

Comprehensive Analysis of Metabolic Pathways Through the Combined Use of Multiple Isotopic Tracers

by

Maciek Robert Antoniewicz

Submitted to the Department of Chemical Engineering
on May 19, 2006 in partial fulfillment of the
requirements for the Degree of Doctor of Philosophy
in Chemical Engineering

ABSTRACT

Metabolic Flux Analysis (MFA) has emerged as a tool of great significance for metabolic engineering and the analysis of human metabolic diseases. An important limitation of MFA, as carried out via stable isotope labeling and GC/MS measurements, is the large number of isotopomer equations that need to be solved. This restriction reduces the ability of MFA to fully utilize the power of multiple isotopic tracers in elucidating the physiology of complex biological networks. Here, we present a novel framework for modeling isotopic distributions that significantly reduces the number of system variables without any loss of information. The elementary metabolite units (EMU) framework is based on a highly efficient decomposition algorithm identifies the minimum amount of information needed to simulate isotopic labeling within a reaction network using knowledge of atomic transitions occurring in the network reactions. The developed computational and experimental methodologies were applied to two biological systems of major industrial and medical significance.

First, we describe the analysis of metabolic fluxes in *E. coli* in a fed-batch fermentation for overproduction of 1,3-propanediol (PDO). A dynamic ^{13}C -labeling experiment was performed and nonstationary intracellular fluxes (with confidence intervals) were determined by fitting labeling patterns of 191 cellular amino acids and 8 external fluxes to a detailed network model of *E. coli*. We established for the first time detailed time profiles of in vivo fluxes. Flux results confirmed the genotype of the organism and provided further insight into the physiology of PDO overproduction in *E. coli*.

Second, we describe the analysis of metabolic fluxes in the pathway of gluconeogenesis in cultured primary hepatocytes, i.e. isolated liver cells. We applied multiple ^{13}C and ^2H -labeled tracers and measured isotopomer distributions of glucose fragments. From this overdetermined data set we estimated net and exchange fluxes in the gluconeogenesis pathway. We identified limitations in current methods to estimate gluconeogenesis in vivo, and developed a novel $[\text{U-}^{13}\text{C}, ^2\text{H}_8]\text{glycerol}$ method that allows accurate analysis of gluconeogenesis fluxes independent of the assumption of isotopic steady-state and zonation of tracers. The developed methodologies have wide implications for in vivo studies of glucose metabolism in Type II diabetes, and other metabolic diseases.

Thesis Supervisor: Gregory Stephanopoulos

Title: Professor of Chemical Engineering

TO ROSANNE
AND
TO MY PARENTS

Acknowledgements

This thesis is the result of five years of research and there are many people who both directly and indirectly contributed to it. First, I would like to thank Greg Stephanopoulos for his guidance, support, and inspiration. Joanne Kelleher introduced me to the field of mammalian physiology and our discussions regarding limitations of current methods and the parallels between her world and mine was the inspiration for most of my research. I also had insightful discussions with Dr. McRae regarding algorithms and software, and I am grateful for his advice. I very much enjoyed the collaboration with Dave Kraynie, who turned out to be a master at crashing my software. As a result, Metran is a much better product than it would have been without his feedback. I'm also grateful for my collaboration with Jose Aleman, who performed all of the cultured hepatocyte experiments detailed in this thesis.

I have learned a lot from Sef Heijnen, Walter van Gulik, and Wouter van Winden in the past. Thank you for your mentorship. The Gregstep group members (past and present) have made my stay at MIT enjoyable and scientifically stimulating. I have collaborated closely with Adrian, Hyuntae and Matt. Adrian has been a great friend for many years. I would also like to thank my friends back in Holland -- Bart, Ton, Rob, Michiel, whom I haven't seen as much as I would have liked these last years, but I am still glad that I can count on you guys for a sanity check. I am very grateful to my parents for giving me the inspiration to work hard and never give up, and for always being there for me when I needed them. And thanks also to my brother, Darek, for keeping my car alive. And finally, I cannot imagine having gone through this without my intelligent and beautiful wife Rosanne. Your love, friendship, and honesty give me the strength to be a better person and to follow my dreams. I love you.

Maciek Antoniewicz

May 2006

Table of Contents

Cover page	1
Abstract	3
Acknowledgments	7
Table of Contents	9
List of Figures	17
List of Tables	19
1 Introduction	23
1.1 Metabolic network and flux analysis.....	23
1.2 Metabolite flux balancing.....	24
1.3 Estimating fluxes from stable isotope measurements.....	25
1.4 Previous work.....	27
1.4.1 Isotopomers.....	27
1.4.2 Fractional enrichments.....	29
1.4.3 NMR fine spectra.....	30
1.4.4 Mass isotopomers.....	31
1.4.5 Cumomers.....	31
1.5 Simulating labeling distributions by isotopomer balancing.....	33
1.6 Simulating labeling distributions by cumomer balancing.....	35
1.7 Aim and outline of thesis.....	36

2 Elementary Metabolite Units (EMU): a novel framework for modeling isotopic distributions	39
2.1 Introduction	39
2.1.1 Metabolic flux analysis	39
2.1.2 Limitations of isotopomer modeling method	40
2.1.3 Alternative modeling methods.....	41
2.1.4 A novel framework for modeling isotopic tracer systems	42
2.2 Theory	42
2.2.1 Elementary Metabolite Units (EMU)	42
2.2.2 EMU reactions	43
2.2.3 Decomposing metabolic networks into EMU reactions	46
2.2.4 Setting up EMU balances and simulating labeling distribution.....	53
2.2.5 Calculating first order derivatives of simulated measurements	57
2.2.6 Global stability and computation time of EMU simulations.....	59
2.2.7 Identifying equivalent EMUs of metabolites.....	61
2.2.8 Simulating NMR measurements using EMUs	70
2.3 Practical applications	73
2.3.1 Simple network model	73
2.3.2 Tricarboxylic acid cycle	74
2.3.3 Reducing EMU balances.....	80
2.3.4 Central carbon metabolism of <i>E. coli</i>	82
2.3.5 Gluconeogenesis pathway	86
3 Determination of fluxes and confidence intervals from stable isotope measurements	91
3.1 Introduction	91
3.2 Methods	93
3.2.1 Flux estimation.....	93
3.2.2 Goodness-of-fit analysis	97

3.2.3	Local linearized statistical properties	98
3.2.4	Calculating accurate flux confidence intervals	99
3.2.5	Relative importance of measurements.....	102
3.3	Results	105
3.3.1	Simple example network.....	105
3.3.2	Grid search.....	107
3.3.3	Monte Carlo simulations.....	108
3.3.4	Linearized statistics	111
3.3.5	Comparison of methods for calculating flux confidence intervals	111
3.3.6	Mammalian gluconeogenesis.....	113
3.4	Discussion	121
A	Numerically stable matrix inverse using singular value decomposition	123
B	Algorithm for covariance-weighted flux estimation.....	124
C	Controlling the step size for determination of accurate flux intervals	125
D	Algorithm for accurate determination of confidence intervals of fluxes.....	127
E	Metabolic model of mammalian glucose metabolism.....	129
4	GC/MS analysis of amino acids	131
4.1	Introduction	131
4.1.1	Flux analysis requires accurate data.....	131
4.1.2	Potential sources of error	132
4.1.3	Reported accuracy and precision in literature	132
4.2	Materials and methods	133
4.2.1	Labeled amino acid standards.....	133
4.2.2	Cellular amino acids.....	133
4.2.3	TBDMS derivatization	134
4.2.4	GC/MS Analysis	134
4.2.5	Natural isotope abundances	135

4.3 Results	135
4.3.1 TBDMS derivatization of amino acids	135
4.3.2 Gas chromatography of TBDMS derivatized amino acids	135
4.3.3 Integration of mass chromatograms	139
4.3.4 Concentration dependence of mass isotopomer distributions	140
4.3.5 Validating identity of ion fragments using ¹³ C-standards	145
4.3.6 Validating accuracy of mass isotopomer distributions	147
5 GC/MS analysis of glucose	153
5.1 Introduction	153
5.2 Materials and methods	155
5.2.1 Materials	155
5.2.2 Hepatocyte isolation and cell culture	155
5.2.3 Preparation of experimental samples for glucose derivatization	156
5.2.4 GC/MS analysis	156
5.2.5 Preparation of glucose esters	157
5.2.6 Preparation of aldonitrile esters of glucose	157
5.2.7 Preparation of methyloxime esters of glucose	157
5.2.8 Preparation of di-O-isopropylidene esters of glucose	157
5.2.9 Preparation of permethyl and perethyl derivatives of glucose	158
5.2.10 Data analysis	158
5.3 Results	160
5.3.1 Synthesis and evaluation of glucose derivates	160
5.3.2 Determining deuterium labeling of glucose standards	166
5.3.3 Study of gluconeogenesis	172
5.4 Discussion	177

6	Nonstationary metabolic flux analysis of <i>E. coli</i>	179
6.1	Introduction	179
6.2	Materials and methods	181
6.2.1	Stable isotope tracers	181
6.2.2	Medium	181
6.2.3	Strain and growth conditions	181
6.2.4	Off-gas analysis	183
6.2.5	Sampling and sample processing	183
6.2.6	Biomass concentration	183
6.2.7	HPLC analysis	183
6.2.8	GC/MS analysis	184
6.2.9	GC/MS analysis of cellular amino acids	184
6.2.10	GC/MS analysis of glucose	187
6.2.11	Calculating external fluxes	188
6.2.12	Metabolic network model	188
6.2.13	Flux determination and statistical analysis	189
6.3	Results	189
6.3.1	External fluxes	189
6.3.2	Characterization of glucose feed	192
6.3.3	Dynamics of glucose labeling	192
6.3.4	Dynamics of fed-batch fermentation	195
6.3.5	Nonstationary model for fed-batch fermentation	197
6.3.6	Metabolic flux analysis	199
6.3.7	Evaluation of estimated D and G parameters	209
6.4	Discussion	212
A	Metabolic network model of <i>E. coli</i>	213
B	Validation of carbon balance and degree of reduction balance	217
C	Fermentation data	218
D	Off-gas analysis data	219
E	Calculated external fluxes	220

7 Quantification of net and reversible hepatic fluxes through the combined use of ¹³C and ²H-tracers	221
7.1 Introduction	221
7.2 Methods	222
7.2.1 Metabolic network model	222
7.2.2 Estimating gluconeogenesis fluxes using MIDA	227
7.2.3 Simulating isotopomer distributions for ¹³ C and ² H tracer experiments	228
7.2.4 Analysis of a single tracer experiment	229
7.2.5 Simultaneous analysis of multiple tracer experiments	230
7.2.6 Statistical analysis	232
7.2.7 Materials	232
7.2.8 Hepatocyte isolation and cell culture	233
7.2.9 Derivatization of glucose	233
7.2.10 GC/MS analysis	234
7.2.11 Measurement of metabolite concentrations	235
7.3 Results	235
7.3.1 External fluxes	235
7.3.2 Reproducibility of cell experiments	237
7.3.3 Characterization of glycerol	237
7.3.4 Incorporation of deuterium into lactate and ketone bodies	241
7.3.5 Incorporation of ¹³ C and ² H into glucose	241
7.3.6 Flux estimation and model validation	247
7.3.7 Evaluation of estimated fluxes	252
7.3.8 Comparing estimated fluxes vs. MIDA	252
7.3.9 Sources of NADH	254
7.4 Discussion	255

8 Application of elementary metabolite units and [U-¹³C,²H₈]glycerol to estimate fluxes of gluconeogenesis	259
8.1 Introduction	259
8.2 Methods	261
8.2.1 Metabolic network model.....	261
8.2.2 Simulating isotopomer distributions using elementary metabolite units	261
8.2.3 Computational methods	262
8.2.4 Determining deuterium enrichment of glucose	262
8.2.5 Materials	263
8.2.6 Hepatocyte isolation and hepatocyte suspension experiments.....	263
8.2.7 Derivatization of glucose	264
8.2.8 GC/MS analysis	265
8.3 Results	266
8.3.1 Incorporation of deuterium into glucose from ² H ₂ O.....	266
8.3.2 Incorporation of labeling into glucose from [U- ¹³ C, ² H ₈]glycerol	272
8.3.2 Labeling incorporation into glucose from [U- ¹³ C, ² H ₈]glycerol and ² H ₂ O.....	276
8.3.3 Flux estimation and model validation.....	279
8.3.4 Evaluation of fluxes in the gluconeogenesis pathway.....	279
8.3.5 Estimation of fluxes using extended model	281
8.4 Discussion	285
References	287
Appendix A: GC/MS analysis of TBDMS derivatized amino acids	295
Appendix B: GC/MS analysis of glucose derivatives	363

List of Figures

1-1	A schematic of metabolic flux estimation from tracer experiments.....	26
1-2	Isotopomers of a 3-atom molecule.....	28
1-3	Fractional enrichments are linear functions of isotopomer fractions.....	29
1-4	Mass isotopomer abundances are linear functions of isotopomer fractions.....	31
1-5	Simple metabolic network used as example for generating isotopomer balances.....	34
2-1	Definition of elementary metabolite units (EMU).....	44
2-2	Three types of biochemical reactions and the corresponding EMU reactions.....	45
2-3	Simple metabolic network used to illustrate EMU decomposition.....	47
2-4	Schematic overview of the algorithm for EMU decomposition.....	52
2-5	Independent EMU reaction networks generated for metabolite F.....	54
2-6	A schematic of the algorithm for simulating labeling distributions using EMUs.....	60
2-7	Stereospecific atom transitions for the reaction catalyzed by aconitase.....	62
2-8	Equivalent EMUs of pyruvate.....	64
2-9	Malic enzyme converts malate to pyruvate.....	65
2-10	Differences between molecules with a rotation axis and center of inversion.....	67
2-11	Equivalent EMUs of the rotationally symmetric fumarate.....	69
2-12	Simplified model of the tricarboxylic acid cycle.....	76
2-13	EMU reaction networks generated for glutamate from EMU decomposition.....	78
2-14	EMU balances for the EMU networks of TCA cycle.....	79
2-15	Simplified EMU reaction networks for glutamate.....	81
2-16	Reactions of the gluconeogenesis pathway.....	87
3-1	Simple metabolic network used for computation of confidence intervals.....	106
3-2	Determination of confidence intervals of metabolic fluxes.....	109
3-3	Histogram of estimated fluxes v_2 and v_4 from 10,000 Monte Carlo simulations.....	110

3-4	Metabolic model of mammalian glucose metabolism.....	114
3-5	Confidence intervals of the gluconeogenesis flux from selected studies.....	119
4-1	Schematic of TBDMS derivatization of polar side groups	136
4-2	Representative total ion chromatogram from GC/MS analysis of amino acids.....	137
4-3	Comparison of three methods for integration of mass chromatograms	141
4-4	Concentration dependence of mass isotopomer abundances	143
4-5	Electron ionization mass spectra of TBDMS derivatized alanine	146
5-1	Schematic of the two step procedure for generating glucose derivatives.....	161
5-2	Positional information obtained from the selected glucose fragments.....	163
5-3	Electron impact mass spectra of the selected glucose derivatives	164
6-1	A schematic of fed-batch fermentation setup and measurement points	182
6-2	Representative total ion chromatogram of cellular amino acids	185
6-3	Characterization of external fluxes in the fed-batch culture.....	190
6-4	Measured isotopic composition of glucose in the medium as a function of time.....	193
6-5	Time profiles of isotopic enrichment of four intermediate metabolite pools in the pathway from glucose to biomass	196
6-6	Two parameter model for modeling nonstationary tracer experiments	198
6-7	Evaluation of goodness-of-fit for models with and without D and G-parameters ...	201
6-8	Metabolic fluxes of <i>E. coli</i> grown in carbon-limited fed-batch culture	204
6-9	Time profiles of selected intracellular fluxes	206
6-10	Time profiles of estimated and predicted D and G parameters.....	211
7-1	Reactions of the gluconeogenesis network model used for flux calculations	224
7-2	Algorithm for flux determination from analysis of multiple tracer experiments.....	231
7-3	Time profiles of glucose, glycerol, lactate and glutamine in hepatocytes cultures	236
7-4	Mass isotopomer distributions of glycerol in the medium.....	239
7-5	Loss of ^2H from $[\text{}^2\text{H}_5]\text{glycerol}$ in cultured hepatocytes	240
7-6	Deuterium incorporation into lactate and 3-hydroxybutyrate.....	242
8-1	Reactions involved in hydrogen exchange and hydrogen incorporation into glucose in the gluconeogenesis pathway.....	271

List of Tables

2-1	EMU reactions corresponding to the three reactions in Figure 2-2.....	46
2-2	Stoichiometry and atom transformations in the example metabolic network.....	48
2-3	Complete list of EMU reactions generated for metabolite F.....	50
2-4	Complete list of EMUs generated for metabolite F.....	51
2-5	Comparison of three modeling approaches for simulating isotopomer labeling.....	75
2-6	Stoichiometry and atom transformations for the reactions of the TCA cycle.....	77
2-7	Comparison of modeling approaches for simulating mass isotopomer labeling.....	83
2-8	Ion fragments of amino acids simulated using the EMU framework.....	84
2-9	Comparison of modeling approaches to simulate the labeling amino acid fragments in the <i>E. coli</i> network model.....	85
2-10	Metabolites in the gluconeogenesis pathway.....	88
2-11	Complete list of EMUs generated for glucose from EMU decomposition of the gluconeogenesis pathway.....	89
2-12	Comparison of modeling approaches for simulating glucose labeling in the gluconeogenesis pathway.....	90
3-1	Stoichiometry and atom transformations for reactions in the example network.....	107
3-2	Comparison of methods for the calculation of confidence intervals of fluxes.....	112
3-3	Stoichiometry and carbon transformations for the reactions in the network of mammalian glucose metabolism.....	115
3-4	Measured and fitted mass isotopomer abundances.....	117
3-5	Estimated glucose metabolic fluxes and their 95% confidence intervals.....	118
4-1	Gas chromatography retention times and main ion fragments of TBDMS derivatized amino acids.....	138
4-2	Effect of integration method on the accuracy of mass isotopomer distributions.....	142

4-3	Comparison of measured and theoretical mass isotopomer distribution of TBDMS derivatized alanine.....	148
4-4	Overview of accepted amino acid fragments	150
4-5	Overview of rejected amino acid fragments.....	151
5-1	Overview of 18 derivatives of glucose that were synthesized and analyzed by electron impact GC/MS	162
5-2	Evaluation of accuracy of selected glucose fragments.....	165
5-3	Mass isotopomer distributions of selected ion fragments from glucose standards ...	167
5-4	Estimated deuterium enrichments of glucose standards	169
5-5	Mass isotopomer distributions of mixtures of glucose standards.....	170
5-6	Estimated deuterium enrichments of mixtures of glucose standards.....	171
5-7	Mass isotopomer distributions of experimental samples	174
5-8	Estimated deuterium enrichments of experimental samples	175
5-9	Comparison of previously estimated fluxes and fluxes determined from deuterium incorporation	176
6-1	Ion fragment of TBDMS derivatized amino acids used for flux analysis.....	186
6-2	Measured and fitted mass isotopomer abundances.....	202
7-1	Stoichiometry and atom transitions for reactions of gluconeogenesis network.....	225
7-2	Assessment of biological variability in cell culture experiments	238
7-3	Incorporation of labeling from [¹³ C]glycerol, [² H]glycerol and ² H ₂ O into glucose....	243
7-4	Corrected mass isotopomer distributions of glucose fragments	244
7-5	Metabolic fluxes estimated by mass isotopomer distribution analysis (MIDA)	246
7-6	Comparison of information content of experimental data	249
7-7	Estimated 95% confidence intervals of fluxes for the samples taken at 2 hr	251
7-8	Metabolic fluxes in the gluconeogenesis pathway estimated by combined analysis of multiple tracer data	253
7-9	Predicted fractional contribution of glycerol, water, and unlabeled sources to NADH hydrogen atoms	254

8-1	Mass isotopomer distributions of glucose fragments from $^2\text{H}_2\text{O}$ experiments with isolated hepatocytes from fasted mice.....	267
8-2	Mass isotopomer distributions of glucose fragments from $^2\text{H}_2\text{O}$ experiments with isolated hepatocytes from fed mice.....	268
8-3	Deuterium enrichment of glucose from $^2\text{H}_2\text{O}$ experiments with hepatocytes isolated from fasted and fed mice	269
8-4	Mass isotopomer distributions of glucose from $[\text{U-}^{13}\text{C},^2\text{H}_8]\text{glycerol}$ labeling experiments with isolated hepatocytes from fasted mice	273
8-5	Mass isotopomer distributions of glucose from $[\text{U-}^{13}\text{C},^2\text{H}_8]\text{glycerol}$ labeling experiments with isolated hepatocytes from fed mice	274
8-6	Mass isotopomer distributions of glucose from $[\text{U-}^{13}\text{C},^2\text{H}_8]\text{glycerol} + ^2\text{H}_2\text{O}$ labeling experiments with isolated hepatocytes from fasted mice	277
8-7	Mass isotopomer distributions of glucose from $[\text{U-}^{13}\text{C},^2\text{H}_8]\text{glycerol} + ^2\text{H}_2\text{O}$ labeling experiments with isolated hepatocytes from fed mice	278
8-8	Comparison of information content of isotopomer data.....	280
8-9	Metabolic fluxes estimated from labeling experiments.....	282
8-10	Metabolic fluxes estimated using the basic and extended network models	284

Chapter 1

Introduction

1.1 Metabolic network and flux analysis

Metabolic fluxes of pathways provide a key to quantifying physiology in fields ranging from metabolic engineering to the analysis of human metabolic diseases. Understanding the regulation of cellular processes and intervening in these processes affords insight into treating disease and achieving other biotechnological objectives. Living cells are complex biological entities that are regulated at many levels, e.g. transcription, translation, protein modification, etc. A large number of reactions, comprising a well-organized system of enzymatic activities, accomplish the conversion of relatively simple molecules such as glucose into a wide variety of small- and macromolecules. The conversion of each individual reaction may be overseen easily, however, the result of the overall system of reactions is often not trivial. Identification of targets for pathway manipulation and determining the required magnitude of biological changes requires an enhanced, quantitative understanding of cellular metabolism and regulation. Metabolic flux analysis (MFA) has emerged as an important tool to assess the metabolic state of living cells and to evaluate the effects of genetic and environmental manipulations. Fluxes of metabolic pathways are considered fundamental determinants of cell physiology and informative parameters in evaluating cellular mechanisms, regulation and causes of disease. The key to quantifying metabolic fluxes is to analyze biological systems as integrated and interacting networks, rather than a set of individual components.

1.2 Metabolite flux balancing

Tools for estimating metabolic fluxes are fundamentally different from the tools for obtaining static measurements such as metabolite concentration and transcript levels, which provide relatively little insight into the dynamics of cellular metabolism. Initially, metabolic flux analysis relied solely on balancing fluxes around metabolites within an assumed network stoichiometry. Assuming metabolic steady-state, fluxes (v) are constrained by the stoichiometry matrix (S).

$$S \cdot v = 0 \tag{1.1}$$

Stoichiometric constraints can be combined with the flux measurements matrix (R) that contains a row with a unity entry for each measured external flux. The combined stoichiometry and measurement matrices are then used to obtain the generalized solution to the metabolite flux balancing problem by solving a set of linear equations. The solution to this problem is given by the following expression:

$$v = \begin{pmatrix} S \\ R \end{pmatrix}^{\text{pinv}} \cdot \begin{pmatrix} 0 \\ v_m \end{pmatrix} + \text{null} \begin{pmatrix} S \\ R \end{pmatrix} \cdot \beta \tag{1.2}$$

Here, 'pinv' denotes the pseudo inverse, and 'null' is the null space of the combined stoichiometry and measurement matrix. Vector β contains the linear coefficients of the columns that span the null space. In most practical situations, however, stoichiometric constraints and external flux measurements did not provide enough information to estimate all fluxes of interest in complex biological systems with reversible reactions, parallel pathways and internal cycles. This limitation led to the development of isotopic tracer techniques to determine fluxes.

1.3 Estimating fluxes from stable isotope measurements

A more powerful method for flux determination in complex biological systems is based on the use of stable isotopes. Figure 1-1 shows schematically the procedure for quantifying metabolic fluxes from stable isotope experiments. The first two important decisions are the choice of the isotopic tracer and the structure of the metabolic network model (steps 1 and 6). Methods for experiment design are aimed at finding the most informative tracer(s) for a given set of stable isotope measurements using criteria from linearized statistics and sensitivity analysis (Mollney et al., 1999). Metabolic flux studies further require some prior knowledge of the biochemical reactions involved in the pathway of interest. The decision which reactions and metabolites to include in the network model is still mainly driven by the investigators' insight into the physiology and may in some cases be somewhat arbitrary. However, we will illustrate in Chapter 3 that proper statistical analysis of isotopomer data can be instrumental in identifying the most likely network structure. Steps 2-4 are experimental in nature and require good laboratory skills. In labeling experiments, metabolic conversion of isotopically labeled substrates generates molecules with distinct labeling patterns (i.e. isotopomers) that can be detected by mass spectrometry (MS) and nuclear magnetic resonance (NMR) spectroscopy (Szyperski, 1995; Des Rosiers, 2004) (step 4). In general, the NMR technique requires expensive equipment and a fairly large amount of sample, which limits the use of this technique to a few expert groups. On the other hand, GC/MS analysis is a more rapid and sensitive technique that is readily accessible to many research labs. Raw data from both techniques needs to be further processed before it can be used for flux determination. In both cases, data processing consists of the detection of metabolite peaks in NMR and MS spectra and integration of peak intensities (step 5). The isotope measurements provide many additional independent constraints for MFA. Quantitative interpretation of the isotopomer data requires the use of large-scale mathematical models that describe the relationship between metabolic fluxes and isotopomer abundances (step 7). Schmidt developed an elegant method for automatically generating the complete set of isotopomer balances for any given network using a matrix based method (Schmidt et al., 1997), and more recently Wiechert et al. (1999) provided an efficient method for solving these isotopomer models using the cumomer framework.

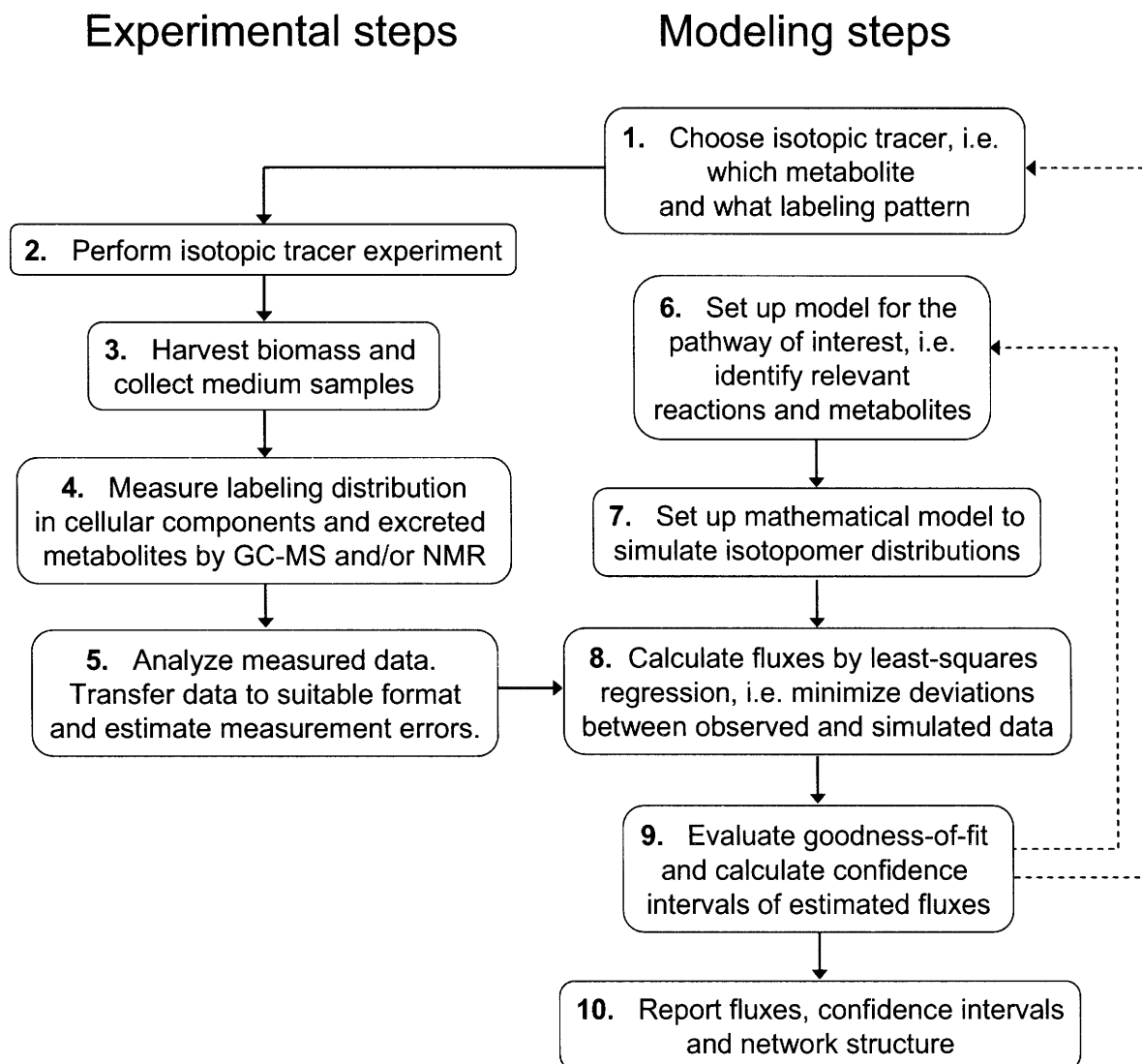


Figure 1-1: A schematic of metabolic flux estimation from tracer experiments. Metabolic flux analysis is characterized by both experimental and analytical steps. The dotted lines indicate that MFA is an iterative process that requires reevaluation of metabolic network assumptions and the choice of optimal tracer.

In the forward calculation, these isotopomer models simulate a unique profile of isotopomer abundances for given steady-state fluxes. In MFA we solve the more challenging inverse problem, i.e. determining the cell's flux state from measurements of isotopomer distributions. Analytical solutions to this inverse problem are only available for very simple systems. Therefore, fluxes in complex biological systems have to be determined by iterative least-squares fitting procedures, where the objective is to evaluate a set of feasible fluxes that best accounts for the observed isotopomer measurements (step 8). At convergence, the goodness-of-fit is evaluated using statistical criteria and confidence intervals of fluxes are determined (step 9). The final result of this whole process is a detailed flux map (with confidence intervals) that describes the contribution of various metabolic reaction pathways to the overall cellular metabolism. The dotted lines in Figure 1-1 illustrate that metabolic flux analysis is an iterative process that requires constant reevaluation of metabolic network assumptions and the choice of optimal tracer.

1.4 Previous work

A range of stable isotopes such as ^{13}C , ^2H , ^{15}N , and ^{18}O can be used to trace metabolic pathways using GC/MS and NMR measurements. Currently, methods based on carbon-13 tracing are most widely used. In this section we provide a short review of the most important concepts currently used in metabolic tracer analysis, i.e. isotopomers, fractional enrichments, NMR fine spectra, mass isotopomers, and cumomers.

1.4.1 Isotopomers

Positional isotopomers (or simply isotopomers) are isomers of a metabolite that differ only in the labeling state of their individual atoms, for example, ^{13}C vs. ^{12}C in carbon-labeling studies, and ^2H vs. ^1H in hydrogen-labeling studies. For a metabolite comprising N atoms that may be in one of two (labeled or unlabeled) states, 2^N isotopomers are possible. Thus, a molecule consisting of 3 atoms can exist in 8 specific labeling states (see Figure 1-2). We can represent the labeling patterns of isotopomers as sequences of ones and zeros that can be interpreted as binary numbers that provide a unique way of ordering the 2^N isotopomers.

The isotopomer distribution vector (IDV) contains the molar fractions of the 2^N isotopomers. For example, the first element in the IDV contains the molfraction of the isotopomer with labeling pattern 000, i.e. unlabeled molecule. The second element corresponds to labeling pattern 001, i.e. molecule with a single labeled atom at the third position, and so forth. Note that by definition, the sum of all elements of IDV equals one. In practice, isotopomer fractions are not measured directly. Instead, available measurements are expressed as functions of isotopomer fractions. The two most widely used techniques for measuring labeling distribution are nuclear magnetic resonance (NMR) spectroscopy and mass spectrometry (MS), which are discussed next.

Isotopomers

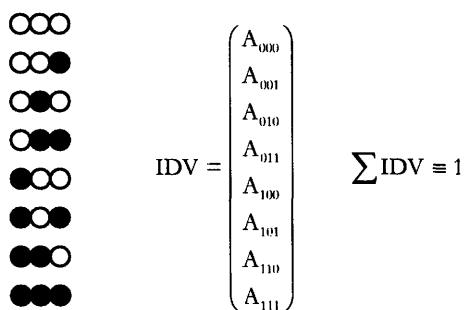


Figure 1-2: Isotopomers of a 3-atom molecule. The 8 ($=2^3$) isotopomers are shown on the left. The spheres represent labeled (full) and unlabeled (open) atoms. The isotopomer distribution vector (IDV) contains the molfractions of all isotopomers. By definition, the sum of all isotopomer fractions equals one.

1.4.2 Fractional enrichments

The NMR technique detects magnetic interaction between ^{13}C -nuclei and adjacent nuclei with magnetic spins, e.g. ^1H and adjacent ^{13}C nuclei. NMR analysis provides two types of labeling information. First, one can determine the fractional abundance of ^{13}C at a specific carbon atom position, which is called the fractional enrichment (FE) measurement.

Determination of fractional enrichments is based on the fact that the ^1H - ^{12}C interaction gives rise to a different peak in the ^1H -NMR spectrum than the ^1H - ^{13}C interaction.

Fractional enrichments of individual carbon atoms can be interpreted as linear functions of isotopomer fractions. For example, consider the fractional enrichment of the first atom of the 3-atom molecule A, i.e. $A_{\#1}$, which is simply the sum of the four isotopomer fractions for which the first atom is labeled (i.e. A_{100} , A_{101} , A_{110} , and A_{111}). Figure 1-3 shows the linear relationship between fractional enrichments and isotopomer fractions. Note that the term fractional enrichment is somewhat misleading, i.e. one doesn't actually measure the enrichment of ^{13}C . The term 'positional abundance of ^{13}C ' would have been more appropriate.

Fractional enrichments

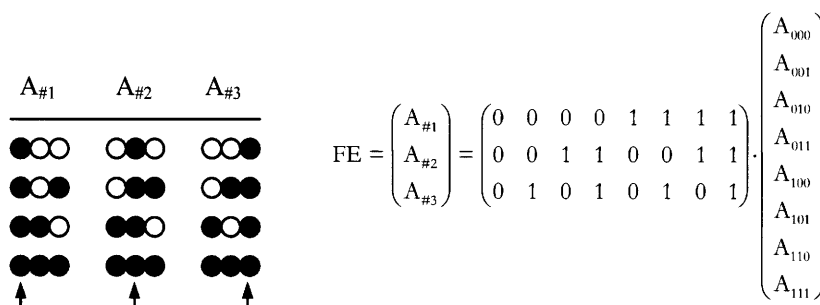


Figure 1-3: Fractional enrichments are linear functions of isotopomer fractions.

1.4.3 NMR fine spectra

Adjacent ^{13}C - ^{13}C nuclei influence each others NMR signal by peak splitting (a phenomenon called J-coupling), which is observed in the ^{13}C -NMR spectrum. Peak splitting leads to the formation of multiple fine structures in the NMR spectrum, e.g. singlets, doublets, triplets, doublets of doublets, etc. The relative contribution of individual multiplets to the resulting overall multiplet pattern provides not only information on the labeling state of individual carbon atoms of a molecule, but also detailed positional information. For example, consider a molecule consisting of 2 carbon atoms. The ^{13}C -multiplet peak areas can be expressed as a nonlinear function of three isotopomer fractions. Eq. 1.3 converts ^{13}C -multiplet peak areas to relative areas, in this case two singlets and a doublet in the ^{13}C -NMR spectrum.

$$\begin{pmatrix} \text{singlet 2} \\ \text{singlet 1} \\ \text{doublet 12} \end{pmatrix} = \begin{pmatrix} A_{01} \\ A_{10} \\ A_{11} \end{pmatrix} \cdot (A_{01} + A_{10} + A_{11})^{-1} \quad (1.3)$$

Eq. 1.4 shows the relationships for a secondary carbon atom, where we also take into account long range ^{13}C - ^{13}C interactions.

$$\begin{pmatrix} \text{singlet 2} \\ \text{doublet 24} \\ \text{doublet 23} \\ \text{double doublet 234} \\ \text{doublet 12} \\ \text{double doublet 124} \\ \text{double doublet 123} \\ \text{quadruple doublet 1234} \end{pmatrix} = \begin{pmatrix} A_{0100} \\ A_{0101} \\ A_{0110} \\ A_{0111} \\ A_{1100} \\ A_{1101} \\ A_{1110} \\ A_{1111} \end{pmatrix} \cdot (A_{0100} + A_{0101} + A_{0110} + A_{0111} + A_{1100} + A_{1101} + A_{1110} + A_{1111})^{-1} \quad (1.4)$$

1.4.4 Mass isotopomers

Mass spectrometry (MS) is an analytical technique where molecules are separated according to their mass to electric charge ratio, i.e. m/z ratio. Isotopomers that have incorporated the same number of labeled atoms, called mass isotopomers, contribute to the intensity of the same ion peak in a mass spectrum. Mass isotopomer distribution reflects the relative amounts of each mass isotopomer (including the unlabeled fraction). Mass isotopomer distribution (MID) can be interpreted as a linear mapping of isotopomer fractions, as is illustrated in Figure 1-4. Note that the sum of the mass isotopomer distribution vector is by definition one.

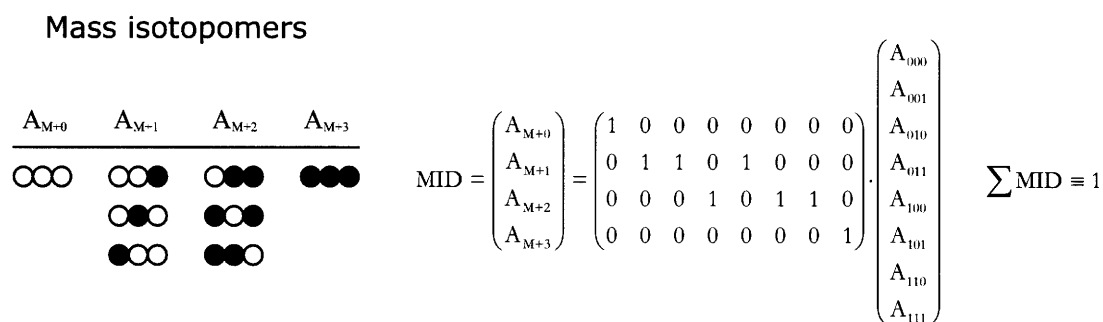


Figure 1-4: Mass isotopomer abundances are linear functions of isotopomer fractions. By definition the sum of all mass isotopomer fractions is one.

1.4.5 Cumomers

Wiechert et. al. (1999) introduced the concept of cumomers, i.e. short for cumulative isotopomers, as a method to simplify isotopomer simulations (see section 1.6). In essence, cumomers are simply a linear mapping of isotopomers. For example, consider a 3-atom molecule A. The so called 0-cumomer fraction is the sum of all isotopomer fractions, and is therefore by definition one.

$$A_{xxx} = \sum_{i,j,k=0}^1 A_{ijk} \equiv 1 \quad (1.4)$$

Here, subscript 'x' has the meaning '0 or 1'. Using the same convention, the 1-cumomer fractions are defined as follows:

$$A_{1xx} = \sum_{j,k=0}^1 A_{1jk} , \quad A_{x1x} = \sum_{i,k=0}^1 A_{i1k} , \quad A_{xx1} = \sum_{i,j=0}^1 A_{ij1} \quad (1.5)$$

Thus, the 1-cumomer fractions are sums of those isotopomer fractions that are labeled at least at the position indicated by the index 1. By this definition, 1-cumomer fractions are identical to fractional enrichments, i.e. $A_{\#1}=A_{1xx}$, $A_{\#2}=A_{x1x}$, and $A_{\#3}=A_{xx1}$. Following the same convention, the 2-cumomer fractions are sums of those isotopomer fractions where at least two of the three atoms are labeled indicated by the index 1:

$$A_{11x} = \sum_{k=0}^1 A_{11k} , \quad A_{1x1} = \sum_{j=0}^1 A_{1j1} , \quad A_{x11} = \sum_{i=0}^1 A_{i11} \quad (1.6)$$

Finally, the 3-cumomer fraction A_{111} corresponds to the fully labeled isotopomer fraction A_{111} .

$$A_{111} \equiv A_{111} \quad (1.7)$$

Wiechert showed that there is always a linear one-to-one relationship between cumomer and isotopomer fractions. For an N atom molecule, the transformation from its 2^N isotopomer fractions to the corresponding 2^N cumomer fractions is given by the transformation matrix T , which is constructed recursively in the following manner.

$$T_0 = 1 , \quad T_i = \begin{bmatrix} T_{i-1} & T_{i-1} \\ 0 & T_{i-1} \end{bmatrix} , \quad \text{for } i=1, \dots, N \quad (1.8)$$

Thus, for a 3-atom molecule the transformation from isotopomer fractions to cumomer fractions is given by Eq. 1.9.

$$\begin{bmatrix} A_{xxx} \\ A_{xxl} \\ A_{xlx} \\ A_{xll} \\ A_{lxx} \\ A_{lxl} \\ A_{llx} \\ A_{lll} \end{bmatrix} = \begin{bmatrix} 1 & 1 & 1 & 1 & 1 & 1 & 1 & 1 \\ 0 & 1 & 0 & 1 & 0 & 1 & 0 & 1 \\ 0 & 0 & 1 & 1 & 0 & 0 & 1 & 1 \\ 0 & 0 & 0 & 1 & 0 & 0 & 0 & 1 \\ \hline 0 & 0 & 0 & 0 & 1 & 1 & 1 & 1 \\ 0 & 0 & 0 & 0 & 0 & 1 & 0 & 1 \\ 0 & 0 & 0 & 0 & 0 & 0 & 1 & 1 \\ 0 & 0 & 0 & 0 & 0 & 0 & 0 & 1 \end{bmatrix} \cdot \begin{bmatrix} A_{000} \\ A_{001} \\ A_{010} \\ A_{011} \\ A_{100} \\ A_{101} \\ A_{110} \\ A_{111} \end{bmatrix} \quad (1.9)$$

The reverse transformation, i.e. from cumomer fractions to isotopomer fractions, is achieved by inverting the transformation matrix. Wiechert showed that the transformation matrix of any size is always full rank, i.e. invertible.

1.5 Simulating labeling distributions by isotopomer balancing

Here, we describe the method that is currently used for simulating labeling distributions in reaction networks. This method was originally based isotopomer balancing, but has been replaced more recently by cumomer balancing. Consider the simple network model shown in Figure 1-5 that consists of 4 metabolites, 3 extracellular fluxes and 3 intracellular reactions. Here, the third reaction is considered reversible and is modeled by separate forward and backward reactions. Metabolite A is the network substrate with known labeling and metabolites C and D are the two products whose labeling pattern we would like to predict for given fluxes. Figure 1-5 (right panel) also shows the assumed atom transitions for the reactions in this network. Similar to metabolite balancing, we can set up material balances for all 12 unknown isotopomers in this system. The complete set of isotopomer balances is shown below.

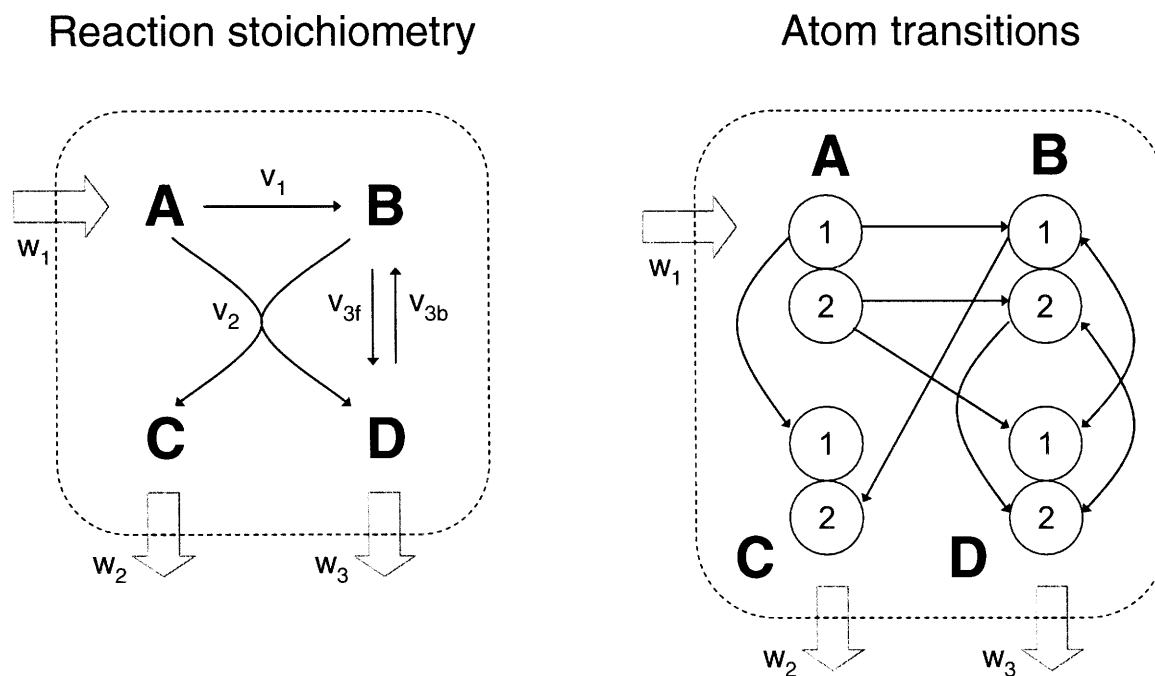


Figure 1-5: Simple metabolic network model used as example for generating isotopomer balances. Reaction stoichiometry is shown in the left panel and the assumed atom transitions are shown in the right panel.

$$0 = v_1 \cdot a_{00} + v_{3b} \cdot d_{00} - (v_{3f} + v_2) \cdot b_{00} \quad (1.10a)$$

$$0 = v_1 \cdot a_{01} + v_{3b} \cdot d_{01} - (v_{3f} + v_2) \cdot b_{01} \quad (1.10b)$$

$$0 = v_1 \cdot a_{10} + v_{3b} \cdot d_{10} - (v_{3f} + v_2) \cdot b_{10} \quad (1.10c)$$

$$0 = v_1 \cdot a_{11} + v_{3b} \cdot d_{11} - (v_{3f} + v_2) \cdot b_{11} \quad (1.10d)$$

$$0 = v_2 \cdot (a_{00} \cdot b_{00} + a_{00} \cdot b_{01} + a_{01} \cdot b_{00} + a_{01} \cdot b_{01}) - w_2 \cdot c_{00} \quad (1.10e)$$

$$0 = v_2 \cdot (a_{00} \cdot b_{10} + a_{00} \cdot b_{11} + a_{01} \cdot b_{10} + a_{01} \cdot b_{11}) - w_2 \cdot c_{01} \quad (1.10f)$$

$$0 = v_2 \cdot (a_{10} \cdot b_{00} + a_{10} \cdot b_{01} + a_{11} \cdot b_{00} + a_{11} \cdot b_{01}) - w_2 \cdot c_{10} \quad (1.10g)$$

$$0 = v_2 \cdot (a_{10} \cdot b_{10} + a_{10} \cdot b_{11} + a_{11} \cdot b_{10} + a_{11} \cdot b_{11}) - w_2 \cdot c_{11} \quad (1.10h)$$

$$0 = v_1 \cdot (a_{00} \cdot b_{00} + a_{00} \cdot b_{10} + a_{10} \cdot b_{00} + a_{10} \cdot b_{10}) + v_{3f} \cdot b_{00} - (v_{3b} + w_3) \cdot d_{00} \quad (1.10i)$$

$$0 = v_1 \cdot (a_{00} \cdot b_{01} + a_{00} \cdot b_{11} + a_{10} \cdot b_{01} + a_{10} \cdot b_{11}) + v_{3f} \cdot b_{01} - (v_{3b} + w_3) \cdot d_{01} \quad (1.10j)$$

$$0 = v_1 \cdot (a_{01} \cdot b_{00} + a_{01} \cdot b_{10} + a_{11} \cdot b_{00} + a_{11} \cdot b_{10}) + v_{3f} \cdot b_{10} - (v_{3b} + w_3) \cdot d_{10} \quad (1.10k)$$

$$0 = v_1 \cdot (a_{01} \cdot b_{01} + a_{01} \cdot b_{11} + a_{11} \cdot b_{01} + a_{11} \cdot b_{11}) + v_{3f} \cdot b_{11} - (v_{3b} + w_3) \cdot d_{11} \quad (1.10l)$$

For given fluxes and labeling input, the isotopomer balances provide 12 nonlinear equations in 12 unknown isotopomer fractions, which can be solved using Newton's iterative method. As the result we obtain the isotopomer fractions for all 12 unknown isotopomers in this system.

1.6 Simulating labeling distributions by cumomer balancing

Wiechert et. al. (1999) recently showed that the complete set of nonlinear isotopomer balances can be converted into a corresponding set of cumomer balances. It was shown that cumomer balances are less strongly coupled than isotopomer balances, which allows cumomer balances to be solved explicitly as a cascade of linear subproblem, from which the 1-, 2-, ... cumomer fractions are successively computed. The cumomer fractions are then transformed to isotopomer fraction as described in section 1.4.5. The major difference between cumomer and isotopomer balances is the fact that cumomer balances are always linear in the unknown variables. Thus, each subproblem can be solved using linear algebra techniques, which significantly reduces computational time. Note, however, that the total

size of the problem is same for both methods, i.e. there are always as many cumomer balances as there are isotopomer balances.

1.7 Aim and outline of thesis

Our research group has actively participated in the development of experimental and computational methods for MFA based on stable isotope experiments. The first general mathematical model for interpreting of fractional enrichments was developed by Zupke and Stephanopoulos (1995). In the last decade MFA has reached a state of relative maturity. The experiments themselves have become a routine procedure, measurement techniques such as GC/MS are widely used, and advanced mathematical procedures are available for quantitative interpretation of stable isotope measurements.

The most important limitation of current methodology for MFA, as carried out via stable isotope labeling and GC-MS measurements, is the large number of isotopomer/cumomer equations that need to be solved, especially when multiple isotopic tracers are used for the labeling of the system. This reduces the ability of MFA to fully utilize the power of multiple isotopic tracers (i.e. ^{13}C and ^2H tracers) in elucidating the physiology of realistic situations comprising complex bioreaction networks. As such, the realm of tracer experiments is currently limited to carbon-13 tracers only. Therefore, the main goal of this thesis work was the development of a novel methodology for comprehensive analysis of metabolic pathways through the combined use of multiple isotopic tracers.

- **Chapter 2** describes the novel framework for modeling isotopic distributions that significantly reduces the number of system variables without any loss of information. The elementary metabolite unit (EMU) framework is based on a highly efficient decomposition algorithm that identifies the minimum amount of information needed to simulate isotopic labeling within a reaction network using the knowledge of atomic transitions occurring in the network reactions. For a typical carbon labeling system the total number of equations that needs to be solved is

reduced by one order-of-magnitude (100s EMUs vs. 1000s cumomers). As such, the EMU framework is most efficient for the analysis of labeling by multiple isotopic tracers. For example, analysis of the gluconeogenesis pathway with ^2H , ^{13}C , and ^{18}O tracers required only 300 EMUs compared to 3,000,000 isotopomers/cumomers.

- **Chapter 3** describes novel methodologies for flux determination and statistical analysis that have been developed. A serious drawback of the flux estimation method in current use is that it does not produce confidence limits for the estimated fluxes. Without this information it is difficult to interpret flux results and expand the physiological significance of flux studies. To address this shortcoming we derived analytical expressions of flux sensitivities with respect to isotope measurements and measurement errors. These tools allow determination of local statistical properties of fluxes and relative importance of measurements. Furthermore, we developed an efficient algorithm to determine accurate nonlinear confidence intervals of fluxes and demonstrated that confidence intervals obtained with this method closely approximate true flux uncertainty.
- **Chapters 4 and 5** describe experimental protocols that were developed for accurate and precise measurement of labeling distributions by GC/MS. In the context of this thesis work, the main focus was on accurate measurement of mass isotopomer distributions of cellular amino acids and glucose. Based on preliminary simulations and sensitivity analysis of realistic metabolic networks we determined that errors in mass isotopomer abundances should be less than 0.5 mol%. The main result of our work is a detailed procedure for the assessment of mass isotopomer distributions of cellular amino acids and glucose with an accuracy of 0.4 mol% and precision of 0.2 mol%, or better.
- **Chapter 6** describes analysis of metabolic fluxes in a nonstationary biological system of with industrial relevance, i.e. microbial fed-batch fermentation of *E. coli* for the overproduction of 1,3-propanediol (PDO). A drawback of current methods for MFA is the requirement of isotopic steady state. To address this shortcoming

and to extend the scope of flux determination from stationary to nonstationary systems we developed a novel modeling strategy that combines key ideas from isotopomer spectral analysis (ISA) and stationary MFA. In this study, metabolic fluxes were determined at multiple time points during a fed-batch culture, and as such we established for the first time detailed time profiles of intracellular fluxes in a fermentation.

- **Chapters 7 and 8** describe analysis of fluxes in the gluconeogenesis pathway from cultured primary hepatocytes, i.e. isolated liver cells. We applied multiple ^{13}C -, and ^2H -labeled tracers and analyzed the resulting mass isotopomer distributions of glucose fragments. From this overdetermined data we estimated, for the first time, both net and exchange fluxes in the gluconeogenesis pathway and calculated confidence intervals for fluxes. We identified limitations in current methods to estimate gluconeogenesis fluxes in vivo, and developed a novel multiple-tracer method for accurate and quantitative analysis of this pathway independent of the isotopic steady-state assumption.

Chapter 2

Elementary Metabolite Units (EMU): a novel framework for modeling isotopic distributions

2.1 Introduction

2.1.1 Metabolic flux analysis

Accurate flux determination is of great importance for the analysis of cell physiology in fields ranging from metabolic engineering to the study of human metabolic diseases (Brunengraber et al., 1997; Hellerstein, 2003; Stephanopoulos, 1999). Initially, metabolic flux analysis (MFA) relied solely on balancing fluxes around metabolites within an assumed network stoichiometry. However, stoichiometric constraints and external flux measurements often cannot provide enough information to estimate all fluxes of interest. A more powerful method for flux determination in complex biological systems is based on the use of stable isotopes (Wiechert et al., 2001). Metabolic conversion of isotopically labeled substrates generates molecules with distinct labeling patterns, i.e. isotope isomers (isotopomers), that can be detected by mass spectrometry (MS) and nuclear magnetic resonance (NMR) (Szyperski et al., 1995). Isotope measurements provide many additional independent constraints for MFA. It has been shown that at metabolic and isotopic steady state the isotopomer composition of metabolic intermediates is fully determined by the cell's flux

state and the administered isotopic label. Quantitative interpretation of isotopomer data requires the use of mathematical models that describes the relationship between metabolic fluxes and the observed isotopomer abundances. Similar to metabolite balancing, balances can be set up around all isotopomers of a particular metabolite. Schmidt described an elegant method for automatically generating the complete set of isotopomer balances using a matrix based method (Schmidt et al., 1997). More recently, Wiechert introduced the concept of cumulative isotopomers (cumomers) and provided an efficient procedure for solving isotopomer models (Wiechert et al., 1999). In the forward calculation, isotopomer models are used to simulate a unique profile of isotopomer abundances for given steady-state fluxes. In MFA we are concerned with the more challenging inverse problem, i.e. to determine the flux state of the cell from measurements of isotopomer distributions. Analytical solutions to the inverse problem are only available for very simple systems. Thus, in general, fluxes in complex biological systems will be determined by iterative least-squares fitting procedures.

2.1.2 Limitations of isotopomer modeling method

Isotopomers are defined as isomers of a metabolite that differ only in the labeling state of their individual atoms, for example, ^{13}C vs. ^{12}C in carbon-labeling studies, and ^2H vs. ^1H in hydrogen-labeling studies. For a metabolite comprising N atoms that may be in one of two (labeled or unlabeled) states, 2^N isotopomers are possible. Consequently, the number of isotopomers can increase quickly when multiple tracers are applied. Consider for example glucose ($\text{C}_6\text{H}_{12}\text{O}_6$). There are only 64 ($=2^6$) carbon atom isotopomers of glucose and 4096 ($=2^{12}$) hydrogen atom isotopomers, but there are 2.6×10^5 ($=2^6 \times 2^{12}$) isotopomers of glucose carbon and hydrogen atoms, and 1.9×10^8 ($=2^6 \times 2^{12} \times 3^6$) isotopomers of glucose carbon, hydrogen and oxygen atoms. Note that oxygen may be present in one of three stable forms, i.e. ^{16}O , ^{17}O , and ^{18}O . Thus, a typical isotopomer model may contain thousands or even millions of isotopomers for multiple isotopic tracers. The number of isotopomers may be reduced somewhat by omitting unstable carboxyl and hydroxyl hydrogen atoms from the model, which exchange with the solvent at rates much faster than biochemical reactions and are also lost in chemical derivatization in preparation for GC/MS analysis. For example, if we consider only the seven stable (i.e. carbon bound) hydrogen atoms of glucose, then there

are 128 ($=2^7$) hydrogen atom isotopomers, 8192 ($=2^6 \times 2^7$) isotopomers of glucose carbon and hydrogen atoms, and 6×10^6 ($=2^6 \times 2^7 \times 3^6$) isotopomers of glucose carbon, hydrogen and oxygen atoms. Thus, even with this reduction there are still too many isotopomers to simulate labeling distributions efficiently for multiple isotopic tracers. Note that the cumomer method suffers from the same problem, because there are always as many cumomers as isotopomers, i.e. there is a one-to-one relationship between cumomers and isotopomers (Chapter 1). As such, the realm of tracer experiments is currently limited solely to ^{13}C -tracers. However, multiple isotopic tracers are more powerful in elucidating the physiology of realistic situations comprising complex bioreaction networks (see Chapters 7 and 8). Therefore, the development of a methodology that extends the capability of MFA beyond the use of a single isotopic tracer is the main goal of this work.

2.1.3 Alternative modeling methods

The isotopomer/cumomer modeling framework is a generic top-down modeling strategy. It provides the most detailed description of the labeling state of a system given by the isotopomer fractions of all metabolites. However, the large number of variables generated in this modeling approach limits its application and has driven the development of alternative modeling methods for specific isotope measurements. For example, it is well known that fractional enrichments of carbon atoms can be simulated efficiently using atom mapping matrices, the method that was originally proposed by Zukpe et al. (1994). More recently, Van Winden et al. (2002) developed the concept of bondomers that allows efficient simulation of NMR fine spectra and MS data without the use of isotopomers. However, the bondomer method is only valid for ^{13}C -labeling data from experiments where a single uniformly ^{13}C -labeled substrate is applied. If multiple carbon sources are present, then all substrates need to be uniformly ^{13}C -labeled with the same enrichment. This requirement significantly limits the applicability of the bondomer method. As such, there is still no general method for simulating mass isotopomer distributions in complex biological systems that avoids the use of isotopomers/cumomers.

2.1.4 A novel framework for modeling isotopic tracer systems

Here, we present a novel framework for modeling isotopic tracer systems that significantly reduces the number of system variables without any loss of information. The elementary metabolite units (EMU) framework is a bottom-up modeling approach that is based on a highly efficient decomposition algorithm that identifies the minimum amount of information needed to simulate isotopic labeling within a reaction network. The functional units generated by the decomposition algorithm, called elementary metabolite units, form the new basis for generating system equations that describe the relationship between fluxes and isotopomer abundances. Isotopomer abundances simulated using the EMU framework are identical to those obtained using the isotopomer and cumomer methods, however, require significantly fewer variables. For a typical carbon labeling system the total number of variables and equations that needs to be solved is reduced by one order-of-magnitude (100s EMUs vs. 1000s isotopomers/cumomers). As such, the EMU framework is most efficient for the analysis of labeling by multiple isotopic tracers. For example, analysis of the gluconeogenesis pathway probed with ^2H and ^{13}C tracers required only 145 EMUs compared to more than 4×10^4 isotopomers/cumomers.

2.2 Theory

2.2.1 Elementary Metabolite Units (EMU)

We define elementary metabolite units as distinct subsets of metabolite's atoms. For example, consider metabolite A consisting of 3 atoms. An EMU is a subset of any number of these 3 atoms. The size of an EMU is defined as the number of atoms that are included in the EMU. There are 7 possible EMUs for metabolite A: 3 EMUs of size 1 (A_1 , A_2 , A_3), 3 EMUs of size 2 (A_{12} , A_{13} , A_{23}), and 1 EMU of size 3 (A_{123}), where the subscript denotes the atoms that are included in the EMU (see Figure 2-1). Note that atoms in an EMU are not necessarily connected by chemical bonds, for example consider EMU A_{13} . In general, for a metabolite comprising N atoms $2^N - 1$ EMUs are possible.

$$\text{Theoretical maximum number of EMUs} = \sum_{i=1}^N \binom{N}{N-i} = 2^N - 1 \quad (2.1)$$

In this Chapter, we will illustrate that the EMU framework can be used for simulation of isotopic labeling within a reaction network using the minimum number of variables, all of which are expressed in terms of EMUs. In most cases, only a small number of all possible EMUs is required to simulate the isotopic labeling. In the next section, we will illustrate the EMU approach for simulating MS measurements, and in section 2.2.8 we will show how NMR measurements can be simulated using EMUs.

2.2.2 EMU reactions

First, we need to introduce the concept of an EMU reaction. Figure 2-2 shows three types of biochemical reactions that we can distinguish: a condensation reaction, a cleavage reaction, and a unimolecular reaction. For each reaction type in Figure 2-2 we would like to determine the minimum amount of information that is needed to determine the mass isotopomer distribution (MID) of product C, i.e. EMU C_{123} . For the condensation reaction, MID of C_{123} is fully determined by the MIDs of EMUs A_{12} and B_1 . For example, the M+0 abundance of C_{123} is equal to the product of M+0 abundances of A_{12} and B_1 , i.e. $C_{123,M+0} = A_{12,M+0} \cdot B_{1,M+0}$. The full MID of C_{123} is obtained from the convolution (or Cauchy product, denoted by '×') of MIDs of A_{12} and B_1 , i.e. $C_{123} = A_{12} \times B_1$. For the cleavage and unimolecular reactions, MID of C_{123} is equal to MID of the EMU A_{123} . Note that for the cleavage reaction atoms of A that are not transferred to C_{123} are not considered in the EMU reaction, i.e. their labeling doesn't affect the labeling state of C. Note also that EMU reactions are always size balanced, i.e. the EMU product is formed either from EMUs of the same size, or by condensation of smaller EMUs such that the total size of substrate EMUs equals the size of the EMU product. Thus, there can only be only two types of EMU reactions: condensation and unimolecular EMU reactions. Table 2-1 shows the EMU reactions corresponding to the biochemical reactions in Figure 2-2.







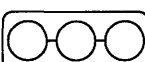
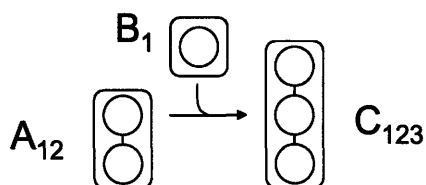
Elementary metabolite unit	Atoms included in the EMU	EMU size
A_1		1
A_2		1
A_3		1
A_{12}		2
A_{13}		2
A_{23}		2
A_{123}		3

Figure 2-1: Elementary metabolite units (EMU) are defined as distinct subsets of metabolite's atoms. There are 7 EMUs for a 3-atom metabolite A. The subscript in the first column denotes the atoms that are included in the respective EMU. The EMU size is defined as the number of atoms included in the EMU.

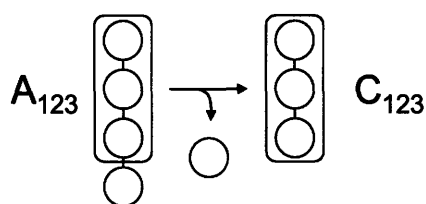
A) Condensation reaction



$$C_{123} = A_{12} \times B_1$$

$$\begin{aligned} C_{123,M+0} &= A_{12,M+0} \cdot B_{1,M+0} \\ C_{123,M+1} &= A_{12,M+0} \cdot B_{1,M+1} + A_{12,M+1} \cdot B_{1,M+0} \\ C_{123,M+2} &= A_{12,M+1} \cdot B_{1,M+1} + A_{12,M+2} \cdot B_{1,M+0} \\ C_{123,M+3} &= A_{12,M+2} \cdot B_{1,M+1} \end{aligned}$$

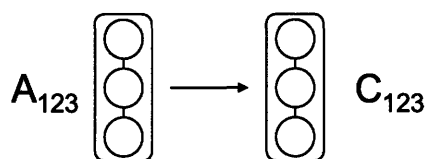
B) Cleavage reaction



$$C_{123} = A_{123}$$

$$\begin{aligned} C_{123,M+0} &= A_{123,M+0} \\ C_{123,M+1} &= A_{123,M+1} \\ C_{123,M+2} &= A_{123,M+2} \\ C_{123,M+3} &= A_{123,M+3} \end{aligned}$$

C) Unimolecular reaction



$$C_{123} = A_{123}$$

$$\begin{aligned} C_{123,M+0} &= A_{123,M+0} \\ C_{123,M+1} &= A_{123,M+1} \\ C_{123,M+2} &= A_{123,M+2} \\ C_{123,M+3} &= A_{123,M+3} \end{aligned}$$

Figure 2-2: Three types of biochemical reactions and the corresponding EMU reactions. Shaded areas indicate atoms included in the EMUs. The mass isotopomer distribution (MID) of product C is fully determined by MID of substrate EMUs. Thus, for the condensation reaction, MID of C_{123} is obtained from the convolution (or Cauchy product, denoted by ‘ \times ’) of MID of A_{12} and B_1 . For the cleavage reaction and unimolecular reaction MID of C_{123} equals MID of A_{123} .

Table 2-1

EMU reactions corresponding to the three reactions shown in Figure 2-2. Note that EMU reactions are always EMU size balanced, i.e. the size of the EMU product always equals the total size of substrate EMUs.

Reaction type	Biochemical reaction	EMU reaction	EMU size balance
Condensation	$A + B \rightarrow C$	$A_{12} + B_1 \rightarrow C_{123}$	$2 + 1 = 3$
Cleavage	$A \rightarrow B + C$	$A_{123} \rightarrow C_{123}$	$3 = 3$
Unimolecular	$A \rightarrow C$	$A_{123} \rightarrow C_{123}$	$3 = 3$

2.2.3 Decomposing metabolic networks into EMU reactions

We will now describe the algorithm that systematically decomposes any biochemical reaction network into EMU reactions using the knowledge of atomic transitions occurring in the network reactions. These EMU reactions will then form the basis for generating model equations for isotopic simulations (see section 2.2.4). Consider the example network shown in Figure 2-3 that will be used to illustrate the theory behind EMU modeling. In this network, metabolite A is the sole substrate and metabolites E and F are two network products. The intermediary metabolites B, C and D are assumed to be at metabolic and isotopic steady state. The stoichiometry and atom transitions for the five reactions are given in Table 2-2, and the assumed flux distribution is shown in Figure 2-3. The structural input that is required for the EMU decomposition is threefold:

1. The assumed metabolic network stoichiometry
2. Atom transitions for all reactions in the network
3. List of metabolites/metabolite fragments that need to be simulated

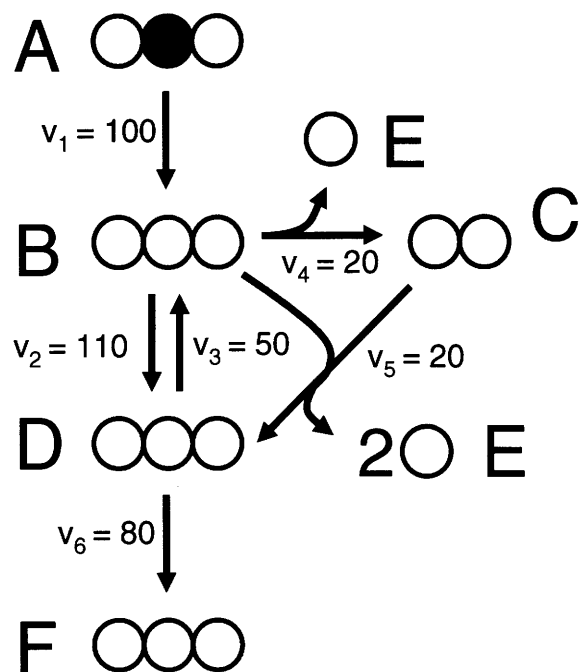


Figure 2-3: Simple metabolic network used to illustrate the decomposition of a metabolic system into EMU reactions. The assumed steady-state fluxes have arbitrary units. The network substrate A is fully labeled on the second atom. Atom transitions for the reactions in this model are given in Table 2-2.

Table 2-2

Stoichiometry and atom transformations for reactions in the example metabolic network. This simple metabolic network is used to illustrate the decomposition of a metabolic system into EMU reactions.

Reaction number	Reaction stoichiometry	Atom transformations*
1	$A \rightarrow B$	$abc \rightarrow abc$
2	$B \leftrightarrow D$	$abc \leftrightarrow abc$
3	$B \rightarrow C + E$	$abc \rightarrow bc + a$
4	$B + C \rightarrow D + E + E$	$abc + AB \rightarrow bcA + a + B$
5	$D \rightarrow F$	$abc \rightarrow abc$

* For each compound atoms are identified using lower case letters to represent successive atoms of each compound. Uppercase letters represent a second compound in the reaction.

In this example, we would like to set up the simplest possible model to simulate the MID of metabolite F, i.e. EMU F_{123} . The following algorithm systematically identifies all EMU reactions that are needed for this simulation model. First, we identify in the network model all EMU reactions that form EMU F_{123} . In this case, F_{123} is formed only in reaction 6 from EMU D_{123} . We record this EMU reaction and the newly identified EMU(s), and repeat this process for all newly identified EMUs starting with the largest size EMU, i.e. D_{123} . Here, D_{123} is formed in two reactions, i.e. in reaction 2 from B_{123} , and in reaction 5 from $B_{23}+C_1$. Next, B_{123} is formed in reactions 1 and 3 from A_{123} and D_{123} , respectively. Note that A_{123} is a network substrate, i.e. it is not produced by any reaction in the network, and D_{123} was already considered in the previous step. Thus, we have identified all EMUs of size 3 that need to be considered. Next, we proceed with EMUs of size 2 that were previously identified, i.e. B_{23} , which is formed in reaction 1 and 3 from A_{23} , and D_{23} , respectively, etc. We complete this process for EMUs of size 2 and 1, until all the EMUs have been traced back to EMUs of network substrate A, or EMUs that were already visited. Table 2-3 shows schematically the complete EMU decomposition for this network. In this case, 18 EMU reactions were identified connecting 14 EMUs. Of these 14 EMUs, 10 EMUs correspond to intermediary metabolites whose labeling is unknown, and 4 EMUs are fully defined by the choice of substrate labeling of metabolite A. The complete list of EMUs for this example is shown in Table 2-4. It should be clear that the described decomposition algorithm is exhaustive, unsupervised, and always identifies the minimal set of EMUs that need to be considered in the simulation model. Furthermore, this algorithm is easy to implement and is computationally efficient, i.e. it converges within seconds even for the largest network model that we have considered. The main advantage of the EMU decomposition is that metabolites are never broken into smaller pieces than is strictly required to describe the labeling state of the selected metabolite(s). In contrast, the isotopomer frameworks always uses all 2^N isotopomers per metabolite to simulate the system. In this case, the complete set of 36 isotopomers describe the system (i.e. 28 unknown isotopomers and 8 substrate isotopomers). Thus, in this example the number of system variables was reduced by more than 50% using the EMU framework. Figure 2-4 shows schematically the complete algorithm for the decomposition of metabolic networks into EMU reaction networks (see sections 2.2.4-2.2.7 for further details).

Table 2-3

Complete list of EMU reactions generated for metabolite F. The complete set of EMU reactions for molecule F was identified using the described decomposition algorithm. The subscripts denote the atoms that are included in the respective EMUs. Note that EMU reactions are always size balanced.

Reaction No.	EMU reaction	EMU reaction size balance
6	$D_{123} \rightarrow F_{123}$	$3 = 3$
2	$B_{123} \rightarrow D_{123}$	$3 = 3$
5	$B_{23} + C_1 \rightarrow D_{123}$	$2 + 1 = 3$
1	$A_{123} \rightarrow B_{123}$	$3 = 3$
3	$D_{123} \rightarrow B_{123}$	$3 = 3$
1	$A_{23} \rightarrow B_{23}$	$2 = 2$
3	$D_{23} \rightarrow B_{23}$	$2 = 2$
2	$B_{23} \rightarrow D_{23}$	$2 = 2$
5	$B_3 + C_1 \rightarrow D_{23}$	$1 + 1 = 2$
4	$B_2 \rightarrow C_1$	$1 = 1$
1	$A_2 \rightarrow B_2$	$1 = 1$
3	$D_2 \rightarrow B_2$	$1 = 1$
2	$B_2 \rightarrow D_2$	$1 = 1$
5	$B_3 \rightarrow D_2$	$1 = 1$
1	$A_3 \rightarrow B_3$	$1 = 1$
3	$D_3 \rightarrow B_3$	$1 = 1$
2	$B_3 \rightarrow D_3$	$1 = 1$
5	$C_1 \rightarrow D_3$	$1 = 1$

Table 2-4

Complete list of EMUs generated for metabolite F from network decomposition. The complete molecule F corresponds to EMU F_{123} . The subscript denotes the atoms that are included in the respective EMUs.

EMU size		
size 1	size 2	size 3
C_1	B_{23}	F_{123}
B_2	D_{23}	D_{123}
D_2	A_{23}	B_{123}
B_3		A_{123}
D_3		
A_2		
A_3		

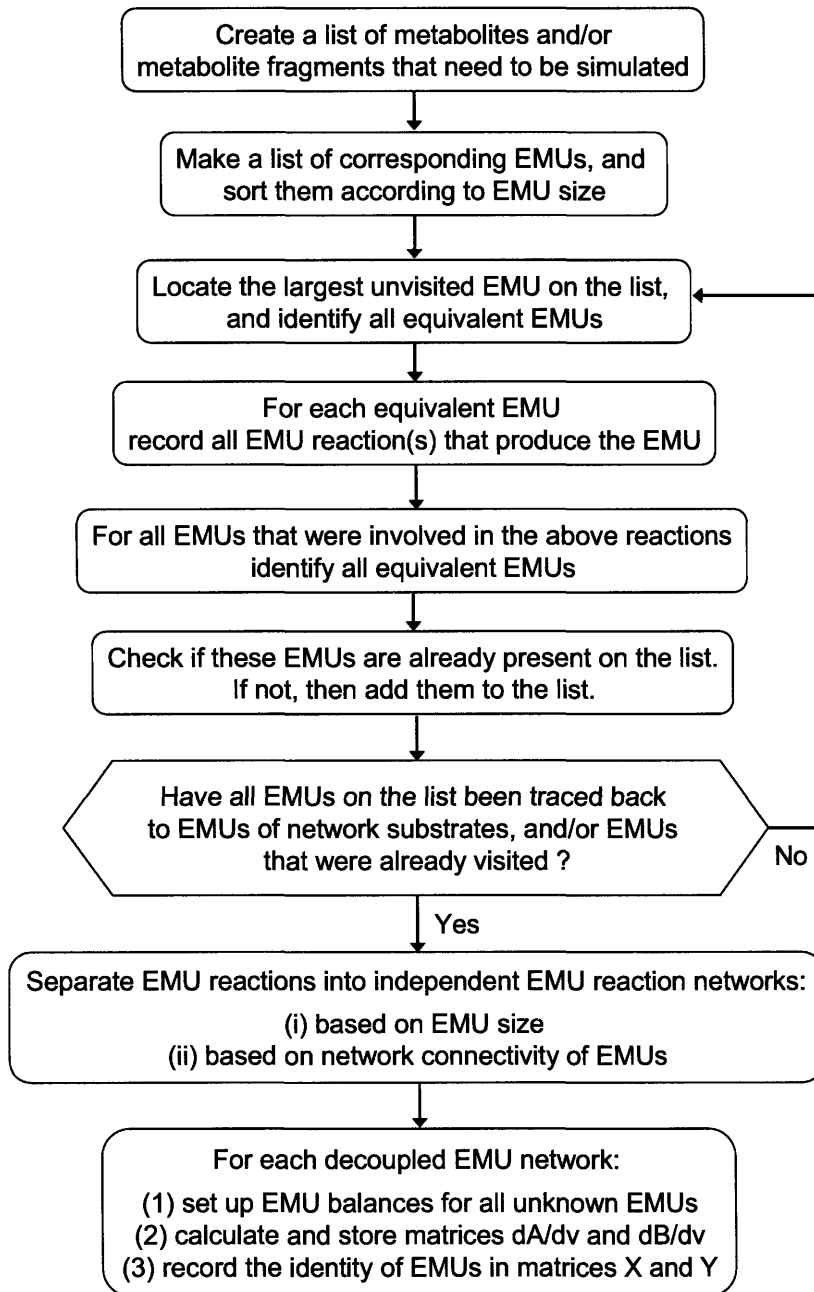


Figure 2-4: Schematic overview of the algorithm for decomposition of metabolic networks into EMU reaction networks. This algorithm systematically identifies the minimal set of EMUs that need to be considered in the simulation model. The algorithm is exhaustive, unsupervised, and efficient (see sections 2.2.4-2.2.7 for further details).

2.2.4 Setting up EMU balances and simulating labeling distribution

The EMU reactions obtained from the decomposition algorithm form the new basis for generating system equations. EMU reactions are much less connected than corresponding isotopomer reactions. Thus, we can group EMU reactions into independent reaction networks based on: (i) the EMU size, and (ii) network connectivity (see section 2.3.4 for an example). For the example network we obtain three independent reaction networks of EMU size 1, 2, and 3, respectively. Figure 2-5 shows the independent EMU reaction networks. Similar to metabolite and isotopomer balancing, we can set up balances around all unknown EMUs.

EMU balances for reaction network of EMU size 1

$$v_4 \cdot C_1 = v_4 \cdot B_2 \quad (2.2a)$$

$$(v_1 + v_3) \cdot B_2 = v_1 \cdot A_2 + v_3 \cdot D_2 \quad (2.2b)$$

$$(v_5 + v_2) \cdot D_2 = v_5 \cdot B_3 + v_2 \cdot B_2 \quad (2.2c)$$

$$(v_1 + v_3) \cdot B_3 = v_1 \cdot A_3 + v_3 \cdot D_3 \quad (2.2d)$$

$$(v_5 + v_2) \cdot D_3 = v_5 \cdot C_1 + v_2 \cdot B_3 \quad (2.2e)$$

EMU balances for reaction network of EMU size 2

$$(v_5 + v_2) \cdot D_{23} = v_5 \cdot (B_3 \times C_1) + v_2 \cdot B_{23} \quad (2.2f)$$

$$(v_1 + v_3) \cdot B_{23} = v_1 \cdot A_{23} + v_3 \cdot D_{23} \quad (2.2g)$$

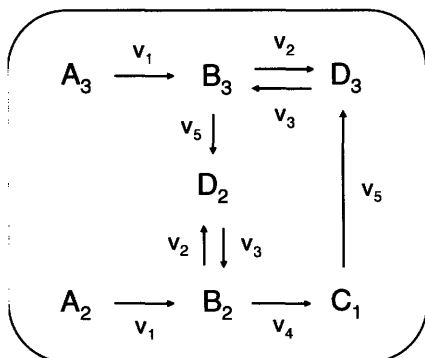
EMU balances for reaction network of EMU size 3

$$v_6 \cdot F_{123} = v_6 \cdot D_{123} \quad (2.2h)$$

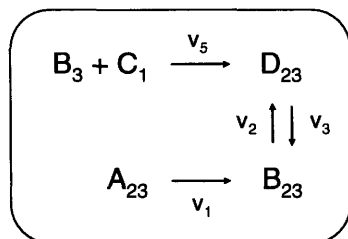
$$(v_5 + v_2) \cdot D_{123} = v_5 \cdot (B_{23} \times C_1) + v_2 \cdot B_{123} \quad (2.2i)$$

$$(v_1 + v_3) \cdot B_{123} = v_1 \cdot A_{123} + v_3 \cdot D_{123} \quad (2.2j)$$

Reaction network for EMU size 1



Reaction network for EMU size 2



Reaction network for EMU size 3

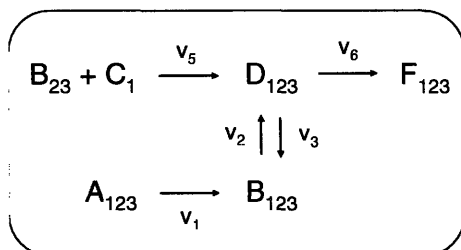


Figure 2-5: Independent EMU reaction networks generated for metabolite F.

In general, EMU balances can be written as a set of linear equations in matrix form:

$$A_{1,k}(v) \cdot X_{1,k} = B_{1,k}(v) \cdot Y_{1,k}(y_1^{in}) \quad (2.3a)$$

$$A_{2,k}(v) \cdot X_{2,k} = B_{2,k}(v) \cdot Y_{2,k}(y_2^{in}, X_1) \quad (2.3b)$$

$$A_{3,k}(v) \cdot X_{3,k} = B_{3,k}(v) \cdot Y_{3,k}(y_3^{in}, X_2, X_1) \quad (2.3c)$$

Here, the first subscript denotes the EMU size and the second the subnetwork number, i.e. in case there are multiple independent EMU networks of the same EMU size. For now we will omit the second subscript. The EMU balances written in matrix corresponding to the EMU networks in Figure 2-5 are shown below.

$$\begin{bmatrix} -v_4 & v_4 & 0 & 0 & 0 \\ 0 & -v_1 - v_3 & v_3 & 0 & 0 \\ 0 & v_2 & -v_2 - v_5 & v_5 & 0 \\ 0 & 0 & 0 & -v_1 - v_3 & v_3 \\ v_5 & 0 & 0 & v_2 & -v_2 - v_5 \end{bmatrix} \cdot \begin{bmatrix} C_1 \\ B_2 \\ D_2 \\ B_3 \\ D_3 \end{bmatrix} = \begin{bmatrix} 0 & 0 \\ -v_1 & 0 \\ 0 & 0 \\ 0 & -v_1 \\ 0 & 0 \end{bmatrix} \cdot \begin{bmatrix} A_2 \\ A_3 \end{bmatrix} \quad (2.4a)$$

$$\begin{bmatrix} -v_5 - v_2 & v_2 \\ v_3 & -v_1 - v_3 \end{bmatrix} \cdot \begin{bmatrix} D_{23} \\ B_{23} \end{bmatrix} = \begin{bmatrix} -v_5 & 0 \\ 0 & -v_1 \end{bmatrix} \cdot \begin{bmatrix} B_3 \times C_1 \\ A_{23} \end{bmatrix} \quad (2.4b)$$

$$\begin{bmatrix} -v_6 & v_6 & 0 \\ 0 & -v_5 - v_2 & v_2 \\ 0 & v_3 & -v_1 - v_3 \end{bmatrix} \cdot \begin{bmatrix} F_{123} \\ D_{123} \\ B_{123} \end{bmatrix} = \begin{bmatrix} 0 & 0 \\ -v_5 & 0 \\ 0 & -v_1 \end{bmatrix} \cdot \begin{bmatrix} B_{23} \times C_1 \\ A_{123} \end{bmatrix} \quad (2.4c)$$

In Eq. 2.3, matrices Y_i and X_i represent the known and unknown EMUs, respectively, and y_i^{in} are EMUs of the network substrate(s). Each row in matrix Y_i and X_i contains the MID for the corresponding EMU. The product term $B_3 \times C_1$ in Eq. 2.4b represents the convolution (or Cauchy product) of MIDs of B_3 and C_1 (see section 2.2.2). Matrices X_2 and Y_2 written out in full for the example network are shown below.

$$\begin{bmatrix} D_{23} \\ B_{23} \end{bmatrix} = \begin{bmatrix} D_{23,M+0} & D_{23,M+1} & D_{23,M+2} \\ B_{23,M+0} & B_{23,M+1} & B_{23,M+2} \end{bmatrix} \quad (2.5)$$

$$\begin{bmatrix} B_3 \times C_1 \\ A_{23} \end{bmatrix} = \begin{bmatrix} B_{3,M+0} \cdot C_{1,M+0} & (B_{3,M+0} \cdot C_{1,M+1} + B_{3,M+1} \cdot C_{1,M+0}) & B_{3,M+1} \cdot C_{1,M+1} \\ A_{23,M+0} & A_{23,M+1} & A_{23,M+2} \end{bmatrix} \quad (2.6)$$

The size matrix A_i depends on the number of unknown EMUs for the corresponding EMU network, and the size of matrix B_i depends on the number of known input EMUs. Thus, for n unknown and m known EMUs, A_i is an $n \times n$ matrix and B_i is an $n \times m$ matrix. Note that matrices A_i and B_i are always strictly linear functions of fluxes. We can therefore easily compute A_i and B_i for given steady-state fluxes from first derivative matrices dA_i/dv_j and dB_i/dv_j , which are constant for a given network:

$$A_i = \sum_j \left(\frac{dA_i}{dv_j} \right) \cdot v_j \quad (2.7)$$

$$B_i = \sum_j \left(\frac{dB_i}{dv_j} \right) \cdot v_j \quad (2.8)$$

To simulate isotopic labeling distribution in the network, EMU balances are solved sequentially starting with the smallest size EMU network(s). Since matrix Y_1 is always known, i.e. it is fully determined by EMUs of network substrate A , we can easily calculate X_1 using standard matrix algebra techniques:

$$X_1 = A_1^{-1} \cdot B_1 \cdot Y_1 \quad (2.9)$$

For subsequent EMU networks, matrices Y_i may depend on previously determined EMUs of smaller size. Thus, for larger EMU sizes we must first update matrix Y_i and then calculate X_i .

$$X_2 = A_2^{-1} \cdot B_2 \cdot Y_2 \quad (2.10)$$

$$X_3 = A_3^{-1} \cdot B_3 \cdot Y_3 \quad (2.11)$$

After all unknown EMUs have been computed we can simply read out the simulated MIDs for the metabolites of interest from the rows of matrices X_i . For example, MID of F_{123} is found in the first row of matrix X_3 .

2.2.5 Calculating first order derivatives of simulated measurements

Here, we present analytical expressions for calculating first order derivatives of simulated measurements with respect to fluxes. Knowledge of these derivatives is important for calculating the optimal search direction of fluxes in least-squares fitting algorithms (Chapter 3). In general, EMU balances are expressed in the following matrix form:

$$A_i \cdot X_i = B_i \cdot Y_i \quad (2.12)$$

Where, matrices A_i and B_i are strictly linear functions of fluxes and matrices X_i and Y_i are nonlinear functions of fluxes. To determine dX_i/dv (which is a 3D-matrix), we take the first order derivative of Eq. 2.12:

$$\frac{d}{dv}(A_i \cdot X_i) = \frac{d}{dv}(B_i \cdot Y_i) \quad (2.13)$$

After applying the product rule we obtain the following expression:

$$\frac{dA_i}{dv} \cdot X_i + A_i \cdot \frac{dX_i}{dv} = \frac{dB_i}{dv} \cdot Y_i + B_i \cdot \frac{dY_i}{dv} \quad (2.14)$$

Note that matrices dA_i/dv_j and dB_i/dv_j are constant for a given network (because A_i and B_i are strictly linear functions of fluxes). After rearrangement of Eq. 2.14 we obtain the following general expression for dX_i/dv :

$$\frac{dX_i}{dv} = A_i^{-1} \cdot \left(\frac{dB_i}{dv} \cdot Y_i + B_i \cdot \frac{dY_i}{dv} - \frac{dA_i}{dv} \cdot X_i \right) \quad (2.15)$$

The above expression may be simplified for the smallest size EMU network. For EMU-seize 1 all terms in matrix Y_1 are constant, i.e. $dY_1/dv=0$. Thus, the solution to the first EMU problem is given by:

$$X_1 = A_1^{-1} \cdot B_1 \cdot Y_1 \quad (2.16)$$

$$\frac{dX_1}{dv} = A_1^{-1} \cdot \left(\frac{dB_1}{dv} \cdot Y_1 - \frac{dA_1}{dv} \cdot X_1 \right) \quad (2.17)$$

For each next EMU network of larger EMU size, matrices Y_i may depend on previously determined EMUs of smaller size, e.g. for the example network model Y_2 was given by:

$$Y_2 = \begin{bmatrix} B_3 \times C_1 \\ A_{23} \end{bmatrix} \quad (2.18)$$

Where, B_3 and C_1 are EMUs of size 1 that are calculated from EMU-size 1 balances. By applying the product rule, we derive the following expression for the first order derivative of the convolution of B_3 and C_1 :

$$\frac{d}{dv}(B_3 \times C_1) = \frac{dB_3}{dv} \times C_1 + B_3 \times \frac{dC_1}{dv} \quad (2.19)$$

Where, dC_1/dv and dB_3/dv matrices that are obtained from dX_1/dv . Note that the second row of Y_2 contains A_{23} which is a network substrate EMU, i.e. it is considered known and constant ($dA_{23}/dv=0$). Thus, we obtain the following expression for dY_2/dv :

$$\frac{dY_2}{dv} = \begin{bmatrix} \frac{dB_3}{dv} \times C_1 + B_3 \times \frac{dC_1}{dv} \\ 0 \end{bmatrix} \quad (2.20)$$

Where, $(dB_3/dv) \times C_1$ denotes the 2D-convolution of matrix (dB_3/dv) and vector C_1 . First order derivatives for any EMU size can be obtained this way. Figure 2-6 summarizes the general procedure for simulating labeling distributions and calculating first order derivatives of simulated measurements with respect to fluxes, using the EMU framework.

2.2.6 Global stability and computation time of EMU simulations

It should be clear that for non-zero fluxes matrices A_i are diagonally dominant, and using Gerhorgin's eigenvalue theorem we can easily prove that therefore matrices A_i are always invertible. In other words, the EMU approach will always compute a unique and stable solution for the unknown EMUs. The most time consuming computation involved in solving EMU balances and calculating first order derivatives is the inversion of matrices A_i , or rather LU decomposition of A_i . In general, the computational time for LU decomposition increases with the size of the matrix, i.e. the number of unknown EMUs. We found empirically that for sparsely connected EMU networks, such as the ones shown in Figure 2-5, the computation time increased linearly with the number of unknown EMUs, i.e. $O(n)$. For more highly connected networks, for example the EMU networks corresponding to central carbon metabolism of *E. coli* (Chapter 6), the computational time increased as $O(n^2)$. Therefore, it is often worthwhile to reduce the number of EMUs by eliminating EMU nodes that only have a single influx, i.e. lumping linear EMU pathways. This will be illustrated in detail in section 2.3.2.

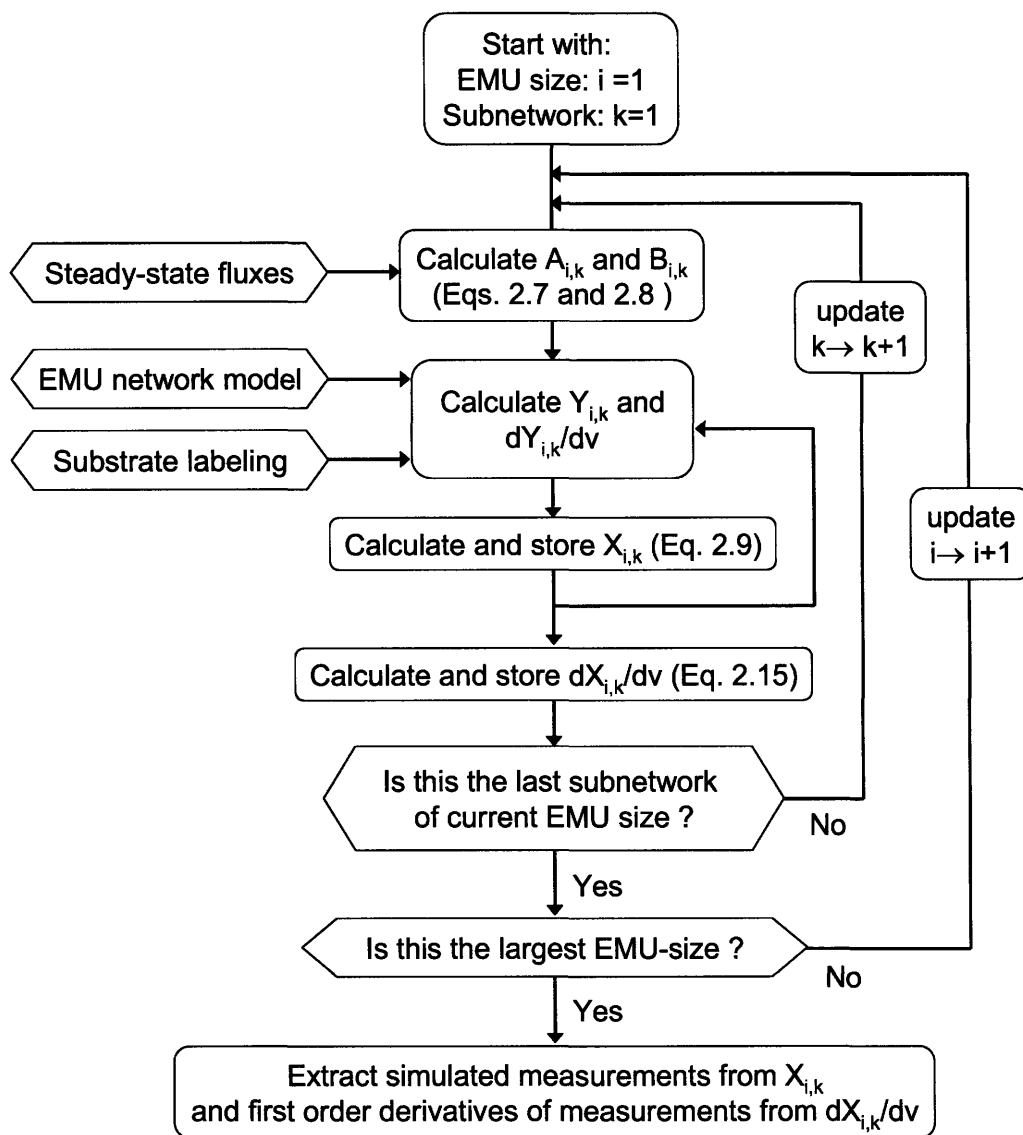


Figure 2-6: A schematic of the algorithm for simulating labeling distributions and calculating sensitivities using EMU balances. EMU balances are solved sequentially starting with the smallest EMU-size networks up to the largest EMU-size network. Simulated measurements and sensitivities are extracted from the matrices X and dX/dv , respectively.

2.2.7 Identifying equivalent EMUs of metabolites

There are a number considerations regarding the chemical structure of metabolites that need to be taken into account to make sure that EMU simulation models are accurate. Here, we will discuss in detail how to account for chiral, prochiral and rotationally symmetric metabolites, and how biochemically equivalent hydrogen and oxygen atoms should be modeled within the EMU framework. These considerations are equally important for the construction of isotopomer models, however, until now they have not received proper attention.

Chiral and prochiral metabolites

Tetrahedral carbon atoms with four different ligands are called chiral, whereas the term prochiral applies to a carbon atoms that hold two stereoheterotopic groups. In other words, prochiral carbon atoms are one step removed from being chiral (Moss, 1996). Many biological metabolites contain one or more chiral and/or prochiral carbon atoms. It is well known that biochemical reactions are highly stereospecific, i.e. enzymes can differentiate between prochiral atoms and prochiral atom groups. Therefore, it is important to keep track of individual prochiral atoms in a network model and assign stereospecific atom transitions to all biochemical reactions. Consider for example the enzymatic reaction catalyzed by aconitase that converts citrate to isocitrate (Figure 2-7). Three of the six carbon atoms of citrate are prochiral, i.e. C2, C3 and C4. The enzyme aconitase stereospecifically transfers the pro-R hydrogen from the pro-R arm (i.e. C1-C2) of citrate to C3 of isocitrate, and produces only one of four possible stereoisomers of isocitrate, i.e. (2R,3S)-isocitrate. Note also that the prochirality of C4 is not altered by aconitase. The absolute stereochemistry for most bioreactions has been worked out in detail and can be found in many biochemistry books, and other general literature.

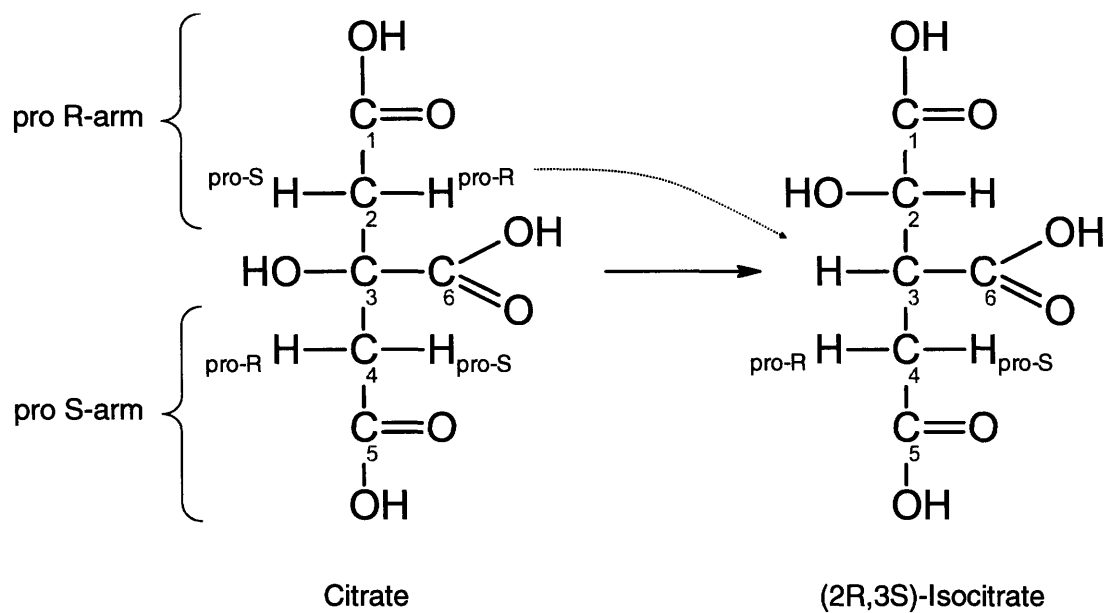


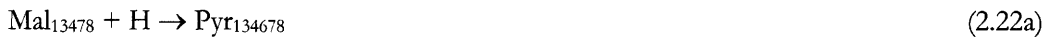
Figure 2-7: Stereospecific atom transitions for the reaction catalyzed by aconitase. Aconitase stereospecifically transfers the pro-R hydrogen from the pro-R arm of citrate to C3 of isocitrate, and produces only one of four possible stereoisomers of isocitrate, i.e. (2R,3S)-isocitrate.

Equivalent hydrogen and oxygen atoms

Biological molecules often contain groups of atoms that are biochemically indistinguishable. Consider for example the chemical structure of pyruvate shown in Figure 2-8. The three hydrogen atoms at C3 are biochemically equivalent, i.e. enzymes cannot distinguish between these atoms. Furthermore, the two oxygen atoms at C1 are biochemically equivalent due to resonance stabilization. Thus, not all of pyruvate's EMUs are independent. For example, there are six equivalent EMUs of pyruvate that contain three carbon atoms, two of the three hydrogen atoms at C3, and one of two oxygen atom at C1. Figure 2-8 shows the six equivalent EMUs. We can predict the number of equivalent EMUs for any EMU as follows:

$$\text{No. of equivalent EMUs} = \prod_{\text{for each group of equivalent atoms}} \left(\frac{(\text{no. of equivalent atoms})!}{(\text{no. of atoms in EMU})! \times (\text{no. of equivalent atoms})!} \right) \quad (2.21)$$

When setting up EMU balances, we need to consider equivalent EMUs. We propose to do that as follows. First, whenever a new EMU is generated during EMU network decomposition, we identify all equivalent EMUs for that EMU. Then, for each equivalent EMU we find the EMU reaction(s) that produce that EMU, and divide the contribution from each reaction by the total number of equivalent EMUs. Note that this way we only introduce one unknown EMU variable for each set of equivalent EMUs. For example, consider the enzymatic reaction catalyzed by malic enzyme that converts malate to pyruvate shown in Figure 2-9 (arbitrary numbering of atoms). The six equivalent EMUs of pyruvate from Figure 2-8 are produced by the following six EMU reactions:



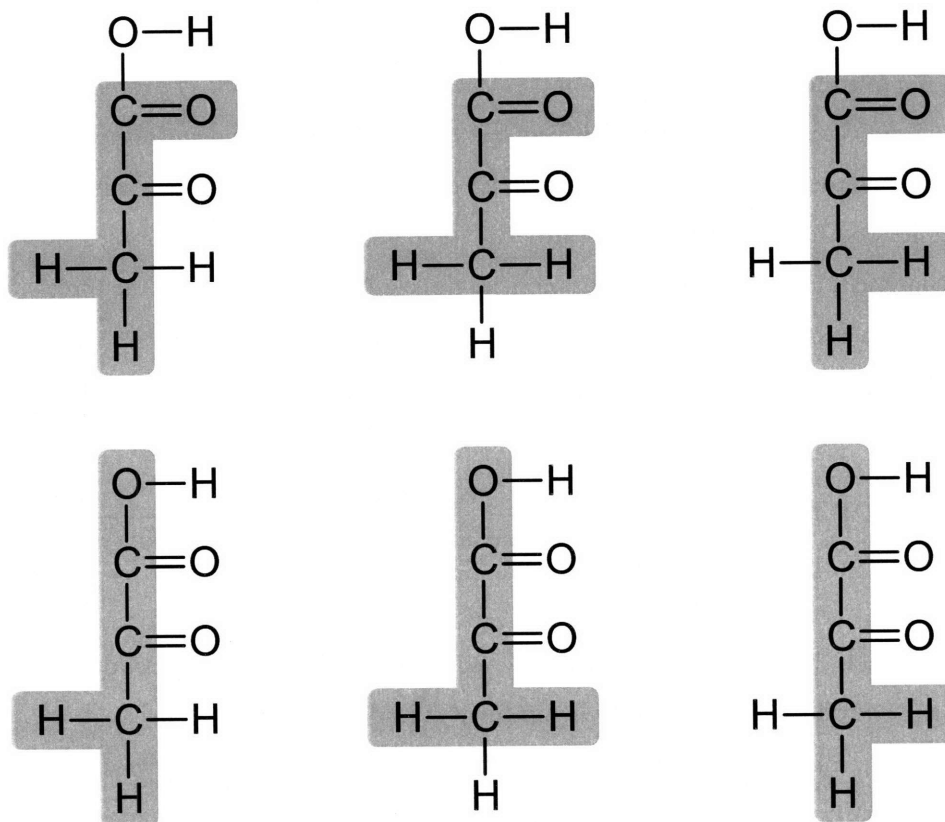


Figure 2-8: Equivalent EMUs of pyruvate. The three hydrogen atoms of pyruvate at C3 are biochemically equivalent. The two oxygen atoms at C1 are also equivalent (due to resonance stabilization). There are six equivalent EMUs of pyruvate containing all three carbon atoms, two of the three hydrogen atoms at C3, and one of two oxygen atom at C1. Shaded areas indicate the atoms that included in the EMUs.

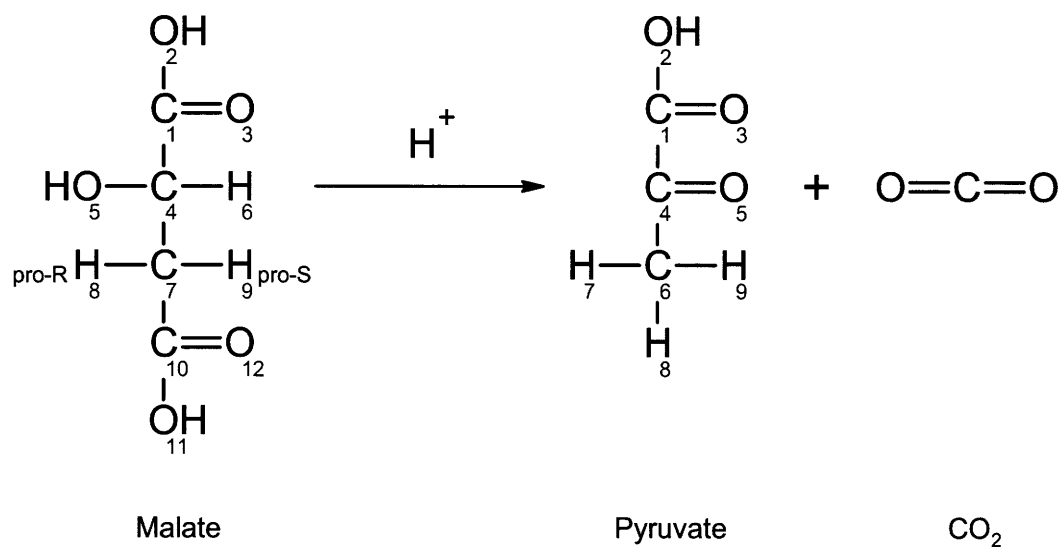
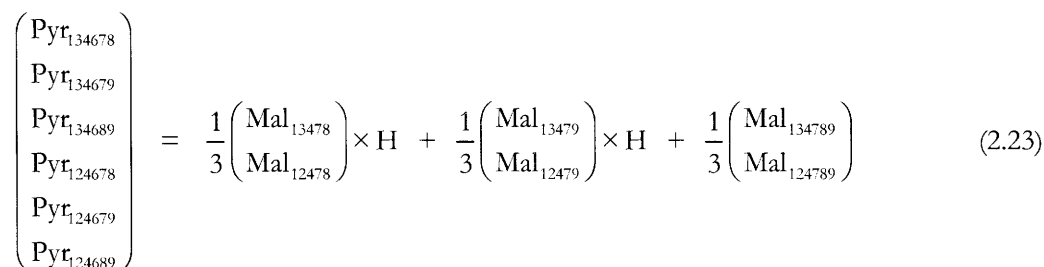


Figure 2-9: Malic enzyme converts malate to pyruvate. Note that one of the three hydrogen atoms at C_{#6} of pyruvate is derived from the solvent. The two prochiral hydrogen atoms of malate at C_{#7} (which are biochemically distinct) become indistinguishable after malate is converted to pyruvate.

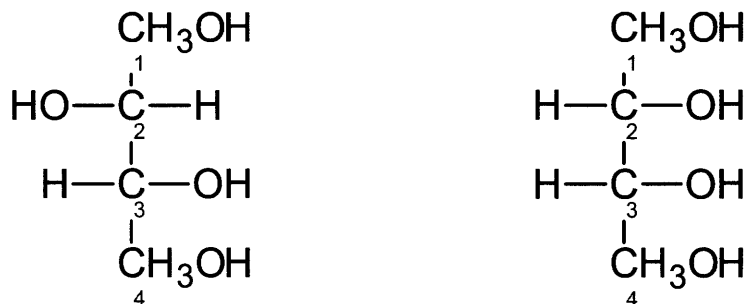
Next, we determine that Mal₁₃₄₇₈ and Mal₁₂₄₇₈; Mal₁₃₄₇₉ and Mal₁₂₄₇₉; and Mal₁₃₄₇₈₉ and Mal₁₂₄₇₈₉ are equivalent EMUs. Taken together, we obtain the following overall EMU reaction:



Note that the two prochiral hydrogen atoms of malate that are initially biochemically distinct become indistinguishable after malate is converted to pyruvate.

Rotationally symmetric metabolites

A number of metabolites of central carbon metabolism are also rotationally symmetric, i.e. they are superposable on themselves by rotation. In isotopic labeling studies these molecules cause scrambling of isotopic labeling. We should note that there is a clear difference between molecules with a center of inversion and molecules with a rotation axis. The two types of symmetry have different characteristics. Only molecules with a rotation axis are superposable on themselves. Figure 2-10 shows the structures of (2S,3R)-butane-1,2,3,4-tetraol (i.e. erythriol) which has a center of inversion, and (2R,3R)-butane-1,2,3,4-tetraol which has a rotation axis. Carbon atoms C1 and C4, and C2 and C3 of erythriol are chemically equivalent (react identically in chemical reactions and have the same chemical properties), however, in enzymatic reactions these atoms are biochemically distinct. In contrast, carbon atoms C1 and C4, and C2 and C3 of (2R,3R)-butane-1,2,3,4-tetraol are both chemically and biochemically equivalent, i.e. they are not distinguished by enzymes.



Name :	(2R,3R)-butane-1,2,3,4-tetraol	(2S,3R)-butane-1,2,3,4-tetraol (i.e. erythritol)
Symmetry :	Rotation axis	Center of inversion
C1 vs. C4 :	Chemically equivalent	Chemically equivalent
C2 vs. C3	Biochemically equivalent	Biochemically different

Figure 2-10: Differences between molecules with a rotation axis and center of inversion.

(2S,3R)-butane-1,2,3,4-tetraol (i.e. erythritol) has a center of inversion; it is not superposable on itself. Therefore, carbon atoms C1 and C4, and C2 and C3 of erythritol are biochemically distinct. (2R,3R)-butane-1,2,3,4-tetraol, on the other hand, has a rotation axis and is superposable on itself. Therefore, carbon atoms C1 and C4, and C2 and C3 are biochemically indistinguishable, which results in scrambling of isotopic labeling.

The most important examples of rotationally symmetric molecules in metabolism are fumarate, succinate, and D-mannitol. Figure 2-11 shows the structure of fumarate (with arbitrary numbering of atoms). It should be clear that fumarate has a rotation axis, i.e. after rotating 180° fumarate superposes on itself. Furthermore, the two oxygen atoms at first carbon and the two oxygen atoms at the last carbon atom of fumarate are biochemically equivalent. These additional characteristics of fumarate need to be considered when we identify equivalent EMUs. The number of equivalent EMUs may increase due to rotational symmetry, i.e. EMUs of rotationally symmetric molecules may have twice as many equivalent EMUs as nonsymmetric molecules:

$$\text{No. of equivalent EMUs} \leq 2 \times \prod_{\text{for each group of equivalent atoms}} \left(\frac{(\text{no. of equivalent atoms})!}{(\text{no. of atoms in EMU})! \times (\text{no. of equivalent atoms})!} \right) \quad (2.24)$$

For example, Figure 2-11 shows the four equivalent EMUs of fumarate Fum_{12467} . However, fumarate EMU F_{1468} has no equivalent EMUs, because its rotational equivalent is F_{1468} itself. Thus, when enumerating equivalent EMUs it is very important that we separate the effect of rotational symmetry, which is a global characteristic of a molecule, from the effect of equivalent hydrogen and oxygen atoms, which are local characteristics of a molecule. To better illustrate this, consider hydrogen atoms #5 and #7 of fumarate. These atoms cannot be treated as equivalent atoms, because that would incorrectly identify Fum_{12465} as being equivalent to Fum_{12467} .

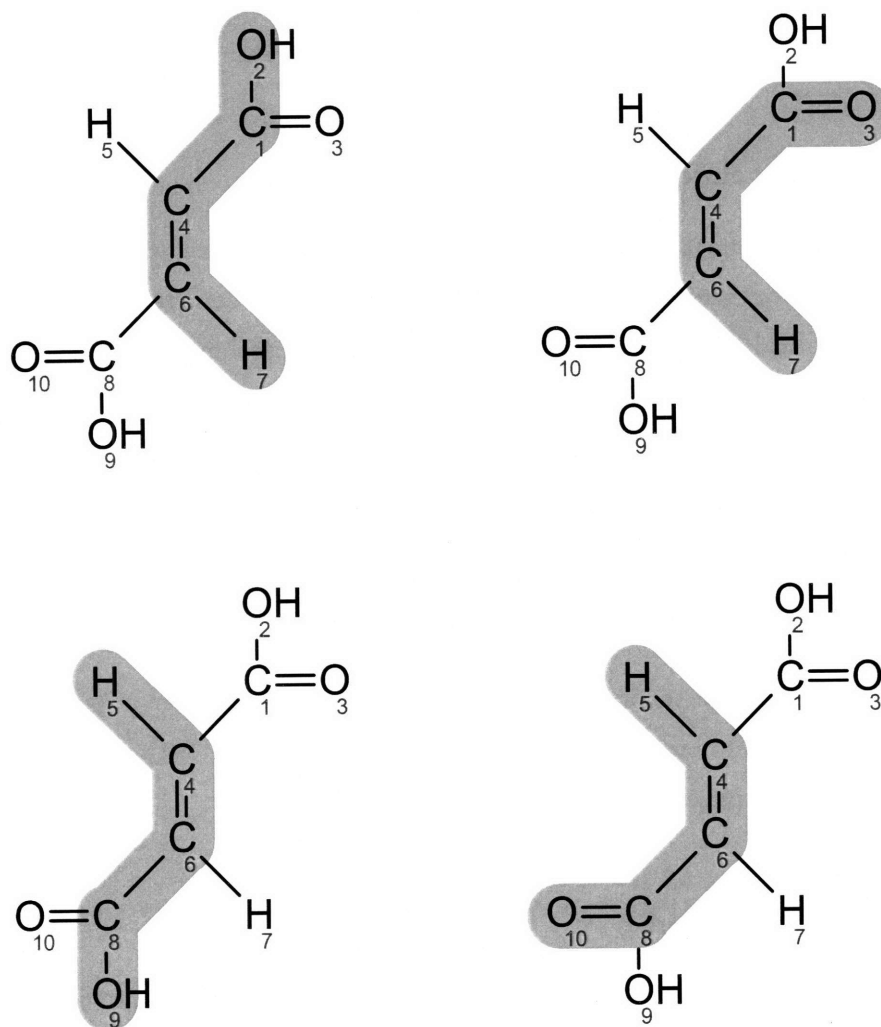


Figure 2-11: Equivalent EMUs of the rotationally symmetric fumarate. Shaded areas indicate atoms included in the EMUs. The following four EMUs are equivalent: Fum₁₂₄₆₇, Fum₁₃₄₆₇, Fum₄₅₆₈₉, and Fum_{4568,10} (numbering of fumarate atoms is arbitrary).

2.2.8 Simulating NMR measurements using EMUs

Thus far, we have shown how MS measurements can be simulated using the EMU approach. We will now illustrate the method for simulating NMR measurements, in particular we will show how fractional enrichment measurements, and NMR fine spectra are simulated.

Simulation of fractional enrichments

Fractional enrichments measure the fractional abundance of ^{13}C -atoms at specific carbon positions in a molecule. For example, Wiechert et al. measured fractional enrichments of 25 carbon atoms of amino acids (Wiechert et al., 1997). Each fractional enrichment measurement provides exactly one flux constraint. In the EMU framework fractional enrichments are modeled by EMUs of size 1 that contain a single carbon atom. In other words, to simulate fractional enrichments we only have to solve EMU balances of size 1. Network decomposition is accomplished with same algorithm as was described before (section 2.2.3). In the EMU balances (Eq. 2.3), however, X_i and Y_i are now vectors (not matrices) that contain values for fractional labeling of carbon atoms. Note that the EMU simulation model for simulating fractional enrichments is very similar to the atom mapping matrix model that was originally proposed by Zupke and Stephanopoulos (1994), and the weight-1 cumomer model as proposed by Wiechert et al. (1999).

Simulation of NMR fine spectra

Data obtained from 2D [$^{13}\text{C},^1\text{H}$] COSY spectra, also known as NMR fine spectra, provide information on the relative amount of ^{13}C - ^{13}C and ^{13}C - ^{12}C carbons at specific carbon positions, where the observed carbon atom is always ^{13}C -labeled and the adjacent carbon atoms are either labeled or unlabeled (Szyperski, 1995). For a secondary carbon atom, NMR fine spectra are expressed as ratios of four isotopomer fractions.

$$\begin{bmatrix} \text{singlet} \\ \text{doublet 3} \\ \text{doublet 1} \\ \text{double doublet} \end{bmatrix} = \begin{bmatrix} A_{010} \\ A_{011} \\ A_{110} \\ A_{111} \end{bmatrix} \cdot (A_{010} + A_{011} + A_{110} + A_{111})^{-1} \quad (2.25)$$

We can obtain these four isotopomer fractions from cumomer fractions A_{x1x} , A_{x11} , A_{11x} , and A_{111} , as was shown previously by van Winden et al. (2002). Alternatively, we have derived that these isotopomer fractions can also be obtained from the following four EMUs A_2 , A_{23} , A_{12} , and A_{123} .

$$\begin{bmatrix} A_{010} \\ A_{110} \\ A_{011} \\ A_{111} \end{bmatrix} = \begin{bmatrix} 1 & 1 & 1 & 1 \\ 0 & 1 & 0 & 1 \\ 0 & 0 & 1 & 1 \\ 0 & 0 & 0 & 1 \end{bmatrix}^{-1} \cdot \begin{bmatrix} A_{x1x} \\ A_{x11} \\ A_{11x} \\ A_{111} \end{bmatrix} = \begin{bmatrix} 1 & 1 & 1 & 1 \\ 0 & 1 & 0 & 1 \\ 0 & 0 & 1 & 1 \\ 0 & 0 & 0 & 1 \end{bmatrix}^{-1} \cdot \begin{bmatrix} A_2 \\ A_{23} \\ A_{12} \\ A_{123} \end{bmatrix} \quad (2.26)$$

In Eq. 2.26, A_{x1x} denotes the weight-1 cumomer fraction for which the second atom is ^{13}C -labeled and the other two atoms are labeled or unlabeled (i.e. $x = 0$ or 1). We can easily show that the cumomer fraction A_{x1x} is equal to the $M+1$ abundance of EMU A_2 . Furthermore, weight-2 cumomer fractions A_{11x} and A_{x11} are equal to the $M+2$ abundances of EMUs A_{23} and A_{12} , respectively (i.e. fully labeled EMUs); and finally, weight-3 cumomer fraction A_{111} is equal to the $M+3$ abundance of EMU A_{123} (i.e. fully labeled EMU). Thus, we can simulate NMR fine spectra either by solving weight-1, 2, and 3 cumomer balances (van Winden et al., 2002), or alternatively by solving EMU balances for the EMUs A_2 , A_{23} , A_{12} , and A_{123} . In this case, in the EMU balances X_i and Y_i are now vectors (not matrices) that contain the fractional abundances of fully labeled EMUs. It should be clear that the number of EMUs generated for the EMUs of size 1, 2, and 3, will always be smaller, or equal to the number of weight-1, 2, and 3 cumomers. Therefore, it is always more efficient to simulate NMR fine spectra using the EMU framework.

The EMU framework can be further extended to include NMR fine spectra for tertiary carbon atoms, and to describe long-range ^{13}C - ^{13}C couplings. In that case, the following eight EMUs of size 1, 2, 3, and 4 are needed: A_2 , A_{12} , A_{23} , A_{24} , A_{123} , A_{234} , A_{124} , and A_{1234} . We can convert the simulated fractional abundances of fully labeled EMUs to isotopomer fractions using Eq. 2.27, and then obtain the NMR signal intensities using Eq. 2.28.

$$\begin{bmatrix} A_{0100} \\ A_{0101} \\ A_{0110} \\ A_{0111} \\ A_{1100} \\ A_{1101} \\ A_{1110} \\ A_{1111} \end{bmatrix} = \begin{bmatrix} 1 & 1 & 1 & 1 & 1 & 1 & 1 & 1 \\ 0 & 1 & 0 & 1 & 0 & 1 & 0 & 1 \\ 0 & 0 & 1 & 1 & 0 & 0 & 1 & 1 \\ 0 & 0 & 0 & 1 & 0 & 0 & 0 & 1 \\ 0 & 0 & 0 & 0 & 1 & 1 & 1 & 1 \\ 0 & 0 & 0 & 0 & 0 & 1 & 0 & 1 \\ 0 & 0 & 0 & 0 & 0 & 0 & 1 & 1 \\ 0 & 0 & 0 & 0 & 0 & 0 & 0 & 1 \end{bmatrix}^{-1} \cdot \begin{bmatrix} A_2 \\ A_{24} \\ A_{23} \\ A_{234} \\ A_{12} \\ A_{124} \\ A_{123} \\ A_{1234} \end{bmatrix} \quad (2.27)$$

$$\begin{bmatrix} \text{singlet} \\ \text{doublet 4} \\ \text{doublet 3} \\ \text{double doublet 34} \\ \text{doublet 1} \\ \text{double doublet 14} \\ \text{double doublet 13} \\ \text{quadruple doublet} \end{bmatrix} = \begin{bmatrix} A_{0100} \\ A_{0101} \\ A_{0110} \\ A_{0111} \\ A_{1100} \\ A_{1101} \\ A_{1110} \\ A_{1111} \end{bmatrix} \cdot (A_{0100} + A_{0101} + A_{0110} + A_{0111} + A_{1100} + A_{1101} + A_{1110} + A_{1111})^{-1} \quad (2.28)$$

Note that in Eqs. 2.27 and 2.28 we assume the observed carbon atom is C2.

2.3 Practical applications

2.3.1 Simple network model

In this example we will compare the EMU framework for simulating mass isotopomer distributions with the isotopomer and cumomer frameworks. Consider the simple network model that was introduced in section 2.2.3 (Figure 2-3). The assumed steady-state fluxes and labeling of substrate A are shown in Figure 2-3. The solution to the EMU balances from Eq. 2.4 are shown below.

Solution of EMU balances for reaction network of EMU size 1

$$\begin{bmatrix} C_1 \\ B_2 \\ D_2 \\ B_3 \\ D_3 \end{bmatrix} = \begin{bmatrix} -20 & 20 & 0 & 0 & 0 \\ 0 & -150 & 50 & 0 & 0 \\ 0 & 110 & -130 & 20 & 0 \\ 0 & 0 & 0 & -150 & 50 \\ 20 & 0 & 0 & 110 & -130 \end{bmatrix}^{-1} \begin{bmatrix} 0 & 0 \\ -100 & 0 \\ 0 & 0 \\ 0 & -100 \\ 0 & 0 \end{bmatrix} \cdot \begin{bmatrix} 0 & 1 \\ 1 & 0 \end{bmatrix} = \begin{bmatrix} 0.0667 & 0.9333 \\ 0.0667 & 0.9333 \\ 0.2000 & 0.8000 \\ 0.9333 & 0.0667 \\ 0.8000 & 0.2000 \end{bmatrix}$$

Solution of EMU balances for reaction network of EMU size 2

$$\begin{bmatrix} D_{23} \\ B_{23} \end{bmatrix} = \begin{bmatrix} -130 & 110 \\ 50 & -150 \end{bmatrix}^{-1} \cdot \begin{bmatrix} -20 & 0 \\ 0 & -100 \end{bmatrix} \cdot \begin{bmatrix} 0.0622 & 0.8756 & 0.0622 \\ 0 & 1 & 0 \end{bmatrix} = \begin{bmatrix} 0.0133 & 0.9733 & 0.0133 \\ 0.0044 & 0.9911 & 0.0044 \end{bmatrix}$$

Solution of EMU balances for reaction network of EMU size 3

$$\begin{bmatrix} F_{123} \\ D_{123} \\ B_{123} \end{bmatrix} = \begin{bmatrix} -80 & 80 & 0 \\ 0 & -130 & 110 \\ 0 & 50 & -150 \end{bmatrix}^{-1} \cdot \begin{bmatrix} 0 & 0 \\ -20 & 0 \\ 0 & -100 \end{bmatrix} \cdot \begin{bmatrix} 0.0003 & 0.0702 & 0.9253 & 0.0041 \\ 0 & 1 & 0 & 0 \end{bmatrix} = \begin{bmatrix} 0.0001 & 0.8008 & 0.1983 & 0.0009 \\ 0.0001 & 0.8008 & 0.1983 & 0.0009 \\ 0.0000 & 0.9336 & 0.0661 & 0.0003 \end{bmatrix}$$

Thus, we find that the simulated MID of F is: 0.0 mol% (M+0), 80.1 mol% (M+1), 19.8 mol% (M+2), and 0.1 mol% (M+3), i.e. the first row in matrix X_3 . These simulated abundances were identical to those obtained using the isotopomer and cumomer methods. The main difference between the methods was the number of equations that needed be solved to simulate the labeling. For the isotopomer method, 28 nonlinear isotopomer balances were solved using Newton's iterative method. For the cumomer method, 4 linear

problems of size 4, 11, 10, and 3, respectively, were solved using standard linear algebra techniques. Note that the total number of cumomers was the same as the number of isotopomers, as expected. Table 2-5 summarizes the main differences between the three modeling methods for this simple example.

2.3.2 Tricarboxylic acid cycle

The second example that we consider is the simplified model of tricarboxylic acid (TCA) cycle shown in Figure 2-12. The stoichiometry and atom transitions for the eight reactions are given in Table 2-6. In this network, acetyl coenzyme A and aspartate are two substrates, and glutamate and carbon dioxide are the products. Here, we simulated the steady-state labeling distribution of glutamate assuming a mixture of 25% [2-¹³C]AcCoA and 25% [1,2-¹³C]AcCoA as the tracer input. The assumed flux distribution is shown in Figure 2-12. In this example, we only consider the labeling of carbon atoms and for simplicity we ignore natural isotope enrichments. The algorithm described in section 2.2.3 decomposed the TCA cycle network into 4 independent EMU reaction networks that are shown in Figure 2-13. The total number of unknown EMUs was 24, i.e. 8 EMUs in the first network (EMU size 1), 5 EMUs in the second (EMU size 2), 8 EMUs in the third (EMU size 3), and 3 EMUs in the fourth network (EMU size 5). The EMU balances for the four decoupled networks are shown in Figure 2-14. The rotational symmetric molecules fumarate and succinate were modeled as described in section 2.2.7. The following groups of EMUs were identified as equivalent: Fum₂ and Fum₃; Suc₂ and Suc₃; Fum₁₂₃ and Fum₂₃₄; Suc₁₂₃ and Suc₂₃₄. The 24 unknown EMUs constituted a significant reduction from the complete set of 176 isotopomers that were required to describe this system (a reduction of 86%). Here, the cumomer model consisted of seven subproblems of size 6, 28, 53, 52, 28, 8, and 1, respectively. As expected, all three modeling methods (i.e. EMU, isotopomer, and cumomer) predicted identical mass isotopomer abundances for glutamate: 34.64 mol% (M+0), 26.95 mol% (M+1), 8.07 mol% (M+2), 2.86 mol% (M+4), and 0.39 mol% (M+5).

Table 2-5

Comparison of three modeling approaches for simulating mass isotopomer labeling. MID of F in the example network (Figure 2-3) was simulated using the EMU, isotopomer, and cumomer methods. The simulated abundances were identical for all methods. The EMU method required only 10 variables to simulate the labeling, as opposed to 28 variables for the isotopomer and cumomer methods (a reduction of 64%).

		isotopomer model	cumomer model	EMU model
Simulated mass isotopomer distribution (MID) of metabolite F (molfractions)	M+0	0.0001	0.0001	0.0001
	M+1	0.8008	0.8008	0.8008
	M+2	0.1983	0.1983	0.1983
	M+3	0.0009	0.0009	0.0009
Type of model equations		nonlinear	linear	linear
Number of variables in each subproblem		28	4, 11, 10, 3	5, 2, 3
Total number of variables		28	28	10

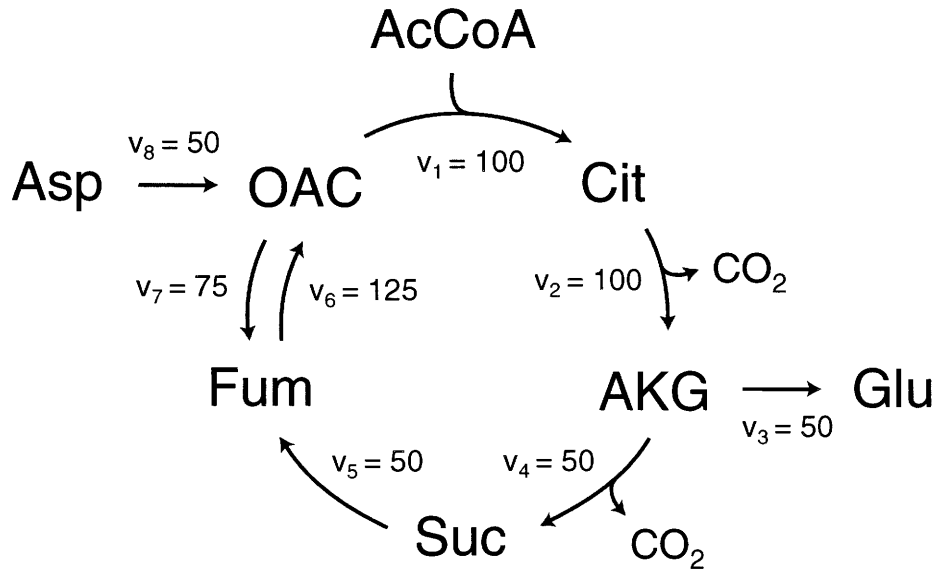


Figure 2-12: Simplified model of the tricarboxylic acid cycle. Abbreviations of metabolites: OAC, oxaloacetate; Asp, aspartate; AcCoA, acetyl coenzyme A; Cit, citrate; AKG, α -ketoglutarate; Glu, glutamate; Suc, succinate. The assumed fluxes have arbitrary units.

Table 2-6

Stoichiometry and atom transformations for the reactions of the TCA cycle. This network model was used simulate the mass isotopomer distribution of glutamine.

Reaction number	Reaction stoichiometry	Atom transformations*
1	OAC + AcCoA → Cit	abcd + AB → dcbBAa
2	Cit → AKG + CO ₂	abcdef → abcde + f
3	AKG → Glu	abcde → abcde
4	AKG → Suc + CO ₂	abcde → bcde + a
5	Suc → Fum	½ abcd + ½ dcba → ½ abcd + ½ dcba
6	Fum → OAC	½ abcd + ½ dcba → abcd
7	OAC → Fum	abcd → ½ abcd + ½ dcba
8	Asp → OAC	abcd → abcd

* For each compound atoms are identified using lower case letters to represent successive atoms of each compound. Uppercase letters represent a second compound in the reaction. Abbreviations of metabolites: OAC, oxaloacetate; Asp, aspartate; AcCoA, acetyl coenzyme A; Cit, citrate; AKG, α -ketoglutarate; Glu, glutamate; Suc, succinate.

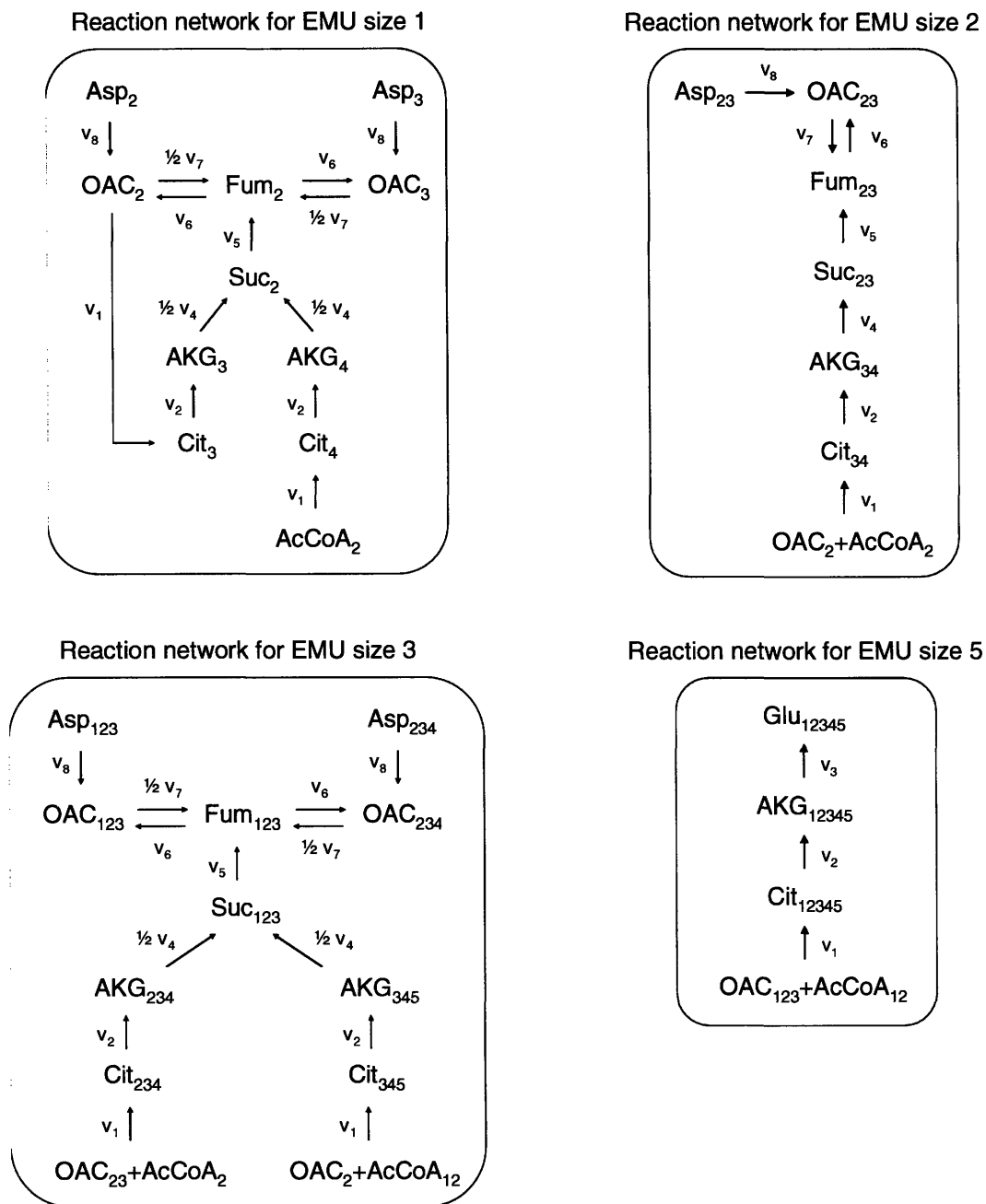


Figure 2-13: EMU reaction networks generated for glutamate from EMU network decomposition. The complete molecule of glutamine corresponds to EMU Glu_{12345} . Subscripts denote carbon atoms that are included in the EMUs. Abbreviations of metabolites are the same as in Figure 2-12.

$$\begin{bmatrix} -v_6 - v_8 & v_6 & \cdot & \cdot & \cdot & \cdot & \cdot & \cdot \\ \frac{1}{2}v_7 & -v_5 - v_7 & \frac{1}{2}v_7 & v_5 & \cdot & \cdot & \cdot & \cdot \\ \cdot & v_6 & -v_6 - v_8 & \cdot & \cdot & \cdot & \cdot & \cdot \\ \cdot & \cdot & \cdot & -v_4 & \frac{1}{2}v_4 & \frac{1}{2}v_4 & \cdot & \cdot \\ \cdot & \cdot & \cdot & \cdot & -v_2 & \cdot & v_2 & \cdot \\ \cdot & \cdot & \cdot & \cdot & \cdot & -v_2 & \cdot & v_2 \\ v_1 & \cdot & \cdot & \cdot & \cdot & \cdot & -v_1 & \cdot \\ \cdot & \cdot & \cdot & \cdot & \cdot & \cdot & \cdot & -v_1 \end{bmatrix} \cdot \begin{bmatrix} \text{OAC}_2 \\ \text{Fum}_2 \\ \text{OAC}_3 \\ \text{Suc}_2 \\ \text{AKG}_3 \\ \text{AKG}_4 \\ \text{Cit}_3 \\ \text{Cit}_4 \end{bmatrix} = \begin{bmatrix} -v_8 & \cdot & \cdot \\ \cdot & \cdot & \cdot \\ \cdot & -v_8 & \cdot \\ \cdot & \cdot & \cdot \\ \cdot & \cdot & \cdot \\ \cdot & \cdot & \cdot \\ \cdot & \cdot & \cdot \\ \cdot & \cdot & -v_1 \end{bmatrix} \cdot \begin{bmatrix} \text{Asp}_2 \\ \text{Asp}_3 \\ \text{AcCoA}_2 \end{bmatrix}$$

$$\begin{bmatrix} -v_8 - v_6 & v_6 & \cdot & \cdot & \cdot \\ v_7 & -v_7 - v_5 & v_5 & \cdot & \cdot \\ \cdot & \cdot & -v_4 & v_4 & \cdot \\ \cdot & \cdot & \cdot & -v_2 & v_2 \\ \cdot & \cdot & \cdot & \cdot & -v_1 \end{bmatrix} \cdot \begin{bmatrix} \text{OAC}_{23} \\ \text{Fum}_{23} \\ \text{Suc}_{23} \\ \text{AKG}_{34} \\ \text{Cit}_{34} \end{bmatrix} = \begin{bmatrix} -v_8 & \cdot \\ \cdot & \cdot \\ \cdot & \cdot \\ \cdot & \cdot \\ \cdot & -v_1 \end{bmatrix} \cdot \begin{bmatrix} \text{Asp}_{23} \\ \text{OAC}_2 \times \text{AcCoA}_2 \end{bmatrix}$$

$$\begin{bmatrix} -v_6 - v_8 & v_6 & \cdot & \cdot & \cdot & \cdot & \cdot & \cdot \\ \frac{1}{2}v_7 & -v_5 - v_7 & \frac{1}{2}v_7 & v_5 & \cdot & \cdot & \cdot & \cdot \\ \cdot & v_6 & -v_6 - v_8 & \cdot & \cdot & \cdot & \cdot & \cdot \\ \cdot & \cdot & \cdot & -v_4 & \frac{1}{2}v_4 & \frac{1}{2}v_4 & \cdot & \cdot \\ \cdot & \cdot & \cdot & \cdot & -v_2 & \cdot & v_2 & \cdot \\ \cdot & \cdot & \cdot & \cdot & \cdot & -v_2 & \cdot & v_2 \\ \cdot & \cdot & \cdot & \cdot & \cdot & \cdot & -v_1 & \cdot \\ \cdot & \cdot & \cdot & \cdot & \cdot & \cdot & \cdot & -v_1 \end{bmatrix} \cdot \begin{bmatrix} \text{OAC}_{123} \\ \text{Fum}_{123} \\ \text{OAC}_{234} \\ \text{Suc}_{123} \\ \text{AKG}_{234} \\ \text{AKG}_{345} \\ \text{Cit}_{234} \\ \text{Cit}_{345} \end{bmatrix} = \begin{bmatrix} -v_8 & \cdot & \cdot & \cdot \\ \cdot & \cdot & \cdot & \cdot \\ \cdot & -v_8 & \cdot & \cdot \\ \cdot & \cdot & \cdot & \cdot \\ \cdot & \cdot & \cdot & \cdot \\ \cdot & \cdot & \cdot & \cdot \\ \cdot & \cdot & -v_1 & \cdot \\ \cdot & \cdot & \cdot & -v_1 \end{bmatrix} \cdot \begin{bmatrix} \text{Asp}_{123} \\ \text{Asp}_{234} \\ \text{OAC}_{23} \times \text{AcCoA}_2 \\ \text{OAC}_2 \times \text{AcCoA}_{12} \end{bmatrix}$$

$$\begin{bmatrix} -v_3 & v_3 & \cdot \\ \cdot & -v_2 & v_2 \\ \cdot & \cdot & -v_1 \end{bmatrix} \cdot \begin{bmatrix} \text{Glu}_{12345} \\ \text{AKG}_{12345} \\ \text{Cit}_{12345} \end{bmatrix} = \begin{bmatrix} \cdot \\ \cdot \\ -v_1 \end{bmatrix} \cdot [\text{OAC}_{123} \times \text{AcCoA}_{12}]$$

Figure 2-14: EMU balances for the EMU networks of the TCA cycle. Subscripts denote carbon atoms that are included in the EMUs. Abbreviations of metabolites are the same as in Figure 2-12. A dot denotes a zero entry.

2.3.3 Reducing EMU balances

In section 2.2.6 we indicated that the computational effort for solving EMU balances depends on the number of unknown EMUs. It is often possible to reduce the number of unknown EMU variables in decomposed EMU networks by eliminating EMU nodes with a single influx. Note that no information is lost in this process. We applied this strategy to simplify the EMU networks for the TCA cycle example from the previous section. The reduced EMU networks are shown in Figure 2-15. In this case, the number of EMUs was reduced from 24 to only 9 unknown EMUs, i.e. 95% reduction compared to the complete set of 176 isotopomers. The corresponding EMU balances are shown below.

$$\begin{bmatrix} -v_8 - v_6 & v_6 & 0 \\ \frac{1}{2}v_7 + \frac{1}{2}v_5 & -v_5 - v_7 & \frac{1}{2}v_7 \\ 0 & v_6 & -v_8 - v_6 \end{bmatrix} \cdot \begin{bmatrix} \text{OAC}_2 \\ \text{Fum}_2 \\ \text{OAC}_3 \end{bmatrix} = \begin{bmatrix} -v_8 & 0 & 0 \\ 0 & 0 & -\frac{1}{2}v_5 \\ 0 & -v_8 & 0 \end{bmatrix} \cdot \begin{bmatrix} \text{Asp}_2 \\ \text{Asp}_3 \\ \text{AcCoA}_2 \end{bmatrix}$$

$$\begin{bmatrix} -v_8 - v_6 & v_6 \\ v_7 & -v_5 - v_7 \end{bmatrix} \cdot \begin{bmatrix} \text{OAC}_{23} \\ \text{Fum}_{23} \end{bmatrix} = \begin{bmatrix} -v_8 & 0 \\ 0 & -v_5 \end{bmatrix} \cdot \begin{bmatrix} \text{Asp}_{23} \\ \text{OAC}_2 \times \text{AcCoA}_2 \end{bmatrix}$$

$$\begin{bmatrix} -v_8 - v_6 & v_6 & 0 \\ \frac{1}{2}v_7 & -v_5 - v_7 & \frac{1}{2}v_7 \\ 0 & v_6 & -v_8 - v_6 \end{bmatrix} \cdot \begin{bmatrix} \text{OAC}_{123} \\ \text{Fum}_{123} \\ \text{OAC}_{234} \end{bmatrix} = \begin{bmatrix} -v_8 & 0 & 0 & 0 \\ 0 & 0 & -\frac{1}{2}v_5 & -\frac{1}{2}v_5 \\ 0 & -v_8 & 0 & 0 \end{bmatrix} \cdot \begin{bmatrix} \text{Asp}_{123} \\ \text{Asp}_{234} \\ \text{OAC}_{23} \times \text{AcCoA}_2 \\ \text{OAC}_3 \times \text{AcCoA}_{12} \end{bmatrix}$$

$$\text{Glu}_{12345} = \text{OAC}_{123} \times \text{AcCoA}_{12}$$

With the reduced EMU model we can simulate the labeling of glutamate in this system for any steady-state fluxes and any substrate labeling by solving four very simple linear problems of size 3, 2, 3, and 1, respectively. The solutions to the EMU balances for the assumed steady-state fluxes and labeling of acetyl-CoA are shown below. As expected, the simulated MID of glutamate was identical to the one obtained with the full EMU model and the isotopomer and cumomer methods. Table 2-7 summarizes the main advantages of the EMU method for the TCA cycle example.

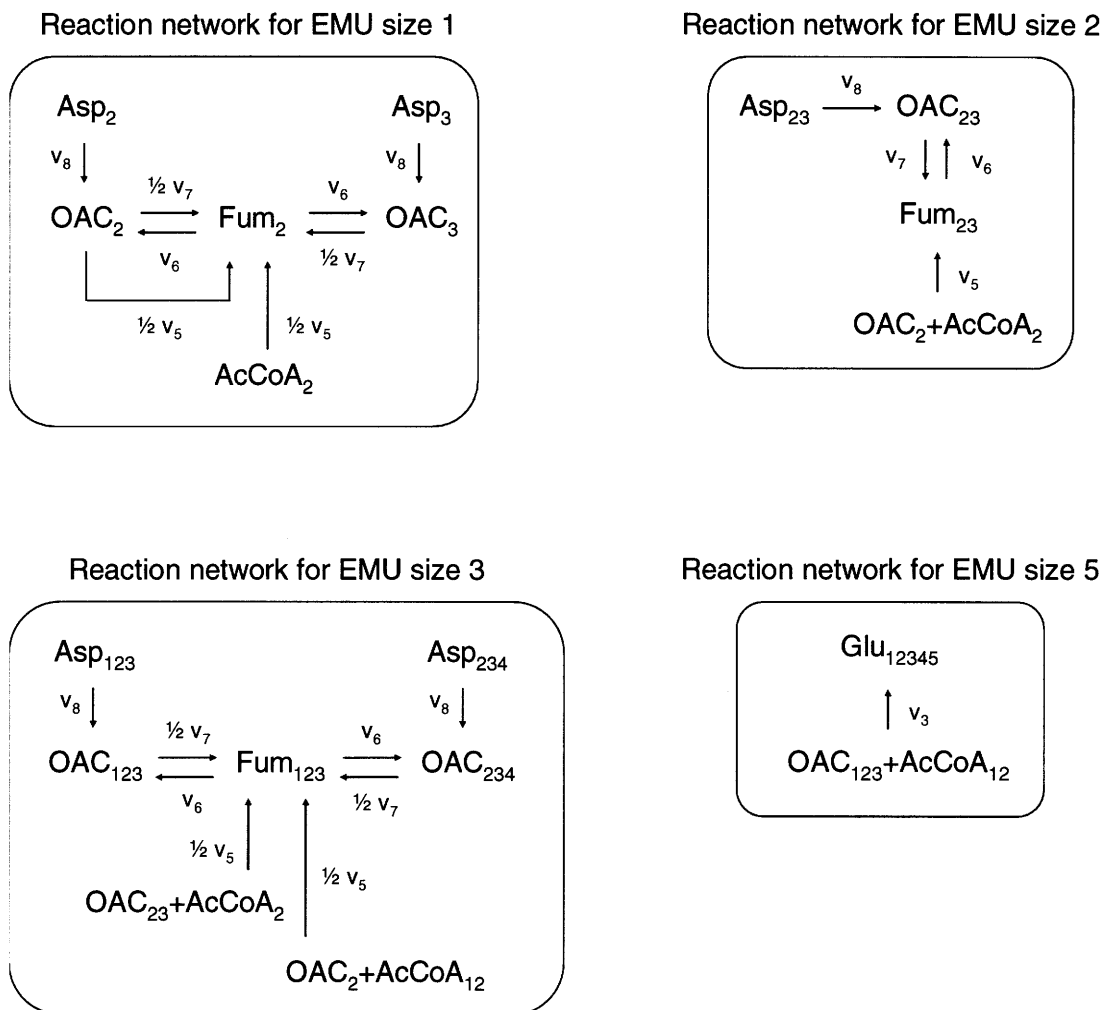


Figure 2-15: Simplified EMU reaction networks for glutamate. EMU networks from Figure 2-13 were simplified by lumping linear EMU nodes, i.e. having only one influx. Abbreviations of metabolites are the same as in Figure 2-12.

Solution of EMU balances for reaction network of EMU size 1

$$\begin{bmatrix} \text{OAC}_2 \\ \text{Fum}_2 \\ \text{OAC}_3 \end{bmatrix} = \begin{bmatrix} -175 & 125 & 0 \\ 62\frac{1}{2} & -125 & 37\frac{1}{2} \\ 0 & 125 & -175 \end{bmatrix}^{-1} \cdot \begin{bmatrix} -50 & 0 & 0 \\ 0 & 0 & -25 \\ 0 & -50 & 0 \end{bmatrix} \cdot \begin{bmatrix} 1 & 0 \\ 1 & 0 \\ 0.5 & 0.5 \end{bmatrix} = \begin{bmatrix} 0.8333 & 0.1667 \\ 0.7667 & 0.2333 \\ 0.8333 & 0.1667 \end{bmatrix}$$

Solution of EMU balances for reaction network of EMU size 2

$$\begin{bmatrix} \text{OAC}_{23} \\ \text{Fum}_{23} \end{bmatrix} = \begin{bmatrix} -175 & 125 \\ 75 & -125 \end{bmatrix}^{-1} \cdot \begin{bmatrix} -50 & 0 \\ 0 & -50 \end{bmatrix} \cdot \begin{bmatrix} 1 & 0 & 0 \\ 0.4167 & 0.5000 & 0.0833 \end{bmatrix} = \begin{bmatrix} 0.7083 & 0.2500 & 0.0417 \\ 0.5917 & 0.3500 & 0.0583 \end{bmatrix}$$

Solution of EMU balances for reaction network of EMU size 3

$$\begin{bmatrix} \text{OAC}_{123} \\ \text{Fum}_{123} \\ \text{OAC}_{234} \end{bmatrix} = \begin{bmatrix} -175 & 125 & 0 \\ 37\frac{1}{2} & -125 & 37\frac{1}{2} \\ 0 & 125 & -175 \end{bmatrix}^{-1} \cdot \begin{bmatrix} -50 & 0 & 0 & 0 \\ 0 & 0 & -25 & -25 \\ 0 & -50 & 0 & 0 \end{bmatrix} \cdot \begin{bmatrix} 1 & 0 & 0 & 0 \\ 1 & 0 & 0 & 0 \\ 0.3542 & 0.4792 & 0.1458 & 0.0208 \\ 0.4167 & 0.2917 & 0.2500 & 0.0417 \end{bmatrix} = \begin{bmatrix} 0.6927 & 0.1927 & 0.0990 & 0.0156 \\ 0.5698 & 0.2698 & 0.1385 & 0.0219 \\ 0.6927 & 0.1927 & 0.0990 & 0.0156 \end{bmatrix}$$

Solution of EMU balance for reaction network of EMU size 5

$$[\text{Glu}_{12345}] = [0.3464 \quad 0.2695 \quad 0.2708 \quad 0.0807 \quad 0.0286 \quad 0.0039]$$

2.3.4 Central carbon metabolism of *E. coli*

In this example we have applied the EMU framework to the realistic metabolic network model of *E. coli* central carbon metabolism. The network is comprised of 73 reactions (with corresponding carbon transitions) utilizing 76 metabolites (5 substrates, 65 balanced intracellular metabolites, and 6 products). The network model included reactions for glycolysis, pentose phosphate pathway, Entner-Doudoroff pathway, TCA cycle, product formation, amphibolic reactions, one-carbon metabolism, and amino acid biosynthesis reactions (see Chapter 6 for details). For this network we simulated the mass isotopomer distributions of 26 amino acid fragments that can be measured experimentally by GC/MS. Table 2-8 provides an overview of the simulated amino acid fragments. To simulate the labeling distribution of the 26 amino acid fragments, the network model was decomposed into 14 independent EMU reaction networks of EMU size 1 to 9. Table 2-9 summarizes the details of the EMU decomposition. The largest EMU subnetwork was the EMU size-1

Table 2-7

Comparison of modeling approaches for simulating mass isotopomer labeling. MID of glutamate in the TCA cycle model (Figure 2-12) was simulated using the EMU, isotopomer, and cumomer methods. The assumed fluxes are shown in Figure 2-12. The assumed labeling of AcCoA was 25% [2-¹³C]AcCoA and 25% [1,2-¹³C]AcCoA. The simulated abundances were identical for all methods. The reduced EMU model required only 9 EMU variables to simulate the labeling of glutamate, as opposed to 176 variables for the isotopomer and cumomer models (a reduction of 95%).

		isotopomer model	cumomer model	EMU full model	EMU reduced model
Simulated mass isotopomer distribution (MID) of glutamate (mol fractions)	M+0	0.3464	0.3464	0.3464	0.3464
	M+1	0.2695	0.2695	0.2695	0.2695
	M+2	0.2708	0.2708	0.2708	0.2708
	M+3	0.0807	0.0807	0.0807	0.0807
	M+4	0.0286	0.0286	0.0286	0.0286
	M+5	0.0039	0.0039	0.0039	0.0039
Type of model equations		nonlinear	linear	linear	linear
Number of variables in each subproblem		176	6, 28, 53, 52, 28, 8, 1	8, 5, 8, 3	3, 2, 3, 1
Total number of variables		176	176	24	9

Table 2-8

Ion fragments of TBDMS derivatized amino acids simulated using the EMU framework.

The identity of amino acid ion fragments was verified previously (Chapter 4).

Amino acid	Monitored intensities	Amino acid carbon atoms	Fragmentation
Ala	232 – 239	2-3	M – C ₅ H ₉ O
	260 – 268	1-2-3	M – C ₄ H ₉
Gly	218 – 224	2	M – C ₅ H ₉ O
	246 – 253	1-2	M – C ₄ H ₉
Val	260 – 269	2-3-4-5	M – C ₅ H ₉ O
	288 – 298	1-2-3-4-5	M – C ₄ H ₉
Leu	274 – 283	2-3-4-5-6	M – C ₅ H ₉ O
Ile	274 – 283	2-3-4-5-6	M – C ₅ H ₉ O
Ser	288 – 296	2-3	M – C ₇ H ₁₅ O ₂ Si
	362 – 370	2-3	M – C ₅ H ₉ O
	390 – 399	1-2-3	M – C ₄ H ₉
Thr	376 – 382	2-3-4	M – C ₅ H ₉ O
	404 – 414	1-2-3-4	M – C ₄ H ₉
Met	292 – 298	2-3-4-5	M – C ₅ H ₉ O
	320 – 327	1-2-3-4-5	M – C ₄ H ₉
Phe	302 – 307	1-2	M – C ₇ H ₇
	308 – 316	2-3-4-5-6-7-8-9	M – C ₅ H ₉ O
	336 – 345	1-2-3-4-5-6-7-8-9	M – C ₄ H ₉
Asp	302 – 309	1-2	M – C ₈ H ₁₇ O ₂ Si
	376 – 382	1-2	M – C ₆ H ₁₁ O
	390 – 397	2-3-4	M – C ₅ H ₉ O
	418 – 428	1-2-3-4	M – C ₄ H ₉
Glu	330 – 336	2-3-4-5	M – C ₇ H ₁₅ O ₂ Si
	404 – 411	2-3-4-5	M – C ₅ H ₉ O
	432 – 443	1-2-3-4-5	M – C ₄ H ₉
Tyr	302 – 307	1-2	M – C ₁₃ H ₂₁ OSi

subnetwork that contained 141 unknown EMUs (i.e. one carbon EMUs). The total number of unknown EMUs was 307, which could be further reduced to 223 unknown EMUs by eliminating EMU nodes with a single influx. In comparison, there were 4,612 isotopomers/cumomers required to simulate the same amino acid fragments, i.e. a reduction of 93-95%. It is interesting to note that there were 241 carbon atoms in this network model, but only 141 EMUs of size 1 were required. Thus, clearly not all individual carbon atoms needed to be simulated in this network. In contrast, the cumomer method required balancing of all 241 weight-1 cumomers. The simulated mass isotopomer distributions from the three methods (i.e. EMU, isotopomer, cumomer) were identical.

Table 2-9

Comparison of modeling approaches to simulate the labeling of 26 amino acid fragments in the *E. coli* network model. With the EMU method, the *E. coli* network model was decomposed 14 EMU networks with 307 unknown EMUs (223 EMUs after further model reduction), compared to 4,612 isotopomers/cumomers, i.e. a reduction of 93-95%.

	isotopomer model	cumomer model	EMU full model	EMU reduced model
Type of model	nonlinear	linear	linear	linear
Number of variables in each subproblem	4,612	54, 241, 527, 771, 876, 832, 655, 404, 183, 57, 11, and 1	(EMU size 1): 141 (EMU size 2): 87 (EMU size 3): 46 (EMU size 4): 12, 8, 1, 1 (EMU size 5): 5, 1, 1, 1, 1 (EMU size 6): none (EMU size 7): none (EMU size 8): 1 (EMU size 9): 1	(EMU size 1): 101 (EMU size 2): 62 (EMU size 3): 32 (EMU size 4): 9, 7, 1, 1 (EMU size 5): 4, 1, 1, 1, 1 (EMU size 6): none (EMU size 7): none (EMU size 8): 1 (EMU size 9): 1
Total number of variables	4,612	4,612	307	223

2.3.5 Gluconeogenesis pathway

In this final example we consider the pathway of gluconeogenesis shown in Figure 2-16. We constructed a detailed biochemical network model for this pathway, where we considered all carbon, hydrogen, and oxygen atom transitions. This pathway is suitable for probing with multiple isotopic tracers, i.e. ^{13}C , ^2H , and ^{18}O . In this example, we simulated the mass isotopomer distribution of glucose. Glucose is the main product of gluconeogenesis and is easily analyzed by GC/MS. The gluconeogenesis network model was comprised of 24 reactions utilizing 21 metabolites, with 5 substrates (oxaloacetate, glycerol, glycogen, NADH, and water), 14 balanced intracellular metabolites, and 2 product (glucose, and CO_2) (see Chapter 7 for details). Table 2-10 shows the number of carbon, hydrogen, and oxygen atoms for each of the 21 metabolites in this system. Here, we only considered stable, i.e. carbon-bound, hydrogen atoms for each metabolite (see section 2.1.2). Simulation of this system using isotopomer and cumomer methods is impossible, because that would require 2,637,120 variables. With the EMU approach, however, the network was decomposed into 60 independent EMU reaction networks of EMU size 1 to 19, with only 493 unknown EMUs, which was further reduced to 354 unknown EMUs by eliminating EMU nodes with a single influx. Table 2-11 shows the details of the EMU decomposition. The largest EMU network contained only 12 unknown EMUs (9 for the reduced EMU model). The simulation of the mass isotopomer distribution of glucose for given fluxes and labeling input took less than 0.1 sec. Thus, in this example we have reduced the computational problem of simulating the gluconeogenesis pathway from an impossible problem to solve, to a problem that is trivial to solve. In Table 2-12 we compare the EMU method vs. the isotopomer/cumomer methods, where we consider alternative labeling strategies. In all cases the EMU method was superior compared to the isotopomer/cumomer method.

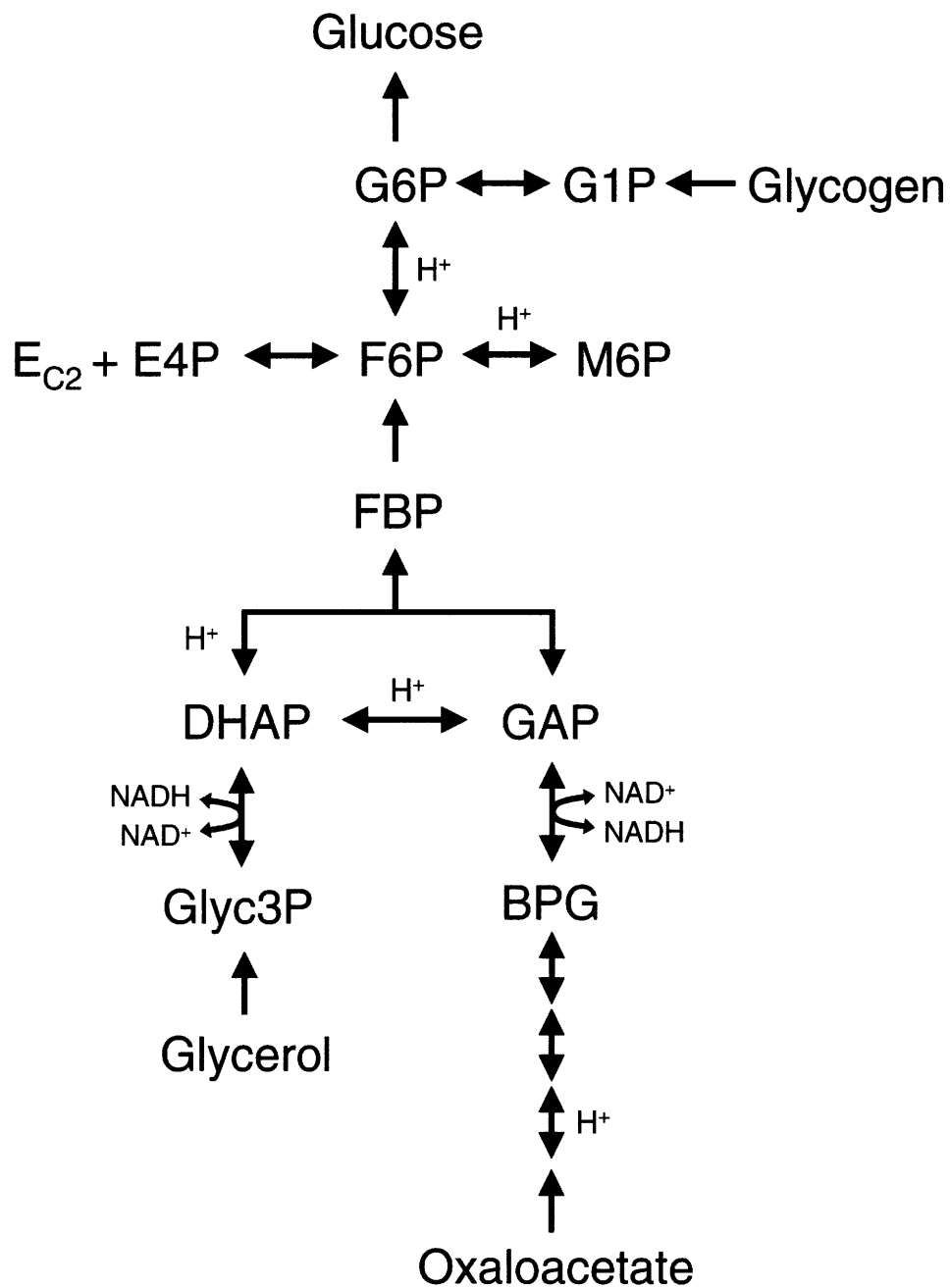


Figure 2-16: Reactions of the gluconeogenesis pathway used to simulate the labeling of glucose.

Table 2-10

Metabolites in the gluconeogenesis pathway. For each metabolite we only considered the stable (i.e. carbon-bound) hydrogen atoms.

Metabolite name	Carbon atoms	Hydrogen atoms	Oxygen atoms	Total atoms
<i>Balanced metabolites</i>				
Glucose 6-phosphate (G6P)	6	7	6	19
Fructose 6-phosphate (F6P)	6	7	6	19
Fructose 1,6,-bisphosphate (FBP)	6	7	6	19
Dihydroxyacetone phosphate (DHAP)	3	4	3	10
Glyceraldehyde 3-phosphate (GAP)	3	4	3	10
1,3-Bisphosphoglycerate (BPG)	3	3	4	10
3-Phosphoglycerate (3PG)	3	3	4	10
2-Phosphoglycerate (2PG)	3	3	4	10
Phosphoenolpyruvate (PEP)	3	2	3	8
Glucose 1-phosphate (G1P)	6	7	6	19
Mannose 6-phosphate (M6P)	6	7	6	19
Glycerol 3-phosphate (Glyc3P)	3	5	3	11
Erythrose 4-phosphate (E4P)	4	5	4	13
Transketolase+C2-unit (E-C2)	2	2	2	6
<i>Products</i>				
Glucose	6	7	6	19
Carbon dioxide	1	0	2	3
<i>Substrates</i>				
Oxaloacetate	4	2	5	11
Glycerol	3	5	3	11
Glycogen	6	7	6	19
NADH	0	1	0	1
Water	0	2	1	3

Table 2-11

Complete list of EMUs generated for glucose from EMU network decomposition of the gluconeogenesis pathway. The EMU method was used to simulate the mass isotopomer distribution of glucose, including all carbon, hydrogen, and oxygen atoms. This required only 493 EMUs (354 EMUs after further model reduction). In comparison 2,637,120 isotopomers/cumomers would have been required with the cumomer modeling approach. In this example, we only considered stable (i.e. carbon-bound) hydrogen atoms for each metabolite.

EMU full model	EMU reduced model
(EMU size 1): 11, 8	(EMU size 1): 8, 5
(EMU size 2): 12, 11, 9	(EMU size 2): 9, 8, 6
(EMU size 3): 11, 11, 11, 10, 9	(EMU size 3): 8, 8, 8, 7, 6
(EMU size 4): 12, 11, 11, 11, 9, 9, 9, 6, 1	(EMU size 4): 9, 8, 8, 8, 6, 6, 6, 4, 1
(EMU size 5): 12, 12, 11, 10, 9, 9, 9, 9, 5, 6, 1, 1, 1	(EMU size 5): 9, 9, 8, 7, 6, 6, 6, 6, 4, 4, 1, 1, 1
(EMU size 6): 12, 10, 10, 10, 10, 9, 9, 9, 5, 1, 1	(EMU size 6): 9, 8, 7, 7, 7, 6, 6, 6, 4, 1, 1
(EMU size 7): 11, 10, 10, 10, 9, 8	(EMU size 7): 9, 7, 7, 7, 6, 6
(EMU size 8): 10, 9, 8	(EMU size 8): 7, 7, 6
(EMU size 9): 9, 5	(EMU size 9): 7, 3
(EMU size 10): 5	(EMU size 10): 3
(EMU size 11): none	(EMU size 11): none
(EMU size 12): none	(EMU size 12): none
(EMU size 13): 6	(EMU size 13): 4
(EMU size 14): none	(EMU size 14): none
(EMU size 15): none	(EMU size 15): none
(EMU size 16): none	(EMU size 16): none
(EMU size 17): 5	(EMU size 17): 4
(EMU size 18): 5, 4	(EMU size 18): 4, 4
(EMU size 19): 6	(EMU size 19): 4
Total number of EMUs = 493	Total number of EMUs = 354

Table 2-12

Comparison of modeling approaches for simulating glucose labeling in the gluconeogenesis pathway. A range of stable isotopes can be used to trace this pathway. Here, we considered ^{13}C -carbon tracers, ^2H -hydrogen tracers, and/or ^{18}O -oxygen tracers. The total number of variables required to simulate the labeling of glucose was determined for the EMU method and the isotopomer/cumomer methods.

Tracer used	Total number of variables		
	isotopomer/cumomer model	EMU full model	EMU reduced model
^{13}C	396	51	35
^2H	768	121	84
^{18}O	420	88	61
$^{13}\text{C} + ^2\text{H}$	42,224	206	145
$^{13}\text{C} + ^{18}\text{O}$	21,392	142	100
$^{18}\text{O} + ^2\text{H}$	42,416	379	268
$^{13}\text{C} + ^{18}\text{O} + ^2\text{H}$	2,637,120	493	354

Chapter 3

Determination of fluxes and confidence intervals from stable isotope measurements

3.1 Introduction

Fluxes of metabolic pathways are fundamental determinants of cell physiology and informative parameters in evaluating cellular mechanisms and causes of disease (Brunengraber et al., 1997; Hellerstein, 2003; Stephanopoulos, 1999). The tools for estimating metabolic fluxes are fundamentally different from the tools for obtaining static measurements, such as concentration profiles or transcript levels. Currently, the most powerful method for metabolic flux determination in complex biological systems is based on the use of stable isotopes (Wiechert et al., 2001). Metabolic conversion of isotopically labeled substrates generates molecules with distinct labeling patterns (i.e. isotopomers) that can be detected by mass spectrometry (MS) and nuclear magnetic resonance (NMR) (Klapa et al., 2003; Szyperski, 1995). The isotopic abundances of metabolites in a metabolic system are strongly dependent on relative flux values. Different flux patterns result in significant tracer redistribution and yield different labeling profiles.

Comprehensive mathematical models that describe the relationship between metabolite labeling patterns and fluxes allow one to simulate isotopic abundances of all metabolites in a network for any set of steady state fluxes. These models are nonlinear because the full set of isotopomer equations contains product terms of fluxes with isotope abundances, and product terms of abundances with abundances due to linear and condensation reactions in

the system (Schmidt et al., 1997). The goal of Metabolic Flux Analysis (MFA) is to find the set of fluxes that minimizes the difference between observed and simulated isotope measurements. In essence, flux determination is a large-scale nonlinear parameter estimation problem. Various iterative search strategies, for example, gradient-based Newton methods, or evolutionary search algorithms may be employed to find the optimal metabolic fluxes (Schmidt et al., 1999; Wiechert et al., 1997). Metabolic flux analysis of this type has been successfully applied to determine fluxes in various prokaryotic and eukaryotic systems (Christensen and Nielsen, 2000; Kelleher, 2004; Malloy et al., 1988; Park et al., 1999; Sauer et al., 1997). However, rigorous statistical analysis of estimated flux has received much less attention. Linearized statistics have been used to describe the uncertainty of fluxes (Arauzo-Bravo and Shimizu, 2003; Dauner et al., 2001; Wiechert et al., 1997). Most often, however, flux estimates are not accompanied by a corresponding range of accuracy/precision, which makes such results difficult to interpret. For example, when the measured isotope abundance is not very different from the simulated abundance, does this mean that the measurement is reliable or does it simply result from a lack of redundancy in the measurement set? A common mistake in assessing the benefit of flux estimation in over-determined systems is to believe that a large redundancy in the measurement set necessarily results in reliable estimates for all fluxes. To address these questions proper nonlinear statistical techniques are needed, otherwise metabolic flux analysis will remain a black box whose inner workings are hard to decipher.

Here, we describe here techniques that can be applied a posteriori to gain insight into the statistical significance of flux estimation results. The same tools may then also be applied a priori for optimal design of tracer experiments. We show how accurate flux confidence intervals are efficiently calculated, and we quantify the relative importance of measurements. We show that approximated confidence intervals obtained from local estimates of standard deviations do not accurately describe the true uncertainty of fluxes. We have applied these tools to analyze the statistical significance of gluconeogenesis fluxes determined from human studies probed with $[U-^{13}C]$ glucose as tracer. We calculated accurate confidence intervals for all fluxes in this system and identified potential flaws in experimental setup that may prevent accurate determination of the gluconeogenesis flux in vivo. The methods presented here are

general in scope and may also be applied to other parameter estimation problems. Furthermore, these algorithms are easily implemented into already developed software platforms for flux estimation.

3.2 Methods

3.2.1 Flux estimation

The methods described here are appropriate for metabolic systems investigated with isotopic tracers at metabolic steady state. Thus, fluxes are required to satisfy the following stoichiometric constraints:

$$S \cdot v = 0 \quad (3.1)$$

Here, S is the stoichiometry matrix and v is the flux vector. For a reaction network with m intermediary metabolites and k fluxes, the stoichiometry matrix is an $m \times k$ matrix.

Reversible reactions are normally modeled as separate forward and backward fluxes, such that all fluxes are additionally required to be non-negative. From a computational standpoint, it is more convenient to work with independent flux variables, also called free fluxes (Schmidt et al., 1997; Wiechert et al., 1997), rather than with all individual fluxes. The number of independent fluxes is usually much smaller than the number of individual fluxes, which significantly reduces the computational time of simulations. Independent fluxes are obtained from the general solution to Eq. 3.1:

$$v = N \cdot u \quad (3.2)$$

Here, N is the null space matrix of S , and u is the vector of independent fluxes. There are many methods to calculate a valid null space matrix (Foster, 1986), and in general there is not a unique null space matrix for any given stoichiometry matrix. The size of the null space matrix and the number of independent flux variables, however, are fully determined by the rank of the stoichiometry matrix. With $r = \text{rank}(S) \leq m$, the null space matrix is a $k \times k-r$

matrix and the number of independent fluxes equals $k-r$. Note that Eq. 3.2 may be used to translate results expressed in terms of independent fluxes into individual fluxes.

At least $k-r$ measurements are needed to determine the $k-r$ independent flux variables. External flux measurements often do not provide enough constraints to estimate all fluxes in complex biological systems containing reversible reactions, parallel pathways and internal cycles (Schmidt et al., 1998). In these cases, isotopic tracer experiments can provide additional constraints from the measurement of isotope incorporation into metabolite pools by techniques such as GC/MS and NMR. The fate of isotopic tracers in a metabolic system is determined by the atoms transitions occurring in biochemical reactions. These transitions are well established for the majority of metabolic pathways and have been documented in biochemical textbooks. Assuming metabolic and isotopic steady state, the mathematical model that is used for isotopic simulations comprises the complete set of isotopomer balances, which may be derived using a matrix based method as described by Schmidt et al. (1997). More recently, alternative modeling strategies were proposed by other authors based on the concept of cumomer balances and bondomer balances (van Winden et al., 2002; Wiechert et al., 1999). In Chapter 2 we described a novel strategy for modeling isotopic distributions based on the concept of elementary metabolite units (EMU). All modeling strategies are equivalent in the sense that they produce the same numerical results, i.e. isotopomer abundances, for a given set of fluxes and substrate labeling. The sensitivity matrix of simulated measurements with respect to flux values, i.e. (dx/du) , may be obtained either by approximation using finite differences, or from algebraic such as the ones derived in Chapter 2 (section 2.2.5). Metabolic fluxes are estimated from labeling data by minimizing the difference between the observed and simulated measurements. Flux estimation is in essence a large-scale constrained least-squares minimization problem:

$$\begin{aligned} \min_{\mathbf{u}} \Phi &= \left(\mathbf{x}(\mathbf{u}) - \mathbf{x}^{obs} \right)^T \cdot \Sigma_x^{-1} \cdot \left(\mathbf{x}(\mathbf{u}) - \mathbf{x}^{obs} \right) \\ \text{s.t.} \quad & \mathbf{N} \cdot \mathbf{u} \geq 0 \end{aligned} \tag{3.3}$$

The objective function Φ is the covariance-weighted sum of squared residuals, $x(u)$ is the vector of simulated measurements, x^{obs} is the vector of experimental data containing both labeling measurements and extracellular rate measurements, and Σ_x is the measurement covariance matrix with measurement variances located on the diagonal. Eq. 3.3 requires an iterative solution scheme, where at each iteration Eq. 3.3 is transformed into a corresponding quadratic programming (QP) subproblem (Gill et al., 1991). First, the simulated measurements are formally expressed as a function of free fluxes using Taylor series expansion:

$$x = x^* + \left(\frac{dx}{du} \right) \cdot \Delta u + O(\Delta u^2) \quad (3.4)$$

Here, x^* is the vector of simulated measurements for the current set of fluxes, (dx/du) is the matrix of sensitivities of the simulated measurements with respect to fluxes, and Δu is the vector of flux changes. Substituting Eq. 3.4 into Eq. 3.3 and neglecting second and higher order terms, we obtain the following expression for the objective function as a function of flux changes:

$$\begin{aligned} \min_{\Delta u} \Phi &= (x^* - x^{obs})^T \cdot \Sigma_x^{-1} \cdot (x^* - x^{obs}) + 2 \cdot \Delta u^T \cdot \left(\frac{dx}{du} \right)^T \cdot \Sigma_x^{-1} \cdot (x^* - x^{obs}) + \Delta u^T \cdot \left(\frac{dx}{du} \right)^T \cdot \Sigma_x^{-1} \cdot \left(\frac{dx}{du} \right) \cdot \Delta u \\ \text{s.t.} \quad & N \cdot u \geq 0 \end{aligned} \quad (3.5)$$

Note that the first term in Eq. 3.5 is the value of the objective function for the current fluxes. We define the change in the objective function as:

$$\Delta \Phi = \Phi - (x^* - x^{obs})^T \cdot \Sigma_x^{-1} \cdot (x^* - x^{obs}) \quad (3.6)$$

With this, we obtain the following QP subproblem at each iteration:

$$\begin{aligned} \min_{\Delta u} \Delta\Phi &= 2 \cdot \Delta u^T \cdot J + \Delta u^T \cdot H \cdot \Delta u \\ \text{s.t.} \quad N \cdot u &\geq 0 \end{aligned} \quad (3.7)$$

$$\text{with} \quad J = \left(\frac{dx}{du} \right)^T \cdot \Sigma_x^{-1} \cdot (x^* - x^{obs}) \quad (3.8a)$$

$$\text{and} \quad H = \left(\frac{dx}{du} \right)^T \cdot \Sigma_x^{-1} \cdot \left(\frac{dx}{du} \right) \quad (3.8b)$$

The Hessian matrix H and the Jacobian J are evaluated at each iteration for the current fluxes. Differentiation of the objective function in Eq. 3.7 with respect to flux changes yields:

$$\frac{d(\Delta\Phi)}{d(\Delta u)} = 2 \cdot J + 2 \cdot H \cdot \Delta u \quad (3.9)$$

The minimum of Eq. 3.7 occurs when $d(\Delta\Phi)/d(\Delta u) = 0$ (Gill et al., 1991), which is the solution to the system of linear equations given in Eq. 3.9. Thus, the optimal search direction for the independent fluxes at each iteration is:

$$\Delta u = -H^{-1} \cdot J \quad (3.10)$$

A numerically stable form for the inverse of H may be obtained from singular value decomposition of H (see Appendix 3.A). The following updated flux vector is obtained at each iteration:

$$u_{k+1} = u_k + \Delta u \quad (3.11)$$

Inequality constraints on fluxes, i.e. $N \cdot u \geq 0$, can be included without difficulty to this general scheme, and all kinds of step controlling strategies can be applied (Byrd et al., 1999; Gill et al., 1991). Flux estimation is generally initiated with random values for all fluxes and the estimation algorithm continues until a predefined convergence criterion is met. The final vector of independent fluxes is then transformed using Eq. 3.2 to obtain the optimal values for all metabolic fluxes in the system. The complete algorithm for covariance-weighted flux estimation is outlined in Appendix 3.B.

3.2.2 Goodness-of-fit analysis

The fact that MFA yields a set of fluxes that minimize the difference between the observed and simulated measurements does not mean that the flux model is adequate. At convergence, the minimized variance-weighted sum of squared residuals, as defined in Eq. 3.3, is a stochastic variable with χ^2 -distribution with the number of degrees of freedom equal to the number of independent measurements (n) minus the number of estimated free fluxes $p = k - r$. The expected value for the minimized sum of squared residuals equals the number of degrees of freedom of the χ^2 -distribution. To test the goodness of fit, we test the null hypothesis that the model is adequate:

$$P(\Phi \geq \Phi(\hat{u}) \mid \Phi \sim \chi^2(n - p)) > \alpha \quad (3.12)$$

Here, \hat{u} are the fluxes at the optimal solution. The null hypothesis is rejected when the calculated P-value is smaller than a certain chosen threshold value α , for example 0.05. If previous investigations have excluded the possibility of gross errors in the measurements, then it must be concluded that the model is not adequate, and thus should be reevaluated.

Individual residuals should also be analyzed at convergence. If the flux model is correct, then the standard deviation-weighted residuals are expected to be normally distributed with a mean of zero and standard deviation of one, i.e. $N(0,1)$. A normal probability plot is a useful tool for assessing whether the residuals are indeed normally distributed. Alternatively, one

can use the Kolmogorov-Smirnov and Lilliefors tests to evaluate the hypothesis that the residuals are normally distributed (Conover, 1999). If the standard deviation of the weighted residuals is significantly different from one, then that indicates that the residuals have been improperly weighted, which may result in biased flux estimates.

3.2.3 Local linearized statistical properties

The first goal of MFA is to improve our knowledge of internal fluxes, however, assessing the reliability of flux estimates is also important. Without this information it is difficult to interpret flux results and expand the physiological significance of flux studies. At convergence, a number of local statistical properties of fluxes are easily derived. First, we calculate the inverse of the Hessian, which gives the local estimate for the covariance matrix of the estimated independent fluxes (Hartmann and Hartwig, 1996):

$$\Sigma_u = H^{-1} \quad (3.13)$$

Combining Eqs. 3.2 and 3.13 we obtain the following covariance matrix for all individual fluxes in the system:

$$\Sigma_v = N \cdot \Sigma_u \cdot N^T = N \cdot H^{-1} \cdot N^T \quad (3.14)$$

We can then calculate local estimates for standard deviations of metabolic fluxes, i.e. the square roots of the diagonal elements of Σ_v . The local approximation for the 95% confidence interval of flux i is thus given by:

$$\text{Approx. 95\% confidence interval}_{(i)} = \text{flux}_{(i)} \pm 2 \cdot \sqrt{\Sigma_{v(i,i)}} \quad (3.15)$$

Similarly, we may also calculate covariance matrices and confidence intervals for other system variables. For example, the covariance matrix for the simulated measurements is given by:

$$\Sigma_x = \left(\frac{dx}{du} \right) \cdot \Sigma_u \cdot \left(\frac{dx}{du} \right)^T \quad (3.16)$$

3.2.4 Calculating accurate flux confidence intervals

Confidence intervals of fluxes obtained from estimated local standard deviations may not accurately describe the true flux uncertainty due to inherent nonlinearities of isotopomer balances. In addition, flux constraints, e.g. $v \geq 0$, may be violated within the approximated confidence interval resulting in overestimation of flux uncertainty. To address these issues we propose an alternative strategy for determination of more accurate flux confidence intervals. This technique is an extension to the flux estimation procedure described in section 3.2.1. In the proposed method, confidence intervals are calculated for each flux individually. The goal is to determine the sensitivity of the objective function, i.e. the minimized sum of squared residuals, as a function of the flux value. Small sensitivities, i.e. large changes in the flux value resulting in small changes in the minimized sum of squared residuals, indicate that the flux cannot be estimated precisely. Large sensitivities, on the other hand, indicate that the flux is well determined. The optimization problem associated with minimizing the sum of squared residuals as a function of one particular flux has $n-p-1$ degrees of freedom, compared to $n-p$ degrees of freedom for the original MFA problem. The difference between the objective function evaluated at the optimal solution and the objective function when one flux is fixed follows a χ^2 -distribution with one degree of freedom:

$$\left(\Phi(u) \Big|_{v_i=v_{i0}} - \Phi(\hat{u}) \right) \sim \chi^2(1) \quad (3.17)$$

It should be noted that Eq. 3.17 assumes that the residuals are correctly weighted. If measurement errors are unknown, or the residuals are incorrectly weighted then Eq. 3.17

may produce inaccurate results. In these cases, the following alternative F-statistic is preferred:

$$\frac{\Phi(\mathbf{u})|_{v_i=v_{i0}} - \Phi(\hat{\mathbf{u}})}{\Phi(\hat{\mathbf{u}}) / (n - p)} \sim F(1, n - p) \quad (3.18)$$

In the above equations, $\Phi(\mathbf{u})|_{v_i=v_{i0}}$ indicates the value of the objective function for the model where one flux i is fixed at v_{i0} , and the other degrees of freedom have been used to minimize the objective function. The $1-\alpha$ confidence interval for flux i is given by all flux values for which the following statement is true:

$$\Phi(\mathbf{u})|_{v_i=v_{i0}} \leq \left(\Phi(\hat{\mathbf{u}}) + \chi^2_{1-\alpha}(1) \right) \quad (3.19)$$

The threshold values for $\chi^2_{1-\alpha}(1)$ corresponding to 80%, 90%, 95% and 99% confidence intervals are 1.64, 2.71, 3.84, and 6.63, respectively. Thus, in order to obtain accurate confidence intervals of fluxes we need to determine the minimized sum of squared residuals as a function of the flux value. Here, we describe an efficient algorithm for this purpose. Starting at the optimal solution, the value of one flux whose sensitivity we seek to determine is increased step-by-step, while the other fluxes are determined by minimizing the objective function. We obtain the following QP subproblem at each iteration:

$$\begin{aligned} \min_{\Delta \mathbf{u}} \Delta \Phi &= 2 \cdot \Delta \mathbf{u}^T \cdot \mathbf{J} + \Delta \mathbf{u}^T \cdot \mathbf{H} \cdot \Delta \mathbf{u} \\ \text{s.t.} \quad \mathbf{N}_i \cdot \Delta \mathbf{u} &= h \\ \mathbf{N} \cdot \mathbf{u} &\geq 0 \end{aligned} \quad (3.20)$$

Eq. 3.20 is similar to Eq. 3.7, with the additional constraint that flux v_i is required to increase with a step size 'h'. In the above equation \mathbf{N}_i denotes the i^{th} row of matrix \mathbf{N} . The above constrained optimization problem is transformed to a problem without equality constraints using the Lagrange formulation (Byrd et al., 1999; Gill et al., 1991):

$$\begin{aligned} \min_{\Delta u, \Delta \lambda} L &= 2 \cdot \Delta u^T \cdot J + \Delta u^T \cdot H \cdot \Delta u + (N_i \cdot \Delta u - h) \cdot \Delta \lambda \\ \text{s.t.} \quad N \cdot u &\geq 0 \end{aligned} \quad (3.21)$$

Here, λ is the Lagrange multiplier. The minimum of Eq. 3.21 occurs when the following stationary conditions are satisfied:

$$\left(\frac{dL}{d(\Delta u)} \right) = 0 \quad \rightarrow \quad 2 \cdot J + 2 \cdot H \cdot \Delta u + N_i^T \cdot \Delta \lambda = 0 \quad (3.22)$$

$$\left(\frac{dL}{d(\Delta \lambda)} \right) = 0 \quad \rightarrow \quad N_i \cdot \Delta u - h = 0 \quad (3.23)$$

We define a square matrix A and vectors b and Δd as follows:

$$A = \begin{bmatrix} 2 \cdot H & N_i^T \\ N_i & 0 \end{bmatrix} \quad (3.24a)$$

$$b = \begin{bmatrix} -2 \cdot J \\ h \end{bmatrix} \quad (3.24b)$$

$$\Delta d = \begin{bmatrix} \Delta u \\ \Delta \lambda \end{bmatrix} \quad (3.24c)$$

The stationary conditions from Eqs. 3.22 and 3.23 can be written as follows:

$$A \cdot \Delta d = b \quad (3.25)$$

Thus, the optimal adjustment of the variables in vector d, i.e. independent fluxes and the Lagrange multiplier, that minimizes the objective function is given by:

$$\Delta d = A^{-1} \cdot b \quad (3.26)$$

and we obtain the following updated variables vector at each iteration:

$$d_{k+1} = d_k + \Delta d \quad (3.27)$$

The flux value is increased this way until either the flux reaches infinity, or the objective function has increased by 3.84 compared to the value at the optimal solution, which then corresponds to the upper bound of the 95% flux confidence interval. The above procedure is then repeated starting at the optimal solution, but now the flux value is gradually decreased, i.e. the linear constraint in Eq. 3.20 is changed to:

$$-N_i \cdot \Delta v = h \quad (3.28)$$

Eqs. 3.21 to 3.24 are also changed accordingly. The selected flux is decreased until either the flux reaches the lower bound, or the objective function has increased by 3.84 compared to the value at the optimal solution, thus corresponding to the lower bound of the 95% flux confidence interval. If the flux model was linear, then the profile of the minimized sum of squared residuals versus the flux value would be a parabola. However, because of the inherent nonlinearities of isotopomer models observed profiles will often deviate from the parabola-shape. In section 3.3.1 we show that confidence intervals of metabolic fluxes obtained with the above described method accurately reflect the true uncertainty of flux estimates. Note that additional fluxes constraints, i.e. $N \cdot u \geq 0$, and step controlling strategies are again easily applied to this general scheme (see Appendix 3.C). The complete algorithm for accurate determination of confidence intervals of fluxes is outlined in Appendix 3.D.

3.2.5 Relative importance of measurements

Next, we address the question how the precision of estimated fluxes is influenced by measurement uncertainty. In particular, we wish to identify measurements that contribute

significantly to the variance of estimated fluxes. This will allow us to quantify the relative importance of measurements and identify key measurements, i.e. measurements for which an enhancement of precision would result in significant improvement in the quality of flux estimates (Heyen et al., 1996). These measurements should be carried out with special attention and it may prove wise to measure them more precisely. First, we rewrite Eq. 3.14 as follows:

$$\Sigma_v = N \cdot H^{-1} \cdot N^T = N \cdot H^{-1} \cdot H \cdot H^{-1} \cdot N^T \quad (3.29)$$

Substitution of the definition for the Hessian matrix from Eq. 3.8 into Eq. 3.29 yields an expression that directly links measurement variances, i.e. on the diagonal of matrix Σ_x , with flux variances, i.e. on the diagonal of matrix Σ_v :

$$\Sigma_v = N \cdot H^{-1} \cdot \left(\frac{dx}{du} \right)^T \cdot \Sigma_x^{-1} \cdot \left(\frac{dx}{du} \right) \cdot H^{-1} \cdot N^T \quad (3.30)$$

We can use Eq. 3.30 to construct the contribution matrix. Elements in this matrix reflect the fractional contribution of the variance of measurement j to the local variance of flux i :

$$\text{Contribution}_{(i,j)} = \frac{\left(N \cdot H^{-1} \cdot \left(\frac{dx}{du} \right)^T \right)_{(i,j)}^2}{\Sigma_{v(i,i)} \cdot \Sigma_{x(j,j)}} \quad (3.31)$$

The sum of each row in the contribution matrix equals one. Matrix elements with large values indicate important measurements. From the contribution matrix we can easily determine the number of redundant measurements for each individual flux. In general, it is desirable that more than one measurement significantly contributes to the flux estimation. Fluxes that depend only on one measurement are very sensitive to errors in that one measurement. We can use this as a criterion to determine the quality of tracer experiment design. For example, a tracer experiment is considered poorly designed if a significant

number of estimated fluxes have little or no redundant measurements. Note that this situation may occur even if the total number of measurements is much greater than the number of unknown fluxes. On the other hand, we may also encounter experiments that are specifically designed to determine only a subset of fluxes which are of interest. In that case, the overall flux estimation problem can be underdetermined, as long as the fluxes of interest are over-determined. Thus, in general there is not a single optimal tracer experiment. Instead, depending on the fluxes that need to be determined, different experimental designs may be optimal. Note that our method for evaluating experiment design places emphasis redundant measurements, which sets it apart from the methods used by other investigators which are based on the D-criterion (Mollney et al., 1999).

In addition to the contribution matrix, we also derived the following expressions for local sensitivities of estimated fluxes with respect to changes in measurement values and assumed measurement errors:

$$\frac{dv}{dx} = N \cdot H^{-1} \cdot \left(\frac{dx}{du} \right)^T \cdot \Sigma_x^{-1} \quad (3.32)$$

$$\frac{dv}{d\sigma_x} = 2 \cdot N \cdot H^{-1} \cdot \left(\frac{dx}{du} \right)^T \cdot \Sigma_x^{-1.5} \cdot \text{diag}(x(\hat{u}) - x^{obs}) \quad (3.33)$$

These two expressions indicate how much flux estimates are affected by a change in a particular measurement. It is clear that different measured values will result in different estimated fluxes. However, the significance of assumed measurement errors on flux estimates is often overlooked. The assumed measurement errors determine the relative weighting of residuals in the objective function, and have a significant impact on flux estimation results. This is particularly true for measurements with very small assumed errors, which may introduce a bias towards these measurements. Therefore, as part of a posteriori analysis it is important to analyze the sensitivity of fluxes with respect to changes in measurement values *and* measurement errors. In particular, high sensitivities with respect to

changes in measurement errors indicate disagreement between the measurement and the network model that should be further investigated. This inconsistency may be caused by measurement gross errors, inappropriate weighting of residuals, or errors in the metabolic network model.

3.3 Results

To illustrate the developed methods two examples are provided. The first example is a simple metabolic system with only six fluxes, where we compare flux confidence intervals calculated by the described method to ‘true’ confidence intervals obtained using an exhaustive grid search and by Monte Carlo simulations. The second system is taken from human physiology literature, i.e. mammalian glucose metabolism evaluated by constant infusion of [U-¹³C]glucose.

3.3.1 Simple example network

Consider the simple network shown in Figure 3-1. This system will serve as the test case for our method of calculating accurate confidence intervals. We will simulate data from this system and then use the simulated data to estimate fluxes and calculate flux confidence intervals as we described in sections 3.2.1 and 3.2.4. In this network, metabolite A is the sole substrate and metabolites E and F are two final products. The intermediary metabolites B, C and D are assumed to be at metabolic and isotopic steady state. Atom transitions for the five reactions are given in Table 3-1. The assumed flux distribution is shown in Figure 3-1. All fluxes are expressed as percentages of the substrate uptake rate, which is fixed at 100. In this example, 100% [2-¹³C]A is chosen as the isotopic tracer and the mass isotopomer distribution (MID) of product F is measured. At isotopic steady state the following MID for metabolite F is obtained, 0.01 mol% (M+0), 80.08 mol% (M+1), 19.83 mol% (M+2), and 0.09 mol% (M+3).

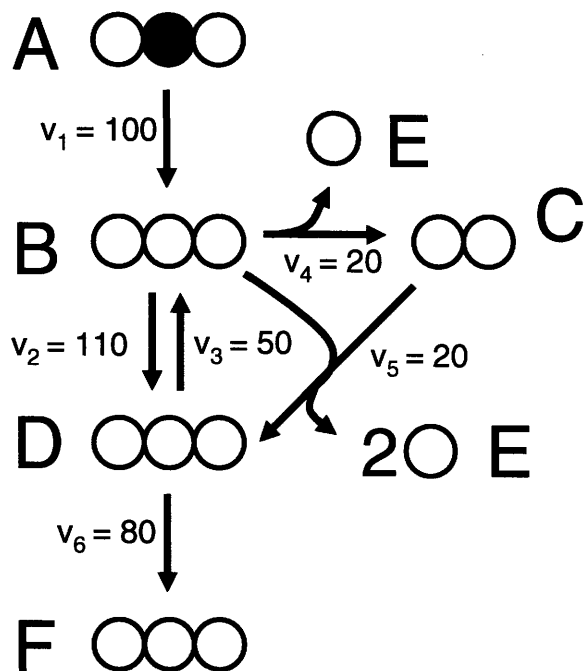


Figure 3-1: Simple metabolic network used here to illustrate the computation of confidence intervals of metabolic fluxes. The assumed steady-state fluxes have arbitrary units. The network substrate A is fully labeled on the second atom. Atom transitions for the reactions in this network are shown in Table 3-1.

Table 3-1

Stoichiometry and atom transformations for reactions in the example metabolic network in Figure 3-1.

Reaction number	Reaction stoichiometry	Atom transformations*
1	$A \rightarrow B$	$abc \rightarrow abc$
2	$B \leftrightarrow D$	$abc \leftrightarrow abc$
3	$B \rightarrow C + E$	$abc \rightarrow bc + a$
4	$B + C \rightarrow D + E + E$	$abc + AB \rightarrow bcA + a + B$
5	$D \rightarrow F$	$abc \rightarrow abc$

* For each compound atoms are identified using lower case letters to represent successive atoms of each compound. Uppercase letters represent a second compound in the reaction.

3.3.2 Grid search

With the substrate uptake rate fixed at 100 this metabolic system has two remaining degrees of freedom. Here, we choose fluxes v_2 and v_4 as the independent fluxes. For this simple problem it is computationally feasible to apply a grid search strategy to determine the sensitivity of the objective function as a function of flux values, from which the uncertainty of fluxes can then be calculated as described in section 3.2.4. Here, we evaluated all combinations of fluxes v_2 ranging from 0 to 500 (with step size 0.5) and v_4 ranging from 0 to 100 (with step size 0.1), i.e. one million flux combinations were evaluated. For each flux combination we calculated the sum of squared residuals assuming a measurement error of 0.3 mol% for all mass isotopomer fractions. Figure 3-2 provides a one-dimensional representation of this 2D-grid search. The dots in Figure 3-2A correspond to the minimal sum of squared residuals for fixed value of v_2 , but variable value of v_4 . In Figure 3-2B flux v_4 was fixed and v_2 varied. Note that for this simple example with two degrees of freedom, the grid search method for calculating flux confidence intervals is closely related to our proposed method described in section 3.2.4.

3.3.3 Monte Carlo simulations

Confidence intervals were also determined using Monte Carlo simulations. For this purpose, we generated 10,000 simulated data sets corrupted with noise with a standard deviation of 0.3 mol%. Metabolic fluxes were estimated from this data and we obtained 10,000 estimates of fluxes v_2 and v_4 . It is expected that the estimated fluxes will differ somewhat from the true flux values (i.e. $v_{2,true}=110$ and $v_{4,true}=20$) due to measurement errors. Furthermore that the spread in the estimated fluxes corresponds to the flux uncertainty. Figure 3-3 shows the histogram of estimated fluxes v_2 and v_4 . To determine flux confidence intervals, flux estimates were first sorted in ascending order. The 80% confidence interval was then obtained by discarding the top 10% and bottom 10% of flux estimates; the 90% confidence interval was obtained by discarding the top 5% and bottom 5% of flux estimates, etc. The calculated confidence intervals for v_2 and v_4 are summarized in Table 3-2.

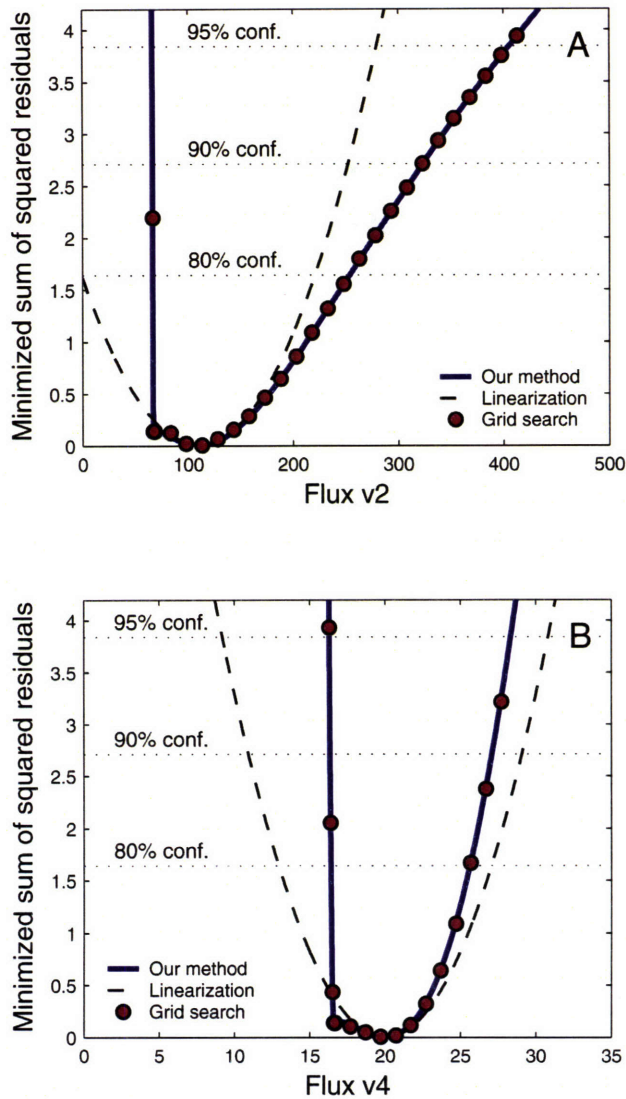


Figure 3-2: Determination of confidence intervals of metabolic fluxes. The minimized sum of squared residuals is plotted against the flux value for fluxes v_2 and v_4 . Circles represent the smallest sum of squared residuals observed for a given flux value from the exhaustive grid search. The solid line represents the profile determined with our method, and the dashed line represents the profile obtained assuming linearized statistics. The dashed horizontal lines represent the threshold values for the 80%, 90% and 95% confidence intervals, respectively (see section 3.2.4 for details).

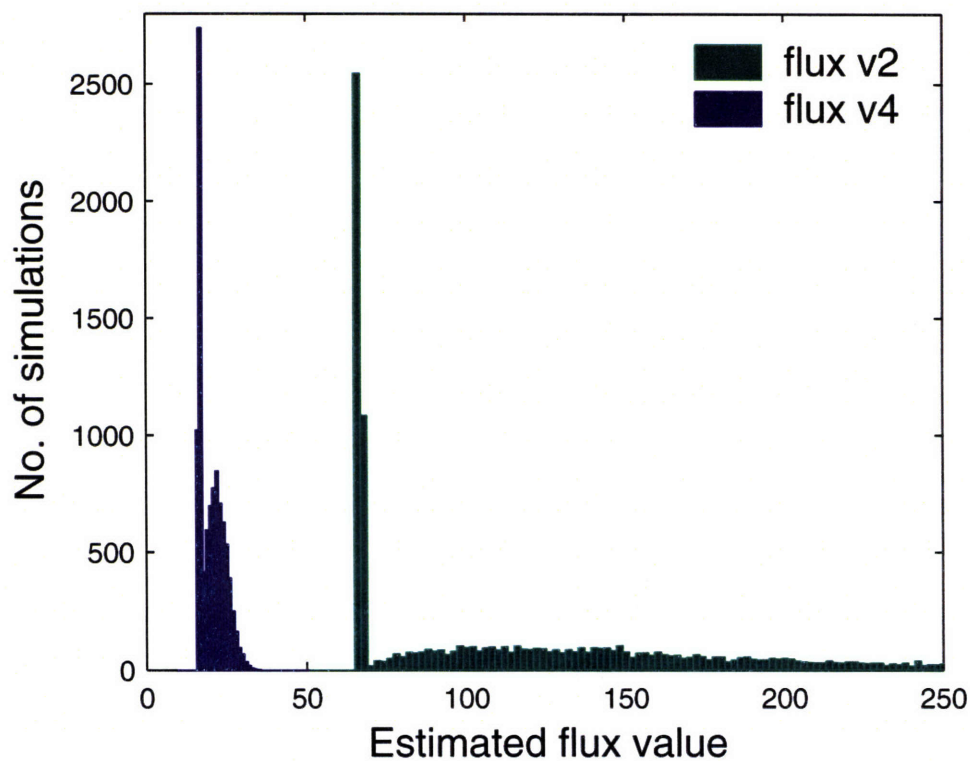


Figure 3-3: Histogram of estimated fluxes v_2 and v_4 from 10,000 Monte Carlo simulations. For each simulation isotopomer data was corrupted with random noise with a standard deviation of 0.3 mol% abundance, and fluxes were estimated by least-square optimization. Estimated fluxes were then collected into bins with a width of 2 for v_2 , and 1 for v_4 (shown here). The estimated fluxes are different from the true flux values due to the introduced measurement errors, i.e. $v_{2,true}=110$ and $v_{4,true}=20$.

3.3.4 Linearized statistics

Approximated confidence intervals were obtained from estimated standard deviations of fluxes after linearization, as described in sections 3.2.1 and 3.2.3. The following optimal solutions for fluxes v_2 and v_4 were obtained: $v_2 = 110 \pm 86.4$; and $v_4 = 20 \pm 5.5$ (best fit \pm SD).

3.3.5 Comparison of methods for calculating flux confidence intervals

Next, confidence intervals of fluxes were determined with our method using the algorithm described in section 3.2.4. The calculated 80%, 90% and 95% confidence intervals for fluxes v_2 and v_4 obtained with all four methods are summarized in Table 3-2. The values obtained using the grid search method, the Monte Carlo simulations and our method agreed well. However, values obtained from linearized statistics differed significantly. In Figure 3-2 we visualize the confidence intervals obtained with the grid search method, linear approximation and our method. It is clearly seen that the confidence intervals in this system are non-symmetric and highly nonlinear. As such, confidence intervals approximated from local estimates of standard deviations agreed well only in a small area surrounding the optimal solution. The lower and upper bounds for flux v_2 were significantly underestimated, and for flux v_4 the size of the 95% confidence interval was overestimated by almost a factor of 2. Note that most metabolic systems of interest will have more than two degrees of freedom, which limits the use of grid search and Monte Carlo simulations due to computational limitations. Even for this simple example network, the grid search method and Monte Carlo simulations required hours of calculations. In contrast, our method took less than one second. It should be noted that the above observations are specific to our particular network structure, substrate labeling, measurements and assumed measurement errors. However, it is clearly illustrated that for reasonable values of measurement errors, highly nonlinear confidence intervals can be expected. In summary, we have shown that approximated flux confidence intervals do not accurately describe true uncertainty of estimated fluxes. Therefore, more accurate flux confidence intervals must be determined using nonlinear tools. We have developed an efficient technique for calculating these intervals without the need to perform computationally demanding grid searches, or Monte Carlo simulations.

Table 3-2

Comparison of methods for the calculation of confidence intervals of fluxes. Confidence intervals were calculated for fluxes v_2 and v_4 in the example network model shown in Figure 3-1.

Method	Confidence intervals for flux v_2			Confidence intervals for flux v_4		
	80%	90%	95%	80%	90%	95%
Grid search	67.0 – 253	66.5 – 323	66.5 – 405	16.5 – 25.6	16.4 – 27.1	16.4 – 28.3
Monte Carlo	66.7 – 251	66.5 – 317	66.4 – 407	16.5 – 25.6	16.4 – 27.0	16.4 – 28.4
Our method	66.5 – 252	66.4 – 322	66.3 – 403	16.4 – 25.6	16.3 – 27.1	16.3 – 28.3
Linearization*	(-0.6) – 220	(-31.8) – 252	(-62.8) – 283	12.9 – 27.1	11.0 – 29.0	9.0 – 31.0

* Confidence intervals were approximated from local estimates of standard deviations for the fluxes after linearization.

3.3.6 Mammalian gluconeogenesis

As the second metabolic system we chose mammalian gluconeogenesis at metabolic and isotopic steady state evaluated by constant infusion of [U-¹³C]glucose. Figure 3-4 shows the metabolic model for mammalian glucose metabolism, which is described in more detail in Appendix 3.E. Investigation of glucose metabolism is of major physiological and clinical significance in the study of obesity, diabetes and other disease (Groop et al., 1989; Landau et al., 1996). Of particular interest are the rates of glucose production and utilization, and the pathways by which glucose is formed during fasting. Tayek and Katz were the first to propose a method for estimating several parameters of glucose metabolism in human from the mass isotopomer distributions of plasma glucose and lactate upon constant infusion of [U-¹³C]glucose as the single isotopic tracer (Tayek and Katz, 1996). However, since the introduction of this method several authors raised questions regarding the reliability of flux estimates from this system (Kelleher, 1999; Landau et al., 1998; Radziuk and Lee, 1999). Here, we address these questions using the developed tools.

We selected two studies from recent literature where the [U-¹³C]glucose method was applied to study glucose metabolism *in vivo*. Tayek et al. investigated glucose metabolism in healthy and diabetic subjects (Tayek and Katz, 1996). Human subjects were infused with [U-¹³C]glucose for 3 hours at a rate of 0.59 $\mu\text{mol}/\text{kg}/\text{min}$. Mass isotopomer distributions (MID) of plasma glucose and plasma lactate were measured at the end of the infusion period and several parameters of glucose metabolism were estimated. The authors found a near linear correlation between hepatic glucose production and plasma glucose levels suggesting a key role of liver metabolism in diabetes. In a more recent publication, Sunehag investigated the effects of supply of parental lipids and amino acids to very premature infants (Sunehag, 2003). After an 8 hr infusion with [U-¹³C]glucose at a rate of 17 $\mu\text{mol}/\text{kg}/\text{min}$, MID of plasma glucose and lactate were measured and the rate of gluconeogenesis was estimated. This study revealed the primary role of lipids in supporting gluconeogenesis in very low birthweight infants. The key difference between the two studies was the rate of tracer infusion. In the study by Tayek [U-¹³C]glucose was infused at a rate corresponding to 4% of

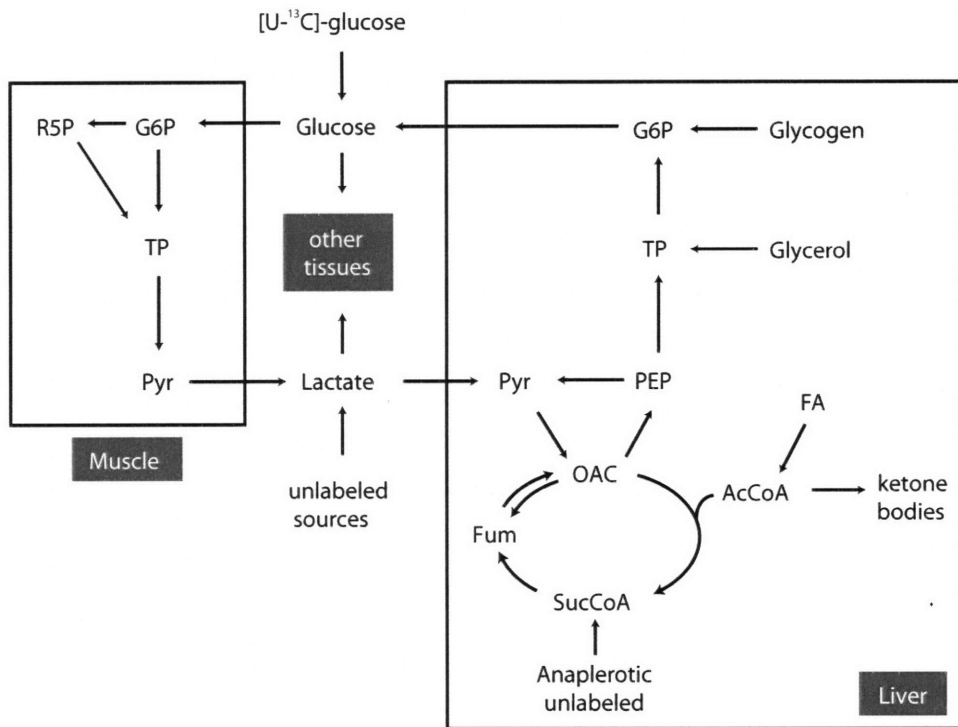


Figure 3-4: Metabolic model of mammalian glucose metabolism evaluated by constant infusion of [U-¹³C]glucose. Abbreviations of metabolites: G6P, glucose-6-phosphate; R5P, ribose-5-phosphate; Pyr, pyruvate; OAC, oxaloacetate; SucCoA, succinyl coenzyme A; Fum, fumarate; AcCoA, acetyl coenzyme A; FA, fatty acids; PEP, phosphoenolpyruvate; TP, triose phosphates.

Table 3-3

Stoichiometry and carbon transformations for the reactions in the network of mammalian glucose metabolism. Abbreviations of metabolites are the same as in Figure 3-4.

Reaction number	Reaction	Carbon transformations*
1	$[U^{13}C]Gluc \rightarrow Gluc$	$abcdef \rightarrow abcdef$
2	$Gluc \rightarrow G6P[M]$	$abcdef \rightarrow abcdef$
3	$G6P[M] \rightarrow TP[M] + TP[M]$	$abcdef \rightarrow cba + def$
4	$G6P[M] \rightarrow R5P[M] + CO_2$	$abcdef \rightarrow bcdef + a$
5	$R5P[M] + R5P[M] \rightarrow S7P[M] + TP[M]$	$abcde + ABCDE \rightarrow abABCDE + cde$
6	$S7P[M] + TP[M] \rightarrow G6P[M] + E4P[M]$	$abcdefg + ABC \rightarrow abcABC + defg$
7	$R5P[M] + E4P[M] \rightarrow G6P[M] + TP[M]$	$abcde + ABCD \rightarrow abABCD + cde$
8	$TP[M] \rightarrow Pyr[M]$	$acb \rightarrow abc$
9	$Pyr[M] \rightarrow Lact$	$abc \rightarrow abc$
10	$Lact[O] \rightarrow Lact$	$abc \rightarrow abc$
11	$Lact \rightarrow other$	$abc \rightarrow abc$
12	$Lact \rightarrow Pyr[L]$	$abc \rightarrow abc$
13	$Pyr[L] + CO_2[L] \rightarrow OAC[L]$	$abc + A \rightarrow abcA$
14	$OAC[L] + AcCoA[L] \rightarrow SucCoA[L] + 2 CO_2$	$abcd + AB \rightarrow ABbc + a + d$
15	$SucCoA[L] \rightarrow Fum[L]$	$abcd \rightarrow (\frac{1}{2} abcd + \frac{1}{2} dcba)$
16	$Fum[L] \leftrightarrow OAC[L]$	$(\frac{1}{2} abcd + \frac{1}{2} dcba) \leftrightarrow abcd$
17	$FA[L] \rightarrow AcCoA[L]$	$ab \rightarrow ab$
18	$AcCoA[L] + AcCoA[L] \rightarrow ketone[L]$	$ab + AB \rightarrow abAB$
19	$OAC[L] \rightarrow PEP[L] + CO_2$	$abcd \rightarrow abc + d$
20	$PEP[L] \rightarrow Pyr[L]$	$abc \rightarrow abc$
21	$PEP[L] \rightarrow TP[L]$	$abc \rightarrow abc$
22	$Glycerol[O] \rightarrow TP[L]$	$abc \rightarrow abc$
23	$TP[L] + TP[L] \rightarrow G6P[L]$	$abc + ABC \rightarrow cbaABC$
24	$Glycogen[L] \rightarrow G6P[L]$	$abcdef \rightarrow abcdef$
25	$G6P[L] \rightarrow Gluc$	$abcdef \rightarrow abcdef$
26	$Gluc \rightarrow other$	$abcdef \rightarrow abcdef$

* For each compound carbon atoms are identified using lower case letters to represent successive carbon atoms of each compound. Uppercase letters represent a second compound in the reaction. Because fumarate is a rotationally symmetric molecule no distinction can be made between carbon atoms 1 and 4, and carbon atoms 2 and 3.

glucose turnover, whereas in the study by Sunehag tracer infusion contributed very significantly to the total rate of glucose appearance (~58%).

The MIDs of plasma glucose and lactate from these two studies are shown in Table 3-4. One representative data set was selected from each study. The data was corrected for natural isotope enrichments of ^{13}C and other stable isotopes. In keeping with previous conventions, we represent mass isotopomers of glucose as M_i and mass isotopomers of lactate as m_i . We fitted both data sets to the glucose metabolic model assuming measurement errors of 0.1 mol% abundance for all measured abundances. In both cases a good fit was obtained, resulting in a minimized sum of squared residuals of 0.3 and 0.5 for the Tayek and Sunehag data, respectively. We then calculated accurate confidence intervals for all fluxes in the network. The results are summarized in Table 3-5.

One of the key fluxes in this model is the rate of gluconeogenesis, i.e. de novo glucose synthesis from precursors such as lactate, amino acids and glycerol. The calculated confidence intervals for this flux from the two studies were significantly different (see Figure 3-5). For the study by Tayek et al., the observed flat profile of the confidence interval indicates that gluconeogenesis flux cannot be determined precisely. There was a wide range of equally likely solutions for the gluconeogenesis flux, ranging between 3.6 and 14.4 $\mu\text{mol}/\text{kg}/\text{min}$, for which the minimized sum of squared residuals was the same. Other fluxes in this model display similar flat profiles. Thus, in this case we could not identify a unique optimal solution for fluxes, but rather a range of optimal solutions as is indicated in Table 3-5. In cases like this, it is informative to determine the search direction of fluxes at the optimal solution, i.e. Δd from Eq. 3.26. This vector reveals metabolic pathways that cannot be determined independently of one another. Considering the gluconeogenesis flux, we found that it was not possible to distinguish between hepatic glycerol intake and glycogenolysis. Indeed, several authors recently raised concerns regarding the $[\text{U-}^{13}\text{C}]$ glucose method. Based on physiological insight Landau and colleagues concluded that the only fluxes that can be determined from this system are hepatic glucose output (HGO) and the fractional contribution of pyruvate to gluconeogenesis (Landau et al., 1998).

Table 3-4

Measured and fitted mass isotopomer abundances. Mass isotopomer of plasma glucose (M_i) and plasma lactate (m_i) were measured after constant infusion of $[U-^{13}C]$ glucose (molar abundances, mol%). Mass isotopomer abundances were corrected for natural isotope enrichments.

Mass isotopomer	Tayek study*		Sunehag study**	
	Measured	Fitted	Measured	Fitted
M_0	95.20	95.20	28.90	28.91
M_1	0.29	0.31	4.40	4.39
M_2	0.22	0.19	3.36	3.38
M_3	0.33	0.33	3.65	3.66
M_4	0.00	0.00	0.80	0.82
M_5	0.00	0.00	0.47	0.42
M_6	3.96	3.96	58.42	58.43
m_0	98.07	98.07	57.78	57.78
m_1	0.38	0.36	5.48	5.50
m_2	0.19	0.22	5.23	5.21
m_3	1.36	1.36	31.51	31.51

* Data was taken from Tayek et al. (1996) for diabetic subject no. 5 (D5). Tracer infusion rate was $0.59 \mu\text{mol/kg/min}$ $[U-^{13}C]$ glucose.

** Data was taken from Sunehag et al. (2003) for the infant receiving supplementation of glucose, amino acids and parental lipids (g + AA + IL). Tracer infusion rate was $17 \mu\text{mol/kg/min}$ $[U-^{13}C]$ glucose.

Table 3-5

Estimated glucose metabolic fluxes and their 95% confidence intervals. Fluxes ($\mu\text{mol}/\text{kg}/\text{min}$) were estimated from mass isotopomers of glucose and lactate using the network model of mammalian glucose metabolism in Figure 3-4.

Tissue	Flux	Tayek study (1996)		Sunehag study (2003)	
		Best fit*	95% Conf.	Best fit*	95% Conf.
Plasma	Tracer infusion rate	0.59	0.59	17.0	17.0
	Influx of unlabeled lactate	0 – 32	0 – 49	5.6 - 36.1	5.1 – 36.4
Muscle	Cori cycle**	1.8 – 15.0	1.1 – 15.6	4.5 - 29.2	4.2 – 29.3
	Pentose pathway	0	0 – 8.5	3.6 - 23.2	3.1 – 23.8
Liver	Hepatic glucose output (HGO)	14.3	13.7 – 15.0	12.2	12.1 – 12.3
	Glycogenolysis (GL)	0 – 10.7	0 – 11.5	5.3	4.3 – 5.6
	Gluconeogenesis (GNG)	3.6 – 14.4	2.5 – 15.0	6.9	6.6 – 7.9
	Glycerol uptake	0 – 21.5	0 – 23.1	0.3	0 – 3.1
	Unlabeled anaplerotic sources	0 – 9.0	0 – 26.6	0.3	0 – 3.1
	TCA Cycle	10 – 22	0.2 – 180	18.0	14.3 – 21.1
	Pyruvate carboxylase (PC)	15.1	5.3 – 23.9	13.5	12.6 – 14.4
	Pyruvate kinase (PK)	6.0 – 12.1	0 – 22.2	0	0 – 0.8
	Backward flux of fumarase	6 – 19	0 – 550	40.0	28.9 – 56.0
	Ketogenesis	0 – Inf	0 – Inf	0 - Inf	0 – Inf

* 'Best fit' denotes flux value at the optimal solution, or the region of flux values with the same minimized sum of squared residuals.

** Cori cycle refers to the total flux from plasma glucose to plasma lactate.

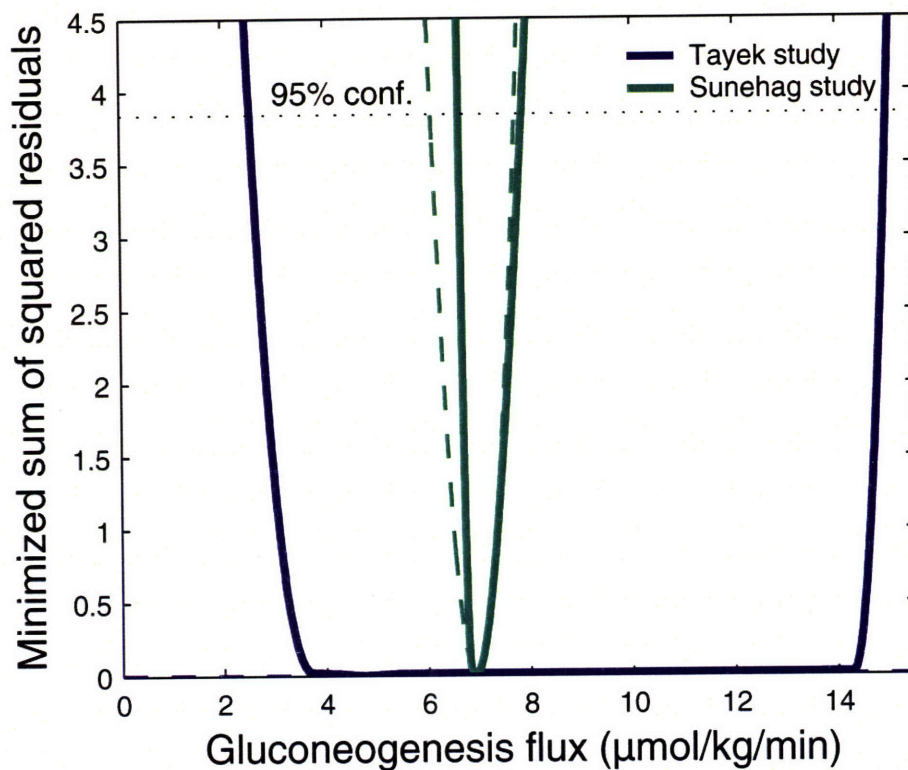


Figure 3-5: Confidence intervals of gluconeogenesis flux for selected studies by Tayek and Sunebag. The minimized sum of squared residuals minus the optimal solution value is plotted against the gluconeogenesis flux. The solid line represents the profile determined with our method, and the dashed line represents the profile obtained from the local estimate of standard deviation. The dashed horizontal line represents the threshold values for the 95% confidence interval of gluconeogenesis flux.

Our results support their conclusions for the Tayek study. Note that the only two fluxes that were uniquely determined were HGO and the pyruvate carboxylase flux, which is the first step in the pathway from pyruvate to glucose.

We also calculated local standard deviations for fluxes at the optimal solution to compare approximated confidence intervals with the results obtained by our method. For most fluxes the approximated values did not agree with the true confidence intervals. The only exception was HGO flux for which the local standard deviation reasonably described the true uncertainty ($14.3 \pm 0.4 \mu\text{mol/kg/min}$). We also determined the most important measurements for the estimated gluconeogenesis flux. The two most important measurements were glucose mass isotopomers M_4 , M_5 . However, in this study neither of these isotopomers were formed in significant abundance. We can therefore conclude that in order to estimate the gluconeogenesis flux in this system one must either find a more precise technique to measure glucose isotopomers M_4 and M_5 , or find an alternative method to quantify either hepatic glycerol uptake or hepatic glycogenolysis.

In contrast, Sunehag applied a significantly higher tracer infusion rate, i.e. $17 \mu\text{mol/kg/min}$ vs. $0.59 \mu\text{mol/kg/min}$ as employed by Tayek et al. Consequently, glucose isotopomers M_4 and M_5 were formed in significant abundance, i.e. 0.80 and 0.47 mol% respectively. In this case, MFA produced a unique solution for the gluconeogenesis flux ($6.9 \mu\text{mol/kg/min}$) with a narrow 95% confidence interval ($6.6 - 7.9 \mu\text{mol/kg/min}$). Here, glucose mass isotopomers M_4 , M_3 and M_5 were the most important measurements for estimating gluconeogenesis flux with relative contributions of 59%, 18% and 9% respectively. Other fluxes in this system were also estimated more precisely than in the Tayek study (see Table 3-5). Here, most fluxes had a well defined optimal flux value, with the notable exceptions of the influx of unlabeled lactate, the Cori cycle flux, the pentose pathway in muscle, and hepatic ketogenesis. Comparing the overall quality of flux results from both studies it is clear that high tracer infusion rates are desirable in order to obtain reliable flux estimates in this system. The main concern is, however, that high infusion rates of glucose may alter endogenous glucose metabolism. Therefore, the optimal infusion rate will depend on the desired precision of fluxes and the ability to measure glucose mass isotopomers M_4 , M_3 and M_5 precisely.

3.4 Discussion

Metabolic flux analysis based on the application of stable isotopes and subsequent measurement of labeling patterns is a powerful technique for measuring metabolic fluxes *in vivo*. However, reliable physiological knowledge can only be obtained from these studies if the statistical significance of estimated fluxes is determined as well. This is complicated by the highly nonlinear relationships inherent to isotopic systems. Unfortunately, detailed statistical analysis of estimated metabolic fluxes is still not common practice. Most often, fluxes obtained from stable isotope studies are reported without any statistical significance. In some cases, linearized statistics have been used to describe the uncertainty (Arauzo-Bravo and Shimizu, 2003; Wiechert et al., 1997). Wiechert et al. showed that linearized statistical properties are inappropriate for large exchange fluxes. A nonlinear mapping of exchange flux improved the approximation for an example network probed with NMR measurements (Wiechert et al., 1997). In this contribution, however, we have shown that even for very simple systems probed with MS measurements confidence intervals of net and exchanges fluxes are highly nonlinear and non-symmetric. The true confidence intervals of fluxes may be much smaller, or much larger than the linearized confidence intervals suggest. For example, van Winden et al. determined the 90% confidence interval for the split ratio between glycolysis and the pentose phosphate pathway in yeast from MS measurements of intracellular metabolites (van Winden et al., 2005). The 90% confidence interval ranged from 0.05 to 0.52, indicating that the split ratio could not be determined precisely due to a correlation with the glycogen flux. In this study, we have also provided examples of fluxes with very large confidence intervals. The gluconeogenesis flux determined from experiments with low [U-¹³C]glucose infusion could not be determined accurately resulting from a correlation between hepatic glycerol influx and glycogenolysis. These types of problems cannot be detected by MFA alone, or using linearized statistics. To eliminate these problems, nonlinear statistical tools are required for careful design of tracer experiments.

In summary, in this contribution we have presented comprehensive techniques that allow accurate determination of the significance of fluxes obtained from stable isotope measurements. The advantage of our approach is that it provides an efficient method to

calculate nonlinear confidence intervals that reflect the true uncertainty of estimated fluxes. It allows the construction of confidence intervals in underdetermined and over-determined systems. The derived analytical expressions for sensitivities of fluxes with respect to measurements and measurement errors allow the identification of key measurements for specific fluxes. We applied these methods to re-analyze the statistical significance of estimated gluconeogenesis fluxes from two human studies with [U-¹³C]glucose as tracer. As a result, we identified a theoretical limitation to estimate the gluconeogenesis flux in one of the studies. We confirmed concerns raised by several authors and identified the source of the limitations, i.e. low isotopic abundance of key mass isotopomers resulting in the inability to distinguish between hepatic glycerol intake and glycogenolysis. Through these examples we have demonstrated the importance of rigorous design and analysis of tracer experiments and the importance of calculating accurate flux confidence intervals for reliable interpretation of physiological studies.

APPENDIX 3.A**Numerically stable form for matrix inverse using singular value decomposition**

Inversion of Hessian matrix H may be numerically unstable if H is singular, or ill conditioned. A numerically stable form for the inverse may be obtained from singular value decomposition of H (Foster, 1986):

$$H = U \cdot S \cdot V^T \quad (3.A1)$$

The diagonal elements of matrix S correspond to the eigenvalues of H . Eigenvalues smaller than a given tolerance, for example $\text{tol} = 10^{-10}$, are considered insignificant. Matrix V is then split into two matrices, $V1$ and $V2$. The columns of $V1$ form an orthogonal basis for the column space of H , while $V2$ provides an orthogonal basis for the null space of H .

$$V = [V1 \mid V2] \quad (3.A2)$$

A numerically stable form for the inverse is then given by:

$$H^{-1} \approx (H + \text{tol} \cdot V2 \cdot V2^T)^{-1} \quad (3.A3)$$

APPENDIX 3.B

Algorithm for covariance-weighted flux estimation

- Choose starting values for free fluxes, in general random values are preferred.
- Set the iteration counter $k = 0$.
- At each iteration k :
 1. Simulate measurements x for current fluxes.
 2. Calculate the sensitivity matrix dx/du .
 3. Calculate the Hessian matrix H and the Jacobian J using Eq. 3.8.
 4. Calculate Δu using Eq. 3.10. Additional inequality constraints may be included here.
 5. Check for convergence. If the error in the necessary condition is smaller than the desired tolerance, then stop. Otherwise, go to step 6.
 6. Update the fluxes using Eq. 3.11.
 7. Set the iteration counter $k \leftarrow k + 1$, and go to step 1.
- Transform the free fluxes into individual metabolic fluxes using Eq. 3.2.

APPENDIX 3.C

Controlling the step size for determination of accurate flux intervals

In order to calculate accurate confidence intervals the step size 'h' in Eq. 3.20 needs to be carefully controlled. Using very small step size increases the number of iterations and is computationally demanding. On the other hand, using a step size that is too large results in significant loss of accuracy due to the inability to follow nonlinearities in the system. Using Taylor series expansion, we can express the increase in the objective function formally as a polynomial function of the step size:

$$\Delta\Phi = a_1 \cdot h + a_2 \cdot h^2 + a_3 \cdot h^3 + \dots \quad (3.B1)$$

The first two coefficients a_1 and a_2 are given by:

$$a_1 = 2 \cdot \Delta u^T \cdot J \quad (3.B2)$$

$$a_2 = \Delta u^T \cdot H \cdot \Delta u \quad (3.B3)$$

Higher order coefficients are normally not calculated, because that would require computation of higher order derivatives of simulated measurements with respect to fluxes, i.e. d^2x/du^2 , d^3x/du^3 , which is computationally demanding and requires large amounts of memory to store multidimensional matrices. However, we can approximate the third coefficient a_3 computationally at each iteration. For this purpose, we calculate the actual increase in the objective function $\Delta\Phi^{\text{actual}}$ for the flux map given by $(u + h \cdot \Delta u)$ and compare this to the predicted increase in the objective function using the quadratic approximation, i.e. $\Delta\Phi^{\text{approx}} = a_1 \cdot h + a_2 \cdot h^2$. The value for a_3 is then approximated from the difference between $\Delta\Phi^{\text{actual}}$ and $\Delta\Phi^{\text{approx}}$:

$$a_3 \approx \frac{|\Delta\Phi^{\text{actual}} - \Delta\Phi^{\text{approx}}|}{h^3} \quad (3.B4)$$

If the difference is too large then the step size needs to be decreased and if the difference is very small then we may increase the step size without loss of accuracy. For our calculations we require the difference to be less than 10^{-4} at each iteration. The step size h is updated at each iteration according to the following formula:

$$h = \sqrt[3]{\frac{10^{-4}}{a_3}} \quad (3.B5)$$

APPENDIX 3.D**Algorithm for accurate determination of confidence intervals of fluxes**

- Calculate the variance-weighted sum of squared residuals at the optimal solution $\Phi(\hat{u})$.
- Choose a confidence level $(1-\alpha)$, and calculate the corresponding threshold value $\chi^2_{1-\alpha}(1)$, e.g. $\chi^2_{0.95}(1) = 3.84$ for the 95% confidence interval.
- For each flux i :
 - Initialize all fluxes at the optimal solution obtained from flux estimation, $u_{(0)} = \hat{u}$.
 - Initialize the Lagrange multiplier at $\lambda_{(0)} = 0$.
 - Initialize the variables vector $d_{(0)} = [u_{(0)} \lambda_{(0)}]^T$.
 - Set the iteration counter $k = 0$.
 - At each iteration k :
 1. Simulate measurements x for current fluxes.
 2. Calculate the sensitivity matrix dx/du .
 3. Calculate the variance-weighted sum of squared residuals $\Phi(u)$.
 4. Calculate the Hessian matrix H and the Jacobian J using Eq. 3.8.
 5. Calculate matrix A and vector b using Eq. 3.24.
 6. Calculate Δd using Eq. 3.26. Additional inequality constraints may be included here.
 7. Update the step size h as described in Appendix 3.C.
 8. Check for convergence. If the flux value for flux i reaches the upper bound, or if $\Phi(u) - \Phi(\hat{u}) > \chi^2_{1-\alpha}(1)$ then stop. Otherwise, go to step 9.
 9. Update the variables vector d using Eq. 3.27.
 10. Transform the free fluxes into individual metabolic fluxes using Eq. 3.2.
 11. Record current value for flux i and the corresponding $\Phi(u)$.
 12. Set the iteration counter $k \leftarrow k + 1$, and go to step 1.
 - Initialize all fluxes at the optimal solution obtained from flux estimation, $u_{(0)} = \hat{u}$.
 - Initialize the Lagrange multiplier at $\lambda_{(0)} = 0$.
 - Initialize the variables vector $d_{(0)} = [u_{(0)} \lambda_{(0)}]^T$.

- Set the iteration counter $k = 0$.
- At each iteration k :
 1. Simulate measurements x for current fluxes.
 2. Calculate the sensitivity matrix dx/du .
 3. Calculate the variance-weighted sum of squared residuals $\Phi(u)$.
 4. Calculate the Hessian matrix H and the Jacobian J using Eq. 3.8.
 5. Replace $-N_i$ for N_i in Eq. 3.24, and calculate matrix A and vector b .
 6. Calculate Δd using Eq. 3.26. Additional inequality constraints may be included here.
 7. Update the step size h as described in Appendix 3.C.
 8. Check for convergence. If the flux value for flux i reaches the lower bound, or if $\Phi(u) - \Phi(\hat{u}) > \chi^2_{1-\alpha}(1)$ then stop. Otherwise, go to step 9.
 9. Update the variables vector d using Eq. 3.27.
 10. Transform the free fluxes into individual metabolic fluxes using Eq. 3.2.
 11. Record current value for flux i and the corresponding $\Phi(u)$.
 12. Set the iteration counter $k \leftarrow k + 1$, and go to step 1.

APPENDIX 3.E

Metabolic model of mammalian glucose metabolism

We constructed a detailed metabolic model for mammalian glucose metabolism in which we consider all major pathways that affect the observed labeling patterns of plasma lactate and glucose (Figure 3-4). Here, [U-¹³C]glucose is infused into the blood, taken up by the tissues and metabolized by glycolysis and pentose phosphate pathway to form lactate, which is then released into circulation. While the infused glucose is comprised of the fully labeled M_6 isotopomer, the action of the glycolysis pathway and scrambling in the pentose pathway produces both fully labeled m_3 , and partially labeled m_1 and m_2 lactate molecules. The labeling of plasma lactate is additionally diluted by unlabeled endogenous sources, such as from glycogen breakdown in the muscle and amino acid oxidation. This dilution of plasma lactate labeling is modeled here by one lumped dilution flux. Lactate then enters the liver where it is converted to pyruvate. We assume that plasma lactate and hepatic pyruvate are at isotopic equilibrium, which has been experimentally validated by several authors (Wykes et al., 1998). In the conversion to glucose, pyruvate undergoes carboxylation to form oxaloacetate that is shared with the TCA cycle. Scrambling of labeling may occur at the point of fumarate since fumarate is rotationally symmetric. The conversion of amino acids to glucose without pyruvate as an intermediate, such as from aspartate and glutamine, is modeled by one lumped dilution flux into the succinyl-CoA pool. Fatty acid oxidation, ketogenesis and the possibility for pyruvate recycling through the action of pyruvate kinase are also considered in the model. Glycerol is another potential gluconeogenic precursor that we consider. Finally, the labeling of hepatic glucose-6-phosphate pool is diluted by glycogenolysis pathway, i.e. the release of unlabeled glucose molecules from glycogen storages. In our model, the reaction between oxaloacetate and fumarate is the only observable reversible reaction. The remaining reactions in the model may therefore be considered irreversible without affecting flux calculations. The list of all reactions in this model together with the corresponding carbon transitions are shown in Table 3-3.

Chapter 4

GC/MS analysis of amino acids

4.1 Introduction

4.1.1 Flux analysis requires accurate data

Accurate assessment of isotopomer distributions of cellular amino acids is of great importance for quantitative analysis of cell physiology. In carbon labeling experiments ^{13}C -distributions measured by gas chromatography / mass spectrometry (GC/MS) and nuclear magnetic resonance (NMR) provide rich information for estimating metabolic fluxes in complex biological systems. The NMR technique requires expensive equipment and fairly high concentration of metabolites. In contrast, GC/MS is a rapid and much more sensitive technique. Powerful computational tools have been developed for quantitative interpretation of mass isotopomer data; however, the statistical significance of carbon-13 tracer studies has been limited due to inaccuracies and imprecision in isotopomer data. Metabolic flux analysis is very sensitive to measurement errors due to the highly nonlinear relationships of models that link fluxes and isotopomer abundances. Thus, small errors in isotopomer data may result in large errors in estimated fluxes. It is therefore essential that isotopomer data are accurate and precise. Based on preliminary sensitivity analysis of realistic metabolic networks we determined that errors in mass isotopomer abundances should be less than 0.5 mol% for most systems. The required accuracy depends mainly on the complexity of the network model (i.e. degrees of freedom), and the number of redundant measurements. In general, complex networks with fewer redundant measurements will require more precise data than more simple systems with large number of measurements.

4.1.2 Potential sources of error

GC/MS analysis of cellular components provides rich information on isotopomer distributions of common metabolites. However, several studies have shown that mass isotopomer data may under-, or overestimate true enrichments. For example, it was reported that metabolite concentration may affect the accuracy of GC/MS data for fatty acid methyl esters (Fagerquist et al., 2001; Patterson & Wolfe, 1993). It was shown that isotopomer ratios deviated significantly from expected natural abundance ratios with increasing metabolite concentration. Although it is uncertain what the exact cause is of this concentration dependence, gas phase ion/molecule chemistry in the ionization chamber appears to be a significant factor (Fagerquist et al., 2001). Klapa et al. reported that mass spectra obtained with ion trap mass spectrometers may suffer from hydrogen abstraction and other artifacts, resulting in inaccurate mass isotopomer ratios and significant M-1 abundances (Klapa et al., 2003). Empirical corrections were proposed to reduce the effect of these artifacts; however, it is unclear how accurate these corrections are for labeled samples. Furthermore, errors may be introduced due to incomplete resolution of mass spectra in time, or in the m/z domain. For example, if compounds are not completely resolved by gas chromatography, co-eluting compounds will contribute to the observed mass spectra. Mass spectra may also overlap in the m/z domain. For example, electron impact ionization typically generates more than 20 ion fragments for each metabolite and some of these fragments may be overlapping. Thus, even if compounds are well separated by chromatography, mass isotopomer distributions of adjacent fragments may still be unresolved. In practice, it is not possible to deconvolute unresolved mass spectra with the desired accuracy of 0.5 mol%. It is important to identify these situations a priori. Finally, errors may be introduced during integration of mass chromatograms due to inaccurate integration algorithms, or failure to account for background noise in MS data.

4.1.3 Reported accuracy and precision in literature

Detailed assessment of accuracy and precision of MS data has received limited attention in the literature. Mass isotopomer abundances from tracer studies are often reported without any indication of error. Dauner and Sauer (2000) were the first to analyze the accuracy of MS

data from TBDMS derivatized amino acid by comparing mass isotopomer abundances of unlabeled amino acids with theoretical abundances. They reported differences between observed and theoretical abundances up to 6 mol%. Of the 38 accepted amino acid fragments, 8 fragments had errors <0.5 mol%, 20 fragments had errors 1-2 mol%, 13 fragments had errors 2-3 mol%, and 10 fragments had errors >2 mol%. Klapa et al. (2003) reported standard deviations for mass isotopomer abundances of TBDMS derivatized amino acids ranging between 0.2 and 4 mol%, with the majority of standard deviations larger than 0.5 mol%. Here, we report our findings from an extensive study of GC/MS analysis of TBDMS derivatized amino acids. In this study we validated the identity of amino acid fragments using ^{13}C -labeled standards, identified potential sources of inaccuracy and imprecision in MS data, and established a technique to minimize these errors. The main result of this work is a procedure for accurate and precise assessment of mass isotopomer distributions of cellular amino acids, with an accuracy of 0.3 mol% and precision of 0.2 mol%, or better.

4.2 Materials and methods

4.2.1 Labeled amino acid standards

A mixture of [^{13}C]algal amino acids (99+ At% ^{13}C) and [^{13}C]aspartic acid (99 At% ^{13}C) were purchased from IsoTec Inc. (Miamisburg, OH). [^{13}C]glutamic acid (99 At% ^{13}C) was purchased from Cambridge Isotope Laboratories Inc. (Andover, MA).

4.2.2 Cellular amino acids

Cellular amino acids were obtained hydrolyzed biomass samples taken from batch cultures of *E. coli*. In one culture no tracers were used (as control), and in a separate culture a mixture of [^{13}C]glucose and [^{13}C]glucose was provided as carbon-13 input. Samples from these cultures were centrifuged and the supernatant separated from the biomass pellet. About 20 mg of wet biomass pellet was transferred to 700 μL of 6 N HCl and heated at 110°C for 24 hrs in a closed vacuum hydrolysis tube. After cooling to room temperature the solvent was

evaporated and the residue dissolved in 150 μ L of distilled water and filtered through a 0.2 μ m pore size filter to remove cell debris. The filtrate was then evaporated to dryness.

4.2.3 TBDMS derivatization

Amino acids were dissolved in 50 μ L pyridine followed by addition of 70 μ L N-methyl-N-(tert-butyldimethyl-silyl)-trifluoroacetamide (MTBSTFA). The mixture was heated at 60°C for 30 min, allowed to cool to room temperature and transferred to injection vial for GC/MS analysis.

4.2.4 GC/MS Analysis

Gas Chromatography-Mass Spectrometry (GC/MS) analysis was performed using HP 5890 Series II GC (Gas Chromatograph) equipped with a DB-1701 [30 m x 0.25 mm (inner diameter) x 0.25 μ m] capillary column, connected to HP 5971 quadrupole MSD (Mass Selective Detector) operating under ionization by electron impact (EI) at 70 eV. The mass spectrometer was calibrated using the 'Max Sensitivity Autotune' setting. The injection volume was 1 μ L and samples were injected in purged splitless mode. The amount of sample analyzed was controlled by varying the purge activation time between 1 sec and 1.5 min. Helium flow was maintained at 0.74 mL/min via electronic pressure control. The injection port temperature was 270°C. The temperature of the column was started at 100°C for 1.5 min, increased to 130°C at 20°C/min and increased to 220°C at 10°C/min and held for 3 min. The temperature was then increased to 280°C at 5°C/min and held for 3 min. The interface temperature was maintained at 300°C. Mass spectra were analyzed in the mass range 195-445 atom mass units (amu) at a rate of 2.7 scans/sec. Measured intensities were corrected for the contribution of noise (baseline correction), and mass isotopomer distributions were obtained by integration. Mass isotopomer values for each fragment were expressed as fractional abundances, i.e. for each fragment the sum of all mass isotopomers equals one.

4.2.5 Natural isotope abundances

Most elements of biological interest (including C, H, O, N, and S) have two or more stable isotopes. Relatively large variations occur for the ^{13}C isotope in nature, varying between 1.097 At% for C4-plants and 1.082 At% for C3-plants (Coplen et al., 2002). This small difference may contribute to significant differences in the calculated natural isotopomer distributions of molecules containing large number of carbon atoms, such as TBDMS derivatized amino acids. For our calculations we used 1.082 At% for the natural abundance of ^{13}C . For other elements we assumed the following isotope abundances: ^2H (0.0156 At%), ^{15}N (0.366 At%), ^{17}O (0.038 At%), ^{18}O (0.204 At%), ^{29}Si (4.69 At%), ^{30}Si (3.09 At%), ^{33}S (0.749 At%), ^{34}S (4.197 At%), ^{36}S (0.015 At%) (Coplen et al. 2002).

4.3 Results

4.3.1 TBDMS derivatization of amino acids

Amino acids are not volatile enough to be analyzed by GC/MS directly. Therefore, chemical modification of the polar side groups, e.g. -OH, -NH₂, -COOH, is required. Here, amino acids were chemically modified to their respective tert-butyldimethylsilyl (TBDMS) derivatives for GC/MS analysis (see Figure 4-1)

4.3.2 Gas chromatography of TBDMS derivatized amino acids

Figure 4-2 shows a representative total ion chromatogram from GC/MS analysis of TBDMS derivatized amino acids from hydrolyzed biomass samples. The retention times of the detected amino acids are reported in Table 4-1. We detected 15 of the 20 amino acids in the hydrolyzed biomass samples. Cysteine and tryptophan were lost in hydrolysis due to oxidation, and glutamine and asparagine were deamidated to glutamate and aspartate, respectively. Histidine was not detected. The insert in Figure 4-2 shows the observed mass spectrum of TBDMS derivatized aspartic acid that eluted at 17.1 min. TBDMS derivatized amino acid displayed characteristic fragmentation patterns resulting from electron impact

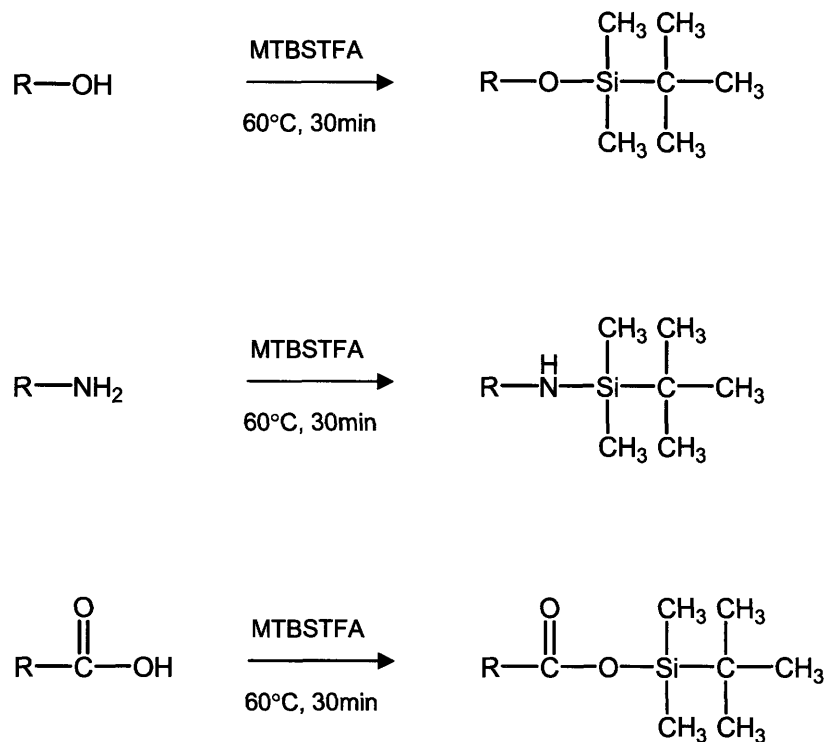


Figure 4-1: Schematic of TBDMS derivatization of polar side groups. Amino acids and other biological metabolites are easily derivatized to their respective TBDMS derivatives in preparation for GC/MS analysis.

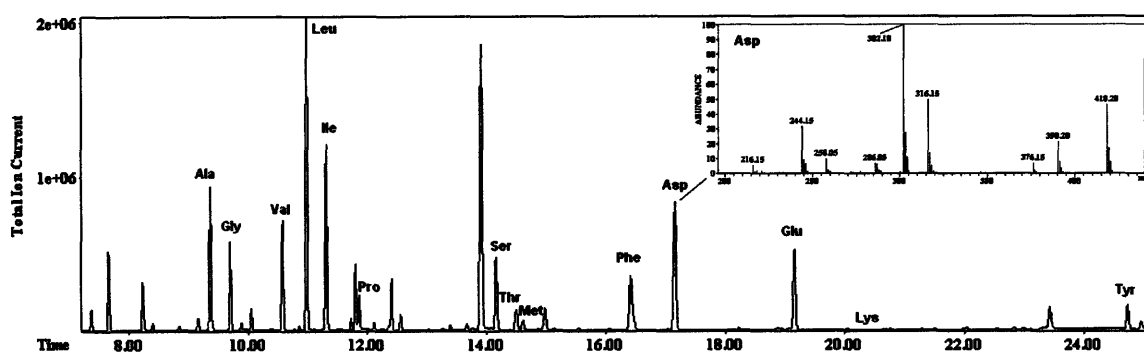


Figure 4-2: Representative total ion chromatogram from GC/MS analysis of TBDMS derivatized amino acids from hydrolyzed biomass. The total ion chromatogram corresponds to the sum of ion intensities measured at each scan. The insert shows the electron ionization mass spectrum of TBDMS derivatized aspartic acid.

Table 4-1

Gas chromatography retention times and main ion fragments of TBDMS derivatized amino acids. Cellular amino acids from hydrolyzed biomass samples were derivatized with TBDMS and analyzed by electron impact GC/MS.

Amino acid	Retention time	Molecular weight*	Main ion fragments (m/z)
Alanine	9.3 min	317	232, 260
Glycine	9.7 min	303	218, 246
Valine	10.5 min	345	260, 288, 302
Leucine	10.9 min	359	200, 274, 302
Isoleucine	11.3 min	359	200, 274, 302
Proline	11.8 min	343	258, 286
Serine	14.1 min	447	230, 288, 302, 362, 390
Threonine	14.4 min	461	376, 404, 417
Methionine	14.6 min	377	218, 244, 292, 320
Phenylalanine	16.4 min	393	234, 302, 308, 336
Aspartate	17.1 min	475	244, 258, 302, 316, 376, 390, 418
Glutamate	19.1 min	489	272, 330, 358, 404, 432
Lysine	20.3 min	488	329, 431
Arginine	22.5 min	515	340, 442
Tyrosine	24.7 min	523	302, 364

* Molecular weight of TBDMS derivatized amino acids.

ionization (EI). Characteristic for TBDMS derivatized amino acids were ion fragments at $m-57$, $m-85$ and $m-159$, where 'm' denotes the molecular weight of the derivatized amino acid.

4.3.3 Integration of mass chromatograms

To obtain accurate mass isotopomer distributions (MIDs) from raw GC/MS data, mass chromatograms have to be integrated over the full peak range of the corresponding amino acid. Mass isotopomer ratios obtained at each scan have a much lower signal-to-ratio and may not reflect the true isotopomer distribution. For example, it is well known that mass isotopomers may separate on the GC column and elute at slightly different times. This effect is generally more significant for ^2H -labeled compounds than for ^{13}C -labeled compounds. In either case, the observed mass isotopomer ratios will be different at the beginning and the end of a metabolite peak. Several software packages allow one to integrate mass chromatograms and calculate mass isotopomer distributions. However, we found that different integration algorithms often produced significantly different integrated mass isotopomer distributions. Here, we will illustrate two potential sources of error due to incorrect integration. First, it is important that all mass chromatograms of a particular metabolite are integrated over the same scan range, i.e. time interval. If peak detection algorithms are applied to each mass chromatogram individually then slightly different integration bounds may be identified for each ion, resulting in biased integrated intensities. Furthermore, it is necessary to correct measured intensities for background noise. This correction should be applied to each mass chromatogram individually, because the level of background noise may be different at each scanned ion. In our experience, good calibration of the mass spectrometer reduced the level of background noise, and the use of high electron multiplier voltages (EMV) increased background noise. To illustrate these effects we quantified the mass isotopomer distribution of glycine ion fragment at m/z 246-250 in the unlabeled biomass sample. Three integration methods were used. In Method 1, fixed integration bounds were used for each mass chromatogram and baseline correction was applied. In Method 2, each mass chromatogram was integrated independently, which could result in slightly different integration bounds for each mass chromatogram. Correction for baseline was applied. In Method 3, fixed integration bounds were used for each mass

chromatogram, but no baseline correction was applied. Figure 4-3 clearly shows the differences between the integration methods. The shaded areas in Figure 4-3 correspond to the integrated intensities. Fractional abundances were obtained from the integrated intensities by dividing the integrated intensity by the sum of all intensities. In Table 4-2 we compare the calculated MID for glycine-246 to the theoretical MID. Overall, the first integration method produced mass isotopomer abundances that corresponded best with theoretical abundances, i.e. less than 0.1 mol% deviation. The second method overestimated M+0 abundance slightly (+0.4 mol%), and underestimated M+1 and M+2 abundances (-0.1 and -0.2 mol%) caused by slightly smaller integration bounds for the M+1 and M+2 mass chromatograms. The third method, i.e. no baseline correction, produced the largest errors. The M+0 abundance was underestimated by 2.2 mol% and other abundances were overestimated by 0.3-0.7 mol%. It should be clear that without baseline correction low abundance isotopomers will always be overestimated, and the most abundant mass isotopomer will be underestimated. Analysis of other amino acid fragments supported all of these findings. Taken together, our results indicate that the first integration method is the most accurate one: using fixed integration bounds for all mass chromatograms and applying baseline correction. This integration method was used in the remainder of this work.

4.3.4 Concentration dependence of mass isotopomer distributions

We found significant correlation between measured mass isotopomer abundances and the amount of amino acid that was analyzed. In this study, all amino acid samples were analyzed 35 times at varying concentrations. The observed abundances varied up to 2 mol% depending on the amount of amino acid analyzed. Figure 4-4 shows the observed mass isotopomer abundances for glycine fragment at m/z 218 plotted against the total ion counts for this fragment (i.e. sum of integrated intensities at m/z 218-222). The dashed horizontal line in Figure 4-4A represents the expected abundances for unlabeled glycine. We found good agreement between the observed and theoretical abundances for low concentrations of the sample, however, the M+0 abundance of unlabeled glycine decreased with increasing glycine concentration and M+1 and M+2 abundances increased. We found a near linear relationship for this concentration effect. All other fragments of TBDMS derivatized amino

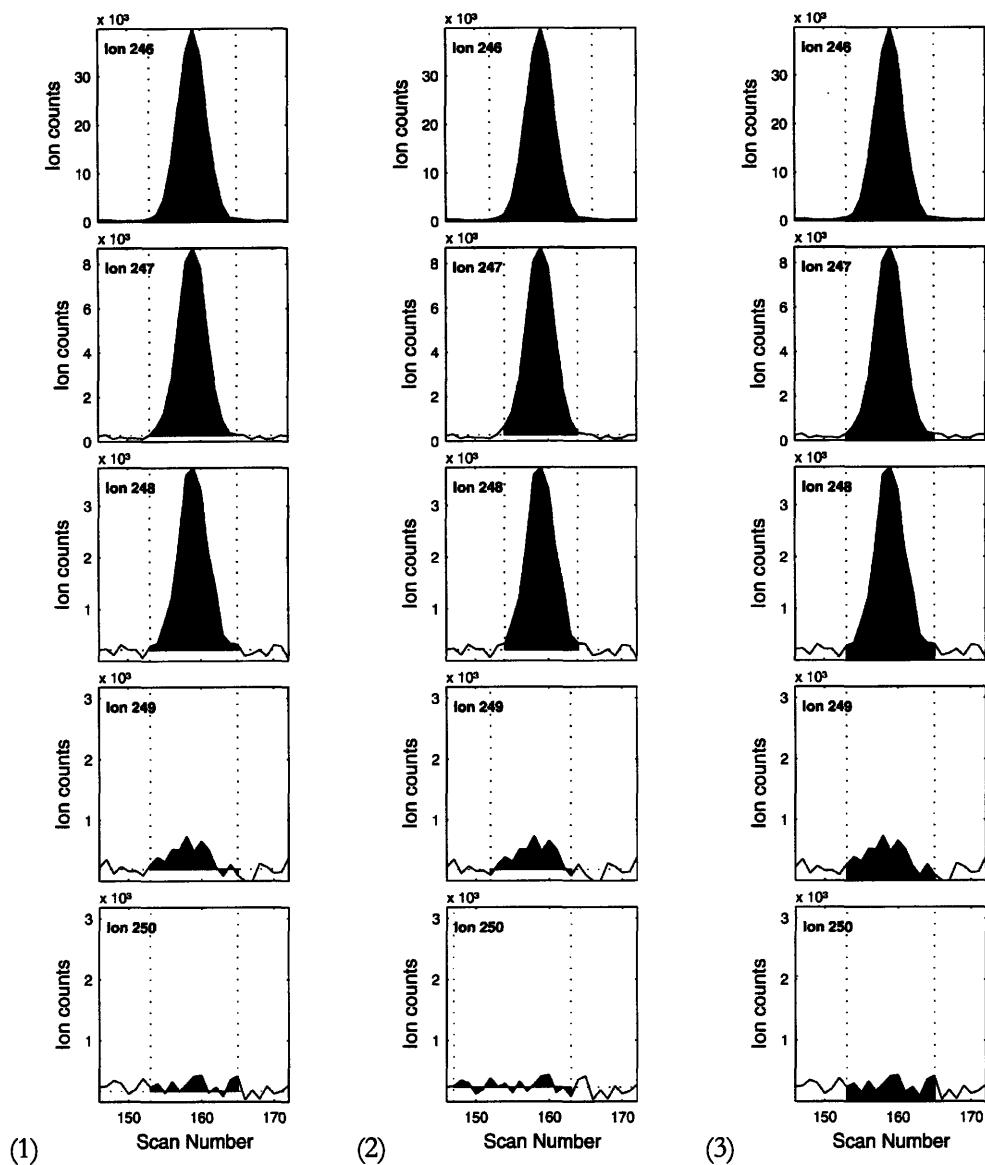


Figure 4-3: Comparison of three methods for integration of mass chromatograms. Mass isotopomer distribution of glycine ion fragment at m/z 246 was determined using three integration methods: (1) fixed integration bounds for all mass chromatograms, and baseline correction; (2) independent integration of each mass chromatogram, resulting in slightly different integration bounds, and baseline correction; (3) fixed integration bounds, but no baseline correction. Shaded areas indicate integrated intensities for each method.

Table 4-2

Effect of integration method on the accuracy of calculated mass isotopomer distributions. MID of glycine fragment at m/z 246-250 was determined by integration using three different integration methods. The calculated isotopomer abundances were compared to theoretical natural isotope abundances (molar abundances, mol%).

		METHOD 1		METHOD 2		METHOD 3	
		Fixed integration bounds and baseline correction		Independent integration and baseline correction		Fixed integration bounds no baseline correction	
Ion		Fig. 4.3 (1)		Fig. 4.2 (2)		Fig. 4.2 (3)	
m/z	Theory	Data	Error	Data	Error	Data	Error
246	75.4	75.4	0.0	75.8	+0.4	73.2	-2.2
247	16.5	16.4	-0.1	16.4	-0.1	16.8	+0.3
248	6.9	7.0	+0.1	6.7	-0.2	7.4	+0.5
249	1.0	1.1	+0.1	1.0	0.0	1.7	+0.7
250	0.2	0.2	0.0	0.1	-0.1	0.9	+0.7

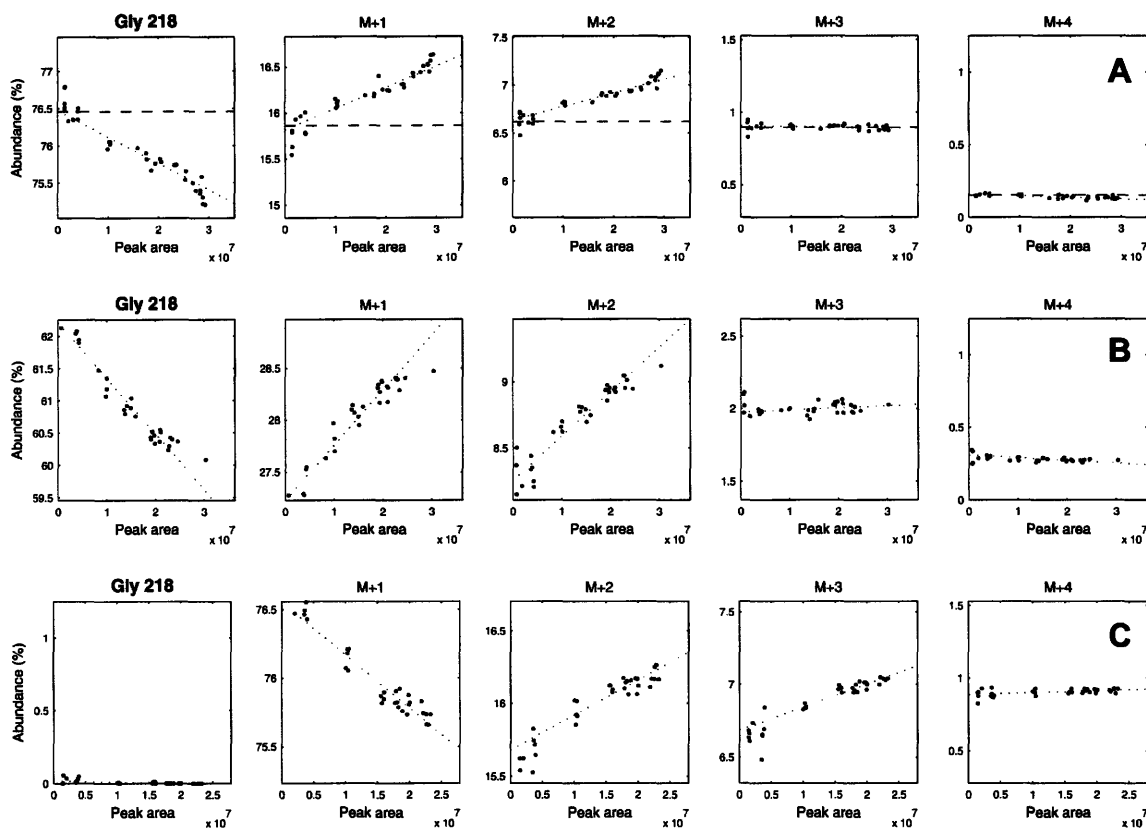


Figure 4-4: Concentration dependence of mass isotopomer abundances of TBDMS derivatized glycine. Glycine samples were analyzed 35 times at different concentrations. Mass isotopomer distributions were obtained by integration of mass chromatograms. Peak area (plotted on the x-axis) denotes the sum of integrated intensities at m/z 218-222. (A) Mass isotopomer abundances for unlabeled glycine. The dashed horizontal line represents the theoretical mass isotopomer abundances; (B) abundances for glycine from ^{13}C -labeled biomass sample; (C) abundances for $[\text{U-}^{13}\text{C}]$ glycine standard. Glycine ion fragment at m/z 218 contains only the second carbon atom of glycine.

acid fragments displayed a similar linear correlation (see Appendix A). Figure 4-4B shows the concentration dependence for glycine from a ^{13}C -labeled biomass sample, and Figure 4-4C shows the concentration dependence for $[\text{U-}^{13}\text{C}]$ glycine standard. In all three samples we observed a linear relationship between mass isotopomer abundances and metabolite concentration. We identified the following pattern for this concentration effect: the intensity of the most abundant mass isotopomers always decreased with increasing concentration, whereas intensities of the other mass isotopomers increased. Furthermore, the magnitude of this effect became smaller for less abundant mass isotopomers. Further investigation revealed that this sample effect could not be explained by nonlinearities of the detector. When we re-analyzed the samples at increasing electron multiplier voltages (EMV) for the detector, the ion counts increased up to 10-fold, however, the observed mass isotopomer distributions did not change significantly (less than 0.3 mol% difference) and the concentration effect remained. Taken together, these findings indicate that this effect is most likely caused during ion formation/fragmentation. A similar effect of sample concentration on the accuracy of GC/MS data was reported for fatty acid methyl esters (Fagerquist et al. 2001; Patterson & Wolfe 1993). To our best knowledge, this is the first time that a sample size effect is reported for TBDMS derivatized amino acids. After careful analysis of all data we concluded that mass isotopomer abundances extrapolated to a theoretical zero concentration (i.e. infinite dilution) correlated best with theoretical abundances. Mass isotopomer abundances obtained this way deviated less than 0.3 mol% from theoretical abundances for all accepted amino acid ion fragments (see section 4.3.6). We found that extrapolation produced more accurate and precise MIDs than could be obtained solely from diluted samples. This was caused by the low signal-to-noise ratio at low concentrations, i.e. the standard deviation of measurements was as high as 0.6 mol% for diluted samples compared to <0.2 mol% for samples at high concentrations. In addition, we observed a slight underestimation of low abundance mass isotopomers in the diluted samples, again caused by low signal-to-noise ratio. Therefore, we strongly recommend that MIDs are always obtained using the extrapolation technique. The main disadvantage of using this method is that it requires multiple injections of samples at different concentrations, which is time consuming. However, MIDs obtained this way are both very accurate (<0.3 mol% error) and very precise (SD <0.2 mol%), which is required for detailed analysis of metabolic fluxes. In

the remainder of this work mass isotopomer abundances of TBDMS derivatized amino acids were always obtained using the extrapolation technique.

4.3.5 Validating identity of ion fragments using ^{13}C -standards

TBDMS derivatized amino acids have characteristic fragmentation patterns resulting from electron impact ionization (EI). The most common ion fragment (m -57) results from the loss of a tert-butyl group (C_4H_9) of the derivatizing agent. This fragment contains the complete carbon backbone of the amino acid. Ion fragments at m -85 and m -159 are formed from cleavage of tert-butyl-CO ($\text{C}_5\text{H}_9\text{O}$) and CO_2 -TBDMS ($\text{C}_7\text{H}_{15}\text{O}_2\text{Si}$) groups, respectively, where the carboxyl group of the amino acid is lost. Another common ion fragment is found at m/z 302. This fragment is formed by cleavage of the carbon bond between α - and β -carbon atoms, i.e. this fragment retains the first two carbon atoms of the amino acid. To validate the assumed identity of ion fragments of TBDMS derivatized amino acids we measured mass spectra for unlabeled and $[\text{U}-^{13}\text{C}]$ labeled amino acids. For example, consider the mass spectrum of unlabeled and $[\text{U}-^{13}\text{C}]$ alanine shown in Figure 4-5. Ala-232 (m -85) ion fragment in unlabeled alanine corresponded to Ala-234 in $[\text{U}-^{13}\text{C}]$ alanine, which was consistent with cleavage of the carboxyl group of alanine. Ala-260 (m -47) ion fragment in unlabeled alanine corresponded to Ala-263 in $[\text{U}-^{13}\text{C}]$ alanine, which was in agreement with cleavage of just the tert-butyl group of the derivatizing agent. However, Ala-302 in unlabeled alanine corresponded to Ala-305 in $[\text{U}-^{13}\text{C}]$ alanine, which was not in agreement with the cleavage of the bond between α - and β -carbon atoms. This fragment clearly contained all three carbon atoms of alanine, and must have been formed by an alternative fragmentation where the methyl group of the derivatizing agent was cleaved. This example clearly illustrates the importance of validating the assumed identity of fragments using ^{13}C -labeled standards to avoid mistakes in the interpretation of mass isotopomer data for metabolic flux analysis. In Appendix A we show the mass spectra for all TBDMS derivatized unlabeled and $[\text{U}-^{13}\text{C}]$ labeled amino acids.

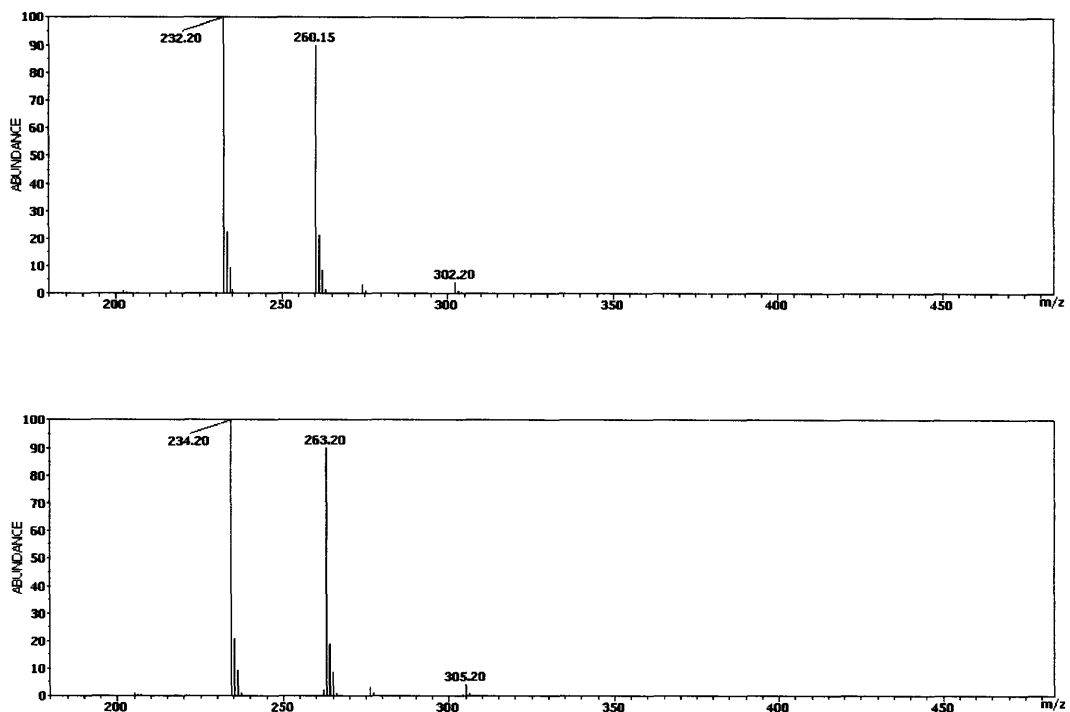


Figure 4-5: Electron ionization mass spectra of TBDMS derivatized alanine. Top spectrum was obtained for unlabeled alanine, and the bottom spectrum for $[\text{U-}^{13}\text{C}]$ alanine standard (99+ At% ^{13}C).

We identified three amino acids where the ion at m/z 302 was formed from multiple fragmentations, i.e. Val-302, Leu-302 and Ile-302. Val-302 in unlabeled valine corresponded to two peaks in $[U-^{13}C]$ alanine mass spectrum, i.e. Ala-304 and Ala-306. Two ion fragments of valine were clearly overlapping here, one fragment containing the first two carbon atoms of valine (m/z 302 \rightarrow 304) and a second fragment containing four of the five carbon atoms of valine (m/z 302 \rightarrow 306), i.e. either $C_{1,2,3,4}$ or $C_{1,2,3,5}$. Leu-302 and Ile-302 ion fragments corresponded to two peaks in $[U-^{13}C]$ labeled amino acid standards, i.e. at m/z 304 and 308. The peak m/z 304 resulted from a fragmentation in which the first two carbon atoms of the respective amino acid were retained (i.e. cleavage of the bond between α - and β -carbon atom), whereas the peak at m/z 308 resulted from the loss of the tert-butyl group of the derivatizing agent, i.e. all carbon atoms of the amino acid were retained. Data from these fragments cannot be used for flux analysis, because we have no means of deconvoluting individual mass isotopomer distributions from the observed mass spectrum.

Fragments of aspartate and glutamate required additional validation with specifically labeled standards. Aspartate and glutamate each have two carboxyl groups, and it was not known a priori which of the two carboxyl groups was cleaved in the m/z 159 (Asp-316 and Glu-330) and m/z 85 (Asp-390 and Glu-404) fragmentations. Therefore, we measured mass spectra for $[4-^{13}C]$ aspartic acid and $[5-^{13}C]$ glutamic acid. For $[4-^{13}C]$ aspartic acid we observed peaks at m/z 317 and 391, and no peaks were observed at m/z 316 and 390. Thus, we concluded that only the first carboxyl group of aspartate was cleaved in these fragmentations. For $[5-^{13}C]$ glutamic acid we observed peaks at m/z 331 and 405, and no peaks were observed at m/z 330 and 404. Thus, only the first carboxyl group of glutamate was cleaved.

4.3.6 Validating accuracy of mass isotopomer distributions

Next, we determined the accuracy of measured mass isotopomer distributions for all accepted amino acid ion fragments by comparing the observed mass isotopomer distributions from unlabeled and $[U-^{13}C]$ labeled amino acids to theoretical distributions. Table 4-3 compares the measured and theoretical abundances for alanine ion fragment at m/z 260. Abundances in Table 4-3 were normalized with respect to the most abundant ion.

Table 4-3

Comparison of measured and theoretical mass isotopomer distribution of TBDMS derivatized alanine. Shown are the measured and theoretical mass isotopomer abundances for unlabeled and [U-¹³C]alanine (99+ At% ¹³C), for the alanine ion fragment at m/z 260.

Abundances were normalized to the most abundant ion.

Ala-260				[U-¹³C]-Ala			
Formula :	C ₁₁ H ₂₆ O ₂ NSi ₂						
Exact mass :	260.150						
C-atoms :	1-2-3						
m/z	theory	data	difference	m/z	theory	data	difference
259	0.0	0.0	0.0	259	0.0	0.0	0.0
260	100.0	100.0	0.0	260	0.0	0.3	+0.3
261	23.0	23.2	+0.2	261	0.0	0.4	+0.4
262	9.4	9.4	0.0	262	3.1	3.3	+0.2
263	1.4	1.4	0.0	263	100.0	100.0	0.0
264	0.3	0.2	-0.1	264	19.9	20.5	+0.6
265	0.0	0.0	0.0	265	8.7	9.0	+0.3
266	0.0	0.0	0.0	266	1.1	1.2	+0.1
267	0.0	0.0	0.0	267	0.2	0.1	-0.1
268	0.0	0.0	0.0	268	0.0	0.0	0.0

We found very good agreement for the Ala-260 fragment. The maximum difference between measured and theoretical abundances was less than 0.2 mol%. As expected, we observed larger differences for [U-¹³C]alanine standard, which was caused mainly by incomplete ¹³C-labeling (99 At% ¹³C-labeling according to manufacturers' specifications). Taking into account potentially incomplete labeling of [U-¹³C]alanine, the observed agreement for [U-¹³C]labeled alanine was acceptable. In Appendix A we show tables for all 47 amino acid fragments that were analyzed in detail where we compare measured and theoretical distributions. For our purposes, amino acid fragments for which the observed abundances deviated more than 0.5 mol% from theoretical abundances (for unlabeled amino acids) were considered inaccurate. The following fragments were rejected: for Leu-200 M+0 was too high (+0.9 mol%), for Asp-316 M+3 was too high (+0.7 mol%), and for Glu-404 M+0 was too low (-0.6 mol%). In general, we did not observe M-1 peaks for most amino acid fragments (<0.1 mol%), indicating that hydrogen abstraction was not a problem in our GC/MS analysis. Only two fragments displayed significant M-1 peaks: for Glu-358 M-1 was 1.8% of M+0, and for Lys-431 M-1 was 1.7% of M+0. Proline fragments were omitted from further analysis because proline co-eluted with other compounds that contributed to the measured intensities resulting in inaccurate mass isotopomer abundances. Lys-329 and Tyr-364 were omitted due to low signal-to-noise ratio. Finally, we could not validate the identity of the following fragments: Ser-230, Thr-417, Met-244, Asp-244, Asp-258, and Glu-272.

Taken together, of the 47 amino acid fragments that were analyzed in detail, 29 fragments satisfied our strict criteria, i.e. they had acceptable accuracy (<0.3 mol% error for 28 of the 29 fragments) and acceptable precision (<0.2 mol% SD). The 29 accepted fragments provide 110 independent constraints for carbon-13 flux analysis. Tables 4-4 and 4-5 summarize the results from this extensive study. For the 29 accepted amino acid fragments, Table 4-4 shows the recommended mass range for measuring intensities, the identity of retained carbon atoms, the specific fragmentation mechanism, the maximum observed error between theoretical and measured abundances, and the maximum observed measurement precision. For the 18 rejected amino acid fragments, Table 4-5 shows the scanned mass range, the identity of the retained carbon atoms (if known), the main reason for rejection, and any alternative ion fragments that may be used to obtain the same isotopomer information.

Table 4-4

Overview of accepted amino acid fragments. TBDMS derivatized amino acids were analyzed by electron impact GC/MS. Using ^{13}C -labeled standards we validated the identity of all fragments. Measured mass isotopomer distributions were then analyzed for accuracy and precision.

Amino acid	Mass range	Amino acid carbon atoms	Fragmentation	Max. deviation from theoretical abundances (mol%)	Precision of measurements (mol%)
Ala	232 – 238	2-3	M – C ₅ H ₉ O	0.1	0.1
	260 – 267	1-2-3	M – C ₄ H ₉	0.1	0.1
Gly	218 – 223	2	M – C ₅ H ₉ O	0.1	0.1
	246 – 252	1-2	M – C ₄ H ₉	0.1	0.1
Val	260 – 268	2-3-4-5	M – C ₅ H ₉ O	0.3	0.1
	288 – 297	1-2-3-4-5	M – C ₄ H ₉	0.1	0.1
Leu	274 – 283	2-3-4-5-6	M – C ₅ H ₉ O	0.1	0.1
Ile	200 – 208	2-3-4-5-6	M – C ₇ H ₁₅ O ₂ Si	0.2	0.1
	274 – 283	2-3-4-5-6	M – C ₅ H ₉ O	0.1	0.1
Ser	288 – 294	2-3	M – C ₇ H ₁₅ O ₂ Si	0.1	0.1
	302 – 308	1-2	M – C ₇ H ₁₇ OSi	0.2	0.2
	362 – 369	2-3	M – C ₅ H ₉ O	0.3	0.2
	390 – 398	1-2-3	M – C ₄ H ₉	0.5	0.2
Thr	376 – 382	2-3-4	M – C ₅ H ₉ O	0.3	0.2
	404 – 413	1-2-3-4	M – C ₄ H ₉	0.3	0.2
Met	218 – 226	2-3-4-5	M – C ₇ H ₁₅ O ₂ Si	0.2	0.1
	292 – 298	2-3-4-5	M – C ₅ H ₉ O	0.2	0.2
	320 – 327	1-2-3-4-5	M – C ₄ H ₉	0.2	0.2
Phe	234 – 243	2-3-4-5-6-7-8-9	M – C ₇ H ₁₅ O ₂ Si	0.3	0.1
	302 – 307	1-2	M – C ₇ H ₇	0.3	0.2
	308 – 316	2-3-4-5-6-7-8-9	M – C ₅ H ₉ O	0.1	0.1
	336 – 345	1-2-3-4-5-6-7-8-9	M – C ₄ H ₉	0.1	0.1
Asp	302 – 308	1-2	M – C ₈ H ₁₇ O ₂ Si	0.1	0.1
	376 – 382	1-2	M – C ₆ H ₁₁ O	0.3	0.2
	390 – 398	2-3-4	M – C ₅ H ₉ O	0.3	0.1
	418 – 427	1-2-3-4	M – C ₄ H ₉	0.3	0.1
Glu	330 – 336	2-3-4-5	M – C ₇ H ₁₅ O ₂ Si	0.1	0.1
	432 – 442	1-2-3-4-5	M – C ₄ H ₉	0.1	0.1
Tyr	302 – 305	1-2	M – C ₁₃ H ₂₁ OSi	0.3	0.1

Table 4-5

Overview of rejected amino acid fragments. TBDMS derivatized amino acids were analyzed by electron impact GC/MS. Measured mass isotopomer distributions were analyzed for accuracy and precision. The following 18 amino acid fragments failed to satisfy our criteria for accuracy and precision.

Amino acid	Mass range	Amino acid carbon atoms	Reason for rejection	Alternative fragment
Val	302 – 308	1-2 and 1-2-3-4/5	Overlapping fragments	n/a
Leu	200 – 208	2-3-4-5-6	Inaccurate. M+2 too high (+0.9 mol%)	Leu-274
Leu	302 – 312	1-2 and 1-2-3-4-5-6	Overlapping fragments	n/a
Ile	302 – 312	1-2 and 1-2-3-4-5-6	Overlapping fragments	n/a
Pro	258 – 266	2-3-4-5	Co-eluting with other compounds	Glu-330
Pro	286 – 295	1-2-3-4-5	Co-eluting with other compounds	Glu-432
Ser	230 – 237	unknown	Unknown fragmentation	unknown
Thr	417 – 424	unknown	Inaccurate. M+0 too low (-4.0 mol%)	unknown
Met	244 – 250	unknown	Unknown fragmentation	unknown
Asp	244 – 249	unknown	Unknown fragmentation	unknown
Asp	258 – 266	unknown	Inaccurate. M-1 too high (4.4 % of M+0)	unknown
Asp	316 – 323	2-3-4	Inaccurate. M+3 too high (+0.7 mol%)	Asp-390
Glu	272 – 280	unknown	Unknown fragmentation	unknown
Glu	358 – 367	1-2-3-4-5	Inaccurate. M-1 too high (1.8 % of M+0)	Glu-432
Glu	404 – 408	2-3-4-5	Inaccurate. M+0 too low (-0.6 mol%)	Glu-330
Lys	329 – 336	2-3-4-5-6	Low signal-to-noise ratio	none
Lys	431 – 441	1-2-3-4-5-6	Inaccurate. M-1 too high (1.7 % of M+0)	none
Tyr	364 – 375	2-3-4-5-6-7-8	Low signal-to-noise ratio	Phe-308

Chapter 5

GC/MS analysis of glucose

5.1 Introduction

In the pathway of gluconeogenesis labeled hydrogen atoms are incorporated into glucose from medium containing deuterated water. The amount of label incorporated at each carbon position depends on the deuterium enrichment in the medium, the relative activity of gluconeogenesis (GNG) and glycogenolysis (GL), and the extent of equilibration of reactions in the gluconeogenesis pathway, i.e. phosphoglucose isomerase (PGI) and triose phosphate isomerase (TPI). It has been suggested that the relative contribution of GNG to hepatic glucose production (HGP) can be determined from the ratio of deuterium labeling on C5 vs. C2 of glucose, and that deuterium labeling on C6 vs. C2 corresponds to the contribution of PEP to HGP. Assessment of positional isomers of glucose can be accomplished either by NMR or by GC/MS methods. The NMR technique requires expensive equipment and a fairly large amount of sample. In contrast, GC/MS is a rapid and more sensitive technique. Electron impact (EI) or chemical ionization (CI) of glucose derivatives generates ion fragments containing different carbon and hydrogen atoms of the glucose molecule resulting from carbon bond cleavage at different positions. Mass isotopomer analysis of ion fragments allows determination of ^2H , or ^{13}C -labeling at each position in the glucose molecule. Guo et al. (1992) presented a GC/MS method for quantitative assessment of the ^2H -labeling pattern of glucose from measurements of eight selected ion fragments obtained by two glucose derivatization methods. The aldonitrile pentaacetate derivative of glucose yielded ion fragments at m/z 328, 242, 217, 212, 187, and 145; and the pentaacetate derivative of glucose yielded ion fragments at m/z 331 and 169.

The authors derived expressions to calculate the enrichment of positional isomers of glucose. However, the proposed method required the use of calibration curves and correction factors to account for artifacts in the isotopomer data. For example, significant deuterium-hydrogen exchange was observed for m/z 187 fragment. The authors also reported isotope discrimination for m/z 169 and 328 fragments in samples containing ^2H -labeled glucose diluted with unlabeled glucose. Furthermore, the mass spectrum of m/z 145 fragment contained a constant contaminating ion amounting to 30% of the total ion counts. The authors proposed to correct for this by dividing the observed enrichment at m/z 145 by 0.7 to obtain the 'true' enrichment. However, even after all these corrections the estimated ^2H -enrichments of glucose deviated up to 25% from the expected enrichments for mixtures of glucose standard. Desage et al. (1989) presented a procedure to determine the ^{13}C -labeling pattern of glucose based on 6 methyloxime trimethylsilyl ion fragments of glucose at m/z 103, 160, 205, 217, 262, 319, and the assumption that glucose molecules are labeled symmetrically. Beylot et al. (1993) provided an improved method for analysis of ^{13}C -labeling of glucose based on 21 selected ion fragments from four glucose derivatives, i.e. m/z 314, 242, 225, 217, 212, 200, and 187 from aldonitrile pentaacetate; m/z 319, 217, 205, 160, 117, and 103 from methyloxime trimethylsilyl; m/z 297, 210, 181, and 168 from bisbuthylboronate acetate; and m/z 149, 101, 88, and 75 from permethyl glucose. However, both methods relied on ion fragments that were previously identified as inaccurate. Here, we present an improved protocol for measuring the labeling of glucose by GC/MS. In this study, we critically evaluated the accuracy and precision of more than 200 ion fragments from 18 glucose derivatives. In addition to four widely used derivatization methods we synthesized 14 novel derivatives of glucose that have not been reported previously. We tested all ion fragments for accuracy and validated the assumed fragmentation patterns using ^{13}C - and ^2H -labeled standards, and by carefully prepared mixtures of glucose standards. The accuracy was assessed by comparing the observed mass isotopomer distributions to theoretical abundances for glucose standards. The vast majority of fragments that were analyzed were inaccurate, including a number of the most widely used ion fragments. From the 200+ analyzed ion fragments, we selected six most accurate ion fragments that provided sufficient information for quantitative assessment of deuterium labeling of glucose. The selected fragments were derived from three novel glucose derivatives, i.e. aldonitrile

pentapropionate, di-O-isopropylidene propionate, and methyloxime pentapropionate. The main result of this work is a detailed procedure for accurate assessment of deuterium labeling in glucose for the entire range of enrichments (0 to 100 mol% enrichment), with an accuracy of 0.3 mol% and precision of 0.2 mol%, or better.

5.2 Materials and methods

5.2.1 Materials

[1-²H]glucose (97 At% ²H), [2-²H]glucose (97 At% ²H), and [6,6-²H₂]glucose (98 At% ²H) were purchased from IsoTec Inc. (Miamisburg, OH). [3-²H]glucose (98 At% ²H), [4-²H]glucose (94 At% ²H), [5-²H]glucose (98 At% ²H) were purchased from Omicron Biochemicals (South Bend, IN). [U-¹³C₆]glucose (99 At% ¹³C) and [1,2,3,4,5,6,6-²H₇]glucose (98 At% ²H) were purchased from Cambridge Isotope Laboratories Inc. (Andover, MA). Stock solutions of unlabeled and specifically labeled glucose standards were prepared at 10 mM in distilled water. For each derivatization procedure 50 μL of glucose standard was evaporated to dryness under airflow. Tissue culture media for hepatocyte cultures were obtained from Sigma (St. Louis, MO).

5.2.2 Hepatocyte isolation and cell culture

The procedure for hepatocyte isolation and cell culture was described in detail elsewhere (Chapter 7). Briefly, hepatocytes were isolated from C57BL/6 mice fed ad libitum by modified two step-collagenase perfusion as described by Seglen (1976). Purified cells were suspended in Hepatocyte Attachment Medium (HAM) and seeded in 6-well plates (1.3×10⁶ cells/well) for 90 minutes at 37°C. Attached cells were washed once and cultured overnight in Hepatocyte Growth Medium (HGM). After 18 hr incubation at 37°C and 5% CO₂ the attached hepatocytes were washed once and cultured in glucose-free HGM enriched with gluconeogenic carbon sources, i.e. 1mM glycerol, 10 mM lactate, 1 mM pyruvate, 5 mM glutamine, and 2 mM acetate. The cells were incubated for 2, 5, or 8 hr at 37°C and 5% CO₂

in medium containing $^2\text{H}_2\text{O}$ at 10% enrichment. At the end of the incubation period medium samples were collected and stored at -80°C prior to analysis.

5.2.3 Preparation of experimental samples for glucose derivatization

Deuterium labeling of glucose from experimental samples was determined by GC/MS analysis of glucose aldonitrile pentapropionate, methyloxime pentapropionate and di-O-isopropylidene propionate derivatives. For each derivatization procedure, 100 μL of medium sample (~ 1 mM glucose) was deproteinized by addition of 300 μL of cold acetone, followed by vortexing vigorously for 30 sec, and centrifugation at $2000\times g$ for 1 min. The supernatant was evaporated to dryness under airflow and the residue derivatized as described next.

5.2.4 GC/MS analysis

Gas Chromatography/Mass Spectrometry (GC/MS) analysis was performed using HP 5890 Series II gas chromatograph (GC) equipped with a DB-XLB (30 m x 0.25 mm i.d. x 0.25 μm) capillary column, interfaced with a HP 5971 mass selective detector (MSD) operating under ionization by electron impact (EI) at 70 eV. The mass spectrometer was calibrated using the 'Max Sensitivity Autotune' setting. The injection volume was 1 μL and samples were injected in purged splitless mode. Helium flow was maintained at 0.88 mL/min via electronic pressure control. The injection port temperature was 250°C . The temperature of the column was started at 80°C for 1 min, increased to 280°C at $20^\circ\text{C}/\text{min}$, and held for 4 min. The interface temperature was maintained at 300°C . Mass spectra were recorded over the range of m/z 100-500 at a rate of 2.0 scans/sec. Measured intensities were corrected for the contribution of background noise (baseline correction), and mass isotopomer distributions were obtained by integration. Mass isotopomer values for each fragment were expressed as fractional abundances, i.e. for each fragment the sum of all mass isotopomers equals one. Reported mass isotopomer abundances are averaged values from at least four injections per sample.

5.2.5 Preparation of glucose esters

This procedure is based on that introduced by Biemann et al. (1963). Evaporated glucose samples were dissolved in 50 μL pyridine, followed by addition of 100 μL of acetic, propionic, or butanoic anhydride to obtain the respective acetate esters, or 70 μL of N-methyl-N-trimethylsilyltrifluoroacetamide (MSTFA) + 1% trimethylchlorosilane (TMCS) to obtain the trimethylsilyl (TMS) ether. After 30 min incubation at 60°C, samples were evaporated to dryness, dissolved in 100 μL of ethyl acetate and transferred to injection vials for GC/MS analysis.

5.2.6 Preparation of aldonitrile esters of glucose

This procedure is based on that introduced by Szafranek et al. (1974). Evaporated glucose samples were dissolved in 50 μL of hydroxylamine hydrochloride solution (20 mg/mL in pyridine), heated at 90°C for 60 min, followed by addition of 100 μL of acetic, propionic, or butanoic anhydride to obtain the respective aldonitrile acetate esters, or 70 μL of MSTFA + 1% TMCS to obtain the aldonitrile TMS ether. After 30 min incubation at 60°C, samples were evaporated to dryness, dissolved in 100 μL of ethyl acetate and transferred to injection vials for GC/MS analysis.

5.2.7 Preparation of methyloxime esters of glucose

The basic procedure for preparing methyloxime esters of glucose is based on that introduced by Laine and Sweeley (1971), and is essentially identical to the aldonitrile method, except that methylhydroxylamine hydrochloride solution (20 mg/mL in pyridine) is used in the first reaction instead of hydroxylamine hydrochloride solution.

5.2.8 Preparation of di-O-isopropylidene esters of glucose

This procedure is based on that presented by Hachey et al. (1999). Glucose samples were transferred to a 10 mL screw-cap culture tube and evaporated to dryness. 500 μL of 0.38 M sulfuric acid in acetone was added, and samples were incubated at room temperature for 60

min. 400 μL of 0.44 M sodium carbonate was added to neutralize the reaction, followed by addition of 1 mL of saturated sodium chloride. The di-O-isopropylidene derivatives were extracted by partitioning with 1 mL of ethyl acetate. The upper, organic layer was evaporated to dryness. 100 μL of acetic, propionic, or butanoic anhydride was added to obtain the respective acetate esters, or 70 μL of MSTFA + 1% TMCS to obtain the respective TMS ether. After 30 min incubation at 60°C, samples were evaporated to dryness, dissolved in 100 μL of ethyl acetate and transferred to injection vials for GC/MS analysis.

5.2.9 Preparation of permethyl and perethyl derivatives of glucose

This procedure is based on that introduced by Ciucanu and Kerek (1984) and recently updated by Ciucanu and Caostello (2003). A cloudy suspension of NaOH powder in DMSO was prepared (0.25 g/mL), vortexed vigorously, and 100 μL of the suspension was added to the glucose samples, followed by incubation at room temperature for 3 min. 75 μL of iodomethane, or iodoethane was then added to the samples, and the samples were incubated at room temperature for 6 min to obtain the respective permethyl and perethyl derivatives. 1 mL of chloroform and 2 mL of distilled water were added, and the samples were vortexed vigorously. The top, aqueous layer was removed and the organic layer washed at least three times with 2 mL of distilled water, or until the aqueous layer was no longer basic. The organic layer was then evaporated to dryness, dissolved in 100 μL of ethyl acetate and transferred to injection vials for GC/MS analysis.

5.2.10 Data analysis

The amount of deuterium enrichment at each carbon position was determined using a least-squares approach. First, we constructed a simulation model that predicts the mass isotopomer distributions of selected ion fragments for a given isotopomer distribution of glucose hydrogen atoms. Isotopomers are isomers of a metabolite that differ only in the labeling state of their individual atoms, i.e. ^2H vs. ^1H in deuterium labeling studies. For the seven stable (i.e. carbon bound) hydrogen atoms of glucose that may be in one of two (labeled or unlabeled) states, we have 128 ($=2^7$) possible isotopomers. Our simulation model

predicts mass isotopomer abundances of glucose fragments taking into account natural isotope enrichments of carbon, oxygen, hydrogen, nitrogen and silicon atoms.

$$\mathbf{x} = [\text{mid}_{301}, \text{mid}_{145}, \text{mid}_{173}, \text{mid}_{259}, \text{mid}_{284}, \text{mid}_{370}] = f(\text{IDV}) \quad (5.1)$$

In Eq. 5.1, $\text{mid}_{m/z}$ denotes the simulated mass isotopomer distributions of a particular ion fragment, and IDV is the isotopomer distribution vector. To determine IDV from experimental data we solve the following least-squares regression problem:

$$\begin{aligned} \min \Phi &= (\mathbf{x} - \mathbf{x}^{\text{obs}}) \cdot (\mathbf{x} - \mathbf{x}^{\text{obs}})^T & (5.3) \\ \text{s.t.} \quad \mathbf{x} &= f(\text{IDV}) \\ 0 &\leq \text{IDV}_i \leq 1 \\ \sum \text{IDV}_i &= 1 \end{aligned}$$

Where the objective function Φ is the sum of squared residuals, \mathbf{x} is the vector of simulated mass isotopomer abundances, and \mathbf{x}^{obs} is the vector measured (i.e. uncorrected) mass isotopomer abundances. From the estimated IDV, we then calculated positional deuterium enrichments via a linear transformation:

$$[D_1, D_2, D_3, D_4, D_5, D_{66}] = T \cdot \text{IDV} \quad (5.2)$$

Where T is a constant transformation matrix. We identify the deuterium enrichment of C-H in carbon 1 as D_1 , the enrichment in carbon 2 as D_2 , and so forth. Since there are two hydrogen atoms at carbon 6 that cannot be distinguished, we only determined the average enrichment at carbon 6, i.e. $D_6 = D_{66}/2$.

5.3 Results

5.3.1 Synthesis and evaluation of glucose derivatives

We synthesized 18 glucose derivatives and analyzed them in detail by electron impact GC/MS. We created four families of related glucose derivatives based on four commonly used derivatization methods, i.e. aldonitrile pentaacetate, pentaacetate, methyloxime trimethylsilyl, and permethyl glucose. Figure 5-1 illustrates the basic two step procedure for generating all glucose derivatives. In the first step, we derivatized the carbonyl group at C1 of glucose to produce aldonitrile and methyloxime derivatives via reaction with methylhydroxylamine and hydroxylamine, respectively. Alternatively we produced the di-O-isopropylidene derivate via reaction with acetone. In the second step, we derivatized the hydroxyl groups of glucose with acetic, propionic, or butanoic anhydride to obtain the respective esters, or with iodomethane, iodoethane, or N-methyl-N-trimethylsilyltrifluoroacetamide to obtain the permethyl, perethyl, and trimethylsilyl ethers of glucose, respectively. We successfully generated 18 of the 24 possible glucose derivatives based on this two step procedure. We obtained electron impact mass spectra for all 18 glucose derivatives for unlabeled and specifically labeled glucose standards. The 18 mass spectra for unlabeled glucose are shown in Appendix B. For each glucose derivative we identified the most abundant ion fragments (shown in Table 5-1), and quantified the mass isotopomer distributions. To assign structural positions of glucose carbon and hydrogen atoms to each ion fragment, mass spectra of specifically labeled glucose standards were analyzed: [1-²H]-, [2-²H]-, [3-²H]-, [4-²H]-, [5-²H]-, [6,6-²H₂]-, [1,2,3,4,5,6-²H₇]-, and [U-¹³C₆]glucose. For example, the mass spectrum of aldonitrile pentapropionate glucose was characterized by fragments arising from bond cleavage at C5-C6 (m/z 240 and 370), C4-C5 (m/z 173 and 284), C3-C4 (m/z 259), and C2-C3 (m/z 345) positions. These assignments were apparent from increases in m/z for specifically labeled glucose standards. Based on these assignments we postulated chemical formulae for all ion fragments and calculated theoretical mass isotopomer distributions. We then compared the observed mass isotopomer abundances for unlabeled and singly labeled glucose standards to theoretical abundances. Fragments with abundances deviating more than 0.4 mol% were considered inaccurate.

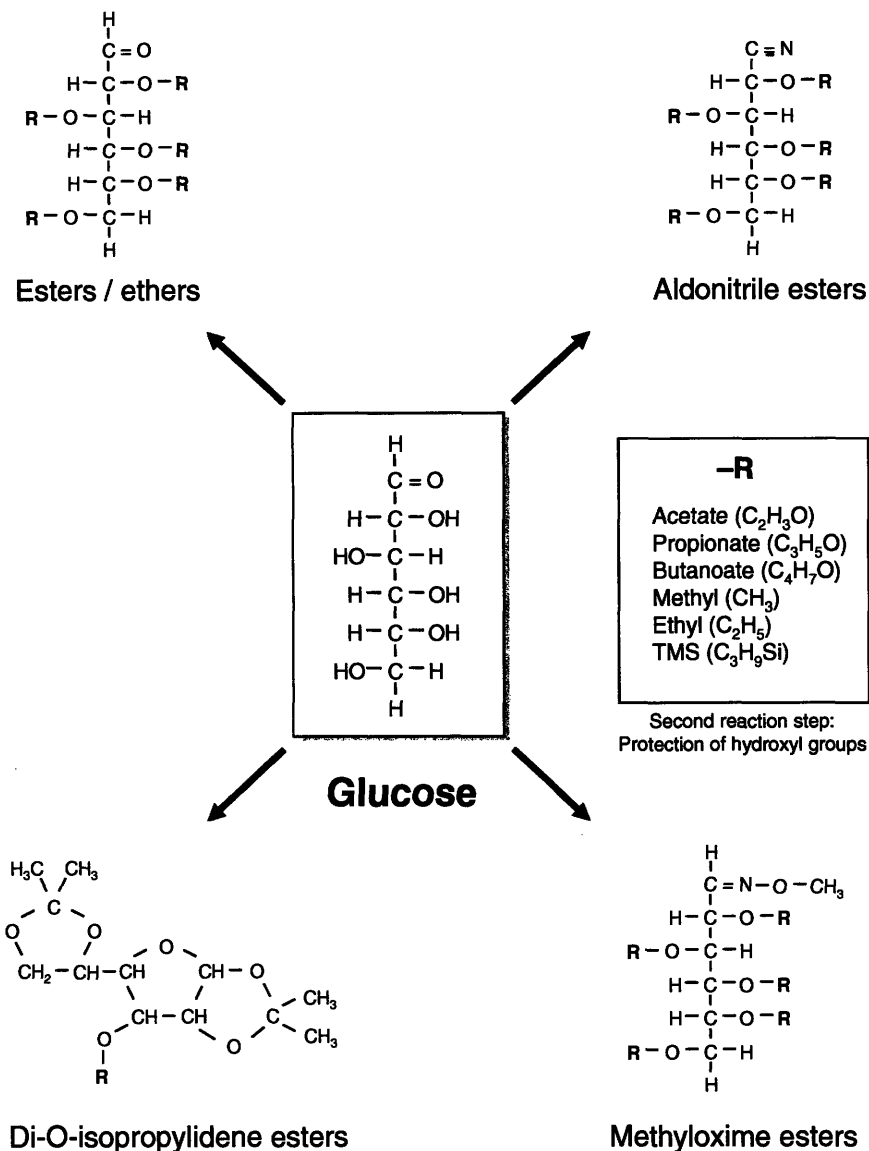


Figure 5-1: Schematic of the two step procedure for generating glucose derivatives. In the first reaction step the carbonyl group at C1 of glucose is derivatized, and in the second reaction step hydroxyl groups of glucose are derivatized. Based on this procedure 18 different glucose derivatives were successfully synthesized and analyzed by GC/MS.

Table 5-1

Overview of 18 derivatives of glucose that were synthesized and analyzed by electron impact GC/MS. For each derivative, the most abundant ion fragments (m/z) were identified and mass isotopomer distributions were analyzed for accuracy. The six most accurate ion fragments are shown in bold and underlined.

1 st reaction step →	none	Isopropylidene	Aldonitrile	Methyloxime
↓ 2 nd reaction step				
Acetate	98, 103, 109, 115, 140, 145, 157, 169, 200, 242, 331	109, 113, 127, 143, 169, 185, 201, 229, 287	103, 115, 127, 141, 145, 157, 187, 212, 217, 225, 242, 272, 314	85, 89, 115, 127, 131, 145, 155, 173, 187, 197, 215, 226, 257, 286, 289, 331
Propionate	109, 129, 131, 154, 183, 185, 187, 210, 227, 284, 387	109, 113, 127, 157, 183, 215, 243, <u>301</u>	129, 131, 141, 155, <u>173</u> , 185, 187, 197, 215, 240, 253, <u>259</u> , <u>284</u> , 345, <u>370</u> , 384	89, 112, 141, <u>145</u> , 155, 198, 201, 215, 254, 328, 345, 384, 387, 416
Butanoate	98, 110, 127, 143, 159, 168, 186, 198, 213, 229, 255, 302, 326, 444	109, 113, 127, 171, 197, 229, 257, 315	112, 143, 155, 159, 169, 193, 201, 211, 213, 229, 243, 268, 281, 301, 326, 370, 426, 440	89, 112, 124, 138, 155, 159, 212, 229, 243, 282, 370, 401, 443
Trimethylsilyl	103, 117, 129, 133, 147, 191, 204, 217, 305	129, 131, 143, 145, 173, 185, 201, 231, 259, 317	103, 117, 129, 133, 147, 157, 189, 191, 205, 217, 229, 291, 319	103, 117, 129, 133, 147, 160, 189, 205, 217, 229, 291, 319, 364
Permethyl*	75, 88, 101, 149	n/a	n/a	n/a
Perethyl*	103, 116, 129, 191	n/a	n/a	n/a

* 'n/a' indicates that we were unable to synthesize this particular derivative of glucose.

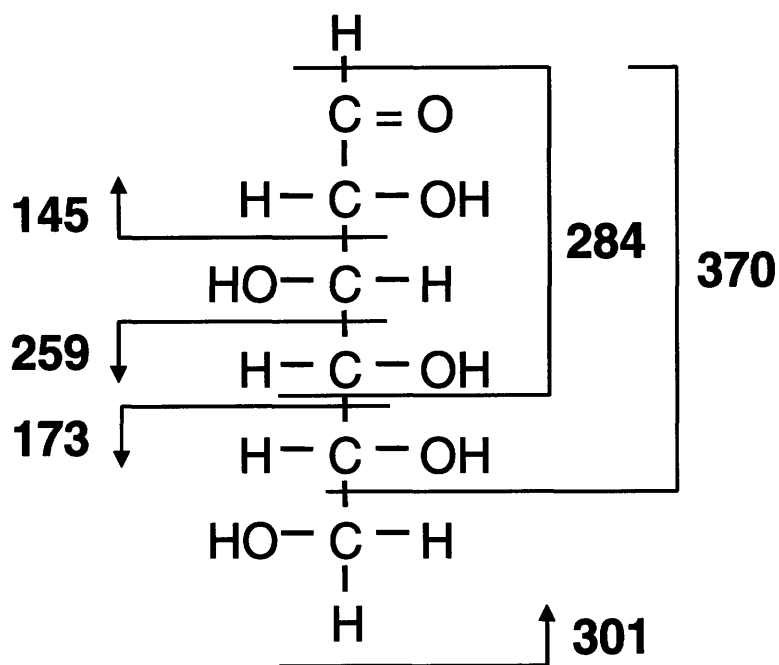


Figure 5-2: Overview of positional information obtained from the selected glucose fragments. Glucose carbon and hydrogen positions included in the selected ion fragments are: m/z 173 (C_{5-6} , H_{5-6}), m/z 259 (C_{4-6} , H_{4-6}), m/z 284 (C_{1-4} , H_{2-4}), and m/z 370 (C_{1-5} , H_{2-5}) all derived aldonitrile pentapropionate glucose; m/z 301 (C_{1-6} , H_{1-6}) derived from di-O-isopropylidene propionate glucose; and m/z 145 (C_{1-2} , H_{1-2}) derived from methyloxime pentapropionate glucose.

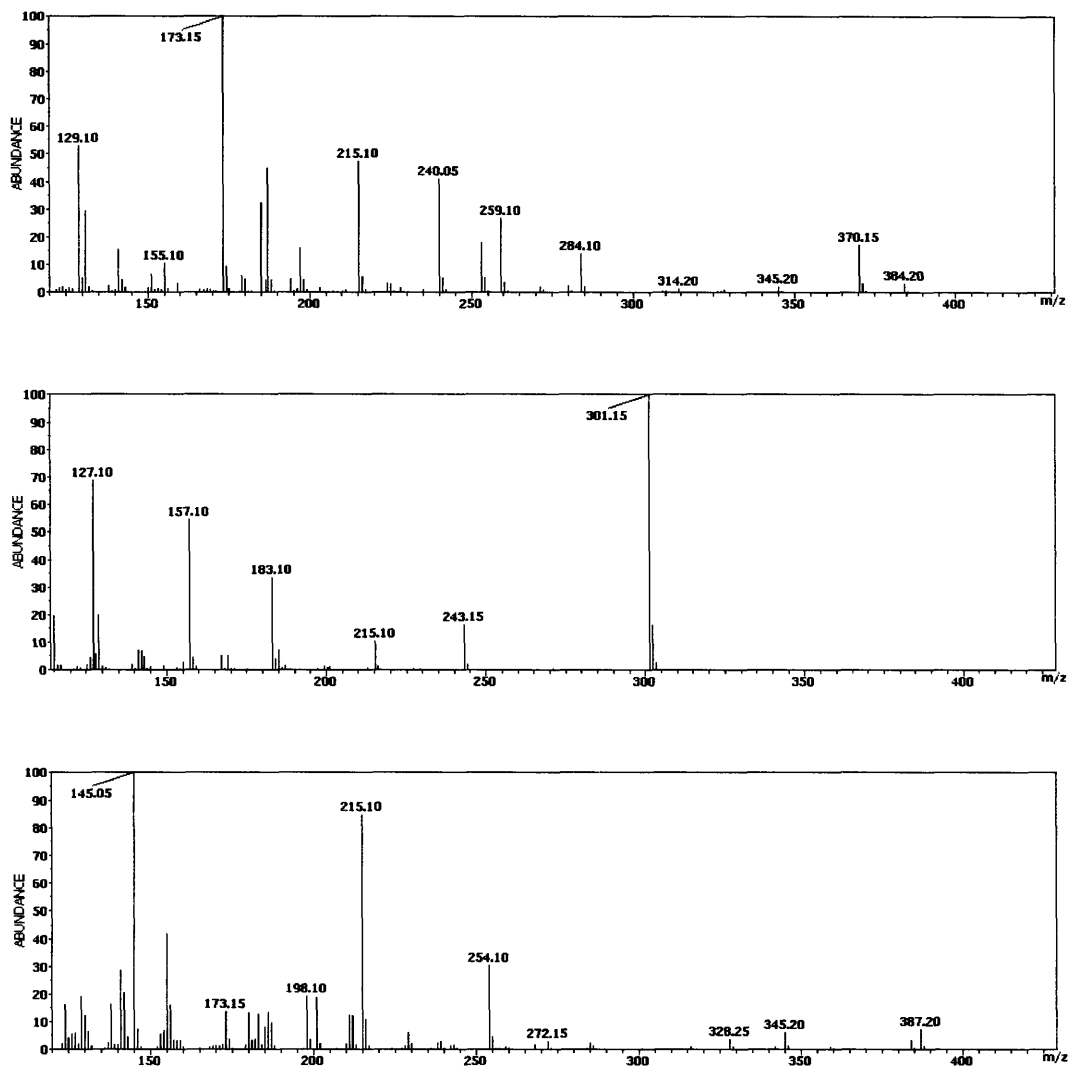


Figure 5-3: Electron impact mass spectra of the selected glucose derivatives. The three panels show the electron impact mass spectra of aldonitrile pentapropionate (top), di-O-isopropylidene propionate (middle), and methyloxime pentapropionate glucose (bottom).

Table 5-2

Evaluation of accuracy of selected glucose fragments. We compared measured and theoretical mass isotopomer abundances of the selected ion fragments at m/z 301 (di-O-isopropylidene propionate), m/z 145 (methyloxime pentapropionate), and m/z 173, 259, 284, and 370 (aldonitrile pentapropionate) for unlabeled glucose. Data shown are mean \pm SD ($n=6$) (molar percentages, mol%).

m/z (formula)	C-H positions		M+0	M+1	M+2	M+3	M+4
301 (C ₁₄ H ₂₁ O ₇)	1,2,3,4,5,6,6	measured	84.1 \pm 0.15	13.5 \pm 0.11	2.2 \pm 0.10	0.2 \pm 0.08	0.0 \pm 0.01
		theory	84.2	13.4	2.2	0.2	0.0
145 (C ₆ H ₁₁ O ₃ N)	1,2	measured	92.3 \pm 0.05	6.8 \pm 0.03	0.8 \pm 0.01	0.1 \pm 0.01	0.0 \pm 0.00
		theory	92.5	6.7	0.8	0.0	0.0
173 (C ₈ H ₁₃ O ₄)	5,6,6	measured	90.6 \pm 0.02	8.2 \pm 0.02	1.1 \pm 0.02	0.1 \pm 0.01	0.0 \pm 0.00
		theory	90.6	8.3	1.1	0.1	0.0
259 (C ₁₂ H ₁₉ O ₆)	4,5,6,6	measured	86.2 \pm 0.09	11.7 \pm 0.07	1.8 \pm 0.02	0.2 \pm 0.01	0.0 \pm 0.00
		theory	86.2	11.8	1.8	0.2	0.0
284 (C ₁₃ H ₁₈ O ₆ N)	2,3,4	measured	85.2 \pm 0.10	12.7 \pm 0.05	1.9 \pm 0.03	0.2 \pm 0.04	0.0 \pm 0.02
		theory	85.0	12.8	1.9	0.2	0.0
370 (C ₁₇ H ₂₄ O ₈ N)	2,3,4,5	measured	81.1 \pm 0.02	15.7 \pm 0.05	2.9 \pm 0.01	0.3 \pm 0.03	0.0 \pm 0.01
		theory	80.9	15.9	2.8	0.4	0.0

Data shown are the observed mass isotopomer abundances obtained from mass chromatogram integration, i.e. not corrected for natural isotope enrichments.

We evaluated over two hundred ion fragments. From these fragments, we then selected the six most accurate fragments that provided sufficient information for quantitative assessment of deuterium labeling at all carbon positions of glucose. These selected fragments were derived from three novel glucose derivatives: aldonitrile pentapropionate ion fragments at m/z 173 (C_{5-6} , H_{5-6}), m/z 259 (C_{4-6} , H_{4-6}), m/z 284 (C_{1-4} , H_{2-4}), and m/z 370 (C_{1-5} , H_{2-5}); di-O-isopropylidene propionate ion fragment at m/z 301 (C_{1-6} , H_{1-6}); and methyloxime pentapropionate ion fragment at m/z 145 (C_{1-2} , H_{1-2}). Figure 5-2 shows schematically the positional information that is obtained from these fragments. The electron impact mass spectra of the three glucose derivatives are shown in Figure 5-3. In Table 5-2 we compare the measured and theoretical mass isotopomer distributions for the selected ion fragments. As expected, we observed very good agreement between the theoretical and observed abundances, i.e. the maximum deviation was 0.2 mol%, and the measurement precision better than 0.15 mol% (i.e. standard deviation of 6 repeated injections).

5.3.2 Determining deuterium labeling of glucose standards

To assess the accuracy of our method for determining positional enrichments of singly labeled glucose, we obtained mass spectra for specifically ^2H -labeled glucose standards, i.e. $[1-^2\text{H}]$ -, $[2-^2\text{H}]$ -, $[3-^2\text{H}]$ -, $[4-^2\text{H}]$ -, $[5-^2\text{H}]$ -, and $[6,6-^2\text{H}_2]$ -glucose, and quantified the mass isotopomer distributions for the selected ion fragments. Table 5-3 shows the observed mass isotopomer distributions (data not corrected for natural isotope enrichments). The deuterium enrichments at the six glucose carbon positions were determined by least-squares regression as described in the Methods section. Table 5-4 shows the estimated enrichments at each carbon position for the purchased glucose standards. The estimated values corresponded well with the expected enrichments based on manufacturers' specifications for isotopic purity. All singly labeled glucose standards showed slight contaminations at various carbon positions. The least pure of the glucose standards was $[4-^2\text{H}]$ glucose, which was 92.3% labeled at C4 and had significant contaminations at C1 and C2 (2.9 mol% and 1.9 mol% enrichment, respectively), compared to 94 At% ^2H -labeling according to manufacturers' specifications. The most pure of the glucose standards was $[5-^2\text{H}]$ glucose, which was 99.8% labeled at C5 and had only a small contamination at C1 (0.8 mol%

Table 5-3

Mass isotopomer distributions of selected ion fragments from ^2H -labeled glucose standards. Specifically labeled glucose standards were derivatized and analyzed by electron impact GC/MS. Data shown have not been corrected for natural isotope enrichments.

m/z	C-H positions	M+0	M+1	M+2	M+3	M+4
[1- ^2H]glucose						
301	1,2,3,4,5,6,6	0.0	82.1	15.1	2.5	0.3
145	1,2	0.2	89.4	9.4	1.0	0.1
173	5,6,6	90.6	8.2	1.1	0.1	0.0
259	4,5,6,6	86.5	11.6	1.8	0.2	0.0
284	2,3,4	82.7	14.9	2.2	0.2	0.1
370	2,3,4,5	78.8	17.5	3.3	0.4	0.0
[2- ^2H]glucose						
301	1,2,3,4,5,6,6	0.0	83.1	14.3	2.4	0.2
145	1,2	0.8	90.4	7.8	0.9	0.1
173	5,6,6	90.5	8.3	1.1	0.1	0.0
259	4,5,6,6	86.3	11.7	1.9	0.2	0.0
284	2,3,4	0.8	84.6	12.6	1.9	0.2
370	2,3,4,5	0.8	80.7	15.4	2.8	0.4
[3- ^2H]glucose						
301	1,2,3,4,5,6,6	1.3	81.3	14.7	2.4	0.3
145	1,2	90.0	8.9	1.0	0.1	0.0
173	5,6,6	90.5	8.3	1.1	0.1	0.0
259	4,5,6,6	86.3	11.6	1.9	0.2	0.0
284	2,3,4	1.1	83.3	13.3	2.0	0.2
370	2,3,4,5	0.9	79.8	16.1	3.0	0.4
[4- ^2H]glucose						
301	1,2,3,4,5,6,6	4.1	80.8	12.7	2.1	0.2
145	1,2	87.5	11.2	1.2	0.1	0.0
173	5,6,6	90.4	8.3	1.1	0.1	0.0
259	4,5,6,6	6.1	81.1	10.9	1.7	0.2
284	2,3,4	5.1	80.9	12.0	1.8	0.2
370	2,3,4,5	4.5	77.5	15.0	2.7	0.3

Table 5-3 (continued)

Mass isotopomer distributions of selected ion fragments from ^2H -labeled glucose standards. Specifically labeled glucose standards were derivatized and analyzed by electron impact GC/MS. Data shown have not been corrected for natural isotope enrichments (molar percentages, mol%).

m/z	C-H positions	M+0	M+1	M+2	M+3	M+4
[5- ^2H]glucose						
301	1,2,3,4,5,6,6	0.0	84.1	13.4	2.2	0.2
145	1,2	91.3	7.7	1.0	0.1	0.0
173	5,6,6	0.0	90.6	8.3	1.1	0.1
259	4,5,6,6	0.0	86.4	11.6	1.8	0.2
284	2,3,4	85.0	12.9	1.9	0.2	0.0
370	2,3,4,5	0.0	81.0	15.7	2.9	0.4
[6,6- $^2\text{H}_2$]glucose						
301	1,2,3,4,5,6,6	0.1	2.9	79.3	14.9	2.6
145	1,2	91.3	7.0	1.6	0.2	0.0
173	5,6,6	0.6	1.5	86.2	10.4	1.3
259	4,5,6,6	0.3	2.3	81.8	13.5	2.2
284	2,3,4	84.8	12.8	2.2	0.2	0.0
370	2,3,4,5	78.6	17.5	3.3	0.4	0.2

Data shown are integrated mass isotopomer abundances not corrected for natural isotope enrichments.

Table 5-4

Estimated deuterium enrichments of glucose standards. Deuterium enrichments (mol% enrichment) at the six glucose carbon positions were determined by least-squares regression of mass isotopomer distributions of selected glucose fragments as described in the Methods section. Numbers in parentheses denote manufacturers' specifications of isotopic purity.

Position	Glucose standard						unlabeled glucose
	[1- ² H]- glucose (97 At%)	[2- ² H]- glucose (97 At%)	[3- ² H]- glucose (98 At%)	[4- ² H]- glucose (94 At%)	[5- ² H]- glucose (98 At%)	[6,6- ² H ₂]- glucose (98 At%)	
D ₁	99.7	2.1	1.4	2.9	0.8	0.8	0.1
D ₂	2.6	98.2	1.6	1.9	0.2	0.2	0.0
D ₃	0.2	1.0	97.8	0.0	0.0	0.0	0.0
D ₄	0.0	0.0	0.0	92.3	0.0	0.2	0.0
D ₅	0.0	0.0	0.0	0.1	99.8	2.4	0.0
D _{66/2}	0.0	0.0	0.0	0.0	0.1	95.8	0.0

Table 5-5

Mass isotopomer distributions of mixtures of glucose standards. Solution of [2-²H]- and [5-²H]glucose was prepared (1:1 mol/mol) and diluted with unlabeled glucose solution to obtain final deuterium enrichments at C2 and C5 of 1%, 5%, 10%, and 50%, respectively.

m/z	C-H positions	M+0	M+1	M+2	M+3	M+4
[2- ² H]glucose + [5- ² H]glucose (50:50)						
301	1,2,3,4,5,6,6	0.0	83.1	14.3	2.4	0.3
145	1,2	46.6	48.7	4.2	0.5	0.0
173	5,6,6	44.5	50.1	4.8	0.6	0.0
259	4,5,6,6	42.3	49.8	6.9	1.0	0.1
284	2,3,4	44.1	47.8	7.1	1.0	0.1
370	2,3,4,5	0.1	81.0	15.7	2.9	0.3
[2- ² H]glucose + [5- ² H]glucose + unlabeled glucose (10:10:80)						
301	1,2,3,4,5,6,6	68.4	26.7	4.3	0.6	0.0
145	1,2	83.3	15.1	1.4	0.1	0.0
173	5,6,6	81.3	16.7	1.9	0.2	0.0
259	4,5,6,6	77.4	19.4	2.8	0.3	0.0
284	2,3,4	77.0	19.5	2.9	0.4	0.1
370	2,3,4,5	65.4	28.4	5.3	0.8	0.1
[2- ² H]glucose + [5- ² H]glucose + unlabeled glucose (5:5:90)						
301	1,2,3,4,5,6,6	76.0	20.2	3.3	0.4	0.0
145	1,2	87.6	11.2	1.1	0.1	0.0
173	5,6,6	85.7	12.6	1.5	0.1	0.0
259	4,5,6,6	81.9	15.6	2.3	0.3	0.0
284	2,3,4	80.8	16.1	2.5	0.4	0.2
370	2,3,4,5	72.9	22.3	4.1	0.6	0.1
[2- ² H]glucose + [5- ² H]glucose + unlabeled glucose (1:1:98)						
301	1,2,3,4,5,6,6	82.4	14.9	2.5	0.3	0.0
145	1,2	91.5	7.7	0.7	0.1	0.0
173	5,6,6	89.6	9.1	1.2	0.1	0.0
259	4,5,6,6	85.2	12.7	2.0	0.2	0.0
284	2,3,4	84.2	13.3	2.2	0.2	0.1
370	2,3,4,5	79.2	17.2	3.2	0.4	0.0

Table 5-6

Estimated deuterium enrichments of mixtures of glucose standards. Deuterium enrichments (mol% enrichment) at the six glucose carbon positions were determined by least-squares regression of mass isotopomer distributions of selected glucose fragments. The estimated enrichments corresponded well with the expected enrichments at C2 and C5 of 0%, 1%, 5%, 10%, and 50%, respectively.

Position	Mixture of standards				
	[2- ² H]glucose + [5- ² H]glucose + unlabeled glucose				
	0:0:100	1:1:98	5:5:90	10:10:80	50:50:0
D ₁	0.1	0.1	0.3	0.2	1.5
D ₂	0.0	1.0	4.9	9.6	48.7
D ₃	0.0	0.0	0.0	0.0	0.0
D ₄	0.0	0.1	0.0	0.0	0.0
D ₅	0.0	1.0	5.0	9.8	51.0
D ₆₆ /2	0.0	0.0	0.0	0.1	0.0

enrichment). The estimated enrichments for the unlabeled glucose standard were not significantly different from zero, i.e. the highest estimated enrichment was 0.1 mol% at C1. These results clearly illustrate the validity of our method and the high accuracy and precision of MS data obtained from the selected ion fragments.

To assess the accuracy of determining deuterium labeling specifically at C2 and C5 positions of glucose, a standard mixture of [2-²H]glucose and [5-²H]glucose was prepared in the proportion 1:1 (mol/mol). Solution of the standard mixture was then diluted with unlabeled glucose solution to obtain final deuterium enrichments at C2 and C5 positions of 1%, 5%, 10%, and 50% (undiluted), respectively. Table 5-5 shows the measured mass isotopomer distributions for the 4 mixtures of glucose standards. Table 5-6 shows the estimated enrichments at each carbon position. The estimated enrichments at C2 and C5 corresponded well with the true enrichments of the prepared mixtures. The deviation from the expected enrichments was less than 0.3 mol%. Furthermore, the estimated enrichments at C1, C3, C4 and C6 positions were not statistically different from zero for three of the four mixtures. The observed 1.5 mol% enrichment at C1 in the 50/50% mixture could be explained by small contaminations at C1 in the [2-²H]glucose and [5-²H]glucose standards (see Table 5-4).

5.3.3 Study of gluconeogenesis

Incorporation of deuterium into glucose in experiments with ²H₂O depends on a number of biochemical reactions where hydrogen atoms are exchanged with, or incorporated from the solvent. Incorporation at C2 occurs mainly via PGI. It is generally assumed that there is rapid exchange between F6P and G6P catalyzed by PGI, and thus we would expect that the labeling at C2 is equal to the enrichment of the solvent. If that is indeed the case, then the overall flux of hepatic glucose production can be measured by the incorporation of deuterium at C2. Incorporation at C5 occurs in the gluconeogenesis pathway, in particular in the reactions catalyzed by enolase and TPI. Deuterium incorporation at C1 and C6 positions occurs via the pyruvate → oxaloacetate → PEP pathway. Therefore, the ratio of enrichment of C5 to that of C2 is a measure of gluconeogenesis relative to glucose production, and the ratio of enrichment of C6 to that of C2 is a measure of the contribution of PEP to glucose

production. The difference between incorporation at C5 and C6 relative to C2 represents the amount of glucose produced from trioses (including glycerol). In a previous study with cultured primary hepatocytes we applied [U-¹³C]glycerol, [²H₅]glycerol and ²H₂O tracers to estimate net and reversible fluxes in the gluconeogenesis pathway (Chapter 7). Our results suggested that TPI and PGI reactions were not fully equilibrated. In particular, we estimated that the PGI reaction was only 80-86% equilibrated. Based on our flux results we predicted that the labeling of GAP-C2 (which eventually becomes C5 of glucose) would be >95% equilibrated with the solvent (mainly via the enolase reaction), and that C2 of glucose would only be 80% equilibrated with the solvent. To validate these predictions we re-analyzed our samples from ²H₂O experiments (10% enrichment) using the newly identified glucose fragments, and estimated the amount of deuterium at each carbon position of glucose. Table 5-7 shows the measured mass isotopomer distributions for three experimental samples taken at 2, 5, and 8 hr, respectively, and Table 5-8 shows the estimated deuterium enrichments at all carbon positions. In all three samples the deuterium labeling at C2 was incomplete. The measured deuterium labeling at C2 varied between 8.1 and 8.6%, indicating 81-86% equilibrium between the solvent and C2 hydrogen of glucose. Thus, these results fully support our previous finding that the PGI reaction was not fully equilibrated. Table 5-9 shows the fractional contributions of gluconeogenesis, glycogenolysis, glycerol, and PEP to glucose production, as we estimated from the deuterium labeling of glucose. Here, gluconeogenesis (GNG) was estimated as the ratio of enrichment of C5 relative to that of the solvent, glycogenolysis (GL) was estimated as 100 – GNG, the flux of PEP to glucose as 2 × enrichment of C6 relative to that of the solvent, and the flux of glycerol to glucose as 2 × GNG – flux of PEP to glucose. Fractional equilibration of the PGI reaction was estimated from the ratio of enrichment of C2 relative to that of the solvent. Table 5-9 compares these estimated fluxes to the previously determined fluxes based on comprehensive analysis of isotopomer data from [U-¹³C]glycerol, [²H₅]glycerol, and ²H₂O experiments. We found good agreement between fluxes estimated from deuterium incorporation and our previous results. Compared to the previous results GNG was slightly underestimated (by about 10%), and GL slightly overestimated. Note that if we used the C5/C2 ratio as a measure of GNG, then we would have overestimated GNG at 85%, 106%, and 105% for the 2, 5, and 8 hr samples, respectively.

Table 5-7

Mass isotopomer distributions of experimental samples. Hepatocytes were cultured in medium containing $^2\text{H}_2\text{O}$ at 10% enrichment. Samples collected after 2, 5, and 8 hrs of incubation were derivatized and analyzed by GC/MS. Shown are mass isotopomer distributions of selected glucose fragments (molar percentages, mol%).

m/z	C-H positions	M+0	M+1	M+2	M+3	M+4
Sample collected after 2 hr of incubation						
301	1,2,3,4,5,6,6	56.3	31.5	9.8	2.2	0.2
145	1,2	81.1	16.6	2.1	0.2	0.0
173	5,6,6	76.5	19.7	3.3	0.4	0.1
259	4,5,6,6	69.1	24.7	5.3	0.8	0.1
284	2,3,4	70.4	23.7	5.0	0.9	0.0
370	2,3,4,5	62.0	29.1	7.6	1.3	0.1
Sample collected after 5 hr of incubation						
301	1,2,3,4,5,6,6	54.1	32.8	10.5	2.3	0.4
145	1,2	80.2	17.6	2.1	0.2	0.0
173	5,6,6	75.7	20.7	3.2	0.4	0.0
259	4,5,6,6	68.0	25.6	5.4	0.9	0.1
284	2,3,4	69.3	24.9	4.9	0.8	0.1
370	2,3,4,5	60.5	29.8	8.0	1.5	0.2
Sample collected after 8 hr of incubation						
301	1,2,3,4,5,6,6	53.1	33.2	10.9	2.4	0.4
145	1,2	79.8	17.9	2.1	0.2	0.0
173	5,6,6	75.0	21.1	3.4	0.4	0.0
259	4,5,6,6	67.3	26.2	5.6	0.9	0.1
284	2,3,4	69.0	25.1	4.9	0.9	0.1
370	2,3,4,5	60.1	30.3	7.9	1.5	0.2

Table 5-8

Estimated deuterium enrichments of experimental samples. Deuterium enrichments (mol% enrichment) at the six glucose carbon positions were determined for three experimental samples from hepatocyte cultures with $^2\text{H}_2\text{O}$ at 10% enrichment.

Position	Length of incubation time		
	2 hr	5 hr	8 hr
D ₁	4.2	5.7	6.1
D ₂	8.6	8.1	8.2
D ₃	5.4	6.4	6.6
D ₄	5.0	5.6	5.7
D ₅	7.3	8.6	8.6
D ₆₆ /2	5.0	4.6	5.1

Table 5-9

Comparison of previously estimated fluxes and fluxes determined from deuterium incorporation. Metabolic fluxes in the gluconeogenesis pathway were previously estimated by fitting experimental data from [U-¹³C]glycerol, [²H₅]glycerol, and ²H₂O experiments to a detailed flux model (Chapter 7). In this study, fluxes were estimated from the incorporation of deuterium into specific carbon positions of glucose from ²H₂O experiments.

Flux	2 hr		5 hr		8 hr	
	This study	Previous study	This study	Previous study	This study	Previous study
Glucose production (fixed at 100)	100	100	100	100	100	100
Gluconeogenesis (GNG)	73	81	86	90	86	90
Glycogenolysis (GL)	27	18	14	10	14	10
Glycerol to glucose flux	46	70	80	72	70	67
PEP to glucose flux	100	92	92	108	102	114
Equilibration of PGI (%)	86%	79%	81%	81%	82%	86%

* 'Previous study' refers to flux results from Chapter 7

* GNG = ²H-C5 / 10%

* GL = 100 – GNG

* PEP to glucose flux = ²H-C6 / 10%

* Glycerol to glucose flux = 2 × GNG – (flux of PEP to glucose)

* Equilibration of PGI = ²H-C2 / 10%

5.4 Discussion

Measured mass isotopomer distributions may deviate from true isotopomer abundances for many reasons, e.g. unresolved metabolite peaks, overlapping mass spectra of adjacent ion fragments, hydrogen abstraction, deuterium-hydrogen exchange, gas phase ion/molecule chemistry in the ionization chamber, isotope discrimination during ionization and detection, sample size effects, and imprecision due to low signal-to-noise ratio and background noise. Mass isotopomer data may therefore underestimate, or overestimate true enrichments. Because positional enrichments are determined from differences in enrichments of different ion fragments, small errors in data propagates to the calculated positional enrichments as large deviations. Thus, mass isotopomer data of individual ion fragments should be as accurate as possible. In this study, we developed a novel protocol for accurate determination of positional deuterium labeling of glucose that avoids the use of calibration curves and correction factors by ensuring that data from the selected ion fragments are very accurate and precise. In order to find the most accurate ion fragments we synthesized 18 different glucose derivatives and evaluated over 200 ion fragments. We used specifically labeled standards for structural assignments and for validating the accuracy of mass isotopomer distributions. The six selected ion fragments provided sufficient information to determine positional ^2H -labeling of glucose hydrogen atoms with precision. Comprehensive analysis of mass isotopomer distributions by least-squares regression allowed quantitative determination of glucose labeling from pure glucose standards, mixtures of glucose standards, and from experimental samples. Our method determines positional enrichments of deuterium with accuracy better than 0.3 mol% and precision better than 0.2 mol%. An example of quantification of deuterium incorporation into glucose was provided in a study of gluconeogenesis in cultured primary hepatocytes. We found that 42-61% deuterium atom was incorporated into C1, 81-86% into C2, 54-66% into C3, 50-57% into C4, 73-86% into C5, and 46-51% into C6 of glucose. These deuterium enrichments indicated that 14-27% of glucose was derived from glycogenolysis and that gluconeogenesis accounted for the remaining 73-86%. In support of our previous finding that suggested incomplete equilibration of PGI, we found that deuterium labeling at C2 of glucose in $^2\text{H}_2\text{O}$ experiments was incomplete.

Chapter 6

Nonstationary metabolic flux analysis of *E. coli*

6.1 Introduction

Isotopic tracer experiments are routinely used to quantify fluxes in biochemical networks (Stephanopoulos, 1999). In a typical carbon-13 labeling experiment, a labeled substrate, e.g. [1-¹³C]glucose, is introduced to the metabolic system where it is taken up and metabolized by the cells. Atoms of the specifically labeled substrate are biochemically rearranged generating molecules with specific labeling patterns that can be detected by nuclear magnetic resonance (NMR) and mass spectrometry (MS) (Klapa, 2003; Szyperski 1995). The labeling patterns of cellular components provide rich information for the estimation of metabolic fluxes. The goal of metabolic flux analysis (MFA) is to extract as much flux information as possible from stable isotope measurements and external flux measurements. Currently, MFA requires that the system is at metabolic and isotopic steady state, i.e. that the labeling of the substrate and the labeling of the sampled pools are equilibrated (Wiechert et al. 2001). For example, this condition is approximated in continuous culture experiments after four or more residence times. The isotopic steady state assumption simplifies the computational problem that needs to be solved for flux determination from a problem with differential-algebraic equations (DAE) to a problem involving only algebraic equations (Wiechert et al., 2005). In this contribution, we extend the scope of MFA to nonstationary systems, i.e. systems that do not approximate isotopic steady state, without increasing the complexity of computations. The extension of MFA to nonstationary systems is important because many systems of industrial

and medical importance never reach isotopic steady state (Drysch et al. 2003; Kelleher 2001). To account for isotopic transients we have developed a novel modeling strategy that combines key ideas from isotopomer spectral analysis (ISA) and stationary MFA. ISA was initially introduced as a general method for modeling polymerization biosynthesis reactions in systems that do not approximate isotopic steady state (Kelleher and Masterson, 1992). In analogy with the ISA method we introduce two dilution parameters to account for the observed isotopic transients. These parameters are the dilution of the tracer before it is metabolized by cells (the D-parameter), and the dilution of labeled products in the sampled pools (the G-parameter). We illustrate the new modeling strategy with a nonstationary system that closely resembles industrial production conditions, i.e. microbial fed-batch fermentation of *E. coli* that overproduces 1,3-propanediol (PDO). In this experiment neither the labeling of the tracer, nor the labeling of the sampled biomass pools were at isotopic steady state. Metabolic fluxes were estimated in this system by fitting labeling profiles of cellular amino acids (measured by GC/MS) and external flux measurements to a detailed model of *E. coli* metabolism that included the additional dilution parameters. We obtained an over-determined system with 66 redundant measurements from which we calculated metabolic fluxes and confidence intervals of fluxes. With the additional D and G parameters we successfully modeled the observed isotopic transients and for the first time determined time profiles of in vivo fluxes during a fed-batch fermentation. The fits were statistically acceptable as judged by the small magnitude of the sum of squared residuals. Flux results provided insights into the physiology of industrial overproduction of PDO. The results indicated that intracellular fluxes were relatively constant during the fed-batch fermentation. The intracellular flux associated with production of PDO increased only by 10% during 20 hr of fermentation, which was in contrast with the efflux of PDO that fluctuated significantly. We observed only a slight decrease in the split ratio at the branch point between glycolysis and pentose phosphate pathway. The TCA cycle flux, on the other hand, remained constant throughout the fermentation. The general modeling strategy that is introduced here is not limited to fed-batch fermentations, but may be used to analyze other metabolic systems that are not at isotopic steady state.

6.2 Materials and methods

6.2.1 Stable isotope tracers

Isotopically labeled glucose tracers, i.e. [1-¹³C]glucose (99 At% ¹³C) and [U-¹³C]glucose (99 At% ¹³C) were purchased from IsoTec Inc. (Miamisburg, OH) and Cambridge Isotope Laboratories Inc. (Andover, MA), respectively.

6.2.2 Medium

Defined mineral salts medium was used for the fermentation. The unlabeled feed contained 46.2 wt% glucose as the carbon source. The ¹³C-labeled feed was chemically identical, but contained 75 wt% [1-¹³C]glucose and 25 wt% [U-¹³C]glucose instead of unlabeled glucose.

6.2.3 Strain and growth conditions

In this study, we used an *E. coli* K12 strain that was metabolically engineered to overproduce 1,3-propanediol (Nakamura, 2003). The cultivation was performed as a fed-batch fermentation (see Figure 6-1). *E. coli* was cultured in an aerobic fermentor with a working volume of 1 L. The pH was controlled at 6.8 ± 0.04 by addition of NH₄OH, the temperature was controlled at 34 °C, and the dissolved oxygen was controlled at $10\% \pm 0.7$ of saturation by adjusting the stirrer speed. The aeration rate was constant at 0.5 standard liters per minute (SLPM). The batch phase was initiated with 45.1 g of unlabeled glucose medium. Glucose feed was initiated after 16.3 hr and controlled such that glucose concentration in the medium was maintained at 45 ± 5 mM. After 18.6 hr, unlabeled glucose feed was replaced with ¹³C-labeled glucose feed containing 75 wt% [1-¹³C]glucose and 25 wt% [U-¹³C]glucose. After 30.0 hr, labeled glucose feed was replaced with unlabeled glucose feed and the fermentation was continued for 14.6 hr.

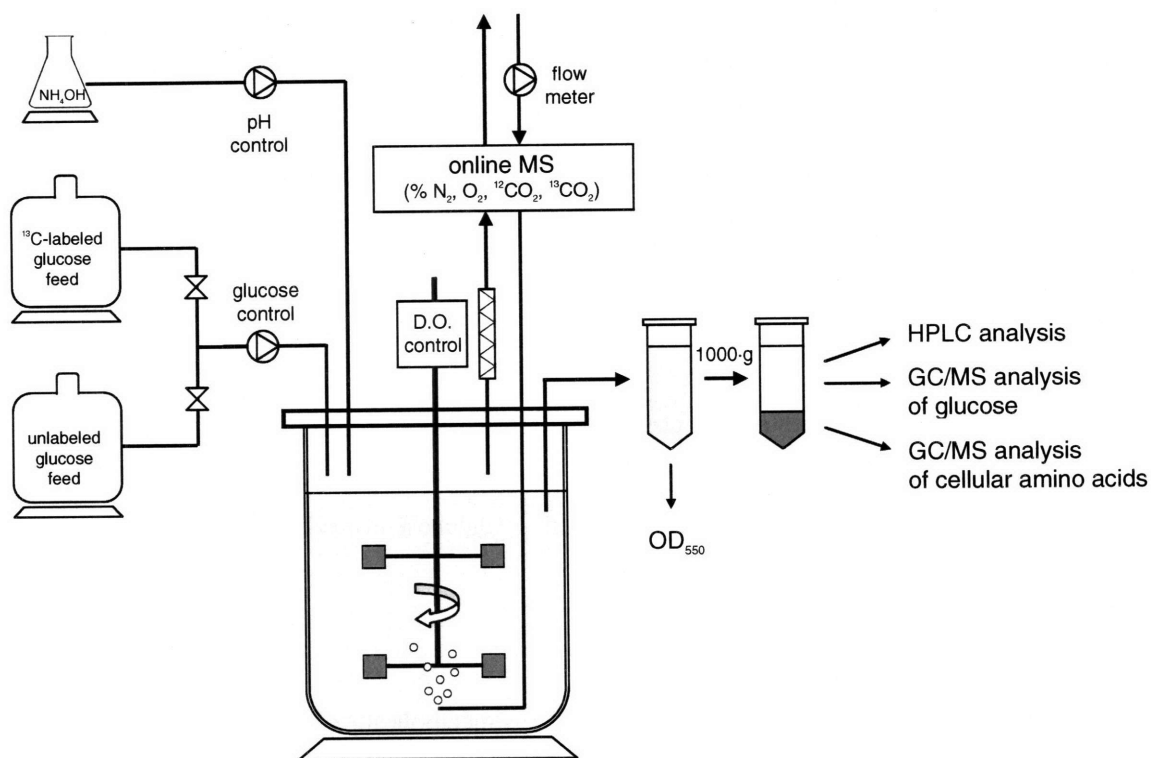


Figure 6-1: A schematic of fed-batch fermentation setup and measurement points. The fed-batch fermentation was performed in an aerobic fermenter with a working volume of 1 L. The pH was controlled at 6.8, the dissolved oxygen at 10% of saturation, and glucose concentration at 45 mM. Online measurements included: weight of the fermenter and feed bottles (scales), flow rate of the inlet air stream (flow meter), the composition of the inlet and outlet air streams (MS). Medium samples were periodically taken for offline analysis: metabolite concentrations (HPLC), biomass concentration (optical density at 550 nm), isotopic labeling of glucose in the medium (GC/MS), and isotopic labeling of cellular amino acids (GC/MS) were measured.

6.2.4 Off-gas analysis

Molfractions of oxygen, carbon dioxide and nitrogen in both the inlet and outlet air streams were measured online by a Prima 600S mass spectrometer (VG Gas, Manchester, UK). The flow rate of the inlet air stream was measured in standard liters per minute (SLPM defined at 1 Atm and 25°C) using a Brooks 5850 series mass flow controller. Fractional labeling of CO₂ in the off-gas was determined from relative intensities of ¹²CO₂ (m/z 44) and ¹³CO₂ (m/z 45).

6.2.5 Sampling and sample processing

Medium samples were periodically taken during the fed batch fermentation for HPLC and GC/MS analysis. In total 21 samples of 11-21 mL were collected between time points 15.4 hr and 44.6 hr. Samples were centrifuged, and the supernatant separated from the biomass pellet. The biomass pellet was stored at -80 °C and the supernatant at -20 °C prior to analysis.

6.2.6 Biomass concentration

Biomass concentration was determined by measuring the optical density at 550 nm (OD₅₅₀), assuming 3.0 g/L/OD₅₅₀ cell dry weight. The molecular weight of dry biomass was assumed to be 25.3 g/C-mol.

6.2.7 HPLC analysis

The concentrations of glucose, glycerol, 1,3-propanediol (PDO), acetate, citrate, and pyruvate in the medium samples were measured by high-performance liquid chromatography (Waters HPLC, Shodex SH1011 sugar column, RI detector).

6.2.8 GC/MS analysis

Gas Chromatography-Mass Spectrometry (GC/MS) analysis was performed using HP 5890 Series II GC (Gas Chromatograph) equipped with a DB-1701 [30 m x 0.25 mm (inner diameter) x 0.25 μ m] capillary column, connected to HP 5971 quadrupole MSD (Mass Selective Detector) operating under ionization by electron impact (EI) at 70 eV. The mass spectrometer was calibrated using the 'Max Sensitivity Autotune' setting. Measured intensities were corrected for the contribution of noise (baseline correction), and mass isotopomer distributions were obtained by integration. Mass isotopomer values for each fragment were expressed as fractional abundances, i.e. for each fragment the sum of all mass isotopomers equals one.

6.2.9 GC/MS analysis of cellular amino acids

Labeling patterns of cellular amino acids were determined by GC/MS analysis of their tert-butyltrimethylsilyl (TBDMS) derivatives. For each derivatization, about 20 mg of wet biomass pellet was transferred to 700 μ L of 6 N HCl and heated at 110 $^{\circ}$ C for 24 hr in a closed vacuum hydrolysis tube. After cooling to room temperature the solvent was evaporated and the residue was dissolved in 150 μ L of distilled water, which was then filtered through a 0.2 μ m pore size filter to remove cell debris. The filtrate was evaporated to dryness. The dried hydrolysate was dissolved in 50 μ L of pyridine followed by addition of 70 μ L of N-(tert-butyltrimethylsilyl)-N-methyl-trifluoroacetamide (MTBSTFA). The mixture was heated at 60 $^{\circ}$ C for 30 min and transferred to an injection vial for GC/MS analysis. The injection volume was 1 μ L and samples were injected in purged splitless mode. The amount of sample analyzed was controlled by varying the purge activation time between 1 sec and 1.5 min. Helium flow was maintained at 0.74 mL/min via electronic pressure control. The injection port temperature was 270 $^{\circ}$ C. The temperature of the column was started at 100 $^{\circ}$ C for 1.5 min, increased to 130 $^{\circ}$ C at 20 $^{\circ}$ C/min and increased to 220 $^{\circ}$ C at 10 $^{\circ}$ C/min and held for 3 min. The temperature was then increased to 280 $^{\circ}$ C at 5 $^{\circ}$ C/min and held for 3 min. The interface temperature was maintained at 300 $^{\circ}$ C. Mass spectra were analyzed in the mass range 195-445 atom mass units at a rate of 2.7 scans/sec. Figure 6-2 shows a representative total ion chromatogram of TBDMS derivatized amino acids from hydrolyzed

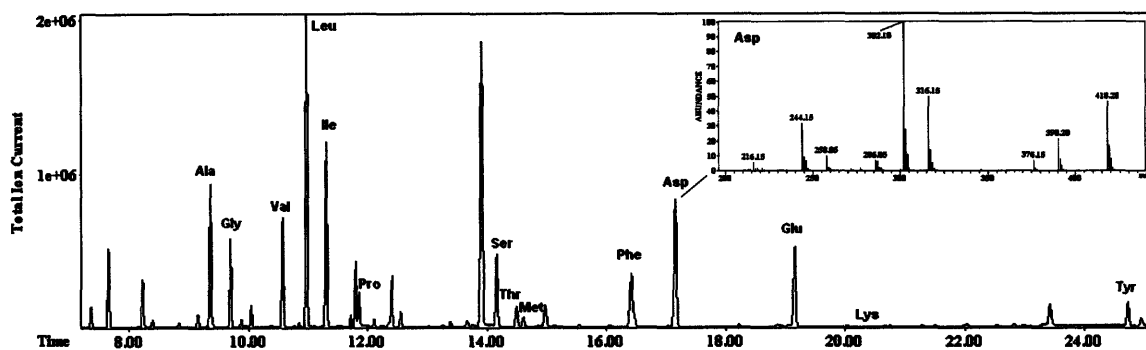


Figure 6-2: Representative total ion chromatogram. Cellular amino acids from hydrolyzed biomass were derivatized by TBDMS and analyzed by electron impact GC/MS. The total ion chromatogram corresponds to the sum of the ion intensities measured at each time point in the analysis. The insert shows the electron ionization mass spectrum for TBDMS derivatized aspartic acid.

Table 6-1

Ion fragment of TBDMS derivatized amino acids used for flux analysis. The identity of amino acid ion fragments was verified previously (Chapter 4). Assignment of precursor metabolites reflects the metabolic network model of *E. coli* shown in Appendix 6.A.

Amino acid	Monitored ions	Amino acid carbon atoms	Fragmentation	Precursor metabolite(s)
Ala	232 – 239	2-3	M – C ₅ H ₉ O	Pyr ₍₂₋₃₎
	260 – 268	1-2-3	M – C ₄ H ₉	Pyr ₍₁₋₂₋₃₎
Gly	218 – 224	2	M – C ₅ H ₉ O	multiple pathways*
	246 – 253	1-2	M – C ₄ H ₉	multiple pathways*
Val	260 – 269	2-3-4-5	M – C ₅ H ₉ O	Pyr ₍₂₋₃₎ + Pyr ₍₂₋₃₎
	288 – 298	1-2-3-4-5	M – C ₄ H ₉	Pyr ₍₁₋₂₋₃₎ + Pyr ₍₂₋₃₎
Leu	274 – 283	2-3-4-5-6	M – C ₅ H ₉ O	AcCoA ₍₂₎ + Pyr ₍₂₋₃₎ + Pyr ₍₂₋₃₎
Ile	274 – 283	2-3-4-5-6	M – C ₅ H ₉ O	OAC ₍₂₋₃₋₄₎ + Pyr ₍₂₋₃₎
Ser	288 – 296	2-3	M – C ₇ H ₁₅ O ₂ Si	multiple pathways*
	362 – 370	2-3	M – C ₅ H ₉ O	multiple pathways*
	390 – 399	1-2-3	M – C ₄ H ₉	multiple pathways*
Thr	376 – 382	2-3-4	M – C ₅ H ₉ O	OAC ₍₂₋₃₋₄₎
	404 – 414	1-2-3-4	M – C ₄ H ₉	OAC ₍₁₋₂₋₃₋₄₎
Met	292 – 298	2-3-4-5	M – C ₅ H ₉ O	OAC ₍₂₋₃₋₄₎ + C-1
	320 – 327	1-2-3-4-5	M – C ₄ H ₉	OAC ₍₁₋₂₋₃₋₄₎ + C-1
Phe	302 – 307	1-2	M – C ₇ H ₇	PEP ₍₁₋₂₎
	308 – 316	2-3-4-5-6-7-8-9	M – C ₅ H ₉ O	PEP ₍₂₋₃₎ + PEP ₍₂₋₃₎ + E4P ₍₁₋₂₋₃₋₄₎
	336 – 345	1-2-3-4-5-6-7-8-9	M – C ₄ H ₉	PEP ₍₁₋₂₋₃₎ + PEP ₍₂₋₃₎ + E4P ₍₁₋₂₋₃₋₄₎
Asp	302 – 309	1-2	M – C ₈ H ₁₇ O ₂ Si	OAC ₍₁₋₂₎
	376 – 382	1-2	M – C ₆ H ₁₁ O	OAC ₍₁₋₂₎
	390 – 397	2-3-4	M – C ₅ H ₉ O	OAC ₍₂₋₃₋₄₎
	418 – 428	1-2-3-4	M – C ₄ H ₉	OAC ₍₁₋₂₋₃₋₄₎
Glu	330 – 336	2-3-4-5	M – C ₇ H ₁₅ O ₂ Si	AKG ₍₂₋₃₋₄₋₅₎
	404 – 411	2-3-4-5	M – C ₅ H ₉ O	AKG ₍₂₋₃₋₄₋₅₎
	432 – 443	1-2-3-4-5	M – C ₄ H ₉	AKG ₍₁₋₂₋₃₋₄₋₅₎
Tyr	302 – 307	1-2	M – C ₁₃ H ₂₁ O ₂ Si	PEP ₍₁₋₂₎

Abbreviations: 3PG, 3-phosphoglycerate; PEP, phosphoenolpyruvate; Pyr, pyruvate; E4P, erythrose-4-phosphate; AKG, α -ketoglutarate; OAC, oxaloacetate; AcCoA, acetyl coenzyme-A; R5P, ribose-5-phosphate; C-1, one-carbon unit.

* Glycine and serine are produced by multiple pathways (see Metabolic Network in Appendix 6.A).

The labeling of these fragments depends on the relative contribution of these pathways.

biomass. We detected 15 of the 20 amino acids in hydrolyzed biomass samples.

Table 6-1 shows the 26 amino acid ion fragments that were used for metabolic flux analysis. All samples were injected 35 times at varying concentrations. For each fragment the integrated mass isotopomer abundances were plotted as a function of total ion counts and extrapolated to a theoretical infinite dilution to correct for the concentration effect of electron impact GC/MS analysis (see Chapter 4).

6.2.10 GC/MS analysis of glucose

Labeling of glucose was determined by GC/MS analysis of aldonitrile pentapropionate derivative of glucose. For each derivatization, 20 μL of medium sample was deproteinized by addition of 300 μL of acetone ($\sim 4^\circ\text{C}$). The mixture was centrifuged and the supernatant evaporated to dryness. 50 μL of 2 wt% hydroxylamine hydrochloride in pyridine was added to the dry residue and the mixture was heated at 90°C for 60 min. This was followed by addition of 100 μL of propionic anhydride and heating at 60°C for another 30 min. After cooling, the sample was evaporated to dryness and dissolved in 100 μL of ethyl acetate and transferred to an injection vial for GC/MS analysis. The injection volume was 1 μL and samples were injected in purged splitless mode. Helium flow was maintained at 0.88 mL/min via electronic pressure control. The injection port temperature was 250°C . The temperature of the column was started at 80°C for 1 min, increased to 280°C at $20^\circ\text{C}/\text{min}$, and held for 4 min. The interface temperature was maintained at 300°C . Mass spectra were analyzed in the mass range 150-450 atom mass units at a rate of 2.3 scans/sec. Labeling of glucose was determined from the ion fragment at m/z 370 ($\text{C}_{17}\text{H}_{24}\text{O}_8\text{N}$) that contained carbon atoms C1-C5 of glucose. Measured mass isotopomer distributions were corrected for natural isotope enrichments as described by Fernandez et al. (1996). The corrected intensity at m/z 370 corresponded to the fraction of naturally labeled glucose, the intensity at m/z 371 corresponded to the fraction of $[1-^{13}\text{C}]$ glucose, and the sum of intensities at m/z 374 and 375 corresponded to the fraction of $[\text{U}-^{13}\text{C}]$ glucose.

6.2.11 Calculating external fluxes

Cumulative consumption of glucose and citrate, and cumulative production of biomass, glycerol, PDO and acetate were calculated from the measured concentrations and fermentor weight, after accounting for losses due to sampling. Consumption and production rates (mol/h) were then determined by fitting a smooth curve through the data points. Rates of total oxygen uptake (TOUR) and total carbon dioxide production (TCER) were calculated from off-gas analysis as follows:

$$\text{TOUR (mol/h)} = \left(x_{\text{O}_2,\text{in}} - x_{\text{O}_2,\text{out}} \cdot \frac{x_{\text{N}_2,\text{in}}}{x_{\text{N}_2,\text{out}}} \right) \cdot \text{SLPM}_{\text{in}} \cdot 2.454 \quad (6.1)$$

$$\text{TCER (mol/h)} = \left(x_{\text{CO}_2,\text{out}} \cdot \frac{x_{\text{N}_2,\text{in}}}{x_{\text{N}_2,\text{out}}} - x_{\text{CO}_2,\text{in}} \right) \cdot \text{SLPM}_{\text{in}} \cdot 2.454 \quad (6.2)$$

The above equations assume that nitrogen is not consumed, produced or accumulated in the system. These equations inherently correct for temperature and pressure differences between the inlet and outlet air streams.

6.2.12 Metabolic network model

A detailed network model for *E. coli* was constructed (see Appendix 6.A). The model was comprised of 73 reactions (with corresponding carbon transitions) utilizing 76 metabolites, with 5 substrates (i.e. glucose, citrate, O₂, NH₃, SO₄), 5 products (i.e. 1,3-propanediol, biomass, CO₂, acetate, and ATP), and 65 balanced intracellular metabolites. Glycerol was allowed to be either a substrate or a product depending on the calculated external flux. The network model included reactions of glycolysis, pentose phosphate pathway, Entner-Doudoroff pathway, TCA cycle, PDO biosynthesis pathway, amphibolic reactions, one-carbon metabolism, and amino acid biosynthesis reactions. Reversible reactions were modeled as separate forward and backward fluxes. Net and exchange fluxes were determined

as: $v_{\text{net}} = v_f - v_b$; $v_{\text{exch}} = \min(v_f, v_b)$. All forward and backward fluxes were required to be non-negative at the final solution.

6.2.13 Flux determination and statistical analysis

Metabolic fluxes were determined by fitting 8 external fluxes and 191 mass isotopomer abundances of cellular amino acid to the metabolic network model of *E. coli* including additional flux parameters to account for isotopic transients (see section 6.3.5). The minimized objective function was the variance-weighted sum of squared deviations between the observed and simulated measurements. The iterative algorithm that was used for least-squares optimization was based on successive quadratic programming (see Chapter 3). At convergence, accurate confidence intervals of fluxes were calculated by evaluating the sensitivity of the objective function with respect to fluxes as described previously (Chapter 3). Flux validation was accomplished by a statistical test for the goodness-of-fit (chi-square test for model adequacy), and a normality test for the weighted residuals. To ensure a global optimum, flux estimation was repeated at least four times starting with random initial values for all fluxes. Sensitivity analysis was used to determine the relative importance of measurements for the estimation of individual fluxes as described previously (Chapter 3).

6.3 Results

6.3.1 External fluxes

Figure 6-3A shows the calculated external fluxes as a function of fermentation time. The calculated external fluxes were consistent, i.e. the carbon balance closed within 2% and degree of reduction balance closed within 4%. Figure 6-3B shows the consumption and production rates expressed as specific fluxes (mmol/h/gDW). The specific fluxes decreased significantly during the fermentation. This indicates that the cells were either becoming less metabolically active, or that the fraction of metabolically active cells decreased, i.e. fraction of dead cells increased. We did not measure cell viability in this experiment, thus the exact cause for the decreased specific fluxes remains uncertain. External fluxes normalized to glucose uptake rate shown in Figure 6-3C. The flux of glucose to biomass decreased in time

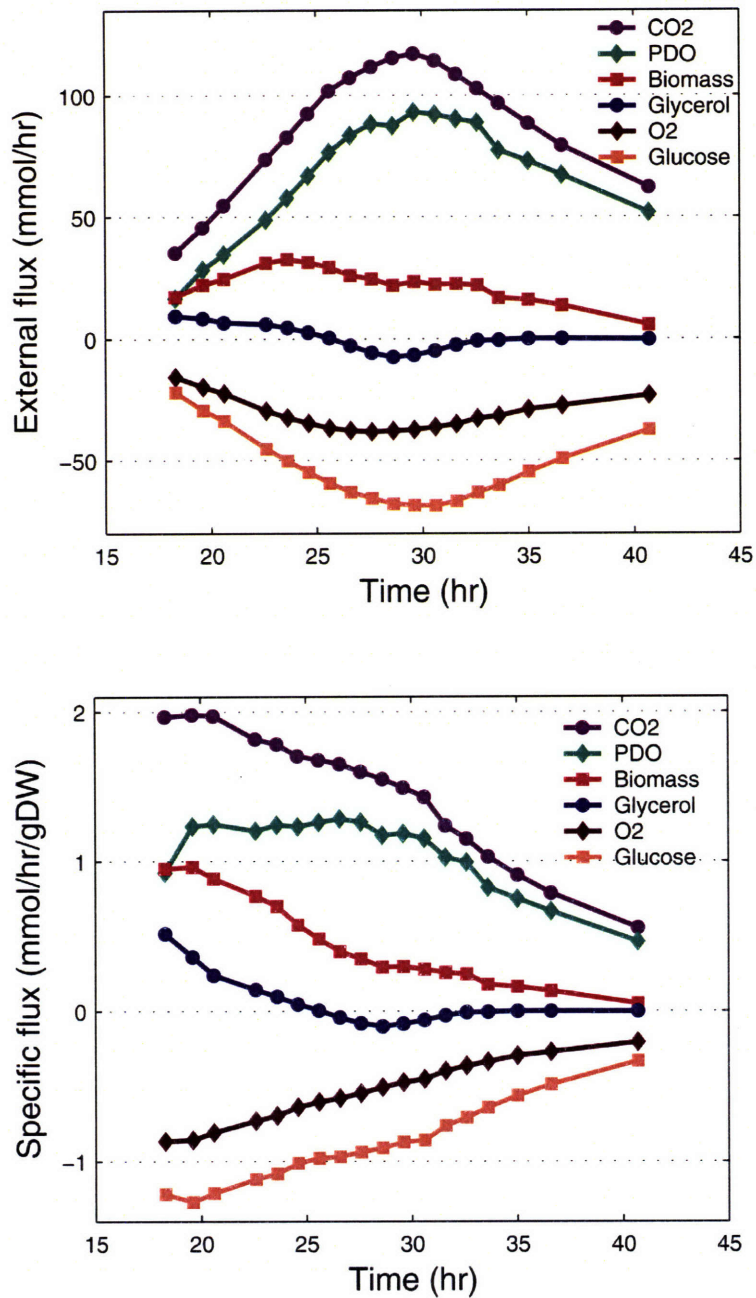


Figure 6-3: Characterization of external fluxes in the fed-batch culture. Top panel shows the observed absolute external fluxes (mmol/h) as a function of fermentation time. Negative fluxes correspond to consumption rates. Bottom panel shows specific external fluxes (mmol/h/gDW) that significantly decreased in time.

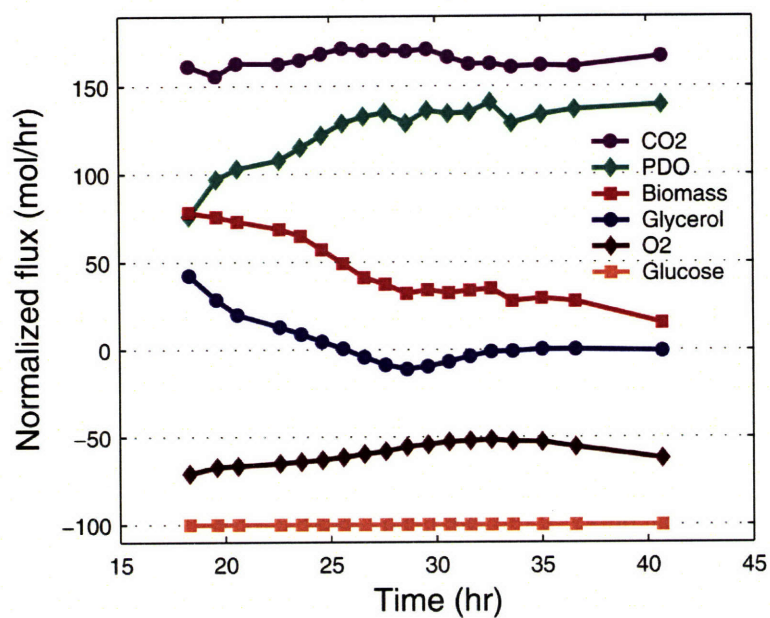


Figure 6-3 (continued): Characterization of external fluxes in the fed-batch culture. Shown are external fluxes normalized to glucose uptake rate that was fixed at -100 (i.e. uptake rate of 100).

and flux towards PDO gradually increased. Note that glycerol was initially produced by the cells, but after 25 hr glycerol was taken up by the cells and co-metabolized with glucose as a carbon source. The rates of acetate production and citrate uptake were negligible compared to the other fluxes (not shown in Figure 6-3; see Appendix 6.E).

6.3.2 Characterization of glucose feed

Based on preliminary simulations and sensitivity analysis of the metabolic system we determined that the optimal labeling of glucose in this study would be 75% [1-¹³C]glucose and 25% [U-¹³C]glucose. The composition of the labeled feed was validated by GC/MS analysis. First, we validated the isotopic purity of the purchased tracers. We measured 99.7 ± 0.2 At% isotopic purity for the [1-¹³C]glucose tracer, and 99.4 ± 0.1 At% isotopic purity for the [U-¹³C]glucose tracer. These enrichments were higher than 99 At% isotopic purity according to manufactures' specifications. The two tracers were mixed as follows: 105 g [1-¹³C]glucose + 35 g [U-¹³C]glucose (i.e. 75/25 wt/wt, or 75.5/24.5 mol/mol). The composition of labeled glucose feed was then validated by GC/MS analysis. The measured composition was 75.4 ± 0.2 mol% [1-¹³C]glucose and 24.6 ± 0.2 mol% [U-¹³C]glucose.

6.3.3 Dynamics of glucose labeling

Figure 6-4 shows the observed isotopic composition of glucose in the medium as a function of fermentation time. Labeled glucose feed was initiated at 18.6 hr and continued until 30.0 hr, when it was replaced with unlabeled glucose feed. The labeling of glucose underwent a transient phase of about 5 hr after the introduction of the tracer (between 18.6 - 23.6 hr), and a second transient phase of about 5 hr after the switch to unlabeled glucose feed (between 30.0 - 35.0 hr). The isotopic composition was constant for samples taken between 23.6 and 29.6 hr, with 75.4% [1-¹³C]glucose and 24.6% [U-¹³C]glucose (measured by GC/MS). The length of the observed isotopic transients is determined by glucose concentration in the reactor and the rate of glucose feed and uptake. In this study, glucose concentration was maintained at 45 ± 5 mM, i.e. much higher than the typical limiting levels of glucose achieved in continuous cultures.

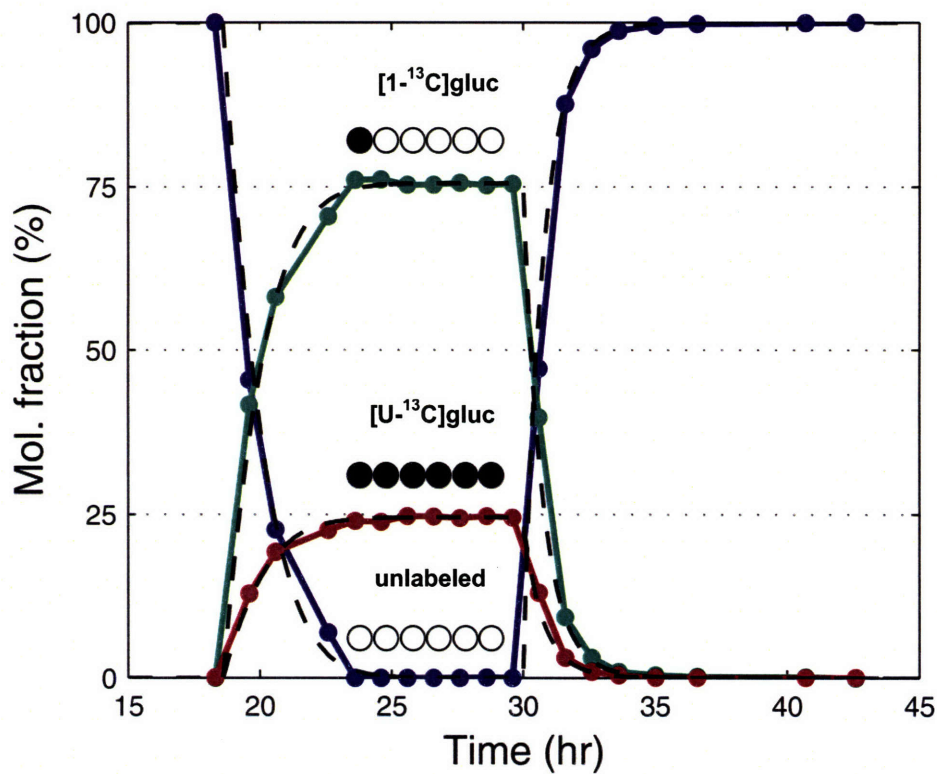


Figure 6-4: Measured isotopic composition of glucose in the medium as a function of time. The isotopic composition of glucose in medium samples was determined by GC/MS analysis. Isotopically labeled glucose was introduced at 18.6 hr. The labeling of glucose approached isotopic steady state at ~ 24 hr. The isotopic composition of glucose was constant for samples between 23.6 and 29.6 hr, with 75.4% $[1-^{13}\text{C}]$ glucose and 24.6% $[U-^{13}\text{C}]$ glucose. After 30.0 hr the feed was switched back to unlabeled glucose feed. The dashed lines represents the predicted composition of glucose based on the balance model in Eq. 6.7.

To describe the observed labeling transients quantitatively, we constructed a simple material balance model assuming ideally mixed reactor. The equations for total glucose concentration and glucose labeling are:

$$\frac{d(V \cdot c_{\text{gluc}})}{dt} = F \cdot c_{\text{gluc},\text{in}} - r_{\text{gluc}} \quad (6.3)$$

$$\frac{d(V \cdot c_{\text{gluc}} \cdot x)}{dt} = F \cdot c_{\text{gluc},\text{in}} \cdot x_{\text{in}} - r_{\text{gluc}} \cdot x \quad (6.4)$$

Here, F (L/hr) is the flow rate of feed to the reactor, c_{gluc} (mmol/L) is glucose concentration in the reactor, $c_{\text{gluc},\text{in}}$ (mmol/L) is the glucose concentration in the feed, V (L) is the reactor volume, r_{gluc} (mmol/hr) is glucose uptake rate, x is the molfraction of labeled glucose in the reactor, and x_{in} is the molfraction of labeled glucose in the feed. In this experiment, glucose concentration and reactor volume were relatively constant during the observed isotopic transients, however, the feed rate changed significantly. Assuming constant glucose concentration and reactor volume, Eq. 6.3 simplifies to:

$$r_{\text{gluc}} = F \cdot c_{\text{gluc},\text{in}} \quad (6.5)$$

Substitution of Eq. 6.5 into Eq. 6.4 yields:

$$\frac{dx}{dt} = \frac{r_{\text{gluc}}}{V \cdot c_{\text{gluc}}} \cdot (x_{\text{in}} - x) \quad (6.6)$$

During the first transient phase, glucose uptake rate increased linearly from 21.7 mmol/h at 18.3 hr to 50.2 mmol/hr at 23.6 hr, i.e. $r_{\text{gluc}} = 5.40 \cdot t - 77$ (linear fit, $R^2=0.99$), while glucose concentration and reactor volume were 43 mmol/L and 0.98 L, respectively. During the second transient phase, glucose uptake rate decreased linearly from 68.7 mmol/h at 30.6 hr to 54.7 mmol/h at 35.0 hr, i.e. $r_{\text{gluc}} = -3.25 \cdot t + 169$ (linear fit, $R^2=0.99$), while glucose

concentration and reactor volume were 48 mmol/L and 1.06 L, respectively. Integration of Eq. 6.6 assuming a linear function for glucose uptake as a function of time ($r_{\text{gluc}}=a+b\cdot t$) yields the following expression for the labeling of glucose as a function of time:

$$x(t) = x_{\text{in}} + (x_0 - x_{\text{in}}) \cdot e^{\left(-\frac{a}{V \cdot c_{\text{gluc}}}t - \frac{b}{2 \cdot V \cdot c_{\text{gluc}}}t^2\right)} \quad (6.7)$$

The dashed lines in Figure 6-4 represent the predicted isotopic composition of glucose based on Eq. 6.7. We found good agreement between the predicted and the observed isotopic transients.

6.3.4 Dynamics of fed-batch fermentation

Atoms of ^{13}C -glucose pass through multiple extracellular and intracellular pools in the pathway from glucose to cellular amino acids. Metabolites in this pathway undergo a transient labeling phase similar to the one observed for glucose labeling in the medium. The characteristic time that describes this process is given by the ratio of the pool size (mmol/L) relative to the turnover rate of the pool (mmol/L/hr). Metabolite pools with short characteristic times relative to the length of the experiment reach isotopic steady state quickly, whereas pools with long characteristic times may never reach isotopic steady state. Figure 6-5 shows time profiles of enrichment for four intermediate metabolite pools in the pathway from glucose to biomass. The first panel shows the labeling of glucose feed that was changed instantaneously from unlabeled glucose to ^{13}C -labeled glucose at 18.6 hr, and visa versa at 30.0 hr. The second panel shows the observed labeling profile of glucose that was discussed in detail in the previous section. The characteristic time for glucose was about 1 hr. The third panel shows the observed enrichment of carbon dioxide in the off-gas, which is a measure of the labeling of intracellular metabolites, i.e. carbon dioxide is produced in the pentose pathway and the TCA cycle from intracellular metabolites. We found that CO_2 enrichment in the off-gas closely followed the profile of glucose labeling in the medium. This suggested that intracellular metabolite pools approximate isotopic steady state, as was expected since intracellular pools are relatively small. The estimated characteristic time for

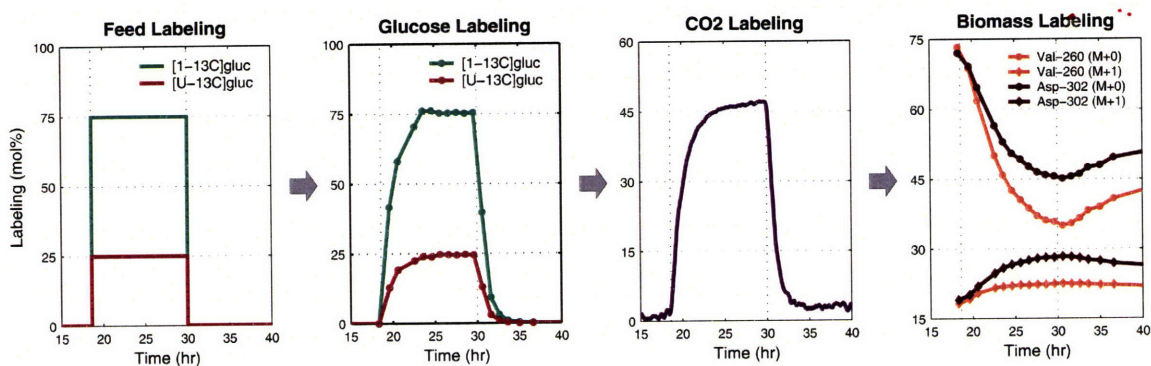


Figure 6-5: Time profiles of isotopic enrichment of four intermediate metabolite pools in the pathway from glucose to biomass. ¹³C-Labeled glucose was introduced between 18.6 hr and 30.0 hr. We observed the first isotopic transient for glucose in the reactor with a characteristic time of about 1 hr. The labeling of carbon dioxide in the off-gas reflects the labeling state of intracellular metabolites, which followed closely the labeling state of glucose in the medium, which suggested pseudo steady state for intracellular metabolites. The labeling of biomass components never reached isotopic steady state. The characteristic time for cellular amino acids was about 10 hr.

intracellular metabolites was on the order of minutes. The last panel in Figure 6-5 shows the enrichment of cellular amino acids as a function of time, where we plotted the time profiles of four representative mass isotopomers. Similar profiles were observed all other amino acid fragments. In this experiment cellular amino acids never reached isotopic steady state. We estimated a characteristic time of about 10 hr for cellular amino acids.

6.3.5 Nonstationary model for fed-batch fermentation

Based on these observations we propose the following nonstationary model for fed-batch fermentation, which is shown in Figure 6-6. This model builds on the classical stationary MFA model with the addition of two dilution parameters, i.e. D and G parameters, that were initially proposed by Kelleher and Masterson (1992) for isotopomer spectral analysis (ISA). ISA is a general method for modeling polymerization biosynthesis reactions in systems that do not approximate isotopic steady state. Here, we distinguish between two dilution effects: dilution of the tracer (i.e. glucose), and dilution of the product (i.e. cellular amino acids). Glucose labeling that is observed by cells during the labeling period is a mixture of ^{13}C -glucose and unlabeled glucose. In this framework, parameter $D(t)$ describes the apparent fractional labeling of glucose during the labeling phase. Thus, the D value is zero if there are no tracers in the system, and is one at isotopic steady state for glucose. The parameter $G(t)$ describes the fraction of ^{13}C -labeled biomass in the sampled biomass pool, while $1-G(t)$ corresponds to the fraction of unlabeled biomass. We could introduce one G parameter for all biomass components, or separate G parameters for each measured amino acid. In the absence of protein turnover we expect the same G value for all cellular amino acids. However, protein turnover may cause differences between G values for proteinogenic amino acids. In our initial model we used a separate G parameters for each amino acid pool. The nonstationary model for fed-batch fermentation closely resembles classical isotopic steady state model. Here, the D and G parameters were included in the model as additional fluxes that were estimated together with the other fluxes. Thus, we could apply the already developed flux estimation tools for stationary MFA to estimate all flux parameters in this system without increasing the complexity of calculations.

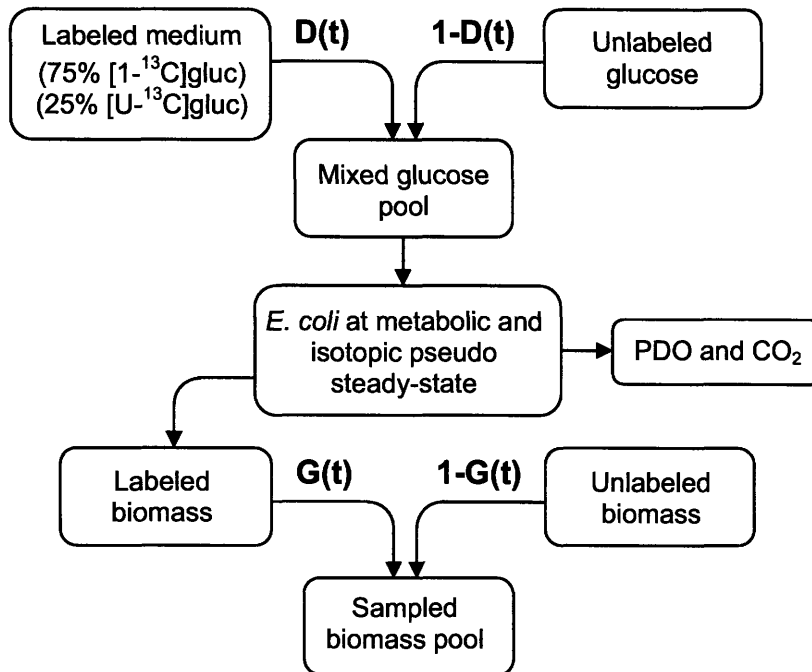


Figure 6-6: Two parameter model for modeling nonstationary tracer experiments. We distinguish two dilution effects: the dilution of the tracer (i.e. glucose), and the dilution of the sampled product (i.e. cellular amino acids). The apparent labeling of glucose observed by the cells during the labeling period is a mixture of ^{13}C -glucose and unlabeled glucose. The value of parameter $D(t)$ reflects the average labeling of glucose during the labeling period. The value of parameter $G(t)$ corresponds to the fraction of total biomass that is ^{13}C -labeled, and $1-G(t)$ is the fraction of unlabeled biomass.

6.3.6 Metabolic flux analysis

We estimated metabolic fluxes for 18 sample points, corresponding to biomass samples taken between 18.3 hr and 40.7 hr. Fluxes were estimated for each sample point individually. For each sample point we fitted 8 external fluxes and 191 mass isotopomer abundances (95 independent mass isotopomers) to a detailed flux model. The minimized objective function was the weighted sum of squared deviations residuals (SSRES) between the observed and simulated measurements. For each sample point we estimated 37 independent flux parameters, i.e. we had $95+8-37 = 66$ redundant measurements. At convergence, the goodness-of-fit was assessed by statistically evaluating SSRES. The maximum allowed value for SSRES was 86 (at 95% confidence level with 66 degrees of freedom; see Chapter 3). Fits where SSRES was larger than 86 were considered statistically not acceptable. To illustrate that both D and G parameters were required, we fitted data using models without D and G parameters. The SSRES values for these fits were statistically not acceptable as is shown in Figure 6-7. Only the model that included both parameters produced statistically acceptable fits for all sample points. The small magnitude of SSRES, the high accuracy and precision of MS data (0.3 mol%), and the large number of redundant measurements gave us very high degree of confidence in the fidelity of the calculated fluxes for all sample points. Table 6-2 shows the optimally-fitted mass isotopomer distributions for sample #12 (taken at 29.6 hr). We found excellent agreement between the observed and predicted mass isotopomer abundances with SSRES=65.2. The maximum deviation between the measured and fitted mass isotopomer abundances was 0.3 mol%. At convergence, nonlinear confidence intervals of estimated fluxes were determined using the method described in Chapter 3. Figure 6-8 shows the estimated fluxes for sample point #12.

Metabolic fluxes were determined at multiple time points during the fed-batch culture. As such we established for the first time detailed time profiles of intracellular fluxes. Fluxes were normalized to glucose uptake rate, which was given the value 100. Figure 6-9 shows time profiles of selected intracellular fluxes, where we plotted the optimally-fitted flux value and 68% confidence interval as a function of fermentation time. The time profiles in Figure 6-9 clearly illustrate that intracellular fluxes were relatively constant during the fed-batch

fermentation. The split ratio between glycolysis and pentose phosphate pathway decreased only slightly from 60/40 at 20 hr to about 50/50 at 40 hr. The flux of lower glycolysis (GAP→Pyr) decreased from 70 ± 2 to 50 ± 2 in the same period of time. On the other hand, the TCA flux remained constant at 47 ± 2 throughout the fermentation. The intracellular flux towards PDO and glycerol increased by about 10% from 118 ± 6 to 130 ± 6 . An interesting finding was that this intracellular flux was relatively constant compared to the large fluctuations in the efflux of PDO, i.e. PDO efflux increased from 78 (at 18.6 hr) to 137 (at 28.6 hr), and to 130 (at 40.7 hr). Our results further indicated that the Entner-Doudoroff pathway was inactive, i.e. the estimated flux of 0.0 ± 0.5 was not statistically different from zero. This result confirmed the known genotype of this organism, i.e. phosphogluconate dehydratase a key enzymes of the Entner-Doudoroff pathway was knocked-out in this strain of *E. coli*. Our flux results revealed the presence of a futile cycle between oxaloacetate and phosphoenolpyruvate. The estimated phosphoenolpyruvate carboxylase and phosphoenolpyruvate carboxykinase fluxes were 14 ± 2 and 5 ± 2 , respectively. The simultaneous activity of these two reactions created a futile cycle where 1 ATP was lost at each turn of the cycle. It is not clear what the physiological significance is of this futile cycle. The total activity of malic enzyme was estimated at 5 ± 1 ; we could not distinguish between the two isoforms of malic enzyme, i.e. NADH and NADPH dependent malic enzyme. Thus, only the combined malic enzyme flux was determined. We estimated only a slightly positive net transhydrogenase flux (i.e. NADH → NADPH) of about 20 ± 15 , which was not statistically different from zero. Finally, we estimated significant net production of ATP of 210 ± 18 , which was not accounted for by the ATP consuming reactions in our model. Potential sinks for this ATP are cell maintenance, transport of metabolites across cell membrane, and futile cycles.

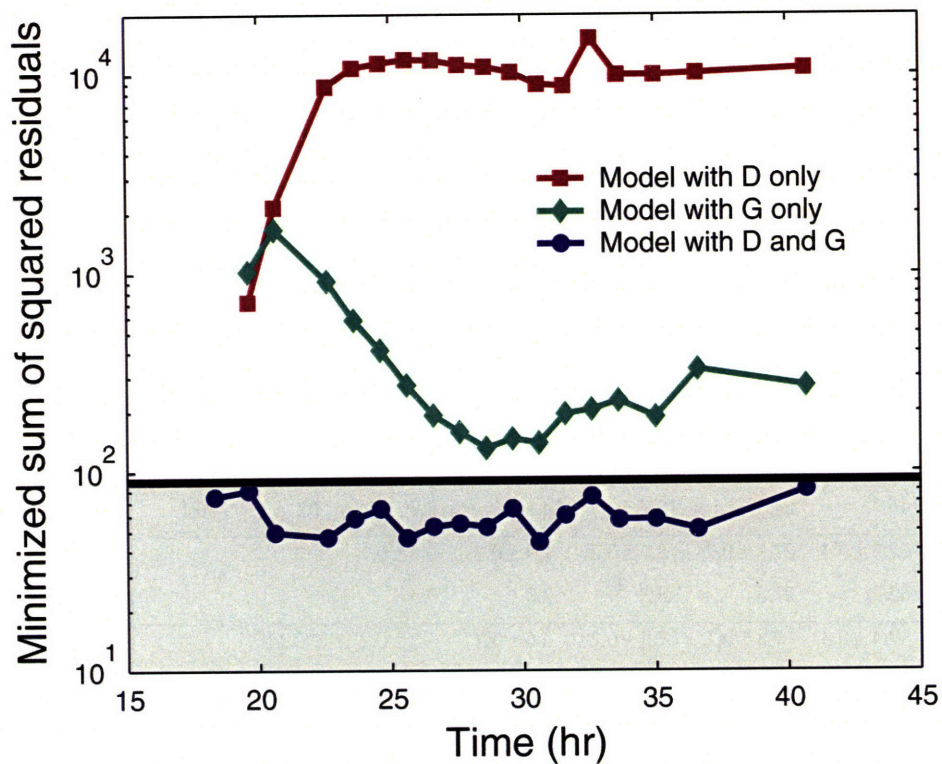


Figure 6-7: Evaluation of goodness-of-fit for models with a D-parameter, a G-parameter and both parameters. Mass isotopomer data from 18 biomass samples were fitted independently to the three models. Shown are the minimized variance-weighted sum of squared residuals for the 18 sample points. Shaded area indicates the statistically acceptable 95% confidence region for the sum of squared residuals. Models lacking the D or G parameters were statistically not acceptable. Only the model that included both parameters produced statistically acceptable fits for all sample points.

Table 6-2

Measured and fitted mass isotopomer abundances. Mass isotopomer abundances of cellular amino acid were measured by GC/MS, after TBDMS derivatization. Data shown are the uncorrected mass isotopomer abundances (molar percentages, mol%) for biomass sample #12 (taken at 29.6 hr) (mean \pm SD). The optimally fitted mass isotopomer distributions ('Calc') corresponded well with the measured values ('Exp').

Fragment		M+0	M+1	M+2	M+3	M+4	M+5	M+6	M+7	M+8
Ala-232	Exp	49.1 \pm 0.2	24.3 \pm 0.2	20.6 \pm 0.2	4.4 \pm 0.2	1.4 \pm 0.2	0.2 \pm 0.1			
	Calc	49.1	24.4	20.5	4.4	1.4	0.2			
Ala-260	Exp	46.6 \pm 0.2	24.4 \pm 0.2	11.0 \pm 0.2	14.0 \pm 0.2	2.9 \pm 0.2	1.1 \pm 0.2	0.1 \pm 0.1		
	Calc	46.7	24.5	10.7	14.1	2.9	1.1	0.1		
Gly-218	Exp	62.5 \pm 0.3	27.1 \pm 0.2	8.2 \pm 0.2	1.9 \pm 0.2	0.3 \pm 0.1				
	Calc	62.2	27.3	8.2	2.0	0.3				
Gly-246	Exp	57.4 \pm 0.3	19.8 \pm 0.2	17.9 \pm 0.2	3.6 \pm 0.2	1.2 \pm 0.2	0.2 \pm 0.1			
	Calc	57.7	19.7	17.7	3.5	1.2	0.2			
Val-260	Exp	35.9 \pm 0.2	22.5 \pm 0.2	23.2 \pm 0.2	11.1 \pm 0.2	5.7 \pm 0.2	1.3 \pm 0.2	0.3 \pm 0.1		
	Calc	36.2	22.7	23.1	10.9	5.6	1.3	0.3		
Val-288	Exp	35.1 \pm 0.2	22.2 \pm 0.2	17.4 \pm 0.2	13.8 \pm 0.2	6.3 \pm 0.2	4.0 \pm 0.2	0.9 \pm 0.1	0.3 \pm 0.1	
	Calc	34.8	22.3	17.6	13.7	6.4	4.0	0.9	0.3	
Leu-274	Exp	28.5 \pm 0.2	22.7 \pm 0.2	21.8 \pm 0.2	15.4 \pm 0.2	7.8 \pm 0.2	3.1 \pm 0.2	0.7 \pm 0.1	0.2 \pm 0.1	
	Calc	28.5	22.5	21.9	15.5	7.8	3.1	0.7	0.2	
Ile-274	Exp	28.7 \pm 0.2	22.6 \pm 0.2	21.8 \pm 0.2	15.3 \pm 0.2	7.8 \pm 0.2	3.0 \pm 0.2	0.7 \pm 0.1	0.2 \pm 0.1	
	Calc	28.7	22.5	21.9	15.4	7.7	3.0	0.7	0.2	
Ser-288	Exp	45.6 \pm 0.2	29.7 \pm 0.2	18.4 \pm 0.2	4.8 \pm 0.2	1.3 \pm 0.2	0.2 \pm 0.1			
	Calc	45.6	29.6	18.5	4.8	1.3	0.2			
Ser-362	Exp	40.9 \pm 0.2	29.8 \pm 0.2	20.1 \pm 0.2	6.5 \pm 0.2	2.1 \pm 0.2	0.4 \pm 0.1	0.1 \pm 0.1		
	Calc	41.0	29.7	20.1	6.5	2.1	0.4	0.1		
Ser-390	Exp	39.0 \pm 0.2	27.2 \pm 0.2	15.5 \pm 0.2	12.6 \pm 0.2	3.9 \pm 0.2	1.4 \pm 0.2	0.3 \pm 0.1	0.1 \pm 0.1	
	Calc	38.9	27.1	15.8	12.5	3.9	1.4	0.3	0.1	
Thr-376	Exp	31.7 \pm 0.2	28.9 \pm 0.2	22.1 \pm 0.2	12.0 \pm 0.2	4.0 \pm 0.2	1.2 \pm 0.2	0.3 \pm 0.1		
	Calc	31.8	28.9	22.0	11.9	3.9	1.2	0.3		
Thr-404	Exp	28.1 \pm 0.2	26.1 \pm 0.2	21.8 \pm 0.2	13.9 \pm 0.2	7.1 \pm 0.2	2.3 \pm 0.2	0.7 \pm 0.1	0.1 \pm 0.1	
	Calc	28.0	26.1	21.8	13.9	7.1	2.3	0.7	0.1	

Table 6-2 (continued)

Measured and fitted mass isotopomer abundances.

Fragment		M+0	M+1	M+2	M+3	M+4	M+5	M+6	M+7	M+8
Met-292	Exp	27.5 ± 0.2	25.9 ± 0.2	23.4 ± 0.2	14.4 ± 0.2	6.3 ± 0.2	1.9 ± 0.2	0.5 ± 0.1		
	Calc	27.7	25.9	23.4	14.3	6.2	1.9	0.5		
Met-320	Exp	25.1 ± 0.2	22.9 ± 0.2	22.2 ± 0.2	15.5 ± 0.2	9.1 ± 0.2	3.7 ± 0.2	1.1 ± 0.2	0.3 ± 0.1	
	Calc	25.0	22.8	22.4	15.7	9.0	3.7	1.1	0.3	
Phe-302	Exp	58.3 ± 0.3	18.3 ± 0.2	17.9 ± 0.2	4.0 ± 0.2	1.3 ± 0.2	0.2 ± 0.1			
	Calc	58.1	18.3	18.0	4.1	1.3	0.2			
Phe-308	Exp	27.7 ± 0.2	18.3 ± 0.2	17.8 ± 0.2	12.5 ± 0.2	10.0 ± 0.2	6.4 ± 0.2	4.3 ± 0.2	2.0 ± 0.2	0.9 ± 0.1
	Calc	27.9	18.0	17.8	12.5	10.0	6.4	4.3	2.0	0.9
Phe-336	Exp	27.3 ± 0.2	17.9 ± 0.2	14.1 ± 0.2	12.9 ± 0.2	10.3 ± 0.2	7.5 ± 0.2	4.8 ± 0.2	2.9 ± 0.2	1.4 ± 0.2
	Calc	27.2	17.9	14.3	13.1	10.4	7.6	4.7	2.8	1.3
Asp-302	Exp	45.7 ± 0.2	28.3 ± 0.2	19.4 ± 0.2	5.0 ± 0.2	1.4 ± 0.2	0.2 ± 0.1			
	Calc	45.8	28.2	19.4	5.0	1.4	0.2			
Asp-376	Exp	41.3 ± 0.2	28.4 ± 0.2	20.8 ± 0.2	6.7 ± 0.2	2.3 ± 0.2	0.5 ± 0.1	0.1 ± 0.1		
	Calc	41.2	28.4	20.8	6.7	2.3	0.5	0.1		
Asp-390	Exp	31.7 ± 0.2	28.9 ± 0.2	22.0 ± 0.2	11.9 ± 0.2	4.0 ± 0.2	1.2 ± 0.2	0.2 ± 0.1		
	Calc	31.7	28.9	22.1	11.9	4.0	1.2	0.3		
Asp-418	Exp	27.8 ± 0.2	26.1 ± 0.2	21.8 ± 0.2	14.0 ± 0.2	7.1 ± 0.2	2.3 ± 0.2	0.7 ± 0.1	0.1 ± 0.1	
	Calc	27.8	26.1	21.9	13.9	7.1	2.3	0.7	0.2	
Glu-330	Exp	29.6 ± 0.2	26.1 ± 0.2	23.0 ± 0.2	13.5 ± 0.2	5.8 ± 0.2	1.5 ± 0.2	0.4 ± 0.1	0.1 ± 0.1	
	Calc	29.5	26.1	23.2	13.4	5.8	1.5	0.4	0.1	
Glu-404	Exp	26.7 ± 0.2	25.4 ± 0.2	23.6 ± 0.2	14.6 ± 0.2	6.8 ± 0.2	2.2 ± 0.2	0.6 ± 0.1	0.1 ± 0.1	
	Calc	26.6	25.5	23.6	14.5	6.9	2.2	0.6	0.1	
Glu-432	Exp	23.5 ± 0.2	22.1 ± 0.2	22.4 ± 0.2	16.6 ± 0.2	9.4 ± 0.2	4.2 ± 0.2	1.3 ± 0.2	0.4 ± 0.1	0.1 ± 0.1
	Calc	23.7	22.2	22.4	16.6	9.3	4.1	1.3	0.4	0.1
Tyr-302	Exp	58.1 ± 0.3	18.3 ± 0.2	18.0 ± 0.2	4.0 ± 0.2	1.3 ± 0.2	0.2 ± 0.1			
	Calc	58.1	18.3	18.0	4.1	1.3	0.2			

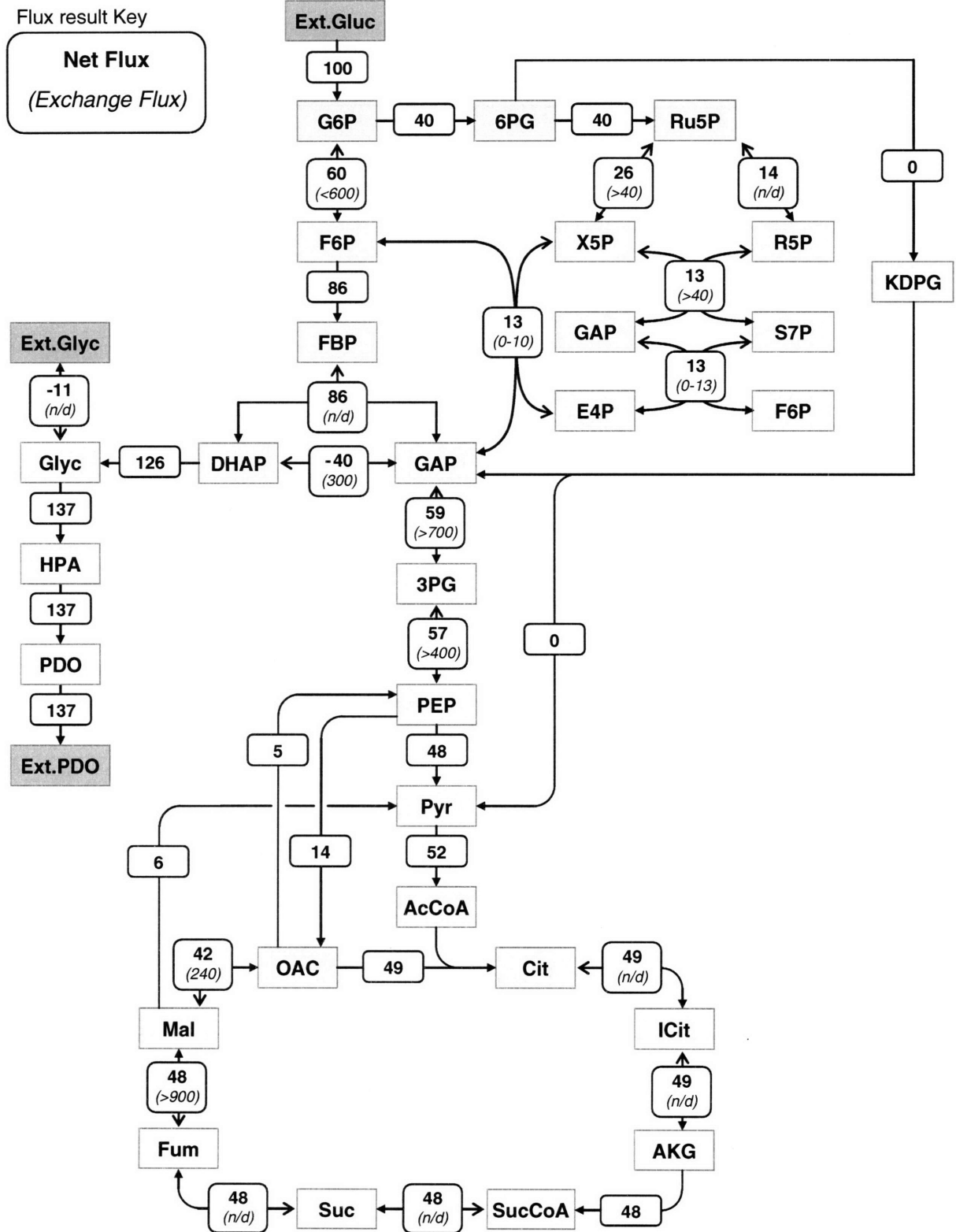


Figure 6-8: Metabolic fluxes of *E. coli* grown in carbon-limited fed-batch culture. Metabolic fluxes were determined by fitting 8 external fluxes and 191 mass isotopomer abundances to a detailed flux model of *E. coli*. Fluxes were normalized to glucose uptake rate. Shown are estimated fluxes for sample point #12 (at 29.6 hr). The top number is the estimated net flux and the bottom number (in *italics* and between brackets) is the estimated exchange flux, where 'n/d' indicates that the flux could not be estimated.

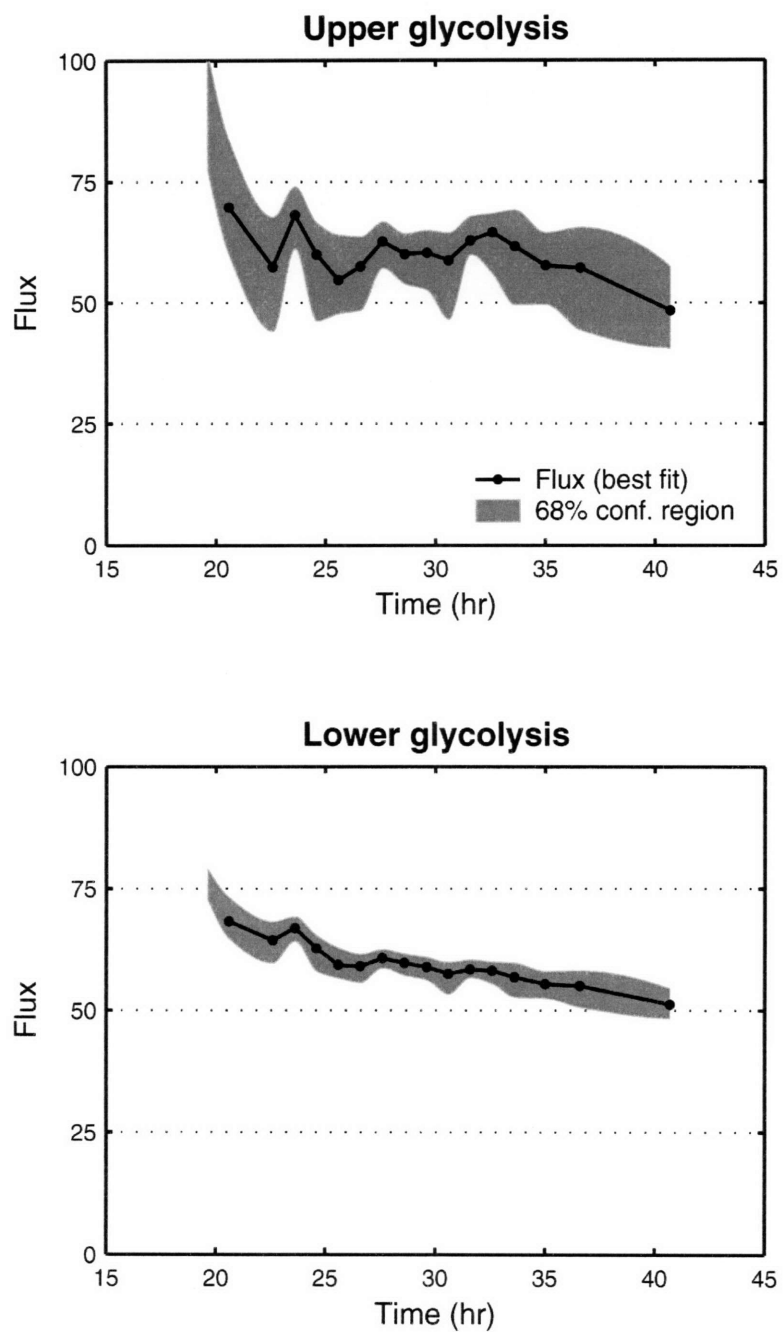


Figure 6-9: Time profiles of selected intracellular fluxes. The best fit (solid line) and the 68% confidence interval (shaded area) are shown as a function of time for the 18 sample points. Fluxes were normalized to glucose uptake rate.

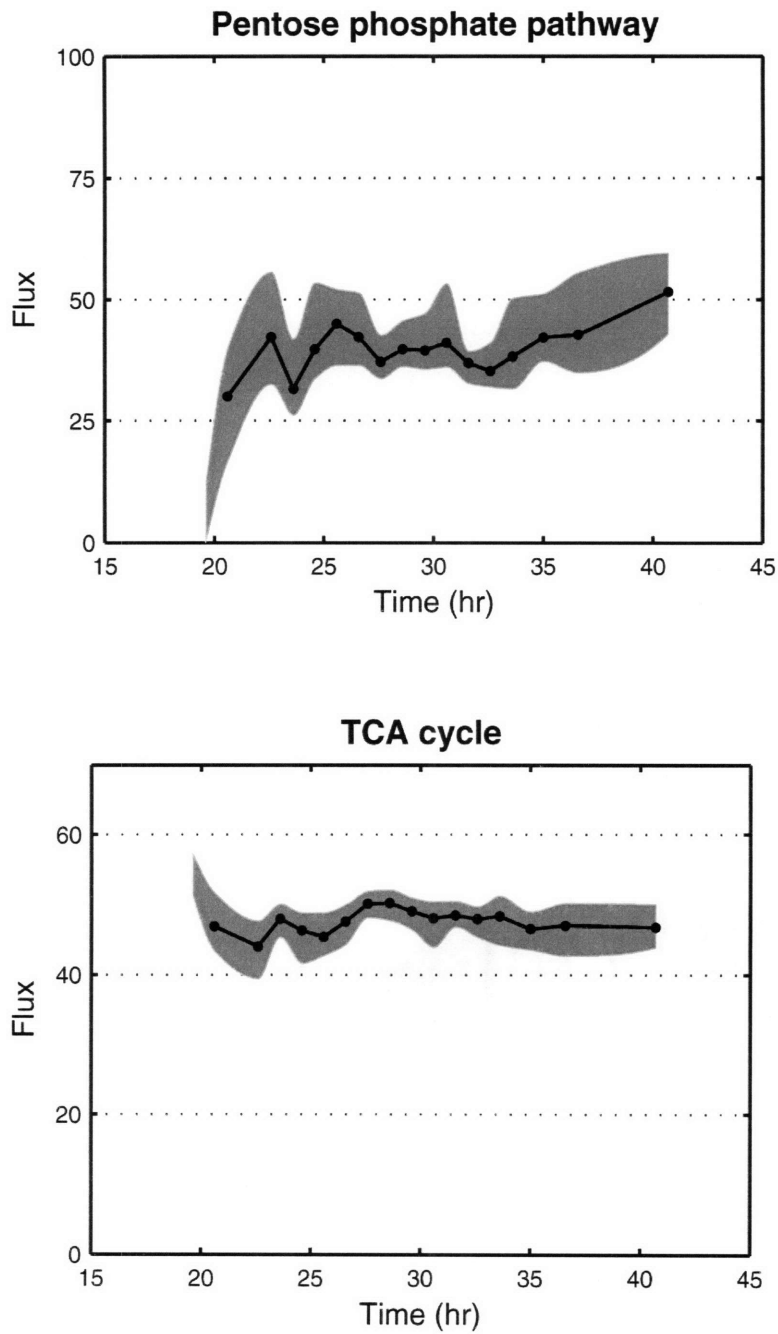


Figure 6-9 (continued): Time profiles of selected intracellular fluxes. The pentose phosphate flux increased slightly in time. The TCA flux was constant at 47 ± 2 .

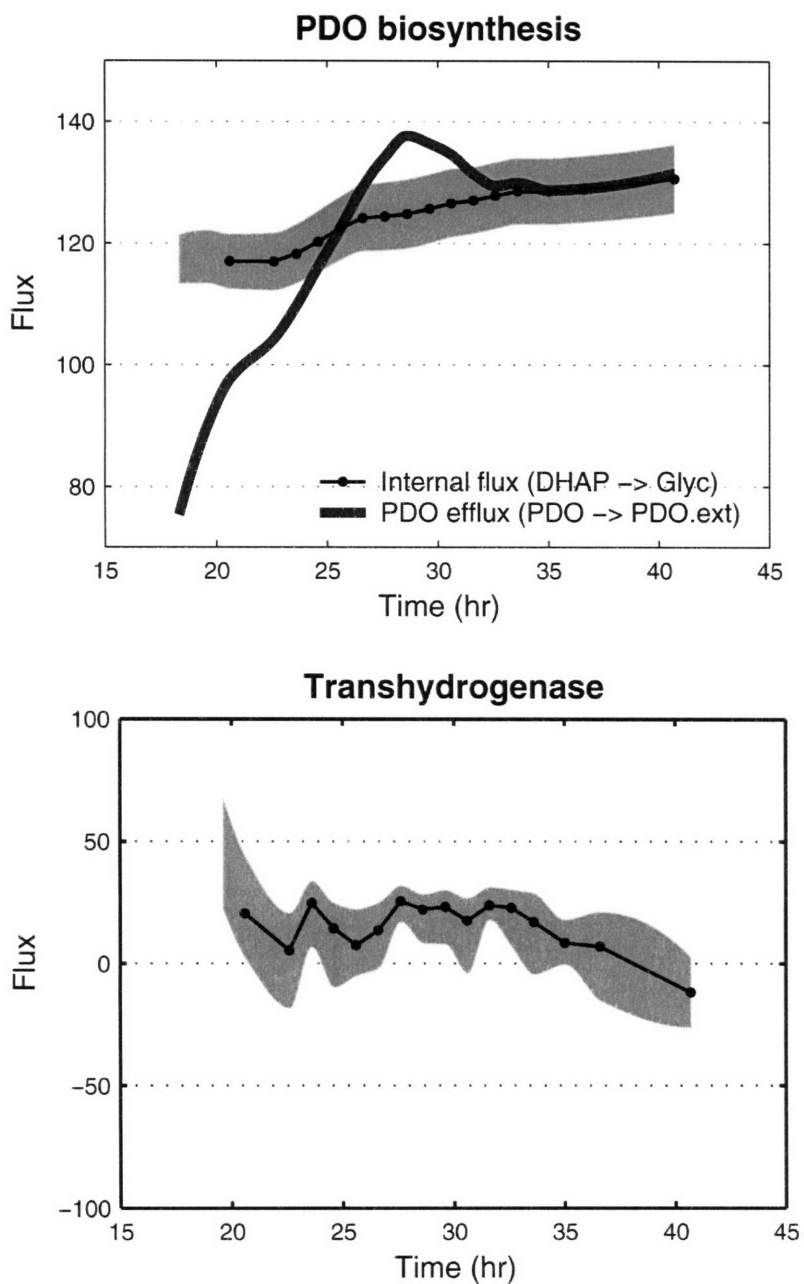


Figure 6-9 (continued): Time profiles of selected intracellular fluxes. The intracellular flux towards glycerol and PDO increased by 10% from 118 ± 6 to 130 ± 6 , whereas the efflux of PDO fluctuated significantly. The transhydrogenase flux was not significantly different from zero.

6.3.7 Evaluation of estimated D and G parameters

As indicated earlier, the key to successful flux determination in this nonstationary system was the introduction of two dilution parameters, the D parameter to account for the dilution of the tracer and the G parameter to account for the dilution of biomass components. Values for both parameters were estimated together with fluxes from mass isotopomer distributions of sampled biomass pools. Our initial model contained 12 individual G parameters, i.e. one G parameter for each of the 12 measured amino acids. The estimated G values for the 12 amino acids were not significantly different from one another, indicating that one G value could be used for all biomass components. When we repeated flux estimation with a single G parameter we obtained the same flux results. The sum of squared residuals increased slightly compared to the model with 12 individual G parameters, however the SSRES was still within statistically acceptable limits, especially when we took into account the fewer number of free flux parameters that were fitted. Time profiles of the estimated D and G parameters are shown in Figure 6-10. We can explain the observed profiles as follows. The G parameter reflects the fraction of biomass that is labeled. Biomass produced before the introduction of tracers was unlabeled, and thus the G value was zero. The observed increase in G value after 18.6 hr reflects the production of labeled biomass, i.e. the fraction of labeled biomass increased. The G value decreased after tracer was depleted reflecting the fact that unlabeled biomass was again produced, i.e. the fraction of labeled biomass decreased. Note that there was a delay between the switch to unlabeled feed at 30.0 h and the first noticeable decrease in the G value at 31.6 hr. This delay reflect the fact that labeled glucose was still present in the reactor for several hours after the feed was switched to unlabeled glucose feed (see Figure 6-5). The D value describes the average enrichment of glucose from which labeled biomass is produced. Figure 6-10 shows that the D value increased starting at 18.6 hr, i.e. reflecting the approach to isotopic steady state of the glucose pool. Note that the D value never reaches unity, because there was always a fraction of biomass that was produced from partially labeled glucose. After the tracer was removed the D value first dropped slightly, i.e. reflecting the second glucose transient, and then remained constant at about 0.9. At that point only unlabeled biomass was produced, which was accounted for by the G

parameter. The constant D value after 31.6 hr indicates biomass turnover was not significant. We set up the following theoretical model for the D and G parameters.

$$D(t) = \frac{\int_0^t \delta(t) \cdot L(t) \cdot \mu(t) \cdot dt}{\int_0^t \delta(t) \cdot \mu(t) \cdot dt} \quad (6.8)$$

$$G(t) = \frac{\int_0^t \delta(t) \cdot \mu(t) \cdot dt}{\int_0^t \mu(t) \cdot dt} \quad (6.9)$$

$$\text{with } \delta(t) = \begin{cases} 0 & \text{if } L(t) < 0.2 \\ 1 & \text{if } L(t) \geq 0.2 \end{cases} \quad (6.10)$$

Here, $L(t)$ is fractional labeling of glucose in the medium (i.e. which corresponds directly to the measured glucose labeling shown in Figure 6-4), $\mu(t)$ is the biomass growth rate, and $\delta(t)$ formally defines what we mean by ‘the labeling phase’. In this case, we define the labeling phase as the timeframe when fractional glucose labeling is at least 20% of isotopic steady state value. This definition was required, otherwise the D and G parameters became highly correlated at low glucose enrichments. In this experiment, $\delta(t)$ was unity between 19.0 h and 31.3 h, and zero everywhere else. We used Eqs. 6.7 and 6.8 to predict time profiles of D and G parameters based on measured labeling of glucose and growth rate as a function time. The predicted time profiles are plotted in Figure 6-10. We found good agreement between the predicted and estimated D and G values, which result further supports the validity of our assumptions and this modeling approach.

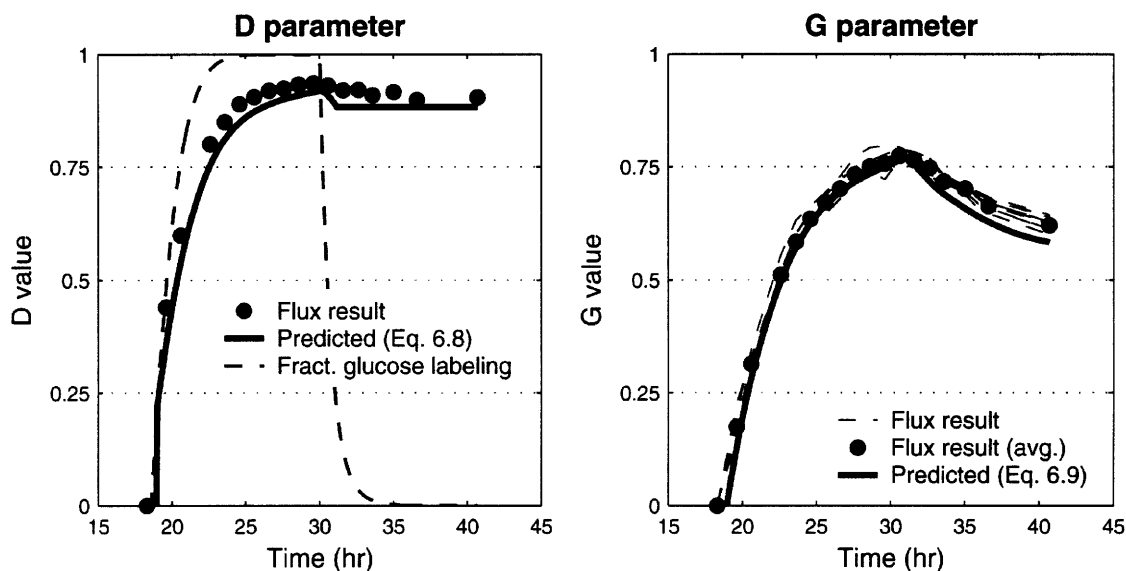
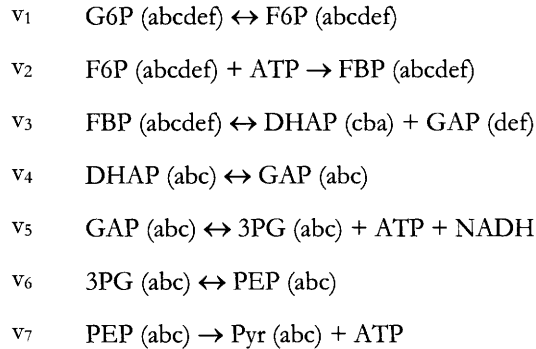
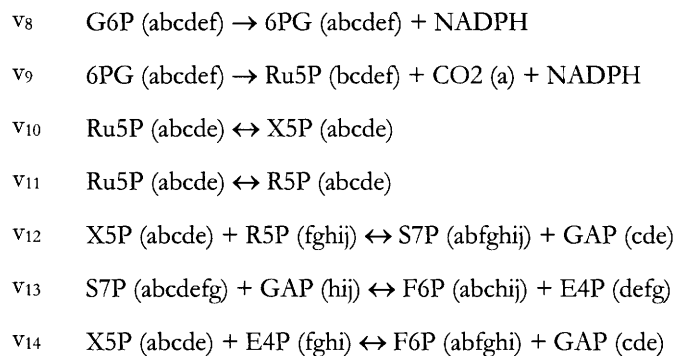
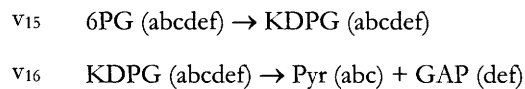
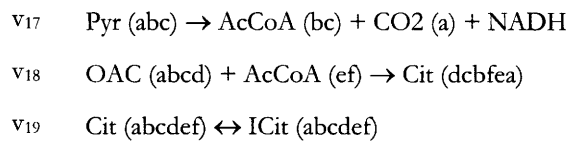


Figure 6-10: Time profiles of estimated and predicted D and G parameters. The dots represent estimated D and G parameters from MFA. The solid line represent the predicted parameters based on Eqs. 6.8 and 6.9. We found good agreement between the predicted and estimated parameter values, in support of the validity of our modeling method. The dashed line in the left panel shows the fractional labeling of glucose, i.e. $L(t)$ in Eq. 6.8. The G values for individual amino acids (dashed lines in right panel) were not significantly different from one another, indicating that one G value could be used for all biomass components.

6.4 Discussion

In this contribution, we presented a novel modeling strategy for metabolic flux analysis in nonstationary systems. Isotopic transients of precursor (i.e. glucose) and products (i.e. sampled biomass components) were captured by two dilution parameters, i.e. D and G parameters, respectively. We applied this modeling strategy to estimate intracellular fluxes of *E. coli* in a fed-batch fermentation. Fluxes were determined by fitting an over-determined data set of external flux measurements and labeling patterns of cellular amino acids to a detailed model of *E. coli*. We obtained highly consistent fits with 66 redundant measurements, which gave us a high degree of confidence in the estimated flux parameters. Metabolic fluxes were determined for multiple time points, and as such we established for the first time detailed time profiles of intracellular fluxes during a fed-batch fermentation. The estimated fluxes provided insight into the overproduction of PDO by *E. coli* and confirmed the genotype of this organism. The additional D and G parameters were estimated together with the fluxes. We related the D and G parameter values to the labeling history of sampled biomass. The G value was the fraction of labeled biomass in the total biomass pool, and the D value was the biomass-averaged glucose labeling. The predicted values for D and G parameters corresponded well with the estimated parameter values from MFA.

APPENDIX 6.A**Metabolic network model of *E. coli*****Glycolysis****Pentose Phosphate Pathway****Entner-Doudoroff Pathway****TCA Cycle**

- v₂₀ ICit (abcdef) \leftrightarrow AKG (abcde) + CO₂ (f) + NADPH
 v₂₁ AKG (abcde) \rightarrow SucCoA (bcde) + CO₂ (a) + NADH
 v₂₂ SucCoA (abcd) \leftrightarrow Suc ($\frac{1}{2}$ abcd + $\frac{1}{2}$ dcba) + ATP
 v₂₃ Suc ($\frac{1}{2}$ abcd + $\frac{1}{2}$ dcba) \leftrightarrow Fum ($\frac{1}{2}$ abcd + $\frac{1}{2}$ dcba) + FADH₂
 v₂₄ Fum ($\frac{1}{2}$ abcd + $\frac{1}{2}$ dcba) \leftrightarrow Mal (abcd)
 v₂₅ Mal (abcd) \leftrightarrow OAC (abcd) + NADH

Amphibolic Reactions

- v₂₆ Mal (abcd) \rightarrow Pyr (abc) + CO₂ (d) + NADPH
 v₂₇ Mal (abcd) \rightarrow Pyr (abc) + CO₂ (d) + NADH
 v₂₈ PEP (abc) + CO₂ (d) \rightarrow OAC (abcd)
 v₂₉ OAC (abcd) + ATP \rightarrow PEP (abc) + CO₂ (d)

Acetic Acid Formation

- v₃₀ AcCoA (ab) \leftrightarrow Ac (ab) + ATP

PDO Biosynthesis

- v₃₁ DHAP (abc) + NADH \leftrightarrow Glyc3P (abc)
 v₃₂ Glyc3P (abc) \rightarrow Glyc (abc)
 v₃₃ Glyc (abc) \rightarrow HPA (abc)
 v₃₄ HPA (abc) + NADPH \rightarrow PDO (abc)

Amino Acid Biosynthesis

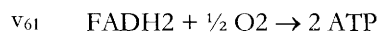
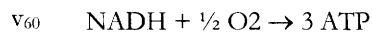
- v₃₅ AKG (abcde) + NADPH + NH₃ \rightarrow Glu (abcde)
 v₃₆ Glu (abcde) + ATP + NH₃ \rightarrow Gln (abcde)
 v₃₇ Glu (abcde) + ATP + 2 NADPH \rightarrow Pro (abcde)
 v₃₈ Glu (abcde) + CO₂ (f) + Gln (ghijk) + Asp (lmno) + AcCoA (pq) + 5 ATP + NADPH \rightarrow
 Arg (abcdef) + AKG (ghijk) + Fum (lmno) + Ac (pq)
 v₃₉ OAC (abcd) + Glu (efghi) \rightarrow Asp (abcd) + AKG (efghi)
 v₄₀ Asp (abcd) + 2 ATP + NH₃ \rightarrow Asn (abcd)

- V41 Pyr (abc) + Glu (defgh) → Ala (abc) + AKG (defgh)
- V42 3PG (abc) + Glu (defgh) → Ser (abc) + AKG (defgh) + NADH
- V43 Ser (abc) ↔ Gly (ab) + MEETHF (c)
- V44 Gly (ab) ↔ CO₂ (a) + MEETHF (b) + NADH + NH₃
- V45 Thr (abcd) → Gly (ab) + AcCoA (cd) + NADH
- V46 Ser (abc) + AcCoA (de) + 3 ATP + 4 NADPH + SO₄ → Cys (abc) + Ac (de)
- V47 Asp (abcd) + Pyr (efg) + Glu (hijkl) + SucCoA (mnop) + ATP + 2 NADPH →
LL-DAP (abcdgfe) + AKG (hijkl) + Suc (½ mnop + ½ ponm)
- V48 LL-DAP (abcdefg) → Lys (abcdef) + CO₂ (g)
- V49 Asp (abcd) + 2 ATP + 2 NADPH → Thr (abcd)
- V50 Asp (abcd) + METHF (e) + Cys (fgh) + SucCoA (ijkl) + ATP + 2 NADPH →
Met (abcde) + Pyr (fgh) + Suc (½ ijkl + ½ lkji) + NH₃
- V51 Pyr (abc) + Pyr (def) + Glu (ghijk) + NADPH → Val (abcef) + CO₂ (d) + AKG (ghijk)
- V52 AcCoA (ab) + Pyr (cde) + Pyr (fgh) + Glu (ijklm) + NADPH →
Leu (abdghe) + CO₂ (c) + CO₂ (f) + AKG (ijklm) + NADH
- V53 Thr (abcd) + Pyr (efg) + Glu (hijkl) + NADPH → Ile (abfcdg) + CO₂ (e) + AKG (hijkl) + NH₃
- V54 PEP (abc) + PEP (def) + E4P (ghij) + Glu (klmno) + ATP + NADPH →
Phe (abcefghij) + CO₂ (d) + AKG (klmno)
- V55 PEP (abc) + PEP (def) + E4P (ghij) + Glu (klmno) + ATP + NADPH →
Tyr (abcefghij) + CO₂ (d) + AKG (klmno) + NADH
- V56 Ser (abc) + R5P (defgh) + PEP (ijk) + E4P (lmno) + PEP (pqr) + Gln (stuvw) + 3 ATP + NADPH →
Trp (abcdklmnoj) + CO₂ (i) + GAP (fgh) + Pyr (pqr) + Glu (stuvw)
- V57 R5P (abcde) + FTHF (f) + Gln (ghijk) + Asp (lmno) + 5 ATP →
His (edcbaf) + AKG (ghijk) + Fum (lmno) + 2 NADH

One-Carbon Metabolism

- V58 MEETHF (a) + NADH → METHF (a)
- V59 MEETHF (a) → FTHF (a) + NADPH

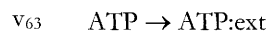
Oxidative Phosphorylation



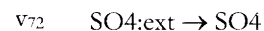
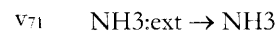
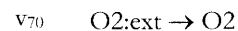
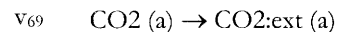
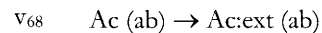
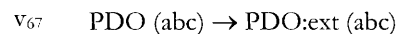
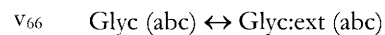
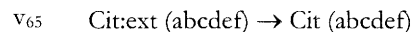
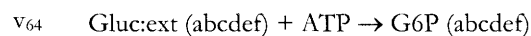
Transhydrogenation



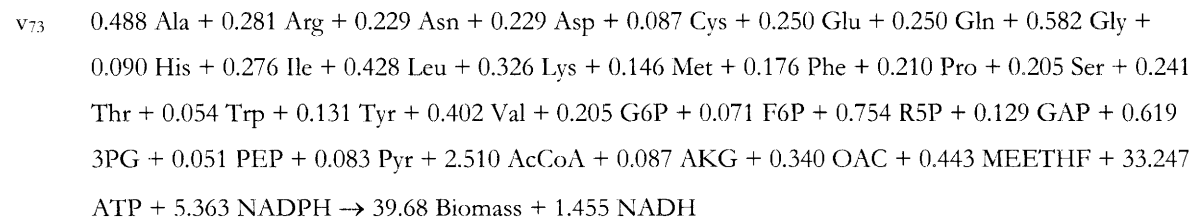
ATP Hydrolysis



Transport



Biomass Formation*



* The biomass formation reaction is based on precursor and cofactor requirements for *E. coli* as described by Neidhardt.

APPENDIX 6.B

Validation of carbon balance and degree of reduction balance

External fluxes were checked for gross errors by validating the carbon balance and the degree of reduction balance. The carbon balance is given by:

$$\frac{\text{carbon}_{\text{in}}}{\text{carbon}_{\text{out}}} = \frac{\sum c_i \cdot v_{i,\text{in}}}{\sum c_i \cdot v_{i,\text{out}}} = \frac{6 \cdot v_{\text{glucose}} + 6 \cdot v_{\text{citrate}}}{v_{\text{biomass}} + 3 \cdot v_{\text{PDO}} + 3 \cdot v_{\text{glycerol}} + v_{\text{CO}_2} + 2 \cdot v_{\text{acetate}}} \quad (6.B1)$$

The degree of reduction balance is given by:

$$\frac{\text{free electrons}_{\text{in}}}{\text{free electrons}_{\text{out}}} = \frac{\sum \gamma_i \cdot v_{i,\text{in}}}{\sum \gamma_i \cdot v_{i,\text{out}}} = \frac{24 \cdot v_{\text{glucose}} + 18 \cdot v_{\text{citrate}} - 4 \cdot v_{\text{O}_2}}{4.2 \cdot v_{\text{biomass}} + 16 \cdot v_{\text{PDO}} + 14 \cdot v_{\text{glycerol}} + 8 \cdot v_{\text{acetate}}} \quad (6.B2)$$

In the above equations c_i is the number of carbon atoms, v_i is the rate of production, and γ_i is the degree of reduction for metabolite i . The degree of reduction corresponds to the number of free electrons, defined such that $\gamma_i=0$ for the following small molecules: H_2O , H^+ , CO_2 , HCO_3^- , NH_4^+ , SO_4^{2-} , PO_4^{3-} . These metabolites are therefore not included in Eq. 6.B2. In general, the degree of reduction for any arbitrary metabolite $\text{C}_c\text{H}_h\text{O}_o\text{N}_n\text{S}_s\text{P}_p^{(\text{charge})}$ is calculated as follows:

$$\gamma = 4 \cdot \text{C} + \text{H} - 2 \cdot \text{O} - 3 \cdot \text{N} + 6 \cdot \text{S} + 5 \cdot \text{P} - \text{charge} \quad (6.B3)$$

APPENDIX 6.C

Fermentation data

Sample (#)	Time (hr)	Unlabeled	Labeled	Reactor	Sample	OD ₅₅₀ (-)	Glucose (mM)	Glycerol (mM)	Acetate (mM)	PDO (mM)	Citrate (mM)**
		Feed (g)***	Feed (g)	Volume (L)*	Volume (mL)						
0	0.1	45.1	0.0	0.99	11	0.1	112.2	0.0	0.0	1.5	9.2
1	15.4	47.1	0.0	0.98	11	3.2	55.3	75.4	0.0	N/A	14.6
2	18.3	56.4	0.0	0.98	21	6.3	40.5	109.3	0.0	28.3	14.1
3	19.6	65.6	10.6	0.97	11	8.1	47.0	114.5	0.0	57.4	13.8
4	20.6	65.6	22.6	0.97	11	9.8	46.9	120.6	1.3	88.1	13.6
5	22.6	65.6	51.6	1.00	15	14.0	37.4	133.4	1.8	175.0	13.0
6	23.6	65.6	71.9	0.99	11	16.1	41.1	135.7	2.4	221.7	12.6
7	24.6	65.6	93.8	0.99	11	18.8	43.0	137.9	3.2	281.8	12.2
8	25.6	65.6	118.6	1.00	11	20.8	47.8	137.4	3.9	350.3	11.5
9	26.6	65.6	145.3	1.01	12	22.0	52.8	132.8	3.8	424.9	10.8
10	27.6	65.6	169.0	1.02	11	23.5	45.6	124.8	4.2	499.7	10.2
11	28.6	65.6	197.7	1.03	11	24.7	50.7	114.5	3.8	577.3	9.6
12	29.6	65.6	227.2	1.04	16	26.0	56.9	103.7	4.4	657.7	9.4
13	30.6	76.8	240.0	1.01	11	27.2	46.4	96.8	4.2	742.4	9.1
14	31.6	104.8	240.0	1.07	12	28.2	48.5	89.8	4.6	806.1	8.7
15	32.6	130.4	240.0	1.06	11	28.8	44.5	86.8	4.0	872.0	8.3
16	33.6	154.2	240.0	1.07	11	30.0	45.6	84.9	5.6	932.4	7.9
17	35.0	185.2	240.0	1.10	11	30.4	43.9	82.0	5.7	1006.6	7.5
18	36.6	220.4	240.0	1.11	11	31.2	49.3	80.8	5.4	1070.8	7.3
19	40.7	288.2	240.0	1.16	11	33.0	47.8	75.8	5.9	1246.4	6.9
20	42.6	315.9	240.0	1.17	11	31.8	52.9	74.5	5.0	1304.1	6.9
21	44.6	345.1	240.0	1.19	17	31.2	62.0	70.3	4.5	1312.0	6.7

* The specific gravity of medium was 1.030 g/mL.

** Citrate data may be inaccurate, i.e. citrate co-eluted with another metabolite in the HPLC analysis.

*** Unlabeled feed contains 46.2 wt% glucose. Labeled feed contains 46.2 wt% glucose (75 wt% [¹³C]glucose and 25wt% [U-¹³C]glucose).

APPENDIX 6.D

Off-gas analysis data

Sample (#)	Time (hr)	Flow Rate (SLPM)*	O _{2,in} (%)	N _{2,in} (%)	¹² CO _{2,out} (%)	¹³ CO _{2,out} (%)	O _{2,out} (%)	N _{2,out} (%)
0	0.1	0.500	20.88	78.19	0.02	0.00	20.87	78.21
1	15.4	0.500	20.86	78.21	1.24	0.01	20.05	77.80
2	18.3	0.500	20.87	78.20	2.77	0.06	19.30	76.98
3	19.6	0.500	20.88	78.19	2.79	0.85	18.89	76.58
4	20.6	0.500	20.87	78.20	2.84	1.48	18.57	76.23
5	22.6	0.500	20.87	78.20	3.33	2.50	17.81	75.49
6	23.6	0.500	20.87	78.21	3.60	2.90	17.53	75.10
7	24.6	0.500	20.87	78.20	3.93	3.28	17.24	74.69
8	25.6	0.500	20.87	78.20	4.23	3.59	17.02	74.31
9	26.6	0.500	20.87	78.20	4.48	3.83	16.85	73.98
10	27.6	0.500	20.87	78.20	4.64	3.98	16.76	73.75
11	28.6	0.500	20.87	78.20	4.74	4.11	16.74	73.56
12	29.6	0.500	20.87	78.21	4.73	4.20	16.75	73.47
13	30.6	0.500	20.87	78.20	6.05	2.61	16.87	73.62
14	31.6	0.500	20.88	78.19	7.57	0.80	17.00	73.77
15	32.6	0.500	20.87	78.20	7.59	0.40	17.19	73.97
16	33.6	0.500	20.86	78.21	7.30	0.26	17.35	74.23
17	35.0	0.500	20.86	78.21	6.72	0.18	17.64	74.59
18	36.6	0.500	20.88	78.20	6.09	0.17	17.90	74.98
19	40.7	0.500	20.87	78.20	4.79	0.12	18.42	75.78
20	42.6	0.500	20.87	78.20	4.30	0.09	18.63	76.11
21	44.6	0.500	20.87	78.20	3.91	0.07	18.78	76.35

* SLPM (standard liters per minute) defined at 1 Atm and 25°C.

APPENDIX 6.E

Calculated external fluxes

Sample (#)	Time (hr)	Glucose (mmol/h)	O ₂ (mmol/h)	CO ₂ (mmol/h)	Biomass (mCmol/h)	Glycerol (mmol/h)	Acetate (mmol/h)	PDO (mmol/h)	Citrate (mmol/h)
2	18.3	-21.7	-15.5	35.3	17.5	9.4	0.2	17.1	-0.1
3	19.6	-29.2	-19.6	45.6	22.6	8.4	0.4	29.1	-0.1
4	20.6	-33.3	-22.3	54.4	25.0	6.6	0.5	35.4	-0.1
5	22.6	-45.3	-29.6	74.1	31.6	5.8	0.6	49.8	-0.2
6	23.6	-50.2	-32.1	83.1	32.9	4.3	0.7	58.9	-0.3
7	24.6	-54.8	-34.7	92.5	31.6	2.3	0.6	68.2	-0.4
8	25.6	-59.4	-36.4	100.9	29.4	0.0	0.5	77.9	-0.4
9	26.6	-63.0	-37.5	107.8	26.0	-3.2	0.2	84.9	-0.4
10	27.6	-65.6	-38.0	112.2	24.4	-6.2	0.2	89.7	-0.3
11	28.6	-68.0	-37.7	115.4	21.6	-8.0	0.2	88.6	-0.3
12	29.6	-68.6	-37.2	116.5	23.2	-7.1	0.2	94.3	-0.2
13	30.6	-68.7	-36.3	112.8	22.0	-5.2	0.2	93.0	-0.2
14	31.6	-67.0	-35.1	108.9	22.3	-2.8	0.3	90.9	-0.2
15	32.6	-63.3	-33.0	103.5	21.8	-1.0	0.5	89.5	-0.1
16	33.6	-60.2	-31.6	97.7	16.4	-0.8	0.4	77.8	-0.2
17	35.0	-54.7	-29.0	88.8	15.8	-0.1	0.4	73.6	-0.1
18	36.6	-49.2	-27.2	80.1	13.5	-0.1	0.1	68.0	0.0
19	40.7	-37.2	-22.9	62.2	5.4	-0.3	-0.1	52.1	0.0

Chapter 7

Quantification of net and reversible hepatic fluxes through the combined use of ^{13}C and ^2H -tracers

7.1 Introduction

Flux determination in mammalian systems is of great importance for detailed analysis of cell physiology. The most powerful method for metabolic flux determination in complex biological systems is based on the use of stable isotopes that, unlike radioisotopes, can be administered safely to subjects in high-risk population groups such as infants, children and pregnant women, making them suitable for in vivo studies. Metabolic conversion of isotopically labeled substrates generates molecules with distinct labeling patterns (i.e. positional isotopomers, or simply isotopomers) that can be detected by gas chromatography mass spectrometry (GC/MS) and nuclear magnetic resonance (NMR). To interpret these data we use large-scale mathematical models that describe the relationship between metabolic fluxes and the observed isotopomer abundances. In the forward calculation, these models simulate a unique profile of isotopomer abundances for given steady-state fluxes. In metabolic flux analysis we solve the more challenging inverse problem, i.e. calculating metabolic fluxes from the enrichments of metabolites using nonlinear least-squares procedures. Powerful mathematical and statistical tools have been developed for quantitative interpretation of isotopomer data. Recently, a generic flux analysis tool was developed, Metran (see Chapter 3), that accepts as input observed isotopomer profiles of metabolites and returns estimated fluxes and their confidence intervals. The accuracy and precision of

estimated fluxes depends on the choice of isotopic tracer, the quality of isotopomer data, and the number of redundant measurements. Methods for experiment design aim at finding the most informative tracer(s) using criteria from linearized statistics (Chapter 3). To maximize the number of redundant measurements, labeling patterns of multiple metabolite pools are sampled. For example, metabolic fluxes have been estimated in cultured cells and in perfused organs by measuring isotopomer distributions of intracellular metabolites such as citrate, alpha-ketoglutarate, succinate, malate, and amino acids by GC/MS (Fernandez, 1995; Khairallah et al., 2004). As powerful as current computational methods may be, many fluxes are still unobservable due to insufficient flux constraints. To address this problem we developed a novel framework for estimating fluxes in complex biological systems through the combined analysis of multiple tracer experiments. Data from experiments with different isotopic tracers are combined and analyzed simultaneously, taking full advantage of the flux information content from each experiment. We illustrate this approach with the detailed analysis of the gluconeogenesis pathway in cultured primary hepatocytes. Here, we applied three isotopic tracers, i.e. $[\text{U-}^{13}\text{C}_3]\text{glycerol}$, $[\text{H}_3]\text{glycerol}$, and $^2\text{H}_2\text{O}$, and measured mass isotopomer distributions of two glucose fragments by GC/MS. From comprehensive analysis of the combined data allowed us to calculate net and reversible fluxes in the gluconeogenesis pathways, which were otherwise unobservable.

7.2 Methods

7.2.1 Metabolic network model

Figure 7-1 shows the gluconeogenesis model used in this study to calculate fluxes. Table 7-1 provides the stoichiometry and atomic transitions for the 21 network reactions. The model contains two explicit gluconeogenic precursors, i.e. oxaloacetate and glycerol. Oxaloacetate is the intrahepatic precursor to glucose that is derived from lactate, pyruvate, glutamine, and other related metabolites. In the metabolic route to glucose oxaloacetate is first converted to phosphoenolpyruvate by the irreversible reaction catalyzed by phosphoenolpyruvate carboxykinase (PEPCK) (reaction 16). The second gluconeogenic precursor, glycerol, enters the gluconeogenesis pathway via DHAP (reactions 10-11). Reactions 8 and 9, i.e.

phosphorylase and phosphoglucomutase, describe glycogenolysis, i.e. breakdown of endogenous glycogen as the second major pathway for glucose production in hepatocytes. Reaction reversibilities and absolute stereochemistry for carbon and hydrogen atom transitions in the model were assigned based on current knowledge. For example, it is known that phosphoglucose isomerase (PGI) transfers specifically the pro-R hydrogen at C1 of fructose 6-phosphate (F6P) to the C2 position of glucose 6-phosphate (G6P). Hydrogen exchange with the solvent was also observed for PGI (Malaisse, 1990; Malaisse, 1991; Seeholzer, 1993). Malaisse et al. (1990, 1991) reported for a single passage in the direction F6P→G6P, 65% intramolecular hydrogen transfer and 35% hydrogen exchange, and for a single passage in the direction G6P→F6P, 72% intramolecular hydrogen transfer and 28% hydrogen exchange. It is also known that triose phosphate isomerase (TPI) has the same stereochemistry as PGI. Phosphomannose isomerase (PMI), on the other hand, has the opposite stereochemistry, i.e. PMI specifically abstracts the pro-S hydrogen of F6P and exchanges it with the solvent. No intramolecular hydrogen transfer was observed for this reaction, i.e. the hydrogen at C2 of mannose 6-phosphate (M6P) always originates from the solvent. The last five reactions in the model (reactions 17-21) account for hydrogen incorporation/metabolism of oxaloacetate and NADH. Oxaloacetate may incorporate hydrogen atoms at C3 from the solvent in reactions of the tricarboxylic acid cycle, e.g. fumarase, or via alanine aminotransferase. Reactions 17-18 describe hydrogen exchange of the pro-S and pro-R hydrogen atoms, respectively. Our model further includes three explicit sources for NADH hydrogen, i.e. 1,3-biphosphoglycerate via GAPDH (reaction 11), hydrogen exchange with the solvent (reaction 19), and from unlabeled endogenous sources (reaction 20). In this model, all fluxes are expressed as percentages of the glucose output flux, which was fixed at 100. There are 17 unknown independent fluxes in this model: flux of glycerol and oxaloacetate to glucose (reactions 10 and 16), hydrogen exchange of pro-S and pro-R hydrogen atoms of oxaloacetate with the solvent (reactions 17-18), fractional contribution of the solvent and unlabeled endogenous sources to NADH (reactions 19-20), and 11 reversible reactions.

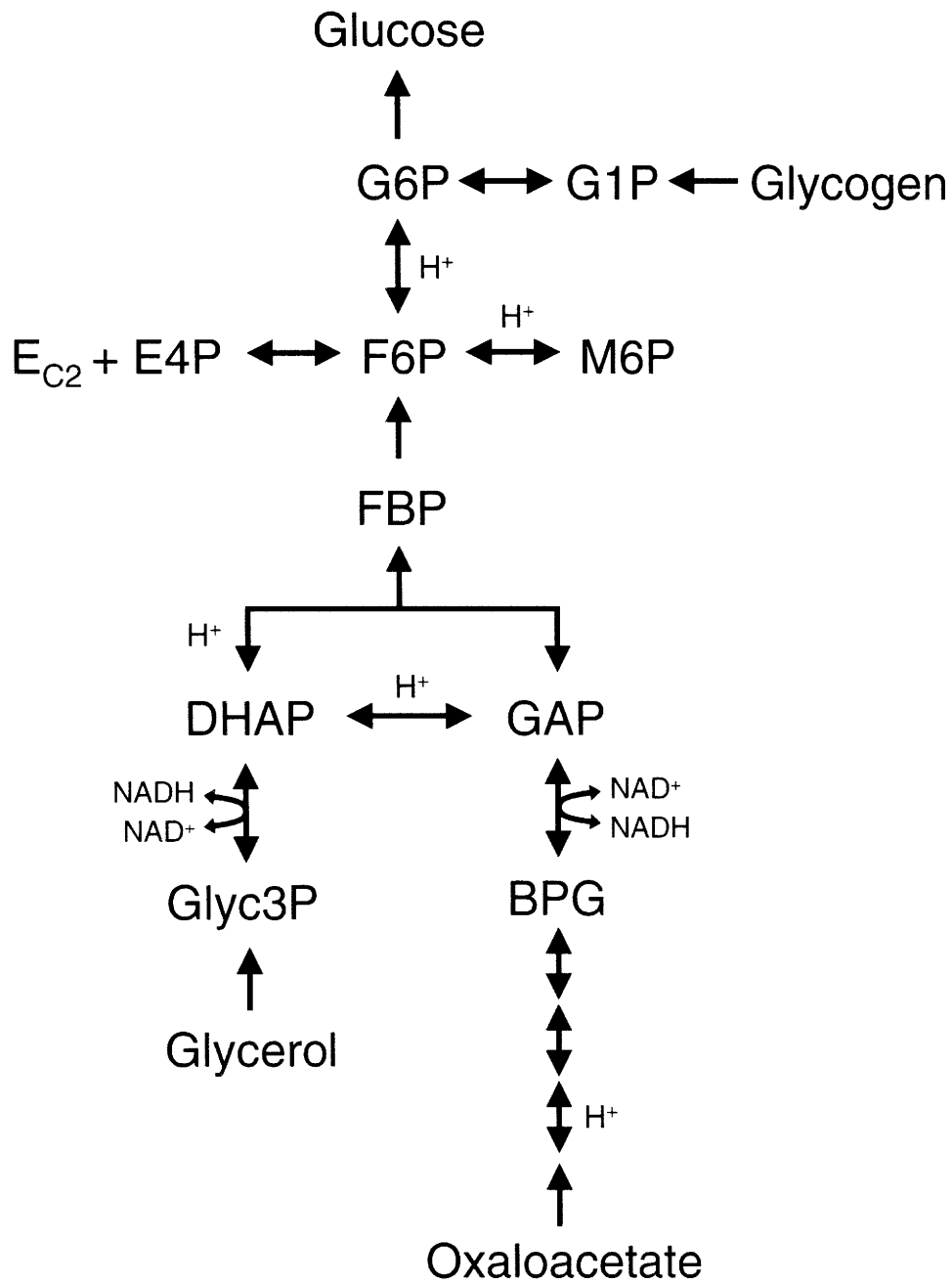


Figure 7-1: Reactions of the gluconeogenesis network model used for flux calculations. The corresponding reaction stoichiometry and atomic transitions for network reactions are given in Table 7-1.

Table 7-1

Stoichiometry and atom transitions for reactions in the gluconeogenesis network model. For each compound carbon atoms are identified using lower case letters to represent successive carbon atoms of each compound. Atom transitions for hydrogen atoms are same as for the corresponding carbon atoms, unless otherwise indicated.

No.	Enzyme	Reaction stoichiometry	Atom transformations
<i>Upper gluconeogenesis</i>			
1	Glucose 6-phosphatase	$\text{G6P} \rightarrow \text{Gluc}$	$\text{abcdef} \rightarrow \text{abcdef}$
2	Phosphoglucose isomerase	$\text{F6P} + 0.3 \text{ H} \leftrightarrow \text{G6P} + 0.3 \text{ H}$	$\text{abcdef} \leftrightarrow \text{abcdef}$ (70%) $\text{C1-H}^{\text{proR}} \leftrightarrow \text{C2-H}$ (30%) $\text{C1-H}^{\text{proR}} + \text{H} \leftrightarrow \text{H} + \text{C2-H}$
3	Fructose 1,6-bisphosphatase	$\text{FBP} \rightarrow \text{F6P}$	$\text{abcdef} \rightarrow \text{abcdef}$
4	Aldolase	$\text{DHAP} + \text{GAP} \leftrightarrow \text{FBP} + \text{H}$	$\text{abc} + \text{def} \leftrightarrow \text{cbadef}$ (DHAP) $\text{C1-H}^{\text{proS}} \leftrightarrow \text{H}$
5	Triose phosphate isomerase	$\text{DHAP} + 0.3 \text{ H} \leftrightarrow \text{GAP} + 0.3 \text{ H}$	$\text{abc} \leftrightarrow \text{abc}$ (70%) $\text{C1-H}^{\text{proR}} \leftrightarrow \text{C2-H}$ (30%) $\text{C1-H}^{\text{proR}} + \text{H} \leftrightarrow \text{H} + \text{C2-H}$
6	Phosphomannose isomerase	$\text{F6P} + \text{H} \leftrightarrow \text{M6P} + \text{H}$	$\text{abcdef} \leftrightarrow \text{abcdef}$ $\text{C1-H}^{\text{proS}} + \text{H} \leftrightarrow \text{H} + \text{C2-H}$
7	Transketolase	$\text{F6P} \leftrightarrow \text{E-C2} + \text{E4P}$	$\text{abcdef} \leftrightarrow \text{ab} + \text{cdef}$
<i>Glycogenolysis</i>			
8	Phosphorylase	$\text{Glycogen} \rightarrow \text{G1P}$	$\text{abcdef} \rightarrow \text{abcdef}$
9	Phosphoglucomutase	$\text{G1P} \leftrightarrow \text{G6P}$	$\text{abcdef} \leftrightarrow \text{abcdef}$
<i>Glycerol metabolism</i>			
10	Glycerol kinase	$\text{Glyc} \rightarrow \text{Glyc3P}$	$\text{abc} \rightarrow \text{abc}$
11	Glycerol 3-phosphate dehydrogenase	$\text{Glyc3P} \leftrightarrow \text{DHAP} + \text{NADH}$	$\text{abc} \leftrightarrow \text{abc}$ $\text{C2-H} \leftrightarrow \text{NADH}$

Table 7-1 (continued)

Stoichiometry and atom transitions for reactions in the gluconeogenesis network model.

<i>Lower gluconeogenesis</i>			
12	Glyceraldehyde 3-phosphate dehydrogenase	$BPG + NADH \leftrightarrow GAP$	$abc \leftrightarrow abc$ $NADH \leftrightarrow C1-H$
13	Phosphoglycerate kinase	$3PG \leftrightarrow BPG$	$abc \leftrightarrow abc$
14	Phosphoglycerate mutase	$2PG \leftrightarrow 3PG$	$abc \leftrightarrow abc$
15	Enolase	$PEP + H \leftrightarrow 2PG$	$abc \leftrightarrow abc$ $H \leftrightarrow C2-H$
16	Phosphoenolpyruvate carboxykinase	$OAC \rightarrow PEP + CO_2$	$abcd \rightarrow abc + d$
<i>Hydrogen incorporation into oxaloacetate and NADH</i>			
17	-	$OAC + H \rightarrow OAC + H$	$abcd \rightarrow abcd$ $C3-H^{proS} + H \leftrightarrow H + C3-H^{proS}$
18	-	$OAC + H \rightarrow OAC + H$	$abcd \rightarrow abcd$ $C3-H^{proR} + H \leftrightarrow H + C3-H^{proR}$
19	-	$H \rightarrow NADH$	$H \rightarrow NADH$
20	-	$unlabeled \rightarrow NADH$	$H^{unlabeled} \rightarrow NADH$
21	-	$NADH \rightarrow other$	$NADH \rightarrow H^{other}$

7.2.2 Estimating gluconeogenesis fluxes using MIDA

Mass isotopomer distribution analysis (MIDA) was proposed as a method for estimating fractional gluconeogenesis from measurements of glucose labeling after incorporation of [^{13}C]glycerol, [^{13}C]lactate, or other ^{13}C -labeled precursors (Neese, 1995). In MIDA, glucose is considered a dimer of two triose phosphate molecules. [^{13}C]Glucose produced by gluconeogenesis may be diluted by unlabeled glucose molecules from glycogenolysis. The mass isotopomer distribution (MID) of glucose is fully determined by the fractional contribution of GNG to glucose production and the labeling of triose phosphates. For example, consider the synthesis of [^{13}C]glucose from [$\text{U-}^{13}\text{C}$]glycerol. Assuming there is no scrambling of ^{13}C -labeling via the TCA cycle, or reactions of the pentose phosphate pathway, the steady-state MID of glucose is given by:

$$M_0 = f \cdot (1 - m_{3,\text{DHAP}}) \cdot (1 - m_{3,\text{GAP}}) + (1 - f) \quad (7.1)$$

$$M_3 = f \cdot (m_{3,\text{DHAP}} \cdot (1 - m_{3,\text{GAP}}) + (1 - m_{3,\text{DHAP}}) \cdot m_{3,\text{GAP}}) \quad (7.2)$$

$$M_6 = f \cdot m_{3,\text{DHAP}} \cdot m_{3,\text{GAP}} \quad (7.3)$$

Here, f is the fraction of glucose produced by GNG, M_i are the mass isotopomers of glucose, and m_i are mass isotopomers of the two triose phosphate pools, i.e. DHAP and GAP. Assuming that TP pools may be unequally labeled, we can introduce the parameter α to describe the extent of equilibration of triose phosphates:

$$\alpha = m_{3,\text{GAP}} / m_{3,\text{DHAP}} \quad (7.4)$$

Note that $\alpha=1$ assumes complete equilibrium of the TP pools. We can solve Eqs. 7.2, 7.3, and 7.4 for the unknown variables $m_{3,\text{DHAP}}$, $m_{3,\text{GAP}}$, and f , and obtain the following expression for fractional GNG as a function of glucose mass isotopomers M_3 and M_6 , and the parameter α :

$$f = \frac{\alpha}{(1 + \alpha)^2} \cdot \frac{(M_3 + 2 \cdot M_6)^2}{M_6} \quad (7.5)$$

From the overall ^{13}C -labeling balance we can additionally derive the following expression for the total flux of [U- ^{13}C]glycerol to glucose:

$$\text{Flux}_{[\text{U}^{13}\text{C}]\text{glycerol} \rightarrow \text{glucose}} = (M_1 + 2 \cdot M_2 + 3 \cdot M_3 + 4 \cdot M_4 + 5 \cdot M_5 + 6 \cdot M_6) / 3 \quad (7.6)$$

7.2.3 Simulating isotopomer distributions for ^{13}C and ^2H tracer experiments

For given steady state fluxes a unique profile of isotopomer abundances can be calculated for all metabolites (Chapter 2). This is done by first enumerating material balances for all possible positional isotopomers, thus generating a comprehensive mathematical model relating isotopomer abundances to fluxes. Positional isotopomers (termed isotopomers from now on) are isomers of a metabolite that differ only in the labeling state of their individual atoms, for example, ^{13}C vs. ^{12}C in carbon-labeling studies, and ^2H vs. ^1H in hydrogen-labeling studies. For a metabolite comprising N atoms that may be in one of two (labeled or unlabeled) states, 2^N isotopomers are possible. Consequently, the number of isotopomers becomes prohibitively large when we consider both carbon and hydrogen atoms. For example, there are only 64 ($=2^6$) carbon atom isotopomers of glucose and 128 ($=2^7$) hydrogen atom isotopomers, but there are 8192 ($=2^{6+7}$) isotopomers of glucose carbon and hydrogen atoms. Note that only the seven stable (i.e. carbon-bound) hydrogen atoms of glucose are considered, i.e. carboxyl and hydroxyl hydrogen atoms of metabolites exchange rapidly with the solvent and are lost during chemical derivatization in preparation for GC/MS analysis. Thus, a typical mathematical model may contain thousands of isotopomers of carbon and hydrogen atoms. To reduce the computational burden of isotopomer simulations we constructed two isotopomer simulation models for the gluconeogenesis network model (Figure 7-1), one isotopomer model where we consider only carbon atom isotopomers, and a model where we consider only hydrogen atom isotopomers. The first model will be used for carbon-labeling simulations, in our case to simulate the [U-

^{13}C]glycerol experiment, and the second model for hydrogen-labeling simulations, in this case for [$^2\text{H}_3$]glycerol and $^2\text{H}_2\text{O}$ experiments.

7.2.4 Analysis of a single tracer experiment

The goal of Metabolic Flux Analysis (MFA) is to estimate metabolic fluxes from measured enrichments of metabolites. Previously we described the MFA algorithm for the analysis of a single tracer experiment (Chapter 3). In short, fluxes are estimated by minimizing the difference between the observed and simulated measurements using a least-squares minimization procedure. The objective of this routine is to evaluate a set of feasible fluxes that best accounts for the observed isotopomer and flux measurements:

$$\min_{\mathbf{u}} \Phi = \left(\mathbf{x}(\mathbf{u}) - \mathbf{x}^{\text{obs}} \right)^T \cdot \Sigma_{\mathbf{x}}^{-1} \cdot \left(\mathbf{x}(\mathbf{u}) - \mathbf{x}^{\text{obs}} \right) \quad (7.7)$$

Here, the objective function Φ is the covariance-weighted sum of squared residuals, $\mathbf{x}(\mathbf{u})$ is the vector of simulated measurements, \mathbf{x}^{obs} is the vector of experimental data, $\Sigma_{\mathbf{x}}$ is the measurement covariance matrix, and \mathbf{u} is the vector of independent flux parameters. Eq. 7.7 is nonlinear and requires an iterative solution scheme, where at each iteration the following quadratic programming (QP) subproblem is solved (see Chapter 3):

$$\min_{\Delta \mathbf{u}} \Delta \Phi = 2 \cdot \Delta \mathbf{u}^T \cdot \mathbf{J} + \Delta \mathbf{u}^T \cdot \mathbf{H} \cdot \Delta \mathbf{u} \quad (7.8)$$

$$\text{with } \mathbf{J} = \left(\frac{d\mathbf{x}}{d\mathbf{u}} \right)^T \cdot \Sigma_{\mathbf{x}}^{-1} \cdot \left(\mathbf{x}(\mathbf{u}) - \mathbf{x}^{\text{obs}} \right) \quad \text{and} \quad \mathbf{H} = \left(\frac{d\mathbf{x}}{d\mathbf{u}} \right)^T \cdot \Sigma_{\mathbf{x}}^{-1} \cdot \left(\frac{d\mathbf{x}}{d\mathbf{u}} \right) \quad (7.9)$$

In other words, \mathbf{J} is the Jacobian and \mathbf{H} is the Hessian matrix. The optimal search direction for the fluxes ($\Delta \mathbf{u}$) at each iteration is given by:

$$\Delta \mathbf{u} = -\mathbf{H}^{-1} \cdot \mathbf{J} \quad (7.10)$$

Thus, to determine Δu at each iteration we first simulate the measurements $x(u)$, calculate the sensitivity matrix of the simulated measurements with respect to fluxes (dx/du), and then evaluate J and H (Eq. 7.9).

7.2.5 Simultaneous analysis of multiple tracer experiments

The above procedure was generalized to allow simultaneous analysis of isotopomer data from multiple experiments for the calculation of the search direction of fluxes at each iteration. In this scheme J and H are constructed as follows:

$$J = \begin{bmatrix} dx_1/du \\ dx_2/du \\ \vdots \\ dx_m/du \end{bmatrix}^T \cdot \begin{bmatrix} \Sigma_{x_1} & 0 & 0 & 0 \\ 0 & \Sigma_{x_2} & 0 & 0 \\ 0 & 0 & \ddots & 0 \\ 0 & 0 & 0 & \Sigma_{x_m} \end{bmatrix}^{-1} \cdot \begin{bmatrix} x_1(u) - x_1^{obs} \\ x_2(u) - x_2^{obs} \\ \vdots \\ x_m(u) - x_m^{obs} \end{bmatrix} \quad (7.11)$$

$$H = \begin{bmatrix} dx_1/du \\ dx_2/du \\ \vdots \\ dx_m/du \end{bmatrix}^T \cdot \begin{bmatrix} \Sigma_{x_1} & 0 & 0 & 0 \\ 0 & \Sigma_{x_2} & 0 & 0 \\ 0 & 0 & \ddots & 0 \\ 0 & 0 & 0 & \Sigma_{x_m} \end{bmatrix}^{-1} \cdot \begin{bmatrix} dx_1/du \\ dx_2/du \\ \vdots \\ dx_m/du \end{bmatrix} \quad (7.12)$$

Here, $x_i(u)$ and dx_i/du are the simulated measurements and measurement sensitivities for experiments $i=1, \dots, m$; and Σ_{x_i} are the corresponding measurement covariance matrices. The two underlying assumptions are: (i) measurements from each experiment are independent, and (ii) metabolic fluxes are identical in each experiment. The first assumption is trivial, and the second assumption is easily validated experimentally by demonstrating reproducible results from multiple experiments for the same conditions. Figure 7-2 shows schematically the proposed algorithm for flux determination through combined analysis of multiple tracer experiments. Flux estimation is initiated with random values for all fluxes. At each iteration, measurements and sensitivities are simulated for each experiment individually, using the same fluxes for each simulation. The simulated isotopomer distributions are then used to

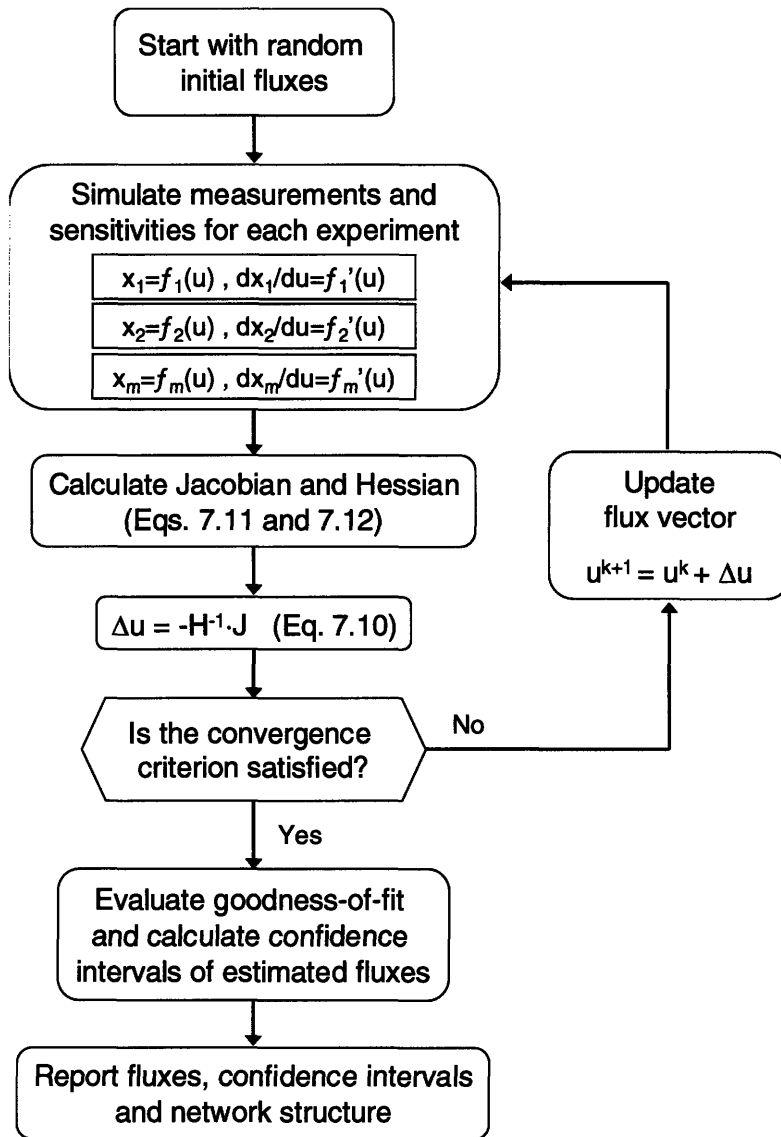


Figure 7-2: A schematic of the algorithm for flux determination through combined analysis of multiple tracer experiments.

construct the Jacobian and Hessian matrices using Eqs. 7.11 and 7.12. The optimal search direction for fluxes is calculated using Eq. 7.10, and the flux vector is updated. The flux estimation algorithm continues until a predefined convergence criterion is met. At convergence, confidence intervals for all fluxes are determined using nonlinear statistical techniques. A nice feature the described method is that the computational effort for calculating J and H increases only linearly with the number of experiments that are included in the analysis. Note that inequality constraints on fluxes can be included without difficulty in this general scheme, and all kinds of step controlling strategies can be applied (Byrd et al., 1999; Gill et al., 1991). This generalized algorithm for MFA was incorporated into our flux analysis software Metran.

7.2.6 Statistical analysis

After the fluxes were calculated, nonlinear statistical techniques were applied to obtain confidence intervals of fluxes by evaluating the sensitivity of the objective function with respect to fluxes as described by previously (Chapter 3). Flux validation was accomplished by a statistical test for the goodness-of-fit (i.e. chi-square test for model adequacy), and a normality test for the weighted residuals. To ensure a global optimum, flux estimation was repeated at least four times starting with random initial values. Sensitivity analysis was employed to determine the relative importance of measurements for individual fluxes as described previously (Chapter 3).

7.2.7 Materials

Biochemicals were obtained from Sigma Chemicals (St. Louis, MO). $[\text{U-}^{13}\text{C}]$ glycerol, and $[\text{U-}^{13}\text{C}]$ glutamine were obtained from Cambridge Isotope Laboratories (Andover, MA). $[\text{H}_5]$ glycerol was obtained from Isotec (Miamisburg, OH). Tissue culture media were obtained from Sigma (St. Louis, MO). Hepatocyte Medium Base was DMEM powder (Sigma) supplemented with 3.7 g/L NaHCO_3 , 30 mg/L proline, 100 mg/L ornithine, 610 mg/L niacinimide, 0.544 mg/L ZnCl_2 , 0.75 mg $\text{ZnSO}_4 \cdot 7\text{H}_2\text{O}$, 0.2 mg/L $\text{CuSO}_4 \cdot 5\text{H}_2\text{O}$, 0.025 mg/L MnSO_4 , 2 g/L bovine serum albumin, 100,000 U penicillin, and 100,000 U

streptomycin. Hepatocyte Attachment Medium consisted of Hepatocyte Medium Base supplemented with 5 nM insulin, 100 nM dexamethasone and 20 mM glucose. Hepatocyte Growth Medium consisted of Hepatocyte Medium Base supplemented with 1 nM insulin, 100 nM dexamethasone and 20 mM glucose.

7.2.8 Hepatocyte isolation and cell culture

Hepatocytes were isolated from C57BL/6 mice fed ad libitum by modified two step-collagenase perfusion as described by Seglen (1976). The cell yield was between $1.0\text{-}1.5\times 10^6$ cells/g mouse with viabilities between 85-90% (Trypan Blue staining). Crude cell suspension was scraped from the liver sac and purified by coarse 100 μm filtration, a second 70 μm filtration, and Percoll fractionation for hepatocytes. Purified cells were suspended in Hepatocyte Attachment Medium (HAM) and seeded in 6-well plates (1.3×10^6 cells/well) for 90 minutes at 37°C . Attached cells were washed once with PBS and cultured overnight in Hepatocyte Growth Medium (HGM). After 18 hr incubation at 37°C and 5% CO_2 the attached hepatocytes were washed once with PBS, and subsequently cultured in glucose-free HGM enriched with gluconeogenic carbon sources: 1mM glycerol, 10 mM lactate, 1 mM pyruvate, 5 mM glutamine, and 2 mM acetate. Four chemically identical isotopically-labeled media were prepared, containing either $[\text{U-}^{13}\text{C}]$ glycerol, $[\text{2H}_5]$ glycerol, 10% $^2\text{H}_2\text{O}$, or no tracers (as control). The cells were then incubated for 2, 5, or 8 hr at 37°C and 5% CO_2 in the labeled media. At the end of the incubation period medium samples were collected and stored at -80°C prior to analysis.

7.2.9 Derivatization of glucose

Glucose labeling patterns were determined by GC/MS analysis of aldonitrile pentaacetate (Szafrank, 1974) and di-O-isopropylidene acetate derivatives of glucose (Hachey, 1999). For each derivatization 200 μL of sample was deproteinized by addition of 500 μL of acetone ($\sim 4^\circ\text{C}$). The mixture was centrifuged and the supernatant evaporated to dryness under air flow. For aldonitrile pentaacetate derivatization, 50 μL of 2 wt% hydroxylamine

hydrochloride in pyridine was added to the dry residue and the sample was heated at 90°C for 60 min. This was followed by addition of $100\ \mu\text{L}$ of propionic anhydride and heating at 60°C for additional 30 min. The sample was then evaporated to dryness, dissolved in $100\ \mu\text{L}$ of ethyl acetate and transferred to an injection vial for GC/MS analysis. For di-O-isopropylidene acetate derivatization, $500\ \mu\text{L}$ of $0.38\ \text{M}$ sulfuric acid in acetone was added to the dry residue and the sample incubated at room temperature for 60 min. $400\ \mu\text{L}$ of $0.44\ \text{M}$ sodium carbonate was added to neutralize the reaction, followed by addition of $1\ \text{mL}$ of saturated sodium chloride. Di-O-isopropylidene derivatives were extracted by partitioning with $1\ \text{mL}$ of ethyl acetate. The upper, organic layer was evaporated to dryness, followed by addition of $150\ \mu\text{L}$ of acetic anhydride in pyridine (2:1 v/v) and heating at 60°C for 30 min. The sample was then evaporated to dryness, dissolved in $100\ \mu\text{L}$ of ethyl acetate and transferred to an injection vial for GC/MS analysis.

7.2.10 GC/MS analysis

Gas Chromatography-Mass Spectrometry (GC/MS) analysis was performed using HP 5890 Series II GC (Gas Chromatograph) equipped with a DB-1701 [$30\ \text{m} \times 0.25\ \text{mm}$ (inner diameter) $\times 0.25\ \mu\text{m}$] capillary column, connected to HP 5971 MSD (Mass Selective Detector) operating under ionization by electron impact (EI) at $70\ \text{eV}$. The mass spectrometer was calibrated using the 'Max Sensitivity Autotune' setting. Helium flow was maintained at $0.737\ \text{mL}/\text{min}$ by electronic control. The temperatures of the injector and the detector were kept at 250°C and 300°C , respectively. The temperature of the column was started at 80°C for 1 min, increased to 280°C at $20^\circ\text{C}/\text{min}$, and held for 4 min. For analysis of aldonitrile pentaacetate glucose, mass spectra were recorded in the mass range 314-322 at 12 scans/sec. The fragment at $m/z\ 314$ ($\text{C}_{13}\text{H}_{16}\text{O}_8\text{N}$) corresponded to C1-C5 carbon atoms, and H2-H5 hydrogen atoms of glucose. For the analysis of di-O-isopropylidene acetate glucose, mass spectra were recorded in the mass range 287-292 at 12 scans/sec. The fragment at $m/z\ 287$ ($\text{C}_{13}\text{H}_{19}\text{O}_7$) corresponded to all six carbon and all seven carbon-bound hydrogen atoms of glucose. Measured intensities were corrected for noise (baseline correction), and mass isotopomer distributions were obtained by integration. All mass

isotopomer values were expressed as fractional abundances, i.e. for each fragment the sum of all mass isotopomers equals one. Reported mass isotopomer distributions are averaged values from at least six injections per sample.

7.2.11 Measurement of metabolite concentrations

Glucose and lactate concentrations were determined by YSI 2300 Stat Plus glucose/lactate analyzer (YSI Inc., Yellow Springs, OH). Glycerol and glutamine concentrations were determined by GC/MS analysis with internal standards. We prepared 1:1 mixtures of the medium sample and a standard with known concentration, in this case either [U- ^{13}C]glutamine (10 mM), [U- ^{13}C]glycerol (1 mM), or unlabeled glycerol (1 mM), which were then derivatized to yield the respective TBDMS derivatives (Chapter 4). Measured intensities for glutamine (m/z 432-444) and glycerol (m/z 173-200) were corrected for natural isotope enrichments, and glutamine and glycerol concentrations were determined from the fractions of labeled/unlabeled molecules.

7.3 Results

7.3.1 External fluxes

Figure 7-3 shows the dynamics of glucose and lactate production, and glycerol and glutamine consumption by cultured hepatocytes over 8 hr period. A linear fit of the data ($R^2 > 0.99$) yielded the following values (in mM/hr/ 10^6 cells): glucose production 0.204 ± 0.005 , lactate production 0.263 ± 0.029 , glycerol uptake 0.133 ± 0.006 , and glutamine uptake 0.333 ± 0.026 . Fluxes expressed as percentages of glucose production were 129 ± 14 for lactate production, 65 ± 3 for glycerol uptake, and 163 ± 13 for glutamine uptake. No glycerol was detected in the samples taken at 8 hr. Based on the linear fit shown in Figure 7-3 we estimated that glycerol was depleted after about 7-7.5 hrs.

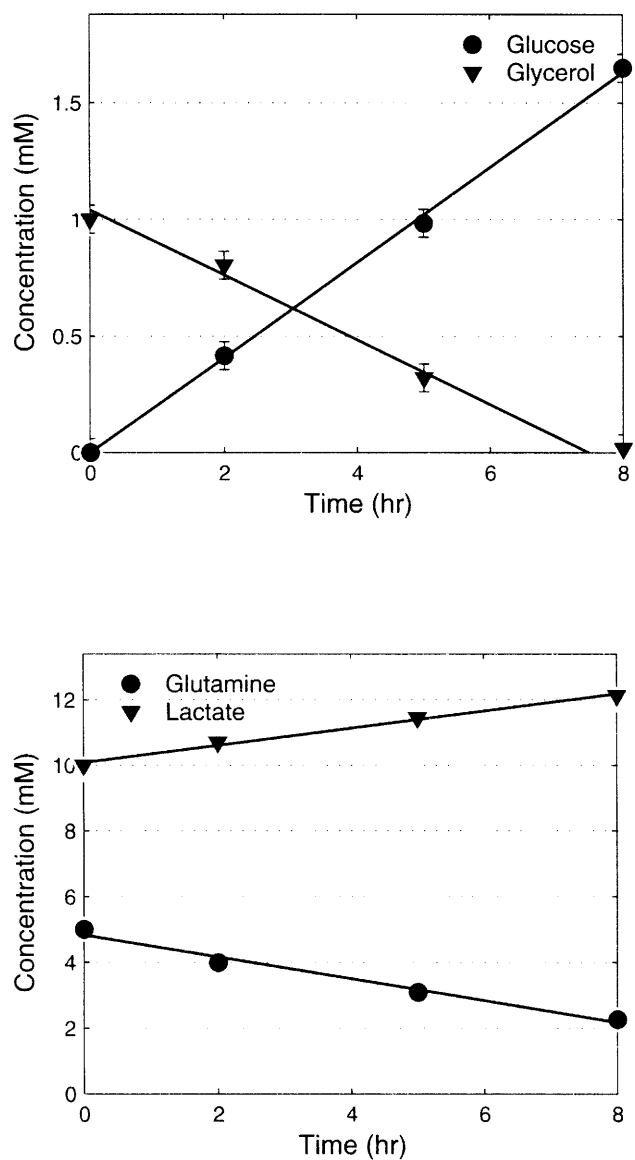


Figure 7-3: Time profiles of glucose, glycerol, lactate and glutamine in hepatocytes cultures. Glucose and lactate accumulated in the medium, while glycerol and glutamine were taken up by hepatocytes and served as precursors for glucose production.

7.3.2 Reproducibility of cell experiments

To characterize the well-to-well variability in our experiments, hepatocytes were incubated in three wells in medium containing $^2\text{H}_2\text{O}$ at 10% enrichment, and a control well with no tracers. Table 7-2 shows the mass isotopomer distribution of two glucose derivatives assayed by GC/MS. The MIDs from three replicate wells were not statistically different from one another ($P>0.1$), but were significantly different from the experiment with no tracers ($P<0.001$). This confirmed that biological variability between wells was small in our experiments.

7.3.3 Characterization of glycerol

Figure 7-4 shows the measured mass isotopomer distributions (MIDs) of glycerol in the medium at 0, 2 and 5 hr from $[\text{U-}^{13}\text{C}]$ glycerol, $[\text{H}_5]$ glycerol, and $^2\text{H}_2\text{O}$ experiments (data shown were corrected for natural isotopes). The MID of glycerol from the $[\text{U-}^{13}\text{C}]$ glycerol experiment at time zero was characterized by 97% M+3 and 3% M+2 isotopomers. The M+2 isotopomer resulted from incomplete labeling of the tracer, i.e. 99 At% ^{13}C -labeling according to manufacturers' specifications. The MID of $[\text{H}_5]$ glycerol at time zero was characterized by 96% M+5 and 4% M+4 isotopomers, which was slightly more labeled than 98 At% ^2H -labeling according to manufacturers' specifications. The enrichment of both glycerol tracers decreased after 5 hr to 75% M+3 enrichment for $[\text{U-}^{13}\text{C}]$ glycerol, and 79% M+5 enrichment for $[\text{H}_5]$ glycerol. The decrease in enrichment occurred mostly due to the release of unlabeled glycerol in the $[\text{U-}^{13}\text{C}]$ glycerol experiment, and release of M+0, M+1, M+2, and M+3 isotopomers in the $[\text{H}_5]$ glycerol experiment. Figure 7-5 shows in more detail the accumulation of M+0 to M+4 glycerol isotopomers in the medium in the $[\text{H}_5]$ glycerol experiment. The release of unlabeled/partially labeled glycerol isotopomers corresponded to about 8-10% of glycerol uptake rate. In the $^2\text{H}_2\text{O}$ experiment we observed a small but significant incorporation of deuterium into glycerol, i.e. the M+1 enrichment of glycerol increased from 0.2 ± 0.2 mol% at time zero to 3.7 ± 0.2 mol% at 5 hr (after correction for natural isotope enrichments).

Table 7-2

Assessment of biological variability in cell culture experiments. Mass isotopomer abundances (mol%) of aldonitrile pentaacetate and di-O-isopropylidene acetate derivatives of glucose from hepatocyte experiments were measured by GC/MS. Experiments were performed in separate wells in a 6-well plate in medium containing 10% $^2\text{H}_2\text{O}$ (wells 1-3), or no tracers (well 4). Mass isotopomer abundances were not significantly different between the three replicate $^2\text{H}_2\text{O}$ experiments, but were significantly different from the experiment with no tracers.

<i>Aldonitrile pentaacetate glucose (m/z 314)</i>				
m/z	10% $^2\text{H}_2\text{O}$ (well 1)	10% $^2\text{H}_2\text{O}$ (well 2)	10% $^2\text{H}_2\text{O}$ (well 3)	no tracers (well 4)
287	54.3 \pm 0.5	53.8 \pm 0.5	53.4 \pm 0.5	84.5 \pm 0.5
288	32.7 \pm 0.4	32.9 \pm 0.4	33.2 \pm 0.4	13.0 \pm 0.4
289	10.4 \pm 0.3	10.6 \pm 0.3	10.7 \pm 0.3	2.2 \pm 0.2
290	2.2 \pm 0.2	2.3 \pm 0.2	2.3 \pm 0.2	0.2 \pm 0.1
291	0.4 \pm 0.2	0.4 \pm 0.2	0.4 \pm 0.2	0.0 \pm 0.1
292	0.0 \pm 0.1	0.0 \pm 0.1	0.0 \pm 0.1	0.0 \pm 0.1
<i>Di-O-isopropylidene acetate glucose (m/z 287)</i>				
m/z	10% $^2\text{H}_2\text{O}$ (well 1)	10% $^2\text{H}_2\text{O}$ (well 2)	10% $^2\text{H}_2\text{O}$ (well 3)	no tracers (well 4)
314	62.8 \pm 0.4	62.4 \pm 0.4	62.4 \pm 0.4	84.9 \pm 0.4
315	28.9 \pm 0.3	29.2 \pm 0.3	29.2 \pm 0.3	12.8 \pm 0.3
316	7.1 \pm 0.2	7.2 \pm 0.2	7.2 \pm 0.2	2.2 \pm 0.2
317	1.2 \pm 0.2	1.2 \pm 0.2	1.2 \pm 0.2	0.1 \pm 0.1
318	0.1 \pm 0.1	0.0 \pm 0.1	0.1 \pm 0.1	0.0 \pm 0.1
319	0.0 \pm 0.1	0.0 \pm 0.1	0.0 \pm 0.1	0.0 \pm 0.1

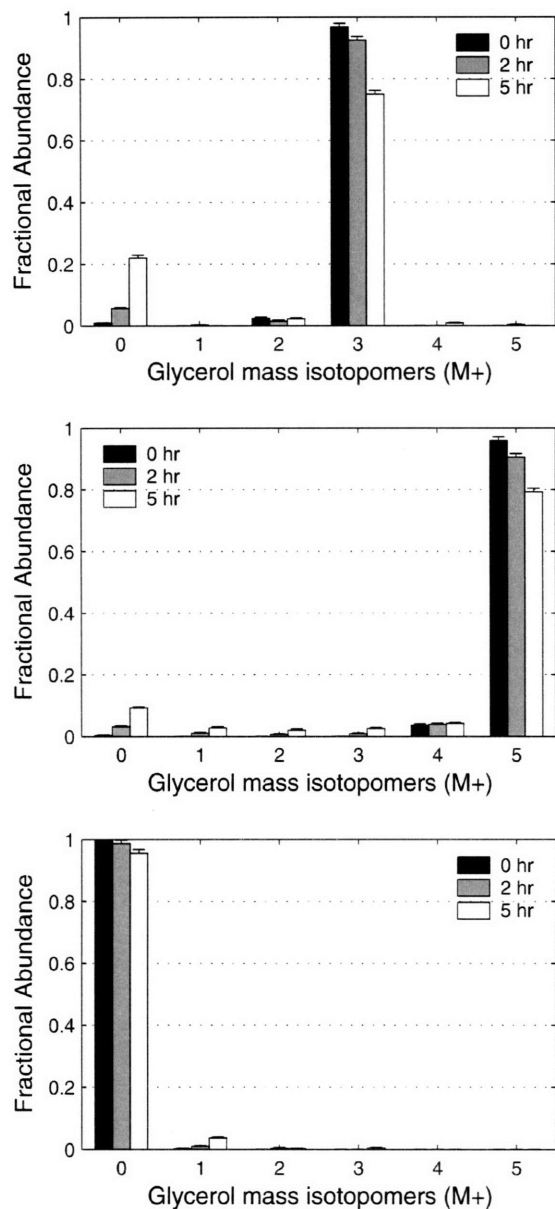


Figure 7-4: Mass isotopomer distributions of glycerol in the medium. Labeling distribution of glycerol from [$\text{U-}^{13}\text{C}$]glycerol (top), [$^2\text{H}_5$]glycerol (middle), and $^2\text{H}_2\text{O}$ (bottom) experiments was analyzed by GC/MS, after TBDMS derivatization. Data shown were corrected for natural isotope enrichments.

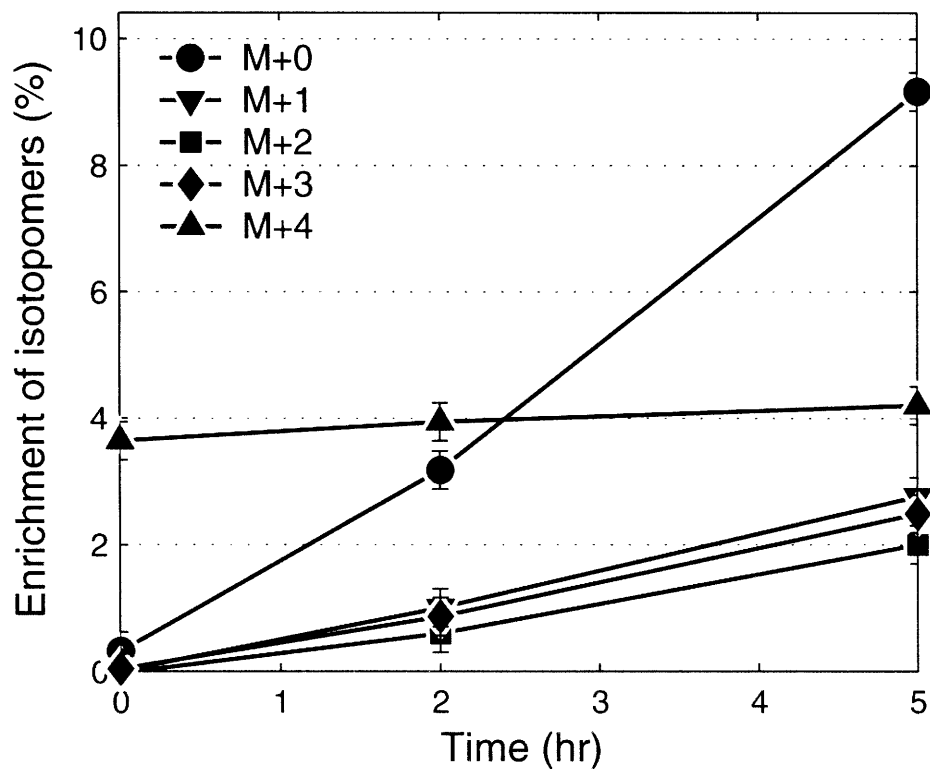


Figure 7-5: Loss of ^2H from $[\text{}^2\text{H}_5]\text{glycerol}$ in cultured hepatocytes. Mass isotopomer distributions of TBDMS derivatized glycerol were measured by GC/MS. Data shown were corrected for natural isotope enrichments.

7.3.4 Incorporation of deuterium into lactate and ketone bodies

We identified two metabolites in the medium that incorporated significant amounts of labeling from $^2\text{H}_5$ glycerol and $^2\text{H}_2\text{O}$, i.e. lactate and 3-hydroxybutyrate. Figure 7-6 shows the enrichment of lactate and 3-hydroxybutyrate, respectively (enrichment = $\sum M_i \times i$). Lactate incorporated labeling from $^2\text{H}_5$ glycerol and $^2\text{H}_2\text{O}$, but not from $[\text{U-}^{13}\text{C}]$ glycerol. The amount of labeling incorporated from $^2\text{H}_2\text{O}$ (at 10% enrichment) could not be explained solely by *de novo* synthesis of lactate, indicating that there was significant exchange between intracellular pyruvate pool and extracellular lactate pool. Pyruvate can incorporate deuterium at C3 in the reaction catalyzed by alanine aminotransferase and lactate can incorporate deuterium at C2 from NADH via lactate dehydrogenase. The amount of labeling incorporated from $^2\text{H}_5$ glycerol was about 6 times less than from 10% $^2\text{H}_2\text{O}$. However, we should note that $^2\text{H}_5$ glycerol can only transfer deuterium atoms to lactate via $^2\text{H}_5$ glycerol \rightarrow $^2\text{H}]$ NADH \rightarrow $^2\text{H}]$ lactate catalyzed by glycerol-3-phosphate dehydrogenase and lactate dehydrogenase, respectively. Taking into account that lactate was present at 10 mM at time zero and the concentration increased to 12.8 mM at 8 hr, and that lactate enrichment increased from 0.0% to $2.9 \pm 0.6\%$, we estimated that about $13 \pm 5\%$ of NADH atoms were derived from glycerol ($= 2.9\% \times 12.8 / (12.8 - 10)$). In contrast, we found that 3-hydroxybutyrate incorporated labeling only from $^2\text{H}_2\text{O}$, and not from $^2\text{H}_5$ glycerol or $[\text{U-}^{13}\text{C}]$ glycerol. In these experiments, 3-hydroxybutyrate was derived solely from *de novo* synthesis, i.e. there was no 3-hydroxybutyrate at time zero (validated by GC/MS analysis). In the 10% $^2\text{H}_2\text{O}$ experiments the enrichment of 3-hydroxybutyrate was more or less constant over 8-hrs at about 22% indicating that on average 2.2 of the 5 hydrogen atoms of 3-hydroxybutyrate were derived from the solvent.

7.3.5 Incorporation of ^{13}C and ^2H into glucose

Table 7-3 shows the mass isotopomer distributions of two glucose fragments measured at 2, 5 and 8 hr from $[\text{U-}^{13}\text{C}]$ glycerol, $^2\text{H}_5$ glycerol, and $^2\text{H}_2\text{O}$ experiments, and Table 7-4 shows the corresponding corrected MIDs. The last column in Table 7-4 shows the total enrichment of glucose, i.e. enrichment = $\sum M_i \times i$. The di-O-isopropylidene acetate derivative of glucose

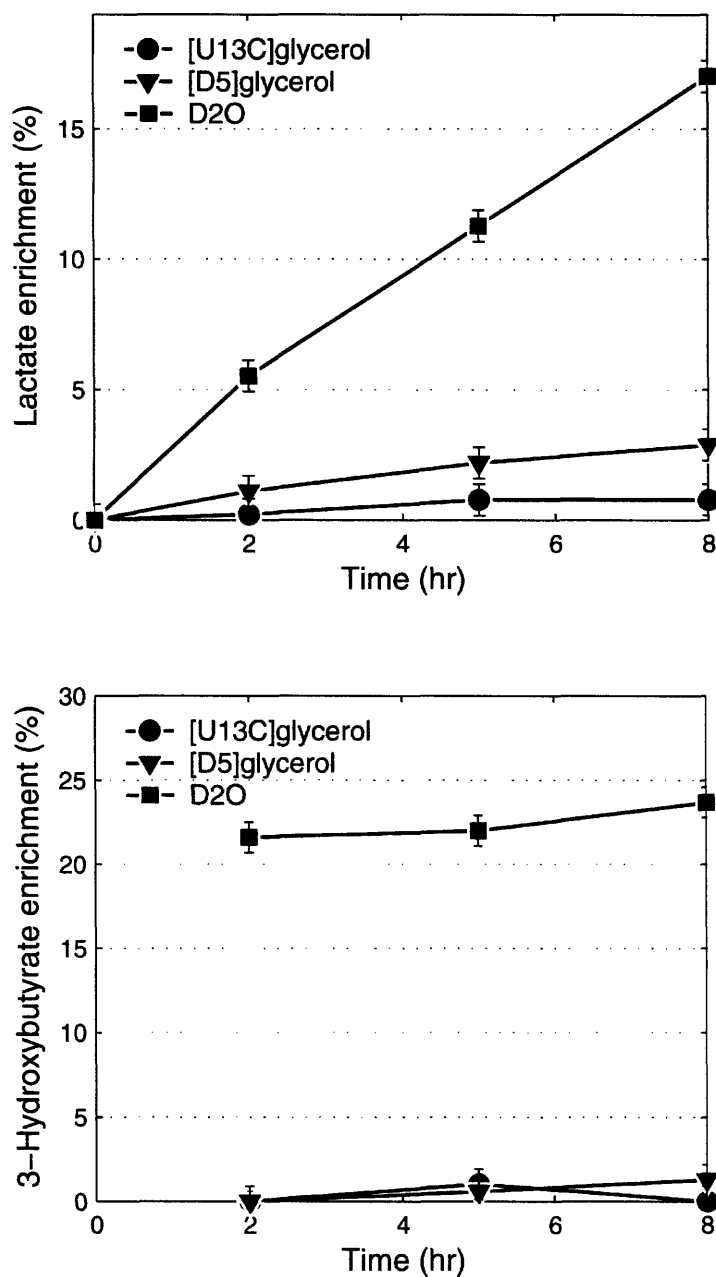


Figure 7-6: Incorporation of deuterium from $^2\text{H}_3$ glycerol and $^2\text{H}_2\text{O}$ into lactate and 3-hydroxybutyrate. Mass isotopomer distributions of TBDMS derivatized lactate and 3-hydroxybutyrate were measured by GC/MS, and isotope enrichment was calculated after correcting for natural isotope enrichments.

Table 7-3

Incorporation of labeling from ^{13}C glycerol, ^2H glycerol and $^2\text{H}_2\text{O}$ into glucose. Shown are the uncorrected mass isotopomer distributions of glucose (molar abundances; mol%), for aldonitrile pentaacetate (m/z 314) and di-O-isopropylidene acetate (m/z 287) derivatives.

Tracer	Time of Sample	Glucose mass isotopomers								
		M+0	M+1	M+2	M+3	M+4	M+5	M+6	M+7	M+8
m/z 287 ion fragment (C1-6, H1-6)										
$[\text{U-}^{13}\text{C}]$ glycerol	2 hr	42.5	7.3	3.0	29.5	4.0	1.8	10.9	0.9	0.1
	5 hr	41.8	7.3	3.2	30.7	4.1	1.8	10.1	0.9	0.1
	8 hr	48.8	8.5	3.3	26.2	3.5	1.4	7.6	0.6	0.1
$[\text{H}_3]$ glycerol	2 hr	43.1	17.4	20.2	11.1	5.7	2.2	0.3	0.0	0.0
	5 hr	42.2	18.0	20.8	11.1	5.4	2.1	0.5	0.1	0.0
	8 hr	45.8	18.6	19.5	9.6	4.4	1.6	0.4	0.1	0.0
$^2\text{H}_2\text{O}$	2 hr	56.9	31.2	9.6	2.1	0.2	0.0	0.0	0.0	0.0
	5 hr	54.7	32.5	10.2	2.2	0.4	0.0	0.0	0.0	0.0
	8 hr	53.7	33.0	10.6	2.3	0.3	0.0	0.0	0.0	0.0
no tracers	2 hr	85.2	12.6	2.1	0.2	0.0	0.0	0.0	0.0	0.0
	5 hr	84.5	13.0	2.2	0.2	0.0	0.0	0.0	0.0	0.0
	8 hr	83.9	13.5	2.3	0.3	0.0	0.0	0.0	0.0	0.0
m/z 314 ion fragment (C1-5, H2-5)										
$[\text{U-}^{13}\text{C}]$ glycerol	2 hr	43.1	7.5	14.0	19.7	3.3	11.1	1.0	0.2	0.0
	5 hr	42.3	7.6	14.8	20.5	3.4	10.3	0.9	0.2	0.0
	8 hr	49.4	8.8	13.2	17.3	2.8	7.7	0.7	0.1	0.0
$[\text{H}_3]$ glycerol	2 hr	65.2	25.3	8.0	1.4	0.1	0.0	0.0	0.0	0.0
	5 hr	64.5	25.8	8.1	1.4	0.1	0.0	0.0	0.0	0.0
	8 hr	67.0	24.4	7.2	1.2	0.1	0.0	0.0	0.0	0.0
$^2\text{H}_2\text{O}$	2 hr	65.0	27.4	6.5	1.0	0.1	0.0	0.0	0.0	0.0
	5 hr	63.0	28.8	6.9	1.1	0.2	0.0	0.0	0.0	0.0
	8 hr	62.6	29.1	7.1	1.1	0.1	0.0	0.0	0.0	0.0
no tracers	2 hr	85.2	12.6	2.1	0.1	0.0	0.0	0.0	0.0	0.0
	5 hr	84.9	12.8	2.1	0.1	0.0	0.0	0.0	0.0	0.0
	8 hr	84.6	13.0	2.2	0.1	0.0	0.0	0.0	0.0	0.0

Table 7-4

Corrected mass isotopomer distributions of glucose fragments. Total enrichment of glucose was calculated from mass isotopomer data after correction for natural isotope enrichments.

Tracer	Time of Sample	Glucose mass isotopomers							Enrichment* (%)
		M+0	M+1	M+2	M+3	M+4	M+5	M+6	
m/z 287 ion fragment (C1-6, H1-6)									
[U- ¹³ C]glycerol	2 hr	49.9	1.2	2.1	33.1	0.7	1.3	11.8	184.5 ± 0.8
	5 hr	49.1	1.3	2.3	34.5	0.6	1.2	10.9	183.7 ± 0.8
	8 hr	57.3	1.5	2.2	29.3	0.5	0.9	8.2	149.9 ± 0.8
[² H ₅]glycerol	2 hr	50.6	13.0	20.6	9.6	4.7	1.6	0.0	109.6 ± 0.7
	5 hr	49.5	13.8	21.2	9.4	4.4	1.5	0.2	110.8 ± 0.7
	8 hr	53.8	13.9	19.5	7.9	3.5	1.1	0.2	97.4 ± 0.7
² H ₂ O	2 hr	66.8	26.7	5.7	0.8	0.0	0.0	0.0	40.5 ± 0.6
	5 hr	64.2	28.7	6.2	0.8	0.1	0.0	0.0	43.9 ± 0.6
	8 hr	63.1	29.5	6.6	0.9	0.0	0.0	0.0	45.1 ± 0.6
no tracers	2 hr	100.0	0.0	0.0	0.0	0.0	0.0	0.0	0.0 ± 0.3
	5 hr	99.4	0.6	0.0	0.0	0.0	0.0	0.0	0.6 ± 0.3
	8 hr	98.8	1.2	0.0	0.0	0.0	0.0	0.0	1.2 ± 0.3
m/z 314 ion fragment (C1-5, H2-5)									
[U- ¹³ C]glycerol	2 hr	50.9	1.1	14.7	20.5	1.0	11.8		154.9 ± 0.8
	5 hr	49.9	1.4	15.6	21.2	1.0	10.9		154.6 ± 0.8
	8 hr	58.3	1.5	13.5	17.8	0.7	8.1		125.4 ± 0.8
[² H ₅]glycerol	2 hr	76.9	18.2	4.6	0.2	0.0	0.0		28.1 ± 0.5
	5 hr	76.2	18.9	4.6	0.2	0.0	0.0		28.9 ± 0.5
	8 hr	79.2	16.9	3.8	0.2	0.0	0.0		24.9 ± 0.5
² H ₂ O	2 hr	76.8	20.7	2.5	0.0	0.0	0.0		25.7 ± 0.5
	5 hr	74.4	22.8	2.7	0.1	0.1	0.0		28.6 ± 0.5
	8 hr	73.9	23.2	2.9	0.0	0.0	0.0		29.0 ± 0.5
no tracers	2 hr	100.0	0.0	0.0	0.0	0.0	0.0		0.0 ± 0.3
	5 hr	99.6	0.4	0.0	0.0	0.0	0.0		0.4 ± 0.3
	8 hr	99.3	0.7	0.0	0.0	0.0	0.0		0.7 ± 0.3

* Enrichment = $\sum M_i \times i$.

(m/z 287) contained all six carbon atoms and all seven carbon-bound hydrogen atoms of glucose, and the aldonitrile pentaacetate derivative (m/z 314) contained carbon atoms C1-C5 of glucose and hydrogen atoms at positions C2-C5. In hepatocytes incubated with $[\text{U-}^{13}\text{C}]$ glycerol the main labeled glucose isotopomers were M+3 (~30 mol%) and M+6 (~10 mol%), with much lower abundances of the other labeled isotopomers (<2.5 mol%). The presence of M+1, M+2, M+4 and M+5 isotopomers can be explained by transketolase activity as suggested by Kurland et al. (2000), or by scrambling of glycerol labeling in the TCA cycle as suggested by Previs et al. (1995). In light of our previous observation that lactate was not labeled from $[\text{U-}^{13}\text{C}]$ glycerol, we concluded the cycling between glycerol and TCA cycle was not significant in our experiments. Thus, there must be some residual transketolase activity in cultured hepatocytes. The higher abundance of M+3 (20.5 mol%; i.e. C1-C3 of glucose) compared to M+2 (14.7 mol%; i.e. C4-C5 of glucose) in the aldonitrile pentaacetate derivative of glucose indicated that DHAP was more labeled than GAP, i.e. the two triose phosphate pools were only at 72% equilibrium ($=14.7/20.5$). The enrichment of glucose from $[\text{U-}^{13}\text{C}]$ glycerol was constant over the first 5 hrs, indicating a constant contribution of $[\text{U-}^{13}\text{C}]$ glycerol to glucose production. The lower enrichments at 8 hr can be explained by the depletion of $[\text{U-}^{13}\text{C}]$ glycerol after about 7 hr (see section 7.3.1). To interpret the data more quantitatively we applied MIDA equations to estimate fractional contribution of GNG to glucose production and the net flux of $[\text{U-}^{13}\text{C}]$ glycerol to glucose. Table 7-5 shows that fractional contribution of GNG was estimated at 66%, 71%, and 63% at 2, 5, and 8 hr, respectively. The value at 8 hr is likely to be an underestimation of GNG due to the depletion of the $[\text{U-}^{13}\text{C}]$ glycerol tracer after 7 hr, i.e. MIDA assumes isotopic steady-state.

In experiments with $[\text{H}_5]$ glycerol we observed significant production of glucose mass isotopomers M+1 to M+5. Similar to the $[\text{U-}^{13}\text{C}]$ glycerol experiment, we found that the fractional contribution of $[\text{H}_5]$ glycerol to glucose production remained constant over the first 5 hrs (i.e. constant enrichment of glucose), and then declined due to $[\text{H}_5]$ glycerol depletion. The amount of deuterium incorporated into glucose from $[\text{H}_5]$ glycerol provided rich information on the relative activity of various gluconeogenic reactions. Deuterium atoms of $[\text{H}_5]$ glycerol may be lost at various points in the pathway from glycerol to glucose.

Table 7-5

Metabolic fluxes estimated by mass isotopomer distribution analysis (MIDA). Glucose mass isotopomers from [U-¹³C]glycerol experiments were measured by GC/MS and corrected for natural isotope enrichments. MIDA equations were used to estimate fluxes of gluconeogenesis pathway. Fluxes shown are expressed as percentages of glucose production rate.

Flux*	2 hr	5 hr	8 hr
Glucose production (fixed at 100)	100	100	100
Gluconeogenesis (parameter f)	66.3	71.0	62.5
Glycogenolysis	33.7	29.0	37.5
Glycerol to glucose flux	61.5	61.2	50.0
Oxaloacetate to glucose flux	71.1	80.8	75.0
Triose phosphate equilibration (%)	72 %	74 %	76 %

* Parameter f was calculated from Eq. 7.5.

* Glycogenolysis = $100 - f$.

* Glycerol to glucose flux was calculated from Eq. 7.6.

* Oxaloacetate to glucose flux = $2 \cdot f - (\text{glycerol to glucose flux})$.

* Triose phosphate equilibration (α in Eq. 7.5) was estimated from the ratio of mass isotopomers (m/z 316)/(m/z317)×100% of aldonitrile pentaacetate derivative of glucose (after correction).

For example, the deuterium at C2 is transferred to NADH in the reaction catalyzed by glycerol-3-phosphate dehydrogenase. The pro-R hydrogen at C1 may be lost in the reaction catalyzed by TPI, and the pro-S hydrogen in reactions catalyzed by aldolase and GAPDH. Finally, the pro-R hydrogen at C3 may be lost in the reaction catalyzed by PGI, and the pro-S hydrogen by PMI and glucose-6-phosphate dehydrogenase reactions. In other words, the presence of M+1 to M+5 mass isotopomers of glucose indicated that one or more of the above reactions were not fully equilibrated. However, without a proper mathematical model it is difficult, if not impossible, to interpret the isotopomer data from [$^2\text{H}_5$]glycerol experiments quantitatively.

In $^2\text{H}_2\text{O}$ experiments deuterium enrichment of glucose increased from 40.5% to 43.9% and 45.1% at 2, 5, and 8 hr, respectively, indicating that gluconeogenesis flux increased by about 11% over the course of the experiment. On average 4.0 to 4.5 of the 7 atoms of glucose were derived from the solvent. The enrichment of the aldonitrile pentaacetate fragment of glucose increased from 25.5% to 28.6% and 29.0% (an increase of 13%), i.e. on average 2.6 to 2.9 of the 4 hydrogen atoms at C2-C5 were derived from the solvent. Note that in the control experiment with no tracers we found a slight increase in glucose enrichment that could not be explained by natural isotope abundances, i.e. from 0.0 ± 0.3 at time zero to 1.2 ± 0.3 at 8 hr. One potential explanation was cross-contamination between adjacent wells in the 6-well plate, i.e. the unlabeled wells were adjacent to the wells with $^2\text{H}_2\text{O}$.

To summarize, qualitative analysis of glucose enrichment data revealed that the flux of glycerol to glucose was constant over the first 5 hrs of the experiment, and that the contribution of non-glycerol precursors to glucose increased by about 10-13%. Finally, we found evidence of some residual transketolase activity in the cultured hepatocytes.

7.3.6 Flux estimation and model validation

To better characterize metabolic fluxes in this system we performed comprehensive analysis of the observed MIDs with the network model shown in Figure 7-1 and Metran software. Fluxes and their confidence intervals were estimated from three data sets individually and

using the combined data of all three experiments. Table 7-6 compares the information content of the data sets. For example, $[\text{U-}^{13}\text{C}]$ glycerol experiments provided 13 mass isotopomers of glucose from which 4 independent fluxes could be estimated, i.e. net fluxes of glycerol and oxaloacetate to glucose, and exchange fluxes of TPI and TK reactions. Thus, there were 9 ($=13-4$) redundant measurements in the $[\text{U-}^{13}\text{C}]$ glycerol data. We found excellent agreement between the observed mass isotopomer abundances and abundances predicted by the model for the optimally fitted fluxes, as judged by the small magnitude of the sum of squared residuals, i.e. 1.8, which was smaller than the critical value 19.0 for the statistical test of model adequacy (at 95% confidence level with 9 degrees of freedom), which indicated that the fit was statistically acceptable. Fits for the $[\text{H}_5]$ glycerol and $^2\text{H}_2\text{O}$ data sets were also statistically acceptable. However, our initial attempts to reconcile data from all three experiments failed. The sum of squared residuals was consistently larger than the critical value for the statistical test. Further analysis revealed that MIDs of glucose from the $[\text{U-}^{13}\text{C}]$ glycerol and $[\text{H}_5]$ glycerol experiments were incompatible with the MIDs of glucose from the $^2\text{H}_2\text{O}$ experiment. Previously, Previs et al. (1998) showed that glycerol and lactate tracers consistently underestimated GNG by 10-30% in isolated hepatocytes. This effect could not be explained from lack of equilibrium of triose phosphates, zonation of glycerol kinase, or differences in substrate concentrations. The authors concluded that there must be different cell populations of hepatocytes that utilize glycerol and lactate/pyruvate to different extent for the production of glucose. The net observed effect was an increased abundance of unlabeled glucose and decreased abundances of labeled glucose isotopomers, resulting in underestimation of GNG. To account for this effect in our model we introduced dilution parameters for glucose labeling from $[\text{U-}^{13}\text{C}]$ glycerol and $[\text{H}_5]$ glycerol experiments, i.e. these parameters quantify the apparent dilution of labeled glucose isotopomers due to differential metabolism of cell populations. Note that these parameters also capture the apparent dilution due to depletion of tracers. Further analysis revealed that no dilution parameter was required for the $^2\text{H}_2\text{O}$ data, i.e. the goodness-of-fit was not statistically improved by adding a dilution parameter for the $^2\text{H}_2\text{O}$ data. Therefore, our model included only two dilution parameters, i.e. for $[\text{U-}^{13}\text{C}]$ glycerol and $[\text{H}_5]$ glycerol experiments. With the updated model we successfully fitted the combined data from all three experiments and estimated fluxes.

Table 7-6

Comparison of information content of experimental data. Individual data sets from [U- ^{13}C]glycerol, [$^2\text{H}_5$]glycerol, and $^2\text{H}_2\text{O}$ experiments were fitted to a detailed model of glucose metabolism. Fluxes were estimated and confidence intervals were evaluated. Analysis of the combined data required two additional parameter to describe the apparent glucose labeling when glycerol tracers were used. The flux results were then statistically evaluated to test for goodness-of-fit.

	10% $^2\text{H}_2\text{O}$	[$^2\text{H}_5$]glycerol	[U- ^{13}C]glycerol	Combined analysis of all three experiments
No. of fitted mass isotopomers	7	9	13	29
No. of estimated fluxes *	2	6	4	11 + 2**
No. of redundant measurements***	5	3	9	16
Sum of weighted squared residuals	1.2	1.8	2.7	12.1
Fit statistically acceptable	Yes	Yes	Yes	Yes

* Number of estimated fluxes equals the number of independent fluxes that were statistically different from zero, as judged by the 95% confidence interval.

** Combined analysis of all three experiments required two additional parameters to account for apparent dilution of glucose labeling from glycerol tracers.

*** Number of redundant measurements = (no. of fitted isotopomers) – (no. of estimated flux)

The minimized sum of squared residuals of 12.1 was smaller than the critical value of 24.8 (at 95% confidence level with 13 degrees of freedom) indicating a statistically acceptable fit. The apparent fractional labeling of glucose was estimated at $87\% \pm 3$ and $86\% \pm 3$ for the $[\text{U-}^{13}\text{C}]$ glycerol and $[\text{H}_5]$ glycerol experiments, respectively, indicating that for both glycerol tracers there was an apparent dilution of glucose by about 13% (i.e. a value of 100% would indicate no dilution). Table 7-7 shows the 95% confidence intervals for the estimated fluxes for the 2-hr experiments.

After comparing the information content of separate data sets with the combined data (Table 7-6), two advantages of our method become apparent: (i) we can estimate more fluxes, and (ii) the number of redundant measurements is significantly increased. Here, 11 fluxes were estimated from the combined data, compared to 2 fluxes from the $^2\text{H}_2\text{O}$ experiment, 6 fluxes from $[\text{H}_5]$ glycerol experiment, and 4 fluxes from $[\text{U-}^{13}\text{C}]$ glycerol experiment. The number of redundant measurements for the combined data was 16 compared to 5, 3, and 9 for $^2\text{H}_2\text{O}$, $[\text{H}_5]$ glycerol, and $[\text{U-}^{13}\text{C}]$ glycerol data, respectively. Redundant measurements are important for metabolic flux analysis, because they allow more accurate estimation of fluxes, validation of modeling assumptions, and identification of missing reactions in the network model. In this study, many modifications to the initially assumed network model were examined for their ability to accurately account for the observed isotopomer data. If a modification explained the data significantly better, i.e. resulted in a statistically smaller magnitude of sum of squared residuals, it was accepted. Such a posteriori changes to the model were the inclusion of the transketolase (TK) and phosphomannose isomerase (PMI) reactions, resulting in a reduction of the sum of squared residuals by more than 80%. The results is shown in Table 7-7 further illustrate that the different isotopic tracers provide different flux information. For example, exchange fluxes of TK and TPI were estimated precisely from $[\text{U-}^{13}\text{C}]$ glycerol data, however, PGI and PMI exchange fluxes could not be determined. On the other hand, $[\text{H}_5]$ glycerol data provided sufficient information to estimate PGI, TPI and PMI exchange fluxes, however, the estimated TK exchange flux was less precise. Note that $^2\text{H}_2\text{O}$ data alone did not provide enough information to determine net and exchange fluxes in this system with precision, however, when supplemented with data from $[\text{U-}^{13}\text{C}]$ glycerol and $[\text{H}_5]$ glycerol tracers, the

Table 7-7

Estimated 95% confidence intervals of fluxes for the samples taken at 2 hr. Metabolic fluxes and their confidence intervals were estimated by fitting glucose mass isotopomer distributions to detailed gluconeogenesis model using Metran software.

<i>Net fluxes</i>	10% D ₂ O	[$^2\text{H}_5$]glycerol	[U- ^{13}C]glycerol	Combined analysis of all three experiments
Glucose production (fixed at 100)	100	100	100	100
Gluconeogenesis (GNG)*	53 – 100	63 – 80	69 – 73	75 – 87
Glycogenolysis (GL)*	0 – 47	20 – 37	27 – 31	13 – 25
Glycerol to glucose flux	0 – 150	57 – 64	60 – 62	65 – 75
Oxaloacetate to glucose flux	29 – 183	65 – 102	77 – 85	85 – 100
<i>Exchange fluxes**</i>				
Phosphoglucose isomerase (PGI)	nd	140 – 380	nd	262 – 728
Aldolase	nd	nd	nd	nd
Triose phosphate isomerase (TPI)	nd	180 – 510	230 – 360	280 – 405
Phosphomannose isomerase (PMI)	nd	0 – 27	nd	0 – 41
Transketolase (TK)	nd	7 – 83	5 – 9	6 – 10
Phosphoglucomutase (PGM)	nd	nd	nd	nd
Glycerol 3-phosphate dehydr.	nd	nd	nd	nd
Glyceraldehyde 3-phosphate dehydr.	nd	nd	nd	nd
Cycling between GAP and PEP	nd	nd	nd	nd
<i>Additional model parameters</i>				
Apparent fractional glucose labeling in [U- ^{13}C]glycerol experiment	-	-	-	87% \pm 3
Apparent fractional glucose labeling in [$^2\text{H}_5$]glycerol experiment	-	-	-	86% \pm 5

* GNG and GL are not independent fluxes, i.e. $\text{GNG} = (v_{\text{glycerol}} + v_{\text{oxaloacetate}})/2$; $\text{GL} = 100 - \text{GNG}$.

** 'nd' (=not determined) indicates that the exchange flux could not be determined, as judged by having a 95% confidence interval from zero to infinity.

$^2\text{H}_2\text{O}$ experiment provided the most informative mass isotopomers for accurate estimation of the gluconeogenesis flux (results based on sensitivity analysis).

7.3.7 Evaluation of estimated fluxes

Table 7-8 shows the estimated fluxes for the 2, 5, and 8-hr samples obtained from analysis of combined isotopomer data for each time point. The small magnitude of the sum of squared residuals and the large number of redundant measurements gave us very high degree of confidence in the fidelity of the calculated fluxes. The estimated fluxes provided important insight into the physiology of cultured hepatocytes. Our results suggest that the phosphoglucose isomerase (PGI) reaction and triose phosphate isomerase (TPI) were not fully equilibrated. The estimated PGI exchange flux of 380 ± 15 corresponds to $79\% \pm 4$ labeling equilibrium between F6P and G6P. Furthermore, the estimated TPI exchange flux of 330 ± 32 corresponds to $76\% \pm 2$ labeling equilibrium between DHAP and GAP. These results are surprising, because it is generally assumed that the PGI and TPI reactions are fully equilibrated. For example, these assumptions are crucial for the widely used $^2\text{H}_2\text{O}$ method for estimating the contribution of gluconeogenesis to hepatic glucose production, as was initially proposed by Landau and colleagues (1995). In this method, fractional gluconeogenesis is determined from the ratio of deuterium labeling at C5 vs. C2 of glucose in experiments with $^2\text{H}_2\text{O}$. Deuterium is incorporated at C5 of glucose in reactions catalyzed by enolase and TPI, whereas deuterium is incorporated at C2 of glucose via PGI reaction. Our flux results indicated that the labeling of GAP-C2 (that eventually becomes C5 of glucose) is $>95\%$ equilibrated with the solvent mainly via enolase reaction, but G6P-C2 (that becomes C3 of glucose) is only 80% equilibrated with the solvent. Thus, in our experiments the C5/C2 ratio would overestimate fractional gluconeogenesis by 20% .

7.3.8 Comparing estimated fluxes vs. MIDA

The estimated fluxes shown in Table 7-8 were significantly different from the fluxes determined by MIDA shown in Table 7-5. MIDA underestimated fractional GNG and the contribution of oxaloacetate to glucose by $18\text{-}31\%$, and overestimated glycogenolysis flux.

Table 7-8

Metabolic fluxes in the gluconeogenesis pathway estimated by combined analysis of multiple tracer data. Fluxes and their confidence intervals (shown as best fit \pm SD) were estimated for the 2, 5, and 8-hr samples by fitting all data for each sample point with Metran.

<i>Net fluxes</i>	2 hr	5 hr	8 hr
Glucose production (fixed at 100)	100	100	100
Gluconeogenesis (GNG)	81 \pm 3	90 \pm 4	91 \pm 4
Glycogenolysis (GL)	19 \pm 3	10 \pm 4	9 \pm 4
Glycerol to glucose flux	70 \pm 3	72 \pm 3	67 \pm 3
Oxaloacetate to glucose flux	92 \pm 4	108 \pm 5	114 \pm 5
<i>Exchange fluxes and percent equilibration*</i>			
Phosphoglucose isomerase (PGI)	380 \pm 115 (79% \pm 4)	390 \pm 150 (81% \pm 4)	527 \pm 200 (86% \pm 5)
Aldolase	nd	nd	nd
Triose phosphate isomerase (TPI)	330 \pm 32 (76% \pm 2)	380 \pm 40 (79% \pm 2)	394 \pm 46 (80% \pm 2)
Phosphomannose isomerase (PMI)	10 \pm 10	13 \pm 14	13 \pm 18
Transketolase (TK)	8.2 \pm 1	9.6 \pm 1	11.2 \pm 1
Phosphoglucomutase (PGM)	nd	nd	nd
Glycerol 3-phosphate dehydr.	nd	nd	nd
Glyceraldehyde 3-phosphate dehydr.	> 295	> 300	> 385
Cycling between GAP and PEP	nd	nd	nd
<i>Additional model parameters</i>			
Apparent fractional glucose labeling in [^{13}C]glycerol experiment	87% \pm 3	85% \pm 3	75% \pm 3
Apparent fractional glucose labeling in [$^2\text{H}_5$]glycerol experiment	86% \pm 5	84% \pm 5	82% \pm 6

* Values in parentheses for PGI and TPI reactions denote the estimated degree of equilibration.

* Percent equilibration = 100% \times (exchange flux) / (100 + exchange flux).

The difference was most striking for the 5-hr and 8-hr samples, where we estimated $90\% \pm 4$ contribution of GNG to glucose production, whereas MIDA estimated 71% and 63%, respectively. Note that our method correctly accounted for the depletion of glycerol tracers, as is indicated by the lower estimate for fractional glucose labeling at 8 hr, i.e. 75% at 8 hr vs. 85% at 2 and 5 hr for the [U-¹³C]glycerol experiments. The estimated GNG flux at 8 hr ($90\% \pm 4$) as identical to the estimated flux at 5 hr ($91\% \pm 4$).

7.3.9 Sources of NADH

The flux results further allowed us to predict the contribution of various sources to the production of NADH. Table 7-9 shows the predicted fractional contribution of glycerol, water, and unlabeled sources to NADH. We estimated that 10% of NADH hydrogen atoms were derived from glycerol, 30-37% from the solvent via hydrogen exchange, and 52-60% from other unlabeled endogenous sources, presumably mainly from lactate via lactate dehydrogenase. The estimated contribution of glycerol to NADH of 10% corresponded well with our previous observation that [²H₅]glycerol transferred deuterium atoms to lactate, from which we estimated that about $13 \pm 5\%$ of NADH was derived from glycerol.

Table 7-9

Predicted fractional contribution of glycerol, water, and unlabeled sources to NADH hydrogen atoms. From the estimated fluxes shown in Table 7-8 we determined the various sources of NADH hydrogen atoms and calculated the following fractional contributions.

	2 hr	5 hr	8 hr
Glycerol	$10 \pm 3\%$	$9 \pm 3\%$	$10 \pm 3\%$
Water	$30 \pm 3\%$	$39 \pm 3\%$	$37 \pm 3\%$
Unlabeled sources	$60 \pm 3\%$	$52 \pm 3\%$	$53 \pm 3\%$

7.4 Discussion

To our best knowledge, this is the first detailed analysis of net and reversible fluxes in the gluconeogenesis pathway in cultured hepatocytes. We demonstrated that an over-determined data set of mass isotopomer abundances obtained from ^{13}C and ^2H -labeling experiments fitted to a detailed model of gluconeogenesis pathway provides precise fluxes, and allows validation of model assumptions using redundant measurements. Our results have wide implications for in vivo studies of glucose metabolism from ^{13}C - and ^2H -tracers. MIDA was originally introduced by Neese et al. (1995) as a method for analysis of the gluconeogenesis pathways from ^{13}C -labeled substrates. This method treats glucose as a dimer of triose phosphates with a constant labeling. Neese et al. showed that lack of equilibrium between the enrichments of triose phosphates had a small impact on the calculation of fractional gluconeogenesis. However, one of the disadvantages of the MIDA framework is that it required the use of ^{13}C -tracers, i.e. it cannot be applied for analysis of mass isotopomer data from ^2H -labeling experiments. Furthermore, MIDA does not accurately capture scrambling of ^{13}C -labeling in the TCA cycle and pentose phosphate pathway reactions resulting in underestimation of the gluconeogenesis pathway. Here, we have developed novel comprehensive analysis tools for analysis of experimental data from multiple tracer experiments. In this contribution, $[\text{U-}^{13}\text{C}]$ glycerol, $[\text{H}_3]$ glycerol, and $^2\text{H}_2\text{O}$ tracer experiments was accomplished with a detailed model of glucose metabolism and rigorous methods for balancing of isotopomers within a reaction network. Analysis of the combined data revealed that MIDs of glucose from glycerol tracers were incompatible with MIDs of glucose from $^2\text{H}_2\text{O}$ experiments. We demonstrated that glycerol tracers consistently underestimated GNG in our experiments. Previs et al. (1995, 1998) reported the same finding from experiments with perfused livers and isolated hepatocytes from starved rats. They attributed the underestimation of GNG to the presence of different cell populations that utilize glycerol to different extent for the production of glucose. Our results support this hypothesis. We concludes that any tracer method that requires the formation of labeled glucose isotopomers from the condensation of two labeled triose phosphate molecules will always underestimate GNG due to differences in enrichments of triose phosphates, and due to zonation and depletion of isotopic tracers. The extent of underestimation of GNG cannot

be determined from MIDA analysis. Here, we applied $^2\text{H}_2\text{O}$ in addition to $[\text{U-}^{13}\text{C}]$ glycerol and $[\text{H}_3]$ glycerol tracers to quantify the underestimation of GNG from glycerol tracers. We showed that in our experiments $[\text{H}_3]$ glycerol and $[\text{H}]$ glycerol tracers consistently underestimated GNG by about 14%.

Previs et al. used $[\text{H}_3]$ glycerol in experiments with perfused livers and noted release of M+0 to M+4 mass isotopomers of glycerol from $[\text{H}_3]$ glycerol. However, without a detailed mathematical model they could only provide qualitative interpretation of the observed mass isotopomers. Based on the release of the M+1 mass isotopomer of glycerol they concluded that there must be cycling between glycerol, PEP, oxaloacetate and pyruvate. In our $[\text{H}_3]$ glycerol experiments we also observed release of M+0 to M+3 mass isotopomers of glycerol from $[\text{H}_3]$ glycerol tracer. However, our results provided a different explanation for the release of M+1 to M+3 isotopomers. The estimated fluxes indicated that there is not any significant cycling between $[\text{H}_3]$ glycerol and pyruvate. In contrast, the presence of M+1 of glycerol was fully explained from deuterium incorporation via $[\text{H}_3]$ glycerol \rightarrow NAD $[\text{H}]$ \rightarrow $[\text{H}]$ glycerol (M+1), catalyzed by glycerol-3-phosphate dehydrogenase. In support of this result we found that deuterium atoms from $[\text{H}_3]$ glycerol were incorporated into lactate, presumably via lactate dehydrogenase (i.e. $[\text{H}_3]$ glycerol \rightarrow NAD $[\text{H}]$ \rightarrow $[\text{H}]$ lactate), and that no ^{13}C -labeling was incorporated into lactate from $[\text{U-}^{13}\text{C}]$ glycerol. Thus, we concluded that in cultured hepatocytes glycerol contributed significantly to the production of NADH. We estimated that about 10% of NADH was derived from glycerol, 30% from the solvent via hydrogen exchange, and 60% from other unlabeled endogenous sources. Our results further indicated that there was rapid exchange between the A- and B-hydrogen atoms of NADH, which was in agreement with the result published by Vind et al. (1987), where the authors showed that in isolated hepatocytes that there is near-equilibrium between the A- and B-hydrogen atoms of NADH.

Our results indicated that the $^2\text{H}_2\text{O}$ method has the best potential to provide an unbiased estimate of GNG flux in vivo. However, the $^2\text{H}_2\text{O}$ method is not without assumptions. For example, it is generally assumed that there rapid incorporation of deuterium at C2 position of glucose via PGI, and at C5 via TPI and enolase. In practice, the extent of equilibration of

these reactions is not easily validated in vivo. In this study, we validated the equilibrium assumptions for the $^2\text{H}_2\text{O}$ method explicitly by estimating reaction reversibilities for PGI and TPI reactions, mainly from the $[\text{}^2\text{H}_3]\text{glycerol}$ data. We found that the PGI and TPI reactions were only 80-86% equilibrated. We estimated that the C2 hydrogen of glucose was no more than 80% equilibrated with the solvent, but the C2 hydrogen of GAP (that eventually becomes C5 of glucose) was more than 95% equilibrated with the solvent, mainly via enolase reaction. Thus, the ratio of deuterium labeling at C5 vs. C2 resulted in 20% overestimation of GNG in our experimental setup. To summarize, we have demonstrated that through combined analysis of mass isotopomer data from $[\text{}^{13}\text{C}]\text{glycerol}$, $[\text{}^2\text{H}]\text{glycerol}$ and $^2\text{H}_2\text{O}$ tracers we can estimate unbiased net and reversible fluxes in the gluconeogenesis pathways and correctly accounted for lack of complete equilibration of reversible reactions in the gluconeogenesis pathway. Furthermore, we provided a method to account for the apparent dilution of glucose labeling from glycerol tracers due to inhomogeneity of hepatocyte populations and depletion of tracers.

Chapter 8

Application of elementary metabolite units and [U-¹³C, ²H₈]glycerol to estimate fluxes of gluconeogenesis

8.1 Introduction

Methods for measuring the metabolic rate of gluconeogenesis (GNG) *in vivo*, relative to hepatic glucose production (HGP), rely on the use of stable isotopes (¹³C and ²H) and the assessment of glucose labeling distribution by gas chromatography mass spectrometry (GC/MS) and nuclear magnetic resonance (NMR) spectroscopy. It has been argued that the algebraic relationships based on the [U-¹³C]glucose tracing method underestimate gluconeogenesis *in vivo*. A major reason is the failure to consider the exchange of labeled precursors in the TCA cycle and the contribution of glycerol to gluconeogenesis. In the early 1990s condensation polymerization methods offered a new approach to estimating biosynthesis. [¹³C]Glycerol tracers were used for quantifying gluconeogenesis using mass isotopomer distribution analysis (MIDA). However, the possibility of zonation of the tracer across the liver has led to questions about the validity of this method. Several studies with isolated hepatocytes, perfused livers, and in whole animals have shown that mass isotopomer distribution (MID) of glucose from [¹³C]glycerol tracers are incompatible with a single constant pool of triose phosphates, presumably due to multiple cell populations with differential preference for various gluconeogenic precursors. Malloy and colleagues (1998) proposed a quantitative approach based on the fate of [U-¹³C]propionate and the analysis of

hepatic glutamate and glucose. This method uncovered a discrepancy between the analyses of different compounds indicative of compartmentation of metabolism. This important finding further complicated the search for a clear quantitative method for estimating hepatic fluxes from carbon labeling data. Recently, we have applied [²H₅]glycerol, [U-¹³C]glycerol and ²H₂O to measure net and exchange fluxes in the gluconeogenesis pathway (Chapter 7). From detailed analysis mass isotopomer distributions of glucose fragments we estimated the extent of equilibration of phosphoglucose isomerase (PGI) and triose phosphate isomerase (TPI) reactions with precision, i.e. 80-86% equilibration for PGI and 79-81% equilibration for TPI in isolated hepatocytes. However, our results also suggested that [²H₅]glycerol and [U-¹³C]glycerol underestimated the flux of GNG by about 15% in our experiments. Currently, the most widely used method for measuring GNG in vivo is the ²H₂O method that was proposed by Landau et al. (1995). It has been argued that this method provides an unbiased estimate of the GNG flux. However, currently this method assumes complete equilibration of PGI and TPI reactions, which is not true in all situations. For example, we have shown previously in isolated hepatocytes that lack of complete equilibration of PGI resulted in 20% overestimation of GNG with the ²H₂O method (Chapters 5 and 7). Thus, despite many decades of experiments, the search for a well-accepted method for quantifying gluconeogenesis from stable isotope tracers continues.

Here, we present a novel two-tracer method for accurate determination of net and reversible fluxes in the gluconeogenesis pathway in vivo. Our method builds on Landau's ²H₂O method with the addition of a novel doubly-labeled glycerol tracer, i.e. [U-¹³C,²H₈]glycerol. In this method we apply the two tracers, i.e. ²H₂O and [U-¹³C,²H₈]glycerol, simultaneously and measure the incorporation of ²H from ²H₂O, and ²H and ¹³C from [U-¹³C,²H₈]glycerol into glucose. Here, we make use of GC/MS analysis to measure the labeling distributions of six fragments of glucose based on three glucose derivatives that were recently introduced, i.e. aldonitrile pentapropionate ion fragments at m/z 173, 259, 284, and 370; methyloxime pentapropionate ion fragment at m/z 145; and di-O-isopropylidene propionate ion fragment at m/z 301. The mass isotopomer distributions of these fragments provide an over-determined data set with 25 redundant measurements from which accurate metabolic fluxes and their confidence intervals are determined. Quantitative interpretation of the complex

labeling patterns was accomplished through the use of rigorous mathematical tools based on the elementary metabolite units (EMU) framework, which was recently developed and shown to be the most efficient method for analyzing mass isotopomer data from labeling experiments. We will illustrate that the proposed two-tracer method allows measurement of net fluxes and the extent of equilibration of reactions in the gluconeogenesis pathway. Furthermore, we show that fluxes estimated with this method are independent of the isotopic steady-state assumption and independent of any potential zonation of glycerol.

8.2 Methods

8.2.1 Metabolic network model

The gluconeogenesis network model that we used for flux calculations was described previously (see Chapter 7; Figure 7-1 and Table 7-1). In short, the network model is comprised of 24 reactions utilizing 26 metabolites, with 5 substrates (oxaloacetate, glycerol, glycogen, water, and NADH from endogenous sources), 3 products (glucose, CO₂, and a metabolic sink for NADH), and 18 balanced intracellular metabolites. Stereospecific atom transitions were assigned for all reactions in the model based on current knowledge.

8.2.2 Simulating isotopomer distributions using elementary metabolite units

Quantitative interpretation of isotopomer data requires the use of mathematical models that describe the relationship between metabolic fluxes and isotopomer abundances. Recently, we presented a novel framework for the modeling of isotopic tracer systems that significantly reduces the number of system variables without any loss of information. The elementary metabolite units (EMU) framework is based on a highly efficient decomposition method that identifies the minimum amount of information needed to simulate isotopic labeling within a reaction network using the knowledge of atomic transitions occurring in the network reactions. Here, the gluconeogenesis network model was decomposed into 60 independent EMU reaction networks with a total of 204 EMU variables, as opposed to the complete set of 42,224 cumomers that would be required to simulate this system using the traditional

cumomer modeling strategy (i.e. a reduction of 99.5%). The functional units generated by the decomposition algorithm, called EMUs, formed the new basis for generating system equations that described the relationship between fluxes and isotopomer abundances (Chapter 2). To simulate the isotopic labeling of glucose, the EMU networks can be solved sequentially starting with the smallest EMU-size network up to the largest EMU-size network. The mathematical simulation model was constructed with the Metran software.

8.2.3 Computational methods

Metabolic fluxes and their confidence intervals were determined by fitting mass isotopomer abundances of glucose fragments to the detailed gluconeogenesis metabolic network model using Metran software. In short, Metran estimates fluxes by minimizing the difference between the observed and simulated measurements using an iterative least-squares minimization procedure. The objective of this routine is to evaluate a set of feasible fluxes that best accounts for the observed isotopomer measurements. After metabolic fluxes were calculated, statistical analysis was automatically performed to obtain accurate standard deviations and confidence intervals of fluxes by evaluating the sensitivity of the objective function with respect to fluxes as described in Chapter 3. Flux validation was accomplished by a statistical test for the goodness-of-fit (i.e. chi-square test for model adequacy), and a normality test for the weighted residuals. To ensure a global optimum, flux estimation was repeated at least four times starting with random initial values. Sensitivity analysis was employed to determine the relative importance of measurements for the estimation of individual fluxes as described previously (Chapter 3).

8.2.4 Determining deuterium enrichment of glucose

The amount of deuterium enrichment at each carbon position of glucose from ²H₂O experiments was determined using a least-squares approach that was previously described in Chapter 5. In short, we constructed a simulation model that predicts the mass isotopomer distributions of selected ion fragments of glucose for given isotopomer distribution of glucose hydrogen atoms, while taking into account natural isotope enrichments. The

isotopomer distribution was determined from experimental data by solving a least-squares regression problem, where the objective was to minimize the sum of squared deviations between simulated and measured mass isotopomer abundances. From the estimated isotopomer distribution we then obtained positional deuterium enrichments via linear transformation. We identify the deuterium enrichment of C-H in carbon 1 as D_1 , the enrichment in carbon 2 as D_2 , and so forth. Since there are two hydrogen atoms at carbon 6 that cannot be distinguished by GC/MS, we could only determine the average enrichment at carbon 6, i.e. $D_6 = D_{66}/2$.

8.2.5 Materials

Biochemicals were obtained from Sigma Chemicals (St. Louis, MO). The custom synthesized glycerol tracer [U-¹³C,²H₈]glycerol (99+ At% ¹³C, 98+ At% ²H) was purchased from Omicron Biochemicals (South Bend, IN). The isotopic purity was of the tracer validated by GC/MS analysis. Tissue culture media were obtained from Sigma (St. Louis, MO).

Hepatocyte medium was DMEM powder (Sigma) supplemented with 3.7 g/L NaHCO₃, 30 mg/L proline, 100 mg/L ornithine, 610 mg/L niacinimide, 0.544 mg/L ZnCl₂, 0.75 mg ZnSO₄·7H₂O, 0.2 mg/L CuSO₄·5H₂O, 0.025 mg/L MnSO₄, 2 g/L bovine serum albumin, 100,000 U penicillin, and 100,000 U streptomycin, and further enriched with gluconeogenic carbon sources: 1mM glycerol, 10 mM lactate, 1 mM pyruvate, 5 mM glutamine, and 2 mM acetate. Four chemically identical labeling media were prepared, containing either ²H₂O (at 10% enrichment); [U-¹³C,²H₈]glycerol + unlabeled glycerol (1:3 mol/mol, i.e. 25% enrichment of tracer); [U-¹³C,²H₈]glycerol + unlabeled glycerol (1:3 mol/mol, i.e. 25% enrichment) prepared in ²H₂O (at 10% enrichment); and medium with no tracers (as control).

8.2.6 Hepatocyte isolation and hepatocyte suspension experiments

Hepatocytes were isolated from C57BL/6 mice by modified two step-collagenase perfusion as described by Seglen (1976). Two mice (~25 gram) were fed ad libitum, and two mice (~25 gram) were fasted 12 hrs prior to hepatocyte isolation. The mice were anesthetized with

tribromoethanol (500 mg/kg IP) for the duration of the procedure. In short, the surgeon exposed the intraperitoneal abdominal contents including the liver, portal vein and inferior vena cava. The portal vein was cannulated with a 24.5G catheter, and the liver was perfused for 15 minutes at a rate of 7 mL/min with calcium-free perfusion buffer to remove blood from the fibrous liver sac. Mouse euthanasia followed exsanguinations after cutting the inferior vena cava to complete the perfusion circuit. The blanched liver was perfused with collagenase solution (200U/mL) for 10 minutes at 7 mL/min to release hepatocytes from the extracellular matrix. The digested liver was excised and placed in preservation buffer, where the digested cells were gently scraped from the liver sac, washed and purified with Percoll to remove dead cells and enrich the hepatocyte fraction. At this point cells were counted and viability assessed by Trypan Blue exclusion. Typical viabilities were between 85-90%, with cell yields of 1.0-1.5×10⁶ cells/g mouse (25-40×10⁶ cells). Purified cells were suspended in media with isotopic tracers and seeded in 6-well plates (10⁶ cells/well) and incubated for 30 minutes at 37°C and 5% CO₂. At the end of the incubation period medium samples were collected (approx. 1 mL), centrifuged for 10 sec, and the supernatant separated from cells pellet. Cells and supernatant were stored at -80 °C prior to analysis.

8.2.7 Derivatization of glucose

Mass isotopomer distributions of glucose were determined from three glucose derivatives, i.e. aldonitrile pentapropionate, methyloxime pentapropionate and di-O-isopropylidene propionate glucose. For each derivatization procedure, 100 µL of medium sample was deproteinized by addition of 300 µL of cold acetone, followed by vortexing vigorously for 30 sec, and centrifugation at 2000×g for 1 min. The supernatant was evaporated to dryness under airflow and the residue derivatized as previously described (Chapter 5). In short, for the aldonitrile pentapropionate and methyloxime pentapropionate derivatizations, 50 µL of 2 wt% hydroxylamine hydrochloride in pyridine, or 2 wt% methoxylamine hydrochloride in pyridine, respectively, was added to the dry residue and the sample heated at 90°C for 60 min. This was followed by addition of 100 µL of propionic anhydride and heating at 60°C for additional 30 min. The sample was then evaporated to dryness, dissolved in 100 µL of

ethyl acetate and transferred to an injection vial for GC/MS analysis. For di-O-isopropylidene propionate derivatization, 500 μ L of 0.38 M sulfuric acid in acetone was added to the dry residue and the sample incubated at room temperature for 60 min. 400 μ L of 0.44 M sodium carbonate was added to neutralize the reaction, followed by addition of 1 mL of saturated sodium chloride. Di-O-isopropylidene derivatives were extracted by partitioning with 1 mL of ethyl acetate. The upper, organic layer was evaporated to dryness, followed by addition of 150 μ L of propionic anhydride in pyridine (2:1 v/v) and heating at 60°C for 30 min. The sample was then evaporated to dryness, dissolved in 100 μ L of ethyl acetate and transferred to an injection vial for GC/MS analysis.

8.2.8 GC/MS analysis

Gas Chromatography-Mass Spectrometry (GC/MS) analysis was performed using HP 5890 Series II GC (Gas Chromatograph) equipped with a DB-1701 [30 m x 0.25 mm (inner diameter) x 0.25 μ m] capillary column, connected to HP 5971 MSD (Mass Selective Detector) operating under ionization by electron impact (EI) at 70 eV. The mass spectrometer was calibrated using the 'Max Sensitivity Autotune' setting. Helium flow was maintained at 0.737 mL/min by electronic control. The temperatures of the injector and the detector were kept at 250°C and 300°C, respectively. The temperature of the column was started at 80°C for 1 min, increased to 280°C at 20°C/min, and held for 4 min. For the analysis of aldonitrile pentapropionate glucose, ion intensities were recorded for the following four ion fragments: m/z 173-178 (C₅₋₆, H₅₋₆), m/z 259-265 (C₄₋₆, H₄₋₆), m/z 284-289 (C₁₋₄, H₂₋₄), and m/z 370-379 (C₁₋₅, H₂₋₅). For di-O-isopropylidene propionate glucose, ion intensities were recorded at m/z 145-149 (C₁₋₂, H₁₋₂). For methyloxime pentapropionate glucose, ion intensities were recorded at m/z 301-313 (C₁₋₆, H₁₋₆). Measured intensities were corrected for noise (baseline correction), and mass isotopomer distributions were obtained by integration. All mass isotopomer values were expressed as fractional abundances, i.e. for each fragment the sum of all mass isotopomers equals one. Samples were injected at least six times and the measured mass isotopomer abundances were averaged. Ions at m/z 148, 149, 178, 288, and 289 contained constant contaminating ions amounting to 0.03, 0.05, 0.27, 0.18, and 0.25 mol% enrichment, respectively, which was corrected by subtraction. In experiments

with [U-¹³C,²H₅]glycerol, intensities of ions at m/z 145, 146, and 147 could be inaccurate (up to 2 mol% inaccuracy) due by overlapping mass spectra from smaller ion fragments. To exclude these data from flux determination we assigned relatively high measurement errors to these ions, i.e. 2 mol% assumed measurement error (compared to <0.4 mol% for all other ions). We should note that sensitivity analysis revealed that ions 145-147 were not important for flux determination, i.e. only the ratio of m/z 148 relative to m/z 149 contained flux information. Thus, inaccuracies in ions 145-147 did not affect flux results.

8.3 Results

8.3.1 Incorporation of deuterium into glucose from ²H₂O

In the pathway of gluconeogenesis labeled hydrogen atoms are incorporated into glucose from medium containing deuterated water. The amount of deuterium incorporated at each carbon position depends on the deuterium enrichment of the solvent, and relative activity of various reversible reactions in the gluconeogenesis pathway. In this study, fresh hepatocytes isolated from fasted and fed mice were incubated in medium containing ²H₂O at 10% enrichment. All experiments were performed in triplicate, i.e. hepatocytes were cultured in 6-well plates for 30 min (10⁶ cells/well). At the end of the incubation period medium samples were collected and glucose was analyzed by GC/MS. The amount of deuterium incorporated at each carbon position was determined by regression analysis of mass isotopomer distributions of six glucose fragments as described previously (Chapter 5). As control, hepatocytes were also cultured in medium with no tracers. Tables 8-1 and 8-2 show the measured mass isotopomer distributions of the six selected glucose fragments from experiments with fasted and fed hepatocytes, respectively. The observed mass isotopomer abundances from the triplicate experiments were not statistically different ($P>0.10$). This confirmed that biological variability between wells was small in our experiments. Table 8-3 shows the deuterium enrichments at all six carbon positions of glucose for the experiments with fasted and fed hepatocytes.

Table 8-1

Mass isotopomer distributions of glucose fragments from ²H₂O experiments with isolated hepatocytes from fasted mice. Hepatocytes were cultured in 6-wells plates in medium containing ²H₂O at 10% enrichment for 30 min, and one control well with no tracers (well #4). Glucose labeling was analyzed by GC/MS. Shown are measured mass isotopomer distributions of six selected glucose fragments (molar percentages, mol%).

m/z (formula)	C-H positions	Well #	M+0	M+1	M+2	M+3	M+4
301 (C ₁₄ H ₂₁ O ₇)	1,2,3,4,5,6,6	1	50.2	34.7	11.9	2.7	0.5
		2	50.4	34.5	11.9	2.7	0.5
		3	50.2	34.6	11.9	2.7	0.5
		4	84.1	13.4	2.4	0.1	0.0
145 (C ₆ H ₁₁ O ₃ N)	1,2	1	79.1	18.5	2.2	0.2	0.0
		2	78.8	18.8	2.2	0.2	0.0
		3	78.9	18.7	2.2	0.2	0.0
		4	92.5	6.7	0.8	0.0	0.0
173 (C ₈ H ₁₃ O ₄)	5,6,6	1	72.3	23.4	3.8	0.4	0.0
		2	72.2	23.5	3.8	0.4	0.0
		3	72.3	23.4	3.8	0.4	0.0
		4	90.7	8.1	1.1	0.1	0.0
259 (C ₁₂ H ₁₉ O ₆)	4,5,6,6	1	64.4	28.1	6.4	1.0	0.0
		2	64.3	28.1	6.4	1.1	0.0
		3	64.4	28.2	6.3	1.0	0.1
		4	86.3	11.6	1.9	0.2	0.0
284 (C ₁₃ H ₁₈ O ₆ N)	2,3,4	1	68.4	25.7	5.1	0.8	0.0
		2	68.2	25.8	5.4	0.7	0.0
		3	68.1	26.0	5.2	0.7	0.0
		4	85.1	12.6	2.1	0.2	0.0
370 (C ₁₇ H ₂₄ O ₈ N)	2,3,4,5	1	58.5	31.1	8.5	1.7	0.2
		2	58.3	31.2	8.6	1.7	0.3
		3	58.4	31.1	8.6	1.7	0.2
		4	81.2	15.6	2.9	0.4	0.0

Data shown are the integrated mass isotopomer distributions not corrected for natural isotope enrichments. Measurements errors were <0.3 mol%. Data from the triplicate wells were not statistically different.

Table 8-2

Mass isotopomer distributions of glucose fragments from ²H₂O experiments with isolated hepatocytes from fed mice. Hepatocytes were cultured in 6-wells plates in medium containing ²H₂O at 10% enrichment for 30 min, and one control well with no tracers (well #4). Glucose labeling was analyzed by GC/MS. Shown are measured mass isotopomer distributions of six selected glucose fragments (molar percentages, mol%).

m/z (formula)	C-H positions	Well #	M+0	M+1	M+2	M+3	M+4
301 (C ₁₄ H ₂₁ O ₇)	1,2,3,4,5,6,6	1	66.0	25.2	7.1	1.5	0.2
		2	65.0	25.8	7.5	1.6	0.2
		3	65.9	25.3	7.2	1.5	0.2
		4	84.2	13.3	2.3	0.2	0.0
145 (C ₆ H ₁₁ O ₃ N)	1,2	1	84.5	13.7	1.7	0.2	0.0
		2	84.5	13.7	1.6	0.1	0.0
		3	84.3	13.9	1.7	0.1	0.0
		4	92.4	6.7	0.9	0.0	0.0
173 (C ₈ H ₁₃ O ₄)	5,6,6	1	82.6	14.9	2.2	0.2	0.0
		2	81.9	15.5	2.3	0.2	0.0
		3	82.2	15.3	2.3	0.2	0.0
		4	90.7	8.0	1.1	0.1	0.0
259 (C ₁₂ H ₁₉ O ₆)	4,5,6,6	1	76.2	19.3	3.8	0.6	0.1
		2	75.4	19.8	4.0	0.6	0.1
		3	75.6	19.7	4.0	0.6	0.1
		4	86.3	11.6	1.9	0.2	0.0
284 (C ₁₃ H ₁₈ O ₆ N)	2,3,4	1	75.2	20.3	3.8	0.6	0.0
		2	74.7	20.7	3.9	0.6	0.0
		3	75.1	20.4	3.8	0.6	0.0
		4	84.9	12.7	2.1	0.2	0.0
370 (C ₁₇ H ₂₄ O ₈ N)	2,3,4,5	1	68.5	24.4	6.0	1.1	0.1
		2	68.0	24.7	6.1	1.1	0.1
		3	68.3	24.5	6.0	1.1	0.1
		4	81.1	15.6	2.9	0.3	0.0

Data shown are the integrated mass isotopomer distributions not corrected for natural isotope enrichments. Measurements errors were <0.4 mol%. Data from the triplicate wells were not statistically different.

Table 8-3

Deuterium enrichment of glucose from ²H₂O experiments with hepatocytes isolated from fasted and fed mice. Hepatocytes isolated from fasted and fed mice were cultured in 6-wells plates in medium containing ²H₂O at 10% enrichment for 30 min, and one control well with no tracers (well #4). Deuterium enrichment at all six glucose carbon position was determined by least-squares regression as described in the Methods section. Results shown are molar percent enrichments (best fit ± SD).

Carbon position	Hepatocytes from fasted mouse				Hepatocytes from fed mouse			
	well #1 ² H ₂ O	well #2 ² H ₂ O	well #3 ² H ₂ O	well #4 no tracers	well #1 ² H ₂ O	well #2 ² H ₂ O	well #3 ² H ₂ O	well #4 no tracers
D ₁	7.3 ± 0.4	6.3 ± 0.4	6.8 ± 0.4	0.1 ± 0.2	4.1 ± 0.3	4.3 ± 0.3	3.7 ± 0.3	0.0 ± 0.2
D ₂	7.9 ± 0.4	9.1 ± 0.4	8.5 ± 0.4	0.0 ± 0.2	4.9 ± 0.3	4.6 ± 0.3	5.4 ± 0.3	0.0 ± 0.2
D ₃	6.5 ± 0.3	5.8 ± 0.3	6.4 ± 0.3	0.0 ± 0.2	4.3 ± 0.4	4.9 ± 0.4	3.6 ± 0.4	0.0 ± 0.2
D ₄	6.6 ± 0.2	6.7 ± 0.2	6.5 ± 0.2	0.0 ± 0.2	3.4 ± 0.2	3.6 ± 0.2	3.7 ± 0.2	0.1 ± 0.2
D ₅	10.6 ± 0.2	10.5 ± 0.2	10.5 ± 0.2	0.0 ± 0.2	5.0 ± 0.2	5.0 ± 0.2	5.1 ± 0.2	0.0 ± 0.2
D _{66/2}	5.7 ± 0.2	5.8 ± 0.2	5.7 ± 0.2	0.0 ± 0.2	2.3 ± 0.2	2.7 ± 0.3	2.5 ± 0.2	0.0 ± 0.2
Total	50.3 ± 0.3	50.0 ± 0.3	50.1 ± 0.3	0.1 ± 0.2	26.4 ± 0.3	27.7 ± 0.4	26.5 ± 0.3	0.1 ± 0.2

To better interpret these results consider Figure 8-1 that schematically illustrates the reactions involved in hydrogen exchange/incorporation into glucose. For example, it is well known that PGI stereospecifically transfers the pro-R hydrogen at C1 of fructose 6-phosphate (F6P) to the C2 position of glucose 6-phosphate (G6P), however, hydrogen exchange with the solvent has also been observed for the PGI reaction (Malaisse, 1990; Malaisse, 1991; Seeholzer, 1993). Malaisse et al. (1990, 1991) reported for a single passage in the direction F6P→G6P, 65% intramolecular hydrogen transfer and 35% hydrogen exchange, and for a single passage in the direction G6P→F6P, 72% intramolecular hydrogen transfer and 28% hydrogen exchange. It is generally assumed that there is rapid exchange between F6P and G6P, in which case we would expect that the labeling at C2 of glucose is equilibrated with the solvent. However, in our experiments the deuterium enrichment at C2 deviated significantly from 10%, i.e. solvent enrichment. In experiments with hepatocytes isolated from fasted and fed mice we found 7.9–9.1% and 4.6–5.4% deuterium enrichment at C2, respectively. These results clearly indicated that the PGI reaction was not fully equilibrated.

Incorporation at C5 of glucose occurs in the gluconeogenesis pathway, mainly via the reactions catalyzed by enolase and TPI (see Figure 8-1). Therefore, the ratio of enrichment of C5 to that of the solvent is a measure of gluconeogenesis relative to total glucose production. In experiments with fasted hepatocytes we found 10.5–10.6% enrichment at C5, indicating that 100% of glucose was produced by GNG, as expected in glycogen-deprived hepatocytes. The observed 0.5 mol% difference between the solvent enrichment and C5 enrichment may have been caused by measurement errors, inaccuracies in our media preparation, or due to a slight isotope effect. In experiments with fed hepatocytes we found 5.0–5.1% enrichment at C5, indicating that about 50% of glucose was produced by GNG. This result is in line with the expected contribution of GNG in hepatocytes isolated from fed mice. Note that in both cases the C5/C2 ratio would overestimate fractional GNG significantly, i.e. if we had used the C5/C2 ratio as a measure of fractional GNG, as proposed by Landau, we would have obtained 123% and 100% for fractional GNG in fasted and fed hepatocytes, respectively, which are both irrational results.

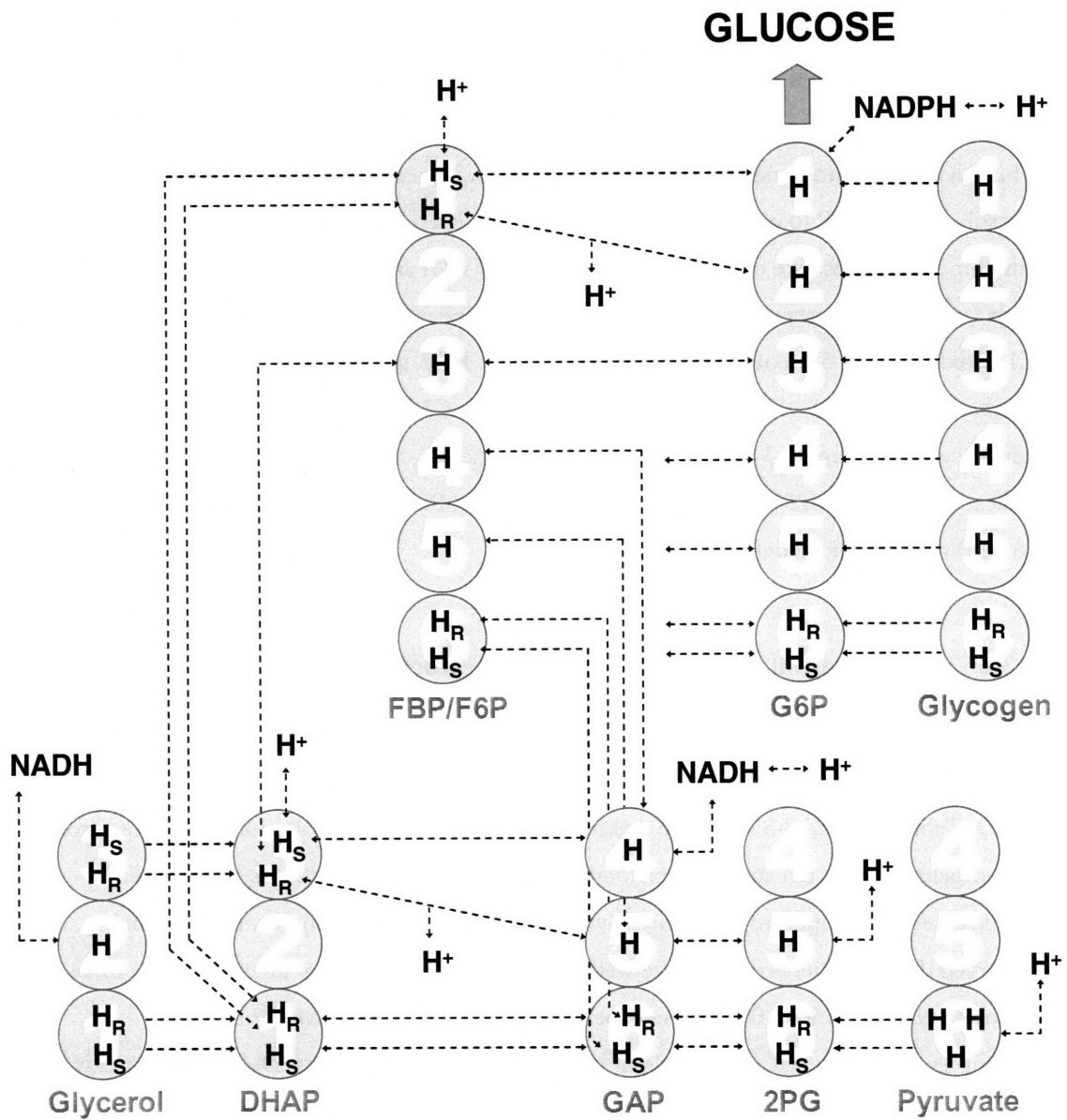


Figure 8-1: A schematic of reactions involved in hydrogen exchange and hydrogen incorporation into glucose in the gluconeogenesis pathway.

Deuterium incorporation at C1 and C6 positions occurs in the pyruvate → oxaloacetate → PEP pathway, more precisely, in reactions catalyzed by alanine aminotransferase and fumarase. Deuterium is additionally incorporated at C1 via reactions catalyzed by phosphomannose isomerase (PMI) and glucose 6-phosphate dehydrogenase (G6PDH). Thus, deuterium enrichment at C6 relative to the solvent enrichment is a measure of the contribution of PEP to glucose production, and the difference between C1 and C6 enrichments is indicative of the combined activity of PMI and G6PDH. In our experiments with fasted hepatocytes we found 5.7–5.8% enrichment at C6 and 6.3–7.3% enrichment at C1, indicating that 57% of glucose was derived from PEP, and that PMI/G6PDH reactions resulted in additional ~1% deuterium incorporation at C1. In experiments with fed hepatocytes we found 2.3–2.7% enrichment at C6 and 3.7–4.3% enrichment at C1, indicating that about 25% of glucose was derived from PEP and that also here there was some PMI/G6PDH activity.

8.3.2 Incorporation of labeling into glucose from [U-¹³C,²H₈]glycerol

Isolated hepatocytes were also incubated with [U-¹³C,²H₈]glycerol at 25% enrichment, i.e. in medium containing a mixture of [U-¹³C,²H₈]glycerol and unlabeled glycerol in the proportion of 1:3. Tables 8-4 and 8-5 show the measured mass isotopomer distributions of glucose from experiments with fasted and fed hepatocytes, respectively. Measured mass isotopomer abundances from triplicate experiments were not statistically different, i.e. the maximum observed deviation between replicate wells was 0.2 mol%. Qualitative interpretation of mass isotopomer distributions from these experiments is more difficult than from ²H₂O experiments, thus we will only highlight a few important observations. Detailed quantitative analysis will be performed in section 8.3.4, where we apply rigorous flux analysis tools to calculate fluxes and confidence intervals from this data. It is important to note that mass isotopomer abundances from [U-¹³C,²H₈]glycerol experiments cannot be corrected for natural isotope enrichments as is often done for other tracer experiments, because here two different isotopes (¹³C and ²H) are incorporated into glucose simultaneously. Thus, we must always analyze the uncorrected data directly.

Table 8-4

Mass isotopomer distributions of glucose from [U-¹³C,²H₈]glycerol labeling experiments with isolated hepatocytes from fasted mice. Hepatocytes were cultured in 6-wells plates in medium containing [U-¹³C,²H₈]glycerol at 25% enrichment for 30 min. Glucose labeling was analyzed by GC/MS. Shown are mass isotopomer distributions of six selected glucose fragments (molar percentages, mol%).

m/z (positions)	Well		M+0	M+1	M+2	M+3	M+4	M+5	M+6	M+7	M+8	M+9	M+10	M+11
	#													
301 (C ₁₋₆ , H ₁₋₆)	1		71.2	13.0	2.5	1.3	2.8	6.1	2.3	0.4	0.1	0.2	0.2	0.1
	2		71.1	13.1	2.6	1.3	2.9	6.0	2.3	0.4	0.1	0.2	0.2	0.1
	3		71.2	13.1	2.5	1.3	2.8	6.0	2.3	0.4	0.1	0.2	0.2	0.0
145* (C ₁₋₂ , H ₁₋₂)	1		82.5	7.7	3.0	4.2	2.7							
	2		82.3	7.7	3.0	4.2	2.8							
	3		82.4	7.7	2.9	4.1	2.8							
173 (C ₅₋₆ , H ₅₋₆)	1		85.8	8.0	1.1	0.4	4.2	0.5						
	2		85.8	7.9	1.2	0.5	4.2	0.5						
	3		85.8	8.0	1.1	0.4	4.2	0.5						
259 (C ₄₋₆ , H ₄₋₆)	1		80.1	12.5	2.1	0.4	0.3	3.7	1.0					
	2		80.0	12.5	2.1	0.4	0.3	3.7	1.0					
	3		80.1	12.3	2.1	0.4	0.3	3.7	1.0					
284 (C ₁₋₄ , H ₂₋₄)	1		72.5	16.6	3.7	2.7	3.1	1.4						
	2		72.7	16.6	3.7	2.6	3.0	1.4						
	3		72.6	16.6	3.7	2.7	3.0	1.4						
370 (C ₁₋₅ , H ₂₋₅)	1		69.4	15.2	6.4	3.6	3.2	1.6	0.5	0.1	0.0	0.0		
	2		69.6	15.1	6.5	3.6	3.2	1.5	0.4	0.1	0.0	0.0		
	3		69.6	15.1	6.5	3.6	3.2	1.5	0.4	0.1	0.0	0.0		

Data shown are the integrated mass isotopomer distributions not corrected for natural isotope enrichments. Measurements errors were <0.3 mol%. Data from the triplicate wells were not statistically different.

* M+0 to M+2 mass isotopomer abundances of ion fragment at m/z 145 may be inaccurate due to overlapping mass spectra.

Table 8-5

Mass isotopomer distributions of glucose from [U-¹³C,²H₈]glycerol labeling experiments with isolated hepatocytes from fed mice. Hepatocytes were cultured in 6-wells plates in medium containing [U-¹³C,²H₈]glycerol at 25% enrichment for 30 min. Glucose labeling was analyzed by GC/MS. Shown are mass isotopomer distributions of six selected glucose fragments (molar percentages, mol%).

m/z (positions)	Well		M+0	M+1	M+2	M+3	M+4	M+5	M+6	M+7	M+8	M+9	M+10	M+11
	#													
301 (C ₁₋₆ , H ₁₋₆)	1		77.3	13.1	2.4	0.9	1.6	3.4	1.1	0.1	0.0	0.0	0.0	0.0
	2		77.3	13.1	2.4	0.9	1.6	3.4	1.1	0.2	0.0	0.1	0.0	0.0
	3		77.3	13.1	2.4	0.9	1.6	3.3	1.1	0.2	0.0	0.0	0.0	0.0
145* (C ₁₋₂ , H ₁₋₂)	1		87.2	7.4	2.1	2.0	1.3							
	2		87.2	7.4	2.1	2.0	1.3							
	3		87.2	7.4	2.1	2.0	1.3							
173 (C ₅₋₆ , H ₅₋₆)	1		87.6	8.0	1.2	0.4	2.6	0.3						
	2		87.6	8.0	1.2	0.4	2.6	0.3						
	3		87.6	8.0	1.2	0.4	2.6	0.3						
259 (C ₄₋₆ , H ₄₋₆)	1		82.5	12.0	2.0	0.3	0.4	2.3	0.5					
	2		82.4	12.0	2.0	0.3	0.4	2.3	0.6					
	3		82.5	12.0	2.0	0.3	0.4	2.3	0.6					
284 (C ₁₋₄ , H ₂₋₄)	1		78.3	15.1	2.9	1.6	1.5	0.6						
	2		78.3	15.1	2.9	1.6	1.5	0.6						
	3		78.2	15.1	2.9	1.6	1.5	0.6						
370 (C ₁₋₅ , H ₂₋₅)	1		75.1	15.3	5.1	2.2	1.5	0.6	0.1	0.0	0.0	0.0		
	2		75.2	15.3	5.1	2.1	1.5	0.7	0.2	0.0	0.0	0.0		
	3		75.1	15.3	5.1	2.1	1.5	0.7	0.1	0.0	0.0	0.0		

Data shown are the integrated mass isotopomer distributions not corrected for natural isotope enrichments. Measurements errors were <0.3 mol%. Data from the triplicate wells were not statistically different.

* M+0 to M+2 mass isotopomer abundances of ion fragment at m/z 145 may be inaccurate due to overlapping mass spectra.

First, consider the mass isotopomer distribution of ion fragment at m/z 301 that contains all carbon and hydrogen atoms of the glucose molecule. In fasted and fed hepatocyte experiments we observed significant abundances of mass isotopomers up to $M+6$. These isotopomers were formed from the incorporation of a single [U-¹³C,²H₈]glycerol molecule into glucose. To minimize probability of condensation of two labeled triose phosphates, we used only 25% enrichment of the tracers in the medium that was further diluted from unlabeled endogenous sources, i.e. oxaloacetate→GAP. This reduced the chance of condensation of two labeled TPs to less than 1%. Of the 8 deuterium atoms in [U-¹³C,²H₈]glycerol only 5 atoms are stable, i.e. hydroxyl hydrogen atoms are rapidly exchanged with the solvent. Furthermore, the C2 hydrogen of glycerol is transferred to NADH in the reaction catalyzed by glycerol 3-phosphate dehydrogenase. Thus, DHAP derived from [U-¹³C,²H₈]glycerol is $M+7$ labeled. If we consider the fate of atoms of DHAP (that eventually becomes the top half of glucose), we find that the pro-S hydrogen at C1 of DHAP is lost to the solvent in the aldolase reaction (see Figure 8-1), and in the PGI reaction the pro-R hydrogen at C1 of F6P may be exchanged with the solvent resulting in $M+5$ glucose, or transferred to C2 of G6P via intramolecular transfer resulting in $M+5$ glucose. $M+4$ and $M+3$ isotopomers of glucose may be formed via additional loss of deuterium atoms in the TPI reaction (loss of C3 hydrogen of glucose), and in the PMI/G6PDH reactions (loss of C1 hydrogen of glucose). In conclusion, the top half of the glucose molecule may be labeled as $M+3$ to $M+6$ from [U-¹³C,²H₈]glycerol depending on the relative fluxes in the pathway from glycerol to glucose. When we trace the path from glycerol to the bottom half of glucose, i.e. glycerol→GAP→glucose, we find that the bottom half of glucose may be labeled as $M+5$, $M+6$, or $M+7$ depending on relative fluxes of TPI, GAPDH, and aldolase reactions. Taken together, the significant abundances of $M+5$ and $M+6$ isotopomers compared to the $M+3$ isotopomer indicated that one or more reactions in the gluconeogenesis pathway was not fully equilibrated. Consider also the m/z 145 fragment of glucose that contains the first two carbon and two hydrogen atoms of glucose. We observed significant $M+3$ and $M+4$ abundances for this fragment from both fasted and fed hepatocytes. The $M+4$ isotopomer is formed only if all four atoms are derived from [U-¹³C,²H₈]glycerol, whereas $M+3$ reflects the fraction of glucose molecules where one of the two deuterium atoms has been lost, i.e. either via PGI (loss of C2 hydrogen), or via

PMI/G6PDH (loss of C1 hydrogen). Thus, the significant abundance of M+4 vs. M+3 provided further evidence that the PGI reaction was not fully equilibrated.

8.3.2 Labeling incorporation into glucose from [U-¹³C,²H₈]glycerol and ²H₂O

Preliminary simulation experiments of the pathway suggested that a combination of [U-¹³C,²H₈]glycerol and ²H₂O tracers would provide much more detailed flux information than could be obtained from either of these tracers alone. The two tracers provide complementary information. With the ²H₂O tracer flux information is obtained from the incorporation of ²H into glucose, whereas with the [U-¹³C,²H₈]glycerol tracer flux information is obtained from the incorporation of ²H relative to ¹³C incorporation into glucose. The ¹³C-carbon backbone of [U-¹³C,²H₈]glycerol is critical for this method, because it provides a measure of the total amount of [U-¹³C,²H₈]glycerol incorporated into glucose, i.e. ¹³C-labeling is not lost in the pathway from glycerol to glucose as opposed to ²H-labeling. Thus, [²H₈]glycerol would provide much less flux information than [U-¹³C,²H₈]glycerol, because the loss of all deuterium atoms from [²H₈]glycerol yields M+0 glucose, which cannot be distinguished from endogenous glucose and glucose derived from glycogenolysis. Preliminary simulation experiments further indicated that we would be able to estimate fluxes in this system independent of the amount of [U-¹³C,²H₈]glycerol that is incorporated into glucose and independent of the isotopic steady state assumption, i.e. fluxes are strictly derived from ratios of labeled mass isotopomers of glucose. Thus, endogenous M+0 glucose will not affect the estimation of fluxes. As such, this method for estimating is fundamentally different from other methods to estimate gluconeogenesis fluxes, e.g. like MIDA, where fluxes are estimated by measuring absolute incorporation of ¹³C-tracers into glucose and assuming isotopic steady state.

Here, isolated hepatocytes were incubated in medium containing the two tracers, i.e. [U-¹³C,²H₈]glycerol at 25% enrichment and ²H₂O at 10% enrichment. Tables 8-6 and 8-7 show the measured mass isotopomer distributions of glucose fragments from triplicate experiments with fasted and fed hepatocytes, respectively. Measured mass isotopomer abundances from triplicate experiments were not statistically different, i.e. the maximum

Table 8-6

Mass isotopomer distributions of glucose from [U-¹³C,²H₈]glycerol + ²H₂O labeling experiments with isolated hepatocytes from fasted mice. Hepatocytes were cultured in 6-well plates in medium containing [U-¹³C,²H₈]glycerol at 25% enrichment and ²H₂O at 10% enrichment for 30 min. Glucose labeling was analyzed by GC/MS. Shown are mass isotopomer distributions of six selected glucose fragments (molar percentages, mol%).

m/z (positions)	Well												
	#	M+0	M+1	M+2	M+3	M+4	M+5	M+6	M+7	M+8	M+9	M+10	M+11
301 (C ₁₋₆ , H ₁₋₆)	1	42.6	30.1	10.8	3.2	2.6	5.1	3.6	1.2	0.3	0.2	0.2	0.1
	2	42.4	30.2	10.9	3.2	2.6	5.1	3.6	1.3	0.3	0.2	0.2	0.1
	3	42.5	30.1	10.8	3.2	2.6	5.1	3.6	1.2	0.3	0.2	0.2	0.1
145* (C ₁₋₂ , H ₁₋₂)	1	69.7	18.2	4.2	4.5	3.4							
	2	69.6	18.4	4.2	4.4	3.5							
	3	69.9	18.2	4.2	4.4	3.3							
173 (C ₅₋₆ , H ₅₋₆)	1	68.7	22.1	3.6	0.8	3.9	0.9						
	2	68.7	22.2	3.6	0.8	3.9	0.9						
	3	68.7	22.2	3.6	0.8	3.9	0.9						
259 (C ₄₋₆ , H ₄₋₆)	1	60.5	27.0	6.3	1.2	0.4	3.2	1.5					
	2	60.4	27.1	6.3	1.2	0.4	3.2	1.5					
	3	60.5	27.0	6.3	1.2	0.4	3.2	1.5					
284 (C ₁₋₄ , H ₂₋₄)	1	58.5	26.5	7.0	3.0	3.2	1.8						
	2	58.4	26.6	7.1	3.0	3.1	1.8						
	3	58.4	26.5	7.0	3.1	3.2	1.8						
370 (C ₁₋₅ , H ₂₋₅)	1	50.4	27.8	10.4	4.8	3.6	2.1	0.7	0.2	0.0	0.0		
	2	50.4	27.7	10.4	4.8	3.6	2.2	0.7	0.2	0.0	0.0		
	3	50.3	27.7	10.4	4.9	3.7	2.1	0.8	0.2	0.0	0.0		

Data shown are the integrated mass isotopomer distributions not corrected for natural isotope enrichments. Measurements errors were <0.3 mol%. Data from the triplicate wells were not statistically different.

* M+0 to M+2 mass isotopomer abundances of ion fragment at m/z 145 may be inaccurate due to overlapping mass spectra.

Table 8-7

Mass isotopomer distributions of glucose from [U-¹³C,²H₈]glycerol + ²H₂O labeling experiments with isolated hepatocytes from fed mice. Hepatocytes were cultured in 6-well plates in medium containing [U-¹³C,²H₈]glycerol at 25% enrichment and ²H₂O at 10% enrichment for 30 min. Glucose labeling was analyzed by GC/MS. Shown are mass isotopomer distributions of six selected glucose fragments (molar percentages, mol%).

m/z (positions)	Well		M+0	M+1	M+2	M+3	M+4	M+5	M+6	M+7	M+8	M+9	M+10	M+11
	#													
301 (C ₁₋₆ , H ₁₋₆)	1		61.8	22.7	6.5	1.8	1.5	2.9	1.9	0.6	0.1	0.1	0.1	0.0
	2		62.1	22.7	6.4	1.7	1.5	2.9	1.8	0.6	0.1	0.1	0.1	0.0
	3		62.0	22.8	6.6	1.8	1.5	2.9	1.9	0.5	0.0	0.0	0.0	0.0
145* (C ₁₋₂ , H ₁₋₂)	1		79.4	14.1	2.8	2.1	1.6							
	2		79.3	14.1	2.8	2.1	1.6							
	3		79.1	14.3	2.8	2.2	1.6							
173 (C ₅₋₆ , H ₅₋₆)	1		80.1	14.2	2.2	0.5	2.4	0.6						
	2		80.1	14.3	2.2	0.5	2.4	0.5						
	3		80.1	14.2	2.2	0.5	2.5	0.5						
259 (C ₄₋₆ , H ₄₋₆)	1		73.6	18.6	3.9	0.7	0.4	2.0	0.9					
	2		73.6	18.6	3.9	0.7	0.4	2.0	0.9					
	3		73.5	18.7	3.9	0.7	0.4	2.0	0.9					
284 (C ₁₋₄ , H ₂₋₄)	1		69.9	21.0	4.8	1.8	1.6	0.8						
	2		70.1	20.9	4.8	1.8	1.5	0.8						
	3		69.8	21.1	4.8	1.8	1.6	0.8						
370 (C ₁₋₅ , H ₂₋₅)	1		64.5	22.6	7.2	2.9	1.7	0.9	0.3	0.0	0.0	0.0		
	2		64.5	22.5	7.2	2.9	1.8	0.9	0.3	0.0	0.0	0.0		
	3		64.3	22.5	7.2	2.8	1.8	0.9	0.3	0.0	0.0	0.0		

Data shown are the integrated mass isotopomer distributions not corrected for natural isotope enrichments. Measurements errors were <0.3 mol%. Data from the triplicate wells were not statistically different.

* M+0 to M+2 mass isotopomer abundances of ion fragment at m/z 145 may be inaccurate due to overlapping mass spectra.

observed deviation was 0.3 mol%. Glucose produced in these experiments was significantly more labeled than in experiments with [U-¹³C,²H₈]glycerol alone, which reflected additional incorporation of ²H from ²H₂O into glucose. For example, we found significant M+7 mass isotopomers (up to 1.2 mol%) for the ion fragment at m/z 301 that contains all carbon and hydrogen atoms of glucose, compared to 0.4 mol% for the experiment with [U-¹³C,²H₈]glycerol alone. Quantitative analysis of the over-determined mass isotopomer data from these experiments is performed in the next section.

8.3.3 Flux estimation and model validation

To better characterize metabolic fluxes in this system we performed comprehensive analysis of the observed mass isotopomer distributions using the network model shown in Figure 8-1 and Metran software. Fluxes and their confidence intervals were estimated for all six experimental data sets, i.e. fasted and fed hepatocytes incubated with either ²H₂O, [U-¹³C,²H₈]glycerol, or ²H₂O+[U-¹³C,²H₈]glycerol as tracers. Table 8-8 compares the information content of the data sets. For example, the ²H₂O experiment with fasted hepatocytes provided 22 mass isotopomers of glucose from which 4 independent fluxes were estimated. Thus, there were 18 (=22-4) redundant measurements in this data. We found excellent agreement between the observed and predicted mass isotopomer abundances for the optimally fitted fluxes, as judged by the small magnitude of the sum of squared residuals, i.e. 2.1, which was smaller than the critical value of 31.5 for the statistical test of model adequacy (at 95% confidence level with 18 degrees of freedom) indicating that the fit was statistically acceptable. Fits for all six data sets were statistically acceptable. Note that 39 mass isotopomers from the [U-¹³C,²H₈]glycerol experiment allowed estimation of 6 fluxes, whereas the 39 mass isotopomers from the ²H₂O+[U-¹³C,²H₈]glycerol experiment provided 9 or 10 fluxes. Clearly, the combined use of ²H₂O and [U-¹³C,²H₈]glycerol provided the most informative data set, as was expected based on preliminary simulations.

8.3.4 Evaluation of fluxes in the gluconeogenesis pathway

Table 8-9 shows the estimated fluxes and standard deviations of fluxes for each of the six data set. Fluxes obtained from the different isotopic tracers were in good agreements.

Table 8-8

Comparison of information content of isotopomer data. Mass isotopomer distributions from six labeling experiments were fitted to a detailed model of glucose metabolism. Fluxes and confidence intervals were determined by nonlinear least-squares regression. The fits were statistically evaluated for the goodness-of-fit.

	Mouse	Isotopic tracers		
		² H ₂ O	[U- ¹³ C, ² H ₅]glycerol	[U- ¹³ C, ² H ₅]glycerol and ² H ₂ O
No. of fitted mass isotopomers	Fasted	22	39	39
	Fed	22	37	38
No. of estimated fluxes*	Fasted	4	6	10
	Fed	2	6	9
No. of redundant measurements**	Fasted	18	33	29
	Fed	20	31	29
Sum of weighted squared residuals	Fasted	2.1	24.3	21.1
	Fed	2.2	17.3	13.0
Fit statistically acceptable	Fasted	Yes	Yes	Yes
	Fed	Yes	Yes	Yes

* Number of estimated fluxes equals the number of independent fluxes that were statistically different from zero, as judged by 95% confidence interval.

** Number of redundant measurements = (no. of fitted isotopomers) – (no. of estimated flux)

For example, the GNG flux was estimated at 100 ± 5 and 50 ± 5 for fasted and fed hepatocytes, respectively, based on ²H₂O data, which was in good agreement with the values of 95 ± 2 and 42 ± 2 , respectively, estimated from the ²H₂O+[U-¹³C,²H₈]glycerol data. Note that [U-¹³C,²H₈]glycerol data alone did not allow precise estimation of the GNG flux, i.e. the 68% confidence interval was 65-100 and 26-100, respectively. Thus, only a lower bound could be determined. This limitation of [U-¹³C,²H₈]glycerol tracer was anticipated based on simulation experiments, which was one of the reasons to use the combination of [U-¹³C,²H₈]glycerol and ²H₂O. Note that the fractional contribution of glycerol and oxaloacetate to glucose was more precisely determined from the ²H₂O+[U-¹³C,²H₈]glycerol data than could be determined from either of the two tracers alone. It is clear from the results shown in Table 8-9 that [U-¹³C,²H₈]glycerol primarily provides information regarding the reversibility of reactions in the gluconeogenesis pathway. Reaction reversibilities were accurately determined from both [U-¹³C,²H₈]glycerol and ²H₂O+[U-¹³C,²H₈]glycerol experiments, but not from ²H₂O data alone. Fractional equilibration for the following four reactions was estimated precisely: $63\% \pm 5$ equilibration for PGI, $72\% \pm 4$ equilibration for TPI, $8\% \pm 3$ equilibration for transketolase, and $18\% \pm 6$ equilibration for the combined activity of PMI and G6PDH reactions. It was interesting that the estimated reaction reversibilities were identical for fasted and fed hepatocytes, suggesting that these fluxes may have a physiological role. To our best knowledge, this is the first methods that allows the estimation of reaction reversibilities in the gluconeogenesis pathway in vivo, which opens up many opportunities for future research. For example, it would be interesting to compare reaction reversibility of healthy hepatocytes with insulin-resistant hepatocytes, or with hepatocytes responding to hormones.

8.3.5 Estimation of fluxes using extended model

In the previous analysis we assumed that all glucose was newly produced and that the enrichment of the tracers was constant and known. These assumptions were clearly satisfied in our well-controlled experiments, however, if we apply these tracers to larger systems, e.g. perfused livers, or whole animal models then these assumptions may not be valid.

Table 8-9

Metabolic fluxes estimated from labeling experiments. Metabolic fluxes and their confidence intervals were estimated by fitting glucose mass isotopomer distributions to a detailed model of gluconeogenesis. Values shown are estimated flux \pm SD, or the 68% confidence interval.

<i>Net fluxes</i>	Mouse	Isotopic tracers		
		² H ₂ O	[U- ¹³ C, ² H ₈]glycerol	[U- ¹³ C, ² H ₈]glycerol and ² H ₂ O
Glucose production (fixed at 100)	Both	[100]	[100]	[100]
Gluconeogenesis (GNG)*	Fasted	100 \pm 5	65 – 100	95 \pm 2
	Fed	50 \pm 5	26 – 100	42 \pm 2
Glycogenolysis (GL)*	Fasted	0 \pm 5	0 – 35	5 \pm 2
	Fed	50 \pm 5	0 – 74	58 \pm 2
Glycerol to glucose flux	Fasted	57 \pm 25	52 \pm 4	52 \pm 1
	Fed	33 \pm 20	29 \pm 1	29 \pm 1
Oxaloacetate to glucose flux	Fasted	137 \pm 24	76 – 150	137 \pm 4
	Fed	67 \pm 22	24 – 173	55 \pm 2
<i>Exchange fluxes and percent equilibration (%)**</i>				
Phosphoglucose isomerase (PGI)	Fasted	0 – 1000 (0 – 91%)	173 \pm 35 (63% \pm 4)	180 \pm 35 (64% \pm 4)
	Fed	0 – 125 (0 – 56%)	164 \pm 54 (62% \pm 6)	145 \pm 35 (59% \pm 5)
Aldolase	Fasted	nd	nd	nd
	Fed	nd	nd	nd
Triose phosphate isomerase (TPI)	Fasted	0 – 400 (0 – 80%)	295 \pm 60 (74% \pm 4)	280 \pm 45 (73% \pm 3)
	Fed	nd	260 \pm 150 (72% \pm 8)	240 \pm 130 (71% \pm 8)
Phosphomannose isomerase (PMI) + Glucose 6-phosphate dehydr. (G6PDH)	Fasted	0 – 520 (0 – 83%)	20 \pm 8 (16% \pm 6)	9 \pm 7 (8% \pm 6)
	Fed	nd	24 \pm 12 (19% \pm 7)	25 \pm 12 (20% \pm 7)
Transketolase (TK)	Fasted	nd	10 \pm 2 (9% \pm 2)	8 \pm 4 (7% \pm 3)
	Fed	nd	10 \pm 4 (9% \pm 3)	8 \pm 5 (7% \pm 4)
Phosphoglucomutase (PGM)	Fasted	nd	nd	nd
	Fed	nd	nd	nd
Glycerol 3-phosphate dehydr.	Fasted	nd	nd	nd
	Fed	nd	nd	nd
Glyceraldehyde 3-phosphate dehydr. (GAPDH)	Fasted	nd	> 320 (>76%)	> 260 (>75%)
	Fed	nd	> 65 (>39%)	> 14 (>12%)
Cycling between GAP and PEP	Fasted	nd	nd	nd
	Fed	nd	nd	nd

* GNG and GL are not independent fluxes, i.e. $GNG = (v_{\text{glycerol}} + v_{\text{oxaloacetate}})/2$; $GL = 100 - GNG$.

** 'nd' (=not determined) indicates that the flux could not be determined, i.e. the confidence interval was 0 – infinity (i.e. 0 – 100% equilibration).

** Percent equilibration = $100\% \times (\text{exchange flux}) / (100 + \text{exchange flux})$.

Therefore, we tested the sensitivity of estimated fluxes with respect to these assumptions. For that purpose we created an extended mathematical model that included three additional parameters that were estimated: (i) fraction of newly produced glucose from tracers, as opposed to endogenous unlabeled glucose; (ii) fractional enrichment of ²H₂O, i.e. in our experiments 10%; and (iii) fractional enrichment of [U-¹³C,²H₈]glycerol tracer, i.e. in our experiments 25%. Fluxes and confidence intervals were estimated for the extended model using Metran. Table 8-10 compares the flux results obtained using the basic model from the previous section with the flux results obtained using the extended model. For example, our results indicate that with the extended model it is not possible to estimate the GNG flux from ²H₂O data. The best estimate for the GNG flux was 100±6 for fasted hepatocytes and 44–100 for fed hepatocytes, thus only a lower bound could be determined in the latter experiment. The fraction of newly synthesized glucose was accurately estimated at 100%±5 for fasted hepatocytes, but was less precisely estimated for fed hepatocytes, i.e. 100%±26. The enrichment of ²H₂O was slightly overestimated at 11%±0.4 and 10.9%±0.4 for fasted and fed hepatocyte experiments, respectively, compared to 10% true enrichment. For the [U-¹³C,²H₈]glycerol experiments the quality of flux results was not significantly affected using the extended model, as we indeed expected based on preliminary simulation experiments. For example, fractional equilibration of fluxes were determined with similar precision as with the basic model. The additional model parameters could not be determined precisely, i.e. the fraction of newly synthesized glucose was estimated at 100%±36 and 100%±22 for fasted and fed hepatocyte experiments, respectively, and the enrichment of [U-¹³C,²H₈]glycerol was estimated at 16–100% and 8–100%, respectively (25% true enrichment). These results were encouraging, because they illustrated that fluxes could be estimated from [U-¹³C,²H₈]glycerol data independent of the amount of glycerol incorporated and independent of the presence of unlabeled endogenous glucose. The same was true for the ²H₂O+[U-¹³C,²H₈]glycerol experiments. Here, both the net and exchange fluxes were estimated precisely with the extended model. For example, with the extended model the GNG flux was estimated at 93±4 and 43±5 for fasted and fed hepatocytes, respectively, which corresponded well with 95±2 and 42±2, respectively, as estimated using the basic model. The slight decrease in precision was due to the reduced number of redundant measurement for the estimation of

Table 8-10

Metabolic fluxes estimated using the basic and extended network models. The extended model included three additional parameters that had to be estimated: fraction of newly produced glucose, fractional enrichment of water, and fractional enrichment of glycerol tracer. Values shown are estimated flux \pm SD, or the 68% confidence interval.

	Mouse	Isotopic tracers					
		² H ₂ O		[U- ¹³ C, ² H ₅]glycerol		[U- ¹³ C, ² H ₅]glycerol and ² H ₂ O	
		Basic Model	Extended Model	Basic Model	Extended Model	Basic Model	Extended Model
<i>Net fluxes</i>							
Glucose production (fixed at 100)	Both	[100]	[100]	[100]	[100]	[100]	[100]
Gluconeogenesis (GNG)	Fasted	100 \pm 5	100 \pm 6	65 – 100	53 – 100	95 \pm 2	93 \pm 4
	Fed	50 \pm 5	44 – 100	26 – 100	25 – 100	42 \pm 2	43 \pm 5
Glycogenolysis (GL)	Fasted	0 \pm 5	0 \pm 6	0 – 35	0 – 47	5 \pm 2	7 \pm 4
	Fed	50 \pm 5	0 – 56	0 – 74	0 – 75	58 \pm 2	57 \pm 5
Glycerol to glucose flux	Fasted	57 \pm 25	66 \pm 30	52 \pm 4	13 – 92	52 \pm 1	36 \pm 12
	Fed	33 \pm 20	51 \pm 45	29 \pm 1	7 – 175	29 \pm 1	31 \pm 12
Oxaloacetate to glucose flux	Fasted	137 \pm 24	132 \pm 30	76 – 150	76 – 187	137 \pm 4	157 \pm 15
	Fed	67 \pm 22	98 \pm 40	24 – 173	14 – 193	55 \pm 2	73 \pm 15
<i>Percent equilibration (%)*</i>							
Phosphoglucose isomerase (PGI)	Fasted	0 – 91%	0 – 91%	63% \pm 4	62% \pm 5	64% \pm 4	62% \pm 4
	Fed	0 – 56%	nd	62% \pm 6	63% \pm 7	59% \pm 5	62% \pm 6
Triose phosphate isomerase (TPI)	Fasted	0 – 80%	0 – 81%	74% \pm 4	75% \pm 3	73% \pm 3	75% \pm 3
	Fed	nd	23 – 100%	72% \pm 8	80% \pm 6	71% \pm 8	74% \pm 8
Phosphomannose isomerase (PMI) + Glucose 6-phosphate dehydr. (G6PDH)	Fasted	0 – 83%	0 – 83%	16% \pm 6	16% \pm 5	8% \pm 6	5% \pm 4
	Fed	nd	nd	19% \pm 7	20% \pm 8	20% \pm 7	17% \pm 8
Transketolase (TK)	Fasted	nd	nd	9% \pm 2	9% \pm 3	7% \pm 3	8% \pm 4
	Fed	nd	nd	9% \pm 3	9% \pm 4	7% \pm 4	8% \pm 5
Glyceraldehyde 3-phosphate dehydr. (GAPDH)	Fasted	nd	nd	> 76%	> 74%	> 72%	> 67%
	Fed	nd	nd	> 39%	> 53%	> 12%	> 80%
<i>Additional model parameters</i>							
Fraction newly produced glucose	Fasted	[100%]	100% \pm 5	[100%]	100% \pm 36	[100%]	87% \pm 12
	Fed	[100%]	100% \pm 26	[100%]	100% \pm 22	[100%]	96% \pm 12
Water enrichment	Fasted	[10%]	11.0% \pm 0.5	[0%]	[0%]	[10%]	9.9% \pm 0.4
	Fed	[10%]	10.9% \pm 0.5	[0%]	[0%]	[10%]	9.0% \pm 0.4
Glycerol enrichment	Fasted	[0%]	[0%]	[25%]	16 – 100%	[25%]	22 – 100%
	Fed	[0%]	[0%]	[25%]	8 – 100%	[25%]	13 – 100%

* 'nd' (=not determined) indicates that the 68% confidence interval was 0 – 100%.

* Percent equilibration = 100% \times (exchange flux) / (100 + exchange flux).

the gluconeogenesis flux, i.e. three additional parameters were estimated in the extended model from the same number of mass isotopomers.

8.4 Discussion

Previously we have shown that net and exchange fluxes in the gluconeogenesis pathway may be estimated through the combined analysis of ²H₂O, [U-¹³C]glycerol, and [²H₅]glycerol experimental data (Chapter 7). Here, we provide a novel two-tracer strategy that allows accurate estimation of the same fluxes from a single experiment. Quantitative analysis of mass isotopomer distributions of glucose resulting from the incorporation of [U-¹³C,²H₈]glycerol into glucose required the use of the elementary metabolite units framework for modeling isotopic distributions. The EMU method reduced the computational problem of isotopic simulations from 42,224 variables, which could not be solved computationally, to only 204 EMU variables that were easily computed. Using the Metran software fluxes and confidence intervals were determined and the fits were statistically evaluated. The methods developed in this study and the insight obtained from these experiments have wide implications for in vivo studies of glucose metabolism in vivo. We have clearly shown that PGI and TPI reactions are not fully equilibrated in isolated hepatocytes. In hepatocytes isolated from fasted and fed mice we found that PGI was only 63%±5 equilibrated and TPI was only 72%±4 equilibrated. This resulted in incomplete equilibration of hydrogen at C2 of glucose and the solvent in ²H₂O experiments, and thus overestimation of fractional GNG from the ratio of deuterium enrichment at C5 vs. C2 of glucose, i.e. 123% for fasted hepatocytes and 100% for fed hepatocytes, compared to the true values of 95% and 42%, respectively. Furthermore, we have illustrated that using [U-¹³C,²H₈]glycerol metabolic fluxes can be determined independent of the isotopic steady state assumption and independent of the amount of glycerol incorporated into glucose, i.e. independent of zonation of glycerol. Thus, this method can be applied to perfused livers and whole animal models without difficulty. And because this method does not require isotopic steady state, tracer experiments can be much shorter (i.e. less expensive) than current experiments that require 4-5 hr constant infusion of tracer to reach isotopic steady state of glucose labeling.

References

- Arauzo-Bravo, M. J. & Shimizu, K. 2003, "An improved method for statistical analysis of metabolic flux analysis using isotopomer mapping matrices with analytical expressions", *J Biotechnol*, vol. 105, no. 1-2, pp. 117-133.
- Beylot, M., Previs, S. F., David, F., & Brunengraber, H. 1993, "Determination of the ¹³C-labeling pattern of glucose by gas chromatography-mass spectrometry", *Anal. Biochem.*, vol. 212, no. 2, pp. 526-531.
- Biemann, K., de Jongh, D. C., & Schnoes, H. K. 1963, "Application of Mass Spectrometry to Structure Problems. XIII. Acetates of Pentoses and Hexoses", *Am J Chem Soc*, vol. 85, no. 12, pp. 1763-1770.
- Brunengraber, H., Kelleher, J. K., & Des, R. C. 1997, "Applications of mass isotopomer analysis to nutrition research", *Annu. Rev. Nutr.*, vol. 17, pp. 559-596.
- Byrd, R. H., Hribar, M. E., & Nocedal, J. 1999, "An interior point algorithm for large scale nonlinear programming", *SIAM J Optim*, vol. 9, no. 4, pp. 877-900.
- Christensen, B. & Nielsen, J. 2000, "Metabolic network analysis of *Penicillium chrysogenum* using (¹³C)-labeled glucose", *Biotechnol Bioeng*, vol. 68, no. 6, pp. 652-659.
- Ciucanu, I. & Costello, C. E. 2003, "Elimination of oxidative degradation during the per-O-methylation of carbohydrates", *J Am Chem Soc*, vol. 125, no. 52, pp. 16213-16219.
- Conover, W. J. 1999, *Practical Nonparametric Statistics*, 3 edn, Wiley, New York.

- Dauner, M. & Sauer, U. 2000, "GC-MS analysis of amino acids rapidly provides rich information for isotopomer balancing", *Biotechnol Prog.*, vol. 16, no. 4, pp. 642-649.
- Des, R. C., Lloyd, S., Comte, B., & Chatham, J. C. 2004, "A critical perspective of the use of (13)C-isotopomer analysis by GCMS and NMR as applied to cardiac metabolism", *Metab Eng*, vol. 6, no. 1, pp. 44-58.
- Desage, M., Guilluy, R., Brazier, J. L., Riou, J. P., Beylot, M., Normand, S., & Vidal, H. 1989, "Positional isotopic analysis of 13C-labelled glucose by mass spectrometry: applications to the study of gluconeogenesis in liver cells", *Biomed. Environ. Mass Spectrom.*, vol. 18, no. 11, pp. 1010-1015.
- Fagerquist, C. K., Hellerstein, M. K., Faubert, D., & Bertrand, M. J. 2001, "Elimination of the concentration dependence in mass isotopomer abundance mass spectrometry of methyl palmitate using metastable atom bombardment", *J Am. Soc. Mass Spectrom.*, vol. 12, no. 6, pp. 754-761.
- Fernandez, C. A. & Des, R. C. 1995, "Modeling of liver citric acid cycle and gluconeogenesis based on 13C mass isotopomer distribution analysis of intermediates", *J Biol. Chem*, vol. 270, no. 17, pp. 10037-10042.
- Foster, L. V. 1986, "Rank and null space calculations using matrix decomposition without column interchanges", *Linear Algebra Appl*, vol. 74, no. 2, pp. 47-71.
- Gill, P. E., Murray, W., & Wright, M. H. 1991, *Numerical linear algebra and optimization, Vol. 1* Addison Wesley, Redwood City, CA.
- Groop, L. C., Bonadonna, R. C., DelPrato, S., Ratheiser, K., Zyck, K., Ferrannini, E., & DeFronzo, R. A. 1989, "Glucose and free fatty acid metabolism in non-insulin-dependent diabetes mellitus. Evidence for multiple sites of insulin resistance", *J Clin. Invest*, vol. 84, no. 1, pp. 205-213.

Guo, Z. K., Lee, W. N., Katz, J., & Bergner, A. E. 1992, "Quantitation of positional isomers of deuterium-labeled glucose by gas chromatography/mass spectrometry", *Anal.Biochem.*, vol. 204, no. 2, pp. 273-282.

Hachey, D. L., Parsons, W. R., McKay, S., & Haymond, M. W. 1999, "Quantitation of monosaccharide isotopic enrichment in physiologic fluids by electron ionization or negative chemical ionization GC/MS using di-O-isopropylidene derivatives", *Anal.Chem.*, vol. 71, no. 20, pp. 4734-4739.

Hartmann, W. M. & Hartwig, R. E. 1996, "Computing the Moore-Penrose inverse for the covariance matrix in constrained nonlinear estimation", *SIAM J Optim*, vol. 6, no. 3, pp. 727-747.

Hellerstein, M. K. 2003, "In vivo measurement of fluxes through metabolic pathways: the missing link in functional genomics and pharmaceutical research", *Annu.Rev.Nutr.*, vol. 23, pp. 379-402.

Heyen, G., Marechal, E., & Kalitventzeff, B. 1996, "Sensitivity calculations and variance analysis in plant measurement reconciliation", *Comput Chem Eng*, vol. 20, p. S539-S544.

Jones, J. G., Solomon, M. A., Sherry, A. D., Jeffrey, F. M., & Malloy, C. R. 1998, "¹³C NMR measurements of human gluconeogenic fluxes after ingestion of [U-¹³C]propionate, phenylacetate, and acetaminophen", *Am J Physiol*, vol. 275, no. 5 Pt 1, p. E843-E852.

Kelleher, J. K. 1999, "Estimating gluconeogenesis with [U-¹³C]glucose: molecular condensation requires a molecular approach", *Am.J Physiol*, vol. 277, no. 3 Pt 1, p. E395-E400.

Kelleher, J. K. 2004, "Probing metabolic pathways with isotopic tracers: insights from mammalian metabolic physiology", *Metab Eng*, vol. 6, no. 1, pp. 1-5.

Khairallah, M., Labarthe, F., Bouchard, B., Danialou, G., Petrof, B. J., & Des, R. C. 2004, "Profiling substrate fluxes in the isolated working mouse heart using ¹³C-labeled substrates: focusing on the origin and fate of pyruvate and citrate carbons", *Am J Physiol Heart Circ.Physiol*, vol. 286, no. 4, p. H1461-H1470.

Klapa, M. I., Aon, J. C., & Stephanopoulos, G. 2003, "Ion-trap mass spectrometry used in combination with gas chromatography for high-resolution metabolic flux determination", *Biotechniques*, vol. 34, no. 4, pp. 832-6, 838, 840.

Klapa, M. I., Aon, J. C., & Stephanopoulos, G. 2003, "Systematic quantification of complex metabolic flux networks using stable isotopes and mass spectrometry", *Eur.J Biochem.*, vol. 270, no. 17, pp. 3525-3542.

Klapa, M. I., Aon, J. C., & Stephanopoulos, G. 2003, "Systematic quantification of complex metabolic flux networks using stable isotopes and mass spectrometry", *Eur.J.Biochem.*, vol. 270, no. 17, pp. 3525-3542.

Kurland, I. J., Alcivar, A., Bassilian, S., & Lee, W. N. 2000, "Loss of [¹³C]glycerol carbon via the pentose cycle. Implications for gluconeogenesis measurement by mass isotope distribution analysis", *J Biol.Chem*, vol. 275, no. 47, pp. 36787-36793.

Laine, R. A. & Sweeley, C. C. 1971, "Analysis of trimethylsilyl O-methyloximes of carbohydrates by combined gas-liquid chromatography-mass spectrometry", *Anal.Biochem.*, vol. 43, no. 2, pp. 533-538.

Landau, B. R., Wahren, J., Chandramouli, V., Schumann, W. C., Ekberg, K., & Kalhan, S. C. 1995, "Use of ²H₂O for estimating rates of gluconeogenesis. Application to the fasted state", *J Clin.Invest*, vol. 95, no. 1, pp. 172-178.

Landau, B. R., Wahren, J., Chandramouli, V., Schumann, W. C., Ekberg, K., & Kalhan, S. C. 1996, "Contributions of gluconeogenesis to glucose production in the fasted state", *J Clin.Invest*, vol. 98, no. 2, pp. 378-385.

- Landau, B. R., Wahren, J., Ekberg, K., Previs, S. F., Yang, D., & Brunengraber, H. 1998, "Limitations in estimating gluconeogenesis and Cori cycling from mass isotopomer distributions using [U-13C6]glucose", *Am.J Physiol*, vol. 274, no. 5 Pt 1, p. E954-E961.
- Malaisse, W. J., Malaisse-Lagae, F., Liemans, V., Ottinger, R., & Willem, R. 1990, "Phosphoglucoisomerase-catalyzed interconversion of hexose phosphates: isotopic discrimination between hydrogen and deuterium", *Mol.Cell Biochem.*, vol. 93, no. 2, pp. 153-165.
- Malaisse, W. J., Liemans, V., Malaisse-Lagae, F., Ottinger, R., & Willem, R. 1991, "Phosphoglucoisomerase-catalyzed interconversion of hexose phosphates. Study by 13C NMR of proton and deuterium exchange", *Mol.Cell Biochem.*, vol. 103, no. 2, pp. 131-140.
- Malloy, C. R., Sherry, A. D., & Jeffrey, F. M. 1988, "Evaluation of carbon flux and substrate selection through alternate pathways involving the citric acid cycle of the heart by 13C NMR spectroscopy", *J Biol.Chem*, vol. 263, no. 15, pp. 6964-6971.
- Mollney, M., Wiechert, W., Kownatzki, D., & de Graaf, A. A. 1999, "Bidirectional reaction steps in metabolic networks: IV. Optimal design of isotopomer labeling experiments", *Biotechnol.Bioeng.*, vol. 66, no. 2, pp. 86-103.
- Moss, G. P. 1996, "Basic terminology of stereochemistry", *Pure Appl Chem*, vol. 68, no. 12, pp. 2193-2222.
- Nakamura, C. E. & Whited, G. M. 2003, "Metabolic engineering for the microbial production of 1,3-propanediol", *Curr.Opin.Biotechnol*, vol. 14, no. 5, pp. 454-459.
- Neese, R. A., Schwarz, J. M., Faix, D., Turner, S., Letscher, A., Vu, D., & Hellerstein, M. K. 1995, "Gluconeogenesis and intrahepatic triose phosphate flux in response to fasting or substrate loads. Application of the mass isotopomer distribution analysis technique with testing of assumptions and potential problems", *J Biol.Chem*, vol. 270, no. 24, pp. 14452-14466.

Park, S. M., Klapa, M. I., Sinskey, A. J., & Stephanopoulos, G. 1999, "Metabolite and isotopomer balancing in the analysis of metabolic cycles: II. Applications", *Biotechnol Bioeng*, vol. 62, no. 4, pp. 392-401.

Patterson, B. W. & Wolfe, R. R. 1993, "Concentration dependence of methyl palmitate isotope ratios by electron impact ionization gas chromatography/mass spectrometry", *Biol.Mass Spectrom.*, vol. 22, no. 8, pp. 481-486.

Previs, S. F., Fernandez, C. A., Yang, D., Soloviev, M. V., David, F., & Brunengraber, H. 1995, "Limitations of the mass isotopomer distribution analysis of glucose to study gluconeogenesis. Substrate cycling between glycerol and triose phosphates in liver", *J Biol.Chem*, vol. 270, no. 34, pp. 19806-19815.

Previs, S. F., Hallowell, P. T., Neimanis, K. D., David, F., & Brunengraber, H. 1998, "Limitations of the mass isotopomer distribution analysis of glucose to study gluconeogenesis. Heterogeneity of glucose labeling in incubated hepatocytes", *J Biol.Chem*, vol. 273, no. 27, pp. 16853-16859.

Radziuk, J. & Lee, W. P. 1999, "Measurement of gluconeogenesis and mass isotopomer analysis based on [U-(13)C]glucose", *Am.J Physiol*, vol. 277, no. 2 Pt 1, p. E199-E207.

Sauer, U., Hatzimanikatis, V., Bailey, J. E., Hochuli, M., Szyperski, T., & Wuthrich, K. 1997, "Metabolic fluxes in riboflavin-producing *Bacillus subtilis*", *Nat.Biotechnol*, vol. 15, no. 5, pp. 448-452.

Schmidt, K., Carlsen, K. M., Nielsen, J., & Villadsen, J. 1997, "Modeling isotopomer distributions in biochemical networks using isotopomer mapping matrices", *Biotechnol Bioeng*, vol. 55, no. 6, pp. 831-840.

Schmidt, K., Marx, A., de Graaf, A. A., Wiechert, W., Sahm, H., Nielsen, J., & Villadsen, J. 1998, "13C tracer experiments and metabolite balancing for metabolic flux analysis: comparing two approaches", *Biotechnol.Bioeng.*, vol. 58, no. 2-3, pp. 254-257.

- Schmidt, K., Nielsen, J., & Villadsen, J. 1999, "Quantitative analysis of metabolic fluxes in *Escherichia coli*, using two-dimensional NMR spectroscopy and complete isotopomer models", *J Biotechnol*, vol. 71, no. 1-3, pp. 175-189.
- Seeholzer, S. H. 1993, "Phosphoglucose isomerase: a ketol isomerase with aldol C2-epimerase activity", *Proc.Natl.Acad.Sci.U.S.A*, vol. 90, no. 4, pp. 1237-1241.
- Seglen, P. O. 1976, "Preparation of isolated rat liver cells", *Methods Cell Biol*, vol. 13, pp. 29-83.
- Stephanopoulos, G. 1999, "Metabolic fluxes and metabolic engineering", *Metab Eng*, vol. 1, no. 1, pp. 1-11.
- Sunehag, A. L. 2003, "The role of parenteral lipids in supporting gluconeogenesis in very premature infants", *Pediatr.Res.*, vol. 54, no. 4, pp. 480-486.
- Szafranek, J., Pfaffenberger, C. D., & Horning, E. C. 1974, "The mass spectra of some per-O-acetylaldononitriles", *Carbohydr.Res.*, vol. 38, pp. 97-105.
- Szyperski, T. 1995, "Biosynthetically directed fractional ¹³C-labeling of proteinogenic amino acids. An efficient analytical tool to investigate intermediary metabolism", *Eur.J Biochem.*, vol. 232, no. 2, pp. 433-448.
- Szyperski, T. 1995, "Biosynthetically directed fractional ¹³C-labeling of proteinogenic amino acids. An efficient analytical tool to investigate intermediary metabolism", *Eur.J.Biochem.*, vol. 232, no. 2, pp. 433-448.
- Tayek, J. A. & Katz, J. 1996, "Glucose production, recycling, and gluconeogenesis in normals and diabetics: a mass isotopomer [U-¹³C]glucose study", *Am.J Physiol*, vol. 270, no. 4 Pt 1, p. E709-E717.
- van Winden, W. A., Heijnen, J. J., & Verheijen, P. J. 2002, "Cumulative bondomers: a new concept in flux analysis from 2D [¹³C,¹H] COSY NMR data", *Biotechnol Bioeng*, vol. 80, no. 7, pp. 731-745.

van Winden, W. A., van Dam, J. C., Ras, C., Kleijn, R. J., Vinke, J. L., van Gulik, W. M., & Heijnen, J. J. 2005, "Metabolic-flux analysis of *Saccharomyces cerevisiae* CEN.PK113-7D based on mass isotopomer measurements of (^{13}C) -labeled primary metabolites", *FEMS Yeast Res.*, vol. 5, no. 6-7, pp. 559-568.

Vind, C., Hunding, A., & Grunnet, N. 1987, "Pathways of reducing equivalents in hepatocytes from rats. Estimation of cytosolic fluxes by means of ^3H -labelled substrates for either A- or B-specific dehydrogenases", *Biochem.J.*, vol. 243, no. 3, pp. 625-630.

Wiechert, W. & deGraaf, A. A. 1997, "Bidirectional reaction steps in metabolic networks .1. Modeling and simulation of carbon isotope labeling experiments", *Biotechnology and Bioengineering*, vol. 55, no. 1, pp. 101-117.

Wiechert, W., Siefke, C., deGraaf, A. A., & Marx, A. 1997, "Bidirectional reaction steps in metabolic networks: II. Flux estimation and statistical analysis", *Biotechnology and Bioengineering*, vol. 55, no. 1, pp. 118-135.

Wiechert, W., Mollney, M., Isermann, N., Wurzel, M., & de Graaf, A. A. 1999, "Bidirectional reaction steps in metabolic networks: III. Explicit solution and analysis of isotopomer labeling systems", *Biotechnol.Bioeng.*, vol. 66, no. 2, pp. 69-85.

Wiechert, W., Mollney, M., Petersen, S., & de Graaf, A. A. 2001, "A universal framework for ^{13}C metabolic flux analysis", *Metab Eng.*, vol. 3, no. 3, pp. 265-283.

Wiechert, W. 2001, " ^{13}C metabolic flux analysis", *Metab Eng.*, vol. 3, no. 3, pp. 195-206.

Wykes, L. J., Jahoor, F., & Reeds, P. J. 1998, "Gluconeogenesis measured with $[U-^{13}\text{C}]$ glucose and mass isotopomer analysis of apoB-100 amino acids in pigs", *Am.J Physiol.*, vol. 274, no. 2 Pt 1, p. E365-E376.

Zupke, C. & Stephanopoulos, G. 1994, "Modeling of isotope distributions and intracellular fluxes in metabolic networks using atom mapping matrices", *Biotechnology Progress*, vol. 10, pp. 489-498.

Appendix A

GC/MS analysis of TBDMS derivatized amino acids

GC/MS analysis of unlabeled and [U-¹³C]-labeled (99 At%) amino acids was performed using HP 5890 Series II GC (Gas Chromatograph) connected to HP 5971 MSD (Mass Selective Detector). The mass spectrometer was calibrated using the 'Max Sensitivity Autotune' setting.

Column Specifications

- Agilent Technologies 122-0732 DB-1701 (Serial No. US4823442H)
- Length: 30 m
- ID: 0.25 mm
- Film: 0.25 μm
- Temperature limits: -20°C to 280°C

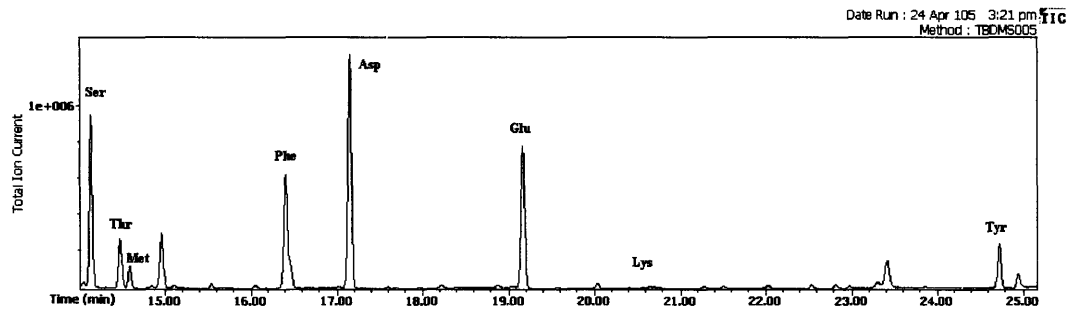
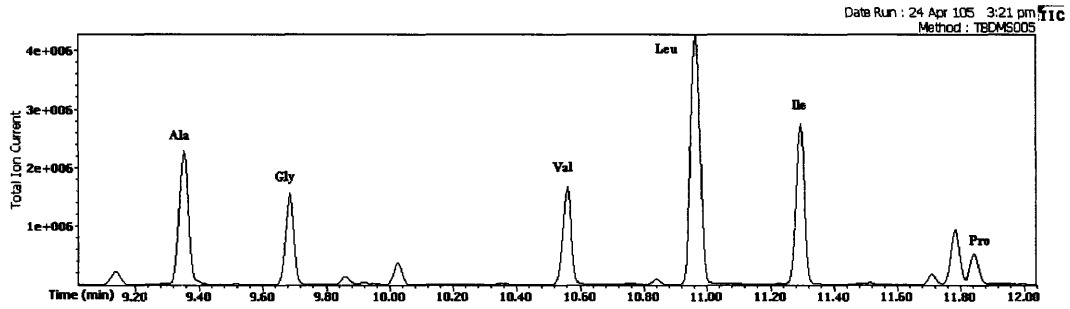
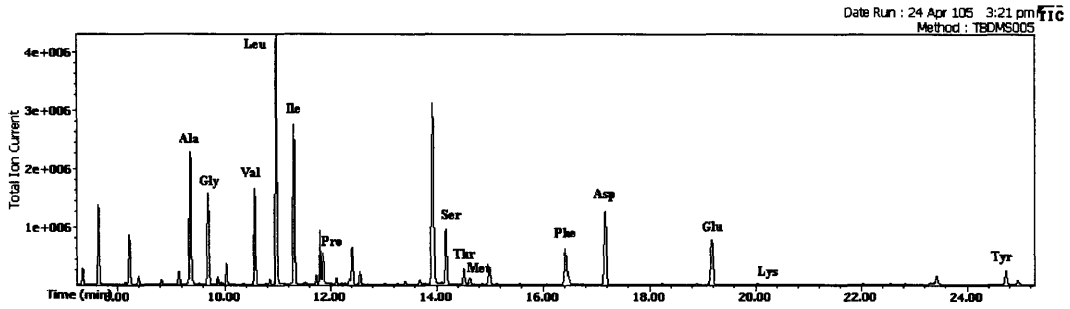
MSD Settings

- Scan mode
- 7 min solvent delay
- 23 min recording time
- Mass range: 195 to 445 amu (approx. 2.7 scans/sec)

GC Settings

- Constant flow 0.737 ml/min (= 6 psi at 80°C; 31.6 cm/sec)
- Injector temp: 270°C
- Transferline temp: 300°C
- Temperature program:
 - 100°C (hold 1.5 min)
 - 20°C/min to 130°C
 - 10°C/min to 220°C (hold 3 min)
 - 5°C/min to 280°C (hold 3 min)

Total Ion Chromatogram



**Recommended fragment ions and corresponding precursor metabolites
(for *E. coli* biosynthesis pathways)**

Amino acid	Mass Range	Carbon atoms	Fragmentation	Precursor metabolite(s)
Ala	232 – 238	2-3	M – C ₅ H ₉ O	Pyr ₍₂₋₃₎
	260 – 267	1-2-3	M – C ₄ H ₉	Pyr ₍₁₋₂₋₃₎
Gly	218 – 223	2	M – C ₅ H ₉ O	3PG ₍₂₎ and C-1 and OAC ₂
	246 – 252	1-2	M – C ₄ H ₉	3PG ₍₁₋₂₎ and 3PG ₍₃₎ + CO ₂ and other
Val	260 – 268	2-3-4-5	M – C ₅ H ₉ O	Pyr ₍₂₋₃₎ + Pyr ₍₂₋₃₎
	288 – 297	1-2-3-4-5	M – C ₄ H ₉	Pyr ₍₁₋₂₋₃₎ + Pyr ₍₂₋₃₎
Leu	274 – 283	2-3-4-5-6	M – C ₅ H ₉ O	AcCoA ₍₂₎ + Pyr ₍₂₋₃₎ + Pyr ₍₂₋₃₎
Ile	200 – 208	2-3-4-5-6	M – C ₇ H ₁₅ O ₂ Si	OAC ₍₂₋₃₋₄₎ + Pyr ₍₂₋₃₎
	274 – 283	2-3-4-5-6	M – C ₅ H ₉ O	OAC ₍₂₋₃₋₄₎ + Pyr ₍₂₋₃₎
Ser	288 – 294	2-3	M – C ₇ H ₁₅ O ₂ Si	3PG ₍₂₋₃₎ and Gly ₍₂₎ + C-1 and other
	302 – 308	1-2	M – C ₇ H ₁₇ OSi	3PG ₍₁₋₂₎ and Gly ₍₁₋₂₎
	362 – 369	2-3	M – C ₅ H ₉ O	3PG ₍₂₋₃₎ and Gly ₍₂₎ + C-1 and other
	390 – 398	1-2-3	M – C ₄ H ₉	3PG ₍₁₋₂₋₃₎ and Gly ₍₁₋₂₎ + C-1 and other
Thr	376 – 382	2-3-4	M – C ₅ H ₉ O	OAC ₍₂₋₃₋₄₎
	404 – 413	1-2-3-4	M – C ₄ H ₉	OAC ₍₁₋₂₋₃₋₄₎
Met	218 – 226	2-3-4-5	M – C ₇ H ₁₅ O ₂ Si	OAC ₍₂₋₃₋₄₎ + C-1
	292 – 298	2-3-4-5	M – C ₅ H ₉ O	OAC ₍₂₋₃₋₄₎ + C-1
	320 – 327	1-2-3-4-5	M – C ₄ H ₉	OAC ₍₁₋₂₋₃₋₄₎ + C-1
Phe	234 – 243	2-3-4-5-6-7-8-9	M – C ₇ H ₁₅ O ₂ Si	PEP ₍₂₋₃₎ + PEP ₍₂₋₃₎ + E4P ₍₁₋₂₋₃₋₄₎
	302 – 307	1-2	M – C ₇ H ₇	PEP ₍₁₋₂₎
	308 – 316	2-3-4-5-6-7-8-9	M – C ₅ H ₉ O	PEP ₍₂₋₃₎ + PEP ₍₂₋₃₎ + E4P ₍₁₋₂₋₃₋₄₎
	336 – 345	1-2-3-4-5-6-7-8-9	M – C ₄ H ₉	PEP ₍₁₋₂₋₃₎ + PEP ₍₂₋₃₎ + E4P ₍₁₋₂₋₃₋₄₎
Asp	302 – 308	1-2	M – C ₈ H ₁₇ O ₂ Si	OAC ₍₁₋₂₎
	376 – 382	1-2	M – C ₆ H ₁₁ O	OAC ₍₁₋₂₎
	390 – 398	2-3-4	M – C ₅ H ₉ O	OAC ₍₂₋₃₋₄₎
	418 – 427	1-2-3-4	M – C ₄ H ₉	OAC ₍₁₋₂₋₃₋₄₎
Glu	330 – 336	2-3-4-5	M – C ₇ H ₁₅ O ₂ Si	AKG ₍₂₋₃₋₄₋₅₎
	432 – 442	1-2-3-4-5	M – C ₄ H ₉	AKG ₍₁₋₂₋₃₋₄₋₅₎
Tyr	302 – 305	1-2	M – C ₁₃ H ₂₁ OSi	PEP ₍₁₋₂₎

3PG: 3-phosphoglycerate

PEP: phosphoenolpyruvate

Pyr: pyruvate

E4P: erythrose-4-phosphate

AKG: α -ketoglutarate

OAC: oxaloacetate

AcCoA: acetyl coenzyme-A

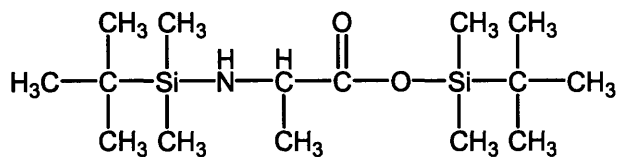
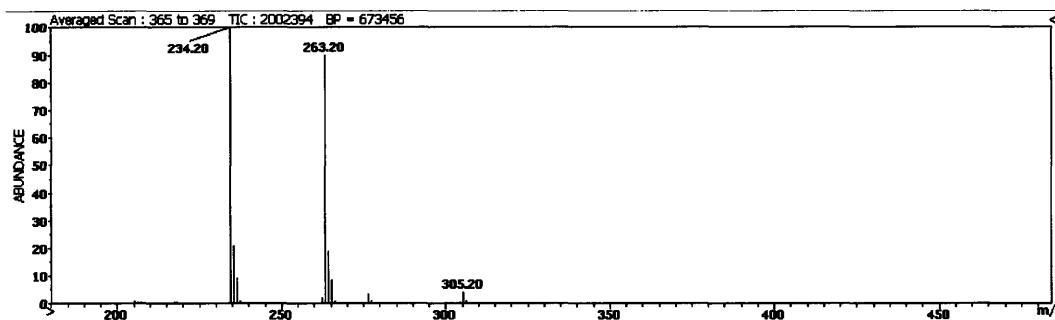
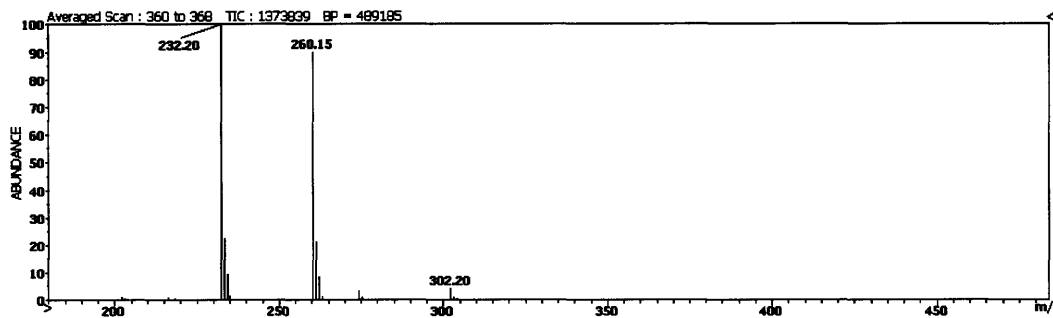
R5P: ribose-5-phosphate

C-1: One-carbon unit

Rejected fragment ions and reason for rejection

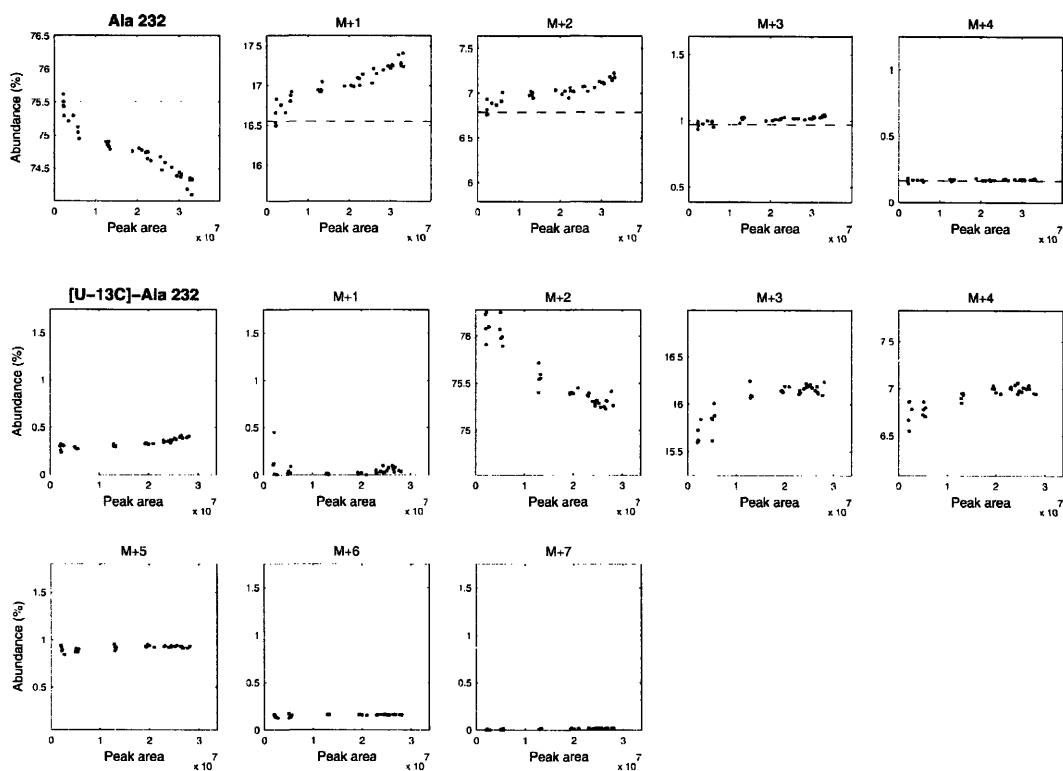
Amino acid	Mass Range	Carbon atoms	Reason for rejection	Alternative fragment
Val	302 – 308	1-2 and 1-2-3-4,5	Overlapping fragments	n/a
Leu	200 – 208	2-3-4-5-6	Inaccurate. M+2 too high (+0.9 mol%)	Leu-274
Leu	302 – 312	1-2 and 1-2-3-4-5-6	Overlapping fragments	n/a
Ile	302 – 312	1-2 and 1-2-3-4-5-6	Overlapping fragments	n/a
Pro	258 – 266	2-3-4-5	Co-eluting with other compounds	Glu-330
Pro	286 – 295	1-2-3-4-5	Co-eluting with other compounds	Glu-432
Ser	230 – 237	unknown	Unknown fragmentation	unknown
Thr	417 – 424	unknown	Inaccurate. M+0 too low (-4.0 mol%)	unknown
Met	244 – 250	unknown	Unknown fragmentation	unknown
Asp	244 – 249	unknown	Unknown fragmentation	unknown
Asp	258 – 266	unknown	Inaccurate. M-1 too high (4.4 % of M+0)	unknown
Asp	316 – 323	2-3-4	Inaccurate. M+3 too high (+0.7 mol%)	Asp-390
Glu	272 – 280	unknown	Unknown fragmentation	unknown
Glu	358 – 367	1-2-3-4-5	Inaccurate. M-1 too high (1.8 % of M+0)	Glu-432
Glu	404 – 408	2-3-4-5	Inaccurate. M+0 too low (-0.6 mol%)	Glu-330
Lys	329 – 336	2-3-4-5-6	Low signal-to-noise ratio	none
Lys	431 – 441	1-2-3-4-5-6	Inaccurate. M-1 too high (1.7 % of M+0)	none
Tyr	364 – 375	2-3-4-5-6-7-8	Low signal-to-noise ratio	Phe-308

Alanine (Ala)



C₁₅H₃₅NO₂Si₂
 Exact Mass: 317.2206

APPENDIX A. GC/MS ANALYSIS OF AMINO ACIDS



Ala 232

Formula : $C_{10}H_{26}ONSi_2$
 Exact mass : 232.155
 C-atoms : 2-3

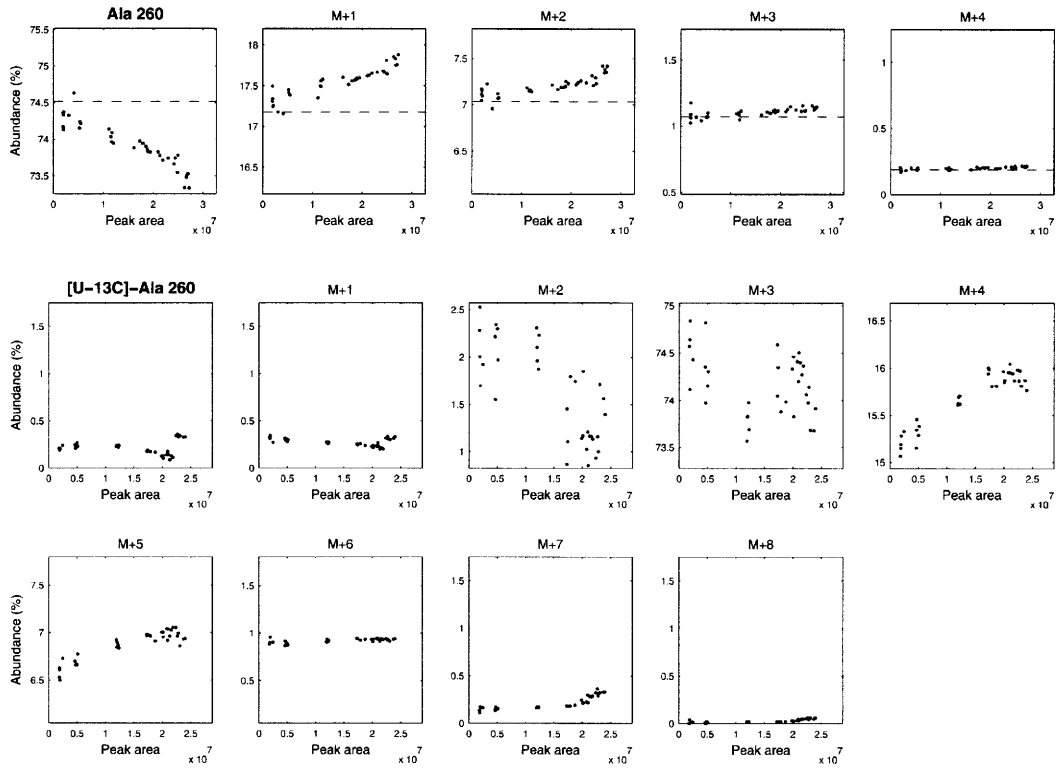
m/z	theory	data	difference
231	0.0	0.0	0.0
232	100.0	100.0	0.0
233	21.9	22.1	0.2
234	9.0	9.1	0.1
235	1.3	1.3	0.0
236	0.2	0.2	0.0
237	0.0	0.0	0.0
238	0.0	0.0	0.0
239	0.0	0.0	0.0

[U-¹³C]-Ala

m/z	theory	data	difference
231	0.0	0.1	0.1
232	0.0	0.3	0.3
233	2.0	0.1	-1.9
234	100.0	100.0	0.0
235	19.8	20.8	1.0
236	8.5	8.9	0.4
237	1.1	1.2	0.1
238	0.2	0.2	0.0
239	0.0	0.0	0.0

This fragment can be used for quantitative analysis.

APPENDIX A. GC/MS ANALYSIS OF AMINO ACIDS



Ala 260

Formula : $C_{11}H_{26}O_2NSi_2$
 Exact mass : 260.150
 C-atoms : 1-2-3

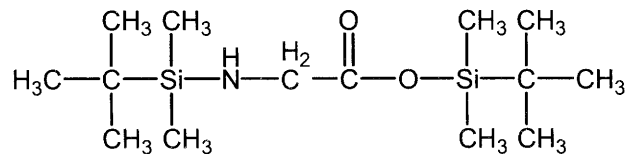
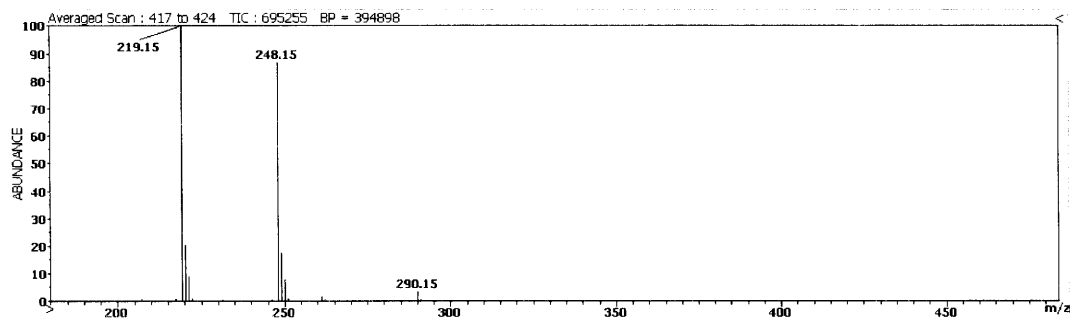
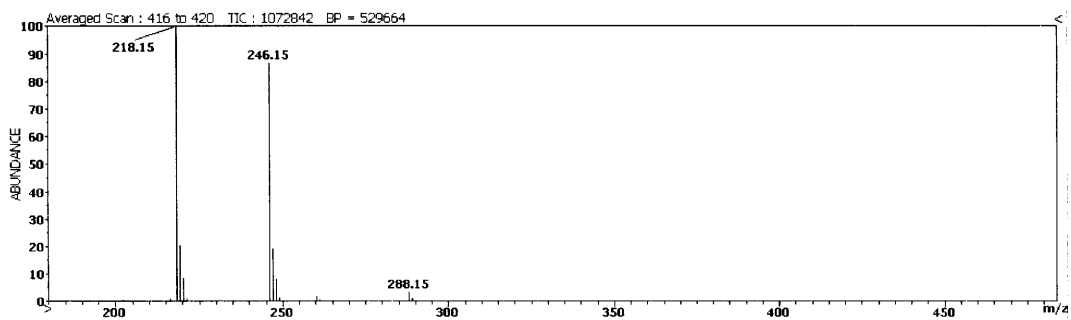
m/z	theory	data	difference
259	0.0	0.0	0.0
260	100.0	100.0	0.0
261	23.0	23.2	0.2
262	9.4	9.4	0.0
263	1.4	1.4	0.0
264	0.3	0.2	0.0
265	0.0	0.0	0.0
266	0.0	0.0	0.0
267	0.0	0.0	0.0
268	0.0	0.0	0.0

[U-¹³C]-Ala

m/z	theory	data	difference
259	0.0	0.0	0.0
260	0.0	0.3	0.3
261	0.0	0.4	0.4
262	3.1	3.3	0.2
263	100.0	100.0	0.0
264	19.9	20.5	0.6
265	8.7	9.0	0.3
266	1.1	1.2	0.1
267	0.2	0.1	-0.1
268	0.0	0.0	0.0

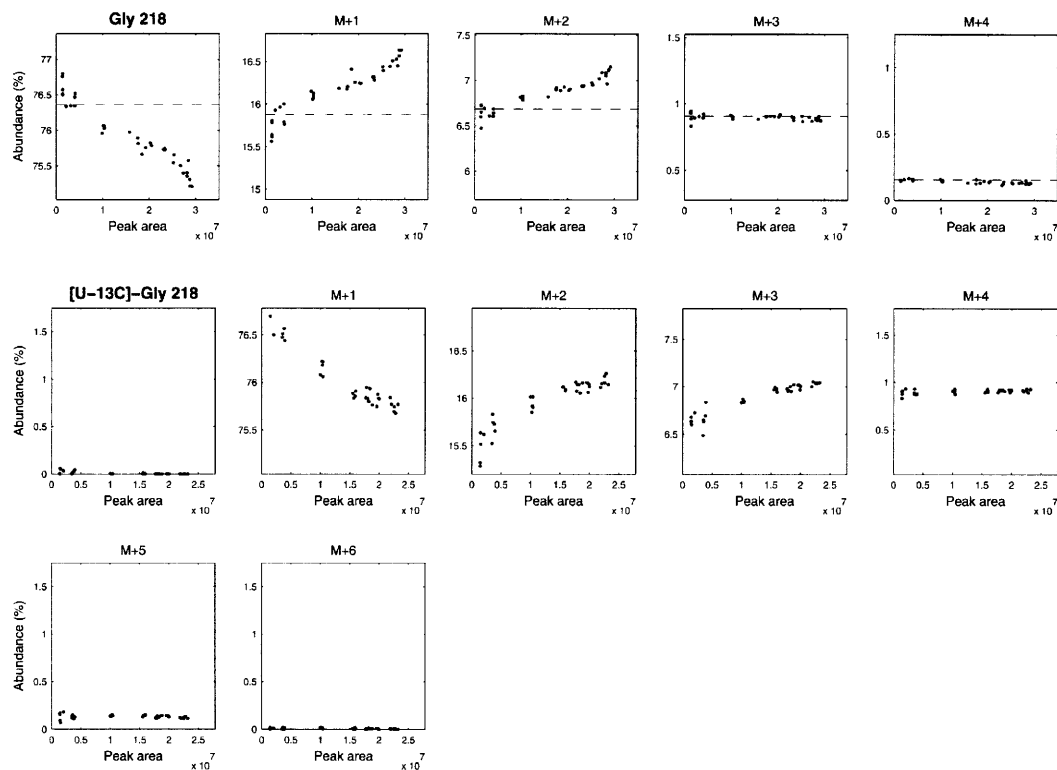
This fragment can be used for quantitative analysis.

Glycine (Gly)



C₁₄H₃₃NO₂Si₂
 Exact Mass: 303.205

APPENDIX A. GC/MS ANALYSIS OF AMINO ACIDS



Gly 218

Formula : $C_9H_{24}ONSi_2$
 Exact mass : 218.140
 C-atoms : 2

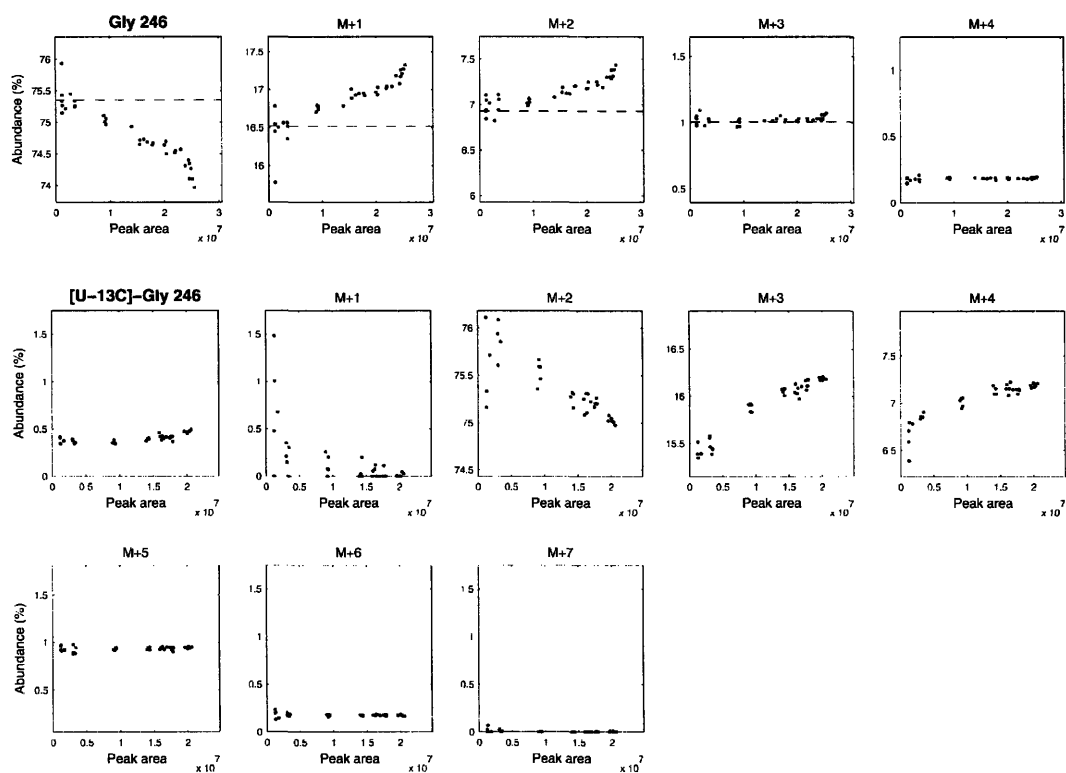
m/z	theory	data	difference
217	0.0	0.0	0.0
218	100.0	100.0	0.0
219	20.8	20.7	-0.1
220	8.8	8.7	-0.1
221	1.2	1.2	0.0
222	0.2	0.2	0.0
223	0.0	0.0	0.0
224	0.0	0.0	0.0

[U- ^{13}C]-Gly

m/z	theory	data	difference
217	0.0	0.9	0.9
218	1.0	0.0	-1.0
219	100.0	100.0	0.0
220	19.7	20.4	0.7
221	8.5	8.7	0.2
222	1.1	1.2	0.1
223	0.2	0.2	0.0
224	0.0	0.0	0.0

This fragment can be used for quantitative analysis.

APPENDIX A. GC/MS ANALYSIS OF AMINO ACIDS



Gly 246

Formula : $C_{10}H_{24}O_2NSi_2$
 Exact mass : 246.135
 C-atoms : 1-2

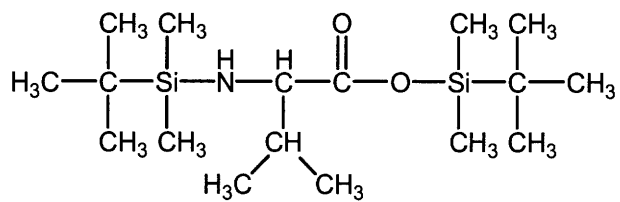
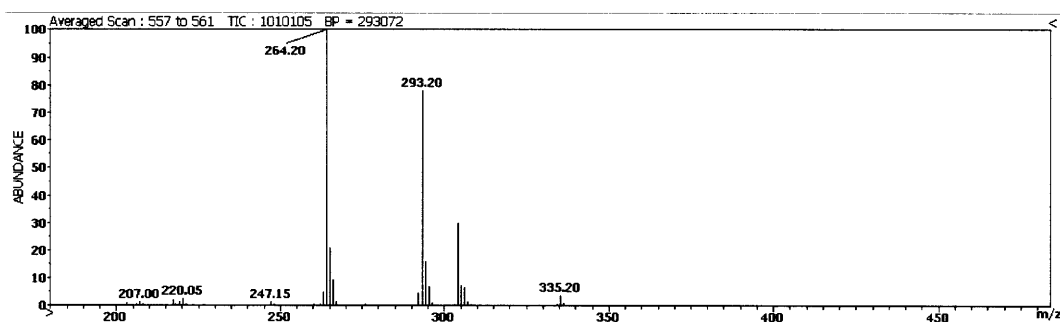
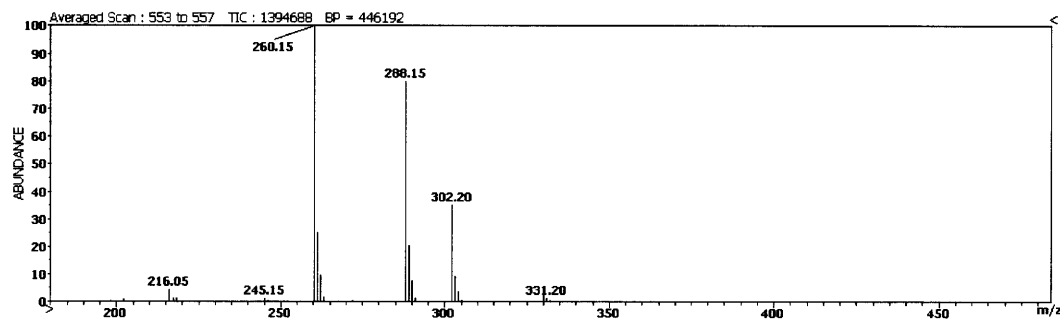
m/z	theory	data	difference
245	0.0	0.0	0.0
246	100.0	100.0	0.0
247	21.9	21.8	-0.1
248	9.2	9.1	-0.1
249	1.3	1.3	0.0
250	0.2	0.2	0.0
251	0.0	0.0	0.0
252	0.0	0.0	0.0
253	0.0	0.0	0.0

[U-¹³C]-Gly

m/z	theory	data	difference
245	0.0	0.0	0.0
246	0.0	0.4	0.4
247	2.0	0.6	-1.4
248	100.0	100.0	0.0
249	19.8	20.3	0.5
250	8.7	8.9	0.2
251	1.1	1.2	0.1
252	0.2	0.2	0.0
253	0.0	0.0	0.0

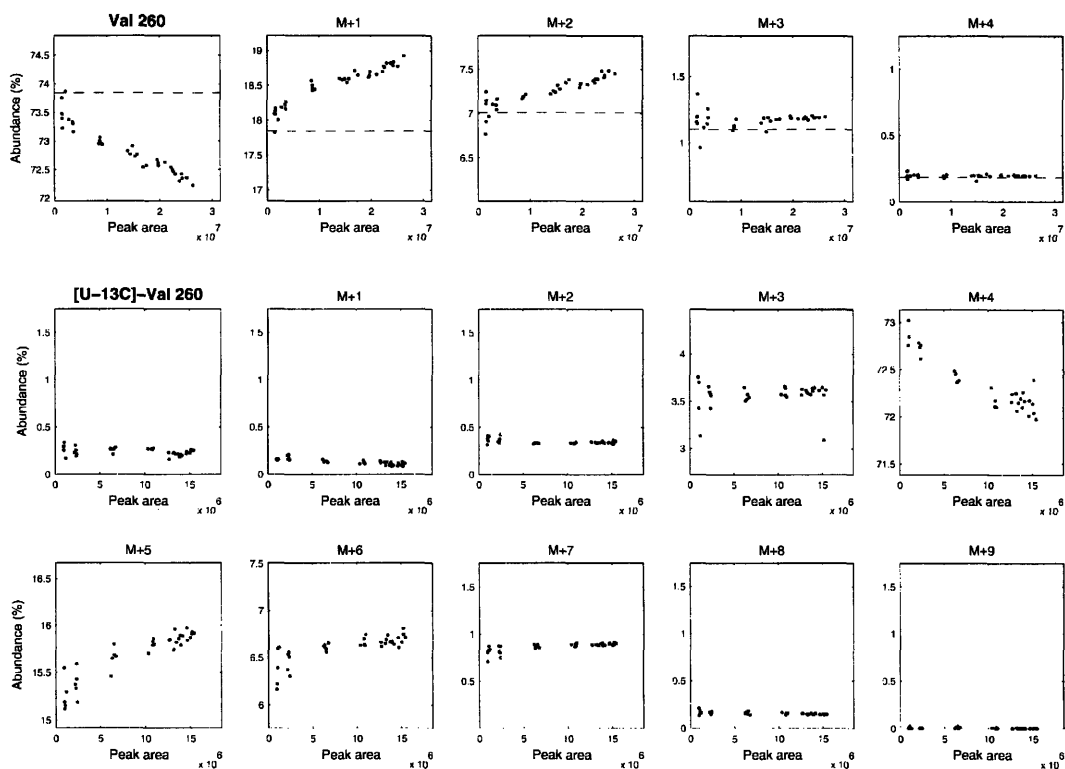
This fragment can be used for quantitative analysis.

Valine (Val)



C₁₇H₃₉NO₂Si₂
 Exact Mass: 345.2519

APPENDIX A. GC/MS ANALYSIS OF AMINO ACIDS



• Val 260

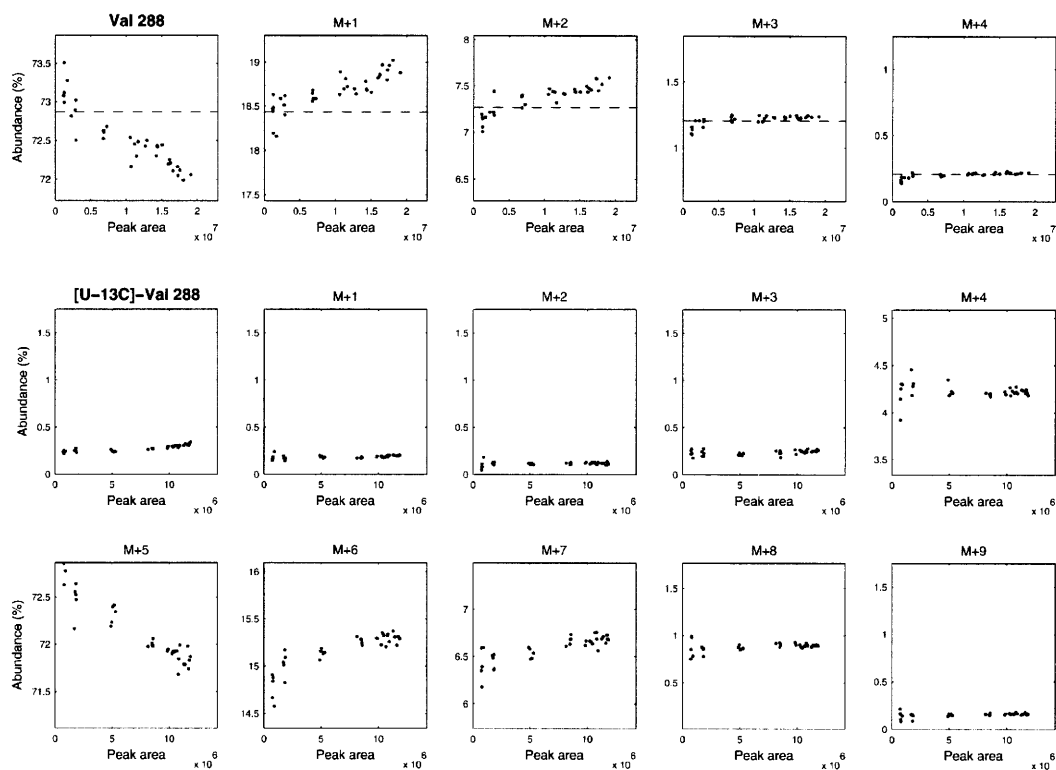
Formula :	C ₁₂ H ₃₀ ONSi ₂		
Exact mass :	260.187		
C-atoms :	2-3-4-5		
m/z	theory	data	difference
259	0.0	0.0	0.0
260	100.0	100.0	0.0
261	24.2	24.7	0.5
262	9.5	9.6	0.1
263	1.5	1.5	0.1
264	0.2	0.3	0.1
265	0.0	0.0	0.0
266	0.0	0.0	0.0
267	0.0	0.0	0.0
268	0.0	0.0	0.0
269	0.0	0.0	0.0

[U-¹³C]-Val

m/z	theory	data	difference
259	0.0	0.0	0.0
260	0.0	0.4	0.4
261	0.0	0.2	0.2
262	0.0	0.5	0.5
263	4.1	4.9	0.8
264	100.0	100.0	0.0
265	20.0	21.1	1.1
266	8.5	8.9	0.4
267	1.1	1.1	0.0
268	0.2	0.2	0.0
269	0.0	0.0	0.0

This fragment can be used for quantitative analysis. Note, however, that M+0 is slightly too low (-0.3 mol%) and M+1 is slightly too high (+0.2 mol%).

APPENDIX A. GC/MS ANALYSIS OF AMINO ACIDS



Val 288

Formula : $C_{13}H_{30}O_2NSi_2$
 Exact mass : 288.182
 C-atoms : 1-2-3-4-5

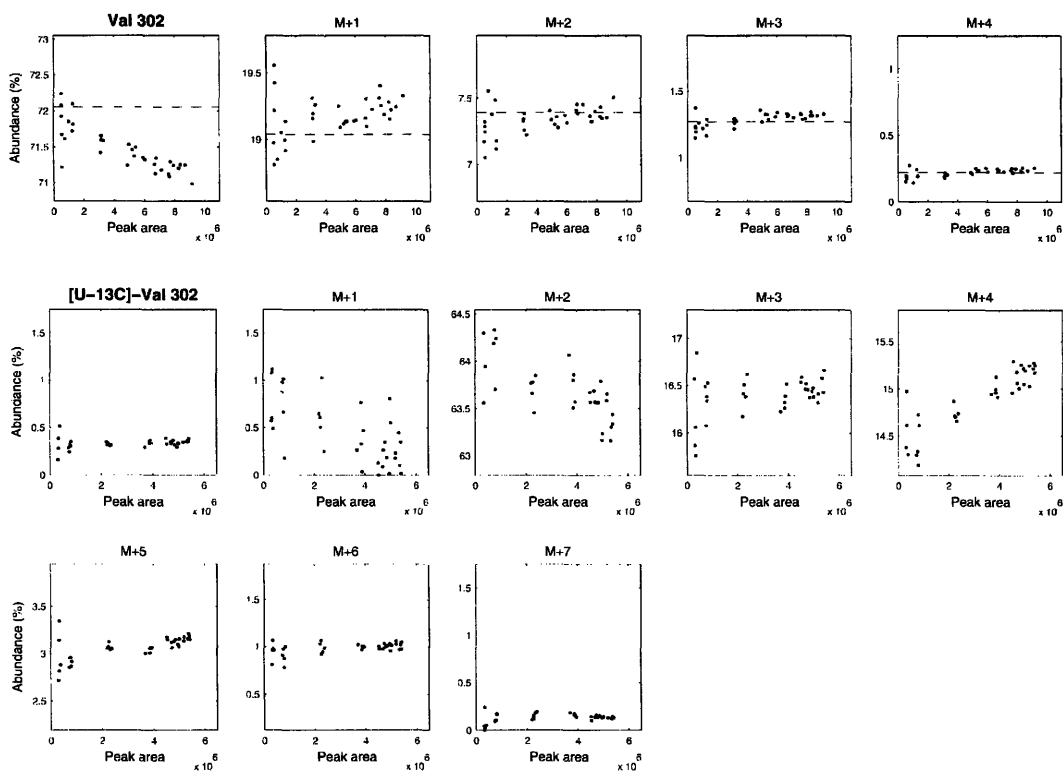
m/z	theory	data	difference
287	0.0	0.0	0.0
288	100.0	100.0	0.0
289	25.3	25.2	-0.1
290	10.0	9.8	-0.2
291	1.7	1.6	-0.1
292	0.3	0.2	-0.1
293	0.0	0.0	0.0
294	0.0	0.0	0.0
295	0.0	0.0	0.0
296	0.0	0.0	0.0
297	0.0	0.0	0.0
298	0.0	0.0	0.0

[U-¹³C]-Val

m/z	theory	data	difference
287	0.0	0.0	0.0
288	0.0	0.3	0.3
289	0.0	0.2	0.2
290	0.0	0.1	0.1
291	0.0	0.3	0.3
292	5.2	5.8	0.6
293	100.0	100.0	0.0
294	20.1	20.5	0.4
295	8.7	8.8	0.1
296	1.1	1.2	0.1
297	0.2	0.2	0.0
298	0.0	0.0	0.0

This fragment can be used for quantitative analysis.

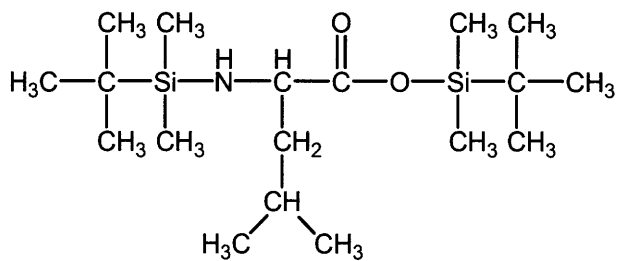
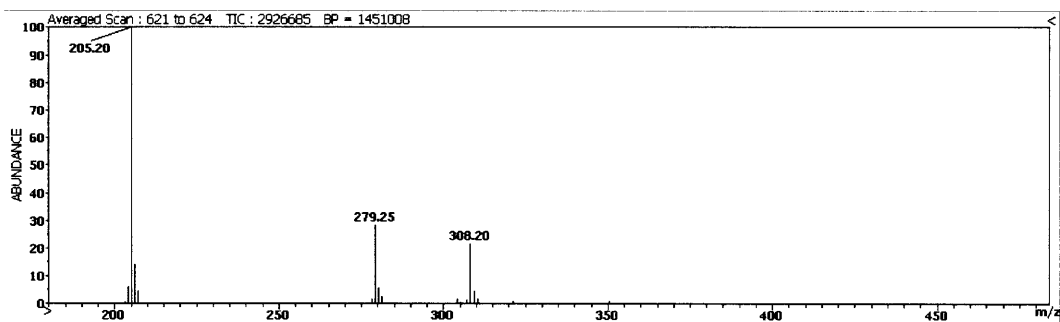
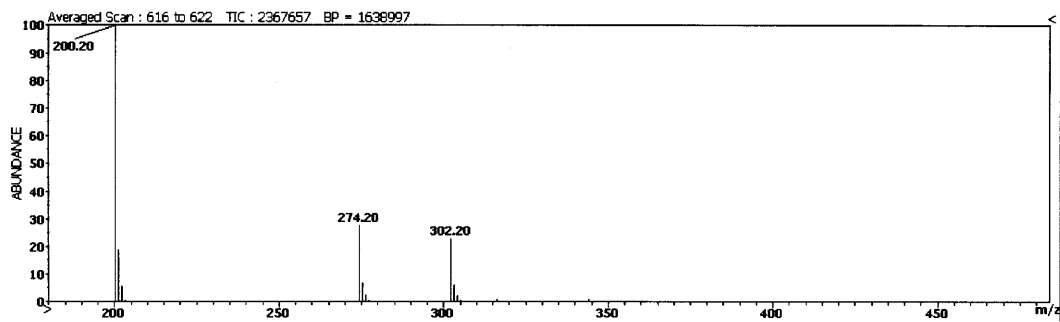
APPENDIX A. GC/MS ANALYSIS OF AMINO ACIDS



Val 302				¹³ C-Val			
Formula :	C ₁₄ H ₃₂ O ₂ NSi ₂						
Exact mass :	302.197						
C-atoms :	unknown						
m/z	theory	data	difference	m/z	theory	data	difference
301	0.0	0.0	0.0	301	0.0	0.0	0.0
302	100.0	100.0	0.0	302	0.0	0.5	0.5
303	26.4	26.5	0.1	303	2.0	1.3	-0.7
304	10.3	10.1	-0.2	304	100.0	100.0	0.0
305	1.8	1.7	-0.1	305	24.3	25.4	1.1
306	0.3	0.3	0.0	306	9.7	22.4	12.7
307	0.0	0.5	0.5	307	1.5	4.6	3.1
308	0.0	0.1	0.1	308	0.3	1.5	1.2
309	0.0	0.0	0.0	309	0.0	0.2	0.2

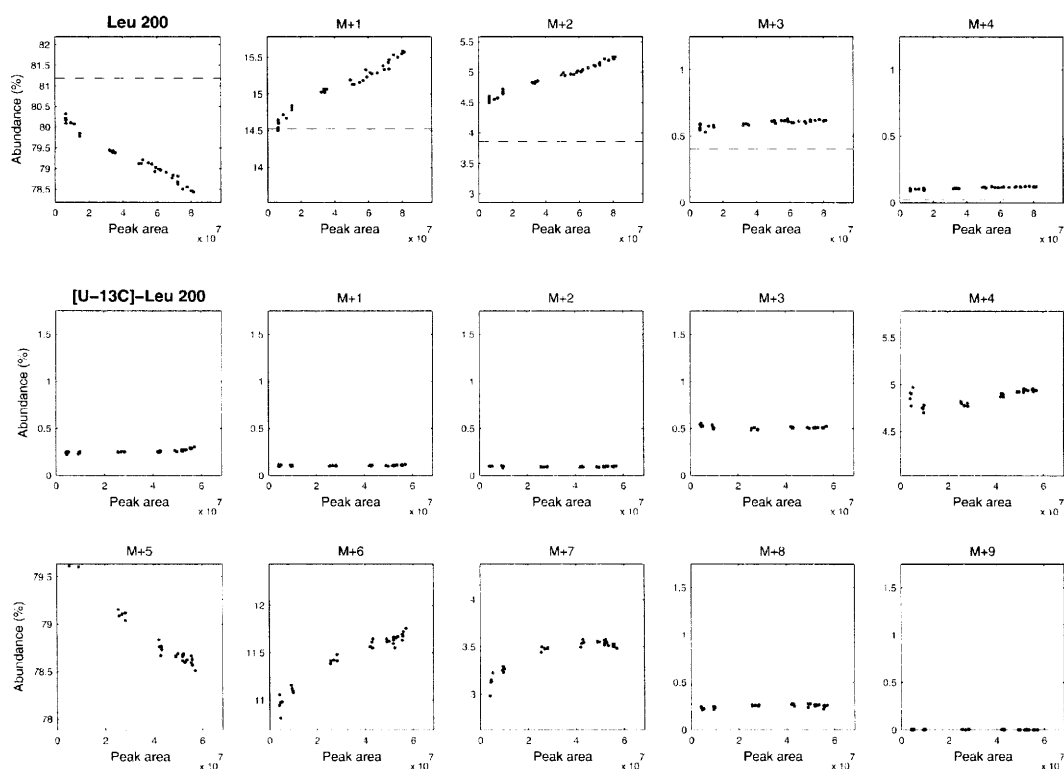
This fragment should not be used. The presence of significant M+2 and M+4 abundances in [¹³C]-valine suggests that two fragments are overlapping.

Leucine (Leu)



C₁₈H₄₁NO₂Si₂
 Exact Mass: 359.2676

APPENDIX A. GC/MS ANALYSIS OF AMINO ACIDS



Leu 200

Formula : $C_{11}H_{26}NSi$
 Exact mass : 200.183
 C-atoms : 2-3-4-5-6

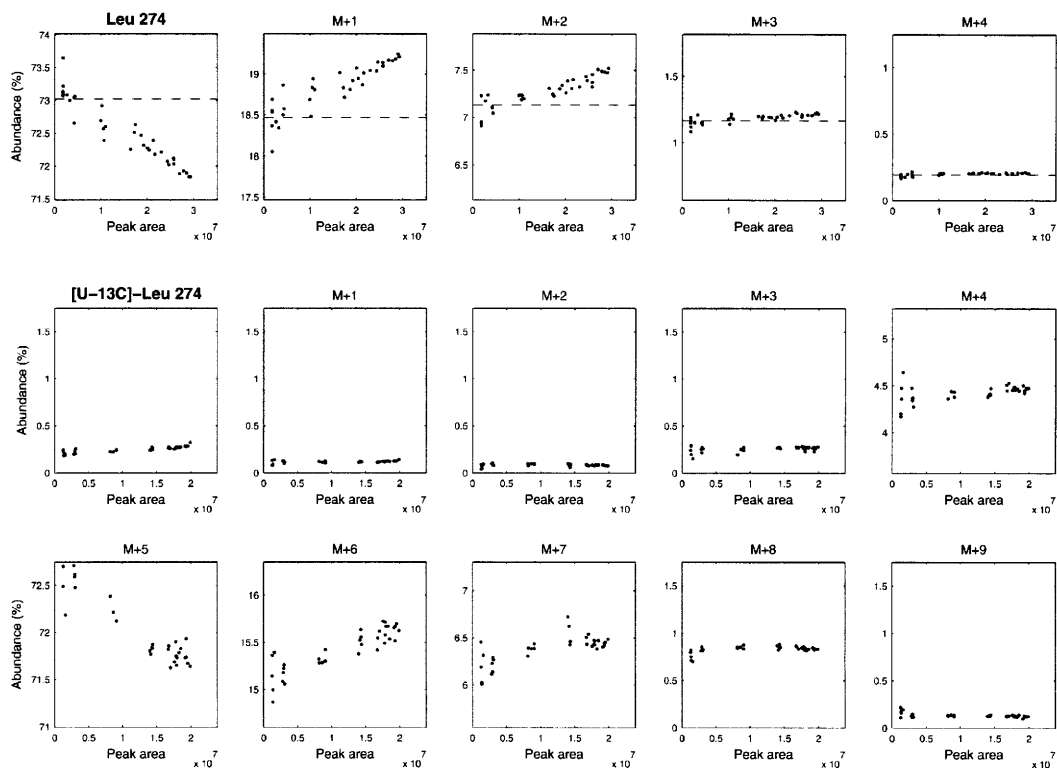
m/z	theory	data	difference
199	0.0	0.0	0.0
200	100.0	100.0	0.0
201	17.9	18.2	0.3
202	4.8	5.7	0.9
203	0.5	0.7	0.2
204	0.0	0.1	0.1
205	0.0	0.0	0.0
206	0.0	0.0	0.0
207	0.0	0.0	0.0
208	0.0	0.0	0.0
209	0.0	0.0	0.0

[U-¹³C]-Leu

m/z	theory	data	difference
199	0.0	0.0	0.0
200	0.0	0.3	0.3
201	0.0	0.1	0.1
202	0.0	0.1	0.1
203	0.0	0.6	0.6
204	5.2	5.9	0.7
205	100.0	100.0	0.0
206	12.5	13.8	1.3
207	3.9	4.1	0.2
208	0.3	0.3	0.0
209	0.0	0.0	0.0

This fragment should not be used. It has a significant bias, M+0 is too low (-1.0 mol%) and M+2 is too high (+0.6mol%). Fragment Leu-274 is preferred.

APPENDIX A. GC/MS ANALYSIS OF AMINO ACIDS



Leu 274

Formula : $C_{13}H_{32}ONSi_2$
 Exact mass : 274.202
 C-atoms : 2-3-4-5-6

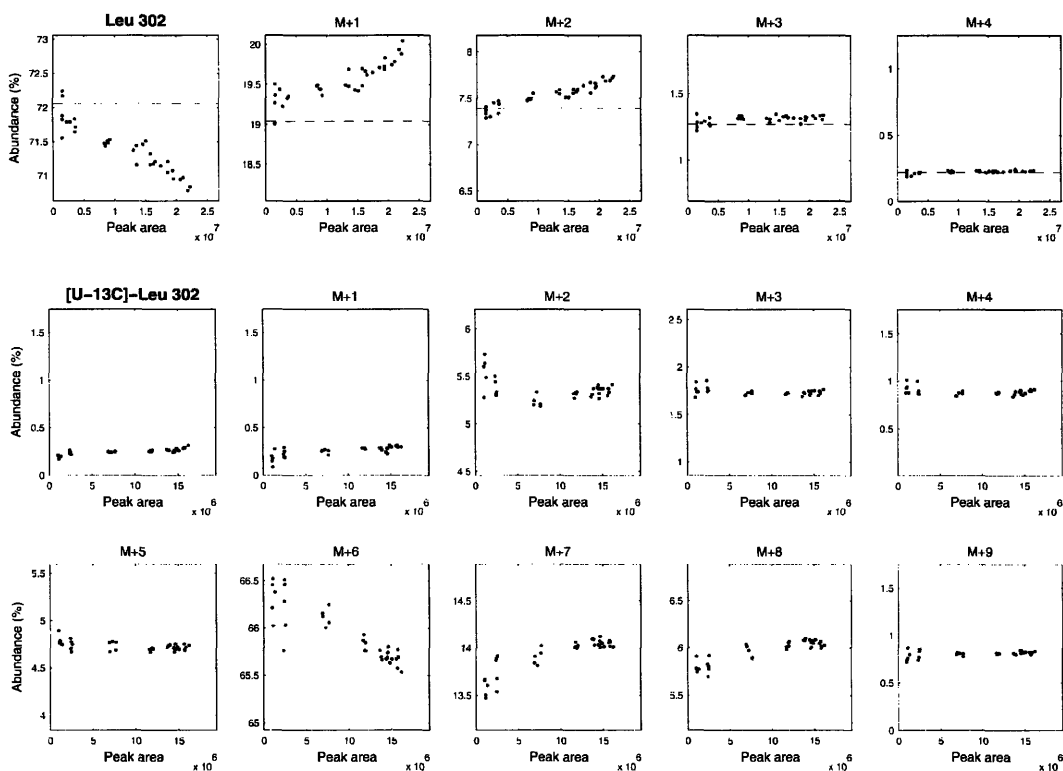
m/z	theory	data	difference
273	0.0	0.0	0.0
274	100.0	100.0	0.0
275	25.3	25.2	-0.1
276	9.8	9.6	-0.2
277	1.6	1.6	0.0
278	0.3	0.3	0.0
279	0.0	0.0	0.0
280	0.0	0.0	0.0
281	0.0	0.0	0.0
282	0.0	0.0	0.0
283	0.0	0.0	0.0
284	0.0	0.1	0.1

[U-¹³C]-Leu

m/z	theory	data	difference
273	0.0	0.0	0.0
274	0.0	0.3	0.3
275	0.0	0.2	0.2
276	0.0	0.1	0.1
277	0.0	0.3	0.3
278	5.2	6.0	0.8
279	100.0	100.0	0.0
280	20.1	20.7	0.6
281	8.5	8.6	0.1
282	1.1	1.1	0.0
283	0.2	0.2	0.0
284	0.0	0.0	0.0

This fragment can be used for quantitative analysis.

APPENDIX A. GC/MS ANALYSIS OF AMINO ACIDS

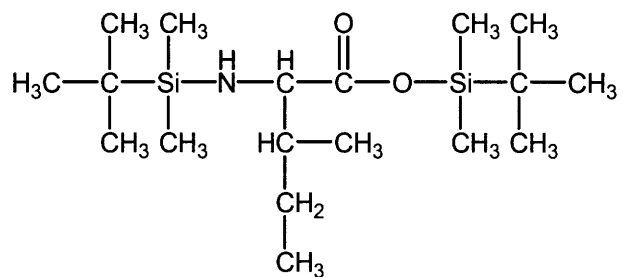
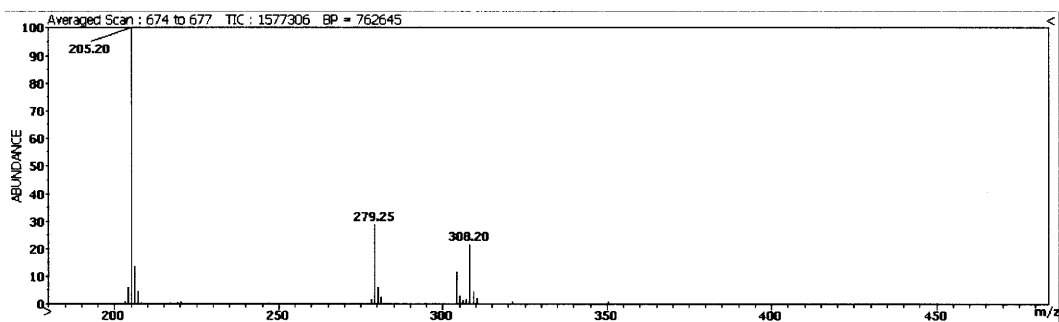
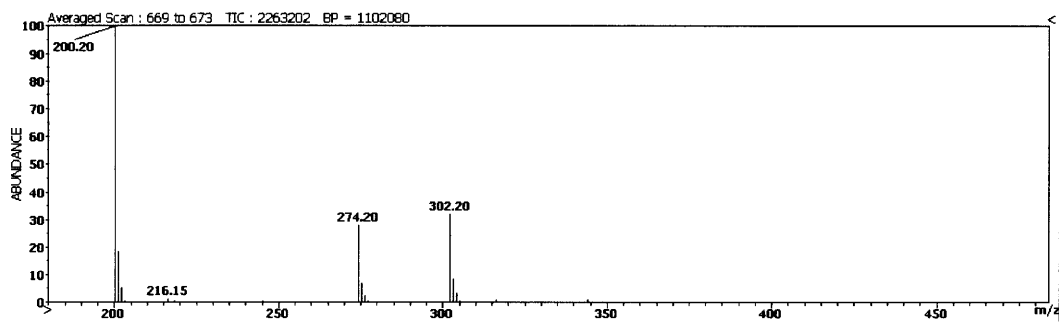


Leu 302			
Formula :	C ₁₄ H ₃₂ O ₂ NSi ₂		
Exact mass :	302.197		
C-atoms :	1-2 and 1-2-3-4-5-6		
m/z	theory	data	difference
301	0.0	0.0	0.0
302	100.0	100.0	0.0
303	26.4	26.6	0.2
304	10.3	10.2	-0.1
305	1.8	1.8	0.0
306	0.3	0.3	0.0
307	0.0	0.0	0.0
308	0.0	0.0	0.0
309	0.0	0.0	0.0
310	0.0	0.0	0.0
311	0.0	0.0	0.0
312	0.0	0.0	0.0
313	0.0	0.0	0.0

[U- ¹³ C]-Leu			
m/z	theory	data	difference
301	0.0	0.0	0.0
302	0.0	0.3	0.3
303	0.0	0.3	0.3
304	0.0	8.1	8.1
305	0.0	2.6	2.6
306	0.0	1.3	1.3
307	6.3	7.2	0.9
308	100.0	100.0	0.0
309	20.2	20.6	0.4
310	8.7	8.8	0.1
311	1.1	1.2	0.1
312	0.2	0.2	0.0
313	0.0	0.0	0.0

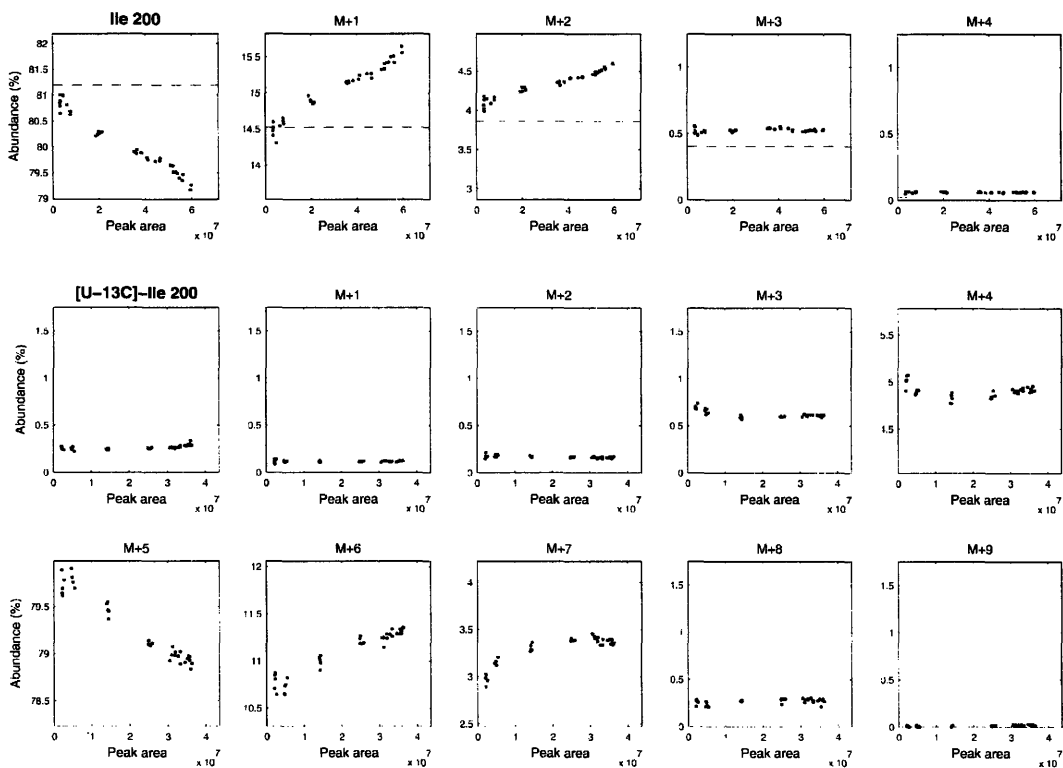
This fragment should not be used. The presence of significant M+2 and M+6 abundances in [U-¹³C]-leucine shows that two fragments with the same chemical formula are overlapping.

Isoleucine (Ile)



C₁₈H₄₁NO₂Si₂
 Exact Mass: 359.2676

APPENDIX A. GC/MS ANALYSIS OF AMINO ACIDS



Ile 200

Formula : $C_{11}H_{26}NSi$
 Exact mass : 200.183
 C-atoms : 2-3-4-5-6

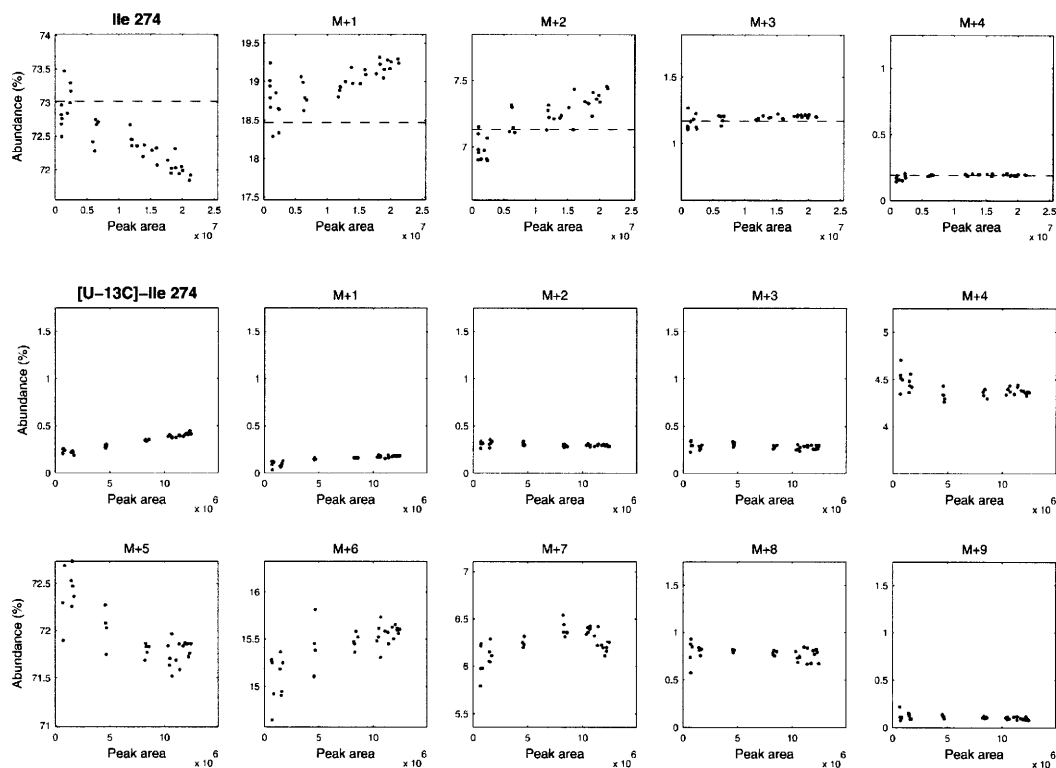
m/z	theory	data	difference
199	0.0	0.0	0.0
200	100.0	100.0	0.0
201	17.9	17.9	0.0
202	4.8	5.0	0.2
203	0.5	0.6	0.1
204	0.0	0.1	0.0
205	0.0	0.0	0.0
206	0.0	0.0	0.0
207	0.0	0.0	0.0
208	0.0	0.0	0.0
209	0.0	0.0	0.0

[U-¹³C]-Ile

m/z	theory	data	difference
199	0.0	0.0	0.0
200	0.0	0.3	0.3
201	0.0	0.1	0.1
202	0.0	0.2	0.2
203	0.0	0.8	0.8
204	5.2	6.1	0.9
205	100.0	100.0	0.0
206	12.5	13.4	0.9
207	3.9	3.9	0.0
208	0.3	0.3	0.0
209	0.0	0.0	0.0

This fragment can be used for quantitative analysis.

APPENDIX A. GC/MS ANALYSIS OF AMINO ACIDS



Ile 274

Formula : $C_{13}H_{32}ONSi_2$
 Exact mass : 274.202
 C-atoms : 2-3-4-5-6

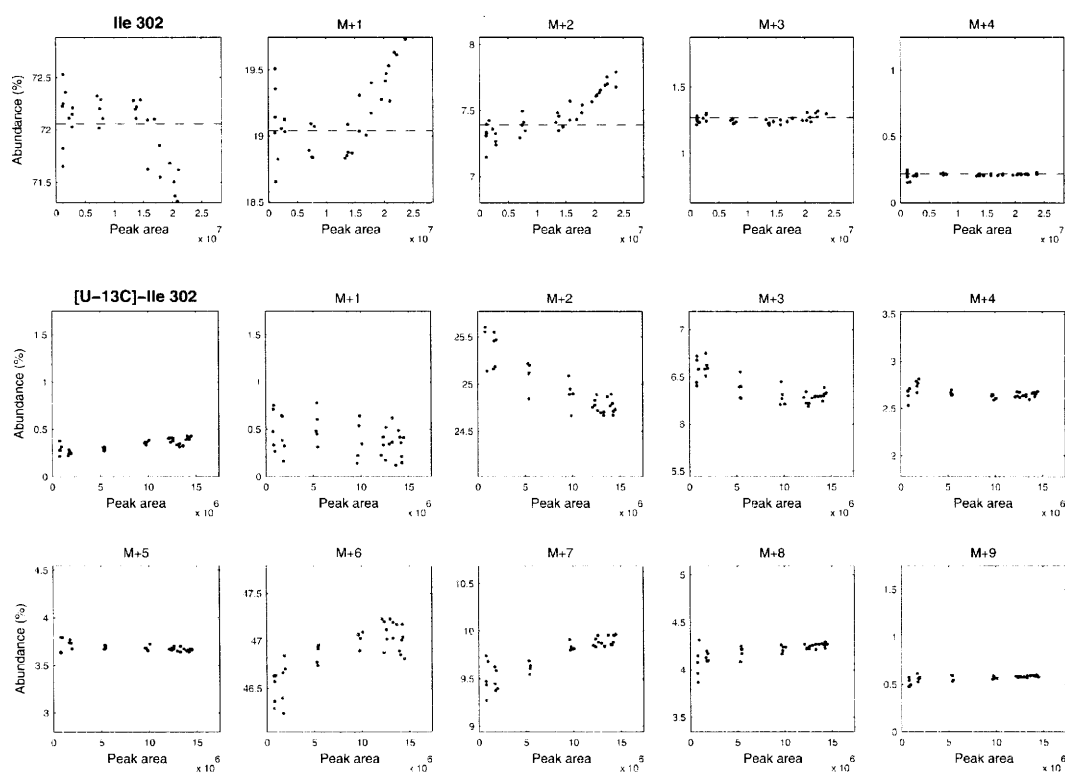
m/z	theory	data	difference
273	0.0	0.0	0.0
274	100.0	100.0	0.0
275	25.3	25.4	0.1
276	9.8	9.6	-0.2
277	1.6	1.6	0.0
278	0.3	0.3	0.0
279	0.0	0.0	0.0
280	0.0	0.0	0.0
281	0.0	0.0	0.0
282	0.0	0.0	0.0
283	0.0	0.0	0.0
284	0.0	0.1	0.1

[U-¹³C]-Ile

m/z	theory	data	difference
273	0.0	0.0	0.0
274	0.0	0.3	0.3
275	0.0	0.1	0.1
276	0.0	0.4	0.4
277	0.0	0.4	0.4
278	5.2	6.1	0.9
279	100.0	100.0	0.0
280	20.1	20.9	0.8
281	8.5	8.5	0.0
282	1.1	1.1	0.0
283	0.2	0.2	0.0
284	0.0	0.0	0.0

This fragment can be used for quantitative analysis.

APPENDIX A. GC/MS ANALYSIS OF AMINO ACIDS



Ile 302

Formula : $C_{14}H_{32}O_2NSi_2$
 Exact mass : 302.197
 C-atoms : 1-2 and 1-2-3-4-5-6

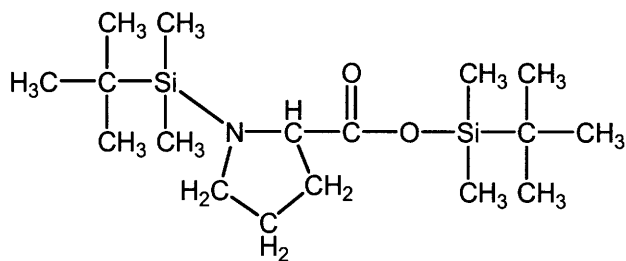
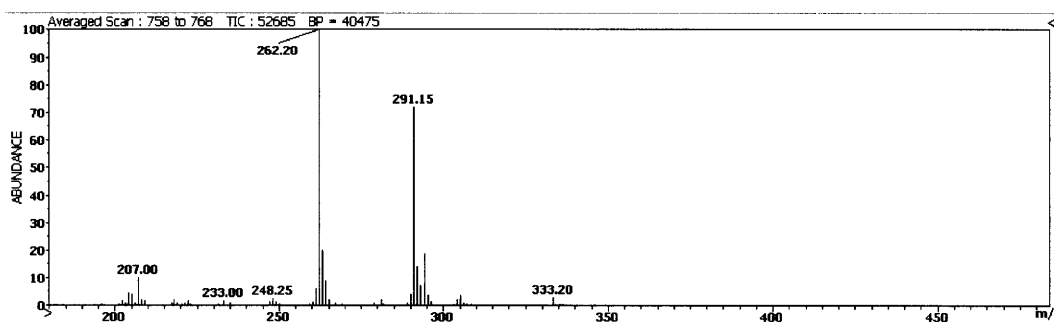
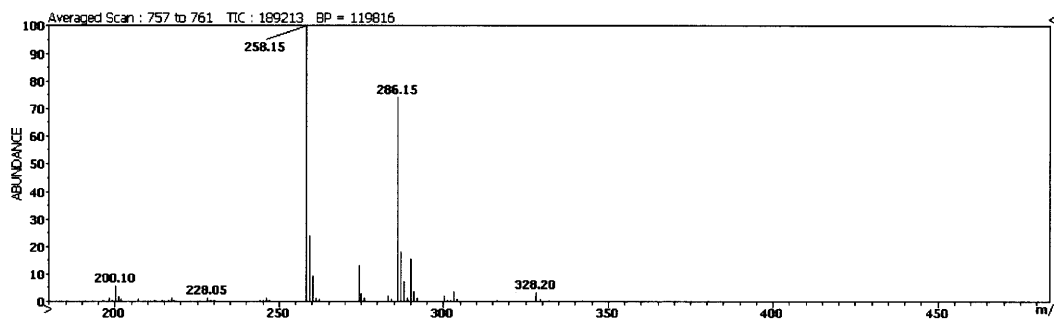
m/z	theory	data	difference
301	0.0	0.0	0.0
302	100.0	100.0	0.0
303	26.4	25.8	-0.6
304	10.3	10.0	-0.3
305	1.8	1.7	-0.1
306	0.3	0.3	0.0
307	0.0	0.0	0.0
308	0.0	0.0	0.0
309	0.0	0.0	0.0
310	0.0	0.0	0.0
311	0.0	0.0	0.0
312	0.0	0.0	0.0
313	0.0	0.0	0.0

[U-¹³C]-Ile

m/z	theory	data	difference
301	0.0	0.0	0.0
302	0.0	0.5	0.5
303	0.0	1.1	1.1
304	0.0	54.6	54.6
305	0.0	14.0	14.0
306	0.0	5.8	5.8
307	6.3	8.0	1.7
308	100.0	100.0	0.0
309	20.2	20.3	0.1
310	8.7	8.8	0.1
311	1.1	1.2	0.1
312	0.2	0.2	0.0
313	0.0	0.0	0.0

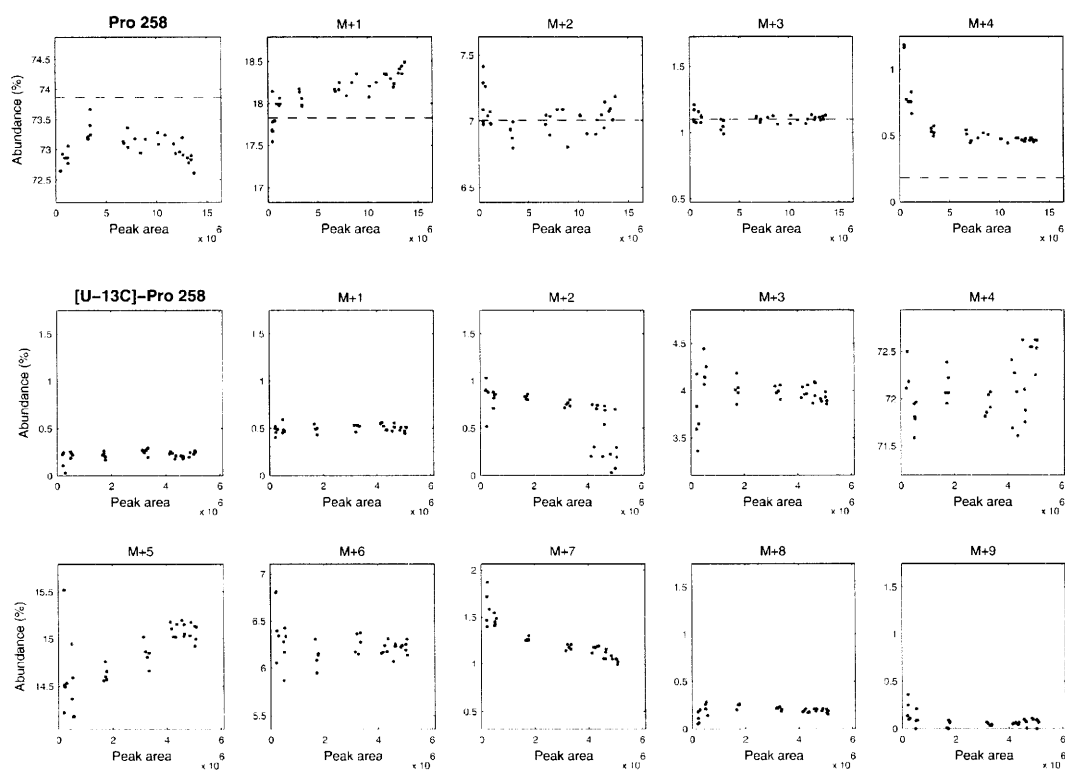
This fragment should not be used. The presence of significant M+2 and M+6 abundances in [U-¹³C]-isoleucine shows that two fragments with the same chemical formula are overlapping.

Proline (Pro)



C₁₇H₃₇NO₂Si₂
 Exact Mass: 343.2363

APPENDIX A. GC/MS ANALYSIS OF AMINO ACIDS



Pro 258

Formula : $C_{12}H_{28}ONSi_2$
 Exact mass : 258.171
 C-atoms : 2-3-4-5

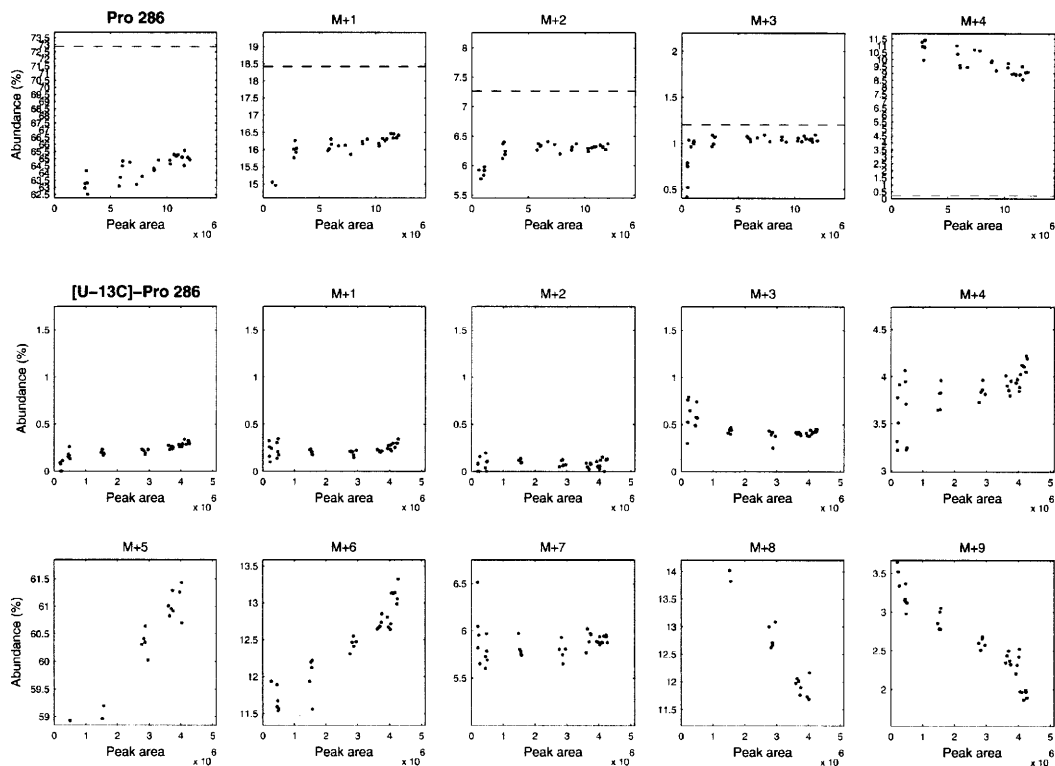
m/z	theory	data	difference
257	0.0	0.0	0.0
258	100.0	100.0	0.0
259	24.1	24.5	0.4
260	9.5	9.4	-0.1
261	1.5	1.4	-0.1
262	0.2	0.8	0.6
263	0.0	0.1	0.1
264	0.0	0.1	0.1
265	0.0	0.0	0.0
266	0.0	0.0	0.0
267	0.0	0.0	0.0

[U- ^{13}C]-Pro

m/z	theory	data	difference
257	0.0	0.1	0.1
258	0.0	0.3	0.3
259	0.0	0.7	0.7
260	0.0	1.5	1.5
261	4.1	5.7	1.6
262	100.0	100.0	0.0
263	20.0	20.0	0.0
264	8.5	8.6	0.1
265	1.1	2.0	0.9
266	0.2	0.3	0.1
267	0.0	0.1	0.1

This fragment should be used with caution. Proline co-elutes with other compounds, which may result in inaccurate values. M+0 is slightly too low (-0.5 mol%) and M+4 is slightly too high (+0.4 mol%). Fragment Glu-330 is preferred.

APPENDIX A. GC/MS ANALYSIS OF AMINO ACIDS



Pro 286

Formula : $C_{13}H_{28}NO_2Si_2$
 Exact mass : 286.166
 C-atoms : 1-2-3-4-5

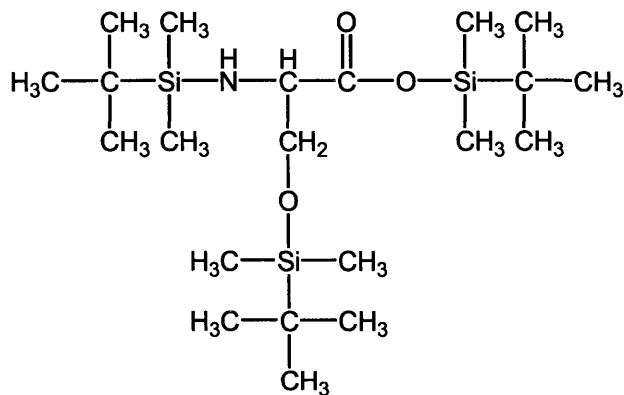
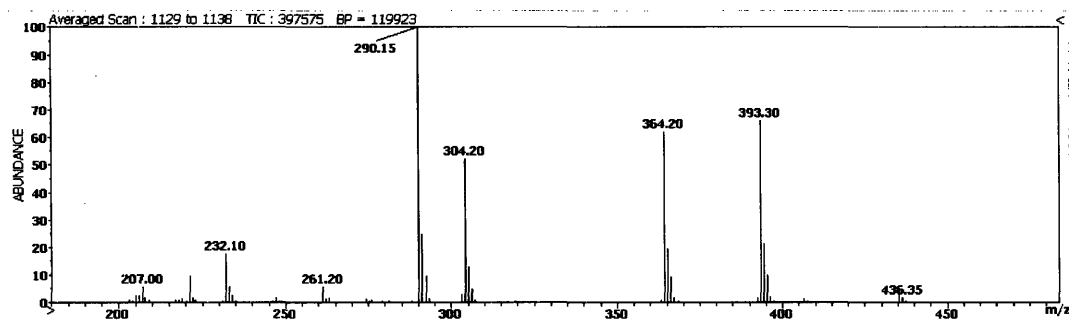
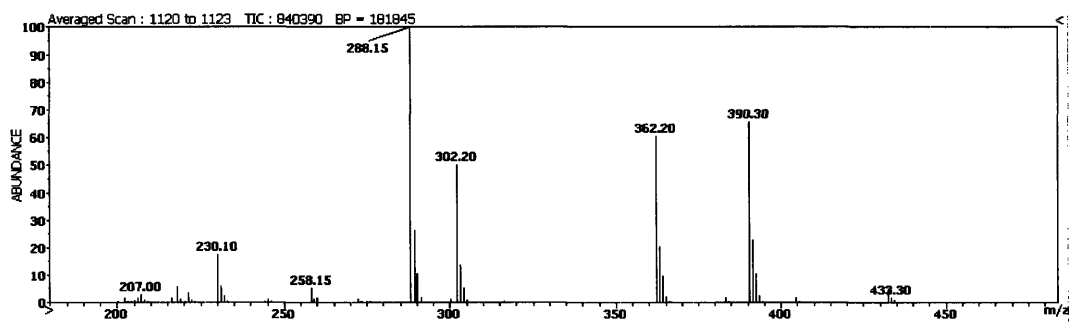
m/z	theory	data	difference
285	0.0	0.0	0.0
286	100.0	100.0	0.0
287	25.3	25.2	-0.1
288	10.0	9.9	-0.1
289	1.6	1.7	0.1
290	0.3	25.4	25.1
291	0.0	6.3	6.3
292	0.0	2.4	2.4
293	0.0	0.5	0.5
294	0.0	0.0	0.0
295	0.0	0.0	0.0
296	0.0	0.0	0.0
297	0.0	0.0	0.0

[U-¹³C]-Pro

m/z	theory	data	difference
285	0.0	0.0	0.0
286	0.0	0.2	0.2
287	0.0	0.3	0.3
288	0.0	0.2	0.2
289	0.0	0.9	0.9
290	5.2	6.4	1.2
291	100.0	100.0	0.0
292	20.1	20.2	0.1
293	8.7	10.1	1.4
294	1.1	29.2	28.1
295	0.2	5.9	5.7
296	0.0	2.7	2.7
297	0.0	0.3	0.3

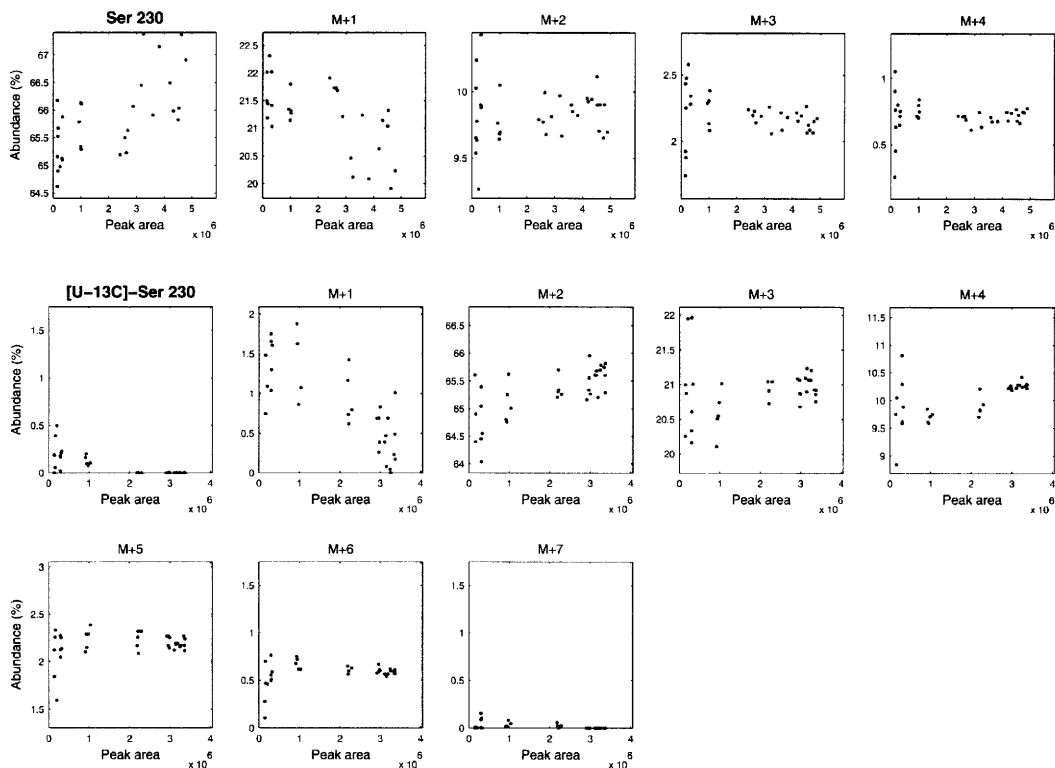
This fragment should not be used. Proline co-elutes with other compounds, which results in inaccurate values. Here, M+4 is significantly too high. Fragment Glu-432 is preferred.

Serine (Ser)



C₂₁H₄₉NO₃Si₃
Exact Mass: 447.302

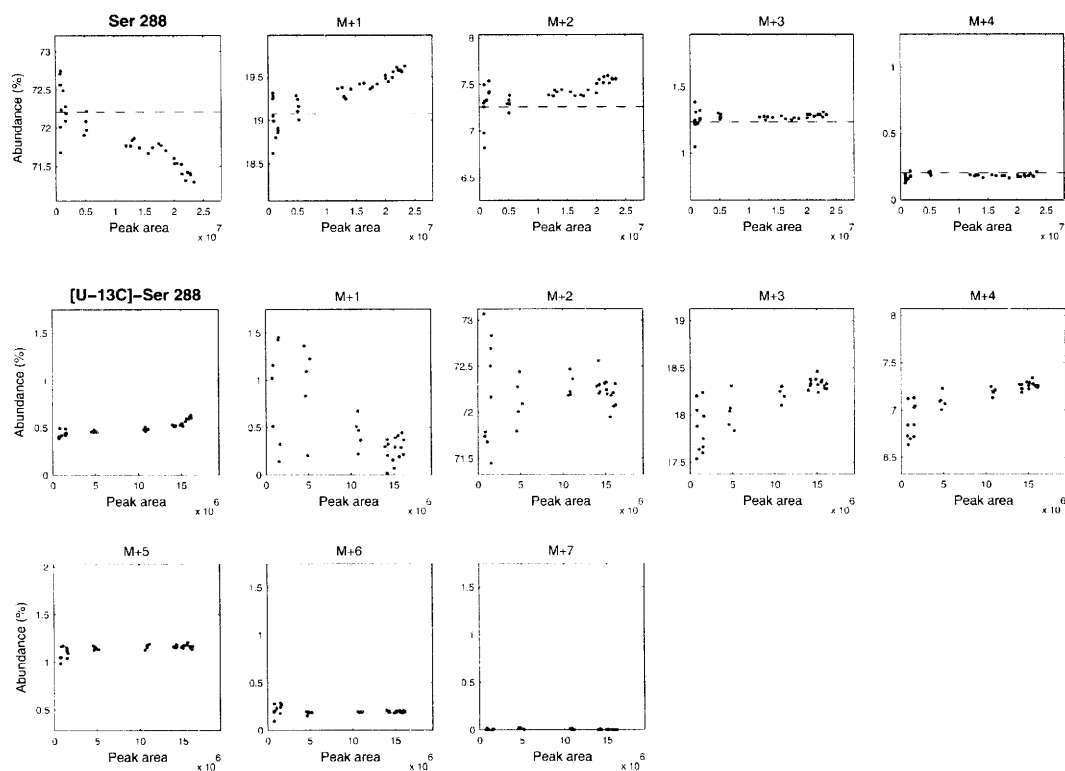
APPENDIX A. GC/MS ANALYSIS OF AMINO ACIDS



Ser 230				[U- ¹³ C]-Ser			
Formula :	unknown						
Exact mass :	unknown						
C-atoms :	unknown						
m/z	theory	data	difference	m/z	theory	data	difference
229		0.0		229		0.0	
230		100.0		230		0.3	
231		33.8		231		2.9	
232		15.0		232		100.0	
233	n/a	3.5	n/a	233	n/a	31.8	n/a
234		1.1		234		14.5	
235		0.2		235		3.4	
236		0.1		236		1.0	
237		0.1		237		0.1	

This fragment cannot be used because the fragmentation is unknown. Furthermore, this fragment is not very abundant and therefore somewhat noisy.

APPENDIX A. GC/MS ANALYSIS OF AMINO ACIDS



Ser 288

Formula : $C_{14}H_{34}NOSi_2$
 Exact mass : 288.218
 C-atoms : 2-3

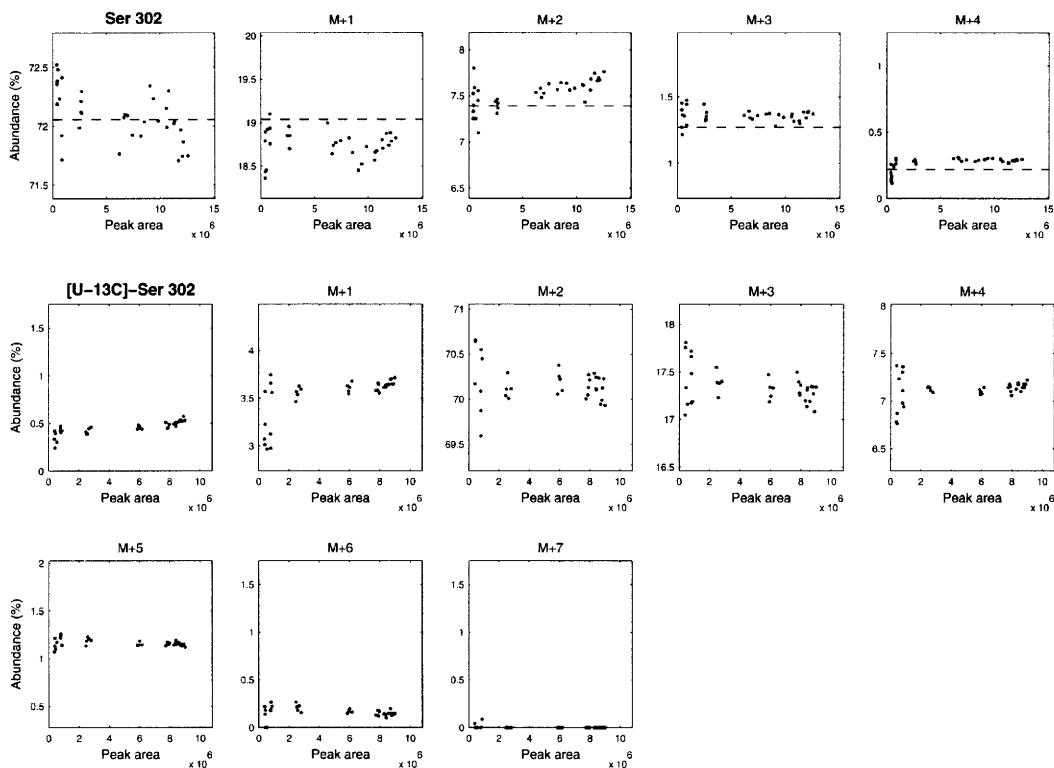
m/z	theory	data	difference
287	0.0	0.0	0.0
288	100.0	100.0	0.0
289	26.4	26.3	-0.1
290	10.1	10.0	-0.1
291	1.7	1.8	0.1
292	0.3	0.3	0.0
293	0.0	0.0	0.0
294	0.0	0.0	0.0
295	0.0	0.0	0.0

[U- ^{13}C]-Ser

m/z	theory	data	difference
287	0.0	0.0	0.0
288	0.0	0.6	0.6
289	2.0	1.7	-0.3
290	100.0	100.0	0.0
291	24.3	24.8	0.5
292	9.5	9.7	0.2
293	1.5	1.6	0.1
294	0.2	0.3	0.1
295	0.0	0.0	0.0

This fragment can be used for quantitative analysis.

APPENDIX A. GC/MS ANALYSIS OF AMINO ACIDS



Ser 302

Formula : $C_{14}H_{32}O_2NSi_2$
 Exact mass : 302.197
 C-atoms : 1-2

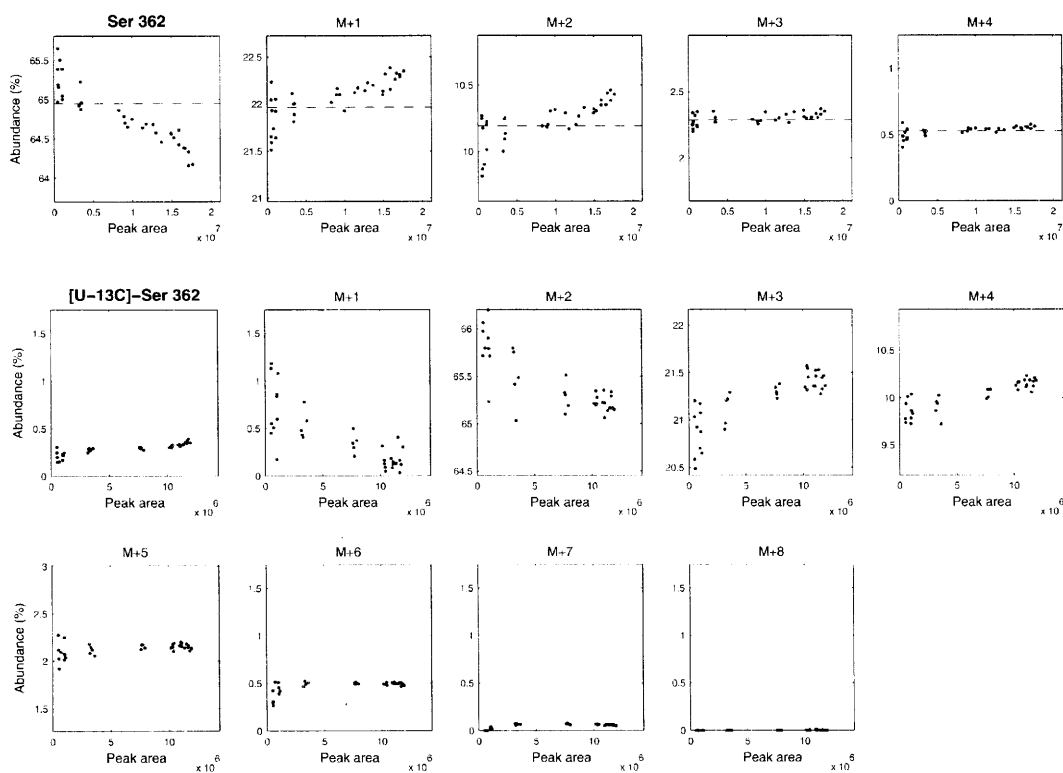
m/z	theory	data	difference
301	0.0	0.0	0.0
302	100.0	100.0	0.0
303	26.4	26.2	-0.2
304	10.3	10.2	-0.1
305	1.8	1.9	0.1
306	0.3	0.4	0.1
307	0.0	0.0	0.0
308	0.0	0.0	0.0
309	0.0	0.0	0.0

[U-¹³C]-Ser

m/z	theory	data	difference
301	0.0	0.0	0.0
302	0.0	0.5	0.5
303	2.0	4.5	2.5
304	100.0	100.0	0.0
305	24.3	24.8	0.5
306	9.7	10.1	0.4
307	1.5	1.7	0.2
308	0.3	0.3	0.0
309	0.0	0.0	0.0

This fragment can be used for quantitative analysis. Note, however, that M+2 of [U-¹³C]-serine is slightly higher than expected.

APPENDIX A. GC/MS ANALYSIS OF AMINO ACIDS



Ser 362

Formula : $C_{16}H_{40}O_2NSi_3$
 Exact mass : 362.237
 C-atoms : 2-3

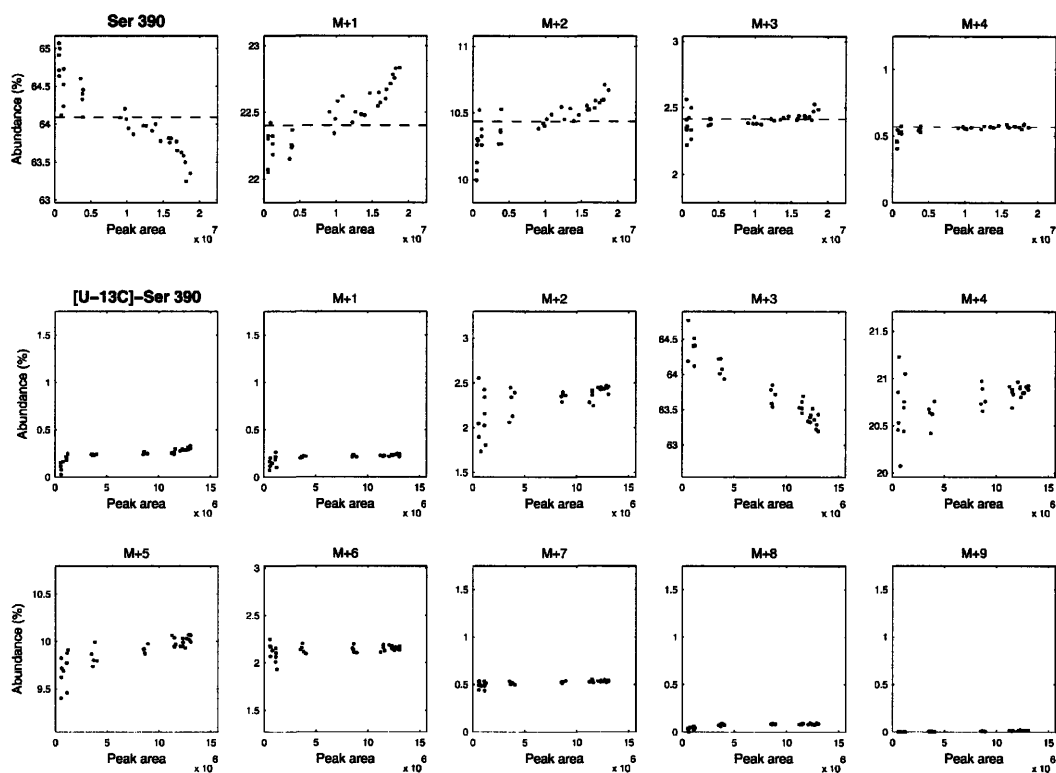
m/z	theory	data	difference
361	0.0	0.0	0.0
362	100.0	100.0	0.0
363	33.8	33.5	-0.3
364	15.7	15.4	-0.3
365	3.5	3.5	0.0
366	0.8	0.8	0.0
367	0.1	0.2	0.0
368	0.0	0.0	0.0
369	0.0	0.0	0.0
370	0.0	0.0	0.0

[U-¹³C]-Ser

m/z	theory	data	difference
361	0.0	0.0	0.0
362	0.0	0.3	0.3
363	2.2	1.5	-0.7
364	100.0	100.0	0.0
365	31.7	31.9	0.2
366	15.0	14.9	-0.1
367	3.2	3.2	0.0
368	0.7	0.7	0.0
369	0.1	0.1	0.0
370	0.0	0.0	0.0

This fragment can be used for quantitative analysis.

APPENDIX A. GC/MS ANALYSIS OF AMINO ACIDS



Ser 390

Formula : $C_{17}H_{40}O_3NSi_3$
 Exact mass : 390.232
 C-atoms : 1-2-3

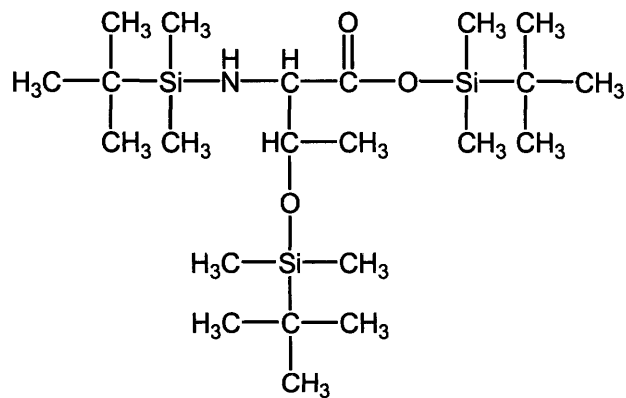
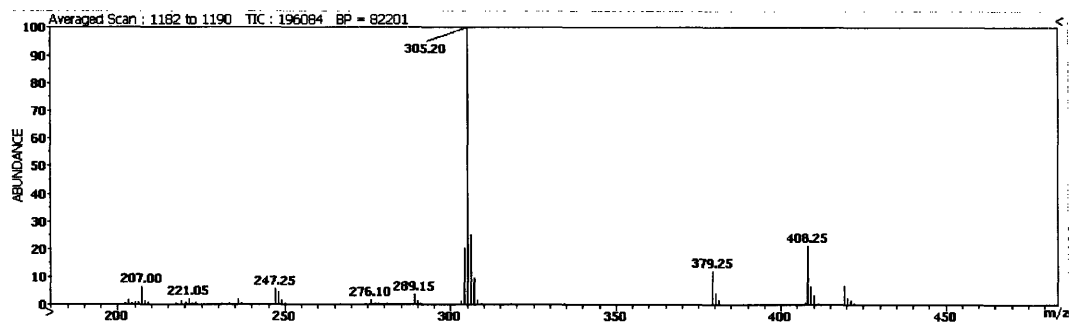
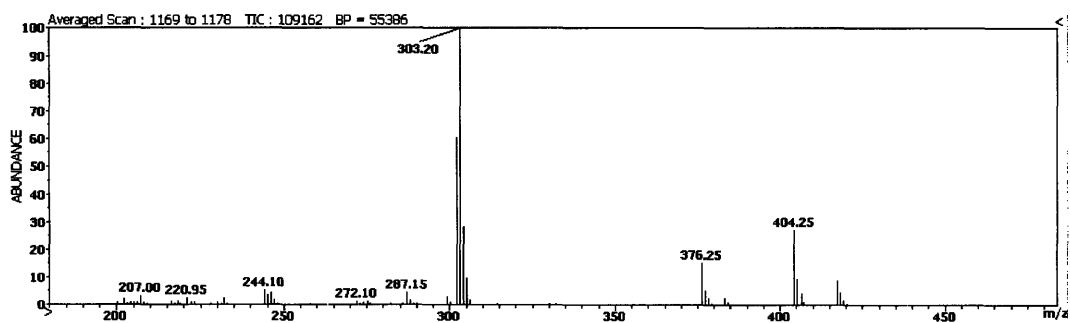
m/z	theory	data	difference
389	0.0	0.0	0.0
390	100.0	100.0	0.0
391	35.0	34.3	-0.7
392	16.3	15.9	-0.4
393	3.8	3.7	-0.1
394	0.9	0.8	-0.1
395	0.1	0.1	0.0
396	0.0	0.0	0.0
397	0.0	0.1	0.1
398	0.0	0.0	0.0
399	0.0	0.0	0.0

[U- ^{13}C]-Ser

m/z	theory	data	difference
389	0.0	0.0	0.0
390	0.0	0.3	0.3
391	0.0	0.3	0.3
392	3.1	3.3	0.2
393	100.0	100.0	0.0
394	31.8	31.9	0.1
395	15.2	15.1	-0.1
396	3.3	3.3	0.0
397	0.8	0.8	0.0
398	0.1	0.1	0.0
399	0.0	0.0	0.0

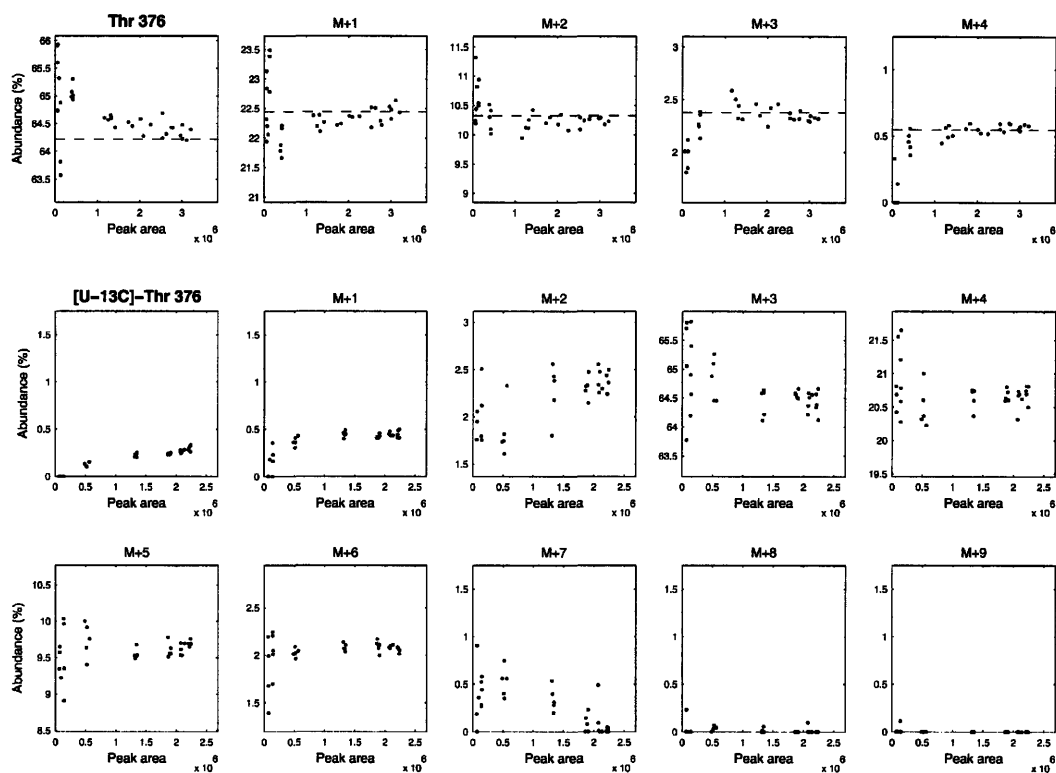
This fragment can be used for quantitative analysis. Note, however, that M+0 is slightly too high (+0.5 mol%) and M+1 is slightly too low (-0.4 mol%).

Threonine (Thr)



$C_{22}H_{51}NO_3Si_3$
Exact Mass: 461.3177

APPENDIX A. GC/MS ANALYSIS OF AMINO ACIDS



Thr 376

Formula : $C_{17}H_{42}O_2NSi_3$
 Exact mass : 376.252
 C-atoms : 2-3-4

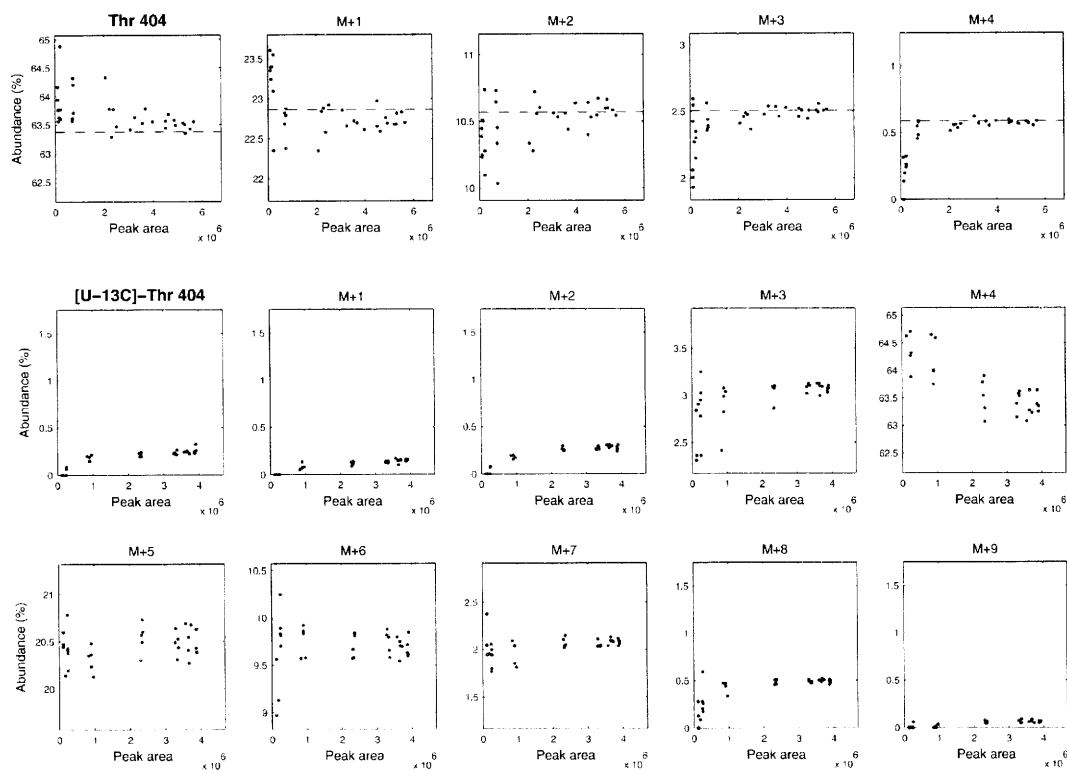
m/z	theory	data	difference
375	0.0	0.0	0.0
376	100.0	100.0	0.0
377	34.9	34.5	-0.4
378	16.1	15.9	-0.2
379	3.7	3.7	0.0
380	0.9	0.7	-0.2
381	0.1	0.0	-0.1
382	0.0	0.0	0.0
383	0.0	0.2	0.2
384	0.0	0.1	0.1
385	0.0	0.0	0.0

[U-¹³C]-Thr

m/z	theory	data	difference
375	0.0	0.0	0.0
376	0.0	0.1	0.1
377	0.0	0.5	0.5
378	3.1	2.8	-0.3
379	100.0	100.0	0.0
380	31.8	31.7	-0.1
381	15.0	14.8	-0.2
382	3.2	3.1	-0.1
383	0.7	0.9	0.2
384	0.1	0.1	0.0
385	0.0	0.0	0.0

This fragment can be used for quantitative analysis. Note, however, that this fragment is noisy at low concentrations.

APPENDIX A. GC/MS ANALYSIS OF AMINO ACIDS



Thr 404

Formula : $C_{18}H_{42}O_3NSi_3$
 Exact mass : 404.247
 C-atoms : 1-2-3-4

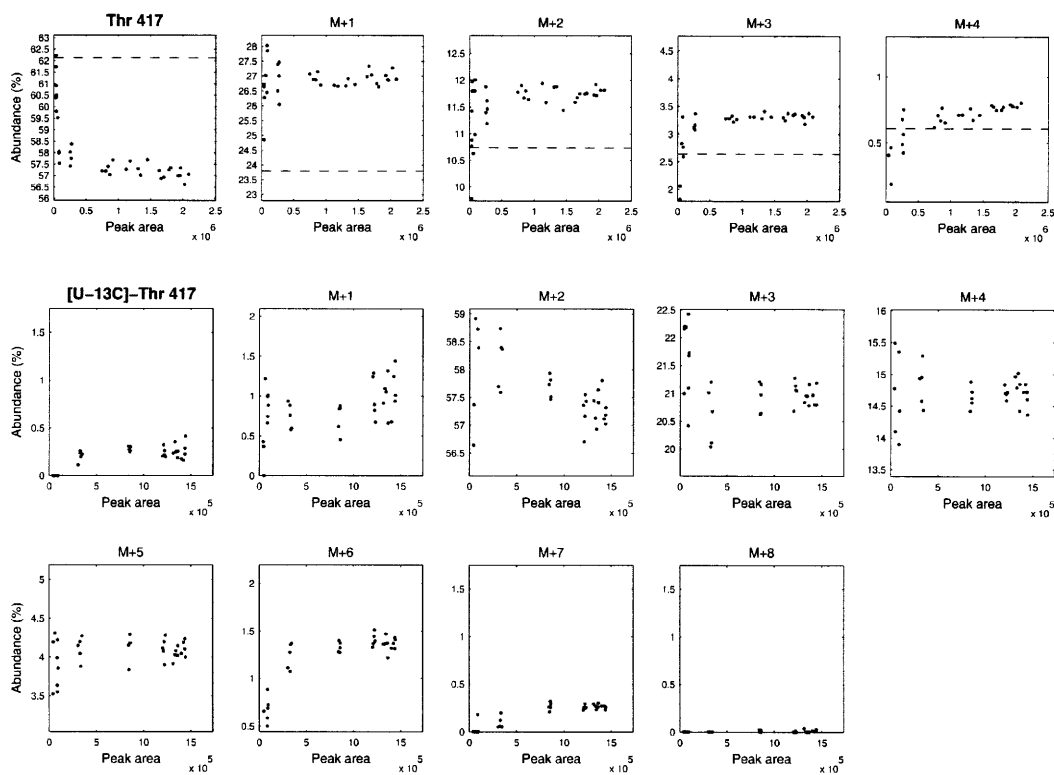
m/z	theory	data	difference
403	0.0	0.0	0.0
404	100.0	100.0	0.0
405	36.1	35.8	-0.3
406	16.7	16.5	-0.2
407	4.0	3.9	-0.1
408	0.9	0.8	-0.1
409	0.2	0.1	-0.1
410	0.0	0.0	0.0
411	0.0	0.0	0.0
412	0.0	0.0	0.0
413	0.0	0.0	0.0
414	0.0	0.0	0.0

[U-¹³C]-Thr

m/z	theory	data	difference
403	0.0	0.0	0.0
404	0.0	0.2	0.2
405	0.0	0.1	0.1
406	0.0	0.2	0.2
407	4.1	4.4	0.3
408	100.0	100.0	0.0
409	31.9	31.6	-0.3
410	15.2	15.2	0.0
411	3.3	3.0	-0.3
412	0.8	0.6	-0.2
413	0.1	0.0	-0.1
414	0.0	0.0	0.0

This fragment can be used for quantitative analysis.

APPENDIX A. GC/MS ANALYSIS OF AMINO ACIDS



Thr 417

Formula : $C_{20}H_{47}NO_2Si_3$
 Exact mass : 417.292
 C-atoms : unknown

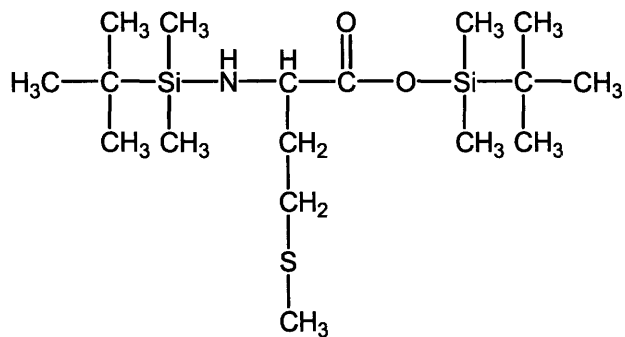
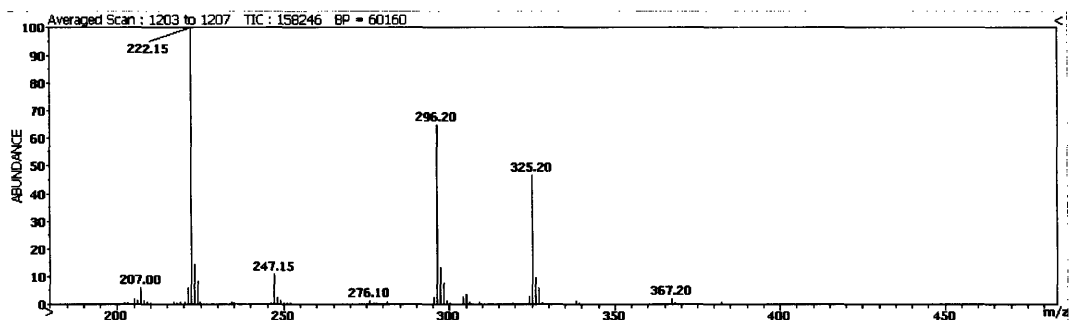
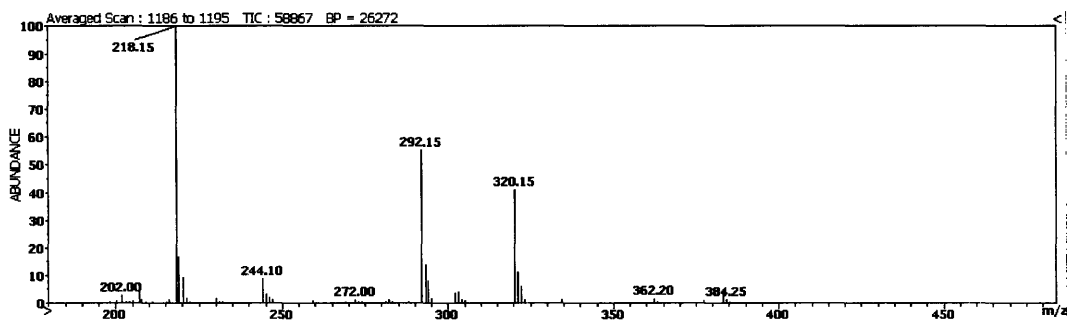
m/z	theory	data	difference
416	0.0	0.0	0.0
417	100.0	100.0	0.0
418	38.3	46.4	8.1
419	17.3	20.1	2.8
420	4.3	5.5	1.2
421	1.0	1.0	0.0
422	0.2	0.0	-0.2
423	0.0	0.0	0.0
424	0.0	0.0	0.0
425	0.0	0.1	0.1

[U-¹³C]-Thr

m/z	theory	data	difference
416	0.0	0.0	0.0
417	0.0	0.3	0.3
418	2.0	1.1	-0.9
419	100.0	100.0	0.0
420	36.2	35.5	-0.7
421	16.4	25.0	8.6
422	3.9	6.9	3.0
423	0.9	1.8	0.9
424	0.1	0.1	0.0
425	0.0	0.0	0.0

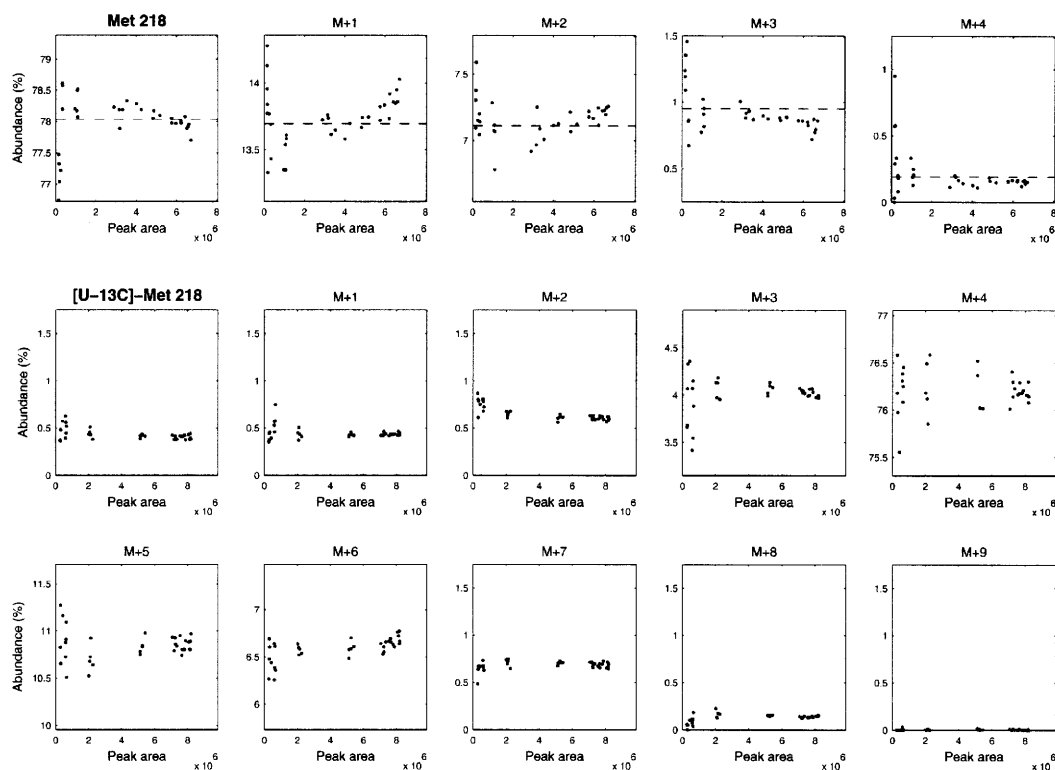
This fragment should not be used. M+0 is too low (-4 mol%) and M+1, M+2, and M+3 are too high.

Methionine (Met)



C₁₇H₃₉NO₂SSi₂
Exact Mass: 377.224

APPENDIX A. GC/MS ANALYSIS OF AMINO ACIDS



Met 218

Formula : $C_{10}H_{24}NSiS$
 Exact mass : 218.114
 C-atoms : 2-3-4-5

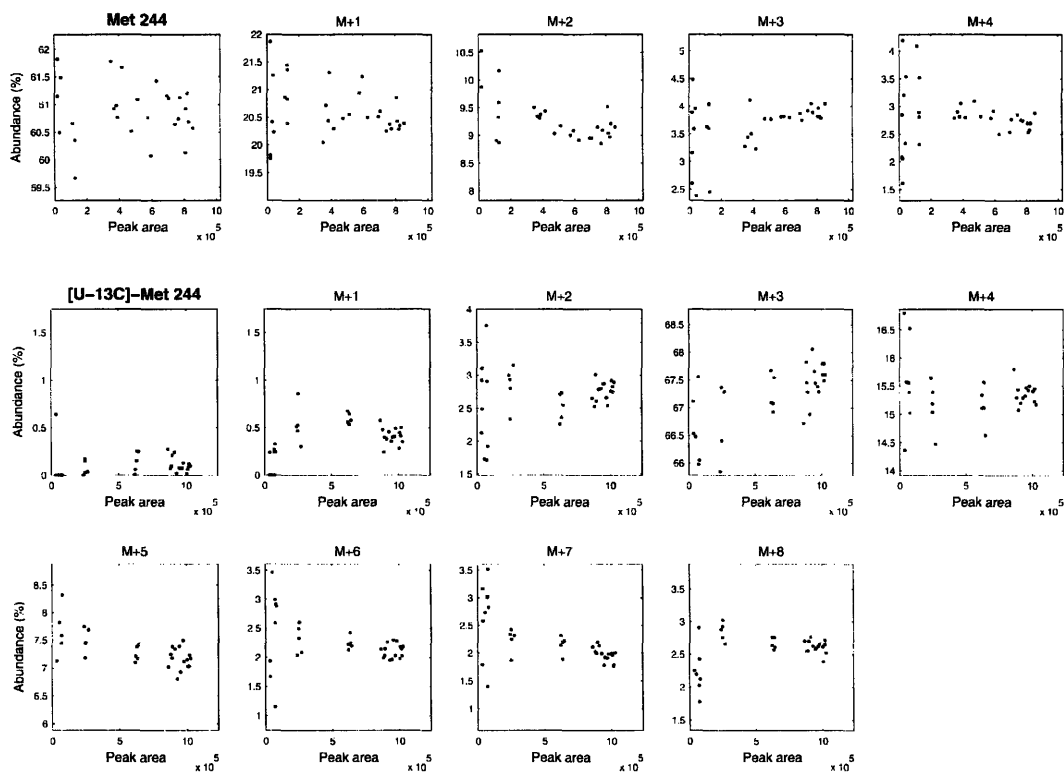
m/z	theory	data	difference
217	0.0	0.0	0.0
218	100.0	100.0	0.0
219	17.6	17.3	-0.3
220	9.1	9.0	-0.1
221	1.2	1.2	0.0
222	0.2	0.3	0.1
223	0.0	0.1	0.1
224	0.0	0.0	0.0
225	0.0	0.0	0.0
226	0.0	0.0	0.0
227	0.0	0.0	0.0

[U-¹³C]-Met

m/z	theory	data	difference
217	0.0	0.7	0.7
218	0.0	0.6	0.6
219	0.0	0.6	0.6
220	0.0	0.9	0.9
221	4.1	5.3	1.2
222	100.0	100.0	0.0
223	13.5	14.1	0.6
224	8.5	8.5	0.0
225	0.8	0.9	0.1
226	0.2	0.2	0.0
227	0.0	0.0	0.0

This fragment can be used for quantitative analysis.

APPENDIX A. GC/MS ANALYSIS OF AMINO ACIDS

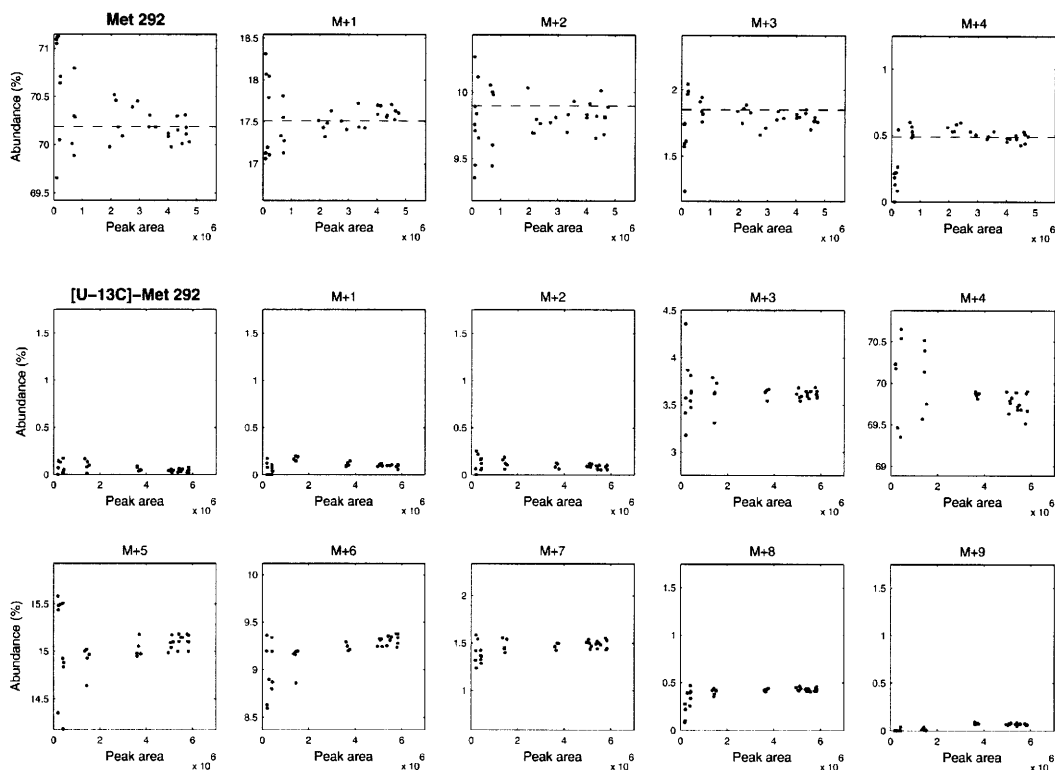


Met 244			
Formula :	unknown		
Exact mass :	unknown		
C-atoms :	unknown		
m/z	theory	data	difference
243		0.1	
244		100.0	
245		34.4	
246		15.5	
247	n/a	5.5	n/a
248		5.1	
249		3.5	
250		1.2	
251		0.2	
252		0.3	

[U- ¹³ C]-Met			
m/z	theory	data	difference
243		0.1	
244		0.2	
245		0.8	
246		3.9	
247	n/a	100.0	n/a
248		23.1	
249		11.8	
250		3.8	
251		3.8	
252		4.1	

This fragment cannot be used because the fragmentation is unknown. However, the relatively high M+1 (34% of M+0) suggests that two fragments are overlapping here.

APPENDIX A. GC/MS ANALYSIS OF AMINO ACIDS



Met 292

Formula : $C_{12}H_{30}NOSi_2S$
 Exact mass : 292.159
 C-atoms : 2-3-4-5

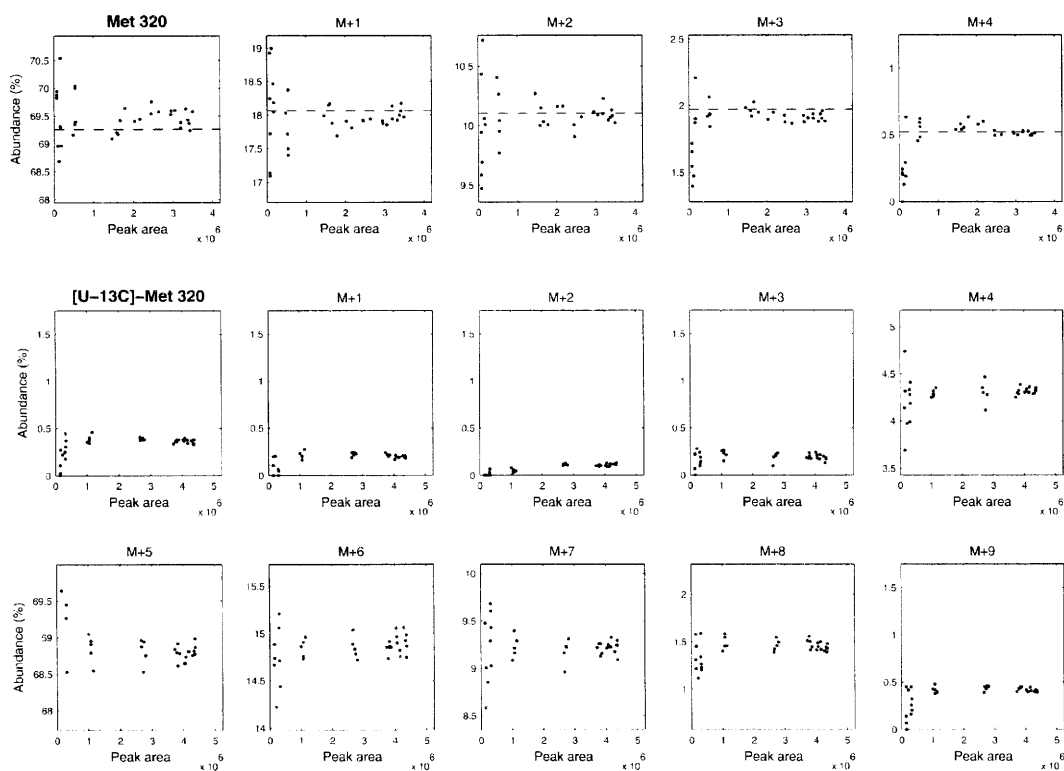
m/z	theory	data	difference
291	0.0	0.0	0.0
292	100.0	100.0	0.0
293	25.0	24.8	-0.2
294	14.1	14.0	-0.1
295	2.6	2.6	0.0
296	0.7	0.8	0.1
297	0.1	0.1	0.0
298	0.0	0.0	0.0
299	0.0	2.1	2.1
300	0.0	0.5	0.5
301	0.0	0.2	0.2

[U- ^{13}C]-Met

m/z	theory	data	difference
291	0.0	0.0	0.0
292	0.0	0.1	0.1
293	0.0	0.2	0.2
294	0.0	0.2	0.2
295	4.1	5.1	1.0
296	100.0	100.0	0.0
297	20.9	21.1	0.2
298	13.1	12.8	-0.3
299	2.1	2.0	-0.1
300	0.6	0.5	-0.1
301	0.1	0.0	-0.1

This fragment can be used for quantitative analysis. Mass isotopomer distributions should be obtained from the mass range 292-298.

APPENDIX A. GC/MS ANALYSIS OF AMINO ACIDS



Met 320

Formula : $C_{13}H_{30}NO_2Si_2S$
 Exact mass : 320.154
 C-atoms : 1-2-3-4-5

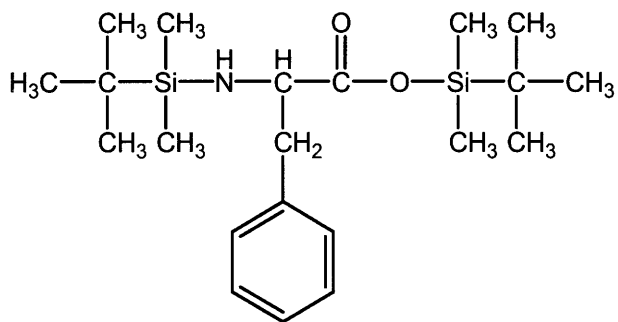
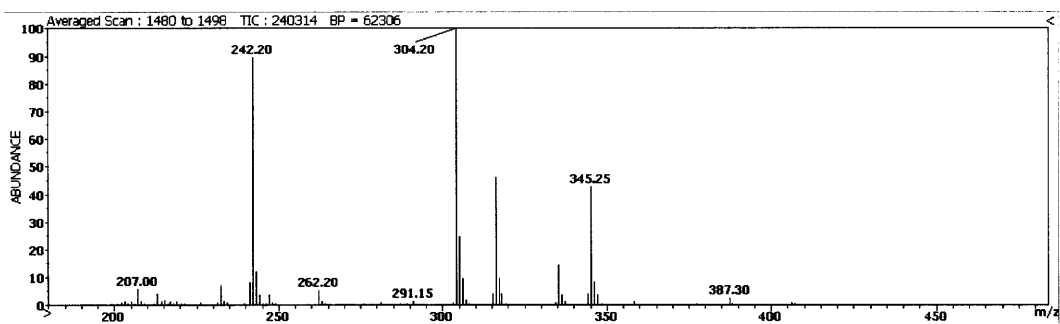
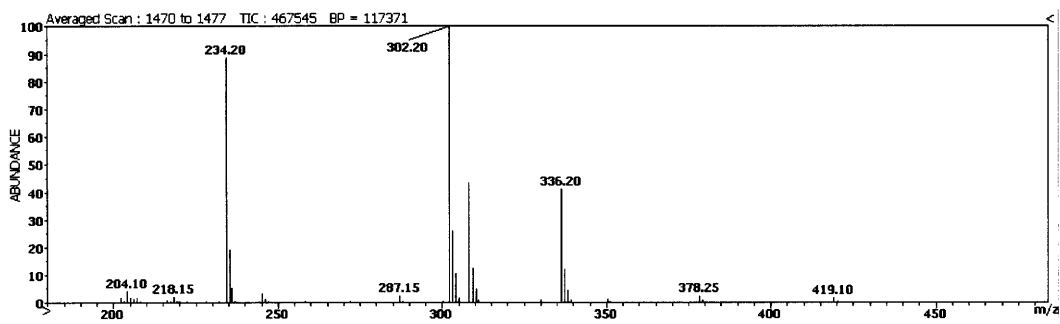
m/z	theory	data	difference
319	0.0	0.0	0.0
320	100.0	100.0	0.0
321	26.1	25.9	-0.2
322	14.6	14.5	-0.1
323	2.8	2.8	0.0
324	0.8	0.8	0.1
325	0.1	0.1	0.0
326	0.0	0.0	0.0
327	0.0	0.0	0.0
328	0.0	0.3	0.3
329	0.0	0.1	0.1
330	0.0	0.2	0.2
331	0.0	0.1	0.1

[U-¹³C]-Met

m/z	theory	data	difference
319	0.0	1.4	1.4
320	0.0	0.5	0.5
321	0.0	0.3	0.3
322	0.0	0.1	0.1
323	0.0	0.3	0.3
324	5.2	6.2	1.0
325	100.0	100.0	0.0
326	21.1	21.4	0.3
327	13.3	13.4	0.1
328	2.1	2.1	0.0
329	0.6	0.6	0.0
330	0.1	0.0	-0.1
331	0.0	0.0	0.0

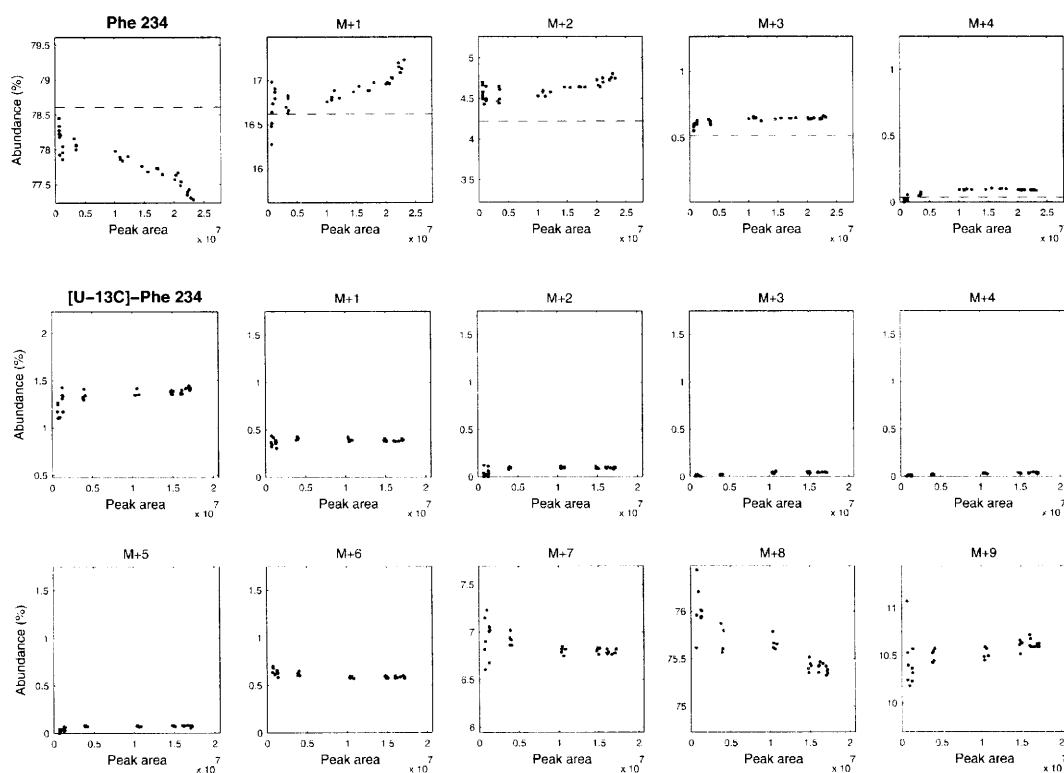
This fragment can be used for quantitative analysis. Mass isotopomer distributions should be obtained from the mass range 320-327.

Phenylalanine (Phe)



C₂₁H₃₉NO₂Si₂
Exact Mass: 393.2519

APPENDIX A. GC/MS ANALYSIS OF AMINO ACIDS



Phe 234

Formula : $C_{14}H_{24}NSi$
 Exact mass : 234.168
 C-atoms : 2-3-4-5-6-7-8-9

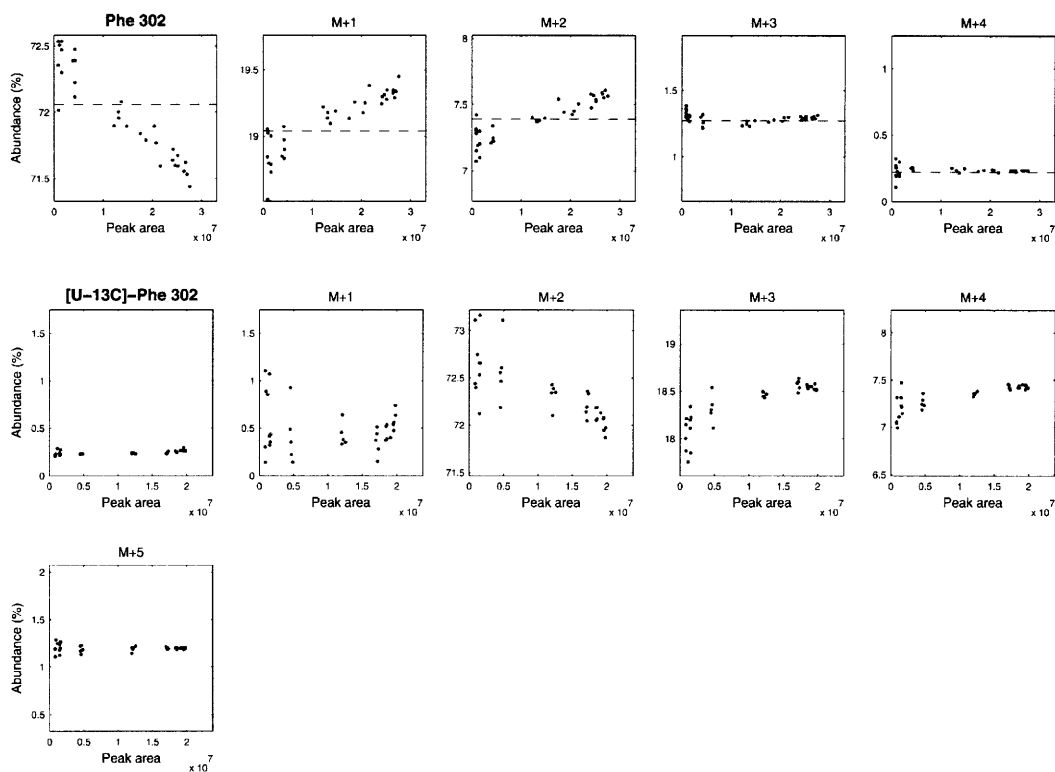
m/z	theory	data	difference
233	0.0	0.0	0.0
234	100.0	100.0	0.0
235	21.1	21.3	0.2
236	5.4	5.7	0.3
237	0.7	0.8	0.1
238	0.0	0.1	0.1
239	0.0	0.0	0.0
240	0.0	0.0	0.0
241	0.0	0.0	0.0
242	0.0	0.0	0.0
243	0.0	0.1	0.1
244	0.0	0.5	0.5
245	0.0	3.7	3.7
246	0.0	1.4	1.4

[U-¹³C]-Phe

m/z	theory	data	difference
233	0.0	4.1	4.1
234	0.0	1.7	1.7
235	0.0	0.5	0.5
236	0.0	0.1	0.1
237	0.0	0.0	0.0
238	0.0	0.0	0.0
239	0.0	0.1	0.1
240	0.0	0.8	0.8
241	8.6	9.2	0.6
242	100.0	100.0	0.0
243	12.6	13.7	1.1
244	3.9	4.2	0.3
245	0.3	0.6	0.3
246	0.0	0.6	0.6

This fragment can be used for quantitative analysis. Mass isotopomer distributions should be obtained from the mass range 234-243.

APPENDIX A. GC/MS ANALYSIS OF AMINO ACIDS



Phe 302

Formula : $C_{14}H_{32}O_2NSi_2$
 Exact mass : 302.197
 C-atoms : 1-2

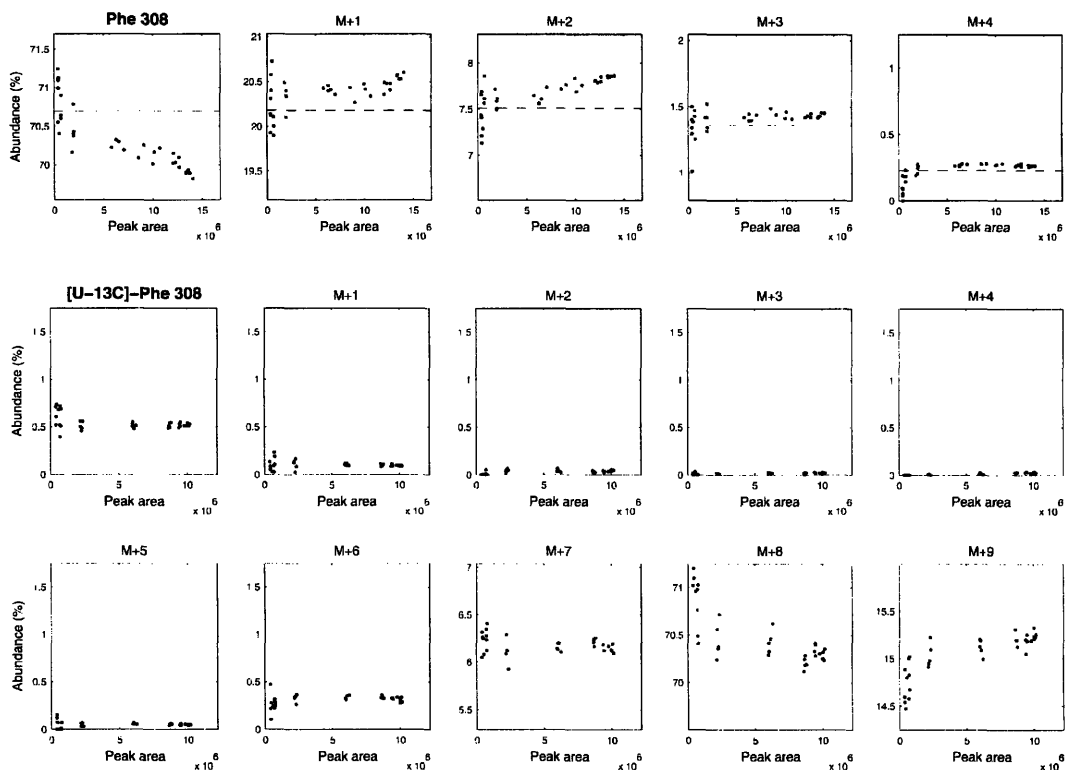
m/z	theory	data	difference
301	0.0	0.0	0.0
302	100.0	100.0	0.0
303	26.4	26.1	-0.3
304	10.3	9.9	-0.4
305	1.8	1.7	-0.1
306	0.3	0.3	0.0
307	0.0	0.0	0.0

[U-¹³C]-Phe

m/z	theory	data	difference
301	0.0	0.0	0.0
302	0.0	0.3	0.3
303	2.0	0.6	-1.4
304	100.0	100.0	0.0
305	24.3	25.0	0.7
306	9.7	9.9	0.2
307	1.5	1.6	0.1

This fragment can be used for quantitative analysis.

APPENDIX A. GC/MS ANALYSIS OF AMINO ACIDS



Phe 308

Formula : $C_{16}H_{30}ONSi_2$
 Exact mass : 308.187
 C-atoms : 2-3-4-5-6-7-8-9

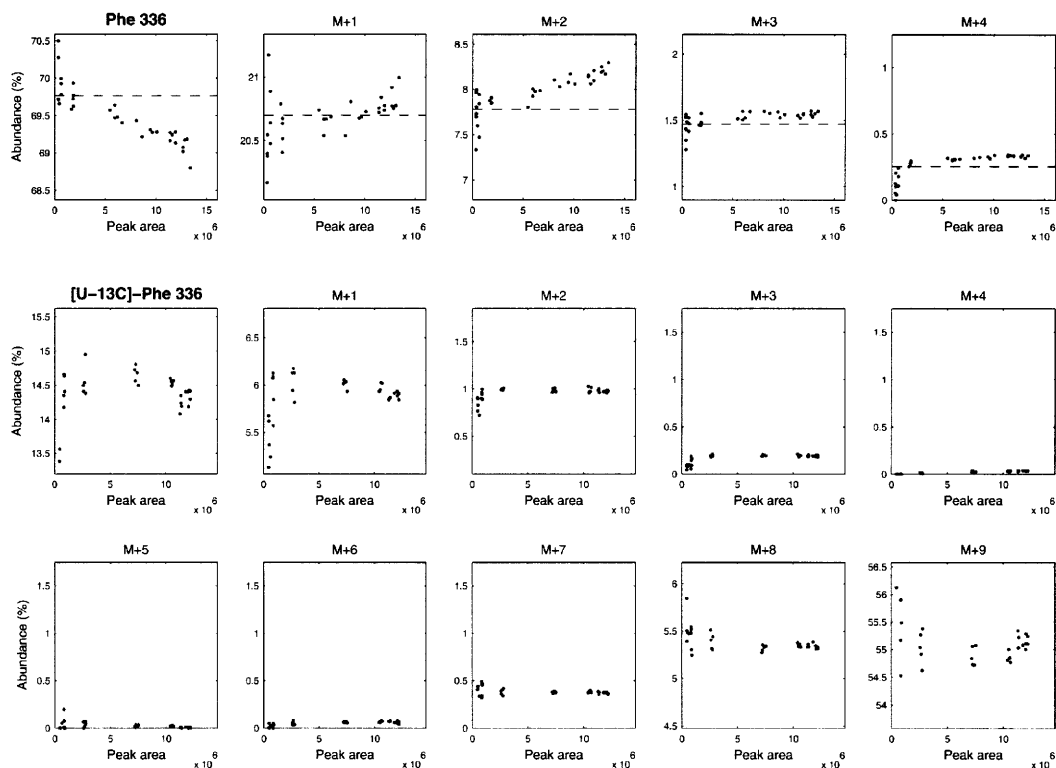
m/z	theory	data	difference
307	0.0	0.0	0.0
308	100.0	100.0	0.0
309	28.5	28.8	0.3
310	10.6	10.6	0.0
311	1.9	2.0	0.1
312	0.3	0.4	0.1
313	0.0	0.0	0.0
314	0.0	0.0	0.0
315	0.0	0.0	0.0
316	0.0	0.0	0.0
317	0.0	0.4	0.4
318	0.0	0.3	0.3
319	0.0	0.1	0.1
320	0.0	0.2	0.2
321	0.0	0.1	0.1

[U- ^{13}C]-Phe

m/z	theory	data	difference
307	0.0	3.5	3.5
308	0.0	0.8	0.8
309	0.0	0.2	0.2
310	0.0	0.1	0.1
311	0.0	0.0	0.0
312	0.0	0.0	0.0
313	0.0	0.1	0.1
314	0.0	0.4	0.4
315	8.5	8.7	0.2
316	100.0	100.0	0.0
317	20.2	21.1	0.9
318	8.5	8.8	0.3
319	1.1	1.3	0.2
320	0.2	0.2	0.0
321	0.0	0.0	0.0

This fragment can be used for quantitative analysis. Mass isotopomer distributions should be obtained from the mass range 308-316.

APPENDIX A. GC/MS ANALYSIS OF AMINO ACIDS



Phe 336

Formula : $C_{17}H_{30}O_2NSi_2$
 Exact mass : 336.182
 C-atoms : 1-2-3-4-5-6-7-8-9

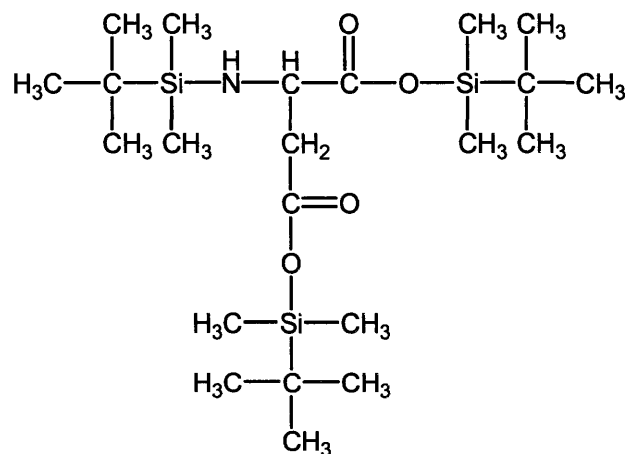
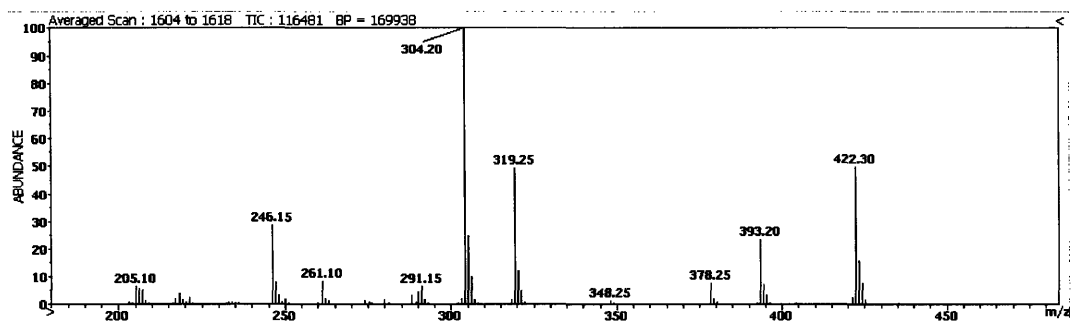
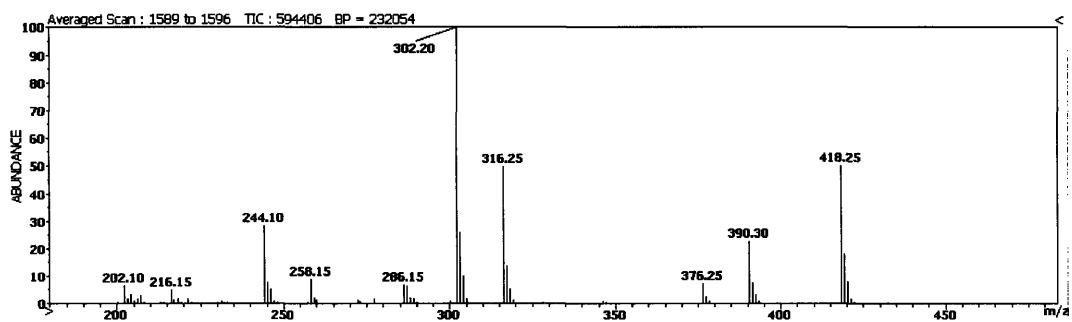
m/z	theory	data	difference
335	0.0	0.0	0.0
336	100.0	100.0	0.0
337	29.7	29.4	-0.3
338	11.2	11.1	-0.1
339	2.1	2.1	0.0
340	0.4	0.4	0.0
341	0.0	0.1	0.1
342	0.0	0.1	0.1
343	0.0	0.0	0.0
344	0.0	0.0	0.0
345	0.0	0.1	0.1
346	0.0	0.1	0.1
347	0.0	0.1	0.1
348	0.0	0.0	0.0
349	0.0	0.4	0.4

[U-¹³C]-Phe

m/z	theory	data	difference
335	0.0	108.4	108.4
336	0.0	26.4	26.4
337	0.0	10.9	10.9
338	0.0	1.8	1.8
339	0.0	0.3	0.3
340	0.0	0.0	0.0
341	0.0	0.1	0.1
342	0.0	0.1	0.1
343	0.0	0.7	0.7
344	9.7	9.8	0.1
345	100.0	100.0	0.0
346	20.3	20.8	0.5
347	8.7	8.9	0.2
348	1.1	1.3	0.2
349	0.2	0.2	0.0

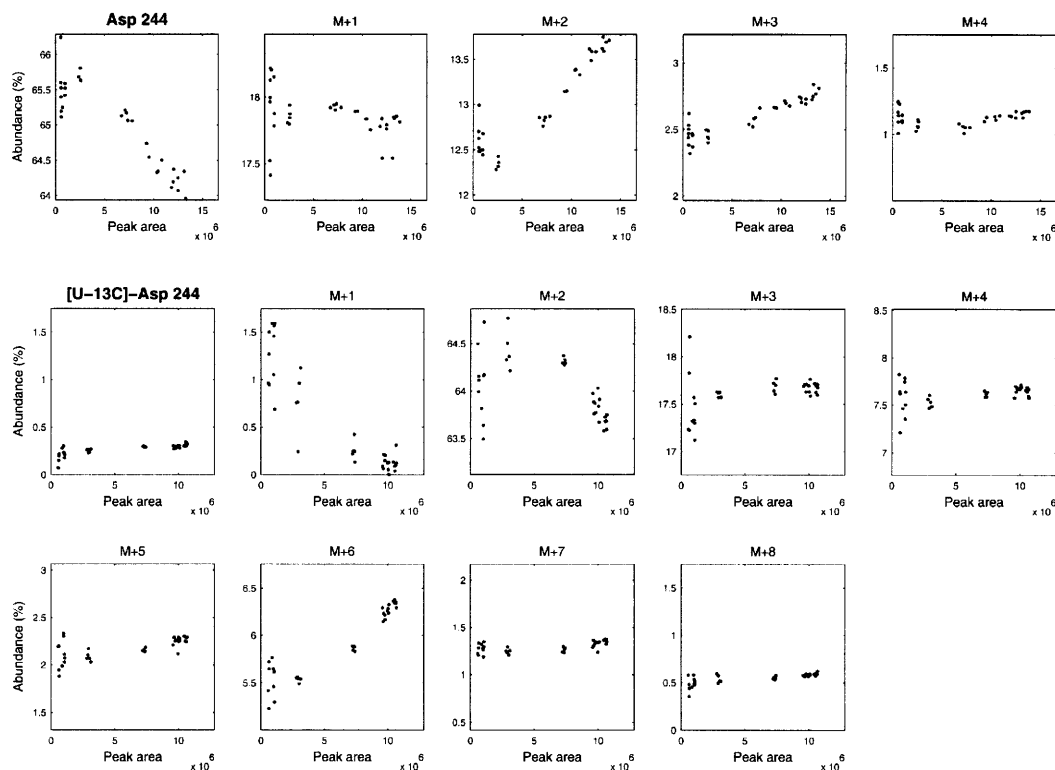
This fragment can be used for quantitative analysis. Phenylalanine must not be M+9 or M+8 labeled for this fragment to be accurate.

Aspartate (Asp)



C₂₂H₄₉NO₄Si₃
 Exact Mass: 475.2969

APPENDIX A. GC/MS ANALYSIS OF AMINO ACIDS



Asp 244

Formula : unknown
 Exact mass : unknown
 C-atoms : unknown

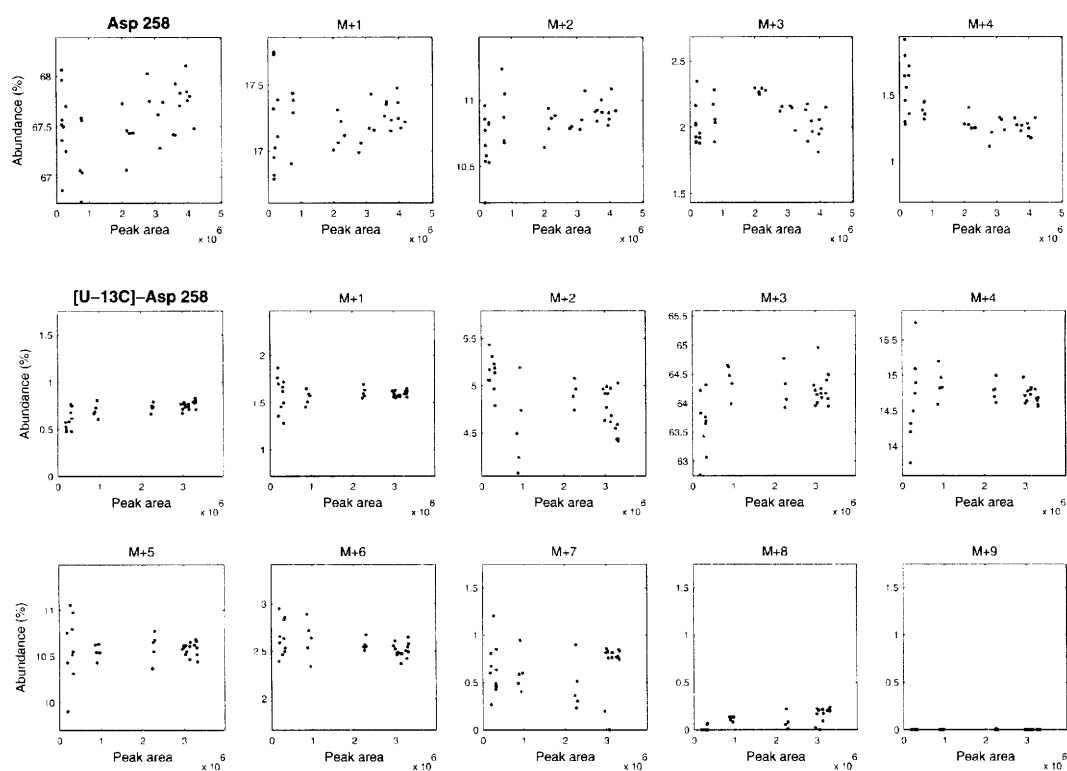
m/z	theory	data	difference
243		0.0	
244		100.0	
245		27.2	
246		18.3	
247	n/a	3.6	n/a
248		1.6	
249		0.7	
250		0.2	
251		0.0	
252		0.0	

[U-¹³C]-Asp

m/z	theory	data	difference
243		0.1	
244		0.3	
245		1.8	
246		100.0	
247	n/a	27.2	n/a
248		11.7	
249		3.2	
250		8.2	
251		1.9	
252		0.8	

This fragment should not be used. The relatively high M+2 (18% of M+0) suggests that two fragments are overlapping. [4-¹³C]-aspartate contains peaks at 244 and 247, which further suggests that two fragments are overlapping.

APPENDIX A. GC/MS ANALYSIS OF AMINO ACIDS



Asp 258

Formula : unknown
 Exact mass : unknown
 C-atoms : unknown

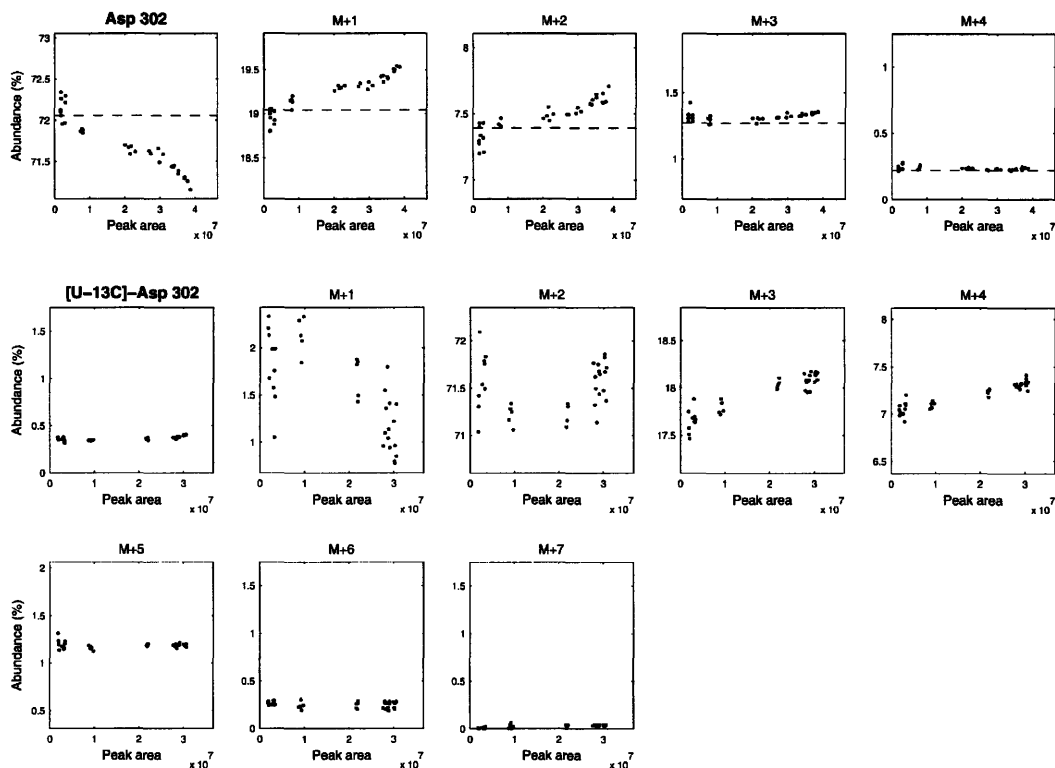
m/z	theory	data	difference
257		4.4	
258		100.0	
259		25.6	
260		16.0	
261	n/a	3.3	n/a
262		2.1	
263		1.8	
264		0.5	
265		0.0	
266		0.0	
267		0.0	

[U-¹³C]-Asp

m/z	theory	data	difference
257		1.8	
258		1.0	
259		2.4	
260		7.6	
261	n/a	100.0	n/a
262		23.2	
263		16.6	
264		4.2	
265		0.8	
266		0.1	
267		0.0	

This fragment should not be used. M-1 is too high (4.4 mol%) and the fragmentation is unknown. [4-¹³C]-aspartate contains a peak at 259 but not at 258, thus this fragment contains C-4.

APPENDIX A. GC/MS ANALYSIS OF AMINO ACIDS



Asp 302

Formula : $C_{14}H_{32}O_2NSi_2$
 Exact mass : 302.197
 C-atoms : 1-2

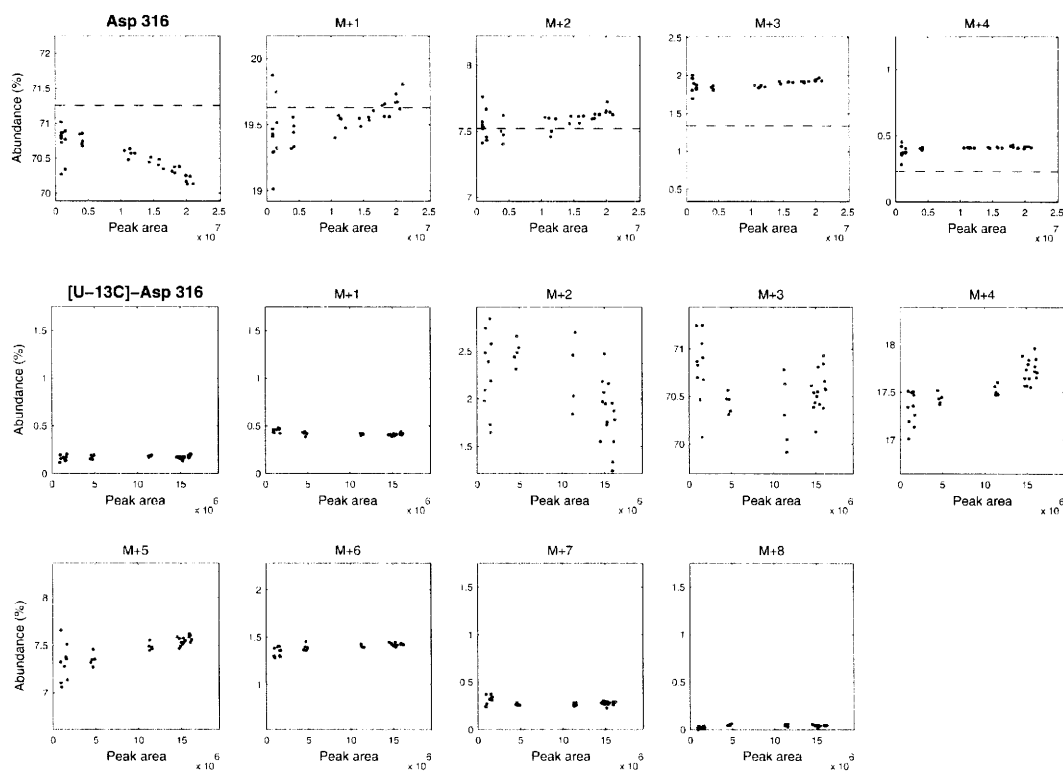
m/z	theory	data	difference
301	0.0	0.0	0.0
302	100.0	100.0	0.0
303	26.4	26.4	0.0
304	10.3	10.2	-0.1
305	1.8	1.8	0.0
306	0.3	0.3	0.0
307	0.0	0.0	0.0
308	0.0	0.0	0.0
309	0.0	0.0	0.0

[U-¹³C]-Asp

m/z	theory	data	difference
301	0.0	0.0	0.0
302	0.0	0.5	0.5
303	2.0	3.1	1.1
304	100.0	100.0	0.0
305	24.3	24.7	0.4
306	9.7	9.8	0.1
307	1.5	1.6	0.1
308	0.3	0.4	0.1
309	0.0	0.0	0.0

This fragment can be used for quantitative analysis. [U-¹³C]-aspartate contains a peak at 302 but not at 303, thus this fragment does not contain C-4.

APPENDIX A. GC/MS ANALYSIS OF AMINO ACIDS



Asp 316

Formula : $C_{15}H_{34}NO_2Si_2$
 Exact mass : 316.213
 C-atoms : 2-3-4

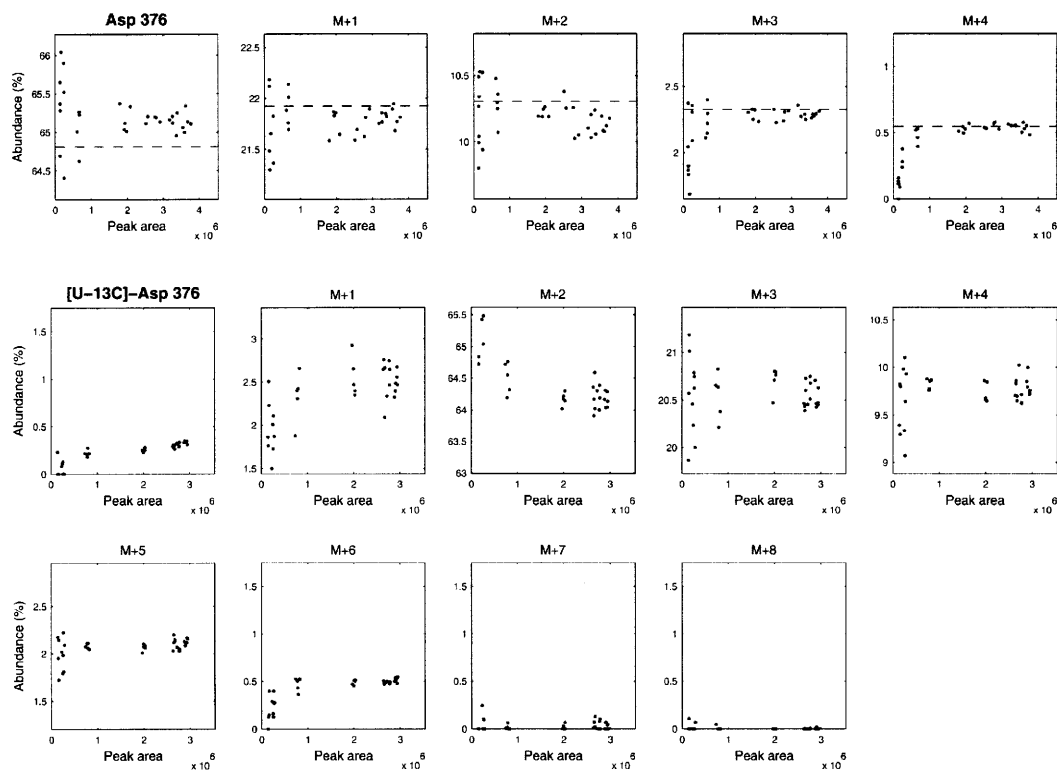
m/z	theory	data	difference
315	0.0	0.0	0.0
316	100.0	100.0	0.0
317	27.5	27.3	-0.2
318	10.6	10.5	-0.1
319	1.9	2.6	0.7
320	0.3	0.6	0.3
321	0.0	0.1	0.1
322	0.0	0.0	0.0
323	0.0	0.0	0.0
324	0.0	0.0	0.0

[U-¹³C]-Asp

m/z	theory	data	difference
315	0.0	0.0	0.0
316	0.0	0.2	0.2
317	0.0	0.6	0.6
318	3.1	3.7	0.6
319	100.0	100.0	0.0
320	24.4	24.5	0.1
321	9.7	10.3	0.6
322	1.5	1.9	0.4
323	0.3	0.4	0.1
324	0.0	0.1	0.1

This fragment should not be used. It has a significant bias, M+0 is too low (-0.3 mol%) and M+3 is too high (+0.7 mol%). [U-¹³C]-aspartate contains a peak at 317 but not at 316, thus this fragment contains C-4.

APPENDIX A. GC/MS ANALYSIS OF AMINO ACIDS



Asp 376

Formula : $C_{16}H_{38}O_3NSi_3$
 Exact mass : 376.216
 C-atoms : 1-2

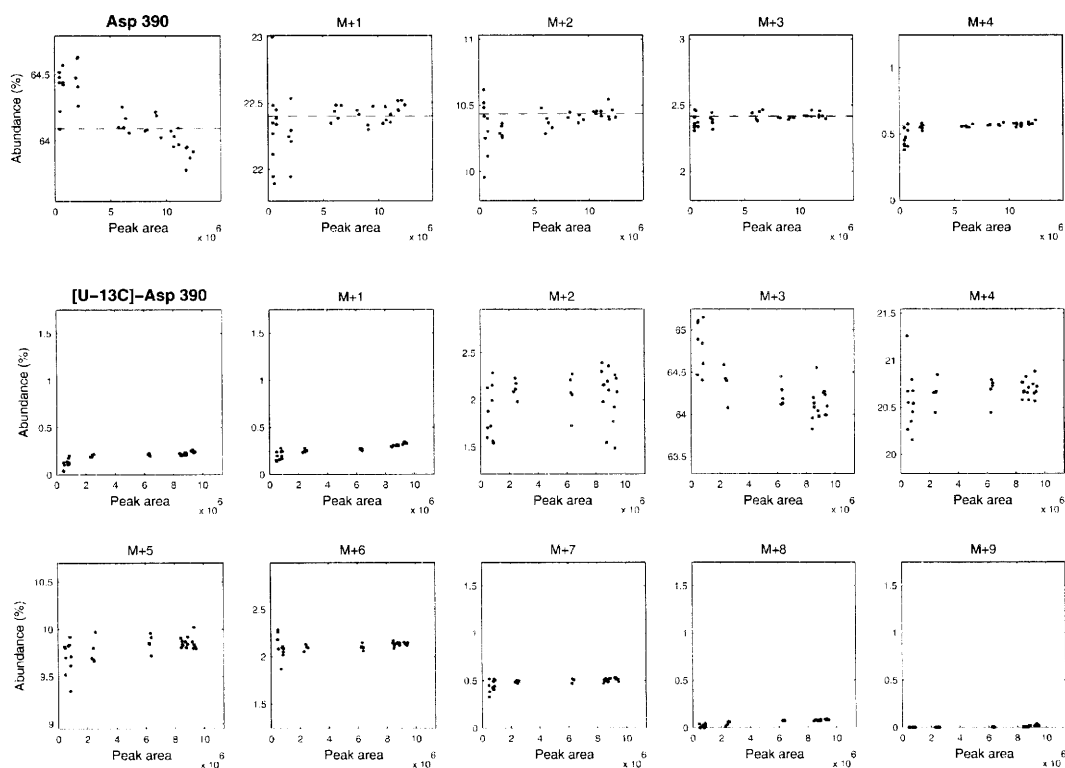
m/z	theory	data	difference
375	0.0	0.1	0.1
376	100.0	100.0	0.0
377	33.8	33.5	-0.3
378	15.9	15.8	-0.1
379	3.6	3.4	-0.2
380	0.8	0.7	-0.1
381	0.1	0.0	-0.1
382	0.0	0.0	0.0
383	0.0	0.1	0.1
384	0.0	0.0	0.0

[U-¹³C]-Asp

m/z	theory	data	difference
375	0.0	0.0	0.0
376	0.0	0.2	0.2
377	2.0	3.2	1.2
378	100.0	100.0	0.0
379	31.7	31.7	0.0
380	15.2	15.0	-0.2
381	3.3	3.1	-0.2
382	0.8	0.5	-0.3
383	0.1	0.0	-0.1
384	0.0	0.0	0.0

This fragment can be used for quantitative analysis. [4-¹³C]-aspartate contains a peak at 376 but not at 377, thus this fragment does not contain C-4.

APPENDIX A. GC/MS ANALYSIS OF AMINO ACIDS



Asp 390

Formula : $C_{17}H_{40}O_3NSi_3$
 Exact mass : 390.232
 C-atoms : 2-3-4

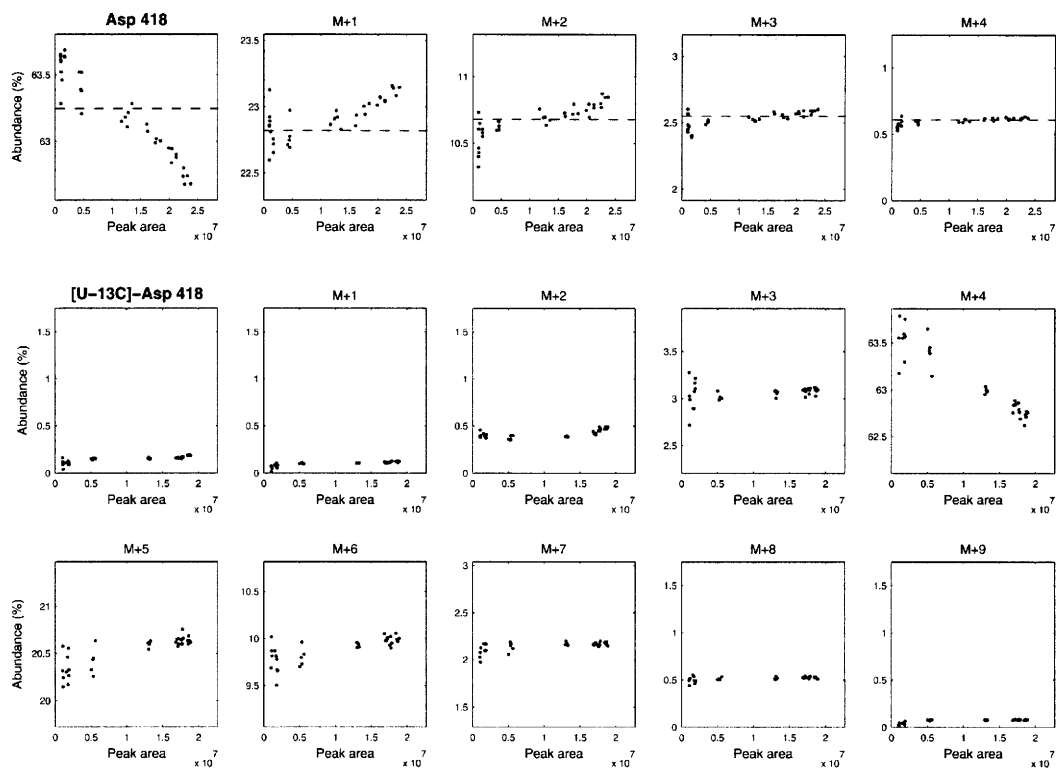
m/z	theory	data	difference
389	0.0	0.0	0.0
390	100.0	100.0	0.0
391	35.0	34.8	-0.2
392	16.3	16.1	-0.2
393	3.8	3.7	-0.1
394	0.9	0.8	-0.1
395	0.1	0.0	-0.1
396	0.0	0.0	0.0
397	0.0	0.0	0.0
398	0.0	0.0	0.0
399	0.0	0.0	0.0

[U-¹³C]-Asp

m/z	theory	data	difference
389	0.0	0.0	0.0
390	0.0	0.2	0.2
391	0.0	0.3	0.3
392	3.1	3.1	0.0
393	100.0	100.0	0.0
394	31.8	31.8	0.0
395	15.2	15.0	-0.2
396	3.3	3.2	-0.1
397	0.8	0.7	-0.1
398	0.1	0.0	-0.1
399	0.0	0.0	0.0

This fragment can be used for quantitative analysis. [4-¹³C]-aspartate contains a peak at 391 but not at 390, thus this fragment contains C-4.

APPENDIX A. GC/MS ANALYSIS OF AMINO ACIDS



Asp 418

Formula : $C_{18}H_{40}O_4NSI_3$
 Exact mass : 418.227
 C-atoms : 1-2-3-4

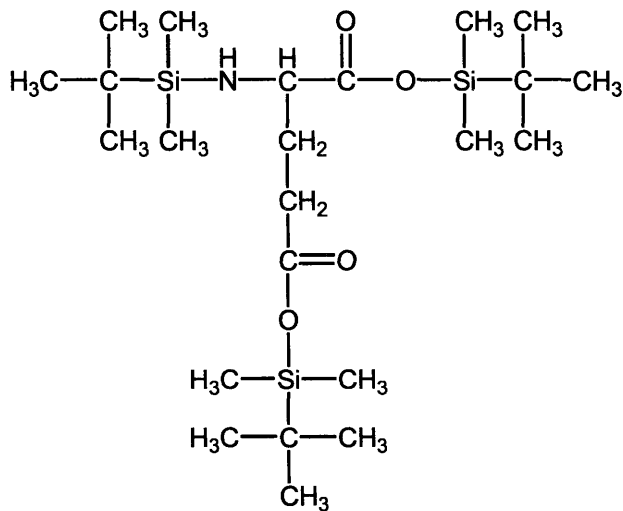
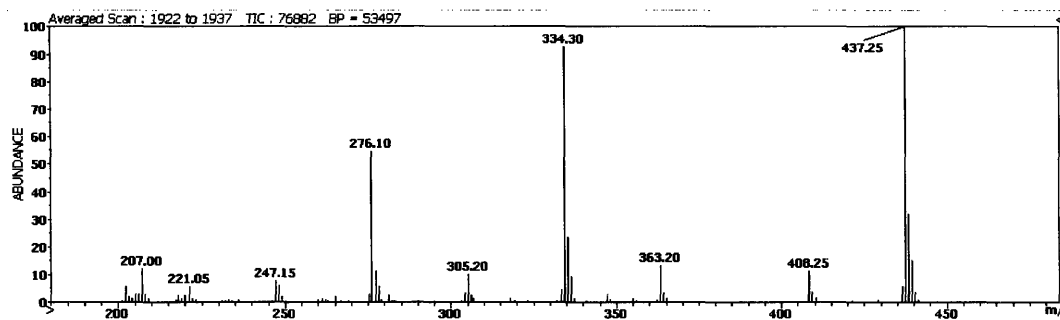
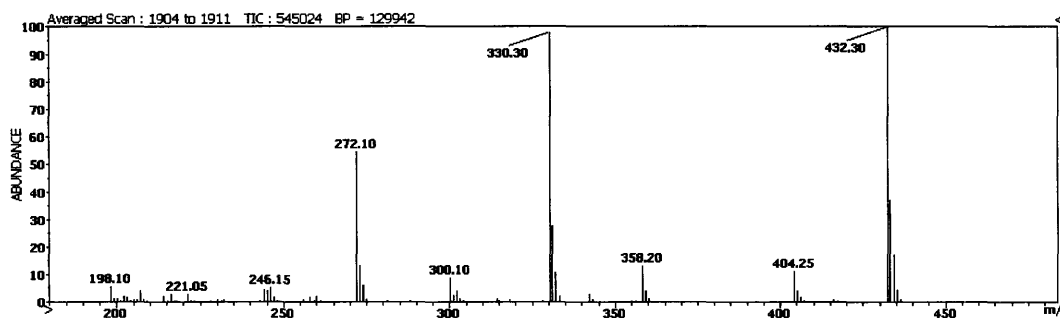
m/z	theory	data	difference
417	0.0	0.0	0.0
418	100.0	100.0	0.0
419	36.1	35.8	-0.3
420	16.9	16.7	-0.2
421	4.0	3.9	-0.1
422	1.0	0.9	-0.1
423	0.2	0.1	-0.1
424	0.0	0.0	0.0
425	0.0	0.0	0.0
426	0.0	0.0	0.0
427	0.0	0.0	0.0
428	0.0	0.0	0.0

[U-¹³C]-Asp

m/z	theory	data	difference
417	0.0	0.0	0.0
418	0.0	0.2	0.2
419	0.0	0.1	0.1
420	0.0	0.6	0.6
421	4.1	4.7	0.6
422	100.0	100.0	0.0
423	31.9	31.9	0.0
424	15.4	15.3	-0.1
425	3.3	3.3	0.0
426	0.8	0.8	0.0
427	0.1	0.1	0.0
428	0.0	0.0	0.0

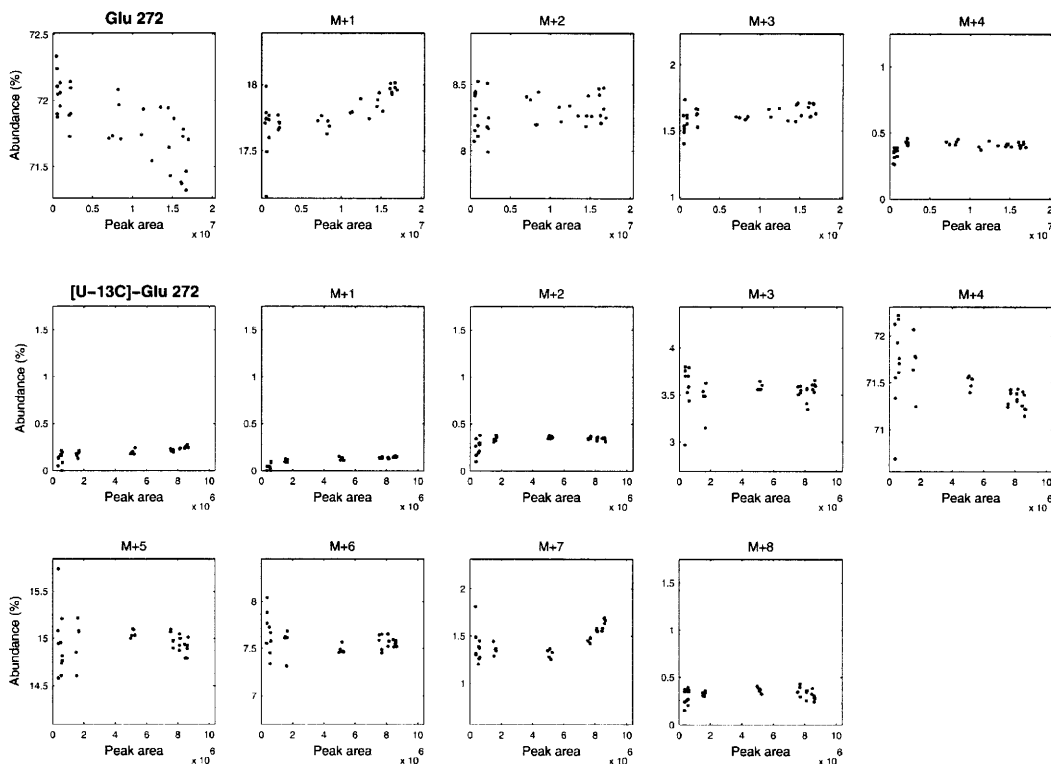
This fragment can be used for quantitative analysis. [4-¹³C]-aspartate contains a peak at 419 but not at 418, thus this fragment contains C-4.

Glutamate (Glu)



C₂₃H₅₁NO₄Si₃
 Exact Mass: 489.3126

APPENDIX A. GC/MS ANALYSIS OF AMINO ACIDS



Glu 272

Formula : unknown
 Exact mass : unknown
 C-atoms : unknown

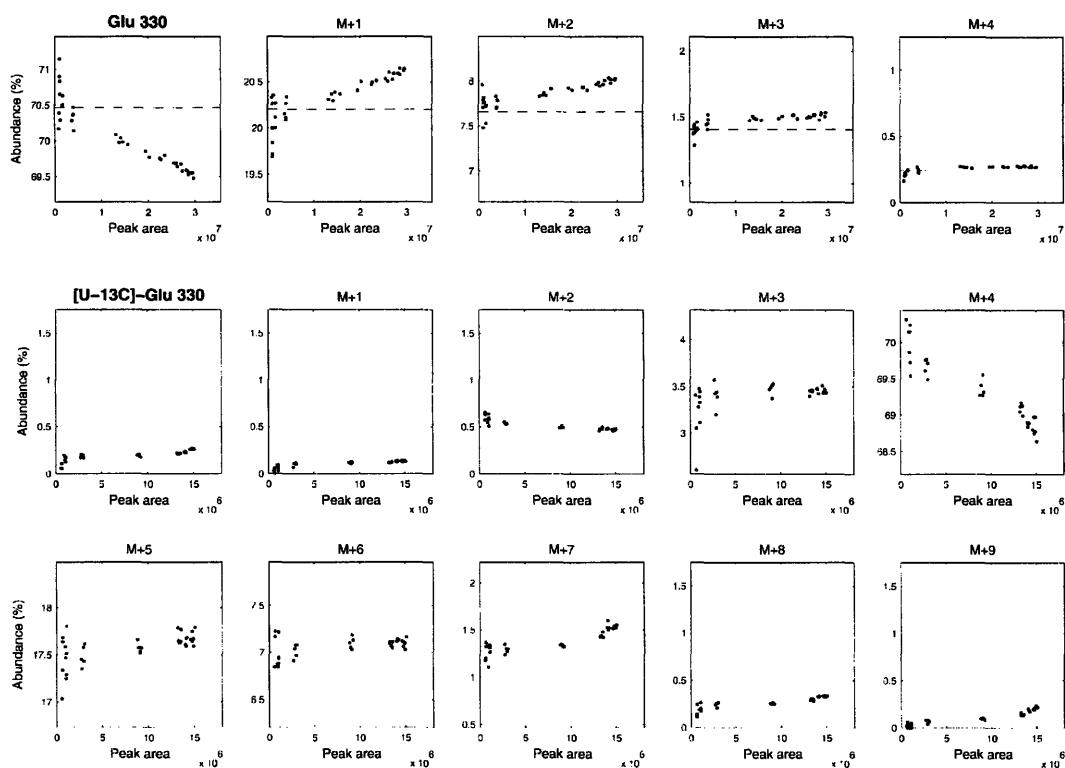
m/z	theory	data	difference
271		0.0	
272		100.0	
273		24.4	
274		11.5	
275	n/a	2.2	n/a
276		0.6	
277		0.1	
278		0.0	
279		0.1	
280		0.0	

[U-¹³C]-Glu

m/z	theory	data	difference
271		0.0	
272		0.2	
273		0.1	
274		0.4	
275	n/a	4.9	n/a
276		100.0	
277		20.8	
278		10.5	
279		1.7	
280		0.5	

This fragment cannot be used because the fragmentation is unknown. [5-¹³C]-glutamine contains a peak at 273 but not at 272, thus this fragment contains C-5. Fragment Glu-432 is preferred.

APPENDIX A. GC/MS ANALYSIS OF AMINO ACIDS



Glu 330

Formula : $C_{16}H_{36}O_2NSi_2$
 Exact mass : 330.228
 C-atoms : 2-3-4-5

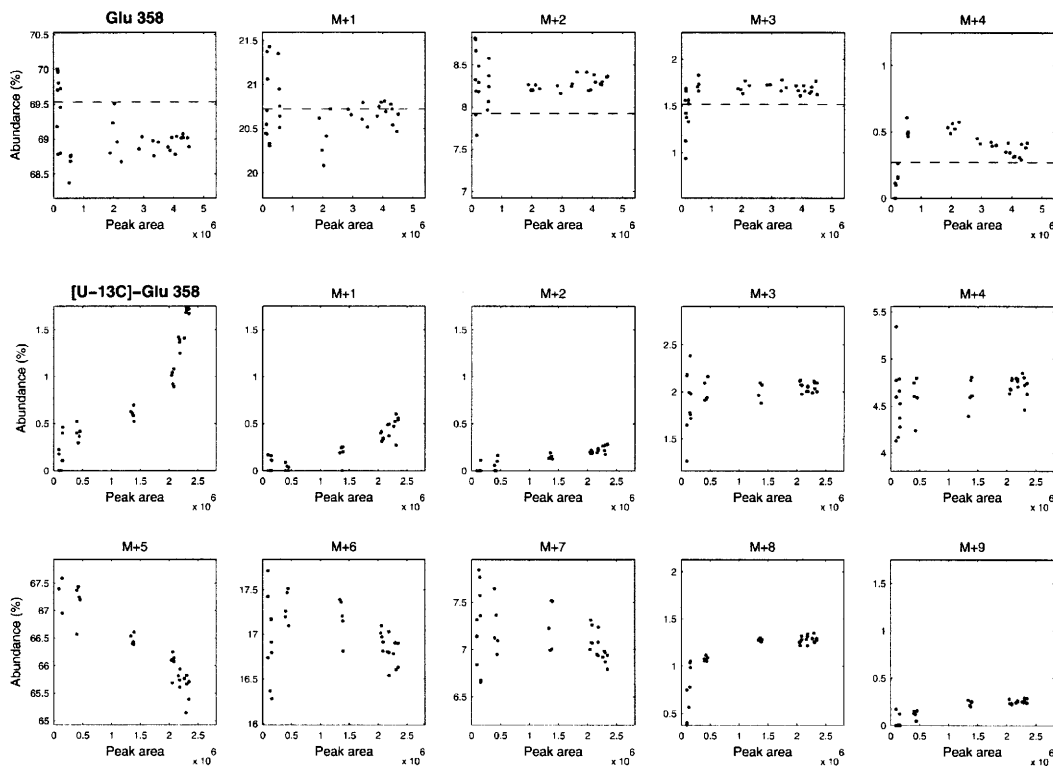
m/z	theory	data	difference
329	0.0	0.0	0.0
330	100.0	100.0	0.0
331	28.7	28.5	-0.2
332	10.9	10.9	0.0
333	2.0	2.1	0.1
334	0.3	0.3	0.0
335	0.0	0.0	0.0
336	0.0	0.0	0.0
337	0.0	0.4	0.4
338	0.0	0.1	0.1
339	0.0	0.1	0.1

[U-¹³C]-Glu

m/z	theory	data	difference
329	0.0	0.0	0.0
330	0.0	0.2	0.2
331	0.0	0.1	0.1
332	0.0	0.8	0.8
333	4.1	4.8	0.7
334	100.0	100.0	0.0
335	24.5	25.0	0.5
336	9.7	10.0	0.3
337	1.6	1.7	0.1
338	0.3	0.3	0.0
339	0.0	0.0	0.0

This fragment can be used for quantitative analysis. Mass isotopomer distributions should be obtained from the mass range 330-336. [5-¹³C]-glutamine contains a peak at 331 but not at 330, thus this fragment contains C-5.

APPENDIX A. GC/MS ANALYSIS OF AMINO ACIDS



Glu 358

Formula : $C_{17}H_{36}NO_3Si_2$
 Exact mass : 358.223
 C-atoms : 1-2-3-4-5

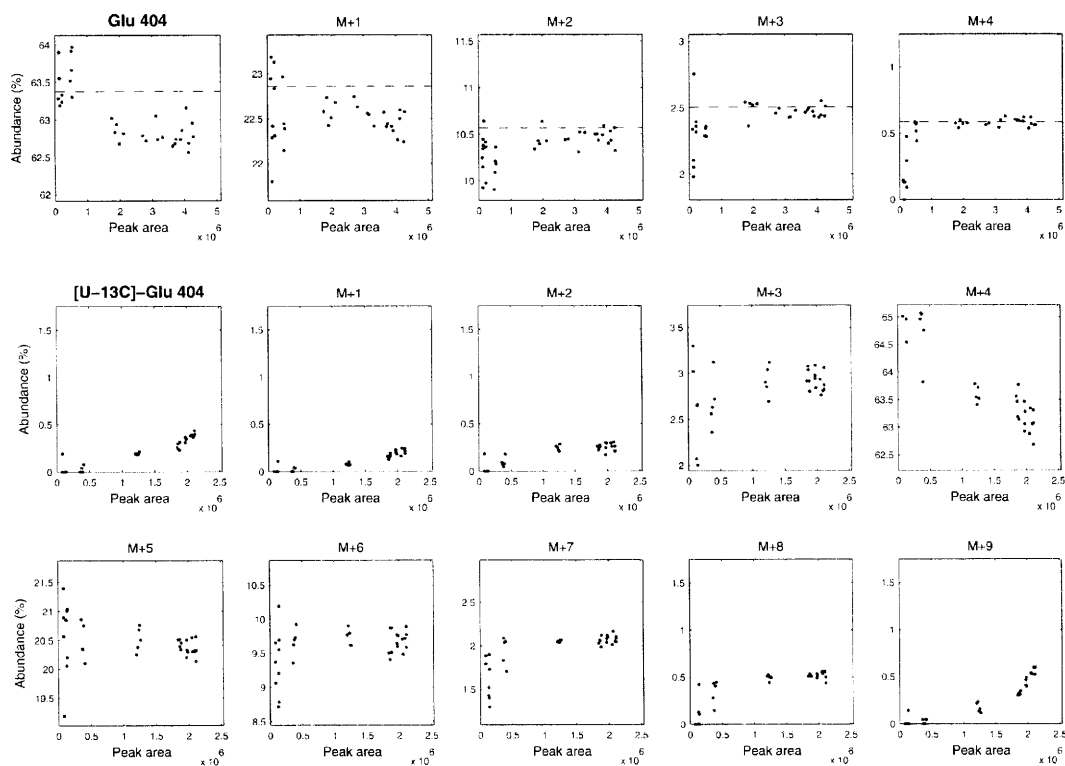
m/z	theory	data	difference
357	0.0	1.8	1.8
358	100.0	100.0	0.0
359	29.8	30.0	0.2
360	11.4	11.9	0.5
361	2.2	2.5	0.3
362	0.4	0.8	0.4
363	0.0	0.1	0.1
364	0.0	0.0	0.0
365	0.0	0.0	0.0
366	0.0	0.0	0.0
367	0.0	0.0	0.0
368	0.0	0.0	0.0

[U- ^{13}C]-Glu

m/z	theory	data	difference
357	0.0	0.2	0.2
358	0.0	0.0	0.0
359	0.0	0.0	0.0
360	0.0	0.1	0.1
361	0.0	2.9	2.9
362	5.2	6.6	1.4
363	100.0	100.0	0.0
364	24.5	25.4	0.9
365	9.9	10.9	1.0
366	1.6	1.4	-0.2
367	0.3	0.2	-0.1
368	0.0	0.0	0.0

This fragment should not be used. M-1 is too high (1.8 mol%). Fragment Glu-432 is preferred. [5- ^{13}C]-glutamine contains a peak at 359 but not at 358, thus this fragment contains C-5.

APPENDIX A. GC/MS ANALYSIS OF AMINO ACIDS



Glu 404

Formula : $C_{18}H_{42}O_3NSi_3$
 Exact mass : 404.247
 C-atoms : 2-3-4-5

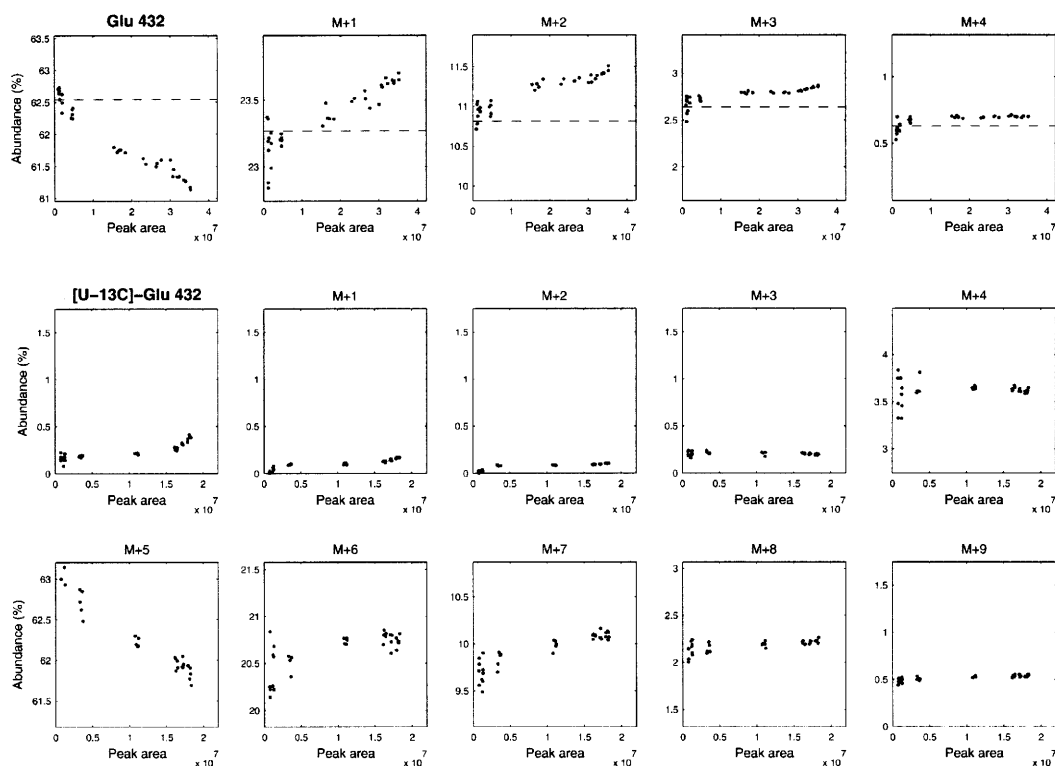
m/z	theory	data	difference
403	0.0	0.0	0.0
404	100.0	100.0	0.0
405	36.1	35.7	-0.4
406	16.7	16.4	-0.3
407	4.0	3.9	-0.1
408	0.9	0.8	-0.1
409	0.2	1.3	1.1
410	0.0	0.3	0.3
411	0.0	0.0	0.0
412	0.0	0.0	0.0
413	0.0	0.0	0.0

[U-¹³C]-Glu

m/z	theory	data	difference
403	0.0	0.0	0.0
404	0.0	0.0	0.0
405	0.0	0.0	0.0
406	0.0	0.1	0.1
407	4.1	3.8	-0.3
408	100.0	100.0	0.0
409	31.9	31.7	-0.2
410	15.2	14.6	-0.6
411	3.3	2.7	-0.6
412	0.8	0.5	-0.3
413	0.1	0.0	-0.1

This fragment should be used with caution. It is not very abundant and therefore noisy. Fragment Glu-330 is preferred. [5-¹³C]-glutamine contains a peak at 405 but not at 404, thus this fragment contains C-5.

APPENDIX A. GC/MS ANALYSIS OF AMINO ACIDS



Glu 432

Formula : $C_{19}H_{42}O_4NSi_3$
 Exact mass : 432.242
 C-atoms : 1-2-3-4-5

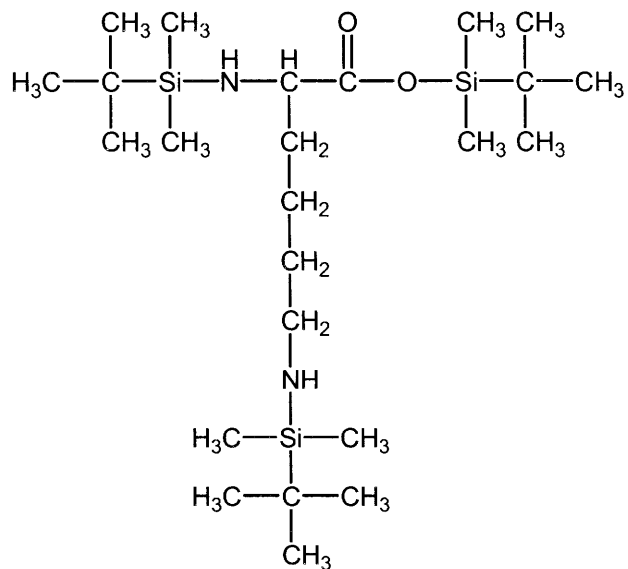
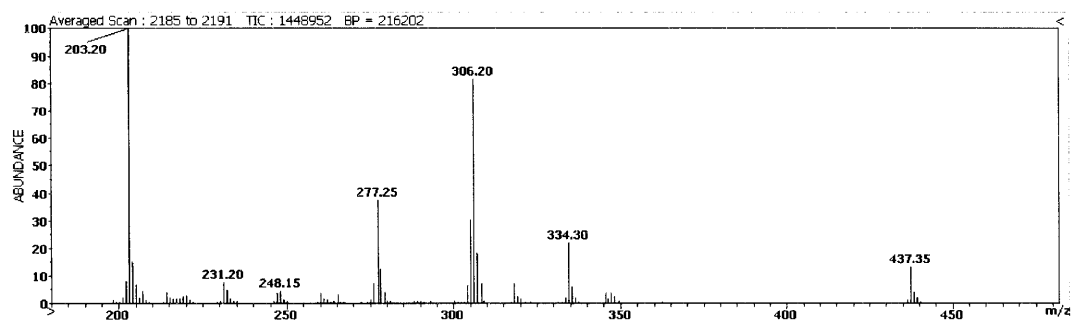
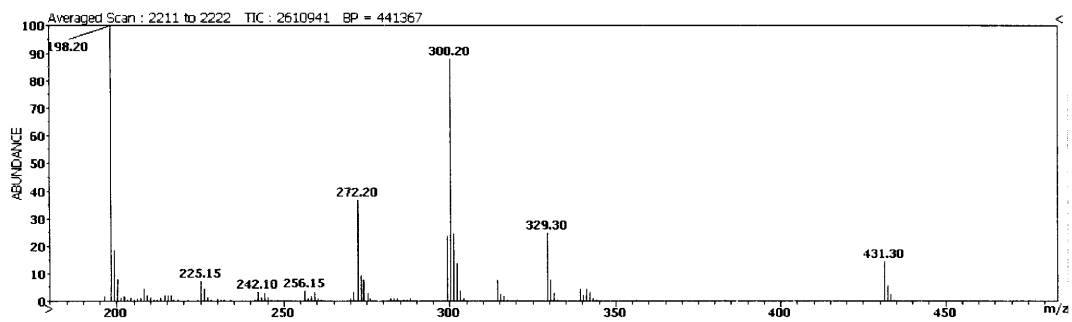
m/z	theory	data	difference
431	0.0	0.0	0.0
432	100.0	100.0	0.0
433	37.2	37.1	-0.1
434	17.3	17.5	0.2
435	4.2	4.4	0.2
436	1.0	1.1	0.1
437	0.2	0.2	0.0
438	0.0	0.0	0.0
439	0.0	0.0	0.0
440	0.0	0.0	0.0
441	0.0	0.0	0.0
442	0.0	0.0	0.0
443	0.0	0.0	0.0

[U-¹³C]-Glu

m/z	theory	data	difference
431	0.0	0.0	0.0
432	0.0	0.2	0.2
433	0.0	0.1	0.1
434	0.0	0.1	0.1
435	0.0	0.3	0.3
436	5.2	5.8	0.6
437	100.0	100.0	0.0
438	32.0	32.5	0.5
439	15.4	15.4	0.0
440	3.3	3.4	0.1
441	0.8	0.8	0.0
442	0.1	0.1	0.0
443	0.0	0.0	0.0

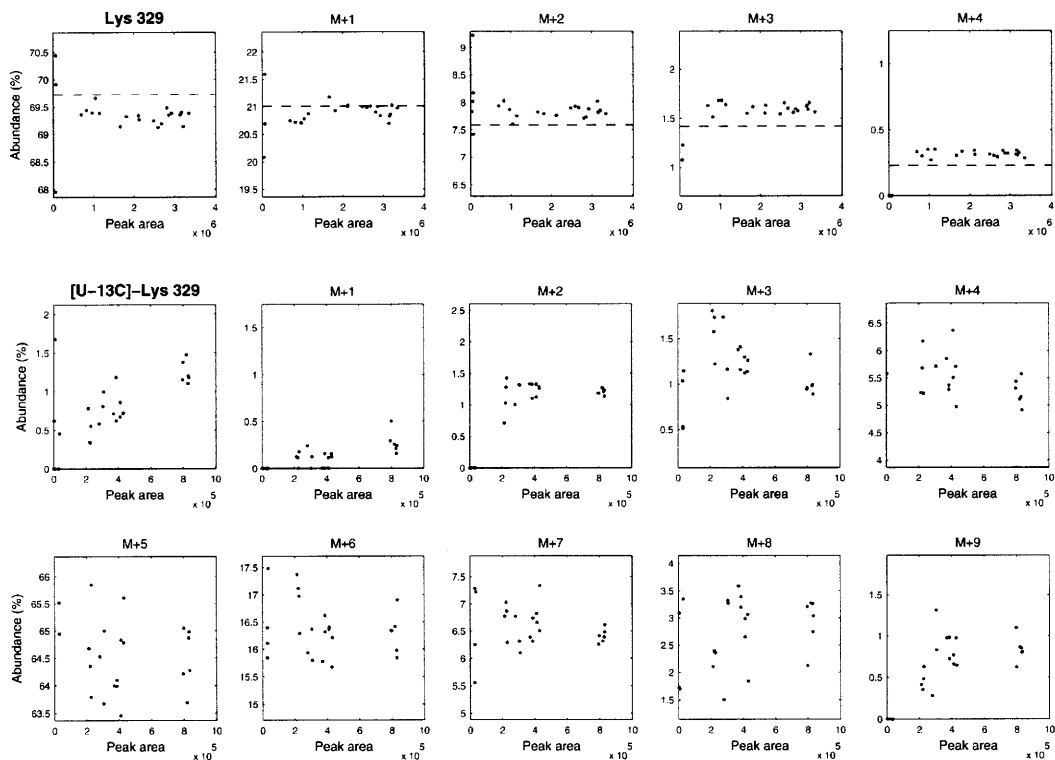
This fragment can be used for quantitative analysis. [5-¹³C]-glutamine contains a peak at 433 but not at 432, thus this fragment contains C-5.

Lysine (Lys)



C₂₄H₅₆N₂O₂Si₃
Exact Mass: 488.365

APPENDIX A. GC/MS ANALYSIS OF AMINO ACIDS



Lys 329

Formula : $C_{17}H_{41}N_2Si_2$
 Exact mass : 329.2808
 C-atoms : 2-3-4-5-6

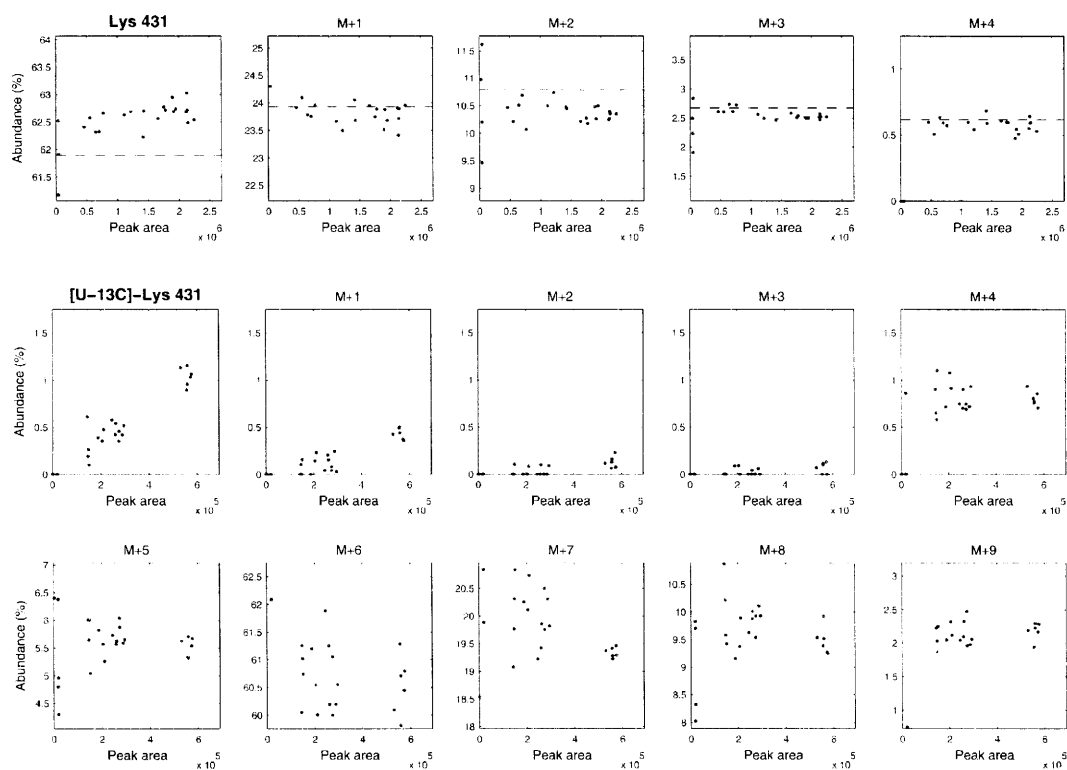
m/z	theory	data	difference
328	0.0	0.6	0.6
329	100.0	100.0	0.0
330	30.1	29.9	-0.2
331	10.9	11.3	0.4
332	2.0	2.2	0.2
333	0.3	0.5	0.2
334	0.0	0.0	0.0
335	0.0	0.0	0.0
336	0.0	0.0	0.0
337	0.0	0.3	0.3
338	0.0	0.1	0.1

[U-¹³C]-Lys

m/z	theory	data	difference
328	0.0	0.0	0.0
329	0.0	0.5	0.5
330	0.0	0.1	0.1
331	0.0	1.8	1.8
332	0.0	2.5	2.5
333	5.2	9.4	4.2
334	100.0	100.0	0.0
335	24.8	25.7	0.9
336	9.4	10.5	1.1
337	1.5	3.8	2.3
338	0.2	0.9	0.7

This fragment should be used with caution. Lysine peak is not very abundant and therefore very noisy.

APPENDIX A. GC/MS ANALYSIS OF AMINO ACIDS



Lys 431

Formula : $C_{20}H_{47}O_2N_2Si_3$
 Exact mass : 431.295
 C-atoms : 1-2-3-4-5-6

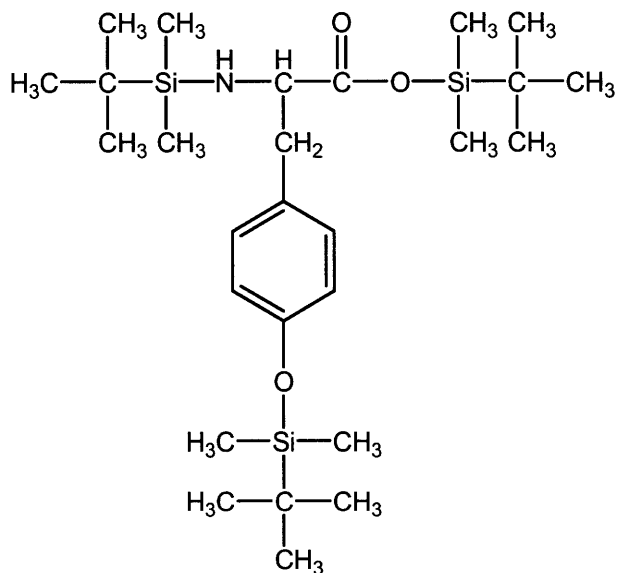
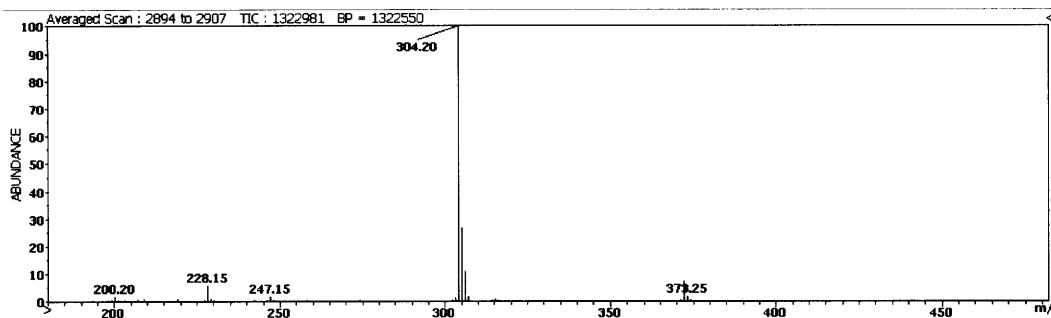
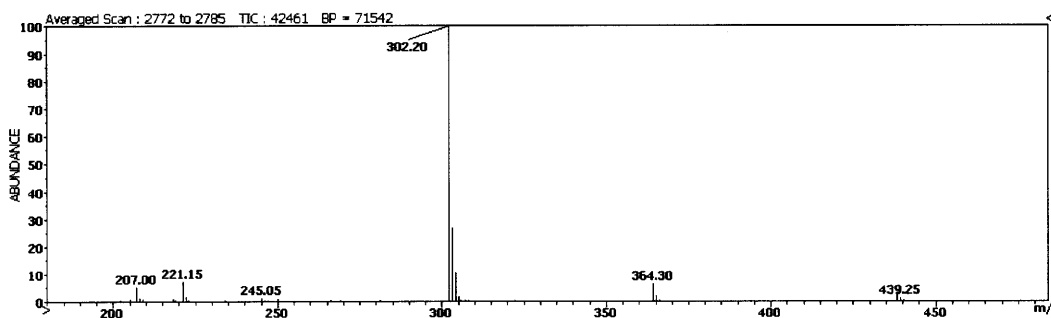
m/z	theory	data	difference
430	0.0	1.7	1.7
431	100.0	100.0	0.0
432	38.7	38.3	-0.4
433	17.4	16.8	-0.6
434	4.3	4.3	0.0
435	1.0	1.0	0.0
436	0.2	0.0	-0.2
437	0.0	0.0	0.0
438	0.0	0.0	0.0
439	0.0	0.0	0.0
440	0.0	0.1	0.1
441	0.0	0.0	0.0
442	0.0	0.0	0.0
443	0.0	0.0	0.0

[U-¹³C]-Lys

m/z	theory	data	difference
430	0.0	0.0	0.0
431	0.0	0.0	0.0
432	0.0	0.0	0.0
433	0.0	0.0	0.0
434	0.0	0.0	0.0
435	0.0	1.4	1.4
436	6.3	9.4	3.2
437	100.0	100.0	0.0
438	32.4	33.5	1.1
439	15.0	16.5	1.5
440	3.2	3.4	0.2
441	0.7	0.3	-0.4
442	0.1	0.0	-0.1
443	0.0	0.0	0.0

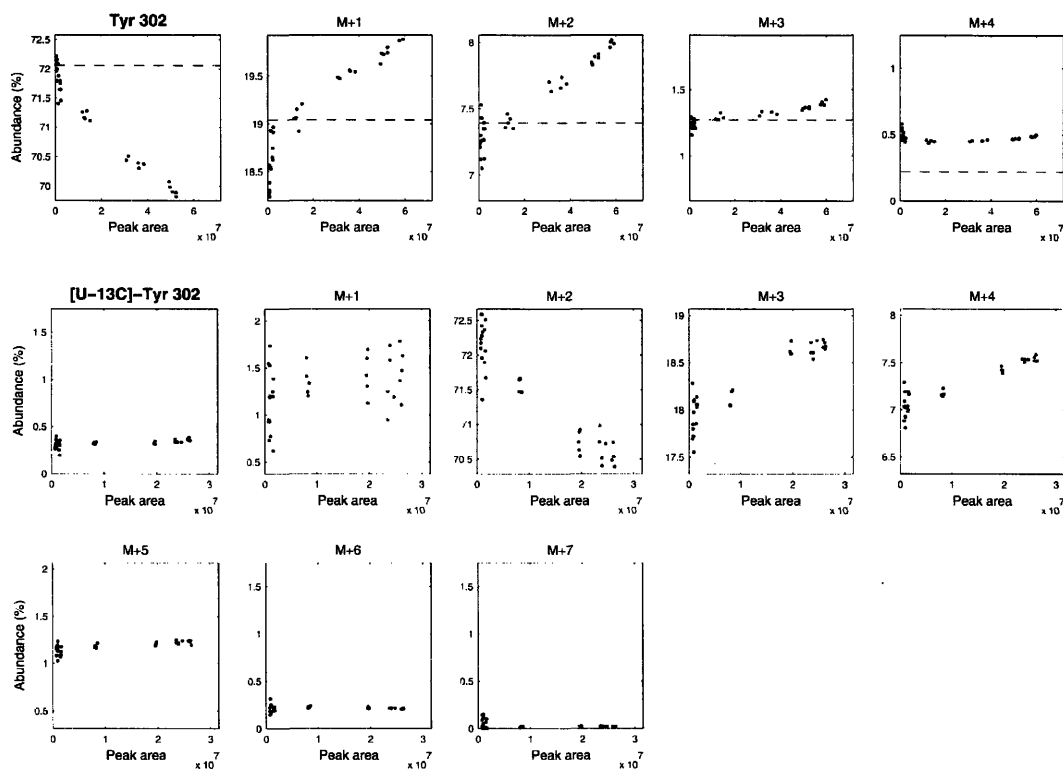
This fragment should not be used. M-1 is too high (1.7 mol%). Lysine peak is not very abundant and therefore very noisy.

Tyrosine (Tyr)



$\text{C}_{27}\text{H}_{53}\text{NO}_3\text{Si}_3$
Exact Mass: 523.3333

APPENDIX A. GC/MS ANALYSIS OF AMINO ACIDS



Tyr 302

Formula : $C_{14}H_{32}O_2NSi_2$
 Exact mass : 302.197
 C-atoms : 1-2

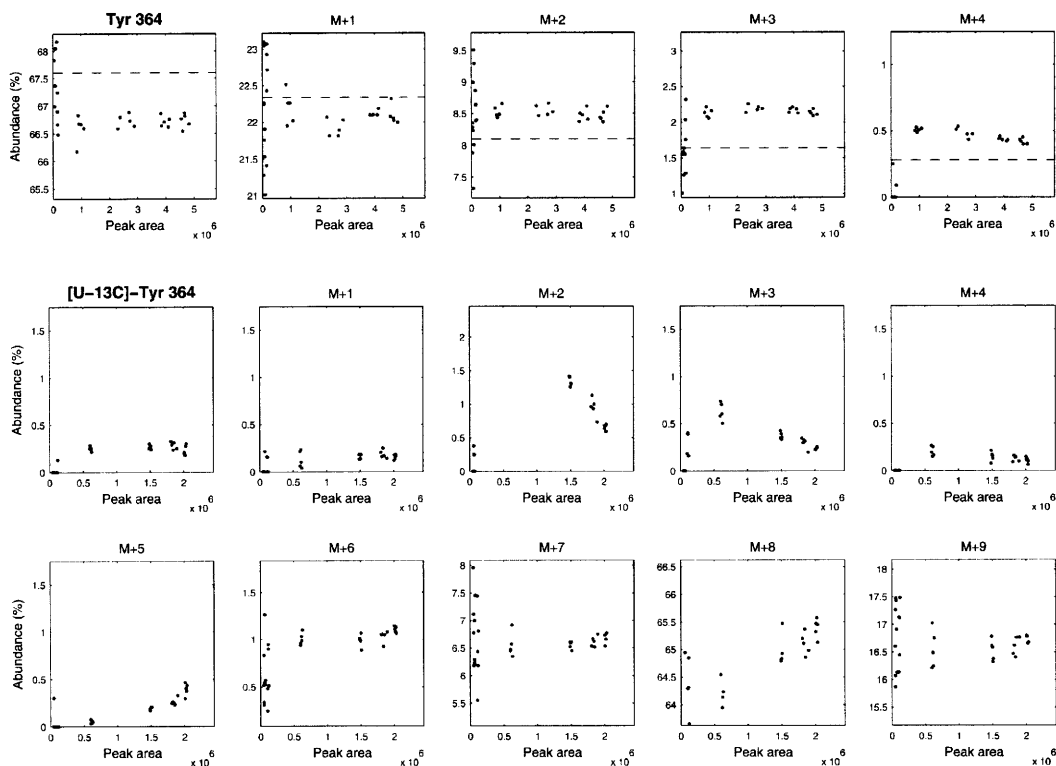
m/z	theory	data	difference
301	0.0	0.0	0.0
302	100.0	100.0	0.0
303	26.4	26.3	-0.1
304	10.3	10.1	-0.2
305	1.8	1.7	-0.1
306	0.3	0.6	0.3
307	0.0	0.8	0.8
308	0.0	0.5	0.5
309	0.0	0.2	0.2

[U-¹³C]-Tyr

m/z	theory	data	difference
301	0.0	0.1	0.1
302	0.0	0.4	0.4
303	2.0	1.8	-0.2
304	100.0	100.0	0.0
305	24.3	24.9	0.6
306	9.7	9.7	0.0
307	1.5	1.6	0.1
308	0.3	0.3	0.0
309	0.0	0.0	0.0

This fragment can be used for quantitative analysis. Mass isotopomer distributions should be obtained from the mass range 302-305.

APPENDIX A. GC/MS ANALYSIS OF AMINO ACIDS



Tyr 364

Formula : $C_{20}H_{38}NOSi_2$
 Exact mass : 364.249
 C-atoms : 2-3-4-5-6-7-8

m/z	theory	data	difference
363	0.0	0.5	0.5
364	100.0	100.0	0.0
365	33.0	33.1	0.1
366	12.0	12.7	0.7
367	2.4	3.0	0.6
368	0.4	0.7	0.3
369	0.1	0.1	0.0
370	0.0	0.0	0.0
371	0.0	0.0	0.0
372	0.0	0.0	0.0
373	0.0	0.0	0.0
374	0.0	0.2	0.2
375	0.0	0.0	0.0
376	0.0	0.8	0.8
377	0.0	0.3	0.3

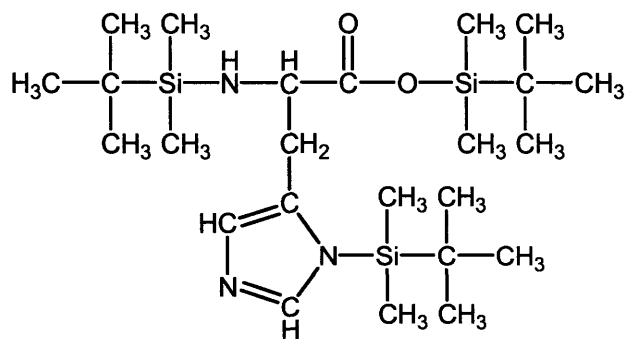
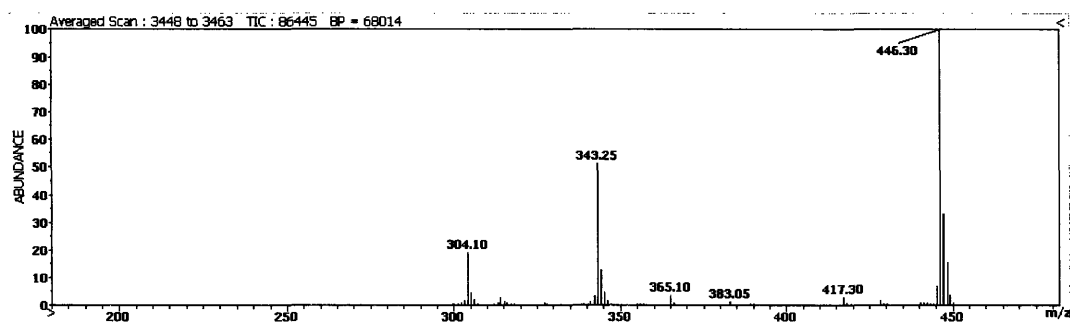
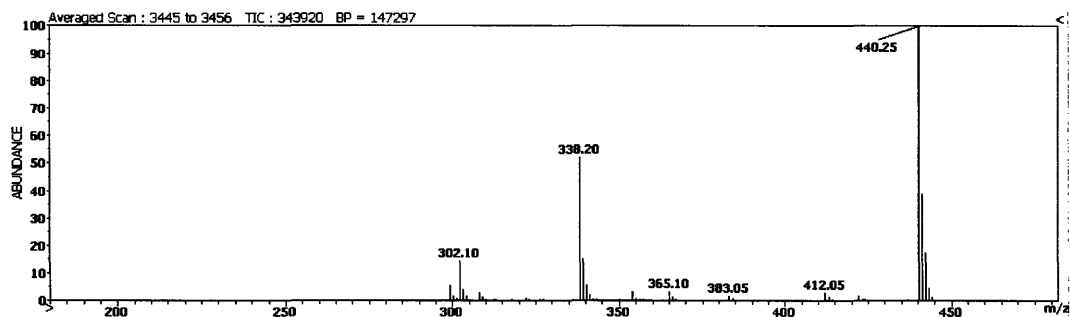
[U- ^{13}C]-Tyr

m/z	theory	data	difference
363	0.0	0.1	0.1
364	0.0	0.4	0.4
365	0.0	0.2	0.2
366	0.0	3.6	3.6
367	0.0	1.0	1.0
368	0.0	0.3	0.3
369	0.0	0.0	0.0
370	0.0	1.3	1.3
371	8.5	10.1	1.6
372	100.0	100.0	0.0
373	24.6	25.9	1.3
374	9.5	9.9	0.4
375	1.5	1.6	0.1
376	0.2	0.2	0.0
377	0.0	0.0	0.0

This fragment should not be used. It is not very abundant and therefore very noisy. Fragment Phe-308 is preferred.

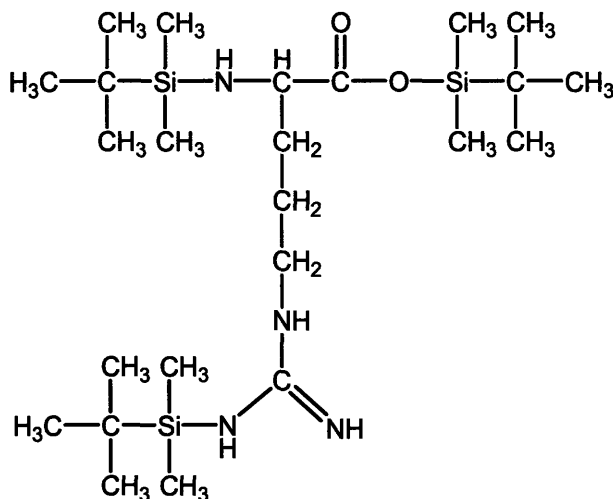
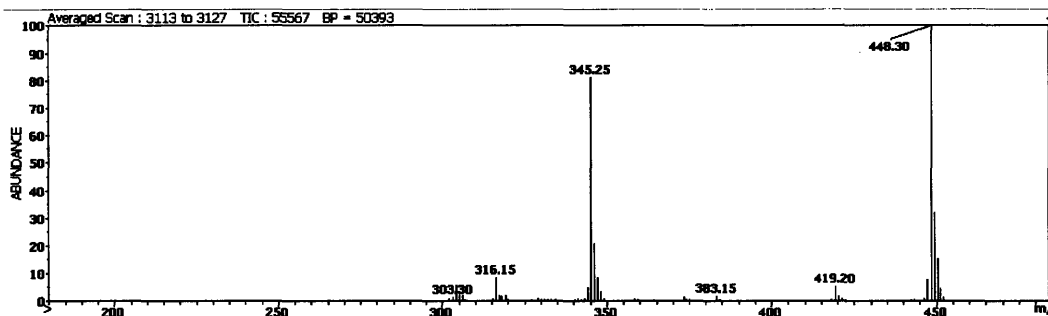
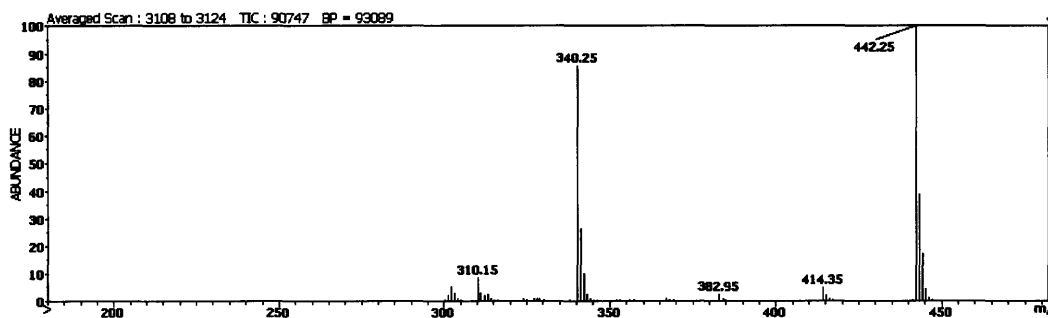
Histidine (His)

Histidine fragments were not investigated in detail because of low signal-to-noise ratio. Histidine was not found in all samples.



$C_{24}H_{51}N_3O_2Si_3$
Exact Mass: 497.3289

Arginine (Arg)



C₂₄H₅₅N₄O₂Si₃
Exact Mass: 515.363

Arginine peak is found at 22.5 min with peaks at m/z 442 (M-57-16) and m/z 340 (M-159-16). The arginine derivative corresponds to a nitrile form derived from loss of a guanidino nitrogen (see Petterson BW et al., Biol Mass Spectrom, 22(9), 518-523). Arginine fragments were not investigated in detail because of low signal-to-noise ratio.

Appendix B

GC/MS analysis of glucose derivatives

GC/MS analysis of unlabeled glucose derivatives was performed using HP 5890 Series II GC (Gas Chromatograph) connected to HP 5971 MSD (Mass Selective Detector). The mass spectrometer was calibrated using the 'Max Sensitivity Autotune' setting.

Column Specifications

- Agilent Technologies 122-1262 DB-XLB (Serial No. 8758214)
- Length: 30 m
- ID: 0.25 mm
- Film: 0.25 μm
- Temperature limits: 30°C to 340°C

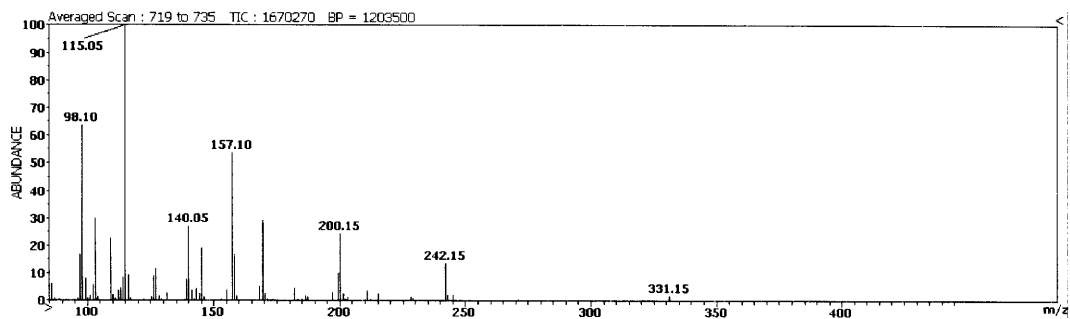
MSD Settings

- Scan mode
- 5 min solvent delay
- 10 min recording time
- Mass range: 100 to 500 amu (approx. 2.0 scans/sec)

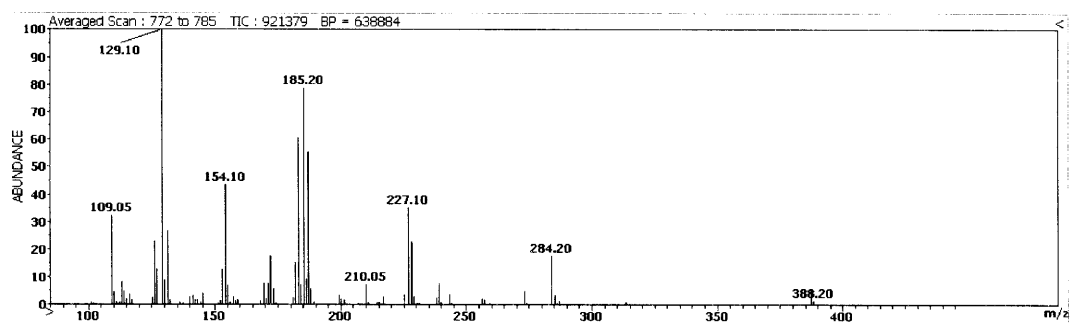
GC Settings

- Constant flow 0.88 mL/min
- Injector temp: 250°C
- Transferline temp: 300°C
- Temperature program:
 - 80°C (hold 1 min)
 - 20°C/min to 280°C (hold 4 min)

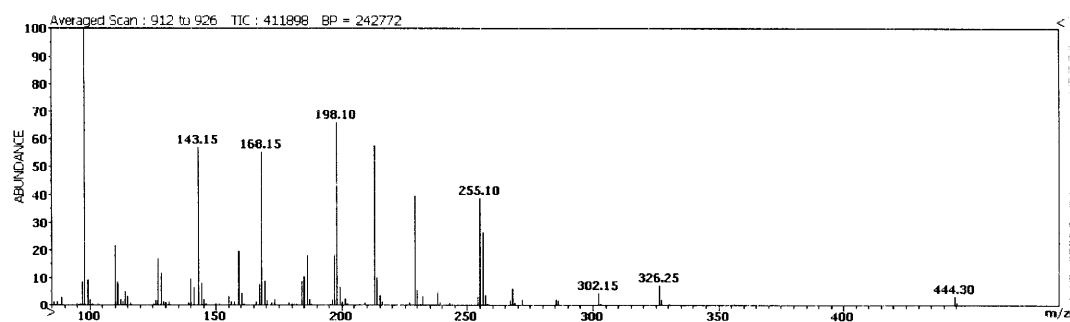
Pentacetate glucose



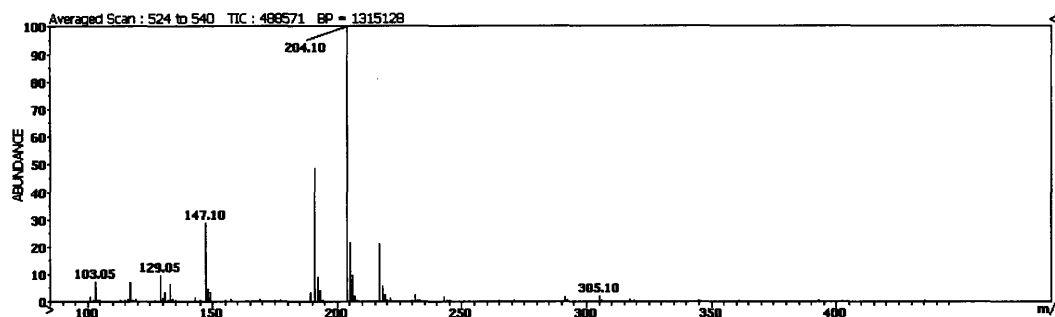
Pentpropionate glucose



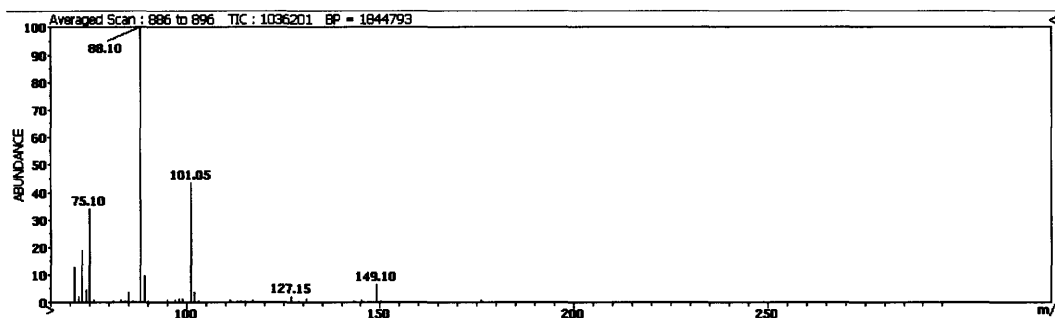
Pentbutanoate glucose



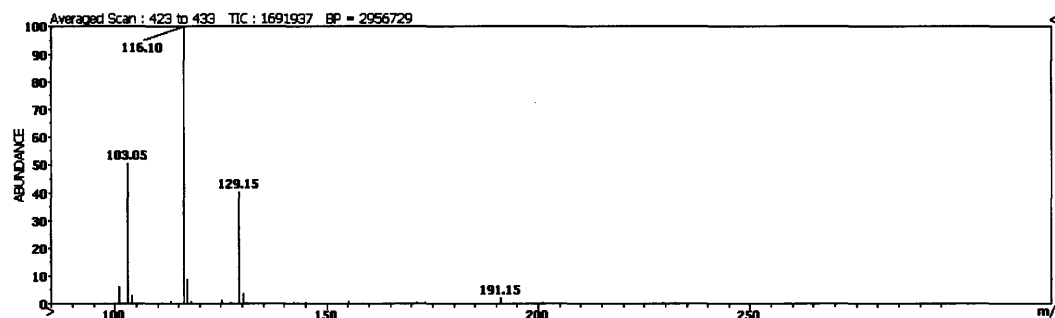
Pentatrimethylsilyl glucose



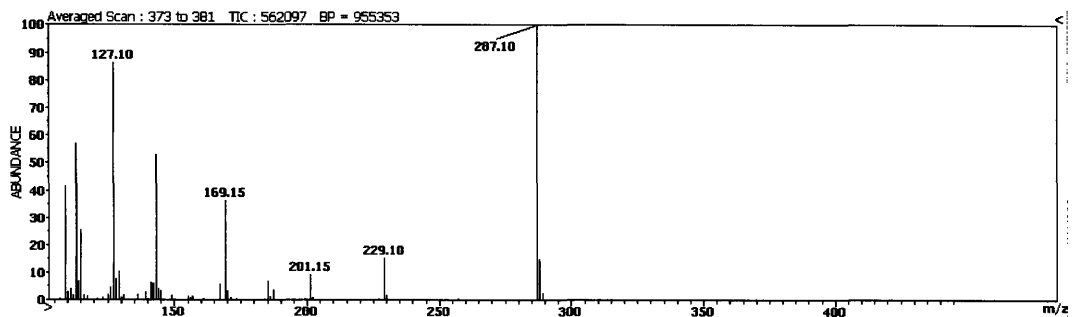
Permethyl glucose



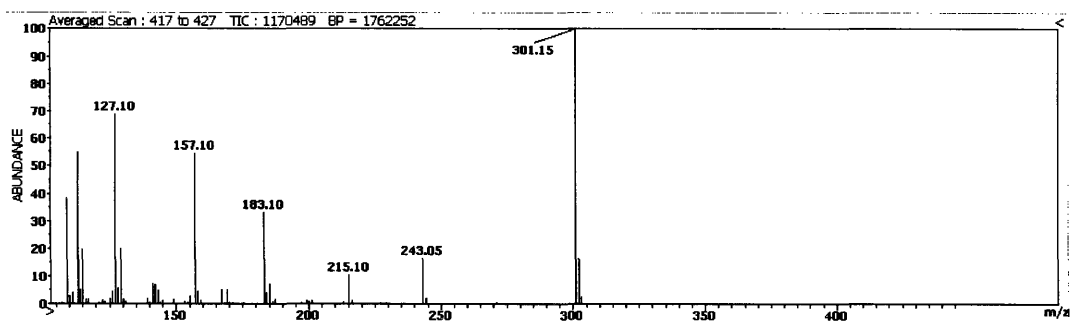
Perethyl glucose



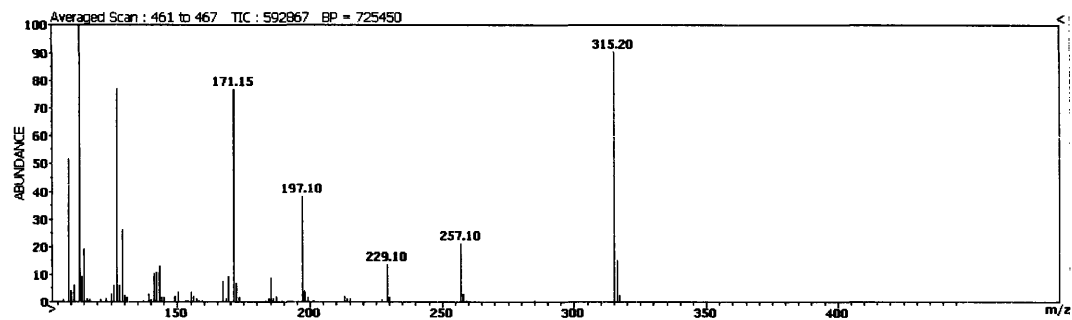
Di-O-isopropylidene acetate glucose



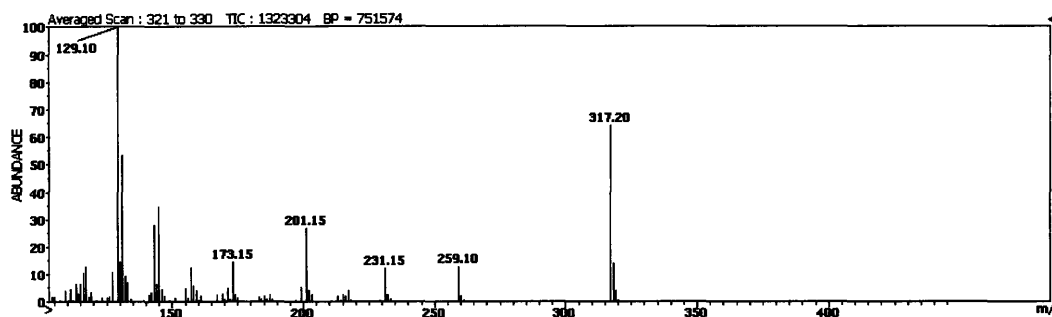
Di-O-isopropylidene propionate glucose



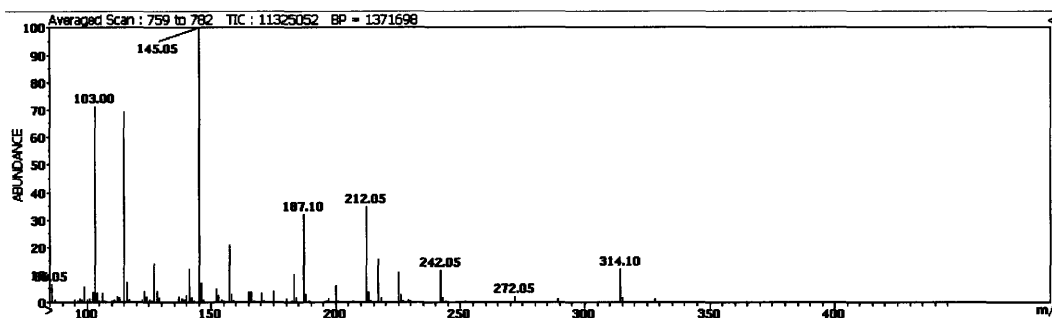
Di-O-isopropylidene butanoate glucose



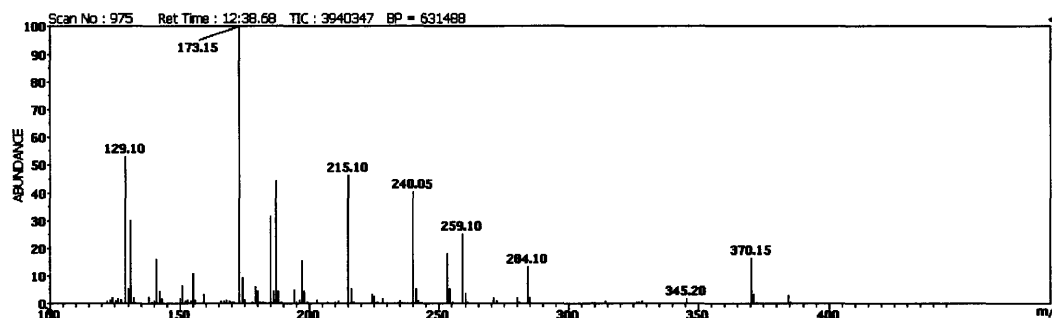
Di-O-isopropylidene trimethylsilyl glucose



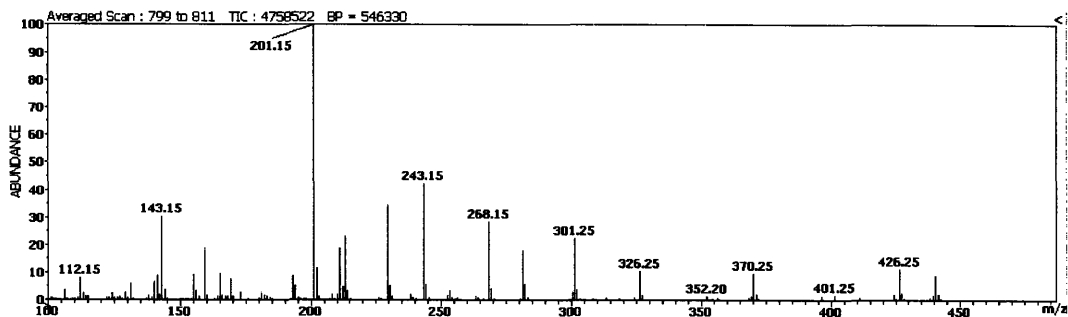
Aldonitrile pentacetate glucose



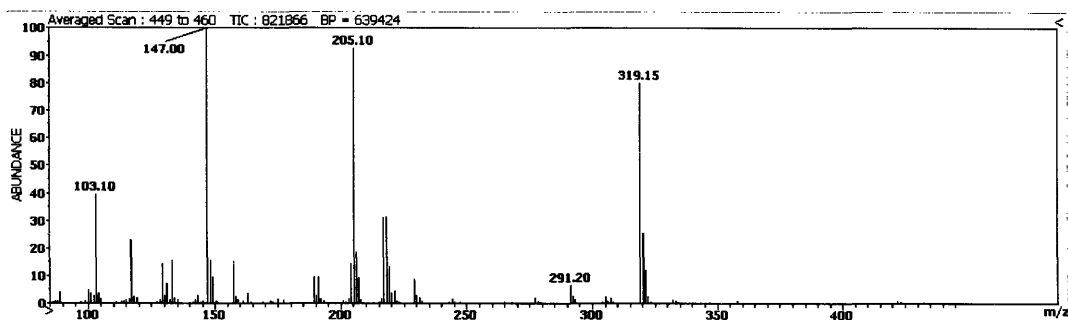
Aldonitrile pentpropionate glucose



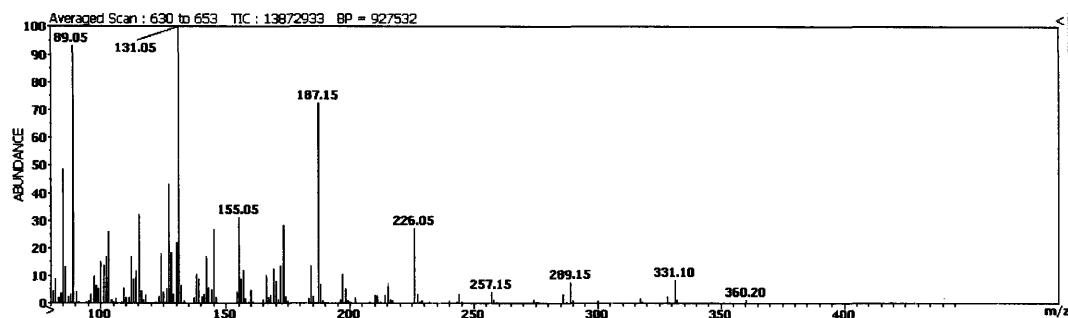
Aldonitrile pentabutanoate glucose



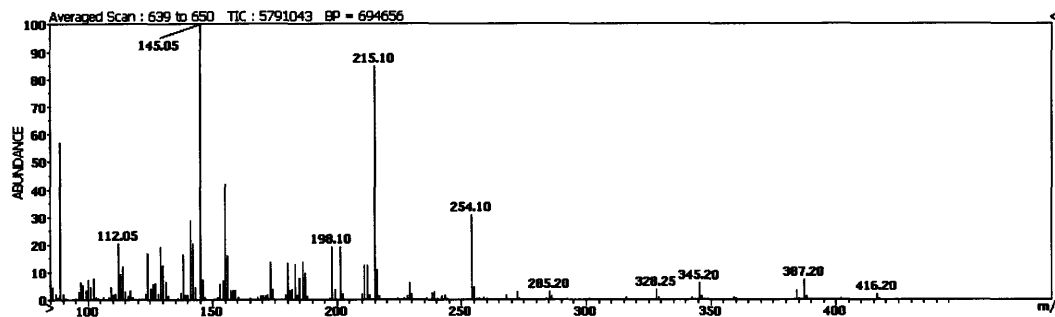
Aldonitrile pentatrimethylsilyl glucose



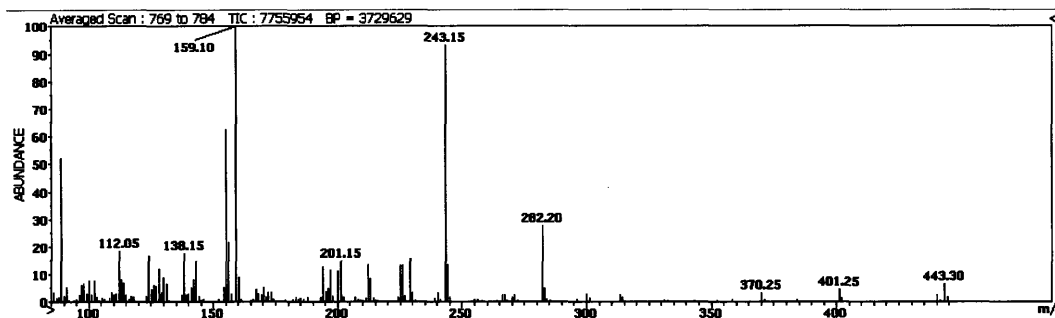
Methyloxime pentacetate glucose



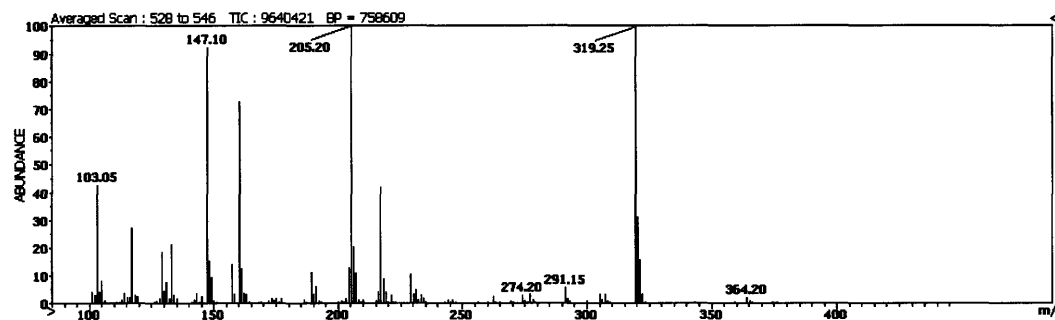
Methyloxime pentapropionate glucose



Methyloxime pentabutanoate glucose



Methyloxime pentatrimethylsilyl glucose



"Until you measure the fluxes, you don't even know if a cell is dead or alive !"